

JAERI-Review
2000-004



JP0050357



研究炉利用における研究成果集
(平成 10 年度)

2000 年 3 月

(編) 豊田政幸・小山芳己

日本原子力研究所
Japan Atomic Energy Research Institute

本レポートは、日本原子力研究所が不定期に公開している研究報告書です。
入手の問合わせは、日本原子力研究所研究情報部研究情報課（〒319-1195 茨城県那珂郡東海村）あて、お申し越し下さい。なお、このほかに財団法人原子力弘済会資料センター（〒319-1195 茨城県那珂郡東海村日本原子力研究所内）で複写による実費頒布を行っております。

This report is issued irregularly.

Inquiries about availability of the reports should be addressed to Research Information Division, Department of Intellectual Resources, Japan Atomic Energy Research Institute, Tokai-mura, Naka-gun, Ibaraki-ken 〒319-1195, Japan.

© Japan Atomic Energy Research Institute, 2000

編集兼発行 日本原子力研究所

研究炉利用における研究成果集（平成10年度）

日本原子力研究所東海研究所研究炉部
（編）豊田 政幸・小山 芳己

（2000年2月7日受理）

本報告書は、平成10年度に研究炉で実験あるいは照射利用を行った利用者（原研外を含む）から成果の提出を受け、これを取りまとめたものである。

Activity Report on the Utilization of Research Reactors
(Japanese Fiscal Year,1998)

(Eds.)Masayuki TOYODA and Yoshimi KOYAMA

Department of Research Reactor
Tokai Research Establishment
Japan Atomic Energy Research Institute
Tokai-mura,Naka-gun,Ibaraki-ken

(Received February 7, 2000)

This is the second issue of the activity report on the utilization of research reactors in the fields of neutron beam experiments, neutron activation analysis, radioisotope production, etc., performed during Japanese Fiscal Year 1998(April 1, 1998- March 31, 1999).

All reports in this volume were described by users from JAERI and also users from the other organizations, i.e., universities, national research institutes and private companies, who have utilized our research reactor utilization facilities for the purpose of the above studies.

Keywords:Research Reactor,Neutron Scattering,Neutron Radiography,Prompt Gamma-ray Analysis,
Neutron Activation Analysis,Neutron Beam,Irradiation

目 次

はじめに	1
研究成果一覧	3
1. 中性子散乱	57
1) 構造・励磁	57
2) 磁 性	79
3) 超伝導現象	151
4) 非晶質・液体	163
5) 材料科学	189
6) 高分子	199
7) 生物学	227
8) 基礎物理学・中性子光学	237
9) 装 置	249
10) その他	261
2. 中性子ラジオグラフィ	269
3. 即発ガンマ線分析	297
4. 放射化分析	309
5. R I の製造	343
6. 原子炉材料照射試験	347
7. その他	351
謝 辞	366
付 録 (1)	367
付 録 (2)	389
付 録 (3)	393

Contents

Preface	1
Research Reports	43
1. Neutron Scattering	57
1) Structure • Excitation	57
2) Magnetism	79
3) Superconductivity	151
4) Amorphous • Liquid	163
5) Material Science	189
6) Polymer	199
7) Biology	227
8) Fundamental Physics • Neutron Optics	237
9) Instrument	249
10) Etc	261
2. Neutron Radiography	269
3. Prompt Gamma-ray Analysis	297
4. Neutron Activation Analysis	309
5. Production of Radio Isotopes	343
6. Irradiation Test of Reactor Materials	347
7. Etc	351
Acknowledgments	366
Appendix (1)	367
Appendix (2)	389
Appendix (3)	393

はじめに

平成10年度における研究炉の利用運転は、JRR-3Mの4サイクルの共同利用運転と、改造工事を終えたJRR-4の9サイクルの試験利用運転、及び12サイクルの共同利用運転であり、これに伴いさまざまな利用が行われた。

本報告書は、利用者（原研外利用者を含む）から当該利用の成果の提出を受け、取りまとめたものである。

提出して頂いた成果の件数は、中性子散乱143件、中性子ラジオグラフィ7件、即発γ線分析3件、放射化分析11件、RIの製造2件、原子炉材料1件、その他4件で合計171件であった。事情により利用成果を提出して頂けなかった利用者については、その利用内容の一覧を付録に掲載した。なお、本報告書では下記の報告書の中から一部を転載させて頂いた。

最後に、原稿を提出して頂いた利用者の皆様の協力に感謝するとともに、今後も研究炉が有効に利用され、種々の研究がさらに進展されることを期待します。

研究炉利用課長

高柳 政二

1) レポート番号：Vol.6（第6巻）

標 題 : ACTIVITY REPORT ON NEUTRON SCATTERING
RESEARCH issued by ISSP-NSL, University of Tokyo
(東京大学物性研究所発行)

編 者 : N.Takesue and H.Yoshizawa (武末尚久, 吉沢英樹)

発 行 年 : 1999年

2) レポート番号：UTRCN-G-28

標 題 : 原研施設利用共同研究成果報告書（平成10年度）

編 者 : 東京大学原子力研究総合センター

発 行 年 : 1999年

This is a blank page.

研究成果一覧

 1. 中性子散乱
 1) 構造・励磁

研究テーマ 「表題」	所 属 担 当 者	利用原子炉 及び装置名	頁
1-1-1 強相関電子系の中性子散乱 による研究 「LaCrO ₃ の粉末中性子回 折」	Advanced Science Research Center,JAERI K.Oikawa,Y.Shimojo,Y.Morii Institute of Materials Science,University of Tsukuba T.Kamiyama Department of Applied Physics,College of Humanities and Sciences,Nihon University T.Hashimoto	JRR-3M 1G (HRPD)	59
1-1-2 強相関電子系の中性子散乱 による研究 「PbZrO ₃ の強誘電相におけ る秩序パラメータの温度依 存性」	Advanced Science Research Center,JAERI S.Katano Department of Physics,Kanazawa University H.Fujishita	JRR-3M 1G (HRPD)	60
1-1-3 水素結合中の水素原子核の イメージング 「マキシマム・エントロピ ー法によるKDPにおける水 素結合中の水素原子核イメ ージング」	School of Science,Kitasato University S.Yamamura,Y.Sugawara Advanced Science Research Center,JAERI S.Kumazawa,Y.Ishii,Y.Morii Department of Applied Physics,Nagoya University E.Nishibori,M.Sakata Department of Material Science,Shimame University M.Takata	JRR-3M 1G (HRPD)	62
1-1-4 水素結合中の水素原子核の イメージング 「マキシマム・エントロピ ー法によるADPにおける水 素結合」	School of Science,Kitasato University S.Yamamura,Y.Sugawara Advanced Science Research Center,JAERI S.Kumazawa,Y.Ishii,Y.Morii Department of Applied Physics,Nagoya University E.Nishibori,M.Sakata Department of Material Science,Shimame University M.Takata	JRR-3M 1G (HRPD)	63
1-1-5 強相関電子系の中性子散乱 による研究 「硫化スピネルCuIr ₂ S ₄ の金 属-非金属転移に対する中 性子散乱」	Advanced Science Research Center,JAERI S.Katano,K.Oikawa National Research Institute for Metals T.Matsumoto	JRR-3M 2G (TAS-1)	64

1. 中性子散乱
1) 構造・励磁

1-1-6 リラクサーPNZの格子振動 「 $\text{Pb}(\text{Zn}_{1/3}\text{Nb}_{2/3})\text{O}_3$ プロペスカイトの格子振動」	Research and Development Center, Toshiba Corporation I.Tomeno, S.Shimanuki School of Science and Engineering, Waseda University Y.Tsunoda Advanced Science Research Center, JAERI Y.Ishii	JRR-3M 2G (TAS-1)	65
1-1-7 精密中性子光学実験法によるNi基超合金単結晶の観察 「クリープ損傷を施したNi基超合金CMSX-4の構造評価(III)」	Advanced Science Research Center, JAERI K.Aizawa, H.Tomimitsu Hitachi Research Laboratory, Hitachi, Ltd. H.Tamaki, A. Yoshinari	JRR-3M 3G (PNO)	66
1-1-8 少数キャリア系Ceモノブニクタイトの格子振動 「少数キャリア系CeSbのフォノン分散」	Department of Physics, Tokyo Metropolitan University K.Iwasa, M.Kohgi Advanced Science Research Center, JAERI Y.Haga, T.Osakabe Laboratoire Léon Brillouin M.Braden, J.-M.Mignot Tsukuba Institute of Science and Technology T.Suzuki	JRR-3M 6G (TOPAN)	67
1-1-9 Yb_4As_3 の価数秩序構造相転移とフォノン分散 「電荷秩序を示す Yb_4As_3 におけるフォノン分散」	Department of Physics, Tokyo Metropolitan University K.Iwase, M.Kohgi Department of Material Science and Technology, Niigata University A.Ochiai Graduate School of Science and Technology, Niigata University H.Aoki Tsukuba Institute of Science and Technology T.Suzuki	JRR-3M 6G (TOPAN)	68
1-1-10 3次元骨格を有するリチウムインターカレーション材料の探索	Department of Chemistry and Chemical Engineering, Faculty of Engineering Niigata University T.Suzuki, H.Ohokawa, M.Saito, K.Uematsu, K.Toda, M.Sato Institute for Material Research, Tohoku University K.Ohoyama	JRR-3M T1-3 (HERMES) (KPD)	70

1. 中性子散乱

1) 構造・励磁

1-1-11 インジウム含有リチウムリン酸塩の構造とイオン伝導性	Department of Chemistry and Chemical Engineering, Faculty of Engineering Niigata University T.Suzuki, N.Hayakawa, K.Yoshikawa, K.Uematsu, K.Toda, M.Sato Institute for Material Research, Tohoku University K.Ohoyama	JRR-3M T1-3 (HERMES) (KPD)	71
1-1-12 軽希土類化合物 RB_2C_2 における結晶場と磁気構造 「正方晶化合物 $\text{Ce}^{III}\text{B}_2\text{C}_2$ 、 $\text{Nd}^{III}\text{B}_2\text{C}_2$ の結晶構造」	Institute for Materials Research, Tohoku University T.Onimaru, K.Ohoyama, H.Yamauchi, H.Onodera, M.Ohashi, Y.Yamaguchi	JRR-3M T1-3 (HERMES) (KPD)	72
1-1-13 ホイスラー型 Ni_2MnGa 系合金の形状記憶効果 「ホイスラー型 $\text{Ni}_2(\text{Pd}_{0.16}\text{Mn}_{0.84})\text{Ga}$ のマルテンサイト型変態と磁気転移」	Faculty of Science and Technology Ryukoku University K.Inoue, K.Enami, M.Igawa Institute for Material Research, Tohoku University Y.Yamaguchi, K.Ohoyama	JRR-3M T1-3 (HERMES) (KPD)	74
1-1-14 中性子散乱による強相関電子系の研究 「 $\text{La}_{2-x}\text{Sr}_x\text{CuO}_4$ の磁場効果」	Advanced Science Research Center, JAERI S.Katano Institute for Material Research, Tohoku University T.Suzuki, T.Fukase Institute for Chemical Research, Tohoku University K.Yamada	JRR-3M T2-4 (TAS-2)	76
1-1-15 半磁性半導体 $\text{Zn}_{1-x}\text{Mn}_x\text{Te}$ の中性子散乱 「希薄磁性半導体 $\text{Zn}_{0.568}\text{Mn}_{0.432}\text{Te}$ における磁気準弾性散乱」	Department of Applied Physics, Graduate School of Engineering, Tohoku University Y.Ono, T.Kamita, T.Kajitani Research Institute for Scientific Measurements, Tohoku University T.Sato, Y.Oka	JRR-3M C3-1-1 (AGNES)	77

1. 中性子散乱
2) 磁 性

1-2-1 遷移金属複合酸化物の構造 磁氣的性質に関する研究 「希土類オルソチタン酸化物の磁氣的及び中性子散乱研究」	Department of Synchrotron radiation Research,JAERI K.Yoshii Department of Materials Science,JAERI A.Nakamura	JRR-3M 1G (HRPD)	81
1-2-2 ペロブスカイト型複合酸化物の磁気構造 「秩序化ペロブスカイト $\text{Sr}_2\text{LnRuO}_6$ (Ln=Ho,Tm) の中性子回折」	Division of Chemistry, Graduate School of Science, Hokkaido University Y.Doi, Y.Hinatsu Advanced Science Research Center, JAERI Y.Shimojo, Y.Morii	JRR-3M 1G (HRPD)	82
1-2-3 ペロブスカイト型複合酸化物の磁気構造 「層状ペロブスカイト $\text{Ca}_{2-x}\text{Sr}_x\text{MnO}_4$ の中性子回折」	Division of Chemistry, Graduate School of Science, Hokkaido University K.Tezuka, M.Inamura, Y.Hinatsu Advanced Science Research Center, JAERI Y.Shimojo, Y.Morii	JRR-3M 1G (HRPD)	83
1-2-4 強相関電子系の中性子散乱による研究 「スピンラダー物質 $\text{Sr}_{1.5}\text{Ca}_{11.5}\text{Cu}_{24}\text{O}_{41}$ のスピングャップと反強磁性に対する圧力効果」	Advanced Science Research Center, JAERI S.Katano Department of Physics, Aoyama-Gakuin University T.Nagata, H.Fujino, J.Akimitsu Neutron Scattering Laboratory, Institute for Solid State Physics, University of Tokyo M.Nishi, K.Kakurai	JRR-3M 2G (TAS-1)	84
1-2-5 強相関電子系の中性子散乱による研究 「 TmB_{12} の磁気構造の中性子回折による研究」	Advanced Science Research Center, JAERI T.Osakabe, S.Hiura, T.Takabatake Advanced Science Matter, Hiroshima University F.Iga	JRR-3M 2G (TAS-1)	86
1-2-6 強相関電子系の中性子散乱による研究 「高圧下におけるCeAsの磁気構造」	Advanced Science Research Center, JAERI T.Osakabe, Y.Haga Department of Physics, Tokyo Metropolitan University M.Kohgi, K.Iwasa Institute for Solid State Physics, University of Tokyo M.Kubota, H.Yoshizawa Tsukuba Institute of Science and Technology T.Suzuki	JRR-3M 2G (TAS-1)	87

1. 中性子散乱

2) 磁 性

1-2-7 希土類十二硼化物の磁気構造 「U ₁ IrGeにおける磁気秩序の探求」	Department of Quantum Matter,ADSM, Hiroshima University F.Iga,T.Takabatake,T.Fujita Hahn-Meitner Institute K.Prokeš Advanced Science Research Center,JAERI T.Osakabe	JRR-3M 2G (TAS-1)	89
1-2-8 La ₂ NiO _{4+δ} のスピンダイナミクスの研究 「酸素ドーピングしたLa ₂ NiO _{4+δ} (δ ≤ 0.11)のスピン波励起」	Neutron Scattering Laboratory,Institute for Solid State Physics,University of Tokyo K.Nakajima,T.Sawada,H.Yoshizawa Department of Physics,Tohoku University Y.Endoh	JRR-3M 4G (GPTAS)	90
1-2-9 二次元希釈反強磁性体の磁気臨界散乱に現れるスピン相関関数 「二次元パーコレーションイジング反強磁性体の磁気臨界散乱」	Department of Physics,Tokyo Metropolitan University K.Iwasa Neutron Scattering Laboratory,Institute of Materials Structure Science,High Energy Accelerator Research Organization H.Ikeda	JRR-3M 4G (GPTAS) C1-1 (HER)	92
1-2-10 Y _{1-x} U _x Ru ₂ Si ₂ (0 ≤ x ≤ 1)における秩序状態の研究 「歪んだ重い電子系(Y,U)Ru ₂ Si ₂ における微弱反強磁性モーメント」	Graduate School of Science,Hokkaido University H.Amitsuka,A.Okumura,K.Kuwahara, M.Yokoyama	JRR-3M 4G (GPTAS)	94
1-2-11 三角格子反強磁性体CuFe(Al)O ₂ におけるスピン波分散 「三角格子反強磁性体CuFe(Al)O ₂ の磁気秩序」	Department of Applied Physics,Fukui University M.Mekata,Y.Kobayashi,K.Taki,Y.Yamada Department of Physics,Osaka University F.Takei,D.Zhao Neutron Scattering Laboratory,Institute for Solid State Physics,University of Tokyo Y.Oohara	JRR-3M 4G (GPTAS) 5G (PONTA)	95
1-2-12 スピンギャップ系BaVS ₃ 化合物の非弾性散乱 「軌道秩序を持つスピン重項系BaVS ₃ の中性子散乱」	Department of Materials Science and Engineering,Kyoto University M.Shiga,H.Nakamura,H.Tanahashi,H.Imai Department of Superconductivity,University of Tokyo K.Kojima Neutron Scattering Laboratory,Institute for Solid State Physics,University of Tokyo K.Kakurai,M.Nishi	JRR-3M 5G (PONTA)	96

1. 中性子散乱

2) 磁 性

1-2-13 CsVCl_3 のスピンの相関関数 「 CsVCl_3 の磁気相関」	Neutron Scattering Laboratory, High Energy Accelerator Research Organization S. Itoh Neutron Scattering Laboratory, Institute for Solid State Physics, University of Tokyo K. Kakurai, K. Nakajima Department of Physics, Tohoku University Y. Endoh Department of Physics, Tokyo Institute of Technology H. Tanaka ISIS Facility, Rutherford Appleton Laboratory M. J. Harris	JRR-3M 5G (PONTA)	97
1-2-14 梯子型化合物の高圧下での 磁性 「梯子格子系物質； $\text{Sr}_{2.5}\text{Ca}_{11.5}\text{Cu}_{24}\text{O}_{41}$ の反強磁性 磁気秩序」	Department of Physics, Aoyama-Gakuin University J. Akimitsu, T. Nagata, H. Fujino Neutron Scattering Laboratory, Institute for Solid State Physics, University of Tokyo M. Nishi, K. Kakurai Advanced Science Research Center, JAERI S. Katano	JRR-3M 5G (PONTA)	99
1-2-15 $\text{Sr}_{14}\text{Cu}_{24}\text{O}_{41}$ の単純鎖の励起 状態に関する研究	The Institute of Physical and Chemical Research (RIKEN) M. Matsuda Neutron Scattering Laboratory, Institute for Solid State Physics, University of Tokyo T. Yoshihama, K. Kakurai Physics Department, Brookhaven National Laboratory G. Shirane	JRR-3M 5G (PONTA)	101
1-2-16 UGa_2 における隠れた磁気 励起 「 UGa_2 における磁気励起 の偏極依存性」	Tokyo Metropolitan University M. Kohgi, K. Iwasa, H. Sagayama Tohoku University N. Sato Neutron Scattering Laboratory, Institute for Solid State Physics, University of Tokyo K. Kakurai	JRR-3M 5G (PONTA)	102
1-2-17 2次元モット転移系 $\text{BaCo}_{1-x}\text{Ni}_x\text{S}_2$ の中性子散乱 「中性子散乱による $\text{BaCo}_{1-x}\text{Ni}_x\text{S}_2$ の金属—絶縁体 転移研究」	Department of Physics, Division of Material Science, Nagoya University H. Sasaki, H. Harashina, K. Kodama, M. Sato Department of Applied Physics, Faculty of Engineering, Tohoku University S. Shamoto Neutron Scattering Laboratory, Institute for Solid State Physics, University of Tokyo M. Nishi, K. Kakurai	JRR-3M 5G (PONTA)	104

1. 中性子散乱
2) 磁 性

1-2-18 $(\text{La}, \text{Sr})_{n+1}\text{MnO}_{3n+1}$ のスピン・電荷ダイナミクス 「層状Mn酸化物 $\text{La}_{2-2x}\text{Sr}_{1+2x}\text{Mn}_2\text{O}_7$ のスピンダイナミクス」	CREST, Department of Physics, Tohoku University H. Fujioka, K. Hirota, Y. Endoh Neutron Scattering Laboratory, Institute for Solid State Physics, University of Tokyo M. Kubota, H. Yoshizawa CIRSE and Department of Applied Physics, Nagoya University Y. Moritomo, Y. Endoh	JRR-3M 6G (TOPAN)	106
1-2-19 DyB_6 の格子ダイナミクスの研究	Institute for Materials Research, Tohoku University H. Nojiri, K. Takahashi, M. Motokawa Department of Physics, Tohoku University S. Kunii, K. Hirota, Y. Endoh Neutron Scattering Laboratory, Institute for Solid State Physics, University of Tokyo K. Kakurai	JRR-3M 6G (TOPAN)	107
1-2-20 $\text{La}_{1-x}\text{Sr}_x\text{MnO}_3$ $x=1/8$ の磁場誘起軌道電荷秩序相の中性子回折	Institute for Materials Research, Tohoku University H. Nojiri, K. Kaneko, M. Motokawa Department of Physics, Tohoku University K. Hirota, Y. Endoh	JRR-3M 6G (TOPAN)	108
1-2-21 希土類化合物 Nd_2Ni_3 単結晶の磁気構造 「 Nd_2Ni_3 単結晶の磁気構造の中性子回折による研究」	Research Reactor Institute, Kyoto University S. Kawano, X. Xu Faculty of School Education, Hiroshima University T. Tsutaoka, T. Kasagi Faculty of Education, Tottori University Y. Andoh Japan Advanced Institute of Science and Technology M. Kurisu	JRR-3M T1-1 (HQR)	109
1-2-22 単結晶 CeGa の中性子回折	Department of Physics, Faculty of Science, Saitama University E. Matsuoka, M. Kosaka, T. Ohki, Y. Uwatoko	JRR-3M T1-1 (HQR)	110
1-2-23 単結晶 $(\text{Fe}_{0.98}\text{Ru}_{0.02})_2\text{P}$ の中性子回折	Department of Physics, Faculty of Science, Saitama University T. Ohki, T. Satoh, M. Kosaka, Y. Uwatoko	JRR-3M T1-1 (HQR)	111

1. 中性子散乱

2) 磁 性

1-2-24 ErNiSnの磁気構造 「ErNiSnの中性子回折」	Faculty of Education, Tottori University Y. Andoh Research Reactor Institute, Kyoto University S. Kawano Japan Advanced Institute of Science and Technology T. Nobata, G. Nakamoto, M. Kurisu Faculty of School Education, Hiroshima University T. Tsutaoka	JRR-3M T1-1 (HQR)	112
1-2-25 高濃度スピングラスにおける長時間緩和	Department of Physics, Faculty of Science and Technology, Science University of Tokyo K. Motoya, T. Kumazawa, J. Kikuchi	JRR-3M T1-1 (HQR) C1-2 (SANS-U)	113
1-2-26 Pd及びPt合金のフェルミ面効果の研究 「PtCr合金の原子短距離秩序とスピングラス」	School of Science and Engineering, Waseda University M. Hirano, Y. Tsunoda	JRR-3M T1-1 (HQR)	114
1-2-27 異方性競合系 $\text{Fe}_x\text{Co}_{1-x}\text{TiO}_3$ の磁場中での新しい(相)転移の研究 「異方性競合系 $\text{Fe}_{0.50}\text{Co}_{0.50}\text{TiO}_3$ の磁場中における履歴現象」	Department of Physics, Ochanomizu University A. Ito, C. Uchikoshi The Institute of Physics and Chemical Research (RIKEN) A. Fukaya Neutron Scattering Laboratory, Institute for Solid State Physics, University of Tokyo K. Nakajima, K. Kakurai	JRR-3M T1-1 (HQR) 5G (PONTA)	115
1-2-28 金属相酸化バナジウムの磁気構造と励起	Department of Physics, Faculty of Science and Technology, Science University of Tokyo K. Motoya, J. Kikuchi, T. Kumazawa, N. Wada Institute for Solid State Physics, University of Tokyo S. Shin	JRR-3M T1-1 (HQR)	117
1-2-29 Pd及びPt合金のフェルミ面効果の研究 「強磁性PdMnの中性子散乱の研究」	Department of Applied Physics, School of Science and Engineering, Waseda University A. Harigae, Y. Tsunoda	JRR-3M T1-1 (HQR)	118
1-2-30 重希土類ヘキサボライド(REB_6 ; RE=Tb, Dy, Ho)の磁気構造の研究 「重希土類ヘキサボライドの磁気構造の研究」	Institute for Materials Research, Tohoku University H. Nojiri, K. Takahashi, M. Motokawa, K. Ohoyama, M. Ohashi, Y. Yamaguchi Department of Physics, Tohoku University S. Kunii	JRR-3M T1-2 (KSD) T1-3 (HERMES) (KPD)	119

1. 中性子散乱

2) 磁 性

1-2-31 重希土類ヘキサボライド (REB ₆ ; RE=Tb, Dy, Ho)の磁 気構造の研究 「重希土類ヘキサボライド の磁気構造の研究」	Institute for Materials Research, Tohoku University H. Nojiri, K. Takahashi, M. Motokawa, K. Ohoyama, M. Ohashi, Y. Yamaguchi Department of Physics, Tohoku University S. Kunii	JRR-3M T1-2 (KSD)	120
1-2-32 近藤化合物Ce(Zn _{1-x} Ga _x)の構 造相転移と磁性 「近藤化合物Ce(Zn _{1-x} Ga _x)で の磁気および構造相転移	Institute for Materials Research, Tohoku University M. Watanabe, K. Ohoyama, H. Onodera, M. Ohashi, Y. Yamaguchi	JRR-3M T1-2 (KSD)	121
1-2-33 ZnCr ₂ O ₄ , ZnFe ₂ O ₄ の中性子 散乱	Department of Physics, Faculty of Science, Kyushu University K. Shiratori, D. Eto Department of Physics, School of Science and Engineering Waseda University K. Kohn, I. Kagomiya Institute of Applied Physics, University of Tsukuba E. Kita, Y. Hata	JRR-3M T1-3 (HERMES) (KPD)	122
1-2-34 フェライト材料の元素置換 による特性改善の機構解明 「LaZn置換Srフェライト の構造」	Department of Applied Chemistry, University of Tokyo K. Kitazawa, N. Hirota Materials Research Center, TDK corporation J. Nakagawa, H. Taguchi ISTE, Superconductivity Research Laboratory K. Iida	JRR-3M T1-3 (HERMES) (KPD)	123
1-2-35 REPb ₂ (RE=rare earth)化合物 の磁気的性質 「CePb ₂ 化合物の磁気構 造」	Department of Materials Science, Tohoku University R. Yamauchi, K. Fukamichi Institute for Materials Research, Tohoku University K. Ohoyama, Y. Yamaguchi	JRR-3M T1-3 (HERMES) (KPD)	124
1-2-36 Ca _{2-x} Y _{2-x} Cu ₃ O ₁₀ の磁気構造に ついての研究	The Institute of Physical and Chemical Research(RIKEN) M. Matsuda Institute for Materials Research, Tohoku University K. Ohoyama Faculty of Engineering, Yamagata University M. Ohashi	JRR-3M T1-3 (HERMES) (KPD)	125

1. 中性子散乱

2) 磁 性

1-2-37 Mn_7Sn_8 の磁気転移の中性子回折による研究	Faculty of Science and Technology, Keio University S. Anzai, T. Kobayashi Institute for Materials Research, Tohoku University Y. Yamaguchi, K. Ohoyama Faculty of Engineering, Yamagata University M. Ohashi	JRR-3M T1-3 (HERMES) (KPD)	126
1-2-38 非晶質ホイスラー合金 $\text{Cu}_2\text{MnAl}_{1-x}\text{Zr}_x$ の中性子回折	Faculty of Science, Ehime University T. Kamimori, Y. Shiraga, K. Konishi, H. Tange, M. Goto Faculty of Engineering, Ehime University S. Tomiyoshi Institute for Materials Research, Tohoku University M. Ohashi, Y. Yamaguchi	JRR-3M T1-3 (HERMES) (KPD)	127
1-2-39 半磁性半導体 $\text{Zn}_{1-x}\text{Mn}_x\text{Te}$ の中性子回折 「希薄磁性半導体 $\text{Zn}_{0.568}\text{Mn}_{0.432}\text{Te}$ における短距離磁気秩序」	Department of Applied Physics, Graduate School of Engineering, Tohoku University Y. Ono, T. Kamiya, S. Shamoto, T. Kajitani Research Institute for Scientific Measurements, Tohoku University T. Sato, Y. Oka	JRR-3M T1-3 (HERMES) (KPD)	128
1-2-40 $\text{La}_{2-2x}\text{Sr}_{1+2x}\text{Mn}_2\text{O}_7$ の高圧化におけるスピン状態 「層状Mn酸化物 $\text{La}_{2-2x}\text{Sr}_{1+2x}\text{Mn}_2\text{O}_7$ の磁気相図」	Neutron Scattering Laboratory, Institute for Solid State Physics, University of Tokyo M. Kubota, H. Yoshizawa CREST, Department of Physics, Tohoku University H. Fujioka, K. Hirota, Y. Endoh CIRSE and Department of Applied Physics, Nagoya University Y. Moritomo	JRR-3M T1-3 (HERMES) (KPD)	129
1-2-41 重い電子系 Ce_2X ($\text{X}=\text{Sb}, \text{Bi}$)での結晶場分裂測定 「重い電子系化合物 Ce_2X ($\text{X}=\text{Sb}, \text{Bi}$)での磁気励起」	Institute for Materials Research, Tohoku University K. Ohoyama, H. Hayashi, H. Onodera, M. Ohashi, Y. Yamaguchi Department of Physics, Tokyo Metropolitan University M. Kohgi Department of Physics, Tohoku University T. Suzuki	JRR-3M T1-3 (HERMES) (KPD)	130

1. 中性子散乱

2) 磁 性

1-2-42 酸素欠損型ペロブスカイト $\text{La}_x\text{Sr}_{(1-x)}\text{MnO}_{(2.5+0.5x)}$ の磁気構造 「酸素欠損型ペロブスカイト $\text{La}_{0.8}\text{Sr}_{0.2}\text{MnO}_{2.9}$ の磁性」	Faculty of Science and Technology Ryukoku University K.Inoue Toyohashi University of Technology T.Mori,N.Kamegashira Institute for Materials Research,Tohoku University Y.Yamaguchi,K.Ohoyama	JRR-3M T1-3 (HERMES) (KPD)	131
1-2-43 ウラン化合物における超伝導の研究 「 UPd_2Al_3 の圧力下中性子散乱による研究」	Advanced Science Research Center,JAERI T.Honma,Y.Haga,E.Yamamoto,N.Metoki, Y.Koike,T.Osakabe Graduate School of Science,Osaka University Y.Onuki	JRR-3M T2-4 (TAS-2)	133
1-2-44 強相関電子系の中性子散乱による研究 「 $\text{Ce}_x\text{La}_{1-x}\text{B}_6$ のIV相の中性子回折による研究」	Tokyo Metropolitan University M.Kohgi,K.Iwasa Niigata University O.Suzuki,T.Goto Advanced Science Research Center,JAERI N.Metoki,Y.Koike,T.Osakabe Tohoku University S.Kunii	JRR-3M T2-4 (TAS-2)	135
1-2-45 DyB_6 の磁場中磁気構造の研究 「10Tマグネットを用いた磁場中での Dy^{11}B_6 の中性子回折」	Institute for Materials Research,Tohoku University K.Takahashi,H.Nojiri,M.Motokawa Advanced Science Research Center,JAERI Y.Matsuoka,N.Metoki Department of Physics,Tohoku University S.Kunii	JRR-3M T2-4 (TAS-2)	137
1-2-46 Ce化合物強相関伝導系における特異な磁気相 「混合原子価をもつ Yb_3S_4 の磁気構造研究」	Department of Physics,Inha University J.-G.Park Department of Physics,Sung Kyun Kwan University Y.S.Kwon Advanced Science Research Center,JAERI Y.Morii Department of Physics,Tokyo Metropolitan University M.Kohgi	JRR-3M T2-4 (TAS-2)	138

1. 中性子散乱
2) 磁 性

<p>1-2-47 $\text{La}_{2-x}\text{Sr}_x\text{CuO}_4$の格子異常と磁気相関 「$\text{La}_{1.88}\text{Sr}_{0.12}\text{CuO}_4$の非整合磁気弾性散乱」</p>	<p>Department of Physics, Tohoku University H. Kimura, H. Matsushita, K. Hirota, Y. Endoh Department of Physics, Brookhaven National Laboratory G. Shirane Department of Physics, Massachusetts Institute of Technology Y. S. Lee, M. A. Kastner, R. J. Birgeneau Institute for Chemical Research, Kyoto University K. Yamada</p>	<p>JRR-3M C1-1 (HER)</p>	<p>140</p>
<p>1-2-48 $\text{La}_{2-x}\text{Sr}_x\text{CuO}_4$のスピン揺動と超伝導の相関 「$\text{La}_{2-x}\text{Sr}_x\text{CuO}_4$の低ドーブ領域における磁気弾性散乱」</p>	<p>Department of Physics, Tohoku University S. Wakimoto, S. Ueki, K. Hirota, Y. Endoh Department of Physics, Brookhaven National Laboratory G. Shirane Department of Physics, Massachusetts Institute of Technology Y. S. Lee, M. A. Kastner, R. J. Birgeneau National Institute of Standards and Technology S. H. Lee, P. M. Gehring Institute for Chemical Research, Kyoto University K. Yamada</p>	<p>JRR-3M C1-1 (HER)</p>	<p>141</p>
<p>1-2-49 LiV_2O_5におけるスピン揺らぎの研究 「LiV_2O_5の高分解能中性子非弾性散乱実験」</p>	<p>Neutron Scattering Laboratory, Institute for Solid State Physics, University of Tokyo Y. Takeo, T. Yoshihama Materials Design and Characterization Laboratory Institute for Solid State Physics, University of Tokyo M. Isobe, Y. Ueda CREST, Japan Science and Technology Corporation K. Kakurai</p>	<p>JRR-3M C1-1 (HER)</p>	<p>142</p>
<p>1-2-50 反強磁性 - 非磁性境界付近の重い電子系化合物における反強磁性相関 「重い電子系CeRu_2Si_2の磁気相関」</p>	<p>Department of Physics, Tokyo Metropolitan University H. Kadowaki Department of Earth and Space Science, Osaka University M. Sato, S. Kawarazaki, Y. Miyako</p>	<p>JRR-3M C1-1 (HER)</p>	<p>143</p>

1. 中性子散乱

2) 磁性

1-2-51 近藤格子上の磁気秩序の研究-CeRu ₂ Si ₂ とその混晶系を中心として 「重い電子系物質CeRu ₂ Si ₂ におけるスピン揺らぎ」	Department of Earth and Space Science, Osaka University M.Sato,M.Miyamura,S.Kawarazaki, Y.Miyako Department of Physics,Tokyo Metropolitan University H.Kadowaki	JRR-3M C1-1 (HER)	144
1-2-52 強磁性ヘビーフェルミオン CeCu _x Al _{4-x} の中性子散乱 「CeCuAl ₃ の磁気秩序」	Neutron Scattering Laboratory,Institute for Solid State Physics,University of Tokyo Y.Oohara Department of Physics,Nagoya University G.Motoyama,T.Nishioka,M.Kontani	JRR-3M C1-1 (HER)	145
1-2-53 中性子散乱によるLi ₂ Ge ₇ O ₁₅ の強誘電相転移に関する ソフトフォノンの研究 「中性子散乱による Li ₂ Ge ₇ O ₁₅ の強誘電相転移の 研究」	Shinshu University M.Wada,Takeda Tohoku University Y.Noda Meisei University T.Yamaguchi Kyoto University Y.Iwata	JRR-3M 4G (GPTAS) C1-1 (HER)	146
1-2-54 CeScSiの粉末中性子回折	Department of Physics,Saitama University M.Yokoyama,M.Kosaka,Y.Uwatoko Factory of Engineering,Yamagata University M.Ohashi Institute for Materials Research,Tohoku University K.Ohoyama,Y.Yamaguchi	JRR-3M T1-3 (HERMES) (KPD)	147
1-2-55 強相関電子系の中性子散乱 の研究 「巨大磁気抵抗効果を示す (La _{1-x} Tb _x) _{2/3} Ca _{1/3} MnO ₃ の小角 散乱」	Advanced Science Research Center,JAERI N.Metoki,J.Suzuki Japan Science and Technology Coporation M.Watahiki Electrotechnical Laboratory J.Nie Waseda University Y.Yamada National Research Institute for Metals M.Tachiki	JRR-3M C3-2 (SANS-J)	148
1-2-56 中性子散乱によるウラン化 合物の磁性研究 「U ₃ Pd ₂₀ Si ₆ の結晶場励起の 観測」	Physics Department,Graduate School of Science,Tohoku University N.Tateiwa,T.Komatsubara Advanced Science Research Center,JAERI N.Metoki,Y.Koike Center for Low Temperature Science,Tohoku University N.Kimura,H.Aoki	JRR-3M 2G (TAS-1)	150

1. 中性子散乱
3) 超伝導現象

1-3-1 高温超伝導体の量子臨界点 近傍の磁気励起 「 $\text{YBa}_2\text{Cu}_3\text{O}_{6+y}$ 系高温超伝導 体の量子臨界点近傍におけ る中性子散乱研究」	Department of Physics, Division of Material Science, Nagoya University M. Kanada Neutron Scattering Laboratory, Institute for Solid State Physics, University of Tokyo K. Kakurai CREST, Japan Science and Technology Corporation (JST) H. Harashina, K. Kodama, M. Sato	JRR-3M 5G (PONTA)	153
1-3-2 梯子格子系における超伝導 とスピングャップ 「梯子格子系物質; $\text{Sr}_{2.5}\text{Ca}_{11.5}\text{Cu}_{24}\text{O}_{41}$ の圧力下で のスピングャップ」	Department of Physics, Aoyama-Gakuin University J. Akimitsu, T. Nagata, H. Fujino Neutron Scattering Laboratory, Institute for Solid State Physics, University of Tokyo M. Nishi, K. Kakurai Neutron Scattering Group, Advanced Science Research Center, JAERI S. Katano	JRR-3M 5G (PONTA)	154
1-3-3 酸化物高温超伝導物質の構 造とダイナミクスの研究 「超伝導体 $\text{YBa}_2\text{Cu}_3\text{O}_{7-x}$ の回 折実験の研究」	Institute of Materials Structure Science, KEK A. W. Garrett, T. Nishijima, M. Arai Department of Physics, Tsukuba University M. Takahashi Department of Physics, Tohoku University Y. Endoh Superconductivity Research Laboratory, ISTEK K. Tomimoto, S. Tajima, Y. Shiohara	JRR-3M T1-2 (KSD)	156
1-3-4 新2次元高温超伝導体 $\text{Li}_x\text{Zr}_{1-y}\text{Hf}_y\text{NCl}$ の構造 「新2次元超伝導体 Na_xHfNCl の構造研究」	Department of Applied Physics, Graduate School of Engineering, Tohoku University S. Shamoto, K. Iizawa, M. Yamada, T. Kajitani Institute for Materials Research, Tohoku University K. Ohoyama, Y. Yamaguchi	JRR-3M T1-3 (HERMES) (KPD)	157
1-3-5 ウラン化合物における超伝 導の研究 「 URu_2Si_2 における磁性と 超伝導の相関」	Advanced Science Research Center, JAERI T. Honma, Y. Haga, E. Yamamoto, N. Metoki, Y. Koike Graduate School of Science, Osaka University H. Ohkuni, Y. Onuki	JRR-3M C2-1 (LTAS)	159
1-3-6 新2次元高温超伝導体 $\text{Li}_x\text{Zr}_{1-y}\text{Hf}_y\text{NCl}$ のフォノン 「新2次元超伝導体 Li_xZrNCl のフォノン」	Department of Applied Physics, Graduate School of Engineering, Tohoku University S. Shamoto, T. Kato, T. Kajitani	JRR-3M C3-1-1 (AGNES)	161

1. 中性子散乱
3) 超伝導現象

1-3-7 強相関電子系の中性子散乱 による研究 「中性子小角散乱法を用い たNb単結晶における磁束 状態の観察」	Department of Materials Science and Engineering, Kyoto University S.Miyata, K.Osamura Advanced Science Research Center, JAERI M.Watahiki, J.Suzuki	JRR-3M C3-2 (SANS-J)	162
---	--	----------------------------	-----

1. 中性子散乱

4) 非晶質・液体

1-4-1 アモルファス高分子の低エネルギー励起のQ依存性 「干渉性非弾性中性子散乱によるグリセロールガラスの低エネルギー励起」	Institute for Chemical Research, Kyoto University I. Tsukushi, T. Kanaya, K. Kaji	JRR-3M 4G (GPTAS)	165
1-4-2 液体金属における電子-イオン相関 「液体亜鉛の電子-イオン相関」	Department of Physics, Faculty of Science, Kyushu University S. Takeda, Y. Kawakita, M. Kanehira, S. Yoshioka	JRR-3M T1-3 (HERMES)	167
1-4-3 dropletマイクロエマルジョンの圧力誘起構造相転移 「三元系マイクロエマルジョンにおける構造形成の温度、圧力効果」	Institute for Solid State Physics, University of Tokyo M. Nagao Faculty of Integrated Arts and Sciences, Hiroshima University H. Seto, Y. Kawabata, T. Takeda	JRR-3M C1-2 (SANS-U)	168
1-4-4 dropletマイクロエマルジョンの圧力誘起構造相転移 「三元系マイクロエマルジョンにおける温度、圧力誘起ラメラ構造」	Institute for Solid State Physics, University of Tokyo M. Nagao Faculty of Integrated Arts and Sciences, Hiroshima University H. Seto, D. Okuhara Department of Applied Chemistry, School of Engineering, Nagoya University Y. Matsushita	JRR-3M C1-2 (SANS-U)	170
1-4-5 アモルファス合金の過冷却液体状態における構造変化過程の直接観察 「バルク合金ガラス転移点付近の中・長距離構造変化過程の中性子小角散乱によるその場観察」	Institute for Materials Research, Tohoku University K. Shibata, T. Higuchi, K. Suzuki National Research Institute for Metals An-Pang Tsai Ochanomizu University M. Imai	JRR-3M C1-2 (SANS-U)	172
1-4-6 水-プロパノール系におけるクラスター形成とクラスターの内部構造 「水-プロパノール系におけるクラスター形成とクラスターの構造」	Department of Chemistry, Faculty of Science, Niigata University M. Misawa, K. Maruyama Graduate School of Science and Technology, Niigata University K. Yoshida, H. Munemura, Y. Hosokawa Institute for Solid State Physics, University of Tokyo M. Nagao Ochanomizu University M. Imai	JRR-3M C1-2 (SANS-U)	174

1. 中性子散乱

4) 非晶質・液体

1-4-7 液体カルコゲンの中性子小角散乱 「液体セレンの中性子小角散乱測定」	Faculty of Integrated Arts and Sciences, Hiroshima University M.Inui Faculty of Science,Niigata University K.Maruyama Faculty of Science,Kyushu University Y.Kawakita,S.Takeda Faculty of Science,Ochanomizu University M.Imai	JRR-3M C1-2 (SANS-U)	175
1-4-8 3元系マイクロエマルジョンの圧力誘起構造相転移におけるダイナミクス 「中性子スピンエコー法を用いた3元系両親媒子系複雑液体の温度及び圧力誘起構造相転移におけるダイナミクス」	Graduate School of Bio-Sphere Science, Hiroshima University Y.Kawabata Institute for Solid State Physics,University of Tokyo M.Nagao Faculty of Integrated Arts and Sciences, Hiroshima University H.Seto,T.Takeda	JRR-3M C2-2 (NSE)	176
1-4-9 両親媒子系複雑液体のスローダイナミクス 「中性子スピンエコー法による両親媒子系複雑液体のスローダイナミクス」	Faculty of Integrated Arts and Sciences, Hiroshima University T.Takeda,Y.Kawabata,H.Seto,S.K.Ghosh Faculty of Science,Ochanomizu University S.Komura Institute for Solid State Physics,University of Tokyo M.Nagao	JRR-3M C2-2 (NSE)	178
1-4-10 多価アミン-多価アルコール二成分系におけるボゾンピークの組成依存性 「多価アミン-多価アルコール二成分系におけるボゾンピーク強度の組成依存性」	Department of Chemistry, Naruto University K.Takeda Department of Chemistry Graduate School of Science Osaka University K.Harabe,O.Yamamuro Institute for Chemical Research,Kyoto University I.Tsukushi,T.Kanaya	JRR-3M C3-1-1 (AGNES)	180
1-4-11 部分的重水素置換によるアルコールガラスのボゾンピークの研究 「部分的に重水素置換したアルコールガラスのボゾンピーク」	Department of Chemistry Graduate School of Science Osaka University O.Yamamuro,K.Harabe,T.Matsuo Institute for Chemical Research,Kyoto University I.Tsukushi,T.Kanaya	JRR-3M C3-1-1 (AGNES)	182

1. 中性子散乱

4) 非晶質・液体

1-4-12 水-ブロパノール系における クラスター分散に果たす 溶媒水の構造化と添加塩効 果 「水-ブロパノール系にお けるクラスター分散に対す る添加塩効果の動的側面」	Department of Chemistry, Faculty of Science, Niigata University M. Misawa, K. Maruyama Graduate School of Science and Technology, Niigata University K. Yoshida, H. Munemura, Y. Hosokawa Graduate School of Engineering, Tohoku University T. Kajitani	JRR-3M C3-1-1 (AGNES)	184
1-4-13 非弾性中性子散乱法による オレイン酸の分子委運動の 研究 「配向オレイン酸結晶の中 性子非干渉性非弾性散乱」	Department of Physics, Kyushu University T. Yokoyama, N. Achiwa Nippon Oil and Fat Corporation M. Suzuki	JRR-3M C3-1-1 (AGNES)	185
1-4-14 永久圧縮石英ガラスの低エ ネルギーダイナミックスの 研究 「圧縮石英ガラスの低エネ ルギーダイナミックスの密 度依存性」	Institute of Materials Structure Science, KEK Y. Inamura, M. Arai, T. Otomo Department of Chemistry, Osaka University O. Yamamuro, A. Inaba, T. Matsuo Government Industrial Research Institute of Osaka N. Kitamura Rutherford Appleton Laboratory S. M. Bennington, A. C. Hannon	JRR-3M C3-1-1 (AGNES)	187

中性子散乱

5) 材料科学

1-5-1 蛍石関連固溶体の構造変化 「高温中性子回折による ZrO_2 -13mol% YO_3 における 正方-立方相転移のその場 観察」	Department of Materials Science and Engineering, Interdisciplinary Graduate School of Science and Engineering, Tokyo Institute of Technology Y. Hatoyama, T. Oketani, M. Yashima Institute for Materials Research, Tohoku University Y. Yamaguchi, K. Ohoyama	JRR-3M T1-2 (KSD)	191
1-5-2 中性子粉末回折用高温電気 炉の開発 「高温における材料の構造 変化のその場観察：空気中 1550℃で得たデータのリー トベルト解析」	Department of Materials Science and Engineering, Interdisciplinary Graduate School of Science and Engineering, Tokyo Institute of Technology M. Yashima, T. Oketani, O. Yokota, Y. Hatoyama, R. Ali, T. Nogami, S. Utsumi, H. Sugawara Institute for Materials Research, Tohoku University M. Ohashi, K. Ohoyama, Y. Yamaguchi	JRR-3M T1-2 (KSD) T1-3 (HERMES) (KDP)	193
1-5-3 TiCoN_xSn の中性子回折 「 CoTiSn 窒化生成物の中 性子回折による研究」	Japan Advanced Institute of Science and Technology G. Nakamoto, T. Nobata, M. Kurisu Department of Physics, Kyushu Kyoritsu University Y. Makihara Faculty of Education, Tottori University Y. Andoh Research Reactor Institute, Kyoto University S. Kawano Faculty of Engineering, Yamagata University M. Ohashi	JRR-3M T1-3 (HERMES) (KDP)	195
1-5-4 ペロブスカイト関連化合物 の構造変化 「高温中性子回折による CaTiO_3 ペロブスカイトの研 究」	Department of Materials Science and Engineering, Interdisciplinary Graduate School of Science and Engineering, Tokyo Institute of Technology R. Ali, M. Yashima, T. Oketani, T. Nogami, H. Sugawara Institute for Materials Research, Tohoku University K. Ohoyama, Y. Yamaguchi	JRR-3M T1-3 (HERMES) (KDP)	196
1-5-5 $(\text{La}, \text{Sr})_{n+1}\text{Mn}_n\text{O}_{3n+1}$ のスピン 電荷ダイナミクス 「層状マンガン酸化物のス ピンバルブMR」	Center for Integrated Research in Science and Engineering, Nagoya University Y. Moritomo Institute for Materials Research, Tohoku University K. Ohoyama, M. Ohashi	JRR-3M T1-3 (HERMES) (KDP)	197

中性子散乱
5) 材料科学

1-5-6 リエントラント液晶の構造	Institute for Molecular Science O.Oishi,S.Miyajima Neutron Scattering Laboratory,Institute for Solid State Physics,University of Tokyo M.Nagao,M.Imai	JRR-3M C1-2 (SANS-U)	198
------------------------------	---	----------------------------	-----

1. 中性子散乱

6) 高分子

1-6-1 高分子多成分系の静的階層構造の研究 「牛血清アルブミンゲルのPNO研究2」	Graduate School of Science and Engineering, Yamagata University Y.Izumi,K.Soma Advanced Science Research Center,JAERI K.Aizawa,S.Koizumi,H.Tomimitsu	JRR-3M 3G (PNO)	201
1-6-2 高分子の結晶構造とダイナミックス 「ポリ-p-フェニレンベンゾビスオキサゾールの中性子構造解析」	Department of Macromolecular Science, Faculty of Science,Osaka University Y.Takahashi	JRR-3M T1-3 (HERMES) (KPD)	202
1-6-3 非晶高分子のダイナミクス 「置換ポリアセチレンの局所運動とガス透過性」	Institute for Chemical Research,Kyoto University T.Kanaya,K.Kaji Department of Polymer Chemistry,Kyoto University M.Teraguchi,T.Masuda	JRR-3M C1-1 (HER)	204
1-6-4 界面活性剤・水系のモルフオロジー転移 「Gyroidドメインのコースニング過程における弾性効果」	Department of Physics,Ochanomizu University M.Imai,K.Nakaya Faculty of Science,Tokyo Metropolitan University T.Kato	JRR-3M C1-2 (SANS-U)	205
1-6-5 ブロック共重合体のマイクロドメインの流動配向化とそのヒステリシスの検討 「スチレン-2ビニルピリジンブロック共重合体のマイクロドメイン構造に対する流動の影響」	Center for Integrated Research in Science and Engineering,Nagoya University Y.Takahashi Graduate School of Engineering,Nagoya University M.Noda,K.Matsuoka,T.Murayama	JRR-3M C1-2 (SANS-U)	206
1-6-6 ループ状の相図を有するブロック共重合体の相転移に関する研究 「ループ状の相図を有するブロック共重合体の相転移」	Department of Polymer Chemistry,Graduate School of Engineering,Kyoto University T.Hashimoto,H.Hasegawa,M.Takenaka,M.Sawamoto Neutron Scattering Laboratory,Institute for Solid State Physics,University of Tokyo M.Nagao,M.Imai	JRR-3M C1-2 (SANS-U)	207
1-6-7 弱電荷ゲルの体積相転移の動力学に関する研究	Department of Polymer Science and Engineering,Kyoto Institute of Technology M.Shibayama,H.Hirose	JRR-3M C1-2 (SANS-U)	208

1. 中性子散乱

6) 高分子

1-6-8 筵型高分子のミクロ相分離構造中の分子形態と界面 「ラメラ状ミクロ相分離構造中のグラフト鎖の分子形態」	Neutron Science Laboratory, KEK N.Torikai Neutron Scattering Laboratory, Institute for Solid State Physics, University of Tokyo J.Suzuki Fuji Film Corporation J.Watanabe School of Engineering, Nagoya University Y.Matsushita	JRR-3M C1-2 (SANS-U)	210
1-6-9 両親媒性環境下におけるポリペプチド鎖の構造解析 「ドデシル硫酸ナトリウム存在下の蛋白質ポリペプチド鎖の分子形態」	National Food Research Institute Y.Watanabe, Y.Sano Advanced Science Research Center, JAERI I.Tanaka, N.Niimura Faculty of Science, Ochanomizu University M.Imai	JRR-3M C1-2 (SANS-U)	211
1-6-10 多糖／水系の高次構造形成と機能発現 「ジェランガム／水系のゾルゲル転移の構造研究」	Graduate School of Science and Engineering, Yamagata University Y.Izumi, Y.Jinbo, K.Soma, S.Saito Institute for Solid State Physics, University of Tokyo M.Nagao, M.Hashimoto, T.Takahashi	JRR-3M C1-2 (SANS-U) C1-3 (ULS)	212
1-6-11 重水素化ポリブタジエン／ポリイソブレン混合系の相溶性におよぼす圧力効果のミクロ構造依存性 「高分子の相溶性に関する圧力効果のミクロ構造依存性」	Department of Polymer Chemistry, Graduate School of Engineering, Kyoto University H.Hasegawa, M.Takenaka, T.Hashimoto Neutron Scattering Laboratory, Institute for Solid State Physics, University of Tokyo M.Nagao, M.Imai	JRR-3M C1-2 (SANS-U)	213
1-6-12 両親媒性ポリマーの水及び有機選択溶媒中における会合体形成挙動	Department of Polymer Chemistry, Kyoto University H.Matsuoka, M.Nakano, M.Kubota, M.Deguchi, Y.Yamamoto, H.Yamaoka	JRR-3M C1-2 (SANS-U)	214
1-6-13 高分子濃厚溶液の濃度揺らぎとセグメント運動の関係 「ポリ酢酸ビニル濃厚溶液のセグメント運動に対する濃度揺らぎの効果」	Department of Macromolecular Science, Graduate School of Science, Osaka University M.Nakazawa, O.Urakawa, K.Adachi	JRR-3M C1-2 (SANS-U)	215

1. 中性子散乱

6) 高分子

1-6-14 セルロース粒子におけるフラクタル構造の研究 「微細結晶性セルロースの大規模構造」	Department of Chemistry and Physics of Condensed Matter, Graduate School, Kyushu University M. Sugiyama Institute of Environmental Systems, Kyushu University K. Hara Department of Applied Physics, Fukuoka University N. Hiramatsu Chemical Technology Department IV, Asahi Chemical Industry Corporation H. Iijima	JRR-3M C1-3 (ULS)	216
1-6-15 ABC型三成分ブロック共重合体の界面構造 「バルク高分子を試料とする中性子反射率測定へのコントラスト・マッチング法の応用」	Neutron Scattering Laboratory, KEK N. Torikai School of Engineering, Nagoya University Y. Matsushita JAERI K. Soyama, N. Metoki, Y. Morii	JRR-3M C2-1 (LTAS)	217
1-6-16 中性子スピンエコー法による両親媒性高分子ミセルの動的挙動の定量的評価	Department of Polymer Chemistry, Kyoto University Y. Yamamoto, H. Matsuoka, H. Yamaoka	JRR-3M C2-2 (NSE)	218
1-6-17 PVAゲルの構造とダイナミクス 「PVAゲルの中性子スピンエコー研究」	Institute for Chemical Research, Kyoto University T. Kanaya, K. Kaji Institute for Solid State Physics, University of Tokyo M. Nagao Faculty of Integrated Arts and Science, Hiroshima University Y. Kawabata, H. Seto, T. Takeda	JRR-3M C2-2 (NSE)	219
1-6-18 低分子量アモルファスポリスチレンのガラス転移温度以下でのダイナミクス 「準弾性中性子散乱で見たガラス転移近傍におけるアモルファスポリスチレンの高分子効果」	Institute for Chemical Research, Kyoto University I. Tsukushi, T. Kanaya, K. Kaji	JRR-3M C3-1-1 (AGNES)	221
1-6-19 中性子反射率法による固・液界面における両親媒性高分子の形態とその集合状態の解析	Department of Polymer Chemistry, Kyoto University H. Endo, K. Kago, R. Yoshitome, K. Matsumoto, H. Matsuoka, H. Yamaoka	JRR-3M C3-1-2 (MINE)	222

1. 中性子散乱
6) 高分子

1-6-20 高分子多成分系のパターン形成に関する研究 「高分子混合系のガラス転移温度近傍における濃度揺らぎの置換基効果」	Kyoto University H.Takeno,T.Hashimoto Advanced Science Research Center,JAERI S.Koizumi	JRR-3M C3-2 (SANS-J)	223
1-6-21 ポリエチレンD/Hブレンド試料におけるD鎖とH鎖の凝集状態：延伸に伴う変化の追跡 「重水素化および水素化ポリエチレンブレンドの1軸延伸試料における分子鎖凝集構造」	Graduate School of Science,Osaka University K.Tashiro,R.Tanaka Advanced Science Research Center,JAERI S.Koizumi	JRR-3M C3-2 (SANS-J)	224

1. 中性子散乱
7) 生物学

1-7-1 コバロキシム錯体結晶の光異性化反応における水素移動 「コバロキシム錯体における2-1光異性化反応」	Department of Chemistry, Tokyo Institute of Technology H.Imura, T.Ohhara, Y.Ohashi Advanced Science Research Center, JAERI I.Tanaka, N.Niimura	JRR-3M 1G-A (BIX-I)	229
1-7-2 中性子回折による生体物質の構造研究 「pH4.9で作成したニワトリ卵白リゾチーム単結晶の中性子回折のデータ収集」	Advanced Science Research Center, JAERI S.Fujiwara, S.Kumazawa, Y.Haga, Y.Minezaki, I.Tanaka, N.Niimura Tsukuba College of Technology Y.Yonezawa	JRR-3M T2-3 (BIX-II)	230
1-7-3 リン脂質膜構造形成においてコレステロール分子の果たす役割に関する研究	Department of Applied Physics, Nagoya University H.Takahashi, I.Hatta Institute for Solid State Physics, University of Tokyo M.Imai Institute of Materials Structure Science, High Energy Accelerator Research Organization T.Adachi	JRR-3M C1-2 (SANS-U)	231
1-7-4 ムコ多糖蛋白質複合体の超分子内部構造 「中性子散乱によるプロテオグリカンの構造研究」	National Food Research Institute Y.Watanabe, Y.Sano Advanced Science Research Center, JAERI I.Tanaka, N.Niimura	JRR-3M C1-2 (SANS-U)	232
1-7-5 中性子溶液散乱による原核生物核様体構造の研究 「DNA結合蛋白質HUのコントラスト変調法を用いた中性子小角散乱による研究」	Advanced Science Research Center, JAERI S.Fujiwara Tsukuba College of Technology Y.Yonezawa Neutron Scattering Laboratory, Institute for Solid State Physics, University of Tokyo M.Nagao	JRR-3M C1-2 (SANS-U)	233
1-7-6 大腸菌外膜蛋白質OmpAの構造変化ならびに両親媒性分子との相互作用の研究 「オクチルグルコシド存在下で可溶化された大腸菌外膜蛋白質OmpAの構造」	Faculty of Engineering, Gifu University K.Kameyama Graduate School of Integrated Science, Yokohama City University M.Sato Department of Biochemistry and Biophysics, University of Rochester S.Ohnishi Neutron Scattering Laboratory, Institute for Solid State Physics, University of Tokyo M.Nagao	JRR-3M C1-2 (SANS-U)	234

1. 中性子散乱
7) 生物学

1-7-7 糖脂質（ガングリオシド） 凝集系の水和構造と熱可逆 相転移 「ガングリオシドミセル構 造の温度依存性」	Department of Physics, Gunma University M.Hirai, H.Iwase, T.Hayakawa, S.Arai, S.Mitsuya Institute for Solid State Physics, University of Tokyo Y.Matsushita	JRR-3M C1-2 (SANS-U)	235
---	--	----------------------------	-----

1. 中性子散乱

8) 基礎物理学・中性子光学

1-8-1 精密中性子光学実験の基礎 と応用の研究 「改3号炉PNOにおける中 性子干渉計実験」	Advanced Science Research Center,JAERI H.Tomimitsu,K.Aizawa Faculty of Engineering,Tokyo University Y.Hasegawa	JRR-3M 3G (PNO)	239
1-8-2 中性子ラーモア回転による パーマロイ単結晶の動力学 回折	Department of Physics,Kyushu University N.Achiwa,G.Shirozu Research Reactor Institute,Kyoto University S.Tasaki,M.Hino,T.Ebisawa,T.Kawai Neutron Scattering Laboratory,Institute for Solid State Physics,University of Tokyo K.Kakurai Graduate School of Engineering,Kyoto University M.Shiga	JRR-3M 5G (PONTA)	241
1-8-3 コヒーレント中性子ビーム による非弾性散乱の研究 「チャンネルカット結晶の ロッキングカーブのテール に現れる散乱の裏面反射の 影響」	Institute for Solid State Physics,University of Tokyo M.Hashimoto,K.Sumitani,S.Nakatani, T.Takahashi	JRR-3M C1-3 (ULS)	243
1-8-4 シリコン単結晶とラーモア 歳差回転を用いた $\uparrow\downarrow$ スピ ン中性子の横方向干渉性の 測定 「スピンスプリッターによ る $\uparrow\downarrow$ スピン中性子の横方 向干渉性の測定」	Research Reactor Institute,Kyoto University M.Hino,T.Ebisawa,S.Tasaki The Institute of Physical and Chemical Research(RIKEN) Y.Otake Department of Nuclear Engineering,Kyoto University H.Tahata Institute for Solid State Physics,University of Tokyo M.Hashimoto,T.Takahashi Department of Physics,Kyushu University N.Achiwa	JRR-3M C3-1-2 (MINE)	244
1-8-5 ラーモア回転による中性子 波束のスピン干渉 「スピン回転による多連結 ファブリペロー磁気膜での 中性子束縛状態の測定」	Department of Physics,Kyushu University N.Achiwa,G.Shirozu Research Reactor Institute,Kyoto University M.Hino,S.Tasaki,T.Ebisawa,T.Kawai Department of Nuclear Engineering,Kyoto University D.Yamazaki	JRR-3M C3-1-2 (MINE)	245

1. 中性子散乱

8) 基礎物理学・中性子光学

1-8-6 中性子ラーモア歳差回転によるトンネル時間とラーモア時計の研究 「吸収の強い磁気膜を透過する中性子のスピン回転」	Research Reactor Institute, Kyoto University M.Hino, S.Tasaki, T.Ebisawa, T.Kawai Department of Physics, Kyushu University N.Achiwa Department of Nuclear Engineering, Kyoto University D.Yamazaki	JRR-3M C3-1-2 (MINE)	246
1-8-7 冷中性子スピン干渉計の開発とその応用 「RF flipper による冷中性子スピン干渉を用いた分光法の開発」	Research Reactor Institute, Kyoto University T.Ebisawa, M.Hino, T.Kawai, S.Tasaki Department of Nuclear Engineering, Kyoto University D.Yamazaki Department of Physics, Kyushu University N.Achiwa SPring8 The Institute of Physical and Chemical Research Y.Otake	JRR-3M C3-1-2 (MINE)	247

1. 中性子散乱

9) 装 置

1-9-1 (1) 生体物質の中性子回折による研究 「生体高分子用中性子イメージングプレート付き改良中性子回折計」	Advanced Science Research Center,JAERI I.Tanaka,K.Kurihara,T.Chatake, Y.Nishimura,Y.Haga,Y.Minezaki, S.Fujiwara,N.Nimura Neutorn Scattering Laboratory(KENS),KEK S.Kumazawa Tsukuba College of Technology Y.Yonezawa Department of Chemistry,University of Southern California R.Bau Faculty of Science,Tohoku University A.Suzuki,E.Otani	JRR-3M 1G-A (BIX-III)	251
1-9-2 高圧下での結晶構造・相変態の研究 「中性子散乱用ミニチュア高圧セル」	School of Engineering Science,Osaka University A.Onodera School of Science,Kyoto University F.Amita Advanced Science Research Center,JAERI Y.Ishii,Y.Morii	JRR-3M T2-4 (TAS-2)	253
1-9-3 研究炉利用高度化の技術開発 「中性子散乱実験用多重極限条件発生装置の性能試験」	Department of Research Reactor,JAERI A.Moriai,S.Ichimura,A.Ohtomo Research Reactor Institute,Kyoto University S.Kawano School of Engineering Science,Osaka University A.Onodera	JRR-3M T2-4 (TAS-2)	254
1-9-4 中性子スピネコー分光器 (IMT) 「改3号炉C2-2中性子スピネコー分光器の改良」	Faculty of Integrated Arts and Sciences, Hiroshima University T.Takeda,H.Seto,Y.Kawabata Neutorn Scattering Laboratory(KENS),KEK S.Satoh,M.Furusaka Institute for Solid State Physics,University of Tokyo M.Nagao,H.Yoshizawa	JRR-3M C2-2 (NSE)	255
1-9-5 薄板基板上的多層膜の中性子反射率測定 「レプリカスーパーミラーの製作と中性子反射率」	Research Reactor Institute,Kyoto University Y.Kawabata,S.Tasaki Department of Research Reactor,JAERI M.Suzuki Faculty of Engineering,Kyoto University K.Somemiya	JRR-3M C3-1-2 (MINE)	256

1. 中性子散乱

9) 装 置

1-9-6 低磁場制御冷中性子偏極パ ルサーの開発 「低磁場制御Permalloy/Ge 磁気鏡のヒステレシス・ル ープ」	Research Reactor Institute,Kyoto University T.Kawai,M.Hino,S.Tasaki,T.Ebisawa SPring8 The Institute of Physical and Chemical Research Y.Otake Physics Department Kyushu University N.Achiwa	JRR-3M C3-1-2 (MINE)	257
1-9-7 高性能多層膜ミラーの開発 「イオンポリッシュ法によ る多層膜中性子ミラーの高 反射率化」	JAERI K.Soyama Nikon Corporation W.Ishiyama,K.Murakami	JRR-3M C2-1 (LTAS)	258
1-9-8 多層膜による中性子反射率 ・透過率の測定 「多層膜による特徴的な非 鏡面干渉性反射の測定と解 析」	Research Reactor Institute,Kyoto University S.Tasaki	JRR-3M C2-1 (LTAS)	259

1. 中性子散乱

10) その他

1-10-1 構造材料の残留応力と疲労 損傷の評価 「残留応力測定に関する VAMASTWA20のプロジェクト」	Nagoya University K.Tanaka,Y.Akiniwa Hitachi Ltd. M.Hayashi,S.Ohkido Advanced Science Research Center,JAERI N.Minakawa,Y.Morii	JRR-3M T2-1 (RESA) T2-4 (TAS-2)	263
1-10-2 構造材料の残留応力と疲労 損傷の評価 「Al ₂ O ₃ /SiCおよび Al ₂ O ₃ /ZrO ₂ 複合材料の残留 応力測定」	Nagoya University K.Tanaka,Y.Akiniwa Advanced Science Research Center,JAERI N.Minakawa,Y.Morii	JRR-3M T2-1 (RESA)	264
1-10-3 工業材料の残留応力と疲労 損傷の評価 「直径40mmの鋼丸棒の残 留ひずみの測定 (II)」	Faculty Science and Technology,Ryukoku University K.Inoue,T.Horikawa,H.Nakamura Advanced Science Research Center,JAERI N.Minakawa,Y.Morii,N.Ikeda Department Materials Science Engineering, Ibaraki University Rudiono	JRR-3M T2-1 (RESA)	265
1-10-4 中性子イメージングプレート を用いた中性子応力測定 による内部残留応力分布状 態の非破壊測定法に関する 研究 「中性子イメージングプレ ートを用いた中性子応力測 定」	Kanazawa University T.Sasaki,Y.Hirose,S.Takago Advanced Science Research Center,JAERI N.Niimura,Y.Morii,N.Minakawa, Y.Tsuchiya Musashi Institute of Technology Y.Yoshioka	JRR-3M T2-1 (RESA)	266

2. 中性子ラジオグラフィ

研究テーマ 「表題」	所 属 担 当 者	利用原子炉 及び装置名	頁
2-1 中性子ラジオグラフィによる沸騰二相流のボイド率計測 「中性子ラジオグラフィ高速度撮影法による瞬間および時間平均ボイド率の計測」	原研 熱流体研究グループ 呉田 昌俊 秋本 肇	JRR-3M 7R (TNRF)	271
2-2 原子炉シビアアクシデント時の溶融炉心冷却に関する基礎研究 「溶融燃料／冷却材相互作用の可視化実験－溶融金属中に落下する水ジェット挙動の可視化－」	原研 原子炉安全工学部 柴本 泰照 中村 秀夫 安濃田 良成	JRR-3M 7R (TNRF)	272
2-3 中性子ビーム利用技術に関する開発研究 「中性子ラジオグラフィ技術の開発研究」	原研 核破碎中性子利用研究室 松林 政仁	JRR-3M 7R (TNRF)	273
2-4 JRR-3M冷中性子を利用するラジオグラフィ高度化技術の開発と応用研究	名古屋大学 工学研究科 玉置 昌義 久木田 豊 辻 義之 親松 和浩 大久保 興平 小田 将広 本田 真彦 八木 貴広 舟橋 隆之 西口 蔵 増永 優作 土田 浩司 原研 核破碎中性子利用研究室 松林 政仁	JRR-3M 7R (TNRF) C2-3 (CNRF)	275
2-5 JRR-3M冷・熱中性子を用いたラジオグラフィ技術の高度化(II) －高温融体と冷却材の混合の可視化に関する研究－	京都大学 原子炉実験所 三島 嘉一郎 日引 俊 齊藤 泰司 原研 炉心損傷安全研究室 杉本 純 森山 清史 原研 核破碎中性子利用研究室 松林 政仁	JRR-3M 7R (TNRF)	279

2. 中性子ラジオグラフィ

2-6 電子撮影方式中性子ラジオグラフィにおける高分解能化に関する研究	武蔵工業大学 持木 幸一 小磯 学 三野 勉稔 岩田 秀規 木原 祥隆 山路 晃弘 木本 亨尚 村田 裕	JRR-3M 7R (TNRF)	289
2-7 植物試料の中性子ラジオグラフィ	東京大学大学院 農学生命科学研究科 中西 友子 古川 純 原研 核破碎中性子利用研究室 松林 政仁	JRR-3M 7R (TNRF)	294

3. 即発ガンマ線分析

研究テーマ 「表題」	所 属 担 当 者	利用原子炉 及び装置名	頁
3-1 畜産および水産研究における原子炉中性子即発ガンマ線分析法の利用 「中性子即発ガンマ線分析法による畜産および水産関係試料中のホウ素およびケイ素の定量」	農林水産省 畜産試験場 宮本 進 西村 宏一 農林水産省 遠洋水産研究所 塩本 明弘 原研 環境科学研究部 安達 武雄 原研 分析科学研究グループ 米沢 伸四郎 松江 秀明 原研 国際原子力総合技術センター 星 三千男	JRR-3M T1-4-1 (PGA)	299
3-2 原子力関連物質の分析化学 「中性子即発γ線分析の研究」	原研 分析科学研究グループ 米沢 伸四郎 松江 秀明	JRR-3M T1-4-1 (PGA)	301
3-3 中性子ビームガイドを用いた中性子吸収反応の核・放射化学への応用(Ⅱ) 「即発ガンマ線エネルギー精密測定法の開発ー光電ピーク形状ー」	熊本大学 工学部 岸川 俊明 上村 実也 原研 分析科学研究グループ 米沢 伸四郎	JRR-3M T1-4-1 (PGA)	303

4. 放射化分析

研究テーマ 「表題」	所 担 当 属 者	利用原子炉 及び装置名	頁
4-1 ラジオアイソトープ技術者の養成 「実習 放射化分析」	原研 東京研修センター 上沖 寛	JRR-3M PN	311
4-2 農林生態系におけるハロゲン元素の動態 「世界の土壌・植物系におけるハロゲン元素の含量レベルと動態の解明ーロシア国 東・中央シベリア高緯度地域の土壌ー」	農業環境技術研究所 結田 康一 森林総研北海道支所 松浦 陽次郎	JRR-3M PN	312
4-3 新アクチバブルトレーサーをマーカーとした家畜消化管内容物移動の解析手法の開発 「ーサマリウム、ランタン等をマーカーとした家畜消化管内容物移動の解析ー」	農林水産省 畜産試験場 松本 光人 宮本 進 山岸 規昭	JRR-3M PN	314
4-4 伊豆小笠原弧背弧域における火成活動および熱水活動に関する研究 「伊豆小笠原弧背弧地域における深成岩と斑岩銅鉱床型熱水活動ー海洋性島弧におけるトーナライトと斑岩銅鉱床ー」	地質調査所 石塚 治 湯浅 真人 宇都 浩三 東京大学 海洋研究所 石井 輝秋 Monterey Peninsula College A.G.Hochstaedter	JRR-4 T Pipe	315
4-5 核融合炉用低放射化構造材料の開発 「SiC繊維(Hi-Nicalon Type S)の不純物定量分析」	原研 材料照射解析研究グループ 井川 直樹 田口 富嗣 山田 禮司 日本カーボン(株) 武田 道夫	JRR-4 PN	316
4-6 多重ガンマ線スペクトルの分析科学への応用 「多重ガンマ線測定装置の中性子放射化分析への応用」	原研 原子核科学研究グループ 初川 雄一 篠原 伸夫 大島 真澄 原研 自由電子レーザー研究グループ 早川 岳人	JRR-4 PN	317

4. 放射化分析

4-7 植物試料の元素分析	東京大学大学院 農学生命科学研究科 中西 友子 古川 純 片岡 達彦	JRR-3M PN-3	319
4-8 放射化分析による海藻由来 の含ハロゲン化合物の生合 成研究	北海道大学大学院 地球環境科学研究科 鈴木 稔 中野 智 高橋 義宣 北海道大学 アイソトープ総合センター 野矢 洋一 大西 俊之	JRR-4 PN JRR-3M PN	323
4-9 生物体類似多元素合成標準 物質の開発と応用	秋田大学 教育学部 Y.Iwata A.Nakamura	JRR-4 T,S-Pipe PN JRR-3M PN	328
4-10 宇宙物質の中性子放射化分 析(2)	東京都立大学大学院 理学研究科 海老原 充 尾崎 大真 孔屏 内野 智功 箕輪 はるか S.K.Latif 石井 友子 日高 洋 大浦 泰嗣 G.W.Kallemeyn 中原 弘道 国立科学博物館 理工学研究部 米田 成一	JRR-3M	334
4-11 放射化分析支援システムの 検証試験	東京大学 原子力研究総合センター 伊藤 泰男 澤幡 浩之 原研 研究炉部 桜井 文雄 大友 昭敏 笹島 文雄	JRR-4 T,S-Pipe PN JRR-3M HR-1 HR-2 PN	339

5. RIの製造

研究テーマ 「表題」	所 属 担 当 者	利用原子炉 及び装置名	頁
5-1 RIの製造技術の開発 「ガドリニウム造影剤の体内分布を高感度で検出－原子炉で放射化し画像で見る新手法を開発－」	原研 アイソトープ開発室 小林 勝利 本石 章司 照沼 久寿男 今橋 強 (株) 生体科学研究所 羽鳥 晶子 重松 昭世	JRR-3M PN	345
5-2 非定常放出に対するガスモニタ校正法の開発 「放射性ガスモニタの校正法の比較」	原研 線量計測課 大石 哲也 吉田 真	JRR-4 T-Pipe	346

6. 原子炉材料照射試験

研究テーマ 「表題」	所 属 担 当 者	利用原子炉 及び装置名	頁
6-1 原子炉用機能性材料の研究 開発 「酸化リチウム単結晶から のヘリウム放出挙動」	原研 材料照射解析研究グループ 八巻 大樹 谷藤 隆昭 原研 企画室 野田 健治	JRR-4 S-Pipe	349

7. その他

研究テーマ 「表 題」	所 属 担 当 者	利用原子炉 及び装置名	頁
7-1 LiAlの電氣的性質の中性子 照射効果の研究II	原研 アイソトープ開発室 須貝 宏行 青森大学 工学部 矢萩 正人 法政大学 工学部 浜中 廣見 内山 周 栗山 一男	JRR-4 D,T-Pipe	353
7-2 黒曜石のフィッション・ト ラック年代測定値の標準化 ー特にAu・Zrモニターに よる放射化反応率測定を試 みー	鹿児島大学 教育学部 鈴木 達郎	JRR-3M PN-1 PN-2	354
7-3 水溶性大環状金属錯体系に おける反跳効果(続) ー水溶性金属フタロシアニ ン系についてー	筑波大学 化学系 荘司 準	JRR-3M PN	358
7-4 石英中の酸素空格子生成: 内部 α 粒子照射による効果 及び γ 線の線量率効果	大阪大学大学院 理学研究科 豊田 新	JRR-3M	362

This is a blank page.

Research Reports

1. Neutron Scattering

1) Structure · Excitation

1-1-1 Neutron Powder Diffraction Study of LaCrO_3	59
K.Oikawa, T.Kamiyama, T.Hashimoto, Y.Shimojo, Y.Morii	
1-1-2 Temperature Dependence of Order Parameters in the Antiferroelectric Phase of PbZrO_3	60
S.Katano, H.Fujishita	
1-1-3 Imaging of Hydrogen Nucleus in the Hydrogen Bond of KDP by Maximum Entropy Method	62
S.Yamamura, S.Kumazawa, E.Nishibori, M.Takata, M.Sakata, Y.Sugawara, Y.Ishii, Y.Morii	
1-1-4 Hydrogen Bond of ADP by the Maximum Entropy Method	63
S.Yamamura, S.Kumazawa, E.Nishibori, M.Takata, M.Sakata, Y.Sugawara, Y.Ishii, Y.Morii	
1-1-5 Neutron Scattering on the Metal-insulator Transition in Thiospinel CuIr_2S_4 ...	64
S.Katano, K.Oikawa, T.Matsumoto	
1-1-6 Lattice Dynamics of Disordered Perovskite $\text{Pb}(\text{Zn}_{1/3}\text{Nb}_{2/3})\text{O}_3$	65
I.Tomeno, S.Shimanuki, Y.Tsunoda, Y.Ishii	
1-1-7 Characterization of Single-crystal Ni-base Superalloy CMSX-4 with Creep Damage(III)	66
K.Aizawa, H.Tomimitsu, H.Tamaki, A.Yoshinari	
1-1-8 Phonon Dispersions in the Low-Carrier Density System CeSb	67
K.Iwasa, M.Kohgi, Y.Haga, T.Osakabe, M.Braden, J.-M.Mignot, T.Suzuki	
1-1-9 Phonon Dispersions in the Charge Ordering System Yb_4As_3	68
K.Iwasa, M.Kohgi, A.Ochiai, H.Aoki, T.Suzuki	
1-1-10 Investigation of Lithium Intercalation Material with 3-Dimensional Framework	70
T.Suzuki, H.Ohokawa, M.Saito, K.Uematsu, K.Ohoyama, K.Toda, M.Sato	
1-1-11 Crystal Structure and Ionic Conductivity of Lithium Phosphate with Indium	71
T.Suzuki, N.Hayakawa, K.Yoshikawa, K.Uematsu, K.Toda, K.Ohoyama, M.Sato	
1-1-12 Crystal Structure Refinement in the Tetragonal Compound $\text{Ce}^{11}\text{B}_2\text{C}_2$ and $\text{Nd}^{11}\text{B}_2\text{C}_2$	72
T.Onimaru, K.Ohoyama, H.Yamauchi, H.Onodera, M.Ohashi, Y.Yamaguchi	

1-1-13 Martensitic and Magnetic Transformations in Heusler-type	
Ni₂(Pd_{0.16}Mn_{0.84})Ga	74
K.Inoue, K.Enami, M.Igawa, Y.Yamaguchi, K.Ohoyama	
1-1-14 Magnetic Field Effects on Superconducting La_{2-x}Sr_xCuO₄	76
S.Katano, T.Suzuki, T.Fukase, K.Yamada	
1-1-15 Magnetic Quasi-elastic Scattering in Diluted Magnetic Semiconductor	
Zn_{1-x}Mn_xTe with x=0.432	77
Y.Ono, T.Kamita, T.Sato, Y.Oka, T.Kajitani	
2) Magnetism	
1-2-1 Magnetic and Neutron Diffraction Studies of Rare-earth Orthotitanates	81
K.Yoshii, A.Nakamura	
1-2-2 Neutron Diffraction Study on Ordered Perovskites Sr₂LnRuO₆ (Ln=Ho, Tm) ...	82
Y.Doi, Y.Hinatsu, Y.Shimojo, Y.Morii	
1-2-3 Neutron Diffraction Study on Layered Perovskites Ca_{2-x}Sr_xMnO₄	83
K.Tezuka, M.Inamura, Y.Hinatsu, Y.Shimojo, Y.Morii	
1-2-4 Pressure Effects on Spin Gap and Antiferromagnetism of the Spin Ladder	
Compound Sr_{2.5}Ca_{11.5}Cu₂₄O₄₁	84
S.Katano, T.Nagata, H.Fujino, J.Akimitsu, M.Nishi, K.Kakurai	
1-2-5 Neutron Diffraction Study on the Magnetic Structure of TmB₁₂	86
T.Osakabe, F.Iga, S.Hiura, T.Takabatake	
1-2-6 Magnetic Structure of CeAs under High Pressure	87
T.Osakabe, M.Kohgi, K.Iwasa, M.Kubota, H.Yoshizawa, Y.Haga, T.Suzuki	
1-2-7 Search for Magnetic Order in UIrGe	89
K.Prokeš, F.Iga, T.Takabatake, T.Fujita, T.Osakabe	
1-2-8 Spin-Wave Excitations in Commensurate Oxygen-Doped	
La₂NiO_{4-δ} (δ ≤ 0.11)	90
K.Nakajima, T.Sawada, H.Yoshizawa, Y.Endoh	
1-2-9 Critical Magnetic Scattering from Two-Dimensional Percolating Ising	
Antiferromagnets	92
K.Iwasa, H.Ikeda	
1-2-10 Weak Antiferromagnetic Moment in Distorted Heavy-Fermion	
System (Y,U)Ru₂Si₂	94
H.Amitsuka, A.Okumura, K.Kuwahara, M.Yokoyama	
1-2-11 Magnetic Ordering in Triangular Lattice Antiferromagnet CuFe(Al)O₂	95
M.Mekata, Y.Kobayashi, K.Taki, Y.Yamada, F.Takei, D.Zhao, Y.Oohara	

1-2-12 Neutron Scattering of an Orbital-Ordered Spin-Singlet System BaVS₃	96
M.Shiga, H.Nakamura, H.Tanahashi, H.Imai, K.Kojima, K.Kakurai, M.Nishi	
1-2-13 Magnetic Correlations in CsVCl₃	97
S.Itoh, K.Kakurai, Y.Endoh, H.Tanaka, K.Nakajima, M.J.Harris	
1-2-14 Antiferromagnetic Ordering in the Hole-Doped Spin Ladder System	
Sr_{2.5}Ca_{11.5}Cu₂₄O₄₁ under Ambient and High Pressure	99
J.Akimitsu, T.Nagata, H.Fujino, M.Nishi, K.Kakurai, S.Katano	
1-2-15 Hole Ordering and Dimerized State in the CuO₂ Chains in Sr₁₄Cu₂₄O₄₁	101
M.Matsuda, T.Yoshihama, K.Kakurai, G.Shirane	
1-2-16 Polarization Dependence of Magnetic Excitations in UGa₂	102
M.Kohgi, K.Iwasa, H.Sagayama, N.Sato, K.Kakurai	
1-2-17 Neutron Scattering Study on Metal-Insulator Transition of BaCo_{1-x}Ni_xS₂	104
H.Sasaki, H.Harashina, K.Kodama, M.Sato, S.Shamoto, M.Nishi, K.Kakurai	
1-2-18 Spin Dynamical Properties of the Layered Perovskite La_{1.2}Sr_{1.8}Mn₂O_{7[1]}	106
H.Fujioka, M.Kubota, K.Hirota, H.Yoshizawa, Y.Moritomo, Y.Endoh	
1-2-19 Study of Lattice Dynamics in DyB₆	107
H.Nojiri, K.Takahashi, M.Motokawa, S.Kunii, K.Hirota, K.Kakurai, Y.Endoh	
1-2-20 Neutron Diffraction Study of the Field Induced Orbital Ordering in	
La_{1-x}Sr_xMnO₃(x=1/8)	108
H.Nojiri, K.Kaneko, M.Motokawa, K.Hirota, Y.Endoh	
1-2-21 Neutron Diffraction Studies of the Magnetic Structures of Nd₂Ni₃ Single	
Crystal	109
S.Kawano, X.Xu, T.Tsutaoka, T.Kasagi, Y.Andoh, M.Kurisu	
1-2-22 Neutron Diffraction Study of CeGa Single Crystal	110
E.Matsuoka, M.Kosaka, T.Ohki, Y.Uwatoko	
1-2-23 Neutron Diffraction Study of (Fe_{0.98}Ru_{0.02})₂P	111
T.Ohki, T.Satoh, M.Kosaka, Y.Uwatoko	
1-2-24 Neutron Diffraction Studies on ErNiSn	112
Y.Andoh, S.Kawano, T.Nobata, G.Nakamoto, M.Kurisu, T.Tsutaoka	
1-2-25 Slow Dynamics in Concentrated Spin Glasses	113
K.Motoya, T.Kumazawa, J.Kikuchi	
1-2-26 Atomic Short Range Order and Spin Glass in PtCr Alloy	114
M.Hirano, Y.Tsunoda	
1-2-27 Competing Anisotropy Origin Hysteretic Behavior of the Mixed Ising-XY	
Antiferromagnet Fe_{0.50}Co_{0.50}TiO₃ in Magnetic Field	115
A.Ito, C.Uchikoshi, A.Fukaya, K.Nakajima, K.Kakurai	

1-2-28 Magnetic Structure and Excitation of Metallic Phase of $(V_{1-x}Ti_x)_2O_3$	117
K.Motoya, J.Kikuchi, T.Kumazawa, N.Wada, S.Shin	
1-2-29 Neutron Scattering Study of Ferromagnetic PdMn	118
A.Harigae, Y.Tsunoda	
1-2-30 Study of Magnetic Structures in ReB_6	119
H.Nojiri, K.Takahashi, M.Motokawa, S.Kunii, K.Ohyama, M.Ohashi, Y.Yamaguchi	
1-2-31 Study of Magnetic Structures in ReB_6	120
H.Nojiri, K.Takahashi, M.Motokawa, S.Kunii, K.Ohyama, M.Ohashi, Y.Yamaguchi	
1-2-32 Magnetic and Structural Phase Transitions in the Kondo Compounds	
Ce($Zn_{1-x}Ga_x$)	121
M.Watanabe, K.Ohoyama, H.Onodera, M.Ohashi, Y.Yamaguchi	
1-2-33 Neutron Scattering Study of $ZnCr_2O_4$ and $ZnFe_2O_4$	122
K.Shiratori, D.Eto, K.Kohn, I.Kagomiya, E.Kita, Y.Hata	
1-2-34 Structural Study of La and Zn Substituted $SrFe_{12}O_{19}$ via Neutron Scattering ...	123
K.Kitazawa, N.Hirota, K.Iida, J.Nakagawa, H.Taguchi	
1-2-35 Magnetic Structure of $CePb_2$ Compound	124
R.Yamauchi, K.Fukamichi, K.Ohyama, Y.Yamaguchi	
1-2-36 Magnetic Ordering of the Edge-Sharing CuO_2 Chains in $Ca_2Y_2Cu_5O_{10}$	125
M..Matsuda, K.Ohoyama, M.Ohashi	
1-2-37 Neutron Diffraction Study of Magnetic Transition in Mn_7Sn_4	126
S.Anzai, T.Kobayashi, Y.Yamaguchi, M.Ohashi, K.Ohoyama	
1-2-38 Neutron Diffraction of Amorphous Heusler Alloy $Cu_2MnAl_{1-x}Y_x$	127
T.Kamimori, Y.Shiraga, K.Konishi, H.Tange, M.Goto, S.Tomiyoshi, M.Ohashi, Y.Yamaguchi	
1-2-39 Short-range Magnetic Order in Diluted Magnetic Semiconductor $Zn_{1-x}Mn_xTe$	
with $x=0.432$	128
Y.Ono, T.Kamiya, S.Shamoto, T.Sato, Y.Oka, T.Kajitani	
1-2-40 Magnetic Phase Diagram of the Bi-Layered Manganite $La_{2-2x}Sr_{1+2x}Mn_2O_7$	
$(0.30 \leq x \leq 0.50)_{[1]}$	129
M.Kubota, H.Fujioka, K.Hirota, Y.Moritomo, H.Yoshizawa, Y.Endoh	
1-2-41 Magnetic Excitations in the Heavy Fermion Compounds Ce_2X ($X=Sb, Bi$)	130
K.Ohoyama, H.Hayashi, H.Onodera, M.Ohashi, Y.Yamaguchi, M.Kohgi, T.Suzuki	
1-2-42 Magnetism of Oxygen Deficient Perovskite, $La_{0.8}Sr_{0.2}MnO_{2.9}$	131
K.Inoue, T.Mori, N.Kamegashira, Y.Yamaguchi, K.Ohoyama	
1-2-43 Neutron Scattering Study of UPd_2Al_3 under External Pressure	133
T.Honma, Y.Haga, E.Yamamoto, N.Metoki, Y.Koike, T.Osakabe, Y.Onuki	

1-2-44 Neutron Diffraction Study of Phase IV of $\text{Ce}_2\text{La}_{1-x}\text{B}_6$	135
M.Kohgi, K.Iwasa, O.Suzuki, T.Goto, N.Metoki, Y.Koike, T.Osakabe, S.Kunii	
1-2-45 Neutron Diffraction Study in Dy^{11}B_6 under Magnetic Fields with 10 T Magnet	137
K.Takahashi, H.Nojiri, Y.Matsuoka, N.Metoki, S.Kunii, M.Motokawa	
1-2-46 Magnetic Structure Study of Mixed Valence YB_2S_4	138
J.-G.Park, Y.S.Kwon, Y.Morii, M.Kohgi	
1-2-47 Neutron Scattering Study of Incommensurate Elastic Magnetic Peaks in $\text{La}_{1-88}\text{Sr}_{0.12}\text{CuO}_{4(1)}$	140
H.Kimura, H.Matsushita, K.Hirota, Y.Endoh, K.Yamada, G.Shirane, Y.S.Lee, M.A.Kastner, R.J.Birgeneau	
1-2-48 Systematic Neutron Scattering Study of Elastic Magnetic Signals in Lightly Doped $\text{La}_{2-x}\text{Sr}_x\text{CuO}_4(0.03 \leq x \leq 0.06)_{(1)}$	141
S.Wakimoto, K.Yamada, S.Ueki, G.Shirane, Y.S.Lee, S.H.Lee, M.A.Kastner, K.Hirota, P.M.Gehring, Y.Endoh, R.J.Birgeneau	
1-2-49 High Resolution Inelastic Neutron Scattering on LiV_2O_5	142
Y.Takeo, T.Yoshihama, K.Kakurai, M.Isobe, Y.Ueda	
1-2-50 Magnetic Fluctuation of the Heavy Fermion CeRu_2Si_2	143
H.Kadowaki, M.Sato, S.Kawarazaki, Y.Miyako	
1-2-51 Spin Fluctuation in the Heavy Fermion Compound CeRu_2Si_2	144
M.Sato, M.Miyamura, H.Kadowaki, S.Kawarazaki, Y.Miyako	
1-2-52 Magnetic Ordering of CeCuAl_3	145
Y.Ohhara, G.Motoyama, T.Nishioka, M.Kontani	
1-2-53 Neutron Inelastic Scattering Study of Ferroelectric Phase Transition in $\text{Li}_2\text{Ge}_2\text{O}_5$	146
M.Wada, Takeda, Y.Noda, T.Yamaguchi, Y.Iwata	
1-2-54 Neutron Powder Diffraction Study of CeScSi	147
M.Yokoyama, M.Kosaka, Y.Uwatoko, M.Ohashi, K.Ohoyama, Y.Yamaguchi	
1-2-55 Small-Angle Neutron Scattering Study on CMR Effect of $(\text{La}_{1-x}\text{Tb}_x)_{2/3}\text{Ca}_{1/3}\text{MnO}_3$	148
M.Watahiki, N.Metoki, J.Suzuki, J.Nie, Y.Yamada, M.tachiki	
1-2-56 The Obsevation of a Crystalline Electric Field Excitation in $\text{U}_3\text{Pd}_{20}\text{Si}_6$	150
N.Tateiwa, N.Metoki, Y.Koike, N.Kimura, H.Aoki, T.Komatsubara	

3) Superconductivity

1-3-1 Neutron Scattering Study on $\text{YBa}_2\text{Cu}_3\text{O}_{6-y}$ System near the Quantum Critical Point	153
H.Harashina, M.Kanada, K.Kodama, M.Sato, K.Kakurai	
1-3-2 Neutron Scattering Study of the Pressure Effect on Spin Gap in the Hole-Doped Spin Ladder System $\text{Sr}_{2.5}\text{Ca}_{11.5}\text{Cu}_{24}\text{O}_{41}$	154
J.Akimitsu, T.Nagata, H.Fujino, M.Nishi, K.Kakurai, S.Katano	
1-3-3 Diffraction Studies in Superconductor $\text{YBa}_2\text{Cu}_3\text{O}_{7-x}$	156
A.W.Garrett, T.Nishijima, M.Arai, M.Takahashi, Y.Endoh, K.Tomimoto, S.Tajima, Y.Shiohara	
1-3-4 Structural Study on Novel 2D Superconductor Na.HfNCI	157
S.Shamoto, K.Iizawa, M.Yamada, K.Ohoyama, Y.Yamaguchi, T.Kajitani	
1-3-5 Interplay between Magnetism and Superconductivity in URu_2Si_2	159
T.Honma, Y.Haga, E.Yamamoto, N.Metoki, Y.Koike, H.Ohkuni, Y.Onuki	
1-3-6 Phonon on Novel 2D Superconductor LiZrNCI	161
S.Shamoto, T.Kato, T.Kajitani	
1-3-7 Observation of Vortex Structure in Nb by Small-angle Neutron Scattering ...	162
S.Miyata, K.Osamura, M.Watahiki, J.Suzuki	

4) Amorphous • Liquid

1-4-1 Low-energy Excitations of Glassy Glycerol As Studied by Coherent Inelastic Neutron Scattering	165
I.Tsukushi, T.Kanaya, K.Kaji	
1-4-2 Electron-Ion Correlation Liquid Zinc by Diffraction Method	167
S.Takeda, Y.Kawakita, M.Kanehira, S.Yoshioka	
1-4-3 Temperature and Pressure Effects on Structural Formations in a Ternary Microemulsion	168
M.Nagao, H.Seto, Y.Kawabata, T.Takeda	
1-4-4 Temperature-and Pressure-Induced Lamellar Structure in a Microemulsion System	170
M.Nagao, H.Seto, D.Okuhara, Y.Matsushita	
1-4-5 In-situ SANS Measurements on Medium and Long Range Structure Evolution in Bulk Metallic Glass $\text{Ni}_{15}\text{Pt}_{60}\text{P}_{25}$ near Glass Transition	172
K.Shibata, T.Higuchi, An-Pang Tsai, M.Imai, K.Suzuki	
1-4-6 Formation and Structure of Clusters in 1-Propanol-Water Solution	174
M.Misawa, K.Yoshida, H.Munemura, Y.Hosokawa, K.Maruyama, M.Nagao, M.Imai	

1-4-7 SANS Measurements of Liquid Se	175
M.Inui, K.Maruyama, Y.Kawakita, S.Takeda, M.Imai	
1-4-8 Neutron Spin Echo Studies on Structural Phase Transitions Induced by Temperature and Pressure in a Ternary Complex Fluids involving Amphiphiles	176
Y.Kawabata, M.Nagao, H.Seto, T.Takeda	
1-4-9 Neutron Spin Echo Investigation on the Slow Dynamics in Complex Fluids Involving Amphiphiles	178
T.Takeda, Y.Kawabata, H.Seto, S.K.Ghosh, S.Komura, M.Nagao	
1-4-10 Composition Dependence of Boson Peak Intensity in Polyamine-Polyalcohol Binary Mixtute	180
K.Takeda, K.Harabe, O.Yamamuro, I.Tsukushi, T.Kanaya	
1-4-11 Boson Peaks in Partially-deuterated Alcohol Glasses	182
O.Yamamuro, K.Harabe, I.Tsukushi, T.Kanaya, T.Matsuo	
1-4-12 Dynamical Aspects for Salt Effect on the Distribution of Clusters in 1-Propanol-Water Solution	184
M.Misawa, K.Yoshida, H.Munemura, Y.Hosokawa, K.Maruyama, T.Kajitani	
1-4-13 Neutron Incoherent Inelastic Scattering of Oriented Oleic Acid Crystal	185
T.Yokoyama, N.Achiwa, M.Suzuki	
1-4-14 Density Dependence of Low Energy Dynamics of Densified Vitreous Silica ...	187
Y.Inamura, M.Arai, O.Yamamuro, A.Inaba, N.Kitamura, T.Otomo, T.Matsuo, S.M.Bennington, A.C.Hannon	
5) Material Science	
1-5-1 In Situ Observation of the Tetragonal-Cubic Phase Transition in the ZrO₂-13mol%YO_{1.5} Using High Temperature Neutron Diffraction	191
Y.Hatoyama, T.Oketani, M.Yashima, Y.Yamaguchi, K.Ohoyama	
1-5-2 In Situ Observations of the Structural Changes in Materials at High Temperatures: Rietveld Refinements of Data Obtained at 1550°C in Air	193
M.Yashima, T.Oketani, O.Yokota, Y.Hatoyama, R.Ali, T.Nogami, S.Utsumi, H.Sugawara, M.Ohashi, K.Ohoyama, Y.Yamaguchi	
1-5-3 Neutron Diffraction Study on Nitrogenation of CoTiSn	195
G.Nakamoto, T.Nobata, M.Kurisu, Y.Makihara, Y.Andoh, S.Kawano, M.Ohashi	
1-5-4 High-Temperature Neutron Diffraction Study of CaTiO₃ Perovskite	196
R.Ali, M.Yashima, T.Oketani, T.Nogami, H.Sugawara, K.Ohoyama, Y.Yamaguchi	

1-5-5 Spin-valve MR in $(\text{La}_{0.9}\text{Nd}_{0.1})_{1.4}\text{Sr}_{1.6}\text{Mn}_2\text{O}_7$	197
Y.Moritomo, K.Ohoyama, M.Ohashi	
1-5-6 Structure of a Reentrant Liquid Crystal	198
O.Oishi, S.Miyajima, M.Nagao, M.Imai	
6) Polymer	
1-6-1 PNO Study on Bovine Serum Albumin Gels 2	201
Y.Izumi, K.Soma, K.Aizawa, S.Koizumi, H.Tomimitsu	
1-6-2 Neutron Structure Analysis of Poly(p-phenylene Benzobisoxazole)	202
Y.Takahashi	
1-6-3 Local Mobility of Substituted Polyacetylenes and Its Relationship with Gas Permeability	204
T.Kanaya, M.Teraguchi, T.Masuda, K.Kaji	
1-6-4 Elasticity Effects on Coarsening of Gyroid Domain	205
M.Imai, K.Nakaya, T.Kato	
1-6-5 Flow Effects on Microdomain Structure of Poly(Styrene-b-2-Vinylpyridine) Solutions	206
Y.Takahashi, M.Noda, K.Matsuoka, T.Murayama	
1-6-6 Phase Transition in Block Copolymers with a Looped Phase Diagram	207
T.Hashimoto, H.Hasegawa, M.Takenaka, M.Sawamoto, M.Nagao, M.Imai	
1-6-7 Kinetics of Volume Phase Transition in Poly (N-isopropylacrylamide-co-acrylic acid) Gels	208
M.Shibayama, H.Hirose	
1-6-8 Conformation of a Graft Polymer Chain in Lamellar Microphase-Separated Structure	210
N.Torikai, J.Suzuki, J.Watanabe, Y.Matsushita	
1-6-9 Chain Conformation of a Protein Polypeptide in the Presence of Sodium Dodecyl Sulfate	211
Y.Watanabe, I.Tanaka, M.Imai, Y.Sano, N.Niimura	
1-6-10 Structural Studies of Sol-Gel Transition of Gellan Gum in Water	212
Y.Izumi, Y.Jinbo, K.Soma, S.Saito, M.Nagao, M.Hashimoto, T.Takahashi	
1-6-11 Microstructure Dependence of Pressure Effects on Polymer Miscibility	213
H.Hasegawa, M.Takenaka, T.Hashimoto, M.Nagao, M.Imai	
1-6-12 Aggregation Behavior of Amphiphilic Polymers in Water and Organic Selective Solvents	214
H.Matsuoka, M.Nakano, M.Kubota, M.Deguchi, Y.Yamamoto, H.Yamaoka	

1-6-13 Effect of Concentration Fluctuation on Segmental Motions in Concentrated Solutions of Polyvinylacetate	215
M.Nakazawa,O.Urakawa,K.Adachi	
1-6-14 Large Scale Structure of Microcrystalline Cellulose in Aqueous Suspension ...	216
M.Sugiyama,K.Hara,N.Hiramatsu,H.Iijima	
1-6-15 Application of Contrast-matching Technique to Neutron Reflectivity Study on Bulk Polymer System	217
N.Torikai,Y.Matsushita,K.Soyama,N.Metoki,Y.Morii	
1-6-16 Neutron Spin-echo Study of the Dynamic Behavior of Amphiphilic Diblock Copolymer Micelles in Aqueous Solution	218
Y.Yamamoto,H.Matsuoka,H.Yamaoka	
1-6-17 Neutron Spin Echo Studies on PVA gels	219
T.Kanaya,K.Kaji,Y.Kawabata,M.Nagao,H.Seto,T.Takeda	
1-6-18 Polymerization Effects of Amorphous Polystyrene by Quasi Elastic Neutron Scattering near T_g	221
I.Tsukushi,T.Kanaya,K.Kaji	
1-6-19 Determination of the Density Profile of Amphiphilic Polymer Adsorbed at Solid/Liquid Interface by Neutron Reflectometry	222
H.Endo,K.Kago,R.Yoshitome,K.Matsumoto,H.Matsuoka,H.Yamaoka	
1-6-20 Effects of Bulky Side Group on Thermal Concentration Fluctuations near the Glass Transition Temperature of Polymer Blends	223
H.Takeno,S.Koizumi,T.Hashimoto	
1-6-21 Aggregation Structure of Chains in Uniaxially-oriented Polyethylene Blends of Deuterated and Hydrogenous Species	224
K.Tashiro,R.Tanaka,S.Koizumi	
 7) Biology	
1-7-1 2-1 Photoisomerization of a Cobaloxime Complex	229
H.Imura,T.Ohhara,Y.Ohashi,I.Tanaka,N.Niimura	
1-7-2 Data Collection of Neutron Diffraction from a Single Crystal of Hen Egg-White Lysozyme at pH 4.9	230
S.Fujiwara,Y.Yonezawa,S.Kumazawa,Y.Haga,Y.Minezaki,I.Tanaka,N.Niimura	
1-7-3 Study on Cholesterol's Roles of a Structure Formation in Phospholipid Membranes	231
T.Adachi,H.Takahashi,M.Imai,I.Hatta	

1-7-4 Structural Study of a Proteoglycan by Neutron Scattering	232
Y.Watanabe, Y.Sano, I.Tanaka, N.Niimura	
1-7-5 A-Small-Angle Neutron Scattering Study on the DNA-Binding Protein HU Using Contrast Variation Method	233
S.Fujiwara, Y.Yonezawa, M.Nagao	
1-7-6 Gross Structure of Escherichia coli Outer Membrane Protein, OmpA Solubilized in the Presence of Octylglucoside	234
K.Kameyama, M.Sato, S.Ohnishi, M.Nagao	
1-7-7 Temperature Dependence of Ganglioside Micellar Structure	235
M.Hirai, H.Iwase, T.Hayakawa, S.Arai, S.Mitsuya, Y.Matsushita	
 8) Fundamental Physics • Neutron Optics	
1-8-1 Neutron Interferometry at PNO in JRR-3M	239
H.Tomimitsu, Y.Hasegawa, K.Aizawa	
1-8-2 Observation of Dynamical Diffraction Phase due to Neutron Spin Precession through Ferromagnetic Crystal of Permalloy	241
N.Achiwa, G.Shirozu, S.Tasaki, M.Hino, T.Ebisawa, T.Kawai, K.Kakurai, M.Shiga	
1-8-3 Influence of Rear Face Reflections on Scattering Appearing in the Tail of the Rocking Curve of Channel-Cut Crystals	243
M.Hashimoto, K.Sumitani, S.Nakatani, T.Takahashi	
1-8-4 Measurement of Transverse Coherent Separation of Spin Precessing Neutron Using Spin Splitters	244
M.Hino, T.Ebisawa, S.Tasaki, Y.Otake, H.Tahata, M.Hashimoto, T.Takahashi, N.Achiwa	
1-8-5 Larmor Precession of Bounded Neutron Spin in Multiply Coupled Magnetic Fabry-Perot Film	245
N.Achiwa, M.Hino, S.Tasaki, T.Ebisawa, T.Kawai, D.Yamazaki, G.Shirozu	
1-8-6 Measurement of Spin Precession Angle of Neutron Transmitted Through Magnetic Thin Film with Absorption	246
M.Hino, S.Tasaki, T.Ebisawa, T.Kawai, N.Achiwa, D.Yamazaki	
1-8-7 Modified Spin Echo Method Using Cold Neutron Spin Interferometry with RF Flippers	247
T.Ebisawa, D.Yamazaki, M.Hino, T.Kawai, S.Tasaki, N.Achiwa, Y.Otake	

9) Instruments

1-9-1 An Upgraded Neutron Diffractometer (BIX-III) for Macromolecules with a Neutron Imaging Plate	251
I.Tanaka, K.Kurihara, T.Chatake, Y.Nishimura, Y.Haga, Y.Minezaki, S.Fujiwara, S.Kumazawa, Y.Yonezawa, N.Niimura, R.Bau, A.Suzuki, E.Otani	
1-9-2 Miniature High Pressure Cell for Neutron Scattering	253
A.Onodera, F.Amita, Y.Ishii, Y.Morii	
1-9-3 Performance Test of a System for Simultaneously Generating Triple Extreme Conditions for Neutron Scattering Experiments III	254
A.Moriai, S.Ichimura, A.Ohtomo, S.Kawano, A.Onodera	
1-9-4 Improvement of Neutron Spin Echo Spectrometer at C2-2 of JRR-3M	255
T.Takeda, H.Seto, Y.Kawabata, S.Satoh, M.Furusaka, M.Nagao, H.Yoshizawa	
1-9-5 Production and Neutron Reflectivity of Replica Supermirrors	256
Y.Kawabata, M.Suzuki, S.Tasaki, K.Somemiya	
1-9-6 Hysteresis Loop of the Permalloy/Ge Magnetic Mirror Working under Low External Magnetic Field	257
T.Kawai, M.Hino, S.Tasaki, T.Ebisawa, Y.Otake, N.Achiwa	
1-9-7 Enhancement of Reflectivity of Multilayer Neutron Mirrors by Ion Polishing	258
K.Soyama, W.Ishiyama, K.Murakami	
1-9-8 Preliminary Measurement of Neutron Reflectivity and Transmissivity from a Multilayer mirror	259
S.Tasaki	

10) Etc

1-10-1 VMASTWA20 Project Measurement of Residual Stress	263
K.Tanaka, Y.Akaniwa, M.Hayashi, S.Ohkido, N.Minakawa, Y.Morii	
1-10-2 Measurement of Residual Stress in Al_2O_3/SiC and Al_2O_3/ZrO_2 Composites	264
K.Tanaka, Y.Akaniwa, N.Minakawa, Y.Morii	
1-10-3 Residual Strain Measurements of a Round Steel Bar with a Diameter of 40mm (II)	265
K.Inoue, T.Horikawa, H.Nakamura, N.Minakawa, Y.Morii, N.Ikeda, Rudiono	
1-10-4 Neutron Stress Measurement Using Neutron Imaging Plate	266
T.Sasaki, N.Niimura, Y.Morii, N.Minakawa, Y.Tsuchiya, Y.Yoshioka, Y.Hirose, S.Takago	

2. Neutron Radiography

- 2-1 Instantaneous and Time-Averaged Void Fraction Measurement Using High-Frame-Rate Neutron Radiography** 271
M.Kureta,H.Akimoto
- 2-2 Visualization of Plunging Jet Behavior dropping into Melt** 272
Y.Shibamoto,H.Nakamura,Y.Anoda
- 2-3 Research and Development on Neutron Radiography Technique** 273
M.Matsubayashi
- 2-4 Development and Application of Advanced Neutron Radiography Techniques Using JRR-3M Cold and Thermal Neutron Beams** 275
M.Tamaki,Y.Kukita,Y.Tsuji,K.Oyamatsu,K.Ohkubo,M.Oda,M.Honda,T.Yagi,
T.Funahashi,O.Nishiguchi,Y.Masunaga,K.Tsuchida,M.Matsubayashi
- 2-5 Development of Advanced Neutron Radiography Techniques Using Thermal and Cold Neutrons from JRR-3M**
-Visualization Study on Molten Metal-Water Interaction- 279
K.Mishima,T.Hibiki,Y.Saito,J.Sugimoto,K.Moriyama,M.Matsubayashi
- 2-6 Development of High Spatial Resolution Neutron Radiography System** 289
K.Mochiki,M.Koiso,K.Mitsuno,H.Iwata,Y.Kihara,A.Yamaji,Y.Kimoto,Y.Murata
- 2-7 Neutron Radiography of Plant Sample** 294
T.Nakanishi,J.Furukawa,M.Matsubayashi

3. Prompt Gamma-ray Analysis

- 3-1 Determination of Boron and Silicone in Animal and Fishery Materials by Reactor Neutron Induced Prompt Gamma-ray Analysis** 299
S.Miyamoto,A.Shiomoto,K.Nishimura,C.Yonezawa,H.Matsue,T.Adachi,M.Hoshi
- 3-2 Study on Neutron Induced Prompt Gamma-ray Analysis** 301
C.Yonezawa,H.Matsue
- 3-3 Nuclear and Radiochemical Application of Neutron Absorption Reactions at the Neutron Beam Guide of JRR-3M (II):Development of the Precise Measurement Method for Energy of Neutron Capture Prompt Gamma-Ray**
-Photpeak profile 303
T.Kishikawa,J.Uemura,C.Yonezawa

4. Neutron Activation Analysis

- 4-1 Determination of Sodium and Copper in Saltwater Clam by Activation Analysis** 311
H.Kamioki
- 4-2 Content Levels of the Halogen Elements in the Soil Plant System of the World -Soils of the East/Central Siberia-**..... 312
K.Yuita,Y.Matsuura
- 4-3 Estimation of Passage Rates by Using Lanthanides(Sm and La)As a Particule Marker** 314
M.Matsumoto,S.Miyamoto,N.Yamagishi
- 4-4 Plutonism and Porphyry Copper-type Hydrothermal Activity in the Back-arc Region of the Izu-Ogasawara arc** 315
O.Ishizuka,M.Yuasa,K.Uto,T.Ishi,A.G.Hochstaedter
- 4-5 Impurity Analysis of Hi-Nicalon Type S SiC Fiber** 316
N.Igawa,T.Taguchi,R.Yamada,M.Takeda
- 4-6 Application of Multidimensional Spectrum for Neutron Activation Analysis ...** 317
Y.Hatsukawa,T.Hayakawa,N.Shinohara,M.Ohoshima
- 4-7 Element Analysis of Plant Sample** 319
T.Nakanishi,J.Furukawa,T.Kataoka
- 4-8 Biosynthetic Study of Halogenated Compounds from Marine Algae by Activation Analysis** 323
M.Suzuki,T.Nakano,Y.Takahashi,Y.Noya,T.Ohnishi
- 4-9 Development of Synthetic Multi-element Reference Materials with Pseudo-Biological Matrix and Its Application** 328
Y.Iwata,A.Nakamura
- 4-10 Neutron Activation Analysis of the Extraterrestrial Materials** 334
M.Ebihara,H.Ozaki,P.Kong,T.Uchino,H.Minowa,S.K.Latif,T.Ishii,Y.Oura,
G.W.Kallemeyn,H.Nakahara,S.Yoneda
- 4-11 Evaluation of the k_0 Standardization Neutron Activation Analysis System** 339
Y.Ito,H.Sawahata,F.Sakurai,A.Ohtomo,F.Sasajima

5. Production of Radio Isotope

- 5-1 A Novel Autoradioluminography Technique for Mesuring the Residual Distribution of a Blood Vessel Imaging Contrast Agent in the Whole-Body ...** 345
K.Kobayashi,S.Motoishi,H.Terunuma,T.Imahashi,M.Hatori,A.Shigematsu

5-2	Comparison of Conversion Factor Obtained by Two Different Calibration Methods for Gas Monitors	346
	T.Ohishi,S.Yoshida	
6.Irradiation Test of Reactor Materials		
6-1	Helium Release from Neutron-Irradiated Li₂O Single Crystals	349
	D.Yamaki,T.Tnifuji,K.Noda	
7.Etc		
7-1	Neutron Irradiation Effects of Electrical Properties on LiAlII	353
	H.Sugai,M.Yahagi,H.Hamanaka,S.Uchiyama,K.Kuriyama	
7-2	Standardization of Obsidian Fission-track ages-an attempt to estimate activation rate with Zr and Au monitors	354
	T.Suzuki	
7-3	Recoil Effect in Water-Soluble Macrocyclic Metal Complex System (Continued) (In the Case of Water-Soluble Metal Phthalocyanine Systems)...	358
	H.Shoji	
7-4	Formation of Oxygen Vacancies in Quartz:The Radiation Effect given by Internal α Particles and The Dose Rate Dependence of External γ Rays	362
	S.Toyoda	

1. 中性子散乱 1) 構造・励磁

1. Neutron Scattering 1) Structure・Excitation

This is a blank page.

研究テーマ：強相関電子系の中性子散乱による研究

表題：LaCrO₃の粉末中性子回折

1-1-1 Neutron Powder Diffraction Study of LaCrO₃

K. Oikawa, T. Kamiyama¹, T. Hashimoto², Y. Shimojo and Y. Morii

Advanced Science Research Center, Japan Atomic Energy Research Institute, Tokai, Ibaraki 319-1195

¹Institute of Materials Science, University of Tsukuba, Tennodai, Tsukuba, Ibaraki 305-8573

²Department of Applied Physics, College of Humanities and Sciences, Nihon University, Setagaya-ku, Tokyo 156-8550

A perovskite-type oxide, La_{1-x}Sr_xCrO₃, is one of the most important material for the industrial applications, e.g., a separator for SOFC, heat resistant ceramics, and so on. It is well known that LaCrO₃ has phase transitions at $T = 15, 260$ and 1030 °C. The first one is due to a magnetic order-disorder transition, the second and the third ones are due to a structural phase transitions^{1, 2)}. The physical properties such as heat capacity and thermal conductivity of LaCrO₃ at a high temperature region have been studied widely, but the precise crystal structure at high temperature region has not been investigated.

Recently, Hashimoto et al. found a negative volume expansion of -0.323 cm³/mol at around 240 °C by high-temperature X-ray diffraction. They also showed the structural phase transition of the LaCrO₃ under high pressure at room temperature using synchrotron X-ray powder diffraction³⁾. They discussed the thermodynamic relation between high-pressure phase and high-temperature phase. To reveal the mechanism of the volume compression of LaCrO₃ at the phase transition, neutron powder diffraction studies are indispensable because the positional parameters of oxygen atoms have to be determined precisely.

Neutron powder diffraction experiments were carried out on HRPD from RT to 410 °C with a high-temperature furnace. The sample was contained in a V holder. The temperature was monitored by a Chromel-Alumel thermocouple and was kept within ± 0.5 K during the measurement. The 16 diffraction data were analyzed by the Rietveld method with RIETAN. Neutron wavelength was refined to be 1.16251 Å. Typical R_{wp} and R_b were ca. 7 % and 3 % respectively. Figure 1 shows

refined lattice constants of an orthorhombic phase and molar volumes vs. temperature. The ΔV was estimated to be -0.0462 cm³/mol at 260 °C, but this value is much smaller than the value reported by Hashimoto et al.³⁾.

The other structural information, such as bond lengths and bond angles, was calculated by ORFFE. The whole understanding of the origin of the volume compression at the phase transition is in progress. Neutron powder diffraction studies on the two-phase region at temperatures between 230 °C and 290 °C using a longer wavelength are planned in near future.

References

- 1) A. C. Momin, E. B. Mirza and M. D. Mathews, J. Mat. Sci. Lett., **10** (1991) 1246.
- 2) S. A. Howard, J. Yau and H. U. Anderson, J. Am. Ceram. Soc. **75** (1991) 1685.
- 3) T. Hashimoto, N. Matsushita, Y. Murakami, N. Kojima, K. Yoshida, H. Tagawa, M. Dokiya and T. Kikegawa, Solid State Communications **108** (1998) 691.

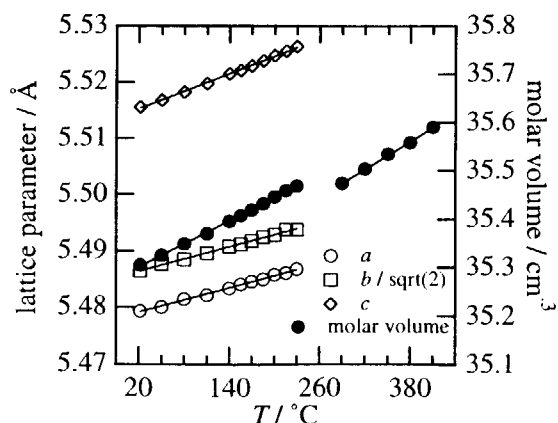


Fig. 1. Refined lattice constants of orthorhombic phase and molar volumes.

研究テーマ：強相関電子系の中性子散乱による研究

表題：PbZrO₃の強誘電相における秩序パラメータの温度依存性

1-1-2 TEMPERATURE DEPENDENCE OF ORDER PARAMETERS IN THE ANTIFERROELECTRIC PHASE OF PbZrO₃

S. Katano and H. Fujishita¹

ASRC, Japan Atomic Energy Research Institute, Tokai, Ibaraki 319-1195

¹ Department of Physics, Kanazawa University, Kanazawa 920-1192

In the shift-type structural phase transitions, the order parameters are atomic shifts, where the superlattice-reflection intensities, the lattice distortion and the birefringence usually show the temperature dependence which is proportional to the square of the order parameters. The temperature dependence of these quantities in the shift-type antiferroelectric phase of PbZrO₃ were measured above room temperature, and the relationships to the order parameter mentioned above were confirmed. Their temperature dependence were furthermore well explained by a phenomenological theory for the first order phase transition.¹⁻⁴⁾

Although physical properties of PbZrO₃ have not been extensively measured below room temperature, recently its crystal structure was studied at 100K by single crystal X-ray diffraction.⁵⁾ The result indicated that the deviation of Pb shifts from the average value is reverse to that above room temperature. Accordingly, the deviation vanishes at around 200K, and the distortion of the sublattice at 100K is significantly different from the line that is extended from room temperature. To examine the existence of such anomalies and the relationships to the order parameters further, neutron diffraction experiments were performed over a wide temperature range.

Neutron diffraction patterns were obtained using a powder diffractometer with 64 detectors installed at JRR-3M. The incident neutron wavelength was 1.163Å. The collimation was 6'-20'-6'. The powder sample was attached in a refrigerator with a closed-cycle

He gas system. The intensities were collected by the scan of the counter system with 0.05° step 2θ over the angle of 2.5°. The data in the 2θ range of 5.0 - 150.0° were analyzed by the Rietveld method.

Figure 1 displays the result of the profile fit of the powder neutron diffraction pattern at 100K. The space group was Pbam (No.55).^{6,7)} The R factors and the lattice parameters were Rwp = 8.8%, Rp = 6.5 % and RI = 2.5 %, *a* = 5.8741(1), *b* = 11.7759(2) and *c* = 8.1969(2). The structure obtained at 100K is almost the same as the structure obtained previously at 100K by X-ray diffraction⁵⁾, except the coordinates Pb1x and Pb2x. The Pb1x and Pb2x are in opposite coordinates in these two structural studies.

The fractional coordinates Pb1x and Pb2x are obtained over a wide temperature range in the present experiment, and they are shown in Fig. 2. The coordinates obtained in the previous powder neutron diffraction^{6,7)} and the single crystal X-ray diffraction⁵⁾ are also shown in the figure. The solid line indicates the square-root of the intensity of the superlattice reflection scaled reasonably with the coordinates. Since the lattice parameter *a* shows only a slight temperature dependence; the changes of the fractional coordinates are directly in proportion to the atomic shifts - the order parameters. These shifts are included in the displacements associated with the antiferroelectric lattice vibrational mode Σ₃(TO) with the wave vector (1/4 1/4 0).²⁾ Because these shifts do not couple with other shifts associated with the lattice vibrational mode

R_{25} ,²⁾ they would not be affected by an existence of those order parameters. Thus we can discuss these shifts by the antiferroelectric order parameter alone. In the present experiments the coordinates Pb1x and Pb2x showed no anomalous temperature dependence. In addition, no clear deviations from the simple phenomenological theory could be detected for the temperature dependence of the coordinates Pb1x and Pb2x. These shows a sharp contrast with the results proposed in the single crystal X-ray diffraction experiments,⁵⁾ as was described before.

Temperature dependence of birefringence in the plane perpendicular to the ab plane, $n_p = n_c - (n_a + n_b)/2$, was reported to be in proportion to that of lattice distortions⁴⁾ and also to that of squares of the Pb shift¹⁾; however, the birefringence in the ab plane $\Delta n_s = n_b - n_a$ was found to show a different temperature dependence with them.^{1,4)} In the present experiment Δn_s above room temperature show the temperature dependence in proportion to that of the superlattice-reflection intensity at R points, as shown in the followings. The fit of Δn_s with the temperature dependence of antiferroelectric superlattice-reflection intensity with the wave vector $(1/4 \ 1/4 \ 0)$, which is identical with the previous fit by the temperature dependence of the square of the Pb shift,¹⁾ is not good. Rather, the fit by the temperature dependence of superlattice-reflection intensity with the wave vector $(1/2 \ 1/2 \ 1/2)$ shows a reasonable result. The temperature dependence of Δn_s is, thus, well in proportion to that of the superlattice-reflection intensity caused by the order parameter of atomic displacements associated with the lattice vibrational mode R_{25} . It might be difficult to understand, however, that the birefringence Δn_s and the square of the antiferroelectric order parameter have the different temperature dependence, because the Δn_s is usually in proportion to the lattice distortion in the ab -plane.

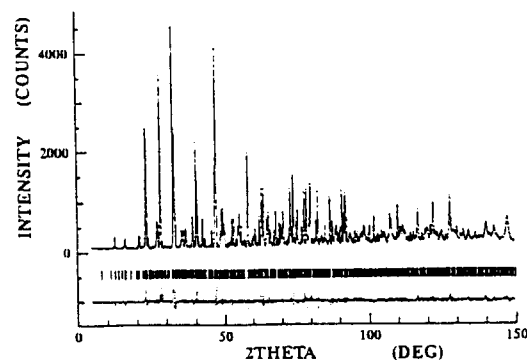


Fig. 1. Neutron Rietveld refinement patterns for PbZrO_3 at 100K.

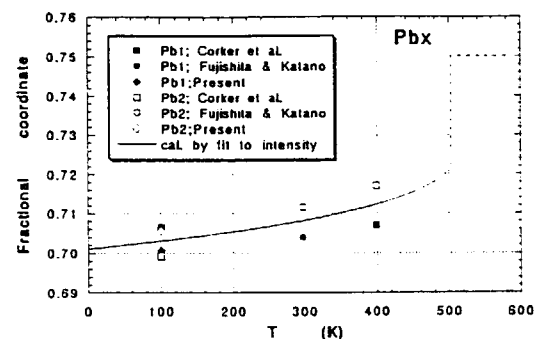


Fig. 2. Temperature dependence of fractional coordinates of the Pb atoms along the a direction.

References

- [1] R. W. Whatmore and A. M. Glazer, *J Phys. C* 12, 1505 (1979).
- [2] H. Fujishita and S. Hoshino, *J. Phys. Soc. Jpn.* 53, 226 (1984).
- [3] E. Sawaguchi, *J. Phys. Soc. Jpn.* 7, 110 (1952).
- [4] F. Jona, G. Shirane and R. Pepinsky, *Phys. Rev.* 97, 1584 (1955).
- [5] D.L. Corker, A. M. Glazer, J. Dec, K. Roleder and R. W. Whatmore, *Acta Cryst. B* 53, 135 (1997).
- [6] H. Fujishita, Y. Shiozaki, N. Achiwa and E. Sawaguchi, *J. Phys. Soc. Jpn.* 51, 3583 (1982).
- [7] H. Fujishita and S. Katano, *J. Phys. Soc. Jpn.* 66 (1997) 3484.

研究テーマ：水素結合中の水素原子核のイメージング

表題：マキシмум・エントロピー法による KDP における水素結合中の水素原子核のイメージング

1-1-3

Imaging of Hydrogen Nucleus in the Hydrogen Bond of KDP by Maximum Entropy Method

Shigefumi YAMAMURA, Shintaro KUMAZAWA¹, Eiji NISHIBORI², Masaki TAKATA³,
Makoto SAKATA², Yoko SUGAWARA, Yoshinobu ISHII¹ and Yukio MORII¹

School of Science, Kitasato University, Sagami-hara 228-8555, Japan

¹Advanced Science Research Center, JAERI, Tokai, Ibaraki 319-1195, Japan

²Department of Applied Physics, Nagoya University, Nagoya 464-8603, Japan

³Department of Material Science, Shimane University, Matsue 690-8504, Japan

For the purpose of examining the nature of hydrogen bond, the nuclear density distribution of KH_2PO_4 (KDP) was obtained by maximum entropy method (MEM)¹⁾. For MEM analyses, neutron powder diffraction data were used without replacing proton by deuteron, in spite of the large incoherent scattering from protons. Because there is strong demand to investigate both protonated and deuterated powder specimens in order to understand the behavior of hydrogen atoms, particularly, for the materials with large isotope effects such as KDP.

The neutron powder diffraction data of KDP were collected at room temperature (RT) and 10 K using HRPD diffractometer installed at the JRR-3M reactor with the neutron wavelength of 1.16 Å. For the accurate evaluation of integrated intensities, each data point was measured with three detectors to improve profile shapes²⁾. The powder data were analyzed by a sophisticated method which is the combination of Rietveld method and MEM^{3,4)}. For the analyses, 255 reflections for RT and 446 reflections for 10 K were used, which corresponded to 0.62 Å resolution in real space for both data. The reliability factor of Rietveld analysis based on Bragg intensities, R_B , was 4.5% for RT and 3.3% for 10 K, respectively. The treatment for the negative coherent scattering length of protons in MEM analysis is described elsewhere⁵⁾.

The nuclear density distributions of hydrogen bond in KDP obtained by MEM are shown in Fig. 1. In Fig. 1(a), it is clearly shown that the distribution of proton has two maxima between two oxygen nuclei. While the proton distribution at 10 K as shown in Fig. 1(b) exhibits single maximum. These figures provide a direct observation of disordered and ordered states of protons.

The present work demonstrated that it is possible to determine the proton distribution in crystalline materials by neutron powder diffraction data, which will be beneficial for studying hydrogen compounds.

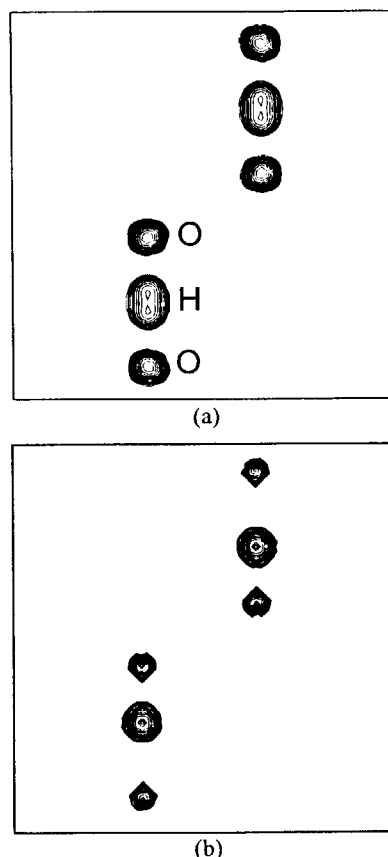


Fig. 1 Nuclear density distributions of hydrogen bond in KDP obtained by MEM at (a) RT, (b) 10 K.

References

- [1] M. Sakata and M. Sato: *Acta Cryst.* **A46** (1990) 263-270.
- [2] S. Kumazawa et al.: JAERI NSL Report April 1995 - March 1996, 99.
- [3] M. Takata et al.: *Nature* **377** (1995) 46-49.
- [4] F. Izumi et al.: *Proc. Int. School on Powder Diffraction*, Allied Publishers, New Delhi (1998) pp.24-36.
- [5] M. Sakata et al.: *J. Appl. Cryst.* **26** (1993) 159-165.

研究テーマ：水素結合中の水素原子核のイメージング

表題：マキシマム・エントロピー法による ADP における水素結合

1-1-4 Hydrogen Bond of ADP by the Maximum Entropy Method

Shigefumi YAMAMURA, Shintaro KUMAZAWA¹, Eiji NISHIBORI², Masaki TAKATA³,
Makoto SAKATA², Yoko SUGAWARA, Yoshinobu ISHII¹ and Yukio MORII¹

School of Science, Kitasato University, Sagamihara 228-8555, Japan

¹Advanced Science Research Center, JAERI, Tokai, Ibaraki 319-1195, Japan²Department of Applied Physics, Nagoya University, Nagoya 464-8603, Japan³Department of Material Science, Shimane University, Matsue 690-8504, Japan

In order to examine the nature of hydrogen bond, it is important to study various types of hydrogen bonds. It is said that $\text{NH}_4\text{H}_2\text{PO}_4$ (ADP) has two kinds of hydrogen bond, one is between O-O and the other is between N-O. In a series of studies which include the present study, it is aimed to investigate both nuclear and electron density distributions for paraelectric and antiferroelectric phases of ADP. In this report, the preliminary results of nuclear density distribution of ADP, which is obtained by a sophisticated imaging technique called the Maximum Entropy Method (MEM)¹⁾, are given. To obtain the nuclear density distribution of ADP, neutron powder diffraction data were used without replacing proton by deuteron, in spite of the large incoherent scattering from protons. It is a part of purpose to demonstrate that there exists no real problem to determine hydrogen nuclear densities from neutron powder data with non-deuterated specimen.

The neutron powder diffraction data of ADP were collected at room temperature using HRPD diffractometer installed at the JRR-3M reactor with the neutron wavelength of 1.16 Å. For the accurate evaluation of integrated intensities, each data point was measured with three detectors to improve profile shapes²⁾. The powder data were analyzed by a sophisticated method which is the combination of Rietveld method and MEM³⁾. For the analyses, 169 reflections which corresponded to 0.74 Å resolution in real space were used. The reliability factor of Rietveld analysis based on Bragg intensities, R_B , was 9.0 %. The treatment for the negative coherent scattering length of protons in MEM analysis has been established⁴⁾.

The nuclear density distributions of hydrogen bond in ADP obtained by MEM are shown in Fig. 1. In Fig. 1(a), it is not very clear whether the distribution of proton has two maxima but the nuclear density of hydrogen is wide spread between two oxygen nuclei. While the proton distribution between N-O as shown in Fig. 1(b) exhibits single maximum near to nitrogen. Furthermore it is very clearly shown that the

location of protons is slightly off the N-O line. It implies that bond nature of O-O and N-O should be rather different.

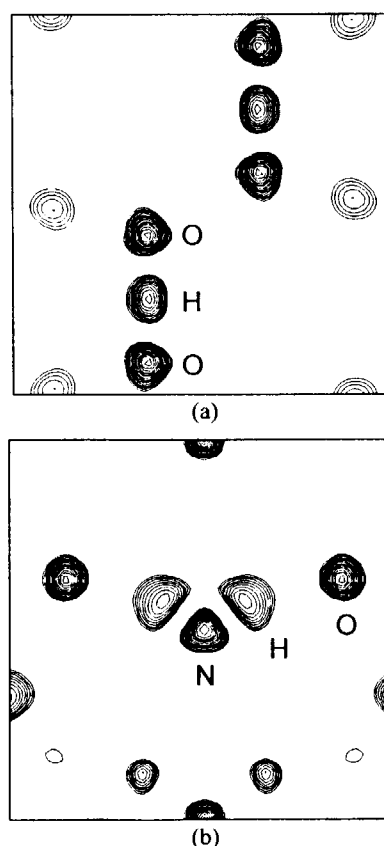


Fig. 1 Nuclear density distributions of hydrogen bond in ADP at room temperature obtained by MEM; (a) O-O bond, (b) N-O bond.

References

- [1] M. Sakata and M. Sato: Acta Cryst. **A46** (1990) 263-270.
- [2] S. Kumazawa et al.: JAERI NSL Report April 1995 - March 1996, 99.
- [3] M. Takata et al.: Nature **377** (1995) 46-49.
- [4] M. Sakata et al.: J. Appl. Cryst. **26** (1993) 159-165.

研究テーマ：強相関電子系の中性子散乱による研究

表題：硫化スピネル CuIr_2S_4 の金属-非金属転移に対する中性子散乱

1-1-5 Neutron scattering on the metal-insulator transition in thiospinel CuIr_2S_4

S. Katano, K. Oikawa and T. Matsumoto¹

ASRC, Japan Atomic Energy Research Institute, Tokai, Ibaraki 319-1195

¹ National Research Institute for Metals, Sengen, Tsukuba 305-0003

Chalcogenide spinel compounds have been extensively studied for their unique crystal structure, magnetism, superconductivity, and so forth. Thiospinel CuIr_2S_4 , which was newly synthesized, is metallic at room temperature, but exhibits a sharp metal-insulator transition at 230 K [1]. This transition accompanies a first-order structural change from cubic to probably tetragonal. Paramagnetic susceptibility at higher temperatures sharply drops at the transition, and becomes diamagnetic. In this insulating phase the X-ray diffraction study suggests a formation of some superstructure. To investigate such superstructures further, and also to examine magnetic properties - possibilities of an antiferromagnetic ordering, or of a spin-singlet state, etc., neutron scattering experiments have been carried out.

The sample was prepared by heating of mixed powder at 850°C for 10 days in a sealed quartz tube. This powdered sample was placed in a cylindrical vanadium holder of the wall thickness of 0.05 mm, and then enclosed in an aluminum can filled with helium exchange gas. The temperature was lowered down to 7 K using a standard closed-cycle refrigerator. Neutron scattering experiments were performed on TAS-1 (a triple-axis spectrometer) in a diffraction arrangement using PG crystals with the neutron energy of 14.7 meV. Inelastic scattering was done with the incident energy of 30.5 and 41 meV at the position of (3/2 3/2 3/2) which corresponds with the superlattice peaks suggested in the previous X-ray dif-

fraction.

Figure shows the temperature dependence of the diffraction pattern around the (220) reflection. The structural transition reported previously was apparently observed; however, reflections which correspond to the superstructures were not detected within the experimental accuracy. The reason of this difference is not clear at present. There may be some delicate problems in the sample preparation. In the present inelastic experiments, no clear excitation peaks were observed over a wide range of energy.

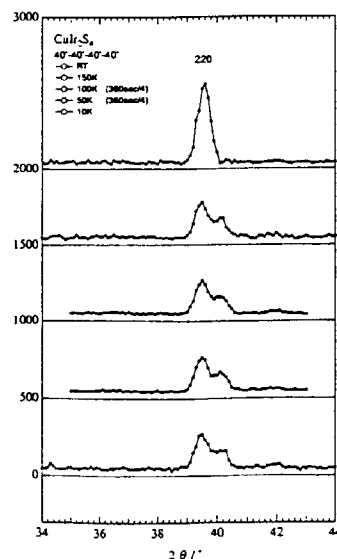


Fig. 1. Diffraction pattern around (220) as a function of temperature.

Reference

- [1] T. Furubayashi, T. Matsumoto, T. Hagino and S. Nagata, J. Phys. Soc. Jpn. 63, 3333 (1994).

研究テーマ：リラクサーPNZの格子振動

表 題：Pb(Zn_{1/3}Nb_{2/3})O₃プロペスカイトの格子振動1-1-6 Lattice dynamics of disordered Perovskite Pb(Zn_{1/3}Nb_{2/3})O₃I. Tomeno, S. Shimanuki, Y. Tsunoda¹, and Y. Ishii²

Research and Development Center, Toshiba Corporation, Saiwai-ku, Kawasaki 210-8582

¹School of Science and Engineering, Waseda University, Shinjuku-ku, Tokyo 169-8555²Japan Atomic Energy Research Institute, Tokai, Ibaraki 319-11

Lead zinc niobate Pb(Zn_{1/3}Nb_{2/3})O₃ (PZN) is typical of relaxor ferroelectrics. PZN has a disordered perovskite-type ABO₃ structure where the B site is randomly occupied by Zn²⁺ or Nb⁵⁺ ions. PZN undergoes a structural phase transition from the low-temperature rhombohedral phase to the high-temperature cubic phase.

Inelastic neutron-scattering measurements were carried out using a triple-axis spectrometer TAS-1 at JRR-3M. PZN single crystals used in this study were grown from a PbO flux by the Bridgman method and had a volume of approximately 0.6 cm³. As ferroelectric domains disappear on warming up, the [100] Bragg intensity is reduced significantly by an extinction effect. The Curie temperature T_c determined in this manner is 380 K.

Figure 1 shows examples of the energy spectra for the [ζ00] TA phonons at ζ=0.1 and 0.5 measured at 470 K. The phonons are well defined in the range ζ ≤ 0.2. The linewidth for the TA phonon becomes sharp in the long wavelength limit. In contrast, the phonon linewidth is extremely broad in the range 0.3 ≤ ζ ≤ 0.5. The phonon lineshape for ζ=0.5 is significantly asymmetric, and its background increases on the high-energy side. The random distribution at the B site has a profound influence on the corresponding short-wavelength phonon. A overdamped phonon picture cannot explain the observed profiles.

Figure 2 shows the phonon dispersion of the TA branch measured at 300, 420 and 470 K along the [ζ00] direction. A combination with preliminary measurements along the [ζζ0]

direction suggests that PZN exhibits relatively isotropic TA phonons. The dispersion relation is practically temperature independent. In typical perovskites, the soft TO mode interacts with the TA mode. The present results suggest that the soft mode behavior is absent in the diffusive phase transition.

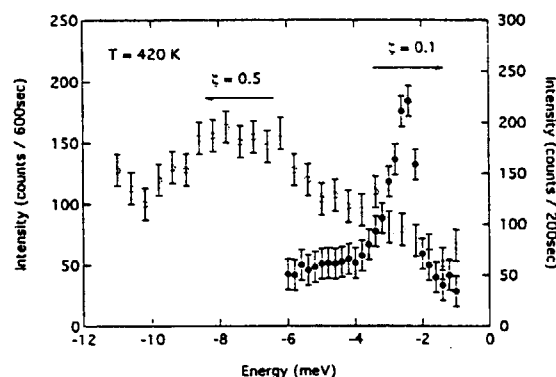


Fig.1 Energy spectra for the [ζ00] TA phonons at ζ=0.1 and 0.5 measured at 470 K.

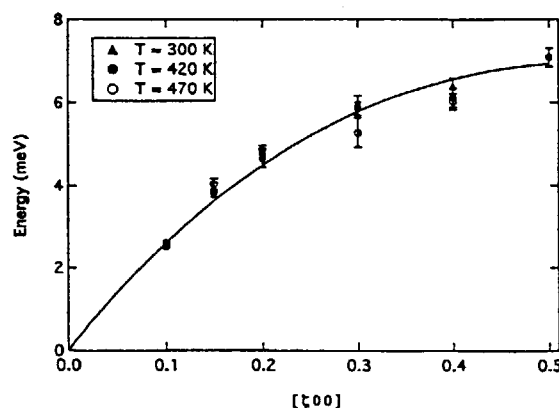


Fig.2 Phonon dispersion relationship of the TA branch. The curve for 420 K is a guide to the eye.

研究テーマ：精密中性子光学実験法によるNi基超合金単結晶の観察

表題：クリープ損傷を施したNi基超合金CMSX-4の構造評価 (III)

1-1-7

Characterization of single-crystal Ni-base superalloy CMSX-4 with creep damage (III)

K. Aizawa, H. Tomimitsu, H. Tamaki¹ and A. Yoshinari¹

Japan Atomic Energy Research Institute, Tokai, Ibaraki, 319-1195

¹Hitachi Research Laboratory, Hitachi, Ltd., Hitachi, Ibaraki, 317-8511

The single crystal Ni-base superalloys have been developed to apply to the blade of gas turbines, which can be operated at higher temperature to achieve higher efficiency. The excellent mechanical properties of these materials at high temperature arise from its morphology. After a standard heat treatment, the γ' phase regularly precipitates with cuboidal shape, which is an ordered phase with $L1_2$ structure, in γ matrix which is a disordered phase with a f.c.c structure. When the tensile stress is loaded, the morphology of this material changes to lamella structure which is aligned normal to the stress axis. So, the morphology is related to the strength of this materials. Therefore, the characterization of morphology of superalloy is very important.

In order to check the possibility of nondestructive testing to the expected life of operated blades made from Ni-base superalloy, we have applied very small-angle neutron scattering (VSANS) experiments to the CMSX-4 superalloy with creep damage as a model case.^{1,2)} In this study, to imitate turbine blades, coating samples, of which one side were treated by thermal barrier coating which deposited alloy layer (CoNiCrAlY) with 0.3 mm and ceramic layer ($ZrO_2-8Y_2O_3$) with 0.1 mm, were measured. The VSANS measurements were carried out using PNO instrument with the q-range ($q=2\pi\theta/\lambda$, θ : scattering angle, λ : neutron wavelength) of 2×10^{-4} – $6 \times 10^{-2} \text{ nm}^{-1}$.

Figure 1 shows the smeared VSANS intensity of coated single crystal CMSX-4 with damage rate from 10% to 85% for creep rupture time. Incident neutron beams were parallel to [100] direction of a sample. Due to large scale particle of coating materials, additional intensity added in a low q-region. However, a contrast of the 1st peak of lamella structure are still good. The dependence of creep damage rate for rupture time of averaged period of lamella structure, d , are shown in Fig. 2 together with the data of non-coating sample and creep curve. The agreement for d between non coating and coating samples is good. This means the influence of the coating for the evaluation of period may be neglected due to high penetrability of neutron. We emphasize that the dependence of d is similar with that of strain. This means the

evolution of the lamella structure correlates the creep strain. Finally, we mention that the all VSANS curves of the coating materials obtained by subtracting the non coating data from coating data lie on a curve. We assumed that the scattering of the coating materials is isotropic and performed a infinite slit height correction. According to Guinier analysis, the radius of gyration of the scatterer is obtained about 2.0 μm .

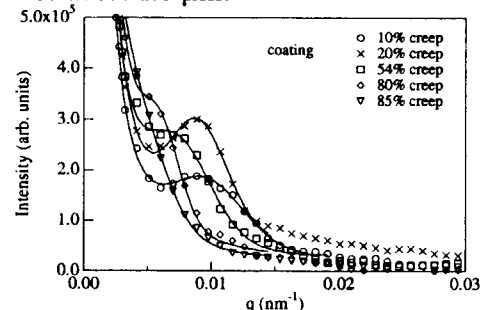


Fig.1 The dependence of VSANS cross section for coating sample with creep damage.

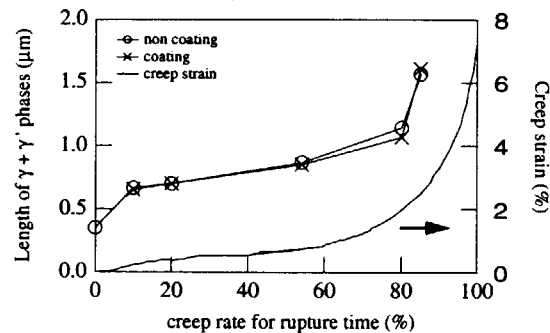


Fig. 2 The dependence of the average distance of lamella structure as a function of damage rate for creep rupture time and creep strain curve.

References

- [1] K. Aizawa, H. Tomimitsu, H. Tamaki and A. Yoshinari: (PROGRESS REPORT ON NEUTRON SCATTERING RESEARCH, April 1, 1996-March 31), 1997, 54
- [2] K. Aizawa, H. Tomimitsu, H. Tamaki and A. Yoshinari: (PROGRESS REPORT ON NEUTRON SCATTERING RESEARCH, April 1, 1997-March 31), 1998, 93

研究テーマ：少数キャリア系 Ce モノプニクタイトの格子振動
表題：少数キャリア系 CeSb のフォノン分散

1-1-8 Phonon Dispersions in the Low-Carrier Density System CeSb

K. Iwasa, M. Kohgi, Y. Haga¹, T. Osakabe¹, M. Braden², J.-M. Mignot² and T. Suzuki³

Department of Physics, Tokyo Metropolitan University, Hachioji, Tokyo 192-0397, Japan

¹ *ASRC, Japan Atomic Energy Research Institute, Tokai, Ibaraki 319-1195, Japan*

² *Laboratoire Léon Brillouin, CEA/Saclay, 91191 Gif-sur-Yvette Cedex, France*

³ *Tsukuba Institute of Science and Technology, Tsukuba, Ibaraki 300-0819, Japan*

Cerium monopnictides (CeX, X = P, As, Sb, Bi) exhibit typical heavy-fermion anomalies despite their extremely low carrier concentration of less than 10^{-2} per Ce ion.¹⁾ They also exhibit complex magnetic structures with various periods of stacking of ferromagnetic (001) planes under high pressures or under magnetic fields at low temperatures.²⁻³⁾ Although the ground state crystal-field level of Ce ions is Γ_7 with a magnetic moment of $0.7\mu_B$, some of the Ce-ion layers exhibit a large magnetic moment of $2\mu_B$. It was confirmed that the magnetic form factor of the Ce ions with the large moment is quite close to the calculated one for the Γ_8 crystal-field state.⁴⁾ The magnetically polarized Ce ions in CeX are considered to be due to strong p-f mixing effect and localization of low-density carrier.⁵⁾

A recent low-temperature X-ray diffraction experiment revealed that crystal-lattice modulations appear in magnetically ordered phases of CeSb.⁶⁾ This phenomenon is interpreted as the result of strong p-f mixing effect of Γ_8 -like state on the crystal lattice.

In order to check effects of low-carrier density and p-f mixing on phonons, CeSb were studied by inelastic neutron scattering at TOPAN (6G) in JRR-3M and at 2T in Orphée reactor of LLB. Figure 1 shows the several dispersions measured at 300 K. A longitudinal optic mode is dispersive in small q region and is degenerate with transverse one at Γ point. This phenomenon

is explained by a model based on a screened Coulomb potential and Born-von Kármán force constants.⁷⁾ Thus a screening effect by low-density carriers is found in this system. Although effects on phonons due to p-f mixing have not been clear yet, temperature dependencies of phonons should be measured.

References

- 1) T. Suzuki: Jpn. J. Appl. Phys. Series 8 (1993) 267.
- 2) see for example, M. Kohgi *et al.*: J. Phys. Soc. Jpn. **65** (1996) Suppl. B 99.
- 3) T. Chattopadhyay *et al.*: Phys. Rev. **B49** (1994) 15096.
- 4) K. Iwasa *et al.*: Physica B **259-261** (1999) 285.
- 5) T. Kasuya and T. Suzuki: J. Phys. Soc. Jpn. **61** (1992) 2628.
- 6) K. Iwasa *et al.*: unpublished.
- 7) N. Wakabayashi and A. Furrer: Phys. Rev. **B13** (1976) 4343.

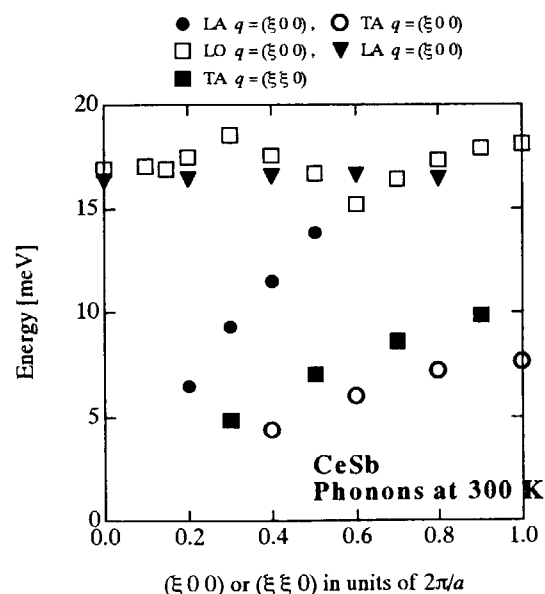


Figure 1. Phonon dispersions of CeSb measured at 300 K.

研究テーマ：Yb₄As₃ の価数秩序構造相転移とフォノン分散
表題：電荷秩序を示す Yb₄As₃ におけるフォノン分散

1-1-9 Phonon Dispersions in the Charge Ordering System Yb₄As₃

K. Iwasa, M. Kohgi, A. Ochiai¹, H. Aoki² and T. Suzuki³

Department of Physics, Tokyo Metropolitan University, Hachioji, Tokyo 192-0397, Japan

¹ *Department of Material Science and Technology, Niigata University, Niigata 950-2181, Japan*

² *Graduate School of Science and Technology, Niigata University, Niigata 950-2181, Japan*

³ *Tsukuba Institute of Science and Technology, Tsukuba, Ibaraki 300-0819, Japan*

Yb₄As₃ has been attracted attention because of its unusual electronic properties. Heavy-fermion-like anomalies have been observed in spite of extremely low carrier concentration.¹⁾ This compound exhibits a structural phase transition at $T_C = 288$ K. Its crystal structure is an anti-Th₃P₄-type cubic one in the high-temperature phase and transforms to a trigonal one below T_C , which is realized by shrinking slightly along the [111] direction of the cubic structure. Magnetic susceptibility measurements or other experimental results suggest that the 4f-electron state is valence fluctuating in the cubic phase and a charge ordered state below T_C expressed as Yb³⁺Yb²⁺₃As₃.

Neutron scattering experiments have also been performed to investigate the charge ordering and the magnetic properties of 4f electrons at low temperature. Polarized-neutron diffraction experiments revealed that the charge ordered state is composed of the Yb³⁺ ions aligning along the shrinking [111] direction and the Yb²⁺ ions on the other lattice sites.²⁾ Magnetic excitations within this one-dimensional chain of Yb³⁺ ions take important roles of low-temperature physical properties in this system.³⁾

Ultrasonic measurement shows that the elastic constant, C_{44} , exhibits a strong decrease near T_C ,⁴⁾ which may indicate a softening of phonons. Increase of entropy with increasing

temperature above T_C was observed in specific heat measurement.⁵⁾ This phenomenon seems to be a precursor of crystal-lattice transformation due to the short-range charge order. Thus, in order to investigate the mechanism of the charge ordering in this system, a measurement of phonons by inelastic neutron scattering should be performed in a temperature range around T_C .

We have performed measurements of lower-energy phonons with propagation vectors along the principal axes using TOPAN (6G) spectrometer. In figure 1, several phonon dispersions along the [111] and [100] directions measured at 300 K are shown. Open squares and filled circles represent the data corresponding to a longitudinal acoustic (LA) mode and a transverse acoustic (TA) one, respectively. Their energies are close to each other, in contrast to usual cases where LA modes take higher energies than those of TA mode. In Sm_{0.75}Y_{0.25}S and TmSe which are typical valence fluctuating systems, the LA phonons propagating along the cubic [111] direction show softening and their energies become slightly lower than those of the TA phonons propagating along the same direction.⁶⁾ The fact that the energy of LA mode is close to that of TA mode in Yb₄As₃ is thought to be a phenomenon of a phonon anomaly as the case in valence fluctuating systems like Sm_{0.75}Y_{0.25}S and TmSe. From the data points near the Brillouin zone center, the elastic constants can be estimated

as $C_{44} = 2.5 \times 10^{11}$ erg/cm³ and $(C_{11} - C_{12})/2 = 5.0 \times 10^{11}$ erg/cm³. The Ultrasonic study reported $C_{44} = 1.83 \times 10^{11}$ erg/cm³ and $(C_{11} - C_{12})/2 = 4.96 \times 10^{11}$ erg/cm³.⁴⁾ The values of C_{44} estimated in this neutron experiment is larger than that by ultrasonic measurement. This fact indicates that the softening of TA phonons along the [100] is expected to occur in the q region closer to the zone center than the measured points of this neutron study.

In order to elucidate the role of phonons for the charge ordering accompanied by the structural phase transition, more detailed inelastic neutron scattering measurements are necessary.

References

- 1) A. Ochiai *et al.*: J. Phys. Soc. Jpn. **59** (1990) 4129.
- 2) M. Kohgi *et al.*: Physica B **230-232** (1997) 638; K. Iwasa *et al.*: unpublished.
- 3) M. Kohgi *et al.*: Phys. Rev. **B56** (1997) R11388.
- 4) T. Goto *et al.*: Physica B **230-232** (1997) 702.
- 5) A. Ochiai *et al.*: Physica B **186-188** (1993) 437.
- 6) H. A. Mook and R. M. Nicklow: Phys. Rev. **B20** (1979) 1656; H. A. Mook and F. Holtzberg: *Valence Fluctuations in Solids* (North Holland, 1981) p. 113.

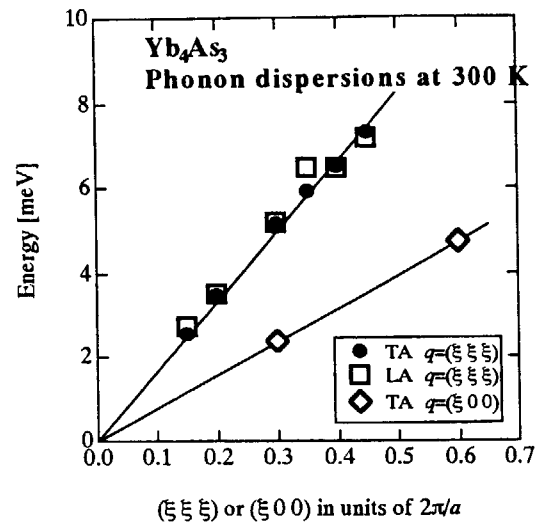


Figure 1. Phonon dispersions of Yb_4As_3 measured at 300 K. Solid lines are fitted linear functions.

研究テーマ：3次元骨格を有するリチウムインターカレーション材料の探索

表題：3次元骨格を有するリチウムインターカレーション材料の探索

1-1-10 Investigation of Lithium Intercalation Material with 3-Dimensional Framework

T. Suzuki, H. Ohokawa, M. Saito, K. Uematsu, K. Ohoyama¹, K. Toda and M. Sato*Department of Chemistry and Chemical Engineering, Faculty of Engineering,
Niigata University, Ikarashi 2 no-cho 8050, Niigata 950-2181, Japan*¹*Institute for Material Research, Tohoku University, Katahira 2-1-1, Aoba-ku,
Sendai 980-0812, Japan*

Cathode materials exhibiting high open voltage, high charge capacity and good cycle property at ambient temperature are expected in order to develop new rechargeable lithium battery systems. β - $\text{Fe}_2(\text{SO}_4)_3$ type $\text{Li}_3\text{V}_2(\text{PO}_4)_3$ has features of high ionic conductivity and easily oxidizable or reduceable element. The fast ion transport of this compound is owing to a 3-dimensional crystal structure similar to $\text{Li}_3\text{In}_2(\text{PO}_4)_3$ and $\text{Li}_3\text{Sc}_2(\text{PO}_4)_3$. However, the disadvantages of it are low charge capacity and poor cycle performance. Reversible two phase transition occurs in $\text{Li}_3\text{V}_2(\text{PO}_4)_3$. The high temperature γ -phase is the highest ionic conduction phase among these three phases. In this study, the stabilization of the γ -phase was performed, and the crystal structure and the cathode property of the stabilized materials were investigated.

$\text{Li}_{3-2x}(\text{V}_{1-x}\text{M}_x)_2(\text{PO}_4)_3$ ($\text{M} = \text{Zr}^{4+}, \text{Ti}^{4+}$) and $\text{Li}_3(\text{V}_{1-x}\text{Al}_x)_2(\text{PO}_4)_3$ were synthesized by a conventional solid state reaction. The sample of $x = 0.05$ had been stabilized in the form of the high temperature γ -phase at room temperature. The highest ionic conductivity was detected in $\text{Li}_{2.8}(\text{V}_{0.9}\text{Zr}_{0.1})_2(\text{PO}_4)_3$. The powder neutron diffraction experiment was carried out by using the HERMES diffractometer installed at the T1-3 beam port of the T1 thermal neutron beam guide of JRR-3M. The crystal structure was refined by the Rietveld analysis for neutron diffraction patterns in order to confirm the site location and site occupancy for Li ions.

In Fig 1, the Li site environment of $\text{Li}_{3-2x}(\text{V}_{1-x}\text{Zr}_x)_2(\text{PO}_4)_3$ with $x = 0.10$ are given. The site occupancy of Li1 site is greater than that of rest Li2 or Li3 site. Although the monoclinic phase and the orthorhombic phase of $\text{Li}_3\text{V}_2(\text{PO}_4)_3$ have almost the same crystal structure, the crucial

difference between the both phases is the different distribution of Li ions. All Li sites are fully occupied in the monoclinic phase, while those sites are partially occupied in the orthorhombic phase. Such partial occupancy behavior over the whole lithium sites is also seen in the $\text{Li}_{2.8}(\text{Sc}_{0.9}\text{Zr}_{0.1})_2(\text{PO}_4)_3$ and $\text{Li}_{2.8}(\text{In}_{0.9}\text{Zr}_{0.1})_2(\text{PO}_4)_3$. These three crystal structures are all the same.

The Rietveld refinement confirmed clearly that a much high disorder was introduced to the three kinds of Li sites in the orthorhombic phase of $\text{Li}_{2.8}(\text{V}_{0.9}\text{Zr}_{0.1})_2(\text{PO}_4)_3$. On charge-discharge measurements, Zr-substituted sample increased the charge capacity about 30% and improved the cycle performance, compared with the unsubstituted sample. The reason can be ascribed to the stabilization of the orthorhombic phase, effective for fast Li ion transport by the introduction of small amounts of Zr^{4+} ions.

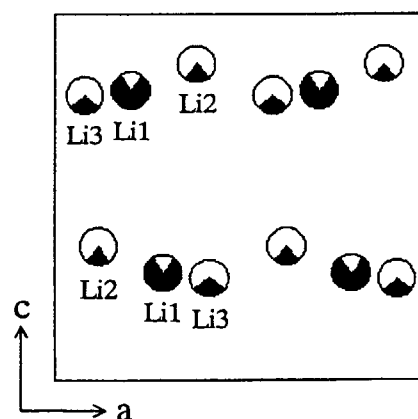


Fig. 1 Li ions distribution of $\text{Li}_{2.8}(\text{V}_{0.9}\text{Zr}_{0.1})_2(\text{PO}_4)_3$ in ac plane. Black painted areas are corresponded to the occupancy rate.

研究テーマ：インジウム含有リチウムリン酸塩の構造とイオン伝導性
表題：インジウム含有リチウムリン酸塩の構造とイオン伝導性

1-1-11 Crystal Structure and Ionic Conductivity of Lithium Phosphate with Indium

T. Suzuki, N. Hayakawa, K. Yoshikawa, K. Uematsu, K. Toda,
K. Ohoyama¹ and M. Sato

Department of Chemistry and Chemical Engineering, Faculty of Engineering,
Niigata University, Ikarashi 2 no-cho 8050, Niigata 950-2181, Japan

¹Institute for Material Research, Tohoku University, katahira 2-1-1, Aoba-ku,
Sendai 980-0812, Japan

Lithium ionic conductors exhibiting high ionic conductivity at ambient temperature are paid attention in order to develop new rechargeable lithium battery systems. Oxide lithium ion conductors are promising solid electrolytes for all solid rechargeable lithium batteries because of easy synthesis, easy handling and stability in air. $\text{Li}_3\text{In}_2(\text{PO}_4)_3$, lithium ion conductor, forms $\beta\text{-Fe}_2(\text{SO}_4)_3$ type structure similar to NASICON type structure. Three phase exists in $\text{Li}_3\text{In}_2(\text{PO}_4)_3$ according to the temperature: a monoclinic α -phase at low temperature, same as another monoclinic β -phase which has a little larger unit cell, and an orthorhombic γ -phase at high temperature. The γ -phase especially indicates good ionic conductivity due to disorder arrangement of Li ions. The purpose in this study is to stabilize the γ -phase at room temperature by substitution of Zr^{4+} ion for In^{3+} sites. The crystal structure of $\text{Li}_{3-2x}(\text{In}_{1-x}\text{Zr}_x)_2(\text{PO}_4)_3$ with $x = 0.10$ was refined by the Rietveld analysis for neutron diffraction pattern in order to confirm the site location for Li ions.

The powder neutron diffraction experiment was carried out by using the HERMES diffractometer installed at the T1-3 beam port of the T1 thermal neutron beam guide of JRR-3M. The crystal structure of $\text{Li}_{2.8}(\text{In}_{0.9}\text{Zr}_{0.1})_2(\text{PO}_4)_3$ was determined by the Rietveld method for the diffraction pattern. In Table 1, the refined

crystallographic data of $\text{Li}_{3-2x}(\text{In}_{1-x}\text{Zr}_x)_2(\text{PO}_4)_3$ and $\text{Li}_{3-2x}(\text{Sc}_{1-x}\text{Zr}_x)_2(\text{PO}_4)_3$ with $x = 0.10$ are given. The lattice parameter a in the indium phosphate is longer than that of scandium phosphate though the unit cell volume is smaller. The expansion of a is effective for Li ion conduction because of the expansion of bottle necks. Actually, the ionic conductivity of $\text{Li}_{2.8}(\text{In}_{0.9}\text{Zr}_{0.1})_2(\text{PO}_4)_3$ ($\sigma = 1.40 \times 10^{-5} \text{ Scm}^{-1}$) is higher than that of $\text{Li}_{2.8}(\text{Sc}_{0.9}\text{Zr}_{0.1})_2(\text{PO}_4)_3$ ($\sigma = 1.14 \times 10^{-5} \text{ Scm}^{-1}$). The crucial difference between the monoclinic phase and the orthorhombic phase of $\text{Li}_3\text{In}_2(\text{PO}_4)_3$ is the different distribution of Li ions. The fact has been obtained that all Li sites are partially occupied in the high temperature form of $\text{Li}_3\text{Sc}_2(\text{PO}_4)_3$ and $\text{Li}_{3-2x}(\text{Sc}_{1-x}\text{M}_x)_2(\text{PO}_4)_3$ ($\text{M} = \text{Ti}, \text{Zr}$) with $x = 0.10$. It is also confirmed that the same situation is heeled in $\text{Li}_{2.8}(\text{In}_{0.9}\text{Zr}_{0.1})_2(\text{PO}_4)_3$.

The Rietveld refinement confirmed clearly that the superionic conduction phase was stabilized at room temperature and that a much highly disordered state was introduced to the three kinds of Li sites by substituting Zr^{4+} ions for In^{3+} sites. The improvement of the ionic conductivity can be ascribed to the introduction of Li ion disorder state and to the creation of a number of vacancies on the available Li sites leading to the expansion of the bottle necks for Li ion conduction.

Table 1 Characteristics of neutron experiment and unit cell parameters of $\text{Li}_{3-2x}(\text{In}_{1-x}\text{Zr}_x)_2(\text{PO}_4)_3$ and $\text{Li}_{3-2x}(\text{Sc}_{1-x}\text{Zr}_x)_2(\text{PO}_4)_3$ with $x = 0.10$.

Compound	Space group	a (Å)	b (Å)	c (Å)	V (Å ³)
$\text{Li}_{2.8}(\text{In}_{0.9}\text{Zr}_{0.1})_2(\text{PO}_4)_3$ 298K	Orthorhombic <i>Pbcn</i>	12.361(2)	8.694(1)	8.837(1)	949.7(3)
$\text{Li}_{2.8}(\text{Sc}_{0.9}\text{Zr}_{0.1})_2(\text{PO}_4)_3$ 298K	Orthorhombic <i>Pbcn</i>	12.3542(5)	8.7946(3)	8.8200(4)	958.29(7)

JRR-3M, KPD, 1. Structure & Excitations

研究テーマ：軽希土類化合物 REB_2C_2 における結晶場と磁気構造

表題：正方晶化合物 $\text{Ce}^{11}\text{B}_2\text{C}_2$ 、 $\text{Nd}^{11}\text{B}_2\text{C}_2$ の結晶構造

1-1-12 Crystal structure refinement in the tetragonal compound $\text{Ce}^{11}\text{B}_2\text{C}_2$ and $\text{Nd}^{11}\text{B}_2\text{C}_2$

T. Onimaru, K. Ohoyama, H. Yamauchi, H. Onodera, M. Ohashi, Y. Yamaguchi,

Institute for Materials Research, Tohoku University, Sendai 980-8577

Magnetic Properties in REB_2C_2 compounds (RE= rare earth) with a tetragonal LaB_2C_2 type crystal structure attract our interest recently. In particular, DyB_2C_2 undergoes an antiferroquadrupolar ordering at $T_Q=24.7\text{K}$ and a transition to a characteristic antiferromagnetic state at 15.3K [1]. Moreover, HoB_2C_2 also shows a complicated phase diagram which may indicate the existence of a quadrupolar ordered state below T_N . To understand the mechanism of quadrupolar interactions in REB_2C_2 , we have investigated the magnetic properties of this system.

Actually, two structure models for this system were reported by X-ray diffraction technique: model-I with the space group $P4_2c$

by Bauer *et al.* [2], and model-II with the space group $P4/mbm$ by Smith *et al.* [3]. Thus, to confirm the crystal structure of this system, we performed neutron powder diffraction experiments. The detail of the results of the experiments has been already reported in ref.4

We measured powder patterns of $\text{Ce}^{11}\text{B}_2\text{C}_2$ and $\text{Nd}^{11}\text{B}_2\text{C}_2$ on Kinken powder diffractometer HERMES(T1-3) at JRR-3M. Natural boron was replaced by ^{11}B , because of the strong neutron absorption effect. Fig.1 shows a powder pattern of $\text{Ce}^{11}\text{B}_2\text{C}_2$ in the paramagnetic state by HERMES, and results of Rietveld analysis by means of RIETAN-97 β with several structure models. Fig.2 shows perspective views of the

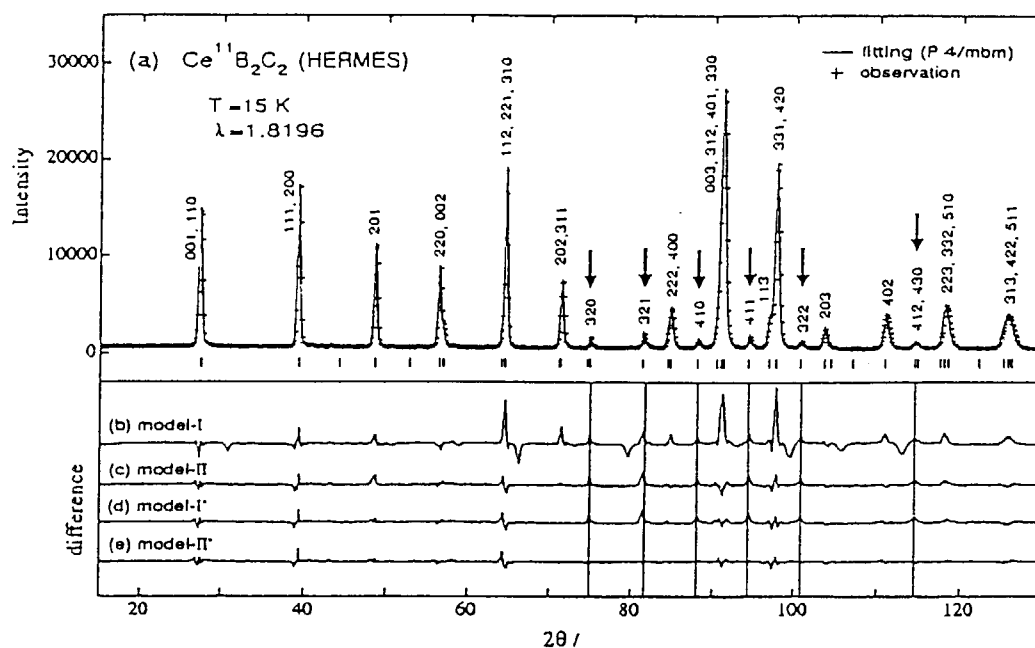


Fig.1 (a) Powder pattern of $\text{Ce}^{11}\text{B}_2\text{C}_2$ at 15 K on HERMES. The solid line is the best results of Rietveld refinement by RIETAN-97 β . (b)-(e) show the differences between observed and calculated patterns by each model. (see Fig.2) Arrows indicates the positions of Bragg peaks which can not be explained by model-I and -II.

JRR-3M, HERMES, 1. Structure

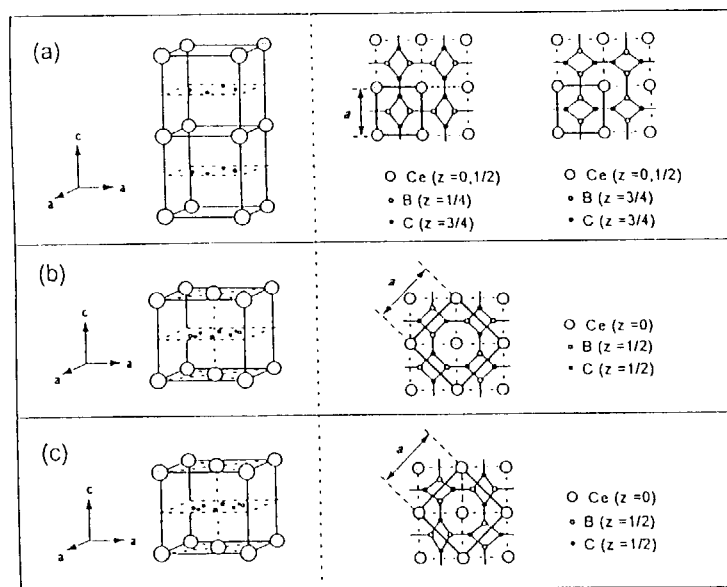


Fig. 2. Perspective views and projections on the c -plane of the models for the tetragonal LaB_2C_2 -type structure with (a) the space groups of $P4_2c$ by Bauer *et al.* (1999) (model I), (b) $P4/mbm$ by Smith *et al.* (1997) (model II) and (c) $P4/mbm$ by the present work (model II').

models. In Fig.1, we observed some characteristic peaks denoted by arrows, which can not be explained by model-I (See Fig.2(a)) by Bauer *et al.* nor model-II (See Fig.2(b)) by Smith *et al.* Almost the same results were observed in powder diffraction experiments in $\text{Nd}^{11}\text{B}_2\text{C}_2$. From some model fitting procedures, we refined the crystal structure of $\text{Ce}^{11}\text{B}_2\text{C}_2$ and $\text{Nd}^{11}\text{B}_2\text{C}_2$; Fig.2(c) shows the best result which explained the powder patterns on HERMES quite well. In this model, the unit cell is different from the model-I by Bauer *et al.*: $[110]$ direction in model-I became $[100]$ direction in our model, that is, the lattice constant, a , is $\sqrt{2}$ times of that of model-I, and c is half of that of model-I. The difference of the model-II by Smith *et al.* is the positional parameters of B and C, x_C and x_B . From Rietveld refinement with our model, x_C and x_B are determined as 0.361 and 0.160, respectively, at 15 K; in the model-II by Smith *et al.*, x_B was determined as 0.352 and $x_C = 0.5 - x_B$.

Since the neutron diffraction technique is effective to determine accurate positions of light atoms in a compounds which includes heavy atoms in comparison with X-ray diffraction

technique, we were able to determine the crystal structure in detail. Since $\text{Ce}^{14}\text{B}_2\text{C}_2$ and $\text{Nd}^{11}\text{B}_2\text{C}_2$ has the same crystal structure, it is highly probable that other RB_2C_2 compounds have the same structure as those of $\text{Ce}^{11}\text{B}_2\text{C}_2$ and $\text{Nd}^{11}\text{B}_2\text{C}_2$. It is necessary, however, to confirm it by neutron powder diffraction in the heavy rare earth compounds.

References

- [1] H. Yamauchi, H. Onodera, K. Ohoyama, T. Onimaru, M. Kosaka, M. Ohashi, Y. Yamaguchi, *J. Phys. Soc. Jpn* 68 (1999) in press
- [2] J. Bauer and J. Debuigne: *C. A. Acad. Sci.* Ser. C274(1972)1271.
- [3] P.K. Smith and P.W. Gilles, *J. Inorg. Nucl. Chem* 29(1967)375.
- [4] T. Onimaru, H. Onodera, K. Ohoyama, H. Yamauchi, Y. Yamaguchi, *J. Phys. Soc. Jpn* 66(1999) in press

研究テーマ：ホイスラー型 Ni_2MnGa 系合金の形状記憶効果

表題：ホイスラー型 $\text{Ni}_2(\text{Pd}_{0.16}\text{Mn}_{0.84})\text{Ga}$ のマルテンサイト型変態と磁気転移

1-1-13 Martensitic and Magnetic Transformations in Heusler-type $\text{Ni}_2(\text{Pd}_{0.16}\text{Mn}_{0.84})\text{Ga}$

K. INOUE, K. ENAMI, M. IGAWA, Y. YAMAGUCHI¹ and K. OHYAMA¹

Fac. Sci & Tech. Ryukoku Univ. Seta, Otsu. 520-2194, Japan

¹*IMR, Tohoku Univ. Aoba-ku, Sendai, 980-8577, Japan*

The Heusler-type Ni_2MnGa alloy shows a thermoelastic martensitic transformation at a temperature, M_s , of about 200K[1], where the magnetic transition occurs from a ferromagnetic phase to another ferromagnetic one. On the other hand, the Curie temperature, T_C , of this Heusler phase is around 370K[1]. If M_s closes to T_C , we may control the phase transformation by changing the external magnetic field instead of temperature. To bring both M_s and T_C close to room temperature, we made slightly non-stoichiometric compounds by replacing some atoms with the other kind of atoms.

In case of $\text{Ni}_2(\text{Pd}_{0.16}\text{Mn}_{0.84})\text{Ga}$, it was found that both M_s and T_C are near the room temperature from the measurement of temperature dependence of the electrical resistivity. To investigate precisely the phenomena occurring around the transformation region, we have made the magnetization measurements by SQUID magnetometer and the powder neutron diffraction by HERMES diffractometer at JRR-3M on this material. The program, RIETAN[2], was used for Rietveld analysis of the diffraction patterns.

The temperature dependence of magnetization measured with increasing and decreasing temperatures at a few field levels is shown in Fig.1. We can see the martensitic transformation and the Curie point occur near the room temperature though the transformation region moves with magnetic field. Neutron diffraction patterns for mother phase at 400(K) and for martensitic phase at 16(K) are shown in Fig.2. Peaks of Al are originated from the sample holder. At high temperature of 400(K), where the compound is paramagnetic, a cubic Heusler structure is only

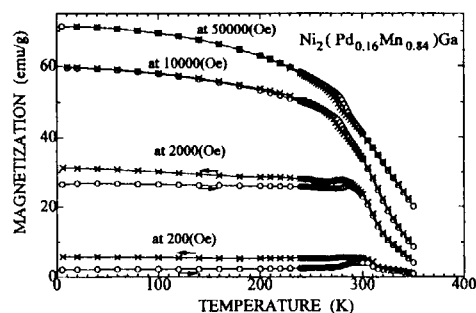


Fig.1. Magnetization versus temperature.

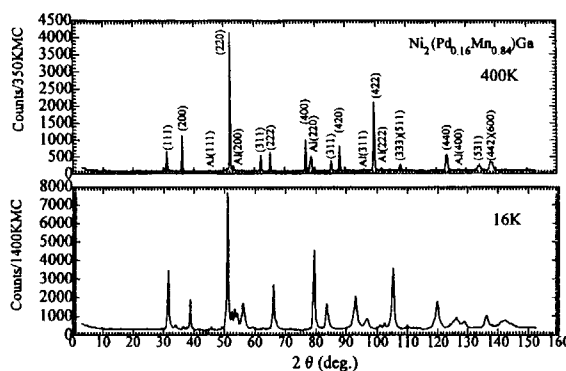


Fig.2. Neutron diffraction patterns at 400K and 16K.

observed. Whereas, at low temperature of 16(K), where the sample is ferromagnetic, the diffraction pattern is quite different from that at 400(K). As the (111) peak of Heusler structure remained at low temperatures and the (200) peak splits into three, the basic structure at low temperatures is presumably orthorhombic distorted from the cubic Heusler structure. To determine the crystal structure, we have made the Rietveld analysis on the diffraction pattern above $2\theta = 70^\circ$, because the effect of magnetic scattering is eliminated at high scattering angle. The best fit was obtained on the assumption that two phase structures coexist at low temperatures. One is an orthorhombic structure distorted from the cubic Heusler one and

the other is a monoclinic one with the shuffling of 6 layers of (220) plane of this orthorhombic one. The basic Heusler structure and the way of shuffling of (220) plane are shown in Fig.3(a) and (b), respectively. The order of 6 layers stacking of (220) plane is A, B', C, A', B and C' in Fig.3(b). The mass fractions of each phase for both increasing and decreasing temperatures are shown in Fig.4.

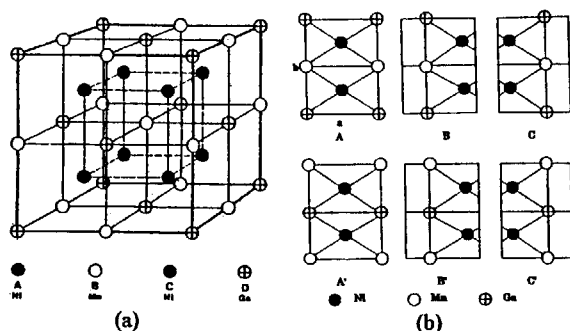


Fig.3. (a) Crystal structure of high temperature cubic phase. (b) 6 layers stacking of (220) plane.

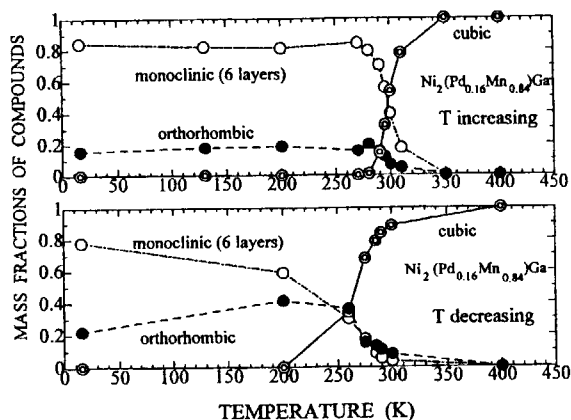


Fig.4. Temperature dependence of mass fractions.

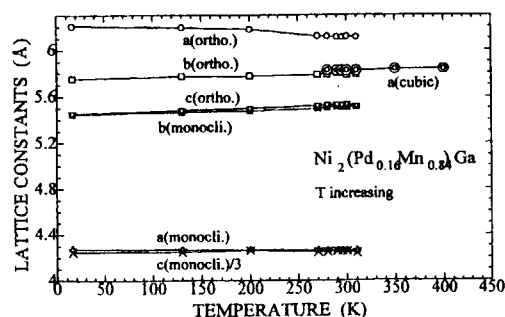


Fig.5. Temperature dependence of lattice constants for three phases.

The temperature dependence of the lattice constants of each structure obtained with increasing temperature is shown in Fig.5. We can see the situation where the cubic Heusler structure is distorted to an orthorhombic one, and this orthorhombic structure is distorted to a monoclinic one with shuffling of 6 layers of (220) plane.

As shown in fig.4, about 80% of the total mass is monoclinic and 20% is orthorhombic at low temperatures. When the temperature increases, between 270(K) and 320(K) the mass fractions of two martensitic phases decreases gradually, whereas that of cubic Heusler phase increases. On the other hand, when the temperature decreases, the change of mass fraction starts at lower temperature region compared to the case of increasing temperature. The hysteresis of the martensitic transformation is obviously observed. The shape of the temperature dependence of the mass fractions is quite different for increasing and decreasing temperatures. This phenomenon indicates that the abundance ratio of these two phases changes easily, because the formation energy of monoclinic phase and that of the orthorhombic one is very close.

If we assume that only the Mn atom has magnetic moment, the moment of Mn is estimated to be $3.88 \mu_B$ from the saturation magnetization. According to the energy equation $\mu_B H = k_B T$, this small moment does not correspond to the measured transformation region which spreads over 50(K).

Better material which has large magnetic moment or narrow temperature region should be developed.

References

- 1) P.J.Webster, K.R.A.Ziebeck, S.L.Town and M.S.Peak: *Philos.Mag.* **49** (1984) 295.
- 2) F.Izumi, *The Rietveld Method*, ed. R.A.Young (Oxford Univ. Press, Oxford, 1993) Chap.13.

研究テーマ：中性子散乱による強相関電子系の研究
表題：La_{2-x}Sr_xCuO₄の磁場効果

1-1-14 Magnetic field effects on superconducting La_{2-x}Sr_xCuO₄

S. Katano, T. Suzuki¹, T. Fukase¹ and K. Yamada²

ASRC, Japan Atomic Energy Research Institute, Tokai, Ibaraki 319-1195

¹ Institute for Material Research, Tohoku University, 2-1-1 Katahira, Sendai 980-8577

² Institute for Chemical Research, Kyoto University, Uji, Kyoto 611-0011

La-based High-*T_c* superconducting cuprates La_{2-x}Sr_xCuO₄ shows a small kink at around $x=0.115$ in the x -*T_c* curve. For this compound an incommensurate magnetic ordering was found clearly [1]; however, the structural phase transition to LTT (the low-temperature tetragonal), which appears apparently in the Ba substituted compound La_{2-x}Ba_xCuO₄ with $x=0.125$ (1/8), has not been observed in the crystal structural studies. On the other hand, in the ultrasonic measurements an anomalous stiffening was observed at low temperatures [2]. The work indicates that in LSCO the LTT structure fluctuates significantly, but that is not a macroscopic one. Recently such a stiffening of the lattice was found to be enhanced by strong magnetic fields [3]. Furthermore, an NMR experiment under high magnetic fields suggested that a structural phase transition occurs accompanied with a spin-flop transition. To examine these peculiar structural and magnetic transitions, neutron scattering experiments have been performed under the fields.

In the experiments a single crystal with $x=0.12$ was used. Its *a* (*b*)-*c* plane was set in the scattering plane, and the magnetic field was applied to the *b* (*a*)-axis. (The crystal consists of twins; thus the scattering both from the *a*-*c* and from the *b*-*c* plane are observed in the scattering plane.) Neutron diffraction experiments were done on TAS-2 (a triple-axis spectrometer) in a diffraction arrangement with the neutron energy of 13.6 meV. Magnetic field effects were studied using a new-type (Liquid-He free) split-pair superconduct-

ing magnet which can apply the fields up to 10T [4].

Figure shows magnetic field dependence of the nuclear peak 200 (and 020 also). The results suggest a change in the population of domains which relate to the twin formation; however, any clear indications of the structural transition were not observed. In this scattering plane a spin-flop transition was also investigated. More detailed experiments, however, are required to discuss the phase transitions under magnetic fields.

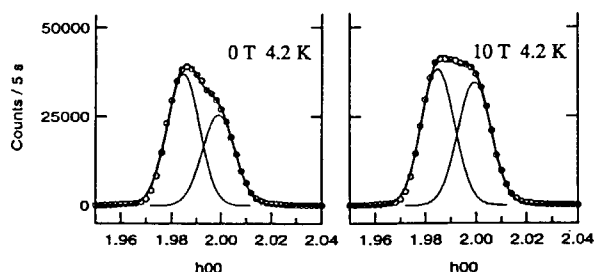


Fig. 1. Magnetic field dependence of the nuclear scattering intensities.

References

- [1] T. Suzuki *et al.*, Phys. Rev. B 57, R3229 (1998).
- [2] Fukase *et al.*, Jpn. J. Appl. Phys. Series 7, 213 (1992).
- [3] T. Goto *et al.*, J. Phys. Soc. Jpn. 66, 2870 (1997).
- [4] S. Katano *et al.*, Proc. of 4th Int. Symposium on Advanced Physical Fields: Quantum Phenomena in Advanced Materials at High Magnetic Fields, 315 (1999).

研究テーマ：半磁性半導体 $\text{Zn}_{1-x}\text{Mn}_x\text{Te}$ の中性子散乱

表題：希薄磁性半導体 $\text{Zn}_{0.568}\text{Mn}_{0.432}\text{Te}$ における磁気準弾性散乱

1-1-15 Magnetic Quasi-elastic Scattering in

Diluted Magnetic Semiconductor $\text{Zn}_{1-x}\text{Mn}_x\text{Te}$ with $x=0.432$

Y.Ono, T.Kamita, T.Sato¹, Y.Oka¹ and T.Kajitani

Department of Applied Physics, Graduate School of Engineering, Tohoku University, Sendai 980-8579

¹ Research Institute for Scientific Measurements, Tohoku University, Sendai 980-8577

Diluted magnetic semiconductor $\text{Zn}_{1-x}\text{Mn}_x\text{Te}$ undergoes spin glass transition below 50 K in the wide manganese concentration range ($0.2 < x < 0.65$). [1] Giebultowicz *et al.* observed damped magnon-like excitations in $\text{Zn}_{0.35}\text{Mn}_{0.65}\text{Te}$ and $\text{Zn}_{0.59}\text{Mn}_{0.41}\text{Te}$ at 4.2 K, but could not detect any critical Lorentzian component from spin relaxational processes in the narrow energy region around the incident neutron peak. [2]

Inelastic neutron scattering experiment for $\text{Zn}_{0.568}\text{Mn}_{0.432}\text{Te}$ was carried out using a TOF cold neutron spectrometer, AGNES ($\lambda = 4.22$ Å), installed at the guide hall of JRR3M.

Quasi-elastic scattering at reciprocal lattice point, $1\ 1/2\ 0$, was fitted with Lorentzian as a function of energy transfer. We obtained FWHM (full-width at half maximum) of the quasi-elastic scattering at 14 K, 17 K, 30 K, 100 K and 293 K, respectively. Figure 1 shows the inverse of FWHM at each temperature, which takes the maximum at the spinglass transition temperature, $T_g=17$ K. The quasi-elastic scattering arises from the magnetic fluctuation related to the spinglass transition.

The quasi-elastic scattering intensity was measured under various scattering conditions in $hk0$ plane at 17 K and integrated over the energy width of ± 1 meV. As shown in Fig.2, the integrated-intensity distribution mainly originates from the type-III antiferromagnetic short-range order, [3] but the peak position is

slightly shifted from $1\ 1/2\ 0$ toward the 100 point. It is suggested that the magnetic fluctuation contains a modulated dynamical component.

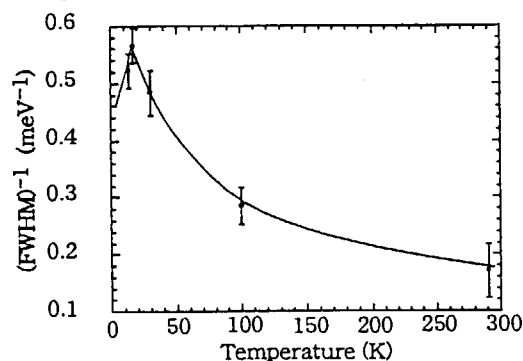


Fig.1 Temperature variation of the inverse of FWHM for quasi-elastic scattering at $1\ 1/2\ 0$.

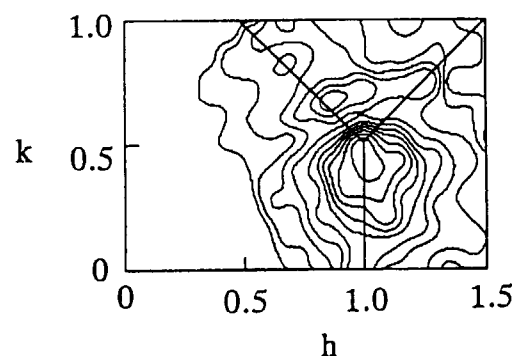


Fig.2 Distribution of quasi-elastic scattering intensity integrated with the width of ± 1 meV at 17 K.

References

- [1] J.K.Furdyna: J.Appl.Phys.64(1988)R29.
- [2] T.M. Giebultowicz : J.Appl.Phys.67 (1990) 5096.
- [3] Y.Ono *et al.* : J.Phys.Chem.Solids, in press

JRR-3M, AGNES(C-3-1-1), 1. Structure & Excitation

This is a blank page.

1. 中性子散乱 2) 磁 性

1. Neutron Scattering 2) Magnetism

This is a blank page.

研究テーマ：遷移金属複合酸化物の構造、磁氣的性質に関する研究
 表題：希土類オルソチタン酸化物の磁氣的及び中性子散乱研究

1-2-1 Magnetic and Neutron Diffraction Studies of Rare-earth Orthotitanates

K. Yoshii and A. Nakamura¹

Japan Atomic Energy Research Institute, Dept. of Synchrotron radiation Research, Mikazuki, Hyogo 679-5143, Japan, and Dept. of Materials Science, Tokai, Ibaraki 319-1195, Japan¹

Rare-earth (Ln) orthotitanates LnTiO_3 containing early trivalent lanthanides (Ln=La to Sm) are known as a canted antiferromagnet. The antiferromagnetic order in these systems readily disappears with slight deviation of Ti valence from $3+(3d^1)$ caused by oxygen excess, Ln-deficiency, the substitution of Ln by alkali-earth ions ($\text{Ln}_{1-x}\text{Sr}_x\text{TiO}_3$), etc. Recently, as a different approach to these systems, the present authors have initiated a systematic study of mixed Ln orthotitanates ($\text{LnLn}'\text{TiO}_3$) to see what further variations of their physical properties are brought about, and found in most of such systems a characteristic susceptibility (χ) peak phenomenon in their χ vs. T plots, as shown in Fig. 1 for $\text{Ce}_{1-x}\text{Nd}_x\text{TiO}_3$: here, the χ peak occurs in the high Nd content region of $x > 0.5$. Whereas, in La-Sm system ($\text{La}_{1-x}\text{Sm}_x\text{TiO}_3$) this occurs in the low Sm content region of $x < 0.3$. In order to elucidate the possible origin of such χ peak phenomenon in these systems, high resolution powder neutron diffraction (HRPD) experiments were performed on each typical system, $\text{Ce}_{0.5}\text{Nd}_{0.5}\text{TiO}_3$ and $\text{La}_{0.75}\text{Sm}_{0.25}\text{TiO}_3$

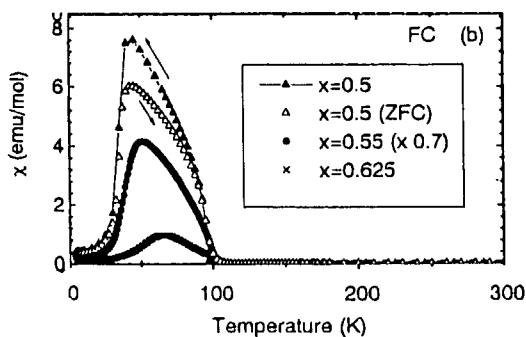


Fig. 1 DC susceptibility (χ) vs. T(K) curves of $\text{Ce}_{1-x}\text{Nd}_x\text{TiO}_3$ over the entire x range.

between room temperature and 10K. The results are shown in Fig. 2 for the former and demonstrate that neither structural nor long range magnetic order take place below T_N and even at the χ peak temperature (=50K) in this system. Similar results were obtained for the latter (but, here, due to the strong neutron adsorption of Sm, the quality of HRPD pattern is much worse.) From these results it is judged that the χ peak in these systems originates from the onset of the cluster(or spin) glass type short range order of the frustrated canted antiferromagnetism in these mixed Ln titanates.

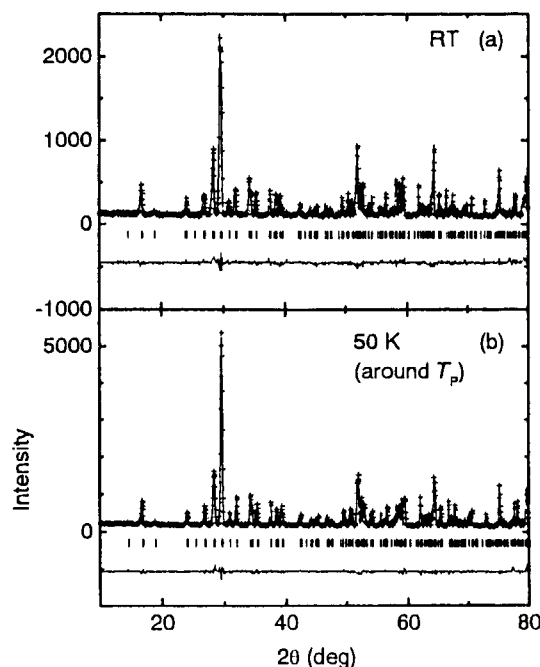


Fig. 2 HRPD pattern of $\text{Ce}_{0.5}\text{Nd}_{0.5}\text{TiO}_3$ at room temp and 50K

研究テーマ:ペロブスカイト型複合酸化物の磁気構造

表題:秩序化ペロブスカイト $\text{Sr}_2\text{LnRuO}_6$ ($\text{Ln}=\text{Ho}, \text{Tm}$) の中性子回折

1-2-2

Neutron Diffraction Study on Ordered Perovskites $\text{Sr}_2\text{LnRuO}_6$ ($\text{Ln}=\text{Ho}, \text{Tm}$)

Y. Doi, Y. Hinatsu, Y. Shimojo¹ and Y. Morii¹

Division of Chemistry, Graduate School of Science, Hokkaido University, Sapporo 060-0810, Japan

¹ Japan Atomic Energy Research Institute, Tokai-mura, Ibaraki 319-1195, Japan

Magnetic properties of ordered perovskite-type compounds $\text{Sr}_2\text{LnRuO}_6$ ($\text{Ln}=\text{Ho}, \text{Tm}$) have been reported. Their magnetic susceptibilities were measured from 5K to 300K. These compounds showed magnetic transitions and their transition temperatures were determined to be *ca.* 36K (Ho compound) and *ca.* 38K (Tm compound).

In order to determine the magnetic structures, powder neutron measurements were performed at room temperature and 10K with a High Resolution Powder Diffractometer (HRPD) in the JRR-3M reactor with a neutron incident wave length ($\lambda = 1.1624\text{\AA}$).

Powder neutron diffraction patterns of $\text{Sr}_2\text{HoRuO}_6$ and the Rietveld analysis are shown in Fig.1. The crystal structure at room temperature is monoclinic with space group $P2_1/n$ (No.14), and the Ln^{3+} and Ru^{5+} ions are structurally ordered at the B sites of the ABO_3 perovskite-type structure. The magnetic structure of $\text{Sr}_2\text{HoRuO}_6$ at 10K is illustrated in Fig.2. The magnetic moment of the Ho^{3+} and Ru^{5+} are ordered antiferromagnetically, respectively. In the *ab* plane, the magnetic moments of Ho^{3+} and Ru^{5+} are coupled ferrimagnetically. The magnetic Bragg peaks of $\text{Sr}_2\text{TmRuO}_6$ are observed, and it is considered that the magnetic structure is antiferromagnetic. However the detailed magnetic structure of $\text{Sr}_2\text{TmRuO}_6$ could not be determined, because their peaks were very weak.

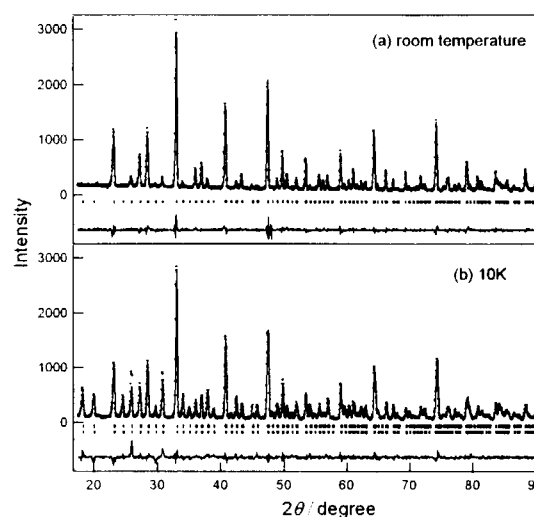


Fig.1 Powder neutron diffraction pattern fitting for $\text{Sr}_2\text{HoRuO}_6$.

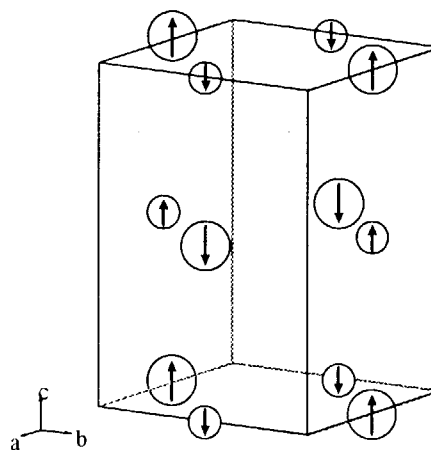


Fig.2 The magnetic structure of $\text{Sr}_2\text{HoRuO}_6$. Diamagnetic ions are omitted. Larger circles Ho^{3+} , smaller circles Ru^{5+} .

研究テーマ：ペロブスカイト型複合酸化物の磁気構造

表題：層状ペロブスカイト $\text{Ca}_{2-x}\text{Sr}_x\text{MnO}_4$ の中性子回折

1-2-3 Neutron Diffraction Study on Layered Perovskites $\text{Ca}_{2-x}\text{Sr}_x\text{MnO}_4$

K. Tezuka, M. Inamura, Y. Hinatsu, Y. Shimojo¹ and Y. Morii¹

Division of Chemistry, Graduate School of Science, Hokkaido University, Sapporo 060-0810, Japan

¹*Japan Atomic Energy Research Institute, Tokai-mura, Ibaraki 319-1195, Japan*

We prepared layered perovskites $\text{Ca}_{2-x}\text{Sr}_x\text{MnO}_4$ ($x = 0 \sim 2.0$ at 0.25 intervals) with Ruddlesden-Popper type structure. The temperature-dependent magnetic susceptibilities were measured with zero-field-cooled (ZFC) and field-cooled (FC) conditions at an applied field of 1000G. The results are shown in Fig. 1. A dramatic difference in magnetic susceptibilities between ZFC and FC was observed below the Néel temperatures for Ca_2MnO_4 and $\text{Ca}_{1.75}\text{Sr}_{0.25}\text{MnO}_4$, which shows the onset of a ferromagnetic moment below these temperatures.

Their precise crystal structures at room temperature and at 10K and magnetic structures at 10K were determined from the neutron diffraction measurements using a High Resolution Powder Diffractometer (HRPD) in the JRR-3M reactor with a neutron incident wave length ($\lambda = 1.823\text{\AA}$). The compounds for $x = 0$ and 0.25 have a tetragonal system with space group $I4_1/acd$ (No. 142). The compounds for $x = 0.5 \sim 2.0$ have a tetragonal system with space group $I4/mmm$ (No. 139) both at room temperature and 10K.

Magnetic structures of $\text{Ca}_{2-x}\text{Sr}_x\text{MnO}_4$ ($x = 0.0, 0.5, 1.0$ and 1.5) solid solutions at 10K have been determined as shown in Fig. 2.

With increasing Ca content, the crystal structure of $\text{Ca}_{2-x}\text{Sr}_x\text{MnO}_4$ becomes distorted and the ferromagnetic component derived from the Dzyaloshinsky-Moriya interaction appears. The interlayer distance becomes shorter with increasing Ca content, and the characteristic of the magnetic interaction between the Mn^{4+} ions becomes three-dimensional from two-dimensional as shown in Fig. 2.

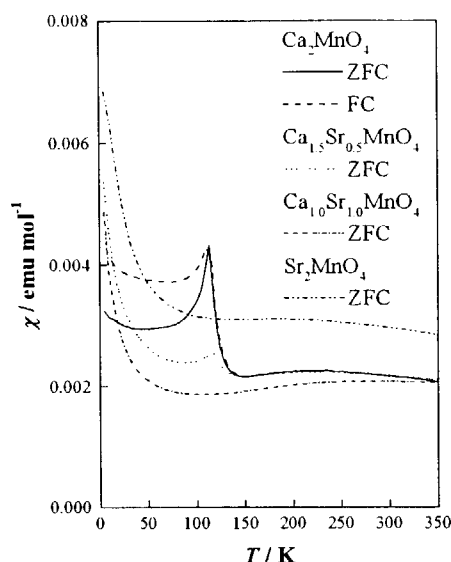


Fig. 1 Magnetic susceptibilities for $\text{Ca}_{2-x}\text{Sr}_x\text{MnO}_4$.

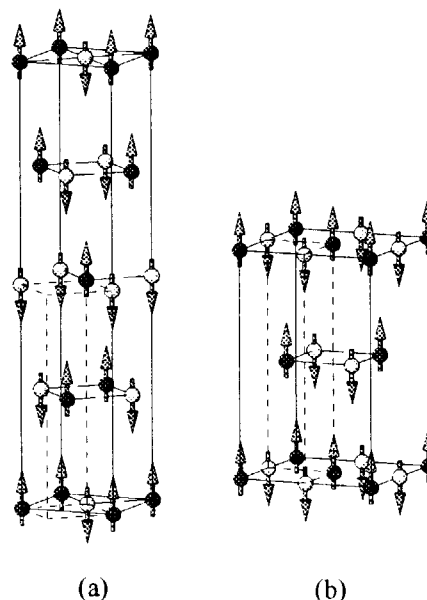


Fig. 2 Magnetic structures of $\text{Ca}_{2-x}\text{Sr}_x\text{MnO}_4$:
(a) Ca_2MnO_4 and (b) $\text{Ca}_{2-x}\text{Sr}_x\text{MnO}_4$ with $x = 0.5 \sim 1.5$.

研究テーマ：強相関電子系の中性子散乱による研究

表題：スピニラダー物質 $\text{Sr}_{2.5}\text{Ca}_{11.5}\text{Cu}_{24}\text{O}_{41}$ のスピンギャップと反強磁性に対する圧力効果

1-2-4

Pressure effects on spin gap and antiferromagnetism of the spin ladder compound



S. Katano, T. Nagata¹, H. Fujino¹, J. Akimitsu¹, M. Nishi², K. Kakurai²

ASRC, Japan Atomic Energy Research Institute, Tokai, Ibaraki 319-1195

¹Department of Physics, Aoyama-Gakuin University, Setagaya-ku, Tokyo 157-8572

²NSL, The Institute of Solid State Physics, The University of Tokyo, Tokai, Ibaraki 319-1106

The magnetic states of the newly discovered spin-ladder systems have received significant attention from both theoretical and experimental viewpoints. After several intense studies on this $S=1/2$ Heisenberg system, the following has been established. Ladders with an odd number of legs show long-range spin correlations, and often exhibit magnetic ordering at low temperature due to interladder interactions. On the other hand, even-leg ladders have short-range magnetic correlations, i.e. a spin liquid ground state with a spin gap. Furthermore, a transition to the superconducting state is expected with hole doping. Recently, such superconductivity has been observed in the heavily doped two-leg ladder system $(\text{Sr}_{1-x}\text{Ca}_x)\text{Cu}_{24}\text{O}_{41}$ - but under high pressures¹⁾. In this unique system, recent neutron scattering studies on a single crystal with $x=\text{Ca } 11.5$ showed that the spin gap does not change from that of the pure system²⁾; moreover, this doped compound exhibits a complex antiferromagnetic ordering below 2K ³⁾.

The present work extends these neutron scattering studies to high pressures. The experiments were carried out on the triple-axis spectrometers at the JRR-3M. The high-pressure experiments were performed at 0.72, 2.1 and 3.0 GPa using a clamp-type pressure cell⁴⁾, which was cooled down to 1.4K in a conventional cryostat. The intensity from the sample was rather small because its volume

was limited to about 0.1 cm^3 in the pressure cell, and there were fairly high background intensities scattered from this pressure cell.

The spin gap energy was measured by neutron inelastic scattering experiments at the antiferromagnetic zone center $(1.5\ 0\ 10.5)$; that is, $(0.5\ 0\ 1.5)$ in the Cu-O-Cu unit. Figure 1 shows the energy dependence of the scattered intensity measured under high pressures. To get statistics, the intensities were corrected for 2 hours per point at 2.1 GPa, and for 1 hour at 0.72 GPa. At ambient pressure where the sample was placed outside the pressure cell, 5 min per point was enough. The errors indicated in the figure were fairly large because of the high background intensities from the pressure cell. Here the intensities

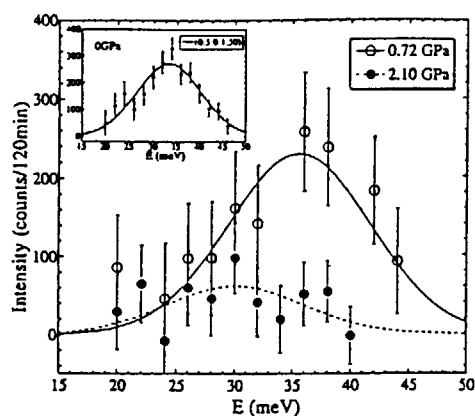


Fig. 1. The constant- Q scan at the antiferromagnetic zone center $(0.5\ 0\ 1.5)$ for the spin gap excitation under high pressures.

at different pressures were normalized by nuclear peak intensities. As shown in this figure, it seems apparent that the intensity decreases progressively under high pressure. There is no clear change in the spectral response below 20 meV. Regarding the spin gap energy, the results are not yet completely conclusive but it appears that the energy gap is around 30 meV. Compared with the detailed experiments at ambient pressure, the spin gap energy does not change significantly from 32 meV²⁾. Since the superconductivity appears at pressures between 3.5 and 8 GPa⁵⁾, the pressure of 2.1 GPa is still some way from this threshold. However, our results imply a characteristic pressure dependence of the spin gap energy and its intensities.

The antiferromagnetic ordering found recently in this Ca substituted system indicates the existence of magnetic order in the spin liquid state³⁾. Since the antiferromagnetism does not appear in the parent compound $\text{Sr}_{14}\text{Cu}_{24}\text{O}_{41}$, this magnetic order must be induced by the holes introduced by the Ca substitution. The ordering appears at 2 K at ambient pressure. As will be explained elsewhere³⁾, this antiferromagnetism is complicated reflecting the complex crystal structure. Although the magnetic ordering seems to be related to the chains, a full determination of the structure has been left. Here, the pressure dependence of this antiferromagnetic ordering was also investigated in connection with its pressure-induced superconductivity. Figure 2 shows the temperature dependence of the intensities from the (1 0 7) magnetic reflection for pressures of 0.72, 2.1 and 3.0 GPa. They were also normalized by the nuclear reflections. The intensity, and the magnetic moment, decrease with increasing pressure, and seem to disappear at the critical pressure for the superconductivity. The Néel temperature, on the other hand, increases a little at a rate of 0.3 K/GPa. These results might be related to the fact that the superconductivity appears at a pressure of 3.5 GPa.

Our results indicate that the spin gap and the Néel temperature are not suppressed

under high pressures. The intensities are, however, greatly decreased with pressure as one approaches the superconducting state. This suggests that pressure promotes the delocalization of electrons and/or holes that are concerned in the magnetism of the system. These conduction carriers would play a role in its superconductivity. To understand the relationships between the magnetism and the superconductivity further, precise experiments under higher pressures are still required.

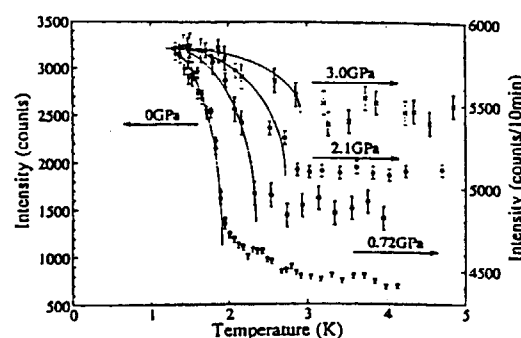


Fig. 2. Pressure dependence of the intensity of the (1 0 7) magnetic reflection as a function of temperature. For the sake of clarity the intensity curves are displaced vertically.

References

- [1] M. Uehara, T. Nagata, J. Akimitsu, H. Takahashi, N. Mori, and K. Kinoshita, *J. Phys. Soc. Jpn.* **65**, 2764 (1996).
- [2] S. Katano, T. Nagata, J. Akimitsu, M. Nishi, and K. Kakurai, *Phys. Rev. Lett.* **82**, 636 (1999).
- [3] T. Nagata, H. Fujino, J. Akimitsu, M. Nishi, K. Kakurai, S. Katano, M. Hiroi, M. Sera, and N. Kobayashi (submitted).
- [4] A. Onodera, Y. Nakai, N. Kunitomi, O.A. Pringle, H.G. Smith, R. M. Nicklow, R.M. Moon, F. Amita, and N. Yamamoto, *Jpn. J. Appl. Phys.* **26**, 152 (1987).
- [5] T. Nagata, M. Uehara, J. Goto, J. Akimitsu, N. Motoyama, H. Eisaki, S. Uchida, H. Takahashi, T. Nakanishi, and N. Môri, *Phys. Rev. Lett.* **81**, 1090 (1998).

研究テーマ：強相関電子系の中性子散乱による研究

表題：TmB₁₂ の磁気構造の中性子回折による研究

1-2-5 Neutron diffraction study on the magnetic structure of TmB₁₂

T. Osakabe, F. Iga¹, S. Hiura and T. Takabatake

Advanced Science Research Center, Japan Atomic Energy Research Institute, Tokai, Ibaraki 319-1195

¹Advanced Science of Matter, Hiroshima Univ., Kagamiyama, Higashi-Hiroshima, Hiroshima 739-8526

RB₁₂ (R=Tb, Dy, Ho, Er, Tm, Yb, Lu) series show NaCl-type crystal structures consisting of R and B₁₂ octahedrons. In this series, R=Yb is well known as a Kondo-semiconductor, which has gaps of about 5 meV and 15 meV at Fermi level and a lot of studies on this compound has been done in order to investigate the origin of gap formation¹⁾. On the other hand, there have been few report on the study of the other compounds, especially on the magnetic structures so far because it has been thought that these compounds show simple antiferromagnetic order due to the RKKY interaction. Recently, Iga et al. have successfully prepared the high-quality sample of these series²⁾. They proposed that the electronic state of TmB₁₂ is similar to that of the Kondo-semiconductor, YbB₁₂. Thus, it is important to study these series systematically in order to investigate the origin of Kondo - semiconductor. In this report, we will show preliminary results of the neutron diffraction experiments on powder sample of TmB₁₂.

The neutron diffraction experiments on TmB₁₂ were carried out on the triple axis spectrometer TAS-1 installed at the 2G beam hole of JRR-3M reactor in JAERI, Tokai.

TmB₁₂ shows the magnetic ordering below 3.4 K. Thus, we measure diffraction patterns at 1.5K and 51K in order to pick out magnetic peaks. Fig. 1 shows the diffraction patterns of TmB₁₂. Some pairs of the magnetic peaks are clearly observed at 1.5 K. Fig. 2 shows the projection of these peak positions on the [100] - [011] scattering plane. The result reveals that TmB₁₂ shows not a simple antiferromagnetic order but a complex long period magnetic order with a wave vector of $k = (0.46, 0.46, 0.46)$. The precise neutron diffraction experiments using high - quality single - crystal samples including other rare - earth compounds in this series are now progressing.

Reference

1) see for example, T. Takabatake, F. Iga, T. Yoshino, Y. Echizen, K. Katoh, K.

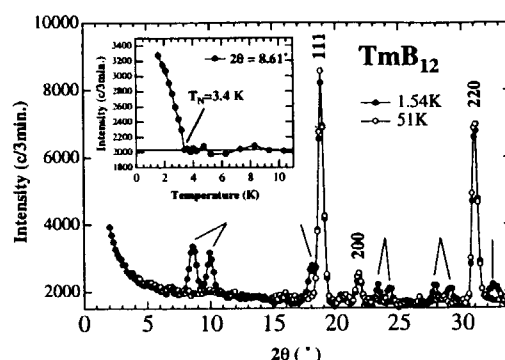


Fig. 1 Neutron diffraction patterns of TmB₁₂

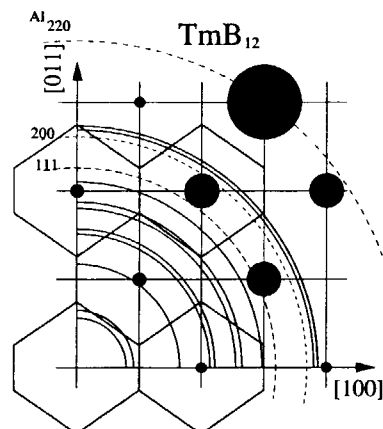


Fig. 2 The projection of the magnetic diffraction peaks of TmB₁₂ on the [100] - [011] plane.

- Kobayashi, M. Higa, N. Shimizu, Y. Bando, G. Nakamoto, H. Fujii, K. Izawa, T. Suzuki, T. Fujita, M. Sera, M. Hiroi, K. Maezawa, S. Mock, H.v. Löhneysen, A. Brückl, K. Neumaier, K. Andres, J. Magn. Mater. 177-181(1998)277
 2) F. Iga, N. Shimizu, T. Takabatake, J. Magn. Mater. 177-181(1998)337

研究テーマ：強相関電子系の中性子散乱による研究

表題：高圧下における CeAs の磁気構造

1-2-6 Magnetic structure of CeAs under high pressure

T. Osakabe, M. Kohgi¹, K. Iwasa¹, M. Kubota², H. Yoshizawa², Y. Haga and T. Suzuki³

Advanced Science Research Center, Japan Atomic Energy Research Institute, Tokai, Ibaraki 319-1195

¹Department of Physics, Tokyo Metropolitan University, Hachioji, Tokyo 192-0397

²Institute of Solid State Physics, University of Tokyo, Tokyo 106-8666

³Tsukuba Institute of Science and Technology, Tsukuba, Ibaraki 300-0819

Ce-monopnictides CeX (X=P, As, Sb, Bi) are low-carrier-density semi metallic compounds with NaCl-type crystal structure. For lighter compound CeP, recent neutron scattering studies using high-quality single-crystal sample made marked advances on the magnetic structures under high pressure. Detailed reports on the experiments were given in Ref. 1)-3). The essential points of the experiments are as follows. The Γ_8 states of Ce ions, which have about $2\mu_B$ magnetic moments in this case, appear among the Γ_7 crystal field ground states of Ce ions at low temperature above critical pressure P_c of about 0.3 GPa. They are forming periodic stacks of the Γ_8 ferromagnetic double (001) planes. The period of the double (001) planes changes quite systematically with increasing applied pressure.

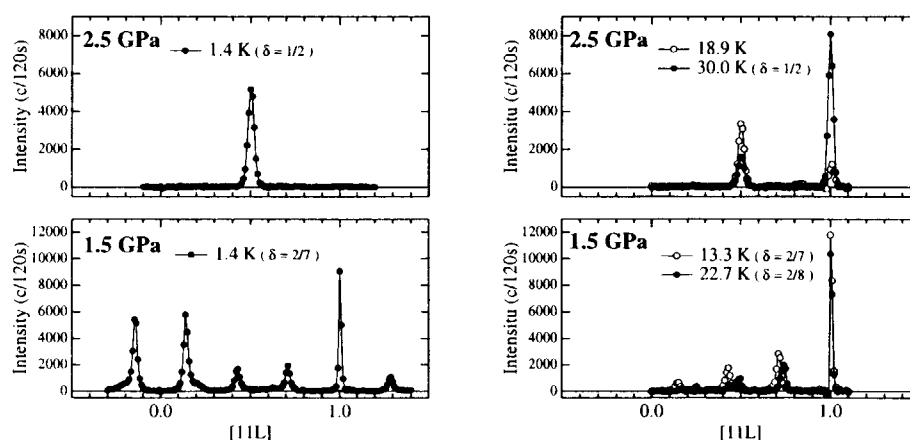
On the other hand, although macroscopic measurements revealed that CeAs shows a pressure versus temperature (P-T, hereafter) phase diagram similar to that of CeP, no evidence that CeAs shows such the novel magnetic structures under high pressure as observed on CeP has been reported so far⁴⁾. Thus, we carried out neutron diffraction experiments under high pressure using high-quality single-crystal sample of CeAs#3. In this paper, we will briefly report the results of our neutron diffraction experiments under high pressure up to 2.5 GPa.

The neutron diffraction experiments on CeAs under pressure up to 2.5 GPa were carried out on the triple axis spectrometer TAS-1 installed at the 2G beam hole of JRR-3M reactor in JAERI, Tokai.

At ambient pressure below 8.0K, CeAs shows a simple type-I antiferromagnetic ordering which consists of an antiferromagnetic stack of ferromagnetic (001) planes with Γ_7 magnetic moments. In contrast, we observed novel magnetic diffraction patterns along [11L] direction above critical pressure P_c of about 1.2

GPa. The majority of the scattering patterns consist of ferromagnetic components at $L = 1.0$ and satellite peaks at regular intervals. The positions of satellite peaks are described by multiples of the wave vector $(2\pi/a)\delta$, where a is the lattice parameter and δ gives the period of the magnetic structure. Fig.1 (a)-(d) show some of the typical magnetic diffraction patterns of CeAs above P_c . The P-T phase diagram and the schematic magnetic structures in the phase diagram determined by the neutron diffraction experiments are summarized in Fig. 2. A systematic change of the period of the magnetic structure is seen in the phase diagram. The detailed feature of the phase diagram is very similar to that of CeP¹⁾⁻³⁾. The apparent difference is pressure values at which the magnetic structures with the same periods appear. This point will be discussed again below. We also observed steep decrease of the volume above P_c with increasing applied pressure. This gives direct evidence for the fact that the states with $2\mu_B$ magnetic moments, which appear among the Γ_7 ground states above P_c , are affected by the strong mixing effect.

In the phase diagram, as expounded on CeP¹⁾⁻³⁾, $T_{c2}(P)$ is correspond to the first-order-like transition temperature below which the Γ_8 Ce ions with $2\mu_B$ magnetic moments appear among the Γ_7 ground state Ce ions suddenly and order in the form of periodic stacks of the Γ_8 ferromagnetic double (001) planes. Since the origin of the Γ_8 ferromagnetic planes is explained within the framework of the p-f mixing model for Ce-monopnictides⁵⁾, it seems that the increase of $T_{c2}(P)$ and the increase of the ratio of the Γ_8 Ce ions with increasing pressure is caused by the increase of the carrier number as a result of the increase of the p-f mixing effect caused by applying pressure. Thus, the difference of the pressure values between CeP and CeAs is due to the difference of their carrier numbers. The

Fig. 1 Magnetic diffraction patterns of CeAs above P_c

macroscopic measurements actually confirmed that the carrier numbers of CeP and CeAs at ambient pressure are estimated to be about 0.01 and about 0.005 per Ce, respectively^{6,7)}. Concerning the present results, more detailed discussions including theoretical aspects are given in Ref. ^{8,9)}.

Reference

- 1) M. Kohgi, T. Osakabe, K. Iwasa, J. M. Mignot, I. N. Goncharenko, Y. Okayama, H. Takahashi, N. Môri, Y. Haga, and T. Suzuki, J. Phys. Soc. Jpn. **65** (1996) suppl. B, p. 99.
- 2) T. Osakabe, M. Kohgi, K. Iwasa, N. Nakajima, J.M. Mignot, I. N. Goncharenko, Y. Okayama, H. Takahashi, N. Môri, Y. Haga, and T. Suzuki, Physica B **230-232** (1997) 645.
- 3) M. Kohgi, T. Osakabe, K. Iwasa, J.M. Mignot, I.N. Goncharenko, P. Link, Y. Okayama, H. Takahashi, N. Môri, Y. Haga and T. Suzuki, Rev. High Pressure Sci. Technol., **7** (1998) 221.
- 4) Y. Okayama, Y. Ohara, S. Mituda, H. Takahashi, H. Yoshizawa, T. Osakabe, M. Kohgi, Y. Haga, T. Suzuki and N. Môri, Physica B **186-188** (1993) 531.
- 5) H. Takahashi and T. Kasuya, J. Phys. C, Solid State Phys. **18** (1985) 2697, 2709, 2721, 2731, 2745 and 2755.
- 6) Y. Haga, Ph.D. thesis, Tohoku University (1995).
- 7) N. Takeda, Y.S. Kwon, Y. Haga, N. Sato, T. Suzuki and T. Komatsubara, Physica B

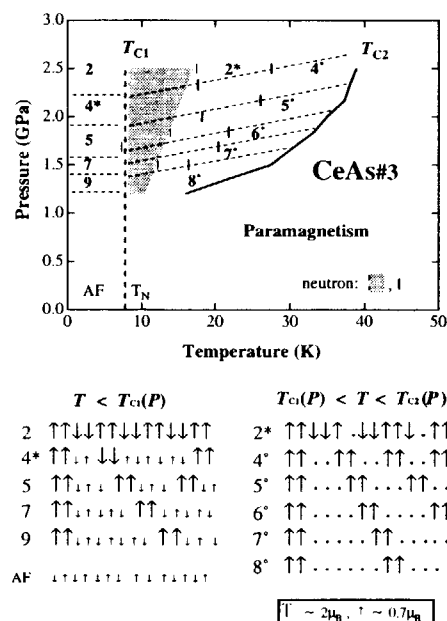


Fig. 2 Phase diagram and schematic magnetic structures of CeAs in the phase diagram determined by the neutron diffraction experiments.

186-188 (1993) 153.

- 8) T. Osakabe, M. Kohgi, K. Iwasa, K. Kakurai, J.M. Mignot, I.N. Goncharenko, Y. Okayama, H. Takahashi, N. Môri, M. Kubota, H. Yoshizawa, Y. Haga and T. Suzuki, JJAP Series 11 p. 123.
- 9) see for example, T. Kasuya, Y. Haga and T. Suzuki, J. Alloys Compounds **219** (1995) 290.

研究テーマ：希土類十二硼化物の磁気構造

表題：UlrGeにおける磁気秩序の探求

1-2-7 Search for Magnetic Order in UlrGe

K. Prokeš¹, F. Iga, T. Takabatake, T. Fujita and T. Osakabe²

Department of Quantum Matter, ADSM, Hiroshima University, Higashi-Hiroshima 739, Japan

¹ At present: Hahn-Meitner Institut, NE, 141 09 Berlin, Germany

² Japan Atomic Energy Research Institute, Tokai, Ibaraki 319 11, Japan

UlrGe belongs to a large group of isostructural UTX compounds and up to now has been studied only in polycrystalline form. It crystallises in the orthorhombic TiNiSi-type of structure (space group Pnma) where U atoms which are responsible for magnetic properties form a zig-zag chain running along the a-axis.

UlrGe is one of the most puzzling cases despite considerable effort of several groups. All bulk properties which have been studied so far point to antiferromagnetism in this compound below 16-18 K. [1-3]. The specific-heat anomaly shifts by 0.5 K to lower temperatures when a field of 5 T is applied [3,6] and the magnetization curves measured on free-powder samples at 4.2 K exhibit two clear metamagnetic transitions at 13 and 19 T, respectively. To a big surprise no indication of magnetic order down to 1.5 K has been provided by neutron powder diffraction experiments [4].

Recently, a single crystal of UlrGe of sufficient quality has been grown by a modified Czochralski technique which has opened the possibility to re-investigate the magnetic structure(s) of this compound at low temperatures. We have performed single-crystal neutron-diffraction experiment at two temperatures, namely at 40 K and at 4.2 K. At higher temperature we have confirmed the proposed crystal structure with the lattice parameters $a=683.7$ pm, $b=429.2$ pm and $c=756.4$ pm.

To detect expected magnetic reflections we have looked to a-c and b-c scattering planes. Note that the b-c plane is magnetically soft plane. Due to the fact that

within the crystallographic unit cell there are four U atoms and therefore antiferromagnetic (AF) coupling can be maintained within the crystallographic unit cell we have also monitored integrated intensities of nuclear reflections. Unfortunately, we did not observe any new reflections which would be due to proposed AF structure nor we have detected any sizable change in the nuclear Bragg peak intensities which would be possible to interpret as to be due to magnetic ordering.

Obtained results strongly suggest that either the magnetic moments are below detection limit of the performed experiment or that the propagation vector of the AF structure is outside the a-c or b-c planes. Most probably, the magnetic structure is incommensurate with the underlying crystallographic structure. It would be desirable to perform diffraction experiment using a wide-angle position-sensitive detector.

References

- [1] Ramirez, A.P., B. Batlogg, and E. Bucher, 1987, J. Appl. Phys. 61, 3189.
- [2] Troc, R. and V.H. Tran, 1988, J. Magn. Magn. Mater. 73, 389.
- [3] Buschow, K.H.J., E. Brück, R.G. van Wierst, F.R. de Boer, L. Havela, V. Sechovsky, P. Nozar, E. Sugiura, M. Ono, M. Date, and A. Yamagishi, 1990, J. Appl. Phys. 67, 5215.
- [4] Tran, V.H., F. Bouree, G. Andre, R. Troc, Solid State Comm. 98 (1996) 111

研究テーマ： $\text{La}_2\text{NiO}_{4+\delta}$ のスピンドYNAMIKSの研究

表題：酸素ドーブした $\text{La}_2\text{NiO}_{4+\delta}$ ($\delta \leq 0.11$) のスピン波励起

1-2-8 Spin-Wave Excitations in Commensurate Oxygen-Doped $\text{La}_2\text{NiO}_{4+\delta}$ ($\delta \leq 0.11$)

K. Nakajima,¹ T. Sawada,¹ H. Yoshizawa,¹ Y. Endoh²

¹Neutron Scattering Laboratory, Institute for Solid State Physics, University of Tokyo

²Department of Physics, Tohoku University

Complicated phenomena triggered by hole doping into transition metal oxides attract much interest. La_2NiO_4 is a 2D Heisenberg antiferromagnet, which belongs to the same family of compounds of so-called 2-1-4 oxide superconductors. Although, in contrast to the cuprates, the system remains insulating even in the rather high concentration range of hole doping, La_2NiO_4 changes its static and dynamical properties drastically on hole doping. Especially, now it is believed that induced holes in the Sr doped La_2NiO_4 or heavily oxidized $\text{La}_2\text{NiO}_{4+\delta}$ ($\delta > 0.11$) are well localized and show a long range ordering in a stripe fashion, which causes a commensurate-incommensurate transition of magnetic correlations. Complicated behavior in the hole doped La_2NiO_4 is a result of co-playing of charge and spins, hence the dynamics of both elements play crucial role in this system. Previously [1], we have measured the spin-wave excitations in $\text{La}_2\text{NiO}_{4.11}$ and have

found that doping induces the additional excitation modes, which show large renormalization in the exchange energy, in the lower energy and the smaller intra-plane momentum transfer q_{2D} region, while the unrenormalized excitations still persist in the higher energy region. To reveal the mechanism of the doping effect on the spin dynamics in detail, critical study on different doping systems is indispensable. Recent two-magnon Raman scattering result suggested a possible coexisting of the unrenormalized and the renormalized spin-waves even in $\text{La}_2\text{NiO}_{4.02}$ [2], which should be examined by neutron scattering.

In the present work, we have performed neutron scattering experiments on single crystals ($\sim 1 \text{ cm}^3$ in average volume) of $\text{La}_2\text{NiO}_{4+\delta}$ with different amount of excessive oxygen ($\delta=0, 0.02$ and 0.11) to measure the spin-wave excitations. Experiment was carried out on a triple-axis spectrometer GPTAS (4G).

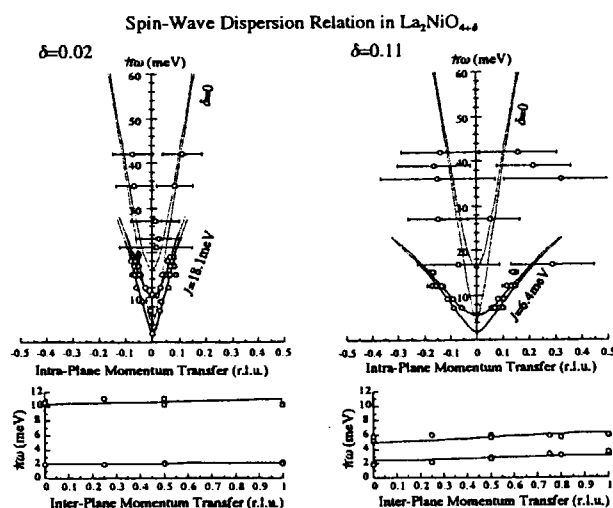


Figure 1 : Spin-wave dispersion relations in $\text{La}_2\text{NiO}_{4.02}$ and $\text{La}_2\text{NiO}_{4.11}$. The horizontal bars of the higher energy data ($\Delta E > 21 \text{ meV}$ of $\delta=0.02$ and $\Delta E > 16 \text{ meV}$ of $\delta=0.11$) indicate the FWHM of the profiles of constant-energy scans. Intra-layer dispersion relation in $\text{La}_2\text{NiO}_{4.00}$ is also indicated by the dashed lines in the figure.

JRR-3M, GPTAS(4G), 2. Magnetism

Resulted spin-wave dispersion relations are shown in Fig. 1. As observed in $\text{La}_2\text{NiO}_{4.11}$, we observed the renormalized spin-wave modes below 20 meV also in $\text{La}_2\text{NiO}_{4.02}$. The renormalized modes are well-defined but can be observed only at the small q_{2D} region. At higher energy region ($\Delta E > 20$ meV), broad and unrenormalized excitations exist. Observed behavior of the spin-wave excitations in $\text{La}_2\text{NiO}_{4.02}$ is qualitatively same as those in $\text{La}_2\text{NiO}_{4.11}$. Mixed spin-wave excitations seem

common nature in oxygen doped $\text{La}_2\text{NiO}_{4+\delta}$ at least in the commensurate region ($\delta \leq 0.11$). Only 2% of oxygen doping (or 4% of hole doping) drastically changes the spin-wave in La_2NiO_4 . The spin-wave velocities of the renormalized mode are 199 meV-Å ($\text{La}_2\text{NiO}_{4.11}$) and 70 meV-Å ($\text{La}_2\text{NiO}_{4.02}$), while the unrenormalized value is 341 meV-Å in $\text{La}_2\text{NiO}_{4.00}$.

In the earlier work, we speculated that the renormalized modes are originated by excitations of impurities, i.e., hole localized Ni^{3+} spins. Present results, however, excludes possibility of an impurity mode. The spin-wave velocity of renormalized modes decreases with increasing the hole number. Scattering intensities also considerably depressed in heavier doped region (Fig. 2 (a)). The evidence can not be expected in a simple impurity system. It should be noted that the Néel temperatures (T_N) are well scaled by the effective exchange interaction of the renormalized modes (Fig. 2 (b)). Since T_N is the ordering temperature of the Ni^{2+} spins, the renormalized modes are considered to be modified spin-waves of Ni^{2+} spins.

In 1D antiferromagnet, multi-modes spin-wave excitations are expected in mixed spin systems [3, 4]. Recently, the spin-wave calculation for doped La_2NiO_4 was performed using Schwinger-boson mean field theory [5]. It is pointed out that the frustration between Ni^{2+} and Ni^{3+} causes the strong renormalization in the spin-wave velocity at lower energy side and the excitations are considerably dumped at the cross-over region. Experimental evidence support this idea. However, further investigations are required to make a definite conclusion for more detailed microscopic mechanism of the doping effect.

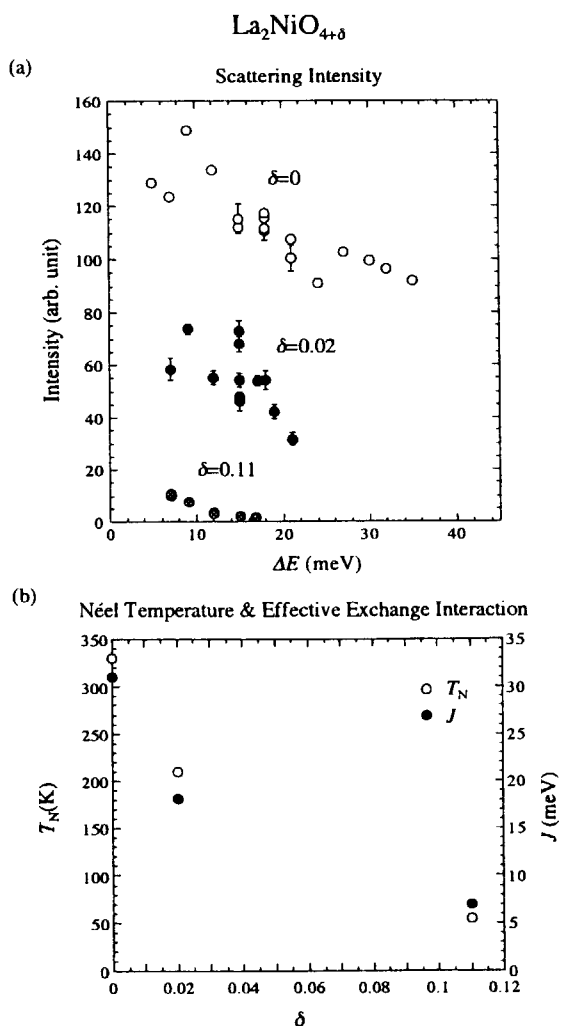


Figure 2 : (a) Intensities obtained from constant-energy-transfer scans across 2D zone center. The instrumental-resolution effects are corrected. Sample volume difference is normalized using phonon intensities. (b) Oxygen concentration dependence of Néel temperature (open circles) and effective exchange interaction (closed circles).

- [1] K. Nakajima, and Y. Endoh: J. Phys. Soc. Jpn. **67** (1998) 1552
- [2] S. Suga *et al.*: J. Phys. Soc. Jpn. **67** (1998) 2992
- [3] M. Saitoh and H. Fukuyama: J. Phys. Soc. Jpn. **66** (1997) 3259
- [4] S. Yamamoto *et al.*: J. Phys. Soc. Jpn. **67** (1998) 3711
- [5] I. Korenblit: Europhys. Lett. **46**, 82 (1999)

研究テーマ：二次元希釈反強磁性体の磁気臨界散乱に現れるスピン相関関数

表題：二次元パーコレーションイジング反強磁性体の磁気臨界散乱

1-2-9

Critical Magnetic Scattering from Two-Dimensional Percolating Ising Antiferromagnets

K. Iwasa and H. Ikeda¹

Department of Physics, Tokyo Metropolitan University, Hachioji, Tokyo 192-0397, Japan

¹ *Neutron Science Laboratory, Institute of Materials Structure Science, High Energy Accelerator Research Organization, Tsukuba, Ibaraki 305-0801, Japan*

Percolating networks have been studied from a concept of fractal structures. Simple systems exhibiting percolating networks are diluted magnets. The fractal structures in two-dimensional (2D) diluted Ising antiferromagnets $\text{Rb}_2\text{Co}_c\text{Mg}_{1-c}\text{F}_4$ have been investigated by neutron experiments,¹⁾ where c corresponds to a magnetic concentration on a 2D square lattice. Their magnetic exchange interaction dominates within the 2D plane and is limited to the nearest neighbors. An infinite spin cluster appears in the system with magnetic concentration above $c_p = 0.593$ (percolation threshold), and it orders in long range. A neutron magnetic Bragg scattering from the near-percolating system with $c = 0.60$ shows a profile with a larger peak width than that of a Gaussian profile which is expected from a δ -function convoluted by the resolution function. The diffraction intensity is reproduced well by a power-law function q^{D_f} , where q is a reduced wave number in the 2D square lattice and $D_f = 1.896$ is a fractal dimension. This fact reveals that the long-range ordered percolating cluster is considered to hold self-similar fractal characters.

Magnetic critical scattering from a homogeneous spin lattice is well known as described by a Lorentzian lineshape as a function of q . On the other hand, the spin-correlation function in a percolating magnet may be different from that in a homogeneous system, because the percolating spin lattice has self-similar structure. It concludes that a scattering profile deviates

from a usual Lorentzian function even in a critical region above T_N . In this study, critical magnetic scattering of $\text{Rb}_2\text{Co}_c\text{Mg}_{1-c}\text{F}_4$ ($c = 0.60$ and 0.65) were measured by double-axis mode of GPTAS (4G) and HER (C1-1) spectrometers.

Figure 1 shows a scattering profile around the magnetic zone center of the $c = 0.60$ sample at 22 K as represented by circles. Néel temperature of this sample was confirmed as 20 K from a temperature dependence of antiferromagnetic Bragg-peak intensity. A solid line represents a result of least-squares fitting of a Lorentzian function convoluted by a resolution function to the experimental data, however it does not reproduce the data. Figure 2 shows the data measured at 31 K. Same fitting procedure was applied to the data, and the result is shown by a solid line. They are in good agreement with each other within statistical errors. In the $c = 0.60$ sample, the deviation of profiles from a Lorentzian function was observed below about $(T_N + 10) = 30$ K. Experiments of the $c = 0.65$ sample, whose ordering temperature was confirmed as 30.8 K, were also performed, and deviation of profiles from a Lorentzian was observed. However, a temperature region where non-Lorentzian profiles of the $c = 0.65$ sample appear is narrower than that in the near-percolating sample with $c = 0.60$. These experimental results can be interpreted as an anomalous critical scattering from percolating systems with fractal geometry.

The deviation of scattering profile from a Lorentzian one is thought to be small in the diluted 2D system, because $D_f = 1.896$ is very close to the Euclidian dimension $D = 2$. In a percolating 3D magnet on a cubic lattice, fractal dimension is 2.48 which has larger difference from the Euclidian dimension ($D = 3$) than that in the 2D magnet. Experimental studies for the diluted 3D magnet are also necessary to determine a generalized spin-correlation function for percolating systems.

Reference

- 1) H. Ikeda, K. Iwasa and K. H. Andersen: J. Phys. Soc. Jpn. 62 (1993) 3832.

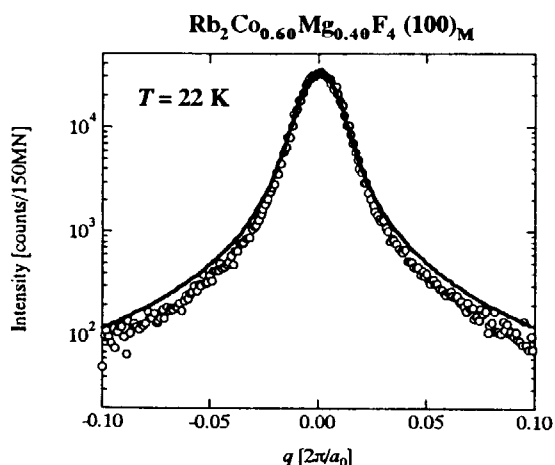


Figure 1. Critical magnetic scattering profile from $\text{Rb}_2\text{Co}_{0.60}\text{Mg}_{0.40}\text{F}_4$ at 22 K obtained by GPTAS (4G) spectrometer. Circles represent the experimental data and a solid line the fitting results.

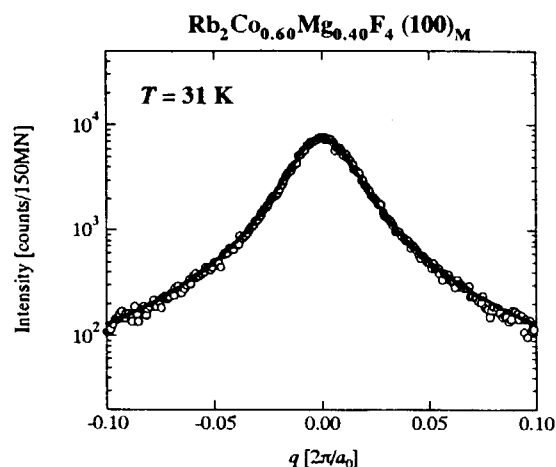


Figure 2. Critical magnetic scattering profile from $\text{Rb}_2\text{Co}_{0.60}\text{Mg}_{0.40}\text{F}_4$ at 31 K obtained by GPTAS (4G) spectrometer. Circles represent the experimental data and a solid line the fitting results.

研究テーマ: $Y_{1-x}U_xRu_2Si_2$ ($0 \leq x \leq 1$) おける秩序状態の研究

表題: 歪んだ重い電子系 $(Y,U)Ru_2Si_2$ における微弱反強磁性モーメント

1-2-10

Weak Antiferromagnetic Moment in Distorted Heavy-Fermion System $(Y,U)Ru_2Si_2$

H. Amitsuka, A. Okumura, K. Kuwahara and M. Yokoyama

Graduate School of Science, Hokkaido University, Sapporo 060-0810, Japan

Antiferromagnetism with extremely weak staggered moment μ_0 ($\sim 10^{-2} \mu_B$) observed in URu_2Si_2 has been one of the most intriguing issues in heavy-fermion physics. This system undergoes a second-order phase transition at $T_0 = 17.5$ K, which is demonstrated by a sharp anomaly in various bulk properties. In spite of intensive studies over the last decade, it remains unsolved how the tiny moments drive the large bulk anomalies, such as a large reduction of entropy ($\sim 0.2R \ln 2$) at T_0 . In addition to various theoretical approaches assuming the dipole to be intrinsic, it has also been argued that there may be some hidden primary order parameter. This latter is supported by a recent neutron study which reports that the onset temperature T_m of the magnetic Bragg intensity deviates from the transition temperature T_0 defined as the midpoint of a jump in C/T .¹⁾ as a result of the absence of annealing procedure.

It is of interest to investigate the relationship between the weak antiferromagnetism and the bulk properties for the same sample by introducing some implicit parameter. Here, we present the results of elastic neutron scattering experiments for the pure and Y 0.5% doped URu_2Si_2 single crystals. This work is an extension of the preliminary experiments of last year, in which we observed a tendency of suppression of μ_0 by doping.

Both samples were grown by using a tri-arc furnace, followed by an annealing in evacuated sealed quartz tubes at 850 °C for one week. The elastic neutron scattering experiments were carried out on the triple axis spectrometer 4G at the JRR-3M reactor. We used a 40'-80'-40'-80 horizontal collimation and double PG(002) filters to reduce the higher-order contaminations.

In Fig. 1, we plot the temperature variations of (100) magnetic Bragg peak intensity I_m normalized by (110) nuclear peak, com-

paring them with the temperature derivative of the c -axis susceptibility. For the pure compound, whole feature of I_m is in good agreement with the previous reports for annealed samples. The saturation moment μ_0 and the correlation length ξ along the a axis at 1.6K are estimated to be $\sim 0.01 \mu_B$ and 178 Å, respectively. By substituting Y for 0.5% of U, it is found that μ_0 is suppressed down to $\sim 0.0075 \mu_B$ with a shorter correlation length of $\xi \sim 102$ Å. T_m also decreases down to 12.5K. These results provide a remarkable contrast to the behavior in the bulk susceptibility, which is hardly affected by doping. The observed discrepancy in the doping effect between $\mu_0(T)$ and χ strongly suggests the tiny moments to be extrinsic to the transition of URu_2Si_2 at T_0 .

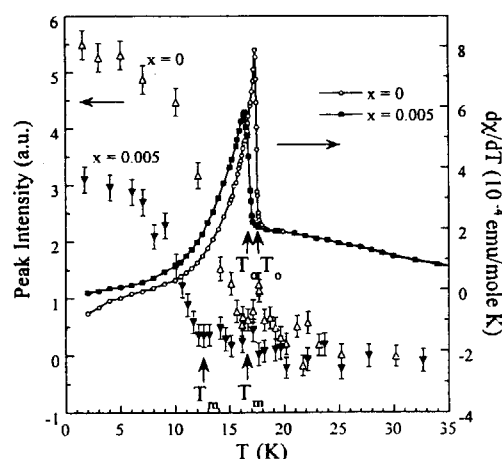


Figure 1: Peak intensity of the (100) Bragg reflection vs. temperature, for $Y_xU_{1-x}Ru_2Si_2$ ($x = 0$ and 0.005), shown together with the temperature derivative of the c -axis magnetic susceptibility.

1) B. Fåk *et al.*, J. Magn. Magn. Mater., 154(1996)339.

研究テーマ：三角格子反強磁性体 $\text{CuFe}(\text{Al})\text{O}_2$ におけるスピン波分散

表題：三角格子反強磁性体 $\text{CuFe}(\text{Al})\text{O}_2$ の磁気秩序

1-2-11

Magnetic Ordering in Triangular Lattice Antiferromagnet $\text{CuFe}(\text{Al})\text{O}_2$

M. Mekata, Y. Kobayashi, K. Taki, Y. Yamada, F. Takei¹, D. Zhao¹
and Y. Oohara²

Department of Applied Physics, Fukui University, Bunkyo, Fukui, 910-8507 Japan

¹ *Department of Physics, Osaka University, Toyonaka, Osaka, 560-0043, Japan*

² *Neutron Scattering Laboratory, ISSP, University of Tokyo, Tokai, Ibaraki, 319-1106 Japan*

In CuFeO_2 why the moments of Fe^{3+} ions in the orbital singlet state behave as Ising spins is the problem to be solved. Neutron diffraction revealed that 2% Al substitution converts the system into a Heisenberg spin system, while high field magnetization measurements showed that Ising character remains up to the 8% substituted compound. To study these problems, the magnetic structure and the phase transition together with the spin fluctuations in a single crystal as well as powder of the 5% substituted compound were studied by means of elastic neutron scattering and neutron spin echo. In spite of extensive trials, no significant signal of magnon excitation was observed.

The T_{N1} for the present compound was found to be 13.5K and some anomaly in the scattered intensity was observed at 11K corresponding to T_{N2} . Figure 1 shows the observed intensity of magnetic peaks at 4K plotted as a function of the calculated intensity based on the helical and the spin density wave structures. Apparently better fitting was obtained for the helical structure. But similar fitting of the data at 12K indicates the system to have the spin density wave (SDW) structure in the intermediate temperature phase. The orientation factor for the scattering vector $(Q_x Q_y Q_z)$, $\langle s_z \rangle^2 + (1 - 2 \langle s_z \rangle^2) Q_z^2$, also shows the existence of the x-y component of the magnetic moment at low temperatures. On the other hand the more diffusive line shape of the (0.2 0.2 1.5) peak than the (0.8 0.8 1.5) peak at 12K may be attributed to the spin density wave structure. Based on these results it is concluded that the

intermediate temperature phase has a collinear spin density wave structure along the c-axis, while in the low temperature phase below 11K a helical structure is stabilized.

Powder diffraction which is free from extinction also gave the consistent results.

Autocorrelation time of spins was measured by neutron spin echo technique up to 150ps at 2K, 8K, 12K and 14K. The time variation of spin echo intensity at 12K is within the data scattering comparing with the results of paramagnetic phase at 14K, but the static nature of the spins at 2K and 8K is obvious from the time dependence of spin echo intensity.

The line profile of the powder pattern deviates appreciably from the Gaussian shape indicating the existence of some randomness frozen in the long range magnetic order which may provide Ising character to the system.

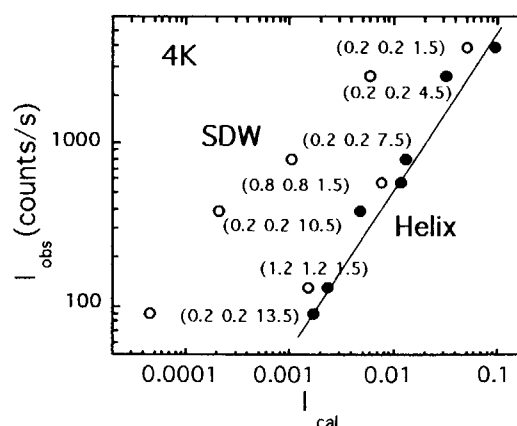


Fig. 1 Magnetic intensity of $\text{CuFe}_{0.95}\text{Al}_{0.05}\text{O}_2$

JRR-3M, 4G & 5G, 2. magnetism

研究テーマ：スピングャップ系 BaVS₃ 化合物の非弾性散乱

表題：軌道秩序を持つスピン-重項系 BaVS₃ の中性子散乱

1-2-12

Neutron Scattering of an Orbital-Ordered Spin-Singlet System BaVS₃

M. Shiga, H. Nakamura, H. Tanahashi, H. Imai, K. Kojima¹, K. Kakurai² and M. Nishi²

Department of Materials Science and Engineering, Kyoto University, Kyoto 606-8501, Japan

¹Department of Superconductivity, The University of Tokyo, Tokyo 113-8656, Japan

²Neutron Scattering Laboratory, The Institute for Solid State Physics, The University of Tokyo, Shirakata, Tokai, Naka, Ibaraki, 319-1106, Japan

BaVS₃, which is a $S = 1/2$ system, exhibits a metal-insulator transition at $T_{MI} \approx 70$ K. Recently, an orbital-ordered spin-singlet state was proposed as the ground state of this compound based on ⁵¹V NMR and NQR results. The crystal structure at room temperature is the hexagonal perovskite type (space group: P6₃/mmc), in which V atoms (at the 2a site) form one-dimensional chains along the c axis and a triangular lattice in the c plane. We performed inelastic neutron scattering experiments of BaVS₃ to detect the spin gap directly and to get information on the nature of the spin singlet and the orbital ordering.

Inelastic neutron scattering experiments were performed for a powder sample of BaVS₃ using the triple axis spectrometer, ISSP-PONTA-5G in the temperature range of $T = 8$ –300 K. All the measurements were made with a fixed final energy $k_f = 2.67 \text{ \AA}^{-1}$ ($E_f = 14.7$ meV).

Figure 1 shows energy scan spectra measured at $Q = 1.2 \text{ \AA}^{-1}$, which was rather arbitrarily selected to be free from phonon scattering. At the lowest temperature, inelastic excitations centered at around the energy transfer $\Delta E = 10$ meV were clearly observed. This result suggests the presence of spin gap with the gap parameter $\Delta \leq 10$ meV. With increasing temperature, the energy of the maximum in the spectra shifts to lower energies, and inelastic excitations

disappear at 75 K ($> T_{MI}$).

We also measured energy scan spectra at a smaller Q ($= 0.8 \text{ \AA}^{-1}$). Even at a low temperature, 8 K, we have observed low energy excitations in addition to the higher-energy inelastic scattering mentioned above. This result seems to be in contrast to the spin singlet ground state picture.

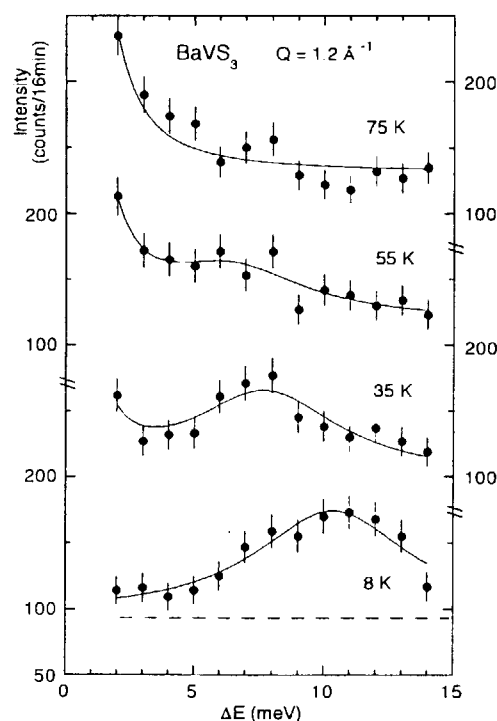


Figure 1. Energy scan spectra measured at $Q = 1.2 \text{ \AA}^{-1}$ and $T = 75, 55, 35$ and 8 K. The origin of the vertical axis is shifted for each temperature. The broken line is the background for $T = 8$ K.

研究テーマ：CsVCl₃のスピン相関関数

表題：CsVCl₃の磁気相関

1-2-13 Magnetic Correlations in CsVCl₃

S. Itoh, K. Kakurai¹, Y. Endoh², H. Tanaka³, K. Nakajima¹ and M. J. Harris⁴

Neutron Science Laboratory, High Energy Accelerator Research Organization, Tsukuba

¹ *Neutron Scattering Laboratory, The University of Tokyo, Tokai*

² *Department of Physics, Tohoku University, Sendai*

³ *Department of Physics, Tokyo Institute of Technology, Tokyo*

⁴ *ISIS Facility, Rutherford Appleton Laboratory, UK*

We have been studying the spin dynamics in CsVCl₃, an $S=3/2$, one-dimensional (1D) Heisenberg antiferromagnet, in order to investigate the crossover behavior in the spin dynamics from the quantum (smaller spin) to the classical (larger spin) limits [1,2]. Classical theory has predicted that the linewidth of the magnetic excitations (Γ) is independent of the 1D momentum transfer (q) and is proportional to the inverse correlation length (κ) at low temperatures, and that Γ is proportional to the temperature (T) as a result of the linear T -dependence of κ [3]. We found that $\Gamma(T)$ is extrapolated to be finite at $T=0$ K [2]. A possible interpretation of the finite Γ is a finite κ in the classical relation between Γ and κ , or an observation of an excitation continuum. In order to obtain an understanding for the behavior of $\Gamma(T)$, we performed measurements of the energy-integrated scattering function to determine $\kappa(T)$. Inelastic neutron-scattering experiments were performed on the ISSP triple-axis spectrometer, PONTA, installed at the 5G beam hole at the JRR-3M reactor and also on the crystal analyzer spectrometer, PRISMA, installed at the ISIS Facility at the Rutherford Appleton Laboratory.

A double-axis measurement was performed on PONTA with E_i fixed to be 30.5 meV using the collimation 15'-20'-20'. The single-crystal sample of CsVCl₃ weighing 1 g was mounted with [110] and [001] in the scattering plane. The scan was performed keeping the 1D reciprocal lattice plane parallel to k_f in order to realize the geometrical condition of the energy-integration at each q . The mosaic spread of the sample crystal was 0.9° (FWHM) and the q -resolution was

measured to be $\Delta q=0.02\text{\AA}^{-1}$ (FWHM). On PRISMA, the single-crystal sample of CsVCl₃ weighing 15 g was mounted with [001] perpendicular to k_i and with [110] horizontal, where the constant- q scan at $q=k_f \sin \phi$ is realized for each detector with its scattering angle ϕ . A 60' collimator was located between the sample and the analyzer crystal. E_f was chosen to be 12.7 meV. The mosaic spread was 2.1° (FWHM), and the q -resolution was measured to be $\Delta q=0.02\text{\AA}^{-1}$ (FWHM). In this experimental set-up, the inelastic spectrum $I(q,E)$ was taken at each q by moving the analyzer-detector arms step by step (i.e. by changing ϕ). Since $I(q,E)$ is the sum of the magnetic scattering cross section $(k_f/k_i)S(q,E)$ and the other background, where E is the energy transfer, the correlation function $S(q)$ was deduced by integrating $(k_i/k_f)I(q,E)$ over E up to 100 meV.

For these two measurements, the q -dependence of the observed intensity was well fitted with the Lorentzian scattering function $(\sim(q^2+\kappa^2)^{-1})$ convoluted with the instrumental resolution, and Fig.1 shows the temperature dependence of inverse correlation length $\kappa(T)$. From these two measurements, the different results on $\kappa(T)$ were obtained, as shown in Fig.1. The magnetic correlation function is defined by the magnetic response $S(q,E)$ integrated over E , and, the inelastic neutron-scattering cross section is proportional to $S(q,E)$ multiplied by the kinematical factor k_f/k_i . This quantity was measured in the PRISMA experiment, with the integration covering all excitation energies up to the zone boundary. On the other hand, the energy-integrated spectrum obtained from the conventional double-axis measurement is the

integration of the cross section without correcting the kinematical factor, but the integration range is bounded by the upper limit E_i , much lower than the zone boundary energy (E_{ZB}). Therefore, the PRISMA results present a more accurate probe of the magnetic correlations. In fact, the energy-integrated spectrum from $I(q, E)$ taken on PRISMA without correcting k_f/k_i was also well fitted to the Lorentzian scattering function, and $\kappa(T)$ obtained by the fit was identical to the result from the double-axis measurement as shown in Fig.1. The difference shown in Fig.1 thus mainly comes from the correction of k_f/k_i . The large error bar of $\kappa(T)$ taken on PRISMA in Fig.1 comes from an enhancement of the poor statistics of the inelastic spectrum at larger E due to the correction of k_f/k_i .

In classical theory, $\kappa(T)$ is expressed by $\kappa(T) = T/(2JS^2a)$, with the exchange constant J and the lattice constant a . The solid line in Fig.1 is $\kappa(T)$ calculated from this formula. Assuming E_{ZB} at $T = 40\text{K}$ [1] to be 4SJ , where R is the renormalization constant [4], J was determined to be $119\text{K} \pm 3\text{K}$. The measured $\kappa(T)$ (on PRISMA) is in good agreement with the theory, κ can be extrapolated to vanish at $T=0\text{K}$. This result is consistent with current theory: half integer spin systems show power-law decay in the spin correlation at $T=0\text{K}$. Correlations with power-law decay represents a sort of a long range ordering, and therefore, $\kappa=0$ at $T=0\text{K}$ in terms of κ [5]. The presently-obtained linear T -dependence of κ at the observed T -range is consistent with the result from the numerical study for an $S=3/2$ system [5].

We previously reported finite Γ at low T [2]. On the other hand, at present we found a linear T -dependence of κ at the observed T -range of $0.34\text{J} \sim 1.7\text{J}$ ($J=119\text{K}$). A classical system exhibits ordering at $T=0\text{K}$, and the dynamical scaling can be applied to the phase transition. The linear relation between Γ and κ is consistent with the scaling. In the present $S=3/2$ system CsVCl_3 , there is no linear relation between $\Gamma(T)$ and $\kappa(T)$. Therefore, the observed finite energy width at low T should

not be attributed to the scaling of $\Gamma(T)$ with $\kappa(T)$ in terms of classical theory, but rather indicates some fluctuations surviving even at low T . A possible reason of the finite energy width is the existence of an excitation continuum. A numerical study has suggested that a half-integer spin system exhibits an excitation continuum and that the energy spread is approximately J for an $S=3/2$ system [6], and, in fact, the observed finite energy width at low T has a value close to the estimated continuum spread.

References

- [1] S. Itoh et al., Phys. Rev. Lett. 74, 2375 (1995).
- [2] S. Itoh et al., Physica B 241-243, 546 (1998).
- [3] G Reiter and A. Sjölander, Phys. Rev. Lett. 39, 1047 (1977).
- [4] S. Yamamoto, Phys Rev. Lett. 75, 3348 (1995).
- [5] N. Hatano and M. Suzuki, J. Phys. Soc. Jpn. 62, 1346 (1993).
- [6] J. Deisz et al., Phys. Rev. B 48, 10227 (1993).

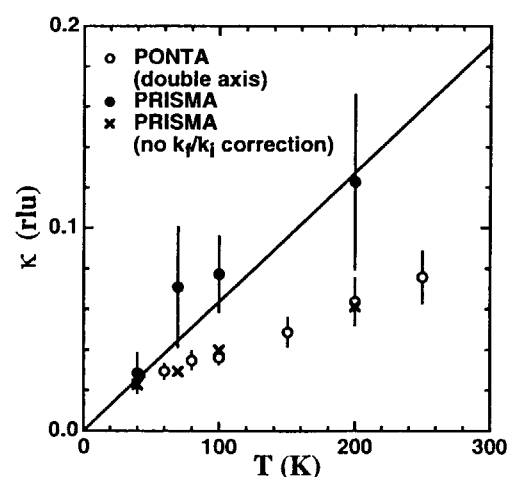


Fig.1 Temperature dependence of the inverse magnetic correlation length $\kappa(T)$ in CsVCl_3 measured with PONTA in the double-axis mode (open circles), with PRISMA (closed circles), and deduced from the PRISMA data without correcting k_f/k_i (crosses). The solid line is the classical prediction for $J=119\text{K}$.

研究テーマ：梯子型化合物の高圧下での磁性

表題：梯子格子系物質； $\text{Sr}_{2.5}\text{Ca}_{11.5}\text{Cu}_{24}\text{O}_{41}$ の反強磁性磁気秩序

1-2-14 Antiferromagnetic Ordering in the Hole-Doped Spin Ladder System $\text{Sr}_{2.5}\text{Ca}_{11.5}\text{Cu}_{24}\text{O}_{41}$ under Ambient and High Pressure.

J. AKIMITSU, T. NAGATA, H. FUJINO, M. NISHI¹, K. KAKURAI¹, and S. KATANO²

Department of Physics, Aoyama-Gakuin University, Setagaya-ku, Tokyo 157-8572

¹Neutron Scattering Laboratory, ISSP, The University of Tokyo, Tokai, Ibaraki 319-1106

²Neutron Scattering Group, Advanced Science Research Center, Japan Atomic Energy Research Institute, Tokai, Ibaraki 319-1195

It has been believed that the ground state of hole-doped spin ladder system $\text{Sr}_{2.5}\text{Ca}_{11.5}\text{Cu}_{24}\text{O}_{41}$ has been confirmed to be spin gap state by NMR¹⁾ and neutron scattering experiment.²⁾ However, we observed the magnetic long range ordering by the specific heat measurement.³⁾ In this report, we describe the neutron scattering experiment concerned with the antiferromagnetic ordering both at ambient and high pressure and we discuss the magnetic structure of the system.

Neutron elastic scattering experiments have been carried out using ISSP-PONTA (5G) and JAERI-TAS-1 (2G) triple-axis spectrometers in JRR-3M with a collimation of 40'-40'-S-80'-80'. In this experiment, we used the neutron wavelength of 2.37 Å and placed the pyrolytic graphite and sapphire filters in front of the sample to eliminate the higher order harmonics. The $\text{Sr}_{2.5}\text{Ca}_{11.5}\text{Cu}_{24}\text{O}_{41}$ single crystal was mounted on a cryostat with liq.He.

In our elastic neutron scattering experiment, we observed a number of Bragg peaks which appeared below 2 K.

Fig. 1 shows the typical elastic neutron scattering results at (1 0 l), (0 1 l) and (h 0 12), these results were plotted after subtracting the intensity at 5 K from that at 1.4 K and the intensities were represented as the integrated intensities. We confirmed that the FWHM of the observed Bragg peaks is nearly the resolution limited.

In order to determine the magnetic structure, we should make clear which layers - ladders or chains - are responsible for the onset of the magnetic long range order. Recent NQR/NMR studies by Ohsugi *et al.*⁴⁾ concluded that (1) the magnetic spins both on ladders and chains are magnetically ordered in this system, (2) spontaneous moments on the ladder sites are rather uniform with small moments less than $\sim 10^{-2} \mu_B$, whereas spontaneous moments on the chain sites are nonuniformly distributed with rather larger moments ($\geq 0.05 \mu_B$).

Considering all these experimental results, we calculated the magnetic structure factor both for chain and ladder planes and compared it with the experimental results. In our calculation, we assumed that the magnetic moments at both sites are directed along a-axis and they are uniformly distributed. The proposed magnetic structures are indicated in Fig. 2. It should be noted that these planes are alternately stacked, i.e. (ladder-A) - (chain-A) - (ladder-B) - (chain-B) ...and so on. The calculated magnetic Bragg peak intensities are shown in the inset of Fig. 1, which are in excellent agreement with the

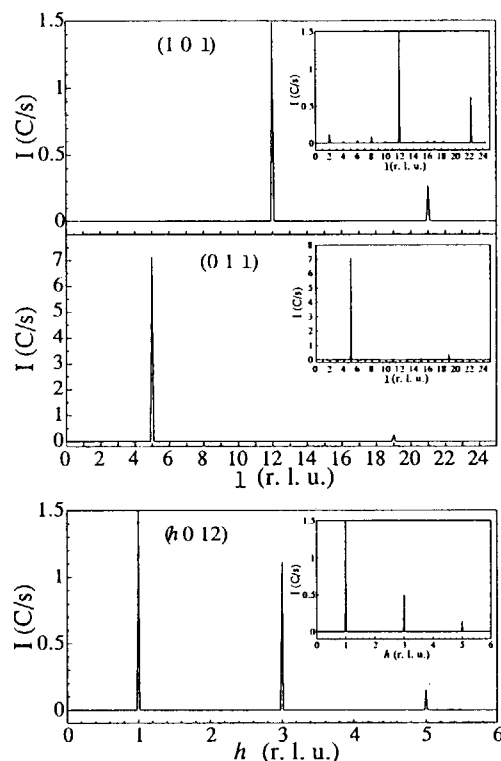


Fig. 1. Typical results by elastic neutron scattering at (1 0 l), (0 1 l) and (h 0 12) of the $\text{Sr}_{2.5}\text{Ca}_{11.5}\text{Cu}_{24}\text{O}_{41}$ single crystal. These results were plotted after subtracting the intensities at 5 K from those at 1.4 K and the intensities were represented as the integrated intensities. Each inset shows the calculated magnetic Bragg peak intensities based on the proposed magnetic structure shown in Fig. 2.

observed values as shown in Fig. 1.

The effective Bohr-magneton (μ_{eff}) at each layer were also evaluated by comparing with the magnetic peak intensities at (1 0 12), (0 1 5) and nuclear Bragg peak intensity at (0 0 24). The magnetic form factor of Cu^{2+} was employed from the reference.⁵⁾ The estimated value of μ_{eff} is about $\mu_{\text{eff}}(\text{chain}) \sim 0.145 \mu_B$ and $\mu_{\text{eff}}(\text{ladder}) \sim 0.035 \mu_B$ per Cu in each layer at 1.4 K, which are qualitatively consistent with the NQR/NMR results.

However, there are some problems in our magnetic

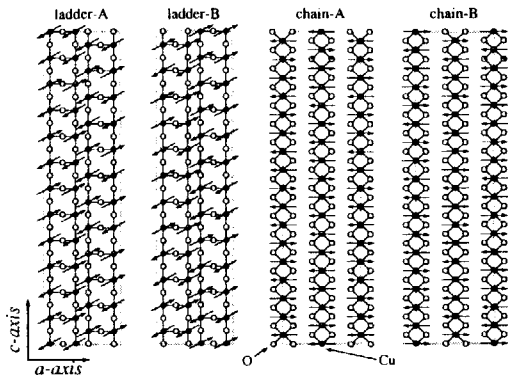


Fig. 2. Magnetic structures of chain and ladder sites in $\text{Sr}_{2.5}\text{Ca}_{11.5}\text{Cu}_{24}\text{O}_{41}$ in the a - c plane. The ladder-A, chain-A, ladder-B and chain-B are stacked along the b -axis, alternately.

structure both at chain and ladder sites.

First for the chain site, we ignore the existence of holes and singlet pairs which might be distributed with some periodicity in the chains. However, it is not yet clear the periodicity of the singlet pair in the chain at Ca-riched $\text{Sr}_{14-x}\text{Ca}_x\text{Cu}_{24}\text{O}_{41}$ system. Secondly, in our model, the magnetic interaction between nearest neighbor Cu spins are ferromagnetic or antiferromagnetic, and these interactions are mixed with some periodicity. This situation seems to be unlikely in usual sense. However, recent crystal structure analysis in $\text{Sr}_{2.5}\text{Ca}_{11.5}\text{Cu}_{24}\text{O}_{41}$ by Gotoh *et al.*⁶⁾ indicated that the angle for Cu-O-Cu bonding and the Cu-Cu distance in the chain varies between 89.5° and 95.5° , and between 2.69 \AA and 2.86 \AA respectively, which might suggest that ferromagnetic and antiferromagnetic interactions coexist in the chain. At the ladder site, the magnetic interaction along the rung direction is ferromagnetic which seems to be unlikely. These are the future problem.

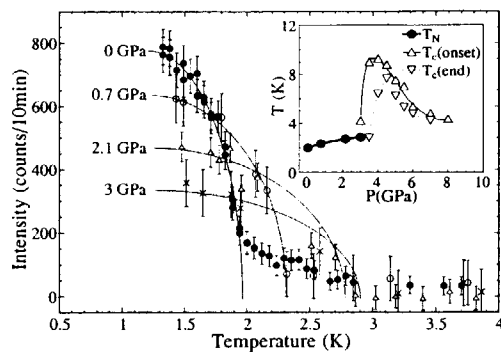


Fig. 3. Temperature dependence of the (1 0 12) reflection under the pressure of the $\text{Sr}_{2.5}\text{Ca}_{11.5}\text{Cu}_{24}\text{O}_{41}$ single crystal. Solid line is drawn for the guides to the eyes. Inset shows the pressure dependence of T_N and T_c .⁷⁾

We also have performed the pressure dependence of this antiferromagnetic ordering in connection with its pressure induced superconductivity. Fig. 3 shows the temperature dependence of the intensities from the magnetic reflection (1 0 12) for the pressure of 0, 0.7, 2.1, and 3 GPa, which was normalized by the nuclear reflections. As shown in the Fig. 3, the intensity decreases with increasing pressure, however, the Néel temperature T_N increases from 2.3 K to 2.8 K at a rate of 0.3 K/GPa, which can be reasonably explained that the three dimensional magnetic interaction in this material will be increased with increasing the pressure. Inset of Fig. 3 shows the pressure dependence of T_N and T_c .⁷⁾ We can find that the transition from antiferromagnetic to superconductor occurs around 3.5 GPa.

- 1) K. Magishi, S. Matsumoto, Y. Kitaoka, K. Ishida, K. Asayama, M. Uehara, T. Nagata and J. Akimitsu, Phys. Rev. B **57** (1998) 11533.
- 2) S. Katano, T. Nagata, J. Akimitsu, M. Nishi and K. Kakurai, Phys. Rev. Lett. **82** (1999) 636.
- 3) T. Nagata, H. Fujino, J. Akimitsu, M. Nishi, K. Kakurai, S. Katano, M. Hiroi, M. Sera and N. Kobayashi, J. Phys. Soc. Jpn. (in press).
- 4) S. Ohsugi, K. Magishi, S. Matsumoto, Y. Kitaoka, T. Nagata and J. Akimitsu, Phys. Rev. Lett. (in press).
- 5) J. Akimitsu and Y. Ito, J. Phys. Soc. Jpn. **40** (1976) 1621.
- 6) Y. Gotoh, (private communication).
- 7) T. Nagata, M. Uehara, J. Goto, J. Akimitsu, N. Motoyama, H. Eisaki, S. Uchida, H. Takahashi, T. Nakanishi and N. Mōri, Phys. Rev. Lett. **81** (1998) 1090.

研究テーマ: $\text{Sr}_{14}\text{Cu}_{24}\text{O}_{41}$ の単純鎖の励起状態に関する研究
 表題: $\text{Sr}_{14}\text{Cu}_{24}\text{O}_{41}$ の単純鎖の励起状態に関する研究

1-2-15

Hole Ordering and Dimerized State in the CuO_2 Chains in $\text{Sr}_{14}\text{Cu}_{24}\text{O}_{41}$

M. Matsuda, T. Yoshihama¹, K. Kakurai¹, and G. Shirane²

The Institute of Physical and Chemical Research (RIKEN), Wako, Saitama 351-0198, Japan

¹*NSL-ISSP, University of Tokyo, Tokai, Ibaraki 319-1195, Japan*

²*Physics Department, Brookhaven National Laboratory, Upton, New York 11973, USA*

$\text{Sr}_{14}\text{Cu}_{24}\text{O}_{41}$, which has simple chains and ladders of copper ions, has been extensively studied since both of the building blocks show interesting ground states. An important feature of this compound is that stoichiometric $\text{Sr}_{14}\text{Cu}_{24}\text{O}_{41}$ contains hole carriers. It has been reported that most of the holes are localized at the oxygen sites in the chain and couple with copper spins to form Zhang-Rice (ZR) singlet.

In this study¹⁾ we are only concerned with the magnetic properties in the chains. First, the dimer is formed between Cu^{2+} spins that are separated by twice the distance between nearest-neighbor Cu ions along the c axis. The exchange interaction ($J \sim 11$ meV) is mediated via a nonmagnetic ZR singlet. Then the question is how the dimers are arranged and interact with each other.

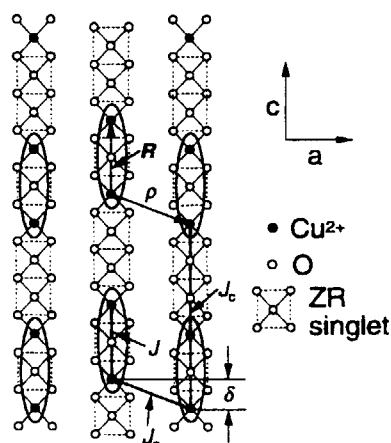


Figure 1 A proposed model for the dimerized state and the ordering of Cu^{2+} and ZR singlet in the ac plane.

JRR-3M, PONTA, 2. Magnetism

We have searched for a simple model of dimers with weak couplings along both c and a directions. Somewhat surprisingly, a specific combination of the two couplings, as described by Leuenberger *et al.* for $\text{Cs}_3\text{Cr}_2\text{Br}_9$,²⁾ produces simple and elegant neutron scattering cross sections that describe properly the measured dispersion and intensities.

We have studied ω - Q dispersion relation perpendicular to the chain direction in considerable detail. By applying a random phase approximation (RPA) treatment, we found that the interdimer coupling along the a axis ($J_a = 0.75$ meV) is also important as well as the interdimer coupling along the c axis ($J_c = 0.75$ meV). The dimer configuration we found in this study, as shown in Fig. 1, indicates a quasi-two-dimensional hole ordering, resulting in an ordering of Cu^{2+} and ZR singlet in the ac plane. These results are consistent with those studied by Eccleston *et al.*³⁾ and Regnault *et al.*⁴⁾

References

- [1] M. Matsuda *et al.*, Phys. Rev. B **59**, (1999) 1060-1067.
- [2] B. Leuenberger *et al.*, Phys. Rev. B **30**, (1984) 6300-6307.
- [3] R.S. Eccleston *et al.*, Phys. Rev. Lett. **81**, (1998) 1702-1705.
- [4] L. P. Regnault *et al.*, Phys. Rev. B **59**, (1999) 1055-1059.

研究テーマ：UGe₂における隠れた磁気励起
表題：UGa₂における磁気励起の偏極依存性

1-2-16

Polarization dependence of magnetic excitations in UGa₂

M. Kohgi,^a K. Iwasa,^a H. Sagayama,^a N. Sato,^b and K. Kakurai^c

^aTokyo Metropolitan University, Hachioji, Tokyo 192-0397, Japan

^bTohoku University, Sendai 980-8578, Japan

^cNeutron Scattering Laboratory, ISSP, University of Tokyo, Tokai, Ibaraki 319-1195, Japan

Microscopic origin of magnetic properties of uranium intermetallic compounds is not so well understood compared to the cases of 3d- or 4f-element intermetallic-compounds. This is due to the intermediate nature of the 5f-electron wave function between localized and itinerant states. In order to shed more light on this problem, we are studying several different types of uranium compounds. UGa₂, which has a hexagonal AlB₂ type structure, is a ferromagnet with a rather high Curie temperature of 125 K.¹⁾ The saturation moment is 2.7 μ_B along *a*-axis, which is close to that of the free ion U³⁺ or U⁴⁺. We have observed a weak magnetic peak at about 30 meV by neutron inelastic scattering using a polycrystalline sample. Well-defined excitations with dispersion of about 4 meV, but with rather large energy gap of about 8 meV, were also observed below the Curie temperature in the experiment using a single crystal sample.²⁾ These results indicate that the 5f-electron state in UGa₂ is well localized as in the case of many rare-earth intermetallic compounds. From neutron scattering point of view, the features of UGa₂ are still interesting because, on the contrary to the case of rare earth compounds, only a little numbers of uranium compounds, such as USb or UPd₃, exhibit such well-defined magnetic low energy response. Therefore this material is a good reference material for the study of other uranium intermetallic compounds, such as UGe₂,³⁾ which show itinerant 5f-electron features.

We have done a polarized neutron scattering experiment to discriminate whether the low energy excitations in UGa₂ are due to spin wave ones or to exciton ones originated from crystal field. The sample is a single crystal of UGa₂ with the diameter of about 5 mm and the length of about 4 cm. It was set inside a cryo-magnet with the <100> axis vertical to the scattering

plane. The experiment was performed on the polarized neutron triple axis spectrometer PONTA (5G) installed at the JRR3M reactor, JAERI. A polarized incident neutron beam with the energy of 34 meV was produced by the Cu₂MnAl polarizer. The scattered neutron energy was analyzed by the pyrolytic graphite analyzer. A set of Sollar collimators of 80'-80'-80'-80' was used.

Measurements were performed at 10 K. A vertical magnetic field of 1 T was applied to the sample. Constant-Q scans at selected Q values were performed in the polarized incident neutron beam mode of the spectrometer.

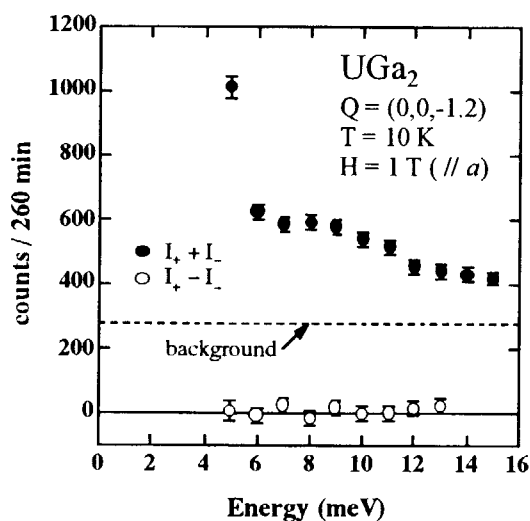


Fig. 1. Sum and difference of the spectra for incident polarization parallel (+) and anti-parallel (-) to the applied magnetic field.

Fig. 1 shows the obtained sum and difference of the spectra at $Q = (0,0,-1.2)$ for polarization parallel (+) and anti-parallel (-) to

the applied magnetic field. The sum of both spectra shows a peak at about 8 meV, which is consistent to the previous unpolarized neutron experiment although the peak width is larger due to the relaxed collimations. It is clear that there is no significant polarization dependence in the data within the experimental accuracy. This indicates that the observed excitations around 10 meV of UGa_2 are not from spin-wave-like modes since spin wave scattering from a ferromagnet at low temperatures should show strong incident polarization dependence if the sample is a single domain one. Therefore, the present experiment suggests that the observed low energy magnetic excitations in UGa_2 are due to exciton-like modes which originate from the combined effects of crystal field splitting and

exchange interaction (or hybridization effect).

Reference

- 1) A. V. Andreev, K.P. Belov, A.V. Deryagin, Z.A. Kazei, R.Z. Leivitin, A. Menovski. Yu. F. Porov and V.I. Silant'ev, Zh. Exsp. Teor. Fiz. 75(1978)2351; Sov. Phys. JETP, **48** (1978) 1187.
- 2) Y. Kuroiwa, M. Kohgi, T. Osakabe, N. Sato and Y. Onuki: Proceedings of the Fifth International Symposium on Advanced Nuclear Energy Research, JAERI-M **93-228** (1993) 314.
- 3) Y. Oniki, S.W. Yun, I. Umehara, K. Satoh, F. Fukuhara, H. Sato, S. Takayanagi, M. Shikama and A. Ochiai, J. Phys. Soc. Jpn., **60** (1991) 2127.

研究テーマ：2次元モット転移系 $\text{BaCo}_{1-x}\text{Ni}_x\text{S}_2$ の中性子散乱
 表題：中性子散乱による $\text{BaCo}_{1-x}\text{Ni}_x\text{S}_2$ の金属-絶縁体転移研究

1-2-17 Neutron Scattering Study on Metal-Insulator Transition of $\text{BaCo}_{1-x}\text{Ni}_x\text{S}_2$

H. Sasaki¹, H. Harashina^{1,2}, K. Kodama^{1,2}, M. Sato^{1,2}, S. Shamoto³, M. Nishi⁴
 and K. Kakurai^{2,4}

¹ Department of Physics, Division of Material Science, Nagoya University, Furo-cho, Chikusa-ku, Nagoya 464-8602

² CREST, Japan Science and Technology Corporation (JST)

³ Department of Applied Physics, Faculty of Engineering, Tohoku University, Aoba, Aramaki, Sendai 980-8577

⁴ Neutron Scattering Laboratory, ISSP, The university of Tokyo, Shirakata 106-1, Tokai, Ibaraki 319-1195

Magnetic excitation spectra of $\text{BaCo}_{1-x}\text{Ni}_x\text{S}_2$, which has a layered structure and exhibits an insulator to metal transition with increasing x and/or with applying pressure,¹⁻³⁾ have been measured by neutron inelastic scattering.^{4,5)} Up to now, crystals with $x=0.0$, 0.18 and 0.24 have been used. Here, results of studies to what extent the imaginary part of the dynamical susceptibility

$$\chi''(q, \omega) \propto \frac{\omega \Gamma_0 \tilde{\chi}_q}{\Gamma_0^2 (\kappa^2 + q^2)^2 \xi_0^4 + \omega^2} \quad (1)$$

deduced by using the random phase approximation (RPA) can describe characteristics of the spectra observed in the metallic state, are presented (Γ_0 , κ are the characteristic energy and

the inverse correlation length, respectively and ξ_0 ~ lattice constant.). It is also presented that Γ_0 of the magnetic excitations of BaCoS_2 measured in the pressure-induced metallic state near the metal-insulator (M-I) phase boundary is much larger than that in the metallic state induced by the Ni-substitution for Co. It indicates the clear difference between the microscopic driving forces of the M-I transitions induced by the two different kinds of means.

Figure 1 shows the neutron scattering profiles of the magnetic excitations of $\text{BaCo}_{0.76}\text{Ni}_{0.24}\text{S}_2$, which is metallic and does not exhibit any magnetic transition. They were taken along $(h, h, 1)$ at 10 K and for various fixed transfer

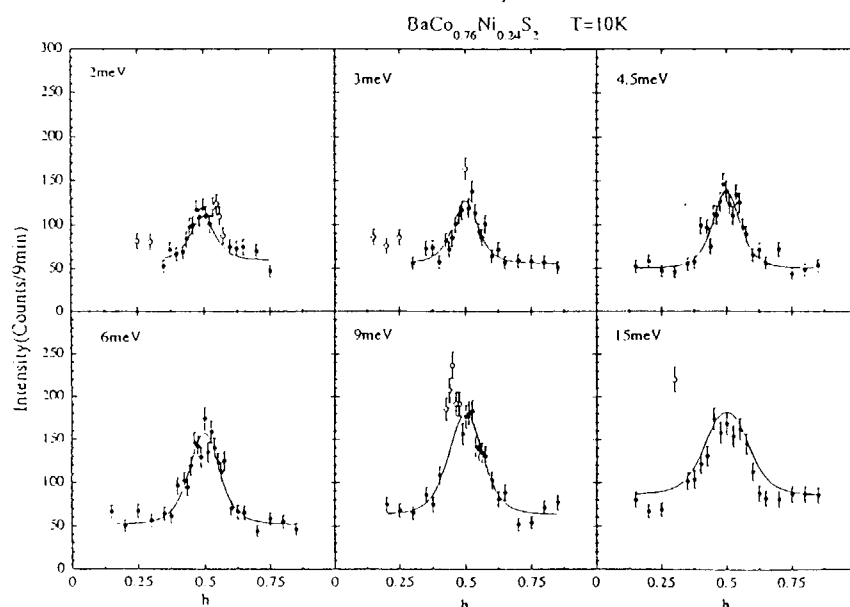


Fig. 1 Magnetic scattering profiles taken for $\text{BaCo}_{0.76}\text{Ni}_{0.24}\text{S}_2$ along $(h, h, 1)$ at 10 K. Curves obtained by the simultaneous fitting to all the profiles are also shown, where $\kappa \sim 0.16 \text{ \AA}^{-1}$ and $\Gamma_0 \sim 13 \text{ meV}$. The open circles have been omitted in the fitting.

energies E . We fitted eq.(1) to all these profiles simultaneously and obtained the solid lines for the parameters $\kappa \sim 0.16\text{\AA}^{-1}$ and $\Gamma_0=13\text{ meV}$, where the RPA expression is found to work rather well. Then, by using this Γ_0 value, eq.(1) was fitted to the profiles taken at $E=3\text{ meV}$ and at various temperatures T with κ^2 being varied as a fitting parameter. The results are shown in Fig. 2 by open squares, together with the values (solid squares) calculated from the full-width-half-maximum w of the observed profiles by using the RPA expression,

$$w = 2\kappa \left\{ \left[2 + \left(\frac{\omega}{\Gamma_0 \kappa^2 \xi_0^2} \right)^2 \right]^{\frac{1}{2}} - 1 \right\}^{\frac{1}{2}} \quad (2)$$

In the figure, κ^2 -values obtained for $x=0.0$ (open circles) and 0.18 (solid circles) are also shown. It is interesting that the approximate relation $\kappa \sim 1/\xi_i$ holds at low temperatures for $x=0.24$, where ξ_i is the average Ni-Ni spacing.

For BaCoS_2 , the magnetic scattering profile is taken at various pressure values p , the examples of which are shown in the inset of Fig. 3. The temperatures at which the measurements were carried out, are always close to T_N . By fitting eq. (1) to the data, the characteristic energy Γ_0 of the magnetic excitation has been determined, where $\kappa^2 \sim 0$ is approximately used. They are shown in Fig. 3, together with the values obtained at ambient pressure for $x=0.18$ (open circle) and 0.24 (triangle). As p approaches the critical values p_c of the M-I transition, Γ_0 increases very rapidly, indicating that the electron band width exhibits a sharp increase. At $p \sim p_c$, Γ_0 is much larger than the values obtained for the Ni-doped samples ($x=0.18$ and 0.24) at ambient pressure (in the metallic state). The results clearly show that the pressure-induced M-I transition is due to the increase of the transfer energy t with respect to the Coulomb repulsive energy U , while the M-I transition induced by the Ni-doping is considered to be due to the change of the electron number from unity (filling-controlled Mott transition).

JRR-3M, PONTA(5G), 2. Magnetism

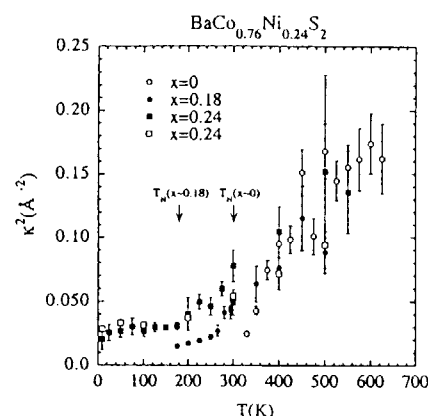


Fig. 2 Values of κ^2 of $\text{BaCo}_{0.76}\text{Ni}_{0.24}\text{S}_2$ deduced from the observed values of w are shown as a function of T by the solid squares. Open squares indicate the κ^2 values determined by the fitting described in the text. The κ^2 values deduced from w -values taken for BaCoS_2 and $\text{BaCo}_{0.82}\text{Ni}_{0.18}\text{S}_2$ are also shown.

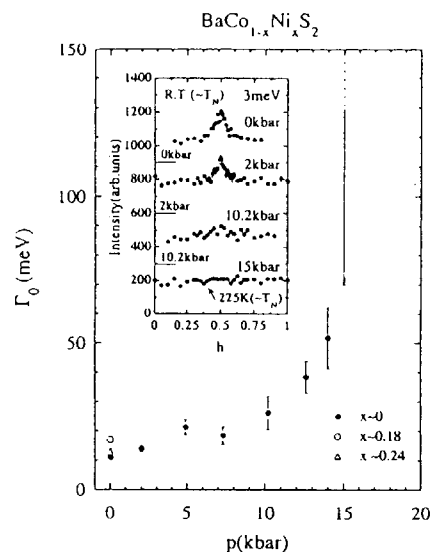


Fig. 3 Pressure dependence of Γ_0 of BaCoS_2 . Values of Γ_0 of $\text{BaCo}_{0.82}\text{Ni}_{0.18}\text{S}_2$ and $\text{BaCo}_{0.76}\text{Ni}_{0.24}\text{S}_2$ under ambient pressure are also shown by the open symbols. Inset shows the Magnetic scattering profiles of BaCoS_2 taken under various p -values. Except for the data at 15 kbar, they were taken at room temperature.

References

- 1) J. Takeda *et al.*, J. Phys. Soc. Jpn. **64** (1995) 2550.
- 2) Y. Yasui *et al.*, J. Phys. Soc. Jpn. **65** (1996) 2757.
- 3) Y. Yasui *et al.*, J. Phys. Soc. Jpn. **66** (1997) 3194.
- 4) S. Shamoto *et al.*, J. Phys. Soc. Jpn. **66** (1997) 1138.
- 5) H. Sasaki *et al.*, J. Phys. Soc. Jpn. **66** (1997) 3975.

研究課題: $(\text{La,Sr})_{1-x}\text{Mn}_x\text{O}_{3-x/2}$ のスピン・電荷ダイナミクス
 標題: 層状Mn酸化物 $\text{La}_{2-2x}\text{Sr}_{1+2x}\text{Mn}_2\text{O}_7$ のスピンダイナミクス

1-2-18

Spin Dynamical Properties of the Layered Perovskite $\text{La}_{1.2}\text{Sr}_{1.8}\text{Mn}_2\text{O}_7$ [1]

H. Fujioka,¹ M. Kubota,² K. Hirota,¹ H. Yoshizawa,² Y. Moritomo³ and Y. Endoh¹

¹CREST, Department of Physics, Tohoku University

²Neutron Scattering Laboratory, Institute for Solid State Physics, University of Tokyo

³CIRSE and Department of Applied Physics, Nagoya University

Inelastic neutron scattering measurements were performed on a single crystal of the layered colossal magnetoresistance (CMR) material $\text{La}_{1.2}\text{Sr}_{1.8}\text{Mn}_2\text{O}_7$ ($T_C \sim 120$ K), in which MnO_2 double layers and $(\text{La,Sr})_2\text{O}_2$ blocking layers are stacked alternatively. Dominant spin-spin interactions should occur between nearest-neighbor Mn atoms, though the in-plane interaction J_{\parallel} and the *intra*-bilayer interaction J_{\perp} might be different. We neglect the *inter*-bilayer interaction J' through a direct exchange, which is supposed to be much weaker. Using the Holstein-Primakoff transformation, we obtain the following dispersion relations:

$$\begin{aligned} \hbar\omega(\mathbf{q}) = & -2J_{\parallel}S(2 - \cos aq_x - \cos aq_y) \\ & -J_{\perp}S(1 \mp 1), \end{aligned} \quad (1)$$

where a and c are the lattice constants. These are classified to two modes, i.e., acoustic (A) and optical (O), when the inter-bilayer coupling J' is neglected.

The spin-wave dispersions along $[h\ 0\ 0]$ were measured at 10 K around $(1\ 0\ 0)$ and $(1\ 0\ 5)$ for the A-branch, and $(1\ 0\ 2.5)$ for the O-branch, as shown in Fig. 1. Error bars correspond to the FWHM of peak profiles. By fitting all the data points for $0 < q \leq 0.25$ r.l.u. simultaneously, we obtain $-J_{\parallel}S = 10.1$ meV and $-J_{\perp}S = 3.1$ meV. The results show that spin-spin correlations are significantly anisotropic. We speculate that x^2-y^2 orbital is dominant in the Mn e_g band, which enhances the double-exchange, i.e., ferromagnetic, interactions within a plane. The in-plane spin wave stiffness constant $D = -J_{\parallel}Sa^2$ is about $151\text{ meV}\text{\AA}^2$, which is corresponding to the nearly cubic perovskite

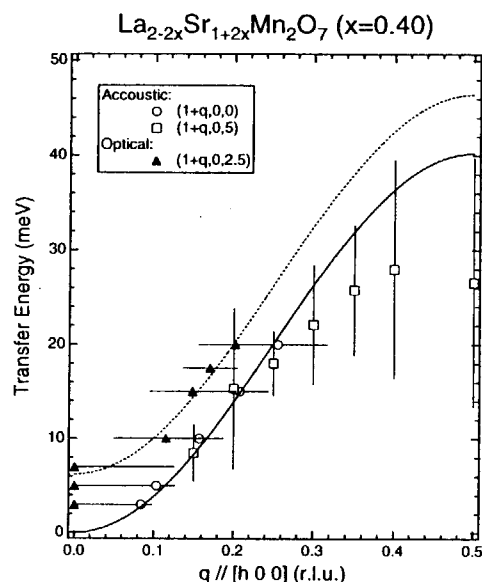


Figure 1: The dispersion relations of spin waves at 10 K.

$\text{La}_{1-x}\text{Sr}_x\text{MnO}_3$ whose D are 188 meV ($x = 0.3, T_C = 370\text{ K}$) [2]. T_C ($\sim 120\text{ K}$) is very much reduced, indicating a large renormalization due to low dimensionality.

References

- [1] H. Fujioka *et al.*, J. Phys. Chem. Solids, in press.
- [2] M. C. Martin *et al.*, Phys. Rev. B **53** (1996) R14285.

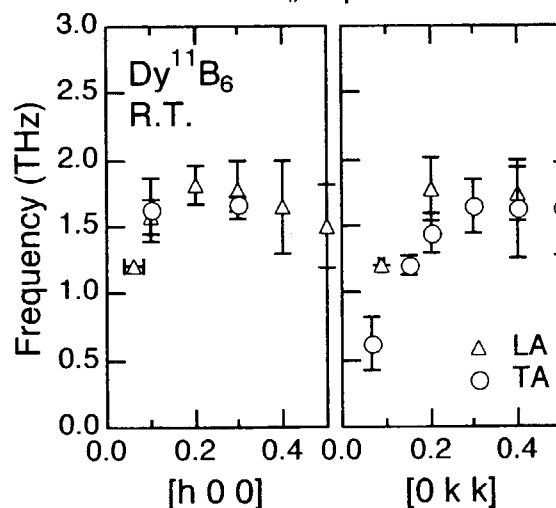
研究テーマ DyB₆の格子ダイナミクスの研究表題 DyB₆の格子ダイナミクスの研究1-2-19 Study of Lattice Dynamics in DyB₆H. Nojiri, K. Tkahashi, M. Motokawa, ¹S. Kunii, ¹K. Hirota, ²K. Kakurai, and ¹Y. Endoh*Institute for Materials Research, Tohoku University, Sendai 980-8577, Japan*¹*Department of Physics, Tohoku University, Sendai 980-8477, Japan*²*Institute for Solid State Physics, University of Tokyo, Roppongi 7-22-1, Tokyo 106, Japan*

The important role of the orbital degree of freedom in magnetism has been a subject of current interest in both 3d transition metal oxides and rare-earth compounds. A heavy rare earth compound DyB₆ has been known as a system with strong electron-lattice coupling. The successive phase transitions occur at 32 K and at 26 K have been explained as the structural phase transition and the magnetic ordering, respectively. For the transition at 32 K, a large softening of the lattice was observed by ultrasonic measurement.^[1] A following universal relation was reported for the phonon dispersion relation of the light rare earth REB₆ compounds such as SmB₆ or CeB₆.^[2] It seems that the phonon dispersion curves of different compounds are nearly identical when its energy is normalized by their Debye temperatures. The purpose of the present study is to investigate the phonon dispersion relation of DyB₆ and compare it with the phonon of other REB₆ compounds.

The phonon dispersion measurements of DyB₆ had not been made so far by neutron scattering. It is because the synthesis of a single crystal is very difficult for the high melting temperature and for the incongruent melting property. Recently, we have succeeded in preparing a ¹¹B enriched single crystal^[3] and we measured the phonon dispersion of DyB₆ for the first time.

Figure 1 shows phonon dispersion relations of DyB₆ for [h 0 0] and [0 k k] directions. The measurement was made at room temperature. Although the intensity is very weak for the imperfect ¹¹B enrichment and an absorption by the Dy, we obtained the dispersion relations for both LA and TA modes. The energy of both modes are

in the range of 1.5-2.0 THz. For [0 k k] direction, the dispersion is less steep up to k=0.2 compared to the mode along [h 0 0]. However, the relation between the anisotropic behavior and the structural phase transition occurs at 32 K is still unclear. A measurement at low temperature is necessary to clarify this point. Another important point is that the above mentioned universal relation of phonon is not simply applied for DyB₆. The phonon energy is more than 20 % lower than the expectation from the ratio of the Debye temperature. It clearly shows that the phonon energy of DyB₆ is relatively lower than that of other REB₆ compounds.

Fig. 1 The phonon dispersion curves of DyB₆ at 300 K.

[1]S. Nakamura, T. Goto, S. Kunii, K. Iwashita and A. Tamaki:J. Phys. Soc. Jpn., 63(1994)623.

[2]S. Kunii: unpublished

[3]K. Takahashi and S. Kunii:J. Sol. Stat. Chem., 133(1997)198.

研究テーマ $\text{La}_{1-x}\text{Sr}_x\text{MnO}_3$ $x=1/8$ の磁場誘起軌道電荷秩序相の中性子回折

表題 $\text{La}_{1-x}\text{Sr}_x\text{MnO}_3$ $x=1/8$ の磁場誘起軌道秩序相の中性子回折

1-2-20 Neutron Diffraction Study of the Field Induced Orbital Ordering in $\text{La}_{1-x}\text{Sr}_x\text{MnO}_3$ ($x=1/8$)

H. Nojiri, K. Kaneko, M. Motokawa, ¹K. Hirota and ¹Y. Edoh

Institute for Materials Research, Tohoku University, Sendai 980-8577, Japan

¹*Department of Physics, Tohoku University, Sendai 980-8477, Japan*

Any evidence of field induced orbital ordering have been observed in $\text{La}_{0.88}\text{Sr}_{0.12}\text{MnO}_3$ above $T_{\text{on}}=145$ K directly by neutron diffraction. We have studied the pseudo cubic phase appears in $\text{La}_{1-x}\text{Sr}_x\text{MnO}_3$ with $x \sim 1/8$ where the JT distortion is not significant. As is well known, the A-type spin structure in LaMnO_3 has been explained by the alternation of the two e_g orbitals in the ab -plane associated with the JT distortion. By substituting Sr for La, the JT distortion tends to be suppressed. At around $x \sim 1/8$, JT distortion disappears and the crystal structure changes to the pseudo cubic phase. Recently, a sharp jump of magnetization was found between T_{on} and $T_c=175$ K. This jump of magnetization is associated by the distinct positive magnetoresistance. These unusual behaviors of macroscopic properties show that the insulating ferromagnetic(FI) phase is more stable than the metallic ferromagnetic(FM) phase driven by double exchange interaction. To investigate the nature of this high field phase, we have measured the field dependence of two kinds of Bragg peaks. Figure 1 shows spectrum for the Bragg peak related to the JT distortion. For the twinning in the crystal, the splitting of the peak is observed for the JT distorted phase at zero field. As shown in Fig. 1, this splitting disappears in high magnetic fields. This change indicates that the JT distortion is removed in the high field phase. Figure 2 shows spectra of the super lattice peak. At zero field, the peak appears only below T_{on} and it has been considered to be caused by the charge ordering or orbital ordering. As shown in Fig. 2, the super lattice peak appears by the application of high magnetic fields even above T_{on} . This behavior indicates that the high field phase observed in magnetization process is the phase with charge

ordering or orbital ordering. The present results indicate directly that the field induced phase transition from FM phase to FI phase is induced by magnetic field and the high field phase is not associated with a significant JT distortion. The important feature of the orbital ordering in the present case shows the significant role of orbital degrees of freedom in CMR manganite.

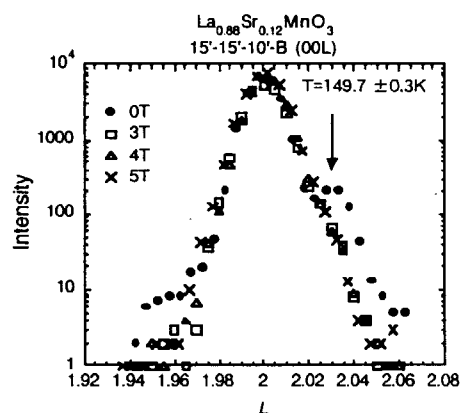


Fig. 1 Field dependence of [002] peak.

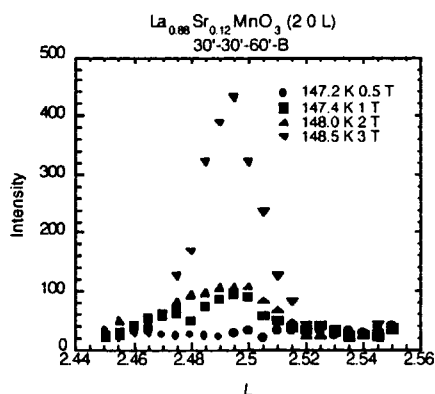


Fig. 2 Field dependence of [202.5] peak.

研究課題：希土類化合物 Nd_7Ni_3 単結晶の磁気構造

表題： Nd_7Ni_3 単結晶の磁気構造の中性子回折による研究

1-2-21 Neutron Diffraction Studies of the Magnetic Structures of Nd_7Ni_3 Single Crystal

S. Kawano¹, X. Xu¹, T. Tsutaoka², T. Kasagi², Y. Andoh³ and M. Kurisu⁴

¹Research Reactor Institute, Kyoto University, Kumatori, Sennan, Osaka 590-0494, Japan

²Faculty of School Education, Hiroshima University, Higashi-Hiroshima 739-8525, Japan

³Faculty of Education, Tottori University, Tottori 680-8551, Japan

⁴Japan Advanced Institute of Science and Technology, Ishikawa 923-1292, Japan

The rare earth compound Nd_7Ni_3 crystallizes in the hexagonal Th_7Fe_3 type structure with the space group $P6_3/mc$ in which Nd occupies three non-equivalent sites. Magnetic susceptibility measurements suggest that this compound has three successive transitions at $T_N=25$ K, $T_C=14$ K, and $T_R=7.8$ K [1]. Previous powder neutron diffraction studies have revealed that at low temperatures $T < T_R$ a magnetic structure is conical with a c -axis ferromagnetic component, and changes to a helix without any ferromagnetic component at elevated temperatures [2]. The aim of the present work is to investigate the detailed magnetic structure, particularly on the intermediate temperature phase around T_C by single crystal neutron diffraction.

The previous measurements on the polycrystalline sample left an ambiguity of an existence of a magnetic reflection at the (100) position which is expected for an existence of the c -axis ferromagnetic component. We have observed clearly the (100) magnetic reflection with the single crystal. Figure 1 gives the temperature dependence of the (100) peak height. At 8 K a sharp decrease of the intensity shows a magnetic transition, which means a disappearance of the c -axis ferromagnetic component, but no anomaly around $T_C=14$ K. This transition temperature corresponds to T_R . Figure 2 shows the temperature dependence of the magnetic propagation vector Q for powdered and single crystal samples. The values for the powdered sample are slightly small in comparison with those for the single crystal. The difference would come from the different heat treatments. However, both curves show a similar temperature dependence of a sharp decrease at 8 K and also of no anomaly around $T_C=14$ K. The temperature variation of both the (100) intensity and Q is very similar. Thus, we have confirmed from single crystal neutron diffraction on Nd_7Ni_3 that

the transition at T_R is to change the magnetic structure from a c -axis cone to a basal plane helix. The transition at T_C in magnetic susceptibility may not be from coherent bulk effect but local/incoherent one, such as impurity or heat treatment.

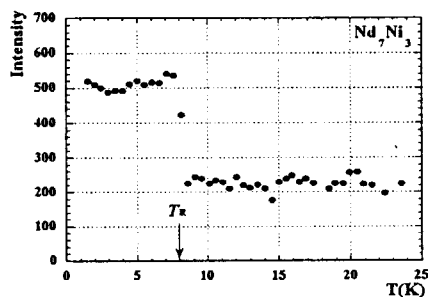


Fig. 1. Temperature dependence of the (100) peak intensity.

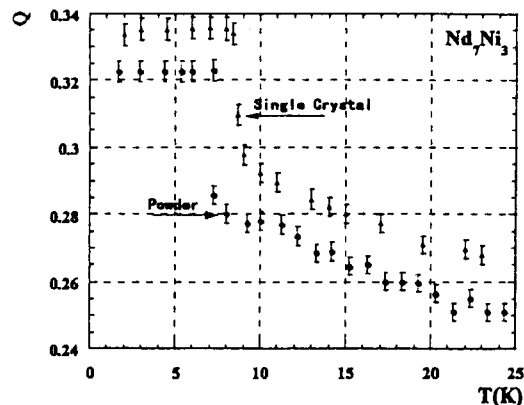


Fig. 2. Temperature dependence of the propagation vector Q for Nd_7Ni_3 single crystal (circles) and polycrystal (triangles).

References

- [1] T. Tsutaoka, et al., J. Magn. Magn. Mater. **167** (1997) 249.
- [2] X. Xu, et al., Physica B **241-243** (1998) 742.

研究テーマ：単結晶 CeGa の中性子回折
表題：単結晶 CeGa の中性子回折

1-2-22

Neutron Diffraction Study of CeGa Single Crystal

E. Matsuoka, M. Kosaka, T. Ohki and Y. Uwatoko

Department of Physics, Faculty of Science, Saitama University, Urawa 338, Japan

CeGa crystallizes in the orthorhombic CrB-type structure and has the antiferromagnetic order below $T_N = 6$ K [1]. Until now, there has been no report about the magnetic structure of CeGa. To clarify the magnetic structure of CeGa, we performed the neutron scattering experiments using the single crystal of CeGa.

The neutron diffraction experiments have been carried out using the HQR diffractometer (T1-1) installed at JRR-3M Guide Hall in JAERI (Tokai). An incident neutron beam with a wave length 2.44 \AA obtained by the (220) reflection of PG.

Figure 1 shows the positions and the intensities of the nuclear reflection and the magnetic reflection in the reciprocal lattice space. The magnetic reflections appear at the positions which are indexed by the propagation vector $\mathbf{q} = (1 \ 0 \ 0.3)$. Therefore, the magnetic structure of CeGa seems to be incommensurate with the crystal lattice. The analysis of the magnetic structure is now in progress.

Figure 2 shows the temperature dependence of the magnetic reflection intensities of the reciprocal lattice positions $(1 \ 0 \ 0.7)$ and $(1 \ 0 \ 1.3)$. The reflections disappear above $T = 6.2$ K. It corresponds well to the susceptibility measurement report [1].

Reference

- [1] E. Matsuoka et al. Physica B 259-261 (1999) 112.

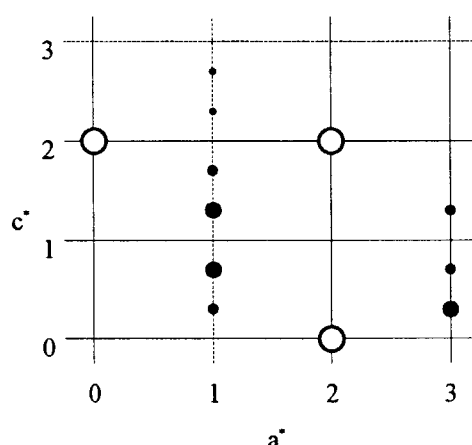


Fig. 1 The positions and the intensities of the nuclear reflection and the magnetic reflection in the reciprocal a^*-c^* plane.

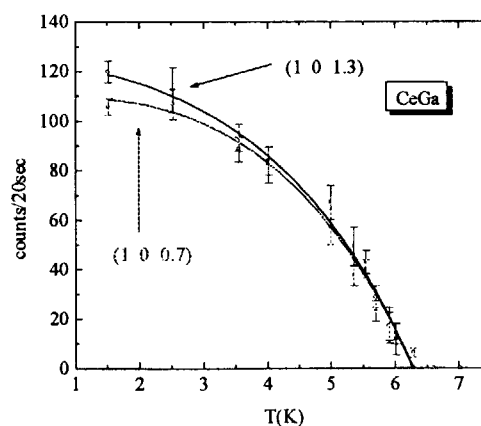


Fig. 2 The temperature dependence of the magnetic reflection intensities of the reciprocal lattice positions $(1 \ 0 \ 0.7)$ and $(1 \ 0 \ 1.3)$.

研究テーマ：単結晶 $(\text{Fe}_{0.98}\text{Ru}_{0.02})_2\text{P}$ の中性子回折
 表題：単結晶 $(\text{Fe}_{0.98}\text{Ru}_{0.02})_2\text{P}$ の中性子回折

1-2-23 Neutron Diffraction Study of $(\text{Fe}_{0.98}\text{Ru}_{0.02})_2\text{P}$

T. Ohki, T. Satoh, M. Kosaka, and Y. Uwatoko

Department of Physics, Faculty of Science, Saitama University, Urawa 338, Japan

**Faculty of Integrated Arts and Sciences, Hiroshima University, Higashi-Hiroshima 739-8521, JAPAN*

$(\text{Fe}_{0.98}\text{Ru}_{0.02})_2\text{P}$ crystallizes in the hexagonal C_{22} type structure (P62m) and has the antiferromagnetic order below $T_N = 140$ K [1]. Until now, we have been studied about the magnetic properties of $(\text{Fe}_{1-x}\text{Ru}_x)_2\text{P}$ sires. To clarify the magnetic structure of $(\text{Fe}_{0.98}\text{Ru}_{0.02})_2\text{P}$, we performed the neutron scattering experiments using the single crystal of $(\text{Fe}_{0.98}\text{Ru}_{0.02})_2\text{P}$.

The neutron diffraction experiments have been carried out using the HQR diffractometer (T1-1) installed at JRR-3M Guide Hall in JAERI (Tokai). An incident neutron beam with a wave length 2.44 \AA obtained by the (220) reflection of PG.

Figure 1 shows the positions and the intensities of the nuclear reflection and the magnetic reflection in the reciprocal lattice space. The magnetic reflections appear at the positions which are indexed by the propagation vector $q = (0.06 \ 0 \ 0)$. Therefore, the magnetic structure of $(\text{Fe}_{0.98}\text{Ru}_{0.02})_2\text{P}$ seems to be incommensurate with the crystal lattice. The analysis of the magnetic structure is now in progress.

Figure 2 shows the temperature dependence of the magnetic reflection intensities of the reciprocal lattice positions $(0.13 \ 0 \ 0)$ and $(0.19 \ 0 \ 0)$. The reflections disappear above $T = 140$ K. It corresponds well to the magnetic measurement report [1].

Reference

- [1] E. Matsuoka et al. Physica B 259-261 (1999) 112.

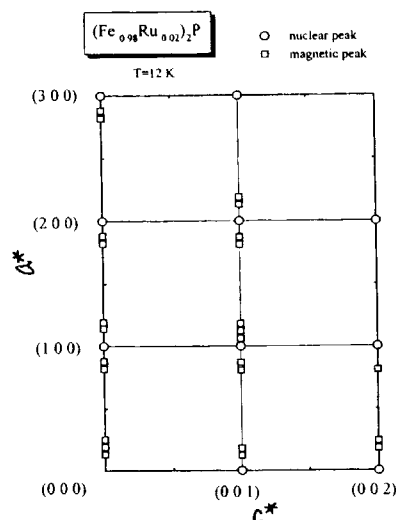


Fig. 1 The positions and the intensities of the nuclear reflection and the magnetic reflection in the reciprocal a^*c^* plane.

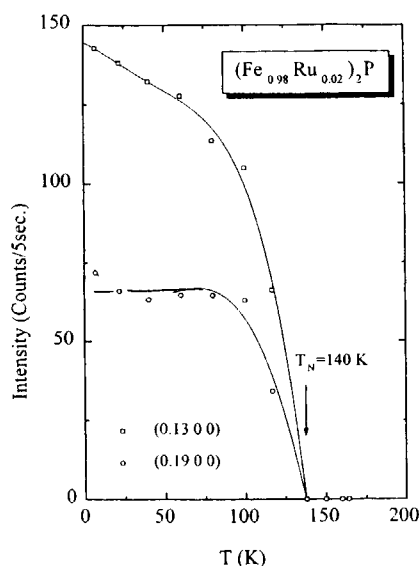


Fig. 2 The temperature dependence of the magnetic reflection intensities of the reciprocal lattice positions $(0.13 \ 0 \ 0)$ and $(0.19 \ 0 \ 0)$.

研究テーマ: ErNiSn の磁気構造

表題: ErNiSn の中性子回折

1-2-24 NEUTRON DIFFRACTION STUDIES ON ErNiSn

Y. ANDOH, S. KAWANO¹, T. NOBATA², G. NAKAMOTO², M. KURISU² and T. TSUTAOKA³

Faculty of Education, Tottori University, Tottori 680-8551, Japan

¹Research Reactor Institute, Kyoto University, Kumatori, Osaka 590-0494, Japan²Japan Advanced Institute of Science and Technology, Ishikawa 923-1292, Japan³Faculty of School Education, Hiroshima University, Higashi-Hiroshima 739-8524, Japan

The ternary compound ErNiSn crystallizes in the orthorhombic (*Pnma*) TiNiSi-type structure and order antiferromagnetically at $T_N=4.0$ K [1]. We reported from powder neutron diffraction measurements that the magnetic structure is characterized by propagation vector $q=(0.285, 0.476, 0.248)$ below $T=1.75$ K and $q=(0.330, 0.494, 0.399)$ for 1.75 K $< T < T_N$ [2]. In this report, we have performed neutron diffraction investigations on ErNiSn single crystals to determine its magnetic structure.

Single crystals were prepared by a Czochralski method using a tri-arc furnace. Neutron diffraction measurements were made using the HQR spectrometer in the guide hall of JRR-3M of JAERI at Tokai in the temperature range from 1.5 K to 30 K. The wavelength of the incident neutrons was 2.445 Å.

Figure 1 shows the neutron diffraction pattern in the a^*-c^* reciprocal plane at 1.8 K for ErNiSn single

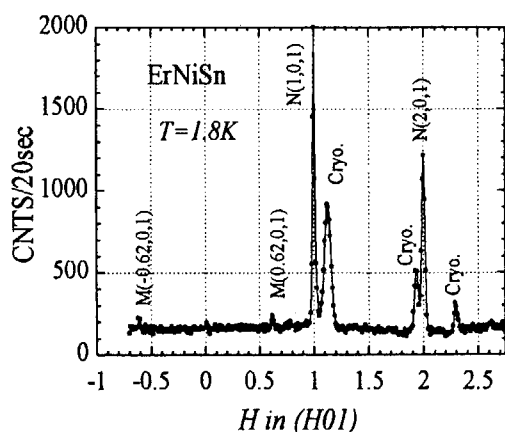


Fig.1 A neutron diffraction pattern in the a^*-c^* reciprocal plane at 1.8 K for ErNiSn single crystal

crystal. The weak magnetic reflections are observed at $(\pm 0.62, 0, 1)$. Any other magnetic reflections are not observed both in the a^*-c^* and the a^*-b^*

reciprocal planes.

The temperature dependence of the peak height of $(\pm 0.62, 0, 1)$ reflections is depicted in Fig. 2. Two anomalies are clearly observed at the Néel temperature $T_N=4.0$ K and 1.7 K. With decreasing

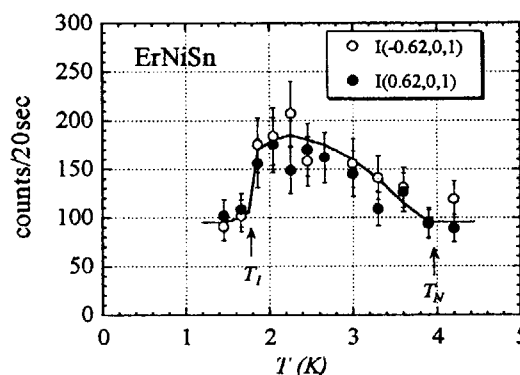


Fig.2 Temperature dependence of the peak height of $(\pm 0.62, 0, 1)$ reflections for ErNiSn.

temperature an abrupt decrease is found at 1.7 K, indicating that a new magnetic phase transition occurs at 1.7 K which is denoted by T_1 . Below T_1 , propagation vector changes and then the $(\pm 0.62, 0, 1)$ reflections are diminished in the a^*-c^* reciprocal plane.

The peak corresponding to $(\pm 0.62, 0, 1)$ positions has been found in powder neutron diffraction. However, these reflections were not indexed with $q=(0.330, 0.494, 0.399)$ even if it considered the higher harmonics reflections. To determine the magnetic structure, more detailed measurements should be done.

[1] Y. Andoh, M. Kurisu, S. Kawano and I. Oguro, J. Magn. Mater. **140-144** (1998) 1063.

[2] Y. Andoh, M. Kurisu, G. Nakamoto, T. Nobata, S. Nakamura, Y. Makiyama, and S. Kawano, Activity Report on Neutron Scattering Research **5** (1998) 124.

研究テーマ：高濃度スピングラスにおける長時間緩和

表題：高濃度スピングラスにおける長時間緩和

1-2-25 Slow Dynamics in Concentrated Spin Glasses

K. Motoya, T. Kumazawa and J. Kikuchi

Department of Physics, Faculty of Science and Technology,

Science University of Tokyo, Noda 278-8510

In order to probe microscopic mechanism of slow dynamics typically observed as time dependent magnetization behavior of spin-glasses, time-resolved small angle neutron scattering study has been made. Previous neutron scattering studies on $\text{Fe}_{65}(\text{Ni}_{1-x}\text{Mn}_x)_{35}$ and $\text{Cu}_2(\text{Mn}_{1-x}\text{Ti}_x)\text{Al}$ alloys showed that the magnetic clusters play an important role on reentrant spin-glass transition.¹⁻³⁾ Based on these studies, we speculate that the mechanism of slow dynamics can most directly be probed by observing the time evolution of magnetic diffuse scattering arising from magnetic clusters. In Fig. 1, magnetic diffuse scattering patterns from $\text{Fe}_{65}(\text{Ni}_{0.66}\text{Mn}_{0.34})_{35}$ taken at $T=8\text{K}$ (SG phase) and $T=50\text{K}$ (FM phase) are shown.

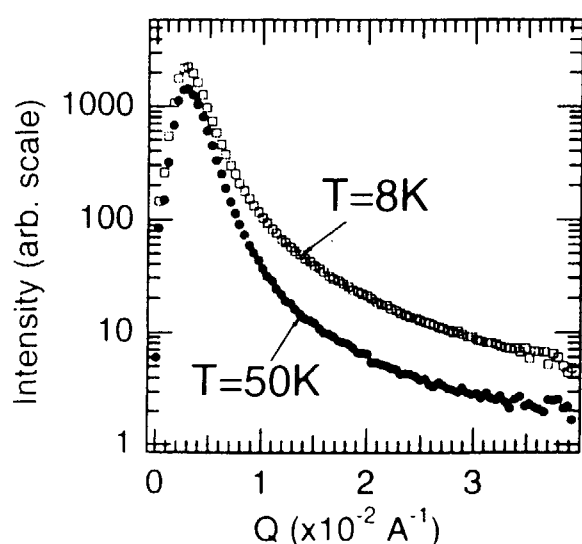


Fig. 1

Figure 2 shows time evolution of diffuse scattering intensity at $Q=0.0056\text{\AA}^{-1}$ measured at $T=8\text{K}$ after rapidly cooled from $T=50\text{K}$. We confirmed by this preliminary measurement that the sensitivity of the apparatus satisfies the necessary condition for the project.

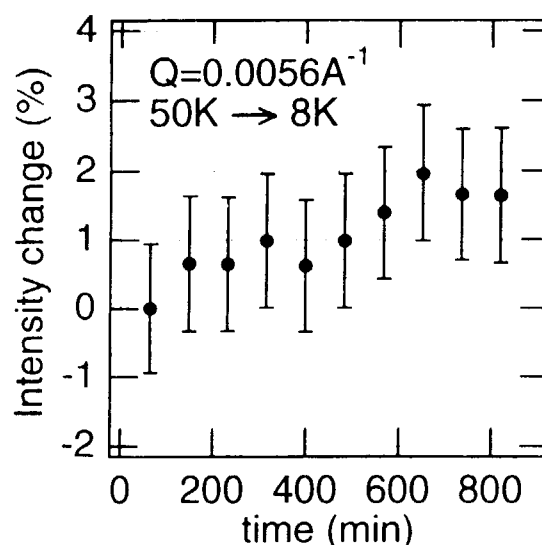


Fig. 2

References

1. K. Motoya and Y. Muraoka: J.Phys.Soc.Jpn. 62 (1993) 2819.
2. K. Motoya, S. Kubota and S.M. Shapiro: J.Mag.Mag.Mater. 140-144. (1995) 75.
3. K. Motoya, K. Nakaguchi and S. Kubota: J.Phys.Soc.Jpn. 68 No-7 (in press)

研究テーマ：Pd及びPt合金のフェルミ面効果の研究

表題：PtCr合金の原子短距離秩序とスピングラス

1-2-26 Atomic Short Range Order and Spin Glass in PtCr Alloy

M. Hirano and Y. Tsunoda

School of Science and Engineering, Waseda University, 3-4-1 Shinjuku, Tokyo 169-8555

PtCr alloy with Cr concentration below 15 at. % are considered to be non-magnetic and these above it show spin glass like behavior. Rather few experimental data were reported for this system until now.

We performed neutron scattering experiments for $Pt_{1-x}Cr_x$ alloy single crystals ($x = 0.07, 0.10, 0.13$ and 0.16) as a link in the chain of the studies on the Fermi surface effects in 3d-Pd and 3d-Pt disordered alloys.

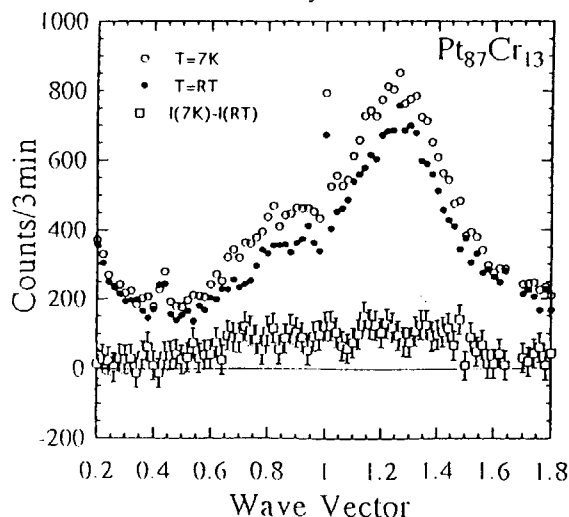
All of neutron scattering data obtained at RT show diffuse satellite peaks with asymmetric peak intensities at both sides of 100. The peak intensities are temperature independent, indicating atomic in origin. The satellite peak positions shift close to the 1 0 0 reciprocal lattice point with increasing Cr concentration. Similar temperature independent satellite reflections are found for PtV alloys at the same symmetric positions and are explained as an atomic concentration wave accompanied with a periodic lattice distortion. Thus, the diffuse scattering in PtCr alloys is ascribed to the concentration wave, which comes from the Friedel oscillation of the screening charge of the impurity potentials. Detailed discussion of the concentration wave is given in ref. 1). Note that the amplitude of the concentration wave is not sensitive to the Cr concentration and even for non-magnetic alloys (7 and 10 %) show

rather strong diffuse satellite reflections.

Magnetic contribution determined by subtracting the RT data from the LT data is observed for 13 and 16 at. % Cr alloys. The experimental data for the 13 at. % alloy are given in the figure. Our susceptibility data also show a cusp-type anomaly for this alloy. Thus the critical concentration for the spin glass phase is slightly lower than that reported in the previous authors. Magnetic scattering is a diffuse peak located around the 1 0 0. The spin glass like behavior of PtCr alloys is again ascribed to the dynamics and freezing processes of the spin density wave clusters just the same as PdMn, PdCr and CuMn spin glass alloys. The crossover of the charge screening and the sd-interaction (the SDW) is very interesting problem for this system.

1) A. Murakami and Y. Tsunoda

submitted to the Phys. Rev. B



研究テーマ：異方性競合系 $\text{Fe}_x\text{Co}_{1-x}\text{TiO}_3$ の磁場中での新しい（相）転移の研究

表題：異方性競合系 $\text{Fe}_{0.50}\text{Co}_{0.50}\text{TiO}_3$ の磁場中における履歴現象

1-2-27

Competing Anisotropy Origin Hysteretic Behavior of the Mixed Ising-XY Antiferromagnet $\text{Fe}_{0.50}\text{Co}_{0.50}\text{TiO}_3$ in Magnetic Field

A. Ito, C. Uchikosi, A. Fukaya¹, K. Nakajima² and K. Kakurai²

Department of Physics, Ochanomizu University, Bunkyo-ku, Tokyo 112-8610, Japan

¹*The Institute of Physics and Chemical Research (RIKEN), Wako, Saitama 351-0198, Japan*

²*Neutron Scattering Laboratory, Institute for Solid State Physics, The University of Tokyo, Shirakata, Tokai 319-1195, Japan*

In the present work, we report results of the field-dependent behavior of the competing anisotropy system $\text{Fe}_{0.5}\text{Co}_{0.5}\text{TiO}_3$, the mixed Ising-XY antiferromagnet [1] examined by neutron scattering measurements. In zero field, the XY(\perp) and the Ising(\parallel) spin component in the present sample makes the order (not real LRO, but domain state [2]) successively at $T_N=36$ K and $T_L=31$ K, accordingly, below T_L the spin system is in the oblique antiferromagnetic (OAF) state and the directions of the spins are tilted from the hexagonal c -axis of the ilmenite structure toward the c -plane.

We show in Fig. 1 a representative example of the temperature variation of magnetizations measured with a magnetic field of $H=10$ kOe applied parallel to the a -axis under the zero-field-cooled (ZFC) and the field-cooled (FC) condition. It is clearly seen that the magnetization vs. temperature curve shows hysteretic behavior below a certain temperature. The ZFC-magnetization M_{ZFC} is smaller than the FC-magnetization M_{FC} at low temperatures. When the temperature increases, M_{ZFC} shows anomalous and rapid increase, and coincides with M_{FC} at a certain higher temperature, which suggests the occurrence of some kind of transition. The transition temperature T_L depends on the value of the applied fields: at $H=10$ kOe, T_c is 7 K as

indicated by an arrow. According to the M_{ZFC} vs. H curve at 6.5 K, the spin-flop (SF) transition of the XY spin component occurs in the c -plane at $H=10$ kOe though it is not complete, the incompleteness of which is supposed to depend on temperature. This strongly suggests that the transition observed in the $M_{\text{ZFC}}-H$ curve corresponds to the SF transition. On the other hand, there appears no anomaly in the M_{FC} vs. T curve at T_c both on heating and cooling.

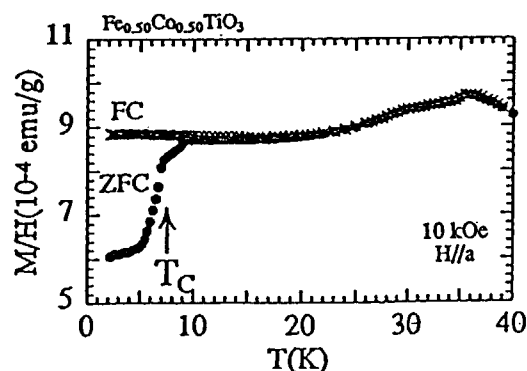


Fig. 1 M_{FC} vs. T and M_{ZFC} vs. T curves measured with 10 kOe applied parallel to the a -axis.

In order to clarify the anomalous behavior of the M vs. T curve, we performed neutron scattering measurements on the triple axis spectrometer ISSP-HQR and -PONTA installed at JRR-3M of JAERI, Tokai: we used it in a double axis

configuration. In Fig. 2, we show the temperature variation of the scattering intensities at the (0 0 1.5) and (1 0 -0.5) reciprocal-lattice position, $I_{0\ 0\ 1.5}$ and $I_{1\ 0\ -0.5}$, measured in 10 kOe applied under the ZFC and FC condition together with those in $H=0$. When $H=0$, the temperature variation of $I_{0\ 0\ 1.5}$ and $I_{1\ 0\ -0.5}$ exhibits no anomaly. On the other hand, when the measurement is made on heating the sample in $H=10$ kOe applied under the ZFC condition, $I_{0\ 0\ 1.5}$ (ZFC) increases rapidly at ~ 6.5 K while $I_{1\ 0\ -0.5}$ (ZFC) largely decreases over several Kelvin around ~ 6.5 K, toward the respective FC-values. This fact indicates that some kind of field-induced transition occurs. The intensity $I_{0\ 0\ 1.5}$ is caused only by $|M_{\perp}|$. Therefore, the increase of $I_{0\ 0\ 1.5}$ (ZFC) at ~ 6.5 K indicates the growth of $|M_{\perp}|$, the XY component. The amount of the growth is estimated to be about 4 %. This value corresponds to the contraction of $|M_{\parallel}|$, the Ising component, by about 6 %, under the assumption that the absolute value $|M|$ does not change at the growth of $|M_{\perp}|$. This corresponds to the increase of θ (spin tilting angle from the c -axis, $\theta \sim 50^\circ$ at $H=0$ kOe) by $\sim 3^\circ$.

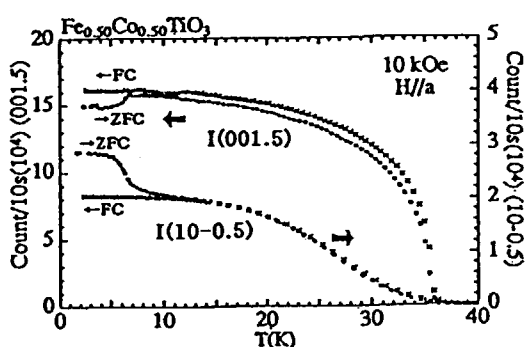


Fig. 2 Neutron scattering intensities at the (0 0 1.5) and (1 0 -0.5) reciprocal-lattice position in a magnetic field of 10 kOe applied parallel to the a -axis under the ZFC and FC condition.

However, we recognize that the decrease of $I_{1\ 0\ -0.5}$ around 6.5 K is much larger than that due to the contraction of $|M_{\parallel}|$ by 6 %. This fact suggests that another transition affecting only $I_{1\ 0\ -0.5}$ occurs simultaneously. This is explained by the fact that the $M_{\text{ZFC}}-H$ curve shows the occurrence of the SF transition in the c -plane at 6.5 K in 10 kOe.

Interestingly, $I_{1\ 0\ -0.5}$ (FC) does not show any anomaly, which indicates that the spin system is not released from the SF state down to 2 K. We attribute the difference between the behavior of $I_{1\ 0\ -0.5}$ (ZFC) and that of $I_{1\ 0\ -0.5}$ (FC) to the subtle balance of the Zeeman and anisotropy energy. As mentioned above, M_{\perp} (ZFC and FC) a few K above 6.5 K is larger than M_{\perp} (ZFC) a few K below 6.5 K. Thus, the XY spin component continues to stay in the SF state down to 2 K under the FC condition in order to keep the Zeeman energy lower. On the other hand, when the sample is cooled in $H=0$, the spin system prefers a large value of M_{\parallel} due to a rather strong Ising anisotropy. Even when a field of 10 kOe is applied, the Zeeman energy gained by the SF transition of M_{\perp} (ZFC) is not large enough to overcome the anisotropy energy at temperatures below ~ 6.5 K. We consider that the coupling between the Ising spin component and the XY one through the off-diagonal terms plays an important role to induce the novel phase transition indicated by the increase of M_{\perp} (ZFC) and the decrease of M_{\parallel} (ZFC) at ~ 6.5 K accompanied by the SF transition and the hysteresis. The details are in press [3].

- [1] A. Ito, S. Morimoto, Y. Someya, Y. Syono and H. Takei, J. Phys. Soc. Jpn. 51 (1982) 3173.
- [2] Q. J. Harris, Q. Feng, Y. S. Lee, R. J. Birgeneau and A. Ito, Phys. Rev. Lett. 78 (1997) 346.
- [3] A. Ito, C. Uchikosi, A. Fukaya, S. Morimoto, K. Nakajima and K. Kakurai, J. Phys. Chem. Solid (1999) in press.

研究テーマ：金属相酸化バナジウムの磁気構造と励起

表題：金属相酸化バナジウムの磁気構造と励起

1-2-28 Magnetic Structure and Excitation of Metallic Phase of $(V_{1-x}Ti_x)_2O_3$

K. Motoya, J. Kikuchi, T. Kumazawa, N. Wada and S. Shin¹

Department of Physics, Faculty of Science and Technology,

Science University of Tokyo, Noda 278-8510

¹*Institute for Solid State Physics, The University of Tokyo, Roppongi, Tokyo 106*

Neutron scattering study on a canonical Mott-Hubbard system $(V_{0.95}Ti_{0.05})_2O_3$ has been made. Development of an incommensurate antiferromagnetic order has been indicated by the appearance of Bragg peaks characterized by the propagation vector $q=1.78c^*$ below $T_N=19K$. In the temperature range $T_R=15K < T < T_N$, no magnetic Bragg peak is observed on the (00ξ) reciprocal line. We propose a spin-density-wave (SDW) magnetic structure. Below T_R , the direction of the magnetic moments deviate from the hexagonal c -axis by $\sim 60^\circ$. In the temperature range $T_R < T < T_N$, the moment direction is parallel to the c -axis. The maximum amplitude of the moment is $\sim 0.5 \mu_B$ at $T=8K$. Inelastic neutron scattering patterns taken by the constant energy scan shows peaks at positions corresponding to the magnetic Bragg points at below and above T_N . For small energy transfer scans, the width of the peaks are relatively narrow but much wider than the instrumental energy resolution. The width of the peaks grow wider with increasing energy transfer. Even far above T_N , scattering pattern still shows clear peaks at magnetic Bragg positions. For small energy transfer scans, peaks around the magnetic Bragg points persist up to $T \sim 10T_N$, which is much different from normal spin-wave excitation.

These characteristics in inelastic scattering properties are similar to those observed in $V_{1.973}O_3$ by Bao *et al.*^{1,2)} We analyzed the result based on the self-consistent renormalization (SCR) theory for weakly itinerant antiferromagnet³⁾ as was done for $V_{1.973}O_3$. The present experiment has shown that a large fluctuating component, which has been observed in the non-stoichiometric system^{1,2)} is also present in this more "homogeneous" system and of which property can be described in terms of the SCR theory for weakly itinerant antiferromagnet.

References

- 1) W. Bao, C. Broholm, S.A. Carter, T.F. Rosenbaum, G. Aeppli, S.F. Trevino, P. Metcalf, J.M. Honig and J. Spalek: *Phys. Rev. Letters* **71** (1993) 766.
- 2) W. Bao, C. Broholm, J.M. Honig, P. Metcalf and S. F. Trevino, *Phys. Rev. B* **54** (1996) 3726.
- 3) K. Nakayama and T. Moriya: *J. Phys. Soc. Jpn.* **56** (1987) 2918.

研究テーマ：Pd及びPt合金のフェルミ面効果の研究
表題：強磁性PdMnの中性子散乱の研究

1-2-29 Neutron Scattering Study of Ferromagnetic PdMn

A. Harigae and Y. Tsunoda

*Dep. of Appl. Phys. School of Science and Engineering, Waseda University
3-4-1 Ohkubo, Shinjuku-ku Tokyo 169-8555 Japan*

It is known that PdMn alloy with Mn concentration below 4 at.% shows ferromagnetism and with above 5 at.% behaves as a spin glass.

Recently, PdMn spin glass alloys were investigated by neutron scattering experiments and the spin glass like behaviour was explained in terms of dynamically fluctuating SDW clusters.

We present here neutron scattering data on a ferromagnetic Pd_{97.5}Mn_{2.5} alloy single crystal. The data were taken at the T1-1 triple axis spectrometer installed at a thermal guide of JRR-3M. Prior to neutron scattering experiments, the specimen was confirmed to be a ferromagnet with the Curie temperature of about 7K by susceptibility measurements.

Fig.1 displays the data obtained by scanning along the [1 0 0] direction passing through the 1 0 0 reciprocal lattice point. These data were taken at 7K and 50K. In order to derive the magnetic contribution, high temperature data were subtracted from the low temperature data. Subtracted data show diffuse satellite peaks at around $1 \pm \delta$ 0 0 ($\delta \sim 0.41$), indicating that the antiferromagnetic spin correlation exist in this ferromagnetic alloy.

We consider several models to explain the incompatible features of the ferromagnetic susceptibility and the diffuse satellite reflections in neutron scattering experiments.

1. Inhomogeneous model

In this model, a specimen is composed of two phases, i.e., ferromagnetic phase and spin glass phase. Since the Curie temperature is

consistent with reported value, Mn concentration is considered to be homogeneous. Three dimensional configuration of Mn atoms may lead to different magnetism.

2. Modulated ferromagnetic model

It was demonstrated in recent neutron scattering measurements that the transverse spin component of the ferromagnetic moment on PdFe and PtFe is modulated with the wave vector incommensurate with the lattice periodicity. The present specimen may be this type.

3. SDW cluster model

The SDW clusters always have a uncanceled spin component as the correlation length is comparable with or shorter than the wavelength. The uncanceled spin component would be strongly susceptible to the applied field and ferromagnetic behaviour results.

All models include some difficulties. We consider that the inhomogeneous model is the most plausible from various experimental data.

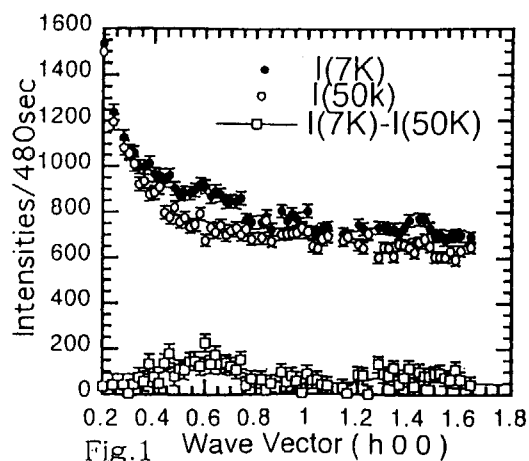


Fig.1 Wave Vector (h 0 0)

研究テーマ 重希土類ヘキサボライド(ReB₆; RE=Tb, Dy, Ho)の磁気構造の研究

表題 重希土類ヘキサボライドの磁気構造の研究

1-2-30 Study of Magnetic Structures in ReB₆H. Nojiri, K. Tkahashi, M. Motokawa, ¹S. Kunii, K. Ohoyama, M. Ohashi, and Y. Yamaguchi*Institute for Materials Research, Tohoku University, Sendai 980-8577, Japan*¹*Department of Physics, Tohoku University, Sendai 980-8477, Japan*

The magnetic structure of DyB₆ has been studied by using a high resolution powder diffractometer HERMES and a single crystal diffractometer KSD. DyB₆ has been known as a system with strong electron-lattice coupling and the successive phase transitions at 32 K and at 26 K have been recognized as the structural phase transition and the magnetic ordering, respectively. A neutron diffraction experiments had not been made so far. It is because the synthesis of a single crystal is very difficult for the high melting temperature and for the incongruent melting property. However, we have succeeded in preparing a ¹¹B enriched single crystal. The high performance of HERMES spectrometer enabled us to perform the high-resolution powder neutron experiments with Dy compounds in which a neutron diffraction is usually difficult.

Figure 1 shows two diffraction patterns at 2.5 K and at 34 K. A number of magnetic peaks are observed for the low temperature phase as indexed M in Fig. 1. Different from the expected magnetic structure inferred by considering the magnetization process^[1], an unexpected long period structure with 4 times larger unit cell is found. A detailed structural analysis shows a model with q-vectors $[1/4 \ 1/4 \ -1/2]$ is most plausible. The experimentally observed structure may be closely related to the lattice distortion from cubic structure to rhombohedral one at 32K. For the breaking of the cubic crystal symmetry, an inequivalence of the exchange coupling is brought into the system and as a result a long period structure is stabilized. Such a strong relation between the crystal structure and the magnetic structure shows a strong electron-lattice coupling in ReB₆ compounds.

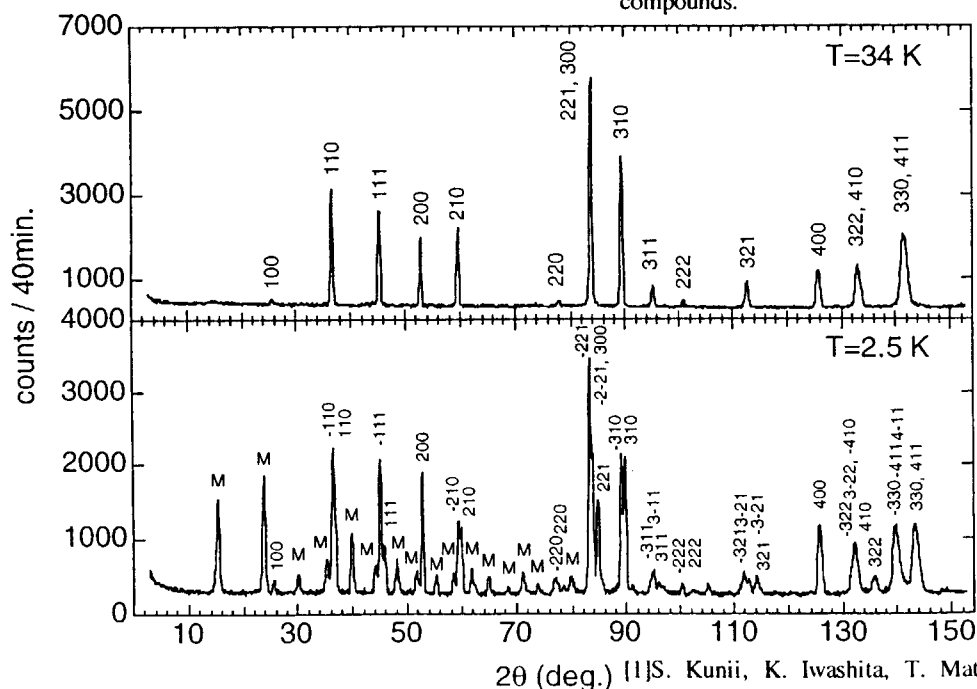


Fig. 1 Diffraction patterns at 2.5 K and at 34 K.

||S. Kunii, K. Iwashita, T. Matsumura, K. Segawa,
186-188(1993)646.

JRR-3M, T1-2, T1-3, 2. Magnetism

研究テーマ 重希土類ヘキサボライド(ReB₆; RE=Tb, Dy, Ho)の磁気構造の研究

表題 重希土類ヘキサボライドの磁気構造の研究

1-2-31 Study of Magnetic Structures in ReB₆H. Nojiri, K. Takahashi, M. Motokawa, ¹S. Kunii, K. Ohoyama, M. Ohashi, and Y. Yamaguchi*Institute for Materials Research, Tohoku University, Sendai 980-8577, Japan*¹*Department of Physics, Tohoku University, Sendai 980-8477, Japan*

The important role of the orbital degree of freedom in magnetism has been a subject of current interest in both 3d transition metal oxides and rare-earth compounds. Among many different kinds of compounds, a series of heavy rare earth compounds such as DyB₆ has been known as a system with strong electron-lattice coupling. The successive phase transitions occur at 32 K and at 26 K have been recognized as the structural phase transition and the magnetic ordering, respectively. However, much attention has not been paid for the effect of the lattice distortion from the cubic structure to the rhombohedral structure for the magnetic property. It is because the synthesis of a single crystal is very difficult for the high melting temperature and for the incongruent melting property. Recently, we have succeeded in preparing a ¹¹B enriched single crystal^[1] and it makes us possible to perform a neutron diffraction experiment.

Figure 1 shows a temperature dependence of the angle α for rhombohedral structure. It should be noted that the α changes gradually below T=32 K and no discontinuous jump of the angle is observed. This second-order-phase-transition like behavior may be related to the considerable softening observed by ultrasonic measurement.^[2] On the other hand, no anomaly is found at the magnetic phase transition temperature of 26 K.

At lower temperature, we found a magnetic Bragg peak at $k=[1/4 \ 1/4 \ -1/2]$ as shown in Fig. 2. The observation of magnetic peak at this reciprocal point shows that the magnetic unit cell is enlarged 4 times from the original unit cell, which is not expected for an antiferromagnet with cubic symmetry. Thus we speculate that this change is closely related to the lattice distortion

from cubic structure to rhombohedral structure. In another word, the breaking of the cubic crystal symmetry may bring the inequivalence of the exchange coupling into the system and as a result a long period structure is stabilized. It shows an essential role of the orbital degrees of freedom to understand the magnetic properties of the ReB₆ compounds. Further experimental studies are necessary to understand the microscopic mechanism for the strong electron-lattice coupling in the present system.

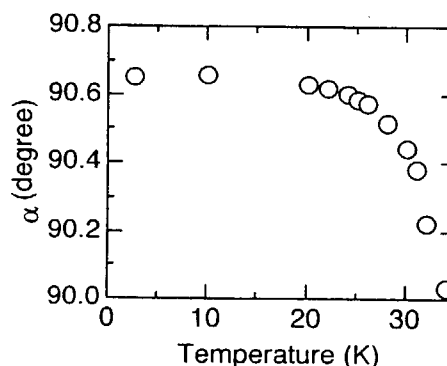
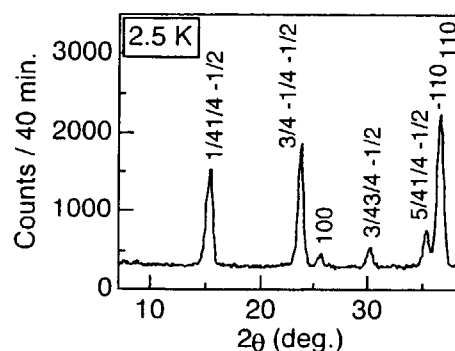
Fig. 1 Temperature dependence of angle α .

Fig. 2 Neutron diffraction pattern at ordered phase.

[1] K. Takahashi and S. Kunii: J. Sol. Stat. Chem., 133(1997)198.

[2] S. Nakamura, T. Goto, S. Kunii, K. Iwashita and A. Tamaki: J. Phys. Soc. Jpn., 63(1994)623.

研究テーマ：近藤化合物 $\text{Ce}(\text{Zn}_{1-x}\text{Ga}_x)$ の構造相転移と磁性

表題：近藤化合物 $\text{Ce}(\text{Zn}_{1-x}\text{Ga}_x)$ での磁気および構造相転移

1-2-32

Magnetic and Structural Phase transitions in the Kondo compounds $\text{Ce}(\text{Zn}_{1-x}\text{Ga}_x)$

M. Watanabe, K. Ohoyama, H. Onodera, M. Ohashi, Y. Yamaguchi,

Institute for Materials Research, Tohoku University, Sendai 980-8577

The Kondo compound CeZn which has the CsCl-type cubic structure at room temperature undergoes an antiferromagnetic ordering at $T_N=30\text{K}$ [1]. Moreover, a structural phase transition occurs at T_N as well; in the magnetic ordered state below T_N , the crystal structure is a tetragonal one with the lattice distortion, $c/a-1$, of 1.9%[1,2]. Thus, we think that CeZn is a system in which the magnetic interaction, lattice distortion and the Kondo effect give important effects for the magnetic behaviour. To understand roles of conduction electrons for the magnetic properties in CeZn , we have investigated the magnetic properties of $\text{Ce}(\text{Zn}_{1-x}\text{Ga}_x)$, because the number of conduction electrons increases with Ga-dope, x , without lattice distortion.

To observe phase transitions, we performed neutron diffraction experiments on single crystals of $\text{Ce}(\text{Zn}_{1-x}\text{Ga}_x)$ ($x=0,0.2,0.3$) using the double axis diffractometer, KSD, at JRR-3M. The receiving collimator of 15° and the incident neutron with a wavelength of 1.52\AA were used.

Fig.1 shows a contour map of 110 nuclear Bragg reflection from a single crystal of $\text{CeZn}_{0.67}\text{Ga}_{0.29}$ in the magnetic ordered state at 2 K. As shown in Fig.1, 110 Bragg peak splits into three Bragg peaks, 110, 101, 011, because of the structural transition to the tetragonal structure. Fig.2 shows the temperature dependence of the lattice constants a and c . As shown in Fig.2, the structural transition occurs at $T_N=20\text{K}$; the lattice distortion at 2K is $c/a-1=1.63\%$. Moreover, we also observed magnetic Bragg peaks below T_N which can be indexed with the same propagation vector as that of CeAn , $k=[0\ 0\ 1/2]$. Almost the same results of neutron diffraction experiments were obtained in $\text{CeZn}_{0.8}\text{Ga}_{0.2}$ as well. Therefore, from the experiments, $\text{Ce}(\text{Zn}_{1-x}\text{Ga}_x)$ show basically the same transition behaviour as that of pure CeZn . From this point of view, $\text{Ce}(\text{Zn}_{1-x}\text{Ga}_x)$ are in the same phase with the

pure CeZn up to $x=0.3$, though T_N rapidly decreases by the Ga doping.

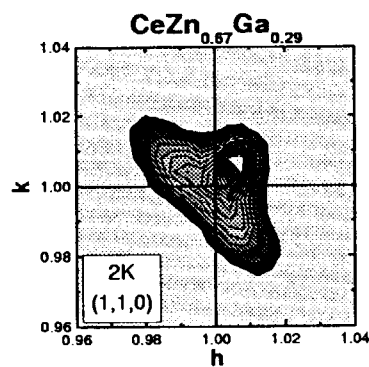


Fig.1: A contour map of 110, 101, 011 nuclear Bragg reflections from a single crystal of $\text{CeZn}_{0.67}\text{Ga}_{0.29}$ at 2 K.

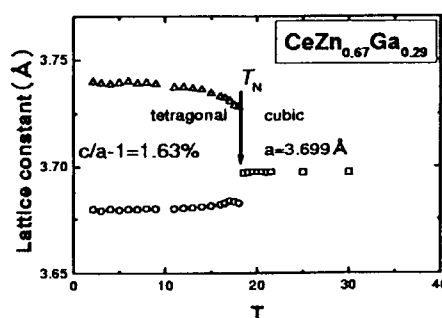


Fig.2: The temperature dependence of the lattice constant, a and c , of a single crystal of $\text{CeZn}_{0.67}\text{Ga}_{0.29}$

References

- [1] K. Pierre, A.P. Murani, R.M. Galere, J. Phys. F Metal Phys. 11(1981)679
- [2] Y. Uwatoko, H. Fujii, M. Nishi, K. Motoya, Y. Ito, Solid State Comm.72(1989)941.

研究テーマ: ZnFe_2O_4 , ZnCr_2O_4 の中性子散乱表題: ZnCr_2O_4 , ZnFe_2O_4 の中性子散乱1-2-33 Neutron Scattering Study of ZnCr_2O_4 and ZnFe_2O_4 K. Siratori, D. Eto, K. Kohn¹, I. Kagomiya¹, E. Kita² and Y. Hata²

Department of Physics, Faculty of Science, Kyushu University, Fukuoka, 812-8581 Japan

¹ Department of Physics, School of Science and Engineering, Waseda University, 169-8555 Japan² Institute of Applied Physics, University of Tsukuba, 305-8573 Japan

ZnFe_2O_4 and ZnCr_2O_4 are cubic spinel type oxides with the magnetic ions only at the B site, a well known frustrated 3-D lattice for the nearest neighbor antiferromagnetic interaction. Indeed, magnetic susceptibility of these oxides deviates from the Curie-Weiss law below about 150 K, though the Néel points are around 10 K. It is to be noted that the "frustration" in this case means that the spin structure, not the spin direction as in the triangular lattice of the Ising spins, cannot be determined uniquely. The exchange energy of the system as a function of the wave vector, $-J(\mathbf{q})$, is minimum for any wave vector with $q_z = 0$.

As a first step of the investigation of the 3-D frustrated Heisenberg spin systems, neutron scattering of polycrystalline specimens was measured by HERMES.

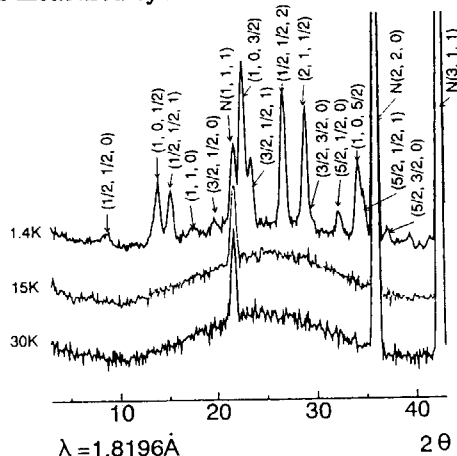


Fig. 1 The low angle part of the neutron scattering of ZnCr_2O_4 above and below T_N . The scale of the coordinate is logarithmic and shifted for each curve.

Figure 1 shows the low angle part of the scattering of ZnCr_2O_4 . A marked diffuse scattering was observed even at about $3 T_N$, which does not vanish completely in the ordered phase. Magnetic Bragg scatterings are observed at the reciprocal lattice points with one or two half integers. In the case of ZnFe_2O_4 , the diffuse peak locates at the lower angle and the magnetic Bragg peaks with two half integers are absent but the situation is similar.

High angle part of the scattering is shown in Fig. 2 for ZnCr_2O_4 . No difference is detected at above and below T_N , indicating that the lattice deformation accompanied by the spin ordering is smaller than $1/500$. This is the same for ZnFe_2O_4 .

Determination of the spin structure will be the next step.

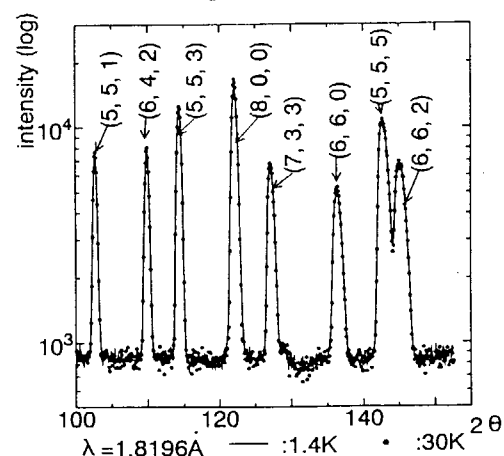


Fig. 2 The high angle part of the neutron scattering of ZnCr_2O_4 above (points) and below (smooth curve) T_N .

研究テーマ:フェライト材料の元素置換による特性改善の機構解明
表題:LaZn 置換 Sr フェライトの構造

1-2-34 Structural Study of La and Zn Substituted $\text{SrFe}_{12}\text{O}_{19}$ via Neutron Scattering

K. Kitazawa¹, N. Hirota¹, K. Iida^{2*}, J. Nakagawa² and H. Taguchi²

¹ Department of Applied Chemistry, University of Tokyo, Bunkyo-ku, Tokyo 113-8656, Japan

² Materials Research Center, TDK corporation, 570-2 Matsugashita, Minami-Hatori, Chiba 286-8588, Japan

*Corresponding author, now at ISTE, Superconductivity Research Laboratory, 1-16-25 Shibaura, Minato-ku, Tokyo 105-0023, Japan

The compound $\text{SrFe}_{12}\text{O}_{19}$ with a hexagonal unit cell, space group $P6_3/mmc$, with $a=0.5879$ nm and $c=2.3029$ nm, is an important material for the creation of a permanent magnet. Recently, we reported that the effects of La and Zn on the magnetic properties of $\text{SrFe}_{12}\text{O}_{19}$ ^[1]. According to our previous studies, $\text{Sr}_{0.7}\text{La}_{0.3}\text{Zn}_{0.3}\text{Fe}_{11.7}\text{O}_{19}$ compound exhibited remarkable magnetic properties accompanied by the enhancement of saturation magnetization. However the structural parameters for this compound have not been clarified precisely. For understanding the origin of the improvement of magnetic properties, an accurate knowledge of the structural parameters is crucial.

In the present study, the structure of $\text{Sr}_{0.7}\text{La}_{0.3}\text{Zn}_{0.3}\text{Fe}_{11.7}\text{O}_{19}$ has been investigated via HERMES, which is installed in JRR-3M at JAERI in Tokai. A polycrystalline sample with a nominal composition of $\text{Sr}_{0.7}\text{La}_{0.3}\text{Zn}_{0.3}\text{Fe}_{11.7}\text{O}_{19}$ was fabricated through a solid-state reaction using the powders of SrCO_3 , La_2O_3 , ZnO and Fe_2O_3 . The details of the sample preparation are described elsewhere^[1]. Neutron scattering experiments of powdered samples with a particle size of < 50 micron were performed at 773 K. This temperature is high enough to occur the magnetic phase transition (i.e. ferrimagnetic to paramagnetic). Based on the neutron diffraction data, the structural analysis were carried out using the Rietveld refinement program; RIETAN97-beta^[2].

We can infer the atomic position of La and Zn is the same that of Sr and Fe, respectively. The compound $\text{SrFe}_{12}\text{O}_{19}$ has five sublattices (2a, 2b, $4f_1$, $4f_2$ and 12k), which are occupied by Fe^{3+} . Judging from the result that magnetization is enhanced by La and Zn substitution, Zn^{2+} as a non-magnetic ion should occupy down-spin sites ($4f_1$ or $4f_2$). Taking into consideration that Zn^{2+} has a strong tetrahedral site-preference in spinel structure, It can be deduced that Zn^{2+} occupy $4f_1$ tetrahedral site.

From the above discussion, we suggested two models;
1) Zn^{2+} ion is occupied $4f_1$ -site (marked as Zn- $4f_1$ model),
2) Zn^{2+} ion is occupied $4f_2$ -site (marked as Zn- $4f_2$ model).

Figure 1 shows both the final fit and the pattern of derivation between calculated intensities and experimental data using the Zn- $4f_1$ model. The refined values for the lattice parameters were $a=0.59104(8)$ nm and $c=2.31805(23)$ nm which were slightly larger than that of room temperature. This slight increase in the lattice was caused by the thermal expansion. The resultant reliability factors were: $R_{wp}=7.52\%$, $R_p=5.69\%$, $R_e=3.34\%$, $R_i=2.49\%$ and $R_f=1.48\%$. The occupancies of La and Zn sites were confirmed 0.19(14) and 0.16(3), which were consistent with the chemical analysis.

On the other hand, we could not derive the meaning solution using the Zn- $4f_2$ model.

Reference

- [1] H.Taguchi, T.Takeishi, K.Suwa, K.Masuzawa and Y.Minachi: Proceedings of The Seventh International Conference on Ferrites (ICF7), C1-311 (Bordeaux, 1997).
- [2] F.Izumi: The Rietveld Method (Oxford University Press, Oxford, 1993) Chap. 13.

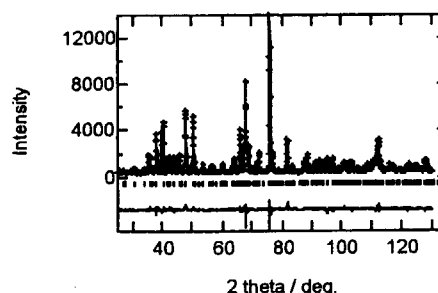


Fig.1 Rietveld refinement of the powder neutron diffraction pattern of $\text{Sr}_{0.7}\text{La}_{0.3}\text{Zn}_{0.3}\text{Fe}_{11.7}\text{O}_{19}$.

JRR3M, 2.Magnetism

研究テーマ: RE₂Pb₂ (RE=rare earth) 化合物の磁気的性質表題: CePb₂ 化合物の磁気構造1-2-35 Magnetic Structure of CePb₂ CompoundR. Yamauchi, K. Fukamichi, K. Ohoyama¹ and Y. Yamaguchi¹*Department of Materials Science, Tohoku University, Aoba-yama 02, Sendai 980-8579, Japan*¹*Institute for Materials Research, Tohoku University, Katahira, Sendai 980-8577, Japan.*

CePb₂ compound has been reported to have a MoSi₂-type (I4/mmm) structure and to be a heavy fermion compound with an antiferromagnetic ordering below 3.6 K⁽¹⁾. To discuss the magnetic moment reduction due to the Kondo effect, we have investigated the magnetic structure and the value of magnetic moment by neutron-diffraction for CePb₂ compound.

Polycrystalline sample was prepared by arc melting by using the constituent elements, 99.9 % pure Ce and 99.999 % pure Pb. The sample was powdered in a globe box filled with He gas. And it was put into a vanadium sample tube filled with He gas in an aluminum cell to prevent the sample from oxidizing and to keep homogeneity of temperature of the sample. The neutron-diffraction experiment was carried out using the HERMES installed at T1-3 port of JRR-3M reactor of JAERI. The neutron-diffraction spectra were measured at 6.0 K in the paramagnetic state, and 1.6 K in the ordered state using an incident wavelength of 1.8196 Å.

Figure 1 shows the observed neutron-diffraction spectrum at 6.0 K and the calculated intensities for MoSi₂- (I4/mmm) and HfGa₂-type (I4₁/amd). For PrPb₂ compound, two kinds of structures, MoSi₂- and HfGa₂-type, have been reported (1, 2). Although these calculated intensities are very similar, low angle spectra can be indexed as the HfGa₂-type crystal structure with $a=4.662\text{Å}$ and $c=32.315\text{Å}$. The present result suggests that CePb₂ compound has the HfGa₂-type crystal structure.

Figure 2 shows the difference between the neutron-diffraction spectra taken at 1.5 K and 6.0 K, which shows the magnetic diffraction peaks. Several magnetic peaks are observed. However, it is not easy to give their indices. The antiferro-

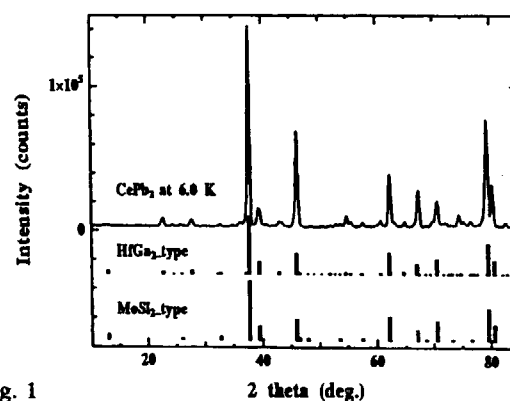


Fig. 1

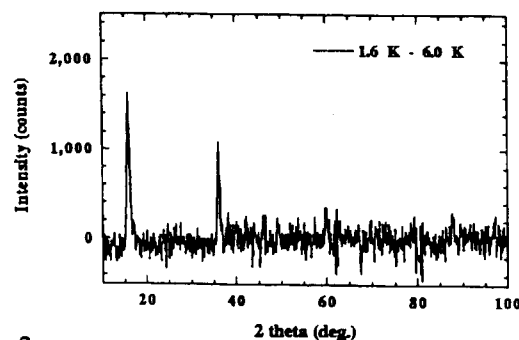


Fig. 2

magnetic structure of CePb₂ compound is considered to be not so simple from the fact that the intensity of the magnetic peaks are very weak, compared with those of the nuclear peaks. Detailed investigations are necessary in order to determine the magnetic structure and the magnitude of the magnetic moment.

This work has been supported by Research Fellowships of the Japan Society for the Promotion of Science for Young Scientists.

References

- (1) Y. Hattori et al., *J. Phys. Condens. Matter*, **6** (1994) 8035.
- (2) O. D. MacMasters et al., *J. Less-Common. Met.*, **45** (1976) 275.

研究テーマ: $\text{Ca}_{2-x}\text{Y}_x\text{Cu}_5\text{O}_{10}$ の磁気構造についての研究
 表題: $\text{Ca}_{2-x}\text{Y}_x\text{Cu}_5\text{O}_{10}$ の磁気構造についての研究

1-2-36 Magnetic Ordering of the Edge-Sharing CuO_2 Chains in $\text{Ca}_2\text{Y}_2\text{Cu}_5\text{O}_{10}$

M. Matsuda, K. Ohoyama¹, and M. Ohashi²

The Institute of Physical and Chemical Research (RIKEN), Wako, Saitama 351-0198, Japan

¹*Institute for Materials Research, Tohoku University, Sendai 980-0812, Japan*

²*Faculty of Engineering, Yamagata University, Jonan 4-3-16, Yonezawa 992-8510, Japan*

$\text{Ca}_{2+x}\text{M}_{2-x}\text{Cu}_5\text{O}_{10}$ ($\text{M}=\text{Y}$, Nd , and Gd) system, which consists of edge-sharing CuO_2 chains, shows a superstructure of the Ca and M ions while the structure of the edge-sharing CuO_2 chains is stable. Recently, Mizuno *et al.* theoretically studied the magnetic properties in various copper oxides with edge-sharing CuO_2 chains.¹⁾ They calculated the exchange interactions in the copper oxides and found a fairly large next-nearest-neighbor interaction J_2 compared with the nearest-neighbor interaction J_1 particularly in $\text{Ca}_2\text{Y}_2\text{Cu}_5\text{O}_{10}$ ($|J_2/J_1|=2.2$; J_1 : ferromagnetic, J_2 : antiferromagnetic), indicating a possibility of frustrated interactions in the chain.

Another important feature in this system is that it is possible to introduce hole carriers in the chain by changing the ratio of the Ca and M ions. It is interesting to study the hole concentration dependence of the magnetic properties. $\text{Ca}_2\text{Y}_2\text{Cu}_5\text{O}_{10}$ shows an antiferromagnetic transition and the transition temperature is decreased in Ca-rich samples²⁾.

We studied the magnetic structure of the end material $\text{Ca}_2\text{Y}_2\text{Cu}_5\text{O}_{10}$ using the neutron powder diffraction method³⁾. Since it is difficult to grow large single crystals in this system, a polycrystalline sample was used in this experiment. The experiment shows that $\text{Ca}_2\text{Y}_2\text{Cu}_5\text{O}_{10}$ has a commensurate long-range

ordering below $T_N \sim 29$ K with ferromagnetic correlations within the chain. The magnetic structure is shown in Fig. 1. The chains are coupled ferromagnetically along the b axis and antiferromagnetically along the c axis. The ordered moment of copper is $\sim 0.9\mu_B$ at 10 K, suggesting that the interchain interactions are fairly large. The observed intensities can be better described by assuming an ordering of oxygen moments which are induced due to the strong hybridization between the copper and oxygen ions.

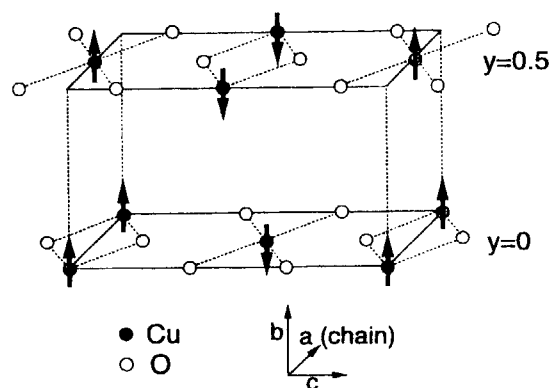


Figure 1 A proposed model for the magnetic structure in the chain.

References

- [1] Y. Mizuno *et al.*, Phys. Rev. B **57**, (1998) 5326-5335.
- [2] M. Matsuda and K. Katsumata, J. Magn. Magn. Mater. **177-181**, (1998) 683-684.
- [3] M. Matsuda, K. Ohoyama, and M. Ohashi, J. Phys. Soc. Jpn. **68**, (1999) 269-272.

研究テーマ : Mn_7Sn_4 の磁気転移の中性子回折による研究

表題 : Mn_7Sn_4 の磁気転移の中性子回折による研究

1-2-37 Neutron Diffraction Study of Magnetic Transition in Mn_7Sn_4

S. Anzai, T. Kobayashi, Y. Yamaguchi¹, M. Ohashi^{1,2}, and K. Ohoyama¹

Faculty of Science and Technology, Keio University

Institute of Materials Research, Tohoku University¹

Faculty of Engineering, Yamagata University²

Ni_2In -type $\text{Mn}_{7+x}\text{Sn}_4$ undergoes a reentrant spin-glass like transition at $T_f=100\sim 70\text{K}$ [1]. Spontaneous magnetization appears between T_f and the Curie temperature $T_c=220\sim 200\text{K}$. Here, the values of T_c and T_f depend on x . Our neutron diffraction investigation discloses an antiferromagnetic reflection (0 0 1/2) which disappears above T_f . Hence, the origin of the reentrant spin-glass like behaviors below T_f is cooperated with the formation of antiferromagnetic order along the c -axis. Concerning the magnetic order-disorder transition at T_c , Kapliencko et al [2] found a discontinuity in the linear thermal expansion coefficient for the a -axis and no anomalous behavior for the c -axis ($x=0.6$ and 1). We investigate the hexagonal lattice parameters a and c through T_f and T_c .

The neutron diffraction patterns of powdered sample ($x=0.4$, 12g; in vanadium cylinder of 10mm ϕ) were taken with the multi-counter type diffractometer (HERMES, Tohoku University) installed at JRR-3M. The wave length of neutron was 0.1824nm.

As seen in Figs. 1(a) and 1(b), the temperature gradient of a decreases above T_c , while that of c hardly changes. Here, the magnetic peaks of (0 0 1/2) and (110) disappears at $T_f=95\text{K}$ and $T_c=202\text{K}$, respectively. It is remarkable that the temperature gradient of a increases at T_f and that

the absolute value of the change is significantly larger than that at T_c . Moreover, the similar change of temperature gradient is observed on the c -axis. The anomalous thermal expansion behavior below the magnetic transition temperatures indicates that the effective magnetic interactions depend on atomic distances. Therefore, the reentrant spin-glass like behavior in $\text{Mn}_{7+x}\text{Sn}_4$ is related to the distance-dependent nature of effective magnetic interactions.

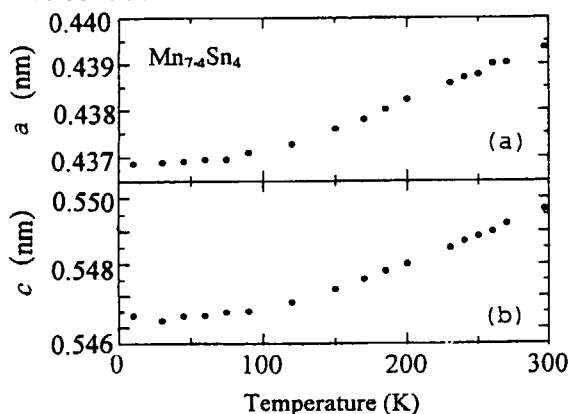


Fig.1 Temperature dependences of a (a) and c (b).

References

- [1] R. Sugi, T. Shimomura, M. Matoba, S. Matsuzaka, S. Fujii, N. Hagiwara and S., Anzai, Phys. Stat. Sol (b) 189 (1995) K65.
- [2] A. I. Kapliencko, b. N. Leonov and V. V. Chekin, Soviet Phys. Solid ; State 12 (1970) 3030.

JRR-3M, HERMES, 2. magnetism

非晶質ホイスラー合金 $\text{Cu}_2\text{MnAl}_{1-x}\text{Zr}_x$ の中性子回折1-2-38 Neutron Diffraction of Amorphous Heusler Alloy $\text{Cu}_2\text{MnAl}_{1-x}\text{Y}_x$ T.Kamimori, Y.Shiraga, K.Konishi, H.Tange, M.Goto, S.Tomiyoshi¹, M.Ohashi² and Y.Yamaguchi²

Faculty of Science, Ehime University, Matsuyama 790-8577

¹Faculty of Engineering, Ehime University, Matsuyama 790-8577²Institute for Material Research, Tohoku University, Sendai 980-8577

A Typical Heusler alloy Cu_2MnAl is well known as a ferromagnet caused by its ordered structure. It arouses an interest of us in magnetism of the alloy in amorphous state. We succeeded to obtain rapidly quenched (R.Q.) Heusler alloy ribbon by substitution of M for Al or Zr, $\text{Cu}_2\text{MnAl}_{1-x}\text{Zr}_x$ or $\text{Cu}_2\text{MnAl}_{1-x}\text{Y}_x$ ^{1,2)}. Magnetic measurements show spin glass behavior at low temperature. A reentrant spin glass behavior was observed for $\text{Cu}_2\text{MnAl}_{0.8}\text{Zr}_{0.2}$ with $T_f \sim 10\text{K}$ and $T_C \sim 50\text{K}$. The neutron diffraction for $M=\text{Y}$ shows anti-ferromagnetic magnetic scattering in 1993²⁾. The magnetic scattering was also found from 20K to 500K that is just below the recrystallization temperature. In the present work, neutron diffraction patterns for $M=\text{Zr}$, $x=0.3$ was measured from 10K to R.T. at JRR-3 of JAERI(Tokai). Fig.1 shows the AF magnetic scattering at R.T. This broad peak can be decomposed into 7 components. Most of these components distributed around $Q \sim 1.5$ that corresponds to the Mn-Mn distance in ordered crystalline Heusler alloy. The broad main peak at $Q=1.58$ and three peaks having the same σ can be understood as scattering from amorphous state and that form disordered crystal state having 2Al, AlZr and 2Zr as nearest neighbour. The distance of AF Mn-Mn pair distance is the same as that of the ferromagnetic Mn-Mn pair in ordered

Heusler alloy. This result shows that the AF property is not caused by appearance of a short distance Mn-Mn pair but caused by long range disordered structure.

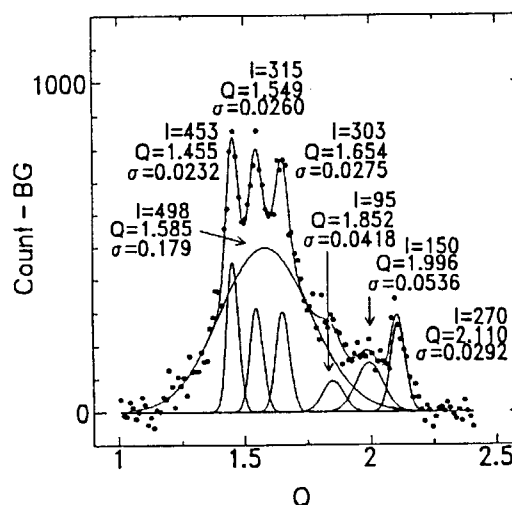


Fig.1 neutron diffraction pattern of amorphous $\text{Cu}_2\text{MnAl}_{0.7}\text{Zr}_{0.3}$ at R.T.

References

- 1) M.Goto, K.Takagi, T.Kamimori and H.Tange; Proceeding of the 2nd International Symposium on Physics of Magnetic Materials. (1992, Beijing, China, International Academic Publications) P.508.
- 2) M.Goto, T.Kamimori, H.Tange, K.Kitao, S.Tomiyoshi, K.Ohoyama and Y.Yamaguchi; J. Magn. Magn. Mater., **140-144**(1995)277.

JRR-3M HERMES Magnetism

研究テーマ：半磁性半導体 $\text{Zn}_{1-x}\text{Mn}_x\text{Te}$ の中性子回折

表題：希薄磁性半導体 $\text{Zn}_{0.568}\text{Mn}_{0.432}\text{Te}$ における短距離磁気秩序

1-2-39 Short-range Magnetic Order in Diluted Magnetic Semiconductor $\text{Zn}_{1-x}\text{Mn}_x\text{Te}$ with $x=0.432$

Y.Ono, T.Kamiya, S.Shamoto, T.Sato¹, Y.Oka¹ and T.Kajitani

Department of Applied Physics, Graduate School of Engineering, Tohoku University, Sendai 980-8579

¹ Research Institute for Scientific Measurements, Tohoku University, Sendai 980-8577

$\text{Zn}_{1-x}\text{Mn}_x\text{Te}$ is a typical frustrated antiferromagnet with 5/2 spins (Mn^{2+}) ($x \leq 0.68$). [1] Single crystal neutron diffraction measurement of $\text{Zn}_{0.568}\text{Mn}_{0.432}\text{Te}$ was carried out using double-axis diffractometer HERMES implemented with multi-counter detection system at JAERI. Highly anisotropic diffuse peaks were clearly observed around the reciprocal lattice point, $1\ 1/2\ 0$ and its equivalent positions at 10 K, 30 K and 100 K, respectively. [2] This is a clear indication of type-III antiferromagnetic short-range order caused by the nearest and next nearest neighbour exchange interactions of Mn^{2+} spins. [3] In this study, degree of short-range order between Mn^{2+} spins, α_{lmn} , was calculated from the observed diffuse intensity using the following equation, [4]

$$\alpha_{\text{lmn}} = \frac{1}{\int_0^1 \int_0^1 \int_0^1 I_D} \int_0^1 \int_0^1 \int_0^1 I_D \times \exp\{2\pi i(lh_1 + mh_2 + nh_3)\} dh_1 dh_2 dh_3, \quad (1)$$

where I_D is diffuse intensity at the reciprocal lattice point, $h_1 h_2 h_3$, being initially corrected by magnetic form factor, Debye-Waller factor and background subtraction. Since the diffuse intensity measurement was restricted within $hk0$ plane, the intensity distribution in the region, $0 < h_1, h_2, h_3 < 1$ was three-dimensionally reconstructed based on that around $1\ 1/2\ 0$. This region was divided into $101 \times 101 \times 101$ pixels for integration in eq. (1).

Figure 1 shows the degree of short-range order between Mn^{2+} spins at 17 K, 30 K and 100 K, respectively. The Mn^{2+} spin at the origin is surrounded by antiparallel nearest neighbour (NN) ones. Parallel spins at NNN site follow them. Such an oscillation gradually diminishes with increasing the distance between Mn^{2+} ions and finally disappears at about 13.2 Å. This distance corresponds to twice of lattice parameter. There is no long-range order at any temperature. The degree of short-range order at the NN site is practically independent from increasing temperature. This indicates that the strong antiferromagnetic exchange interaction still remains between the NN spins at 100 K.

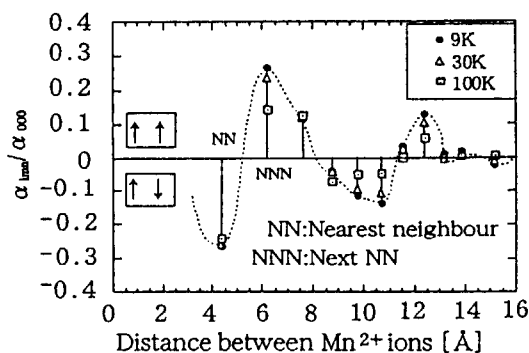


Fig.1 Degree of short-range order vs. distance between Mn^{2+} ions. α_{lmn} is normalized by α_{000} . A dotted line is guide for the eye.

References

- [1] J.K.Furdyna, J.Appl.Phys.64 (1988) R29.
- [2] Y.Ono et al. J.Phys.Chem. Solids, in press
- [3] T.M.Holden et al., Phys.Rev.B26 (1982) 5074.
- [4] J.M.Cowley : J.Appl.Phys.21 (1950) 24.

JRR-3M, HERMES (T-1-3) , 2. Magnetism

研究課題: $\text{La}_{2-2x}\text{Sr}_{1+2x}\text{Mn}_2\text{O}_7$ の高圧化におけるスピン状態
 標題: 層状Mn酸化物 $\text{La}_{2-2x}\text{Sr}_{1+2x}\text{Mn}_2\text{O}_7$ の磁気相図

1-2-40

Magnetic Phase Diagram of the Bi-Layered Manganite $\text{La}_{2-2x}\text{Sr}_{1+2x}\text{Mn}_2\text{O}_7$ ($0.30 \leq x \leq 0.50$)^[1]

M. Kubota¹, H. Fujioka², K. Hirota², Y. Moritomo³, H. Yoshizawa¹ and Y. Endoh²

¹Neutron Scattering Laboratory, Institute for Solid State Physics, University of Tokyo

²CREST, Department of Physics, Tohoku University

³CIRSE and Department of Applied Physics, Nagoya University

The layered Perovskite Mn oxide $\text{La}_{2-2x}\text{Sr}_{1+2x}\text{Mn}_2\text{O}_7$ (LSMO327) exhibits a variety of magnetic structures with changing temperature and the hole concentration x . There have been, however, no systematic study of the magnetism of LSMO327 in a wide temperature and hole concentration range. To establish the magnetic phase diagram, we have carried out extensive neutron-diffraction studies on LSMO327 powder samples, which will be relevant to clarification of colossal magnetoresistive behaviors in this system. Powder diffraction patterns were taken at room temperature, intermediate temperature (~ 120 K), and low temperature (~ 10 K) using the HERMES powder neutron diffractometer. Temperature dependences of magnetic reflections were measured using the triple-axis spectrometers TOPAN and GPTAS.

The powder diffraction patterns for $0.32 \leq x \leq 0.50$ at low temperatures can be explained by a combination of the FM-I and AFM-I phases: the FM-I phase is dominant at low doping region, while the AFM-I phase gradually takes over the FM-I phase with increasing x . A finite canting angle between planar magnetic moments on neighboring planes starts appearing at $x \sim 0.39$ and reaches 180° (A-type antiferromagnet) at $x = 0.48$. We also found that the diffraction pattern at $x = 0.30$ is completely different from the other concentrations, and corresponds to the FM-II phase, in which spins are aligned ferromagnetically along the c -axis. The drastic change in the magnetic structure indicates that there exists a compositional phase boundary around $x = 0.32$.

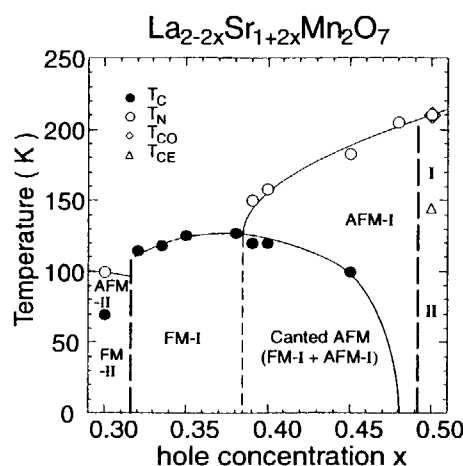


Figure 1: Magnetic phase diagram of $\text{La}_{2-2x}\text{Sr}_{1+2x}\text{Mn}_2\text{O}_7$. FM-I (AFM-II) indicates the planar A-type AFM structure with FM (AFM) intra-bilayer coupling and FM (AFM) inter-bilayer coupling. FM-I and FM-II stand for the FM structures with spin within the ab plane and along the c -axis, respectively. As for $x = 0.50$, only AFM-I exists in the phase I, while AFM-I and CE-type AFM coexist in the phase II.

References

- [1] M. Kubota *et al.*, J. Phys. Chem. Solids, in press.
- [2] Y. Moritomo *et al.*, Nature (London) **380** 141 (1996).

研究課題名：重い電子系 Ce_2X ($\text{X}=\text{Sb}, \text{Bi}$)での結晶場分裂測定

題目：重い電子系化合物 Ce_2X ($\text{X}=\text{Sb}, \text{Bi}$)での磁気励起

1-2-41 Magnetic Excitations in the Heavy Fermion Compounds Ce_2X ($\text{X}=\text{Sb}, \text{Bi}$)

K. Ohoyama, H. Hayashi, H. Onodera, M. Ohashi, Y. Yamaguchi, M. Kohgi^a, T. Suzuki^b

Institute for Materials Research, Tohoku University, Sendai 980-8577

^aDepartment of Physics, Tokyo Metropolitan University, Tokyo 192-0397

^bDepartment of Physics, Tohoku University, Sendai 980-8578

The tetragonal La_2Sb -type compounds Ce_2X ($\text{X}=\text{Sb}, \text{Bi}$) are thought to be Kondo and heavy fermion compounds with antiferromagnetic ground states[1]. This crystal structure includes two kinds of Ce sites, Ce-I at the 4(e) site and Ce-II at the 4(c) site[2]. The distance between the nearest Ce-I atoms is shorter than those in typical valence fluctuation(VF) materials. In contrast, the distance between Ce-II and the nearest Ce atom are about 20 % longer than those of Ce-I, and those in typical VF materials as well. Therefore, we expect that the 4f state of Ce-I shows strong valence fluctuation, while that of Ce-II is relatively localised.

To observed magnetic excitations in Ce_2X , we performed neutron inelastic scattering experiments on polycrystalline samples of Ce_2X using the triple axis spectrometer TOPAN at JRR-3M. The contamination of $\lambda/2$ has been corrected. We have already reported the detail of the results of the experiments in Ref.[3].

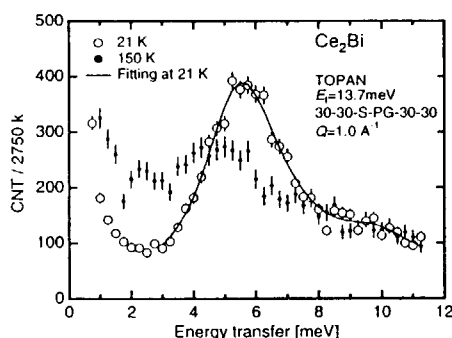


Fig.1 The T-dependence of the energy spectra of Ce_2Bi at $Q=1.0\text{\AA}^{-1}$ at $T=21\text{ K}$ and 150 K . The solid line represents the best result of the fitting procedure.

Fig. 1 shows the spectra of Ce_2Bi at $Q = 1.0\text{\AA}^{-1}$ at $T = 21\text{ K}$ and 150 K . In Fig.1, we observed an obvious peak at 5.5 meV at 21 K . From the T- and Q- dependence of the intensity, it is evident that the obvious peak at 21 K is due to magnetic excitation. Moreover, the obvious peak indicates that the 4f state which occurs the magnetic excitation is well localised. The solid line in Fig.1 represents the best result of the fitting with resolution convolution to the spectrum at 21 K

using two Lorentzian functions. The positions of the Lorentzians are determined as $5.4 \pm 0.1\text{ meV}$ and $9.8 \pm 0.4\text{ meV}$. From the results, we propose a crystalline electric field (CEF) level scheme model of Ce-II in Ce_2Bi : the first and second excited states exist at 5.4 meV and at about 10 meV above the ground state, respectively[3].

Fig. 2 shows the spectra at 21 K at $Q=1.0\text{\AA}^{-1}$ and 4.0\AA^{-1} . We observed broad spectra which shows no obvious temperature dependence. From the Q-dependence of the intensity, there exist magnetic components at about 2 meV and between about 3 and 7 meV at 21 K . The spectra in Ce_2Sb are quite different from those in Ce_2Bi which shows the well defined magnetic peak. Therefore, the present results indicate that the CEF in Ce_2Sb is quite different from that in Ce_2Bi . The difference of CEF in these compounds may be due to the difference of the magnetic anisotropy[1].

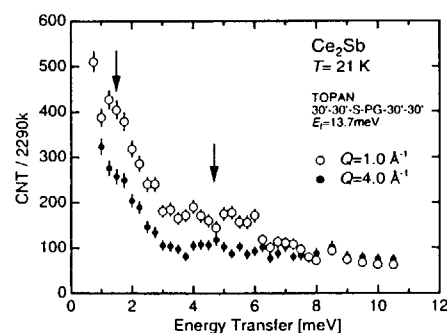


Fig.2 The Q-dependence of the energy spectra of Ce_2Sb at $T=21\text{ K}$ at $Q=1.0\text{\AA}^{-1}$ and 4.0\AA^{-1} . The arrows indicate the positions of magnetic components.

References

- [1] A. Oyamada, A. Isobe, H. Kitazawa, A. Ochiai, T. Suzuki and T. Kasuya: J. Phys. Soc. Jpn. **62** (1993)1750.
- [2] W.N. Stassen, M. Sato and L.D. Calvar: Acta Cryst. **B26**(1970)1534.
- [3] K. Ohoyama, H. Hayashi, H. Onodera, M. Ohashi, Y. Yamaguchi, A. Oyamada, M. Kohgi, T. Suzuki, J. Phys. Chem. Solids in press

研究テーマ：酸素欠損型ペロブスカイト $\text{La}_x\text{Sr}_{(1-x)}\text{MnO}_{(2.5+0.5x)}$ の磁気構造

表題：酸素欠損型ペロブスカイト $\text{La}_{0.8}\text{Sr}_{0.2}\text{MnO}_{2.9}$ の磁性

1-2-42 Magnetism of Oxygen Deficient Perovskite, $\text{La}_{0.8}\text{Sr}_{0.2}\text{MnO}_{2.9}$

K. INOUE, T. MORI¹, N. KAMEGASHIRA¹, Y. YAMAGUCHI², K. OHYAMA²

Fac. Sci. & Tech. Ryukoku Univ. Seta, Otsu 520-2194, Japan

¹*Toyohashi Univ. of Tech. Toyohashi 441-8580, Japan*

²*IMR Tohoku Univ. Aoba-ku, Sendai 980-8577, Japan*

$\text{La}_{0.8}\text{Sr}_{0.2}\text{MnO}_{2.9}$ is a perovskite compound with the oxygen deficiency, where the valence number of Mn ions is controlled to be always three. We have measured the magnetization by SQUID magnetometer and the powder neutron diffraction by HERMES at JRR-3M, to investigate the magnetism of this material.

The temperature dependence of the magnetization and the inverse susceptibility measured at low field of 200 (Oe) is shown in Fig.1, for the cases of zero field cooling and of field cooling at 200(Oe). The field dependence of magnetization at 4.2(K) is shown in Fig.2.

As shown in Fig.1, the behavior of the temperature dependence is quite different for finite-field cooling and for zero-field cooling, whereas the magnetic transition temperature exists at around 138(K) for both cases. In Fig.2, the magnetization gradually increases up to 5(T) and the absolute value of magnetization is very small, although we see a hysteresis near zero field. It seems from these facts that the magnetic order at low temperature is not a simple ferromagnetic state, but presumably a spin-canted state where the ferromagnetic

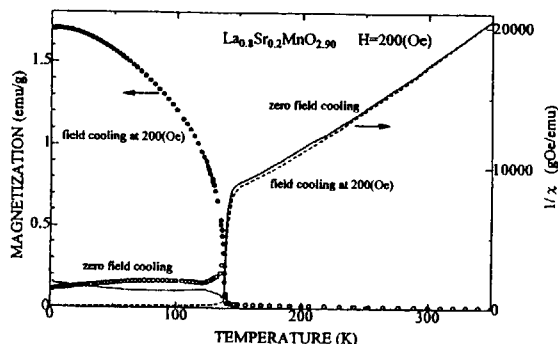


Fig.1. Magnetization and inverse susceptibility versus temperature at low field of 200(Oe).

component and the antiferromagnetic component coexist. In fig.2, the ferromagnetic component obtained from the zero-field magnetization which is extrapolated from the straight line at non zero field, is $0.07 \mu_B/\text{Mn}$. On the other hand, the value of $2S$ per Mn atom, which is obtained from the effective magnetic moment in the paramagnetic region in Fig.1, is $4.95 \mu_B/\text{Mn}$. From these facts, if the magnetic ordered state is assumed to be a spin canted one, the magnetic moment seems almost to be antiferromagnetic.

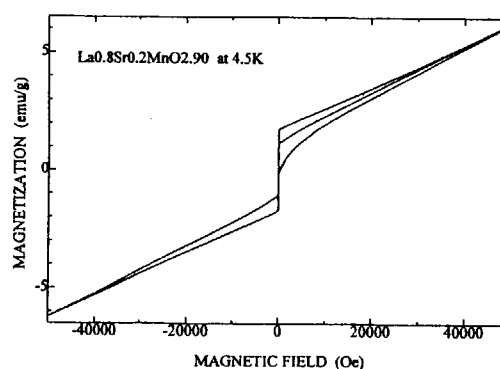


Fig.2. Magnetization versus magnetic field up to 5(T) at 4.2(K).

In Fig.3, the neutron diffraction pattern at 273(K) where the sample is paramagnetic and that at 15(K) where it has magnetic order are shown. The result of Rietveld analysis by the program RIETAN,¹⁾ is shown with a solid line. As shown in the figure, the best fit is obtained by the assumption that the crystal structure at 273(K) is rhombohedral (the space group is R-3c), where the La atom and the Sr atom are mixed at random and the oxygen vacancy exists also at random. The diffraction pattern at low temperature of 15(K) is almost the same as that at 273(K), except the intensity

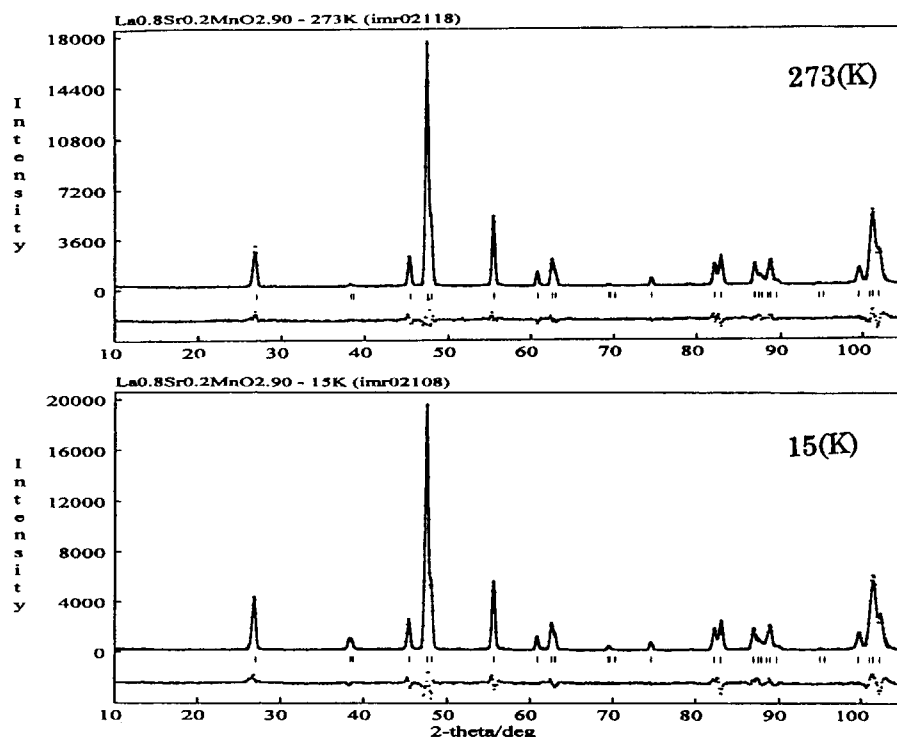


Fig.3. Neutron diffraction patterns and the results of Rietveld analysis at 273(K) and 15(K).

of each peak. The best fit for Rietveld analysis at 15(K) is obtained by the assumption that the magnetic structure is ferromagnetic one with the direction of Mn moment at an angle of about 60° from the [111] direction. The size of the magnetic moment is deduced to be $2.48 \mu_B/\text{Mn}$.

In conclusion, $\text{La}_{0.8}\text{Sr}_{0.2}\text{MnO}_{2.9}$ of which valence number of Mn atom is always controlled to be three by reducing the number of oxygen, shows quite different magnetism from that of $\text{La}_{0.8}\text{Sr}_{0.2}\text{MnO}_3$, which is ferromagnetic with the Curie temperature of about 310(K).²⁾ The magnetic transition temperature of 138(K) for spin-canted $\text{La}_{0.8}\text{Sr}_{0.2}\text{MnO}_{2.9}$ seems to coincide with the extrapolated position from the concentration dependence of the Néel temperatures, T_N , of $\text{La}_{1-x}\text{Sr}_x\text{MnO}_3$, as shown in Fig.4.²⁾ In case of the compound where the valence number of Mn ions is three, the antiferromagnetic region seems to expand up to Sr concentration of 0.2.

At present, the results obtained from the Rietveld analysis on neutron diffraction patterns are contrary to the results obtained

from the magnetization measurements. We have to solve this inconsistency.

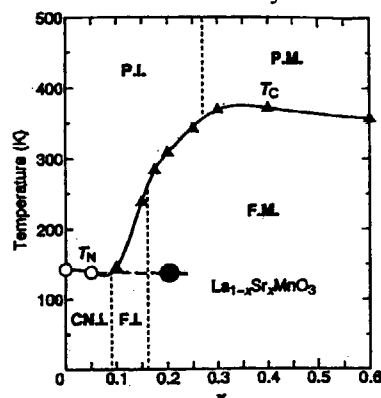


Fig.4. Electronic phase diagram of $\text{La}_{1-x}\text{Sr}_x\text{MnO}_3$.²⁾ The Néel temperature obtained from this experiment is shown by black circle.

References

- 1) F.Izumi, H.Asano, H.Murata and N.Watanabe: J. Appl. Crystallogr. 20(1987) 411.
- 2) A.Urushibara, Y.Moritomo, T.Arima, A. Asamitsu, G.Kido and Y.Tokura: Phys.Rev.B 51(1995)14103.

研究テーマ：ウラン化合物における超伝導の研究
表題：UPd₂Al₃の圧力下中性子散乱による研究

1-2-43 Neutron Scattering Study of UPd₂Al₃ under External Pressure

T. Honma¹, Y. Haga¹, E. Yamamoto¹, N. Metoki¹, Y. Koike¹, T. Osakabe¹ and Y. Ōnuki^{1,2}

¹Advanced Science Research Center, Japan Atomic Energy Research Institute, Tokai, Naka, Ibaraki 319-1195, Japan

²Graduate School of Science, Osaka University, Toyonaka 560-0043, Japan

UPd₂Al₃ with the hexagonal structure is a fascinating magnetic superconductor. Superconductivity with the transition temperature $T_c = 2$ K is realized in the antiferromagnetic state with the Néel temperature $T_N = 14.5$ K.¹⁾ Neutron scattering measurements revealed that the magnetic moments of $0.85 \mu_B/U$ are ferromagnetically oriented along the [1120] direction but are coupled antiferromagnetically along the [0001] direction with the wave vector $Q = (0\ 0\ 0.5)$.²⁾

Pressure is one of the parameters to control both the electric and magnetic properties. In the heavy fermion compounds, those properties are sensitive to pressure because the characteristic temperatures such as the Néel temperature T_N and Kondo temperature T_K are not large in this system. The previous experiments, based on the specific heat and the electrical resistivity under pressure, indicate that T_N of 17.5 K at ambient pressure increases with increasing pressure, makes a maximum around 0.5-1 GPa and decreases rather steeply with increasing pressure.³⁻⁵⁾ The specific heat jump at T_N , reflecting the magnetic phase transition, becomes broad with increasing pressure and the corresponding entropy change becomes small in magnitude compared to that at ambient pressure. This behavior might be correlated with the magnetic moment.

To clarify this interesting tendency, we have done the neutron scattering experiment under

pressure. The single crystal was grown by the Czochralski pulling method in a tetra-arc furnace, as described in ref. 6 in detail. The hydrostatic pressure was introduced by using the McWhan cell. The pressure was calculated from the lattice constant at each pressure and the elastic constants at ambient pressure.⁷⁾ Neutron scattering experiments were carried out by using a thermal neutron triple-axis spectrometer TAS2 installed in the research reactor JRR-3M at the Japan Atomic Energy Research Institute (JAERI).

We have measured the temperature dependence of the (0 0 0.5) antiferromagnetic Bragg intensity. Temperature dependences of a ratio of the (0 0 0.5) magnetic Bragg peak intensity to the (0 0 1) nuclear one under several pressures are shown in Fig. 1.

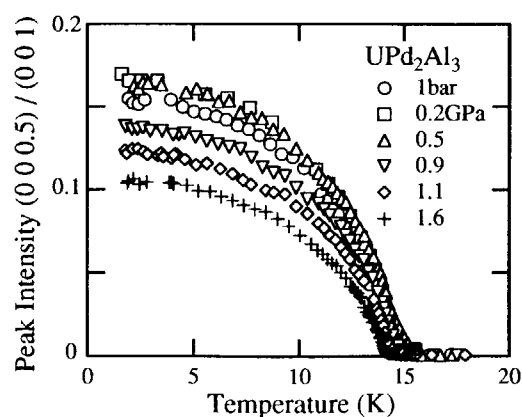


Fig. 1 Temperature dependences of a ratio of the (0 0 0.5) magnetic Bragg peak intensity to the (0 0 1) nuclear one under a several pressures of 0-1.6 GPa.

We determined the magnitude of the ordered moment μ_{ord} under a several pressures of 0-1.6 GPa, which was obtained by comparing the integrated intensity of the magnetic (0 0 0.5) Bragg peak with the one of the nuclear (0 0 3) Bragg peak at 1.8 K. The pressure dependences of the Néel temperature T_N and the ordered moment μ_{ord} are shown in Fig. 2.

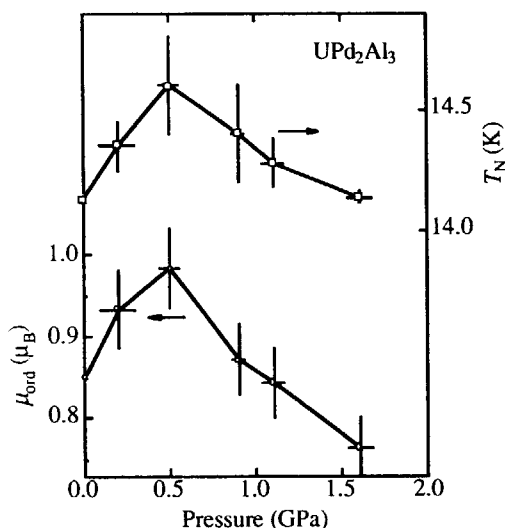


Fig. 2 Pressure dependences of the Néel temperature T_N and the ordered moment μ_{ord} .

The Néel temperature makes a maximum around 0.5 GPa, roughly consistent with the previous result. This unusual pressure dependence of T_N might be due to the deviation from the hydrostatic pressure. From the Ehrenfest relation, the Néel temperature T_N decreases with increasing pressure under the hydrostatic pressure. On the other hand, the thermal expansion of UPd_2Al_3 are strongly anisotropic. Therefore the pressure dependences of T_N under the uniaxial pressure along the [0001] and in the basal plane show an opposite sign.⁸⁾

Interesting is the pressure dependence of the integrated intensity of the magnetic Bragg peak. This is proportional to a square of the magnetic

moment μ_{ord} . The magnetic moment behaves in the same way as T_N does, namely, it makes a maximum of about $1 \mu_B/\text{U}$ around 0.5 GPa and decreases with increasing pressure. Extrapolating the pressure dependence of the ordered moment μ_{ord} linearly, it will vanish at about 7 GPa. This behavior is consistent with the previous results, in which the anomaly at the Néel temperature T_N in the resistivity disappear at about 7 GPa.⁶⁾ The magnetic moment is correlated with the Néel temperature.

In conclusion, we have measured the temperature dependence of the (0 0 0.5) antiferromagnetic Bragg peak intensity under several pressures of 0-1.6 GPa. The Néel temperature and the magnetic ordered moment slightly increase with increasing pressure, make a maximum around 0.5 GPa and decrease with increasing pressure. Extrapolating the pressure dependence of the ordered moment μ_{ord} linearly, it will vanish at about 7 GPa.

References

- 1) C. Geibel et al., Z. Phys. B 84 (1994) 1.
- 2) N. Sato et al., Phys. Rev. B 53 (1996) 14043.
- 3) R. Caspary et al., Phys. Rev. Lett. 71 (1993) 2146.
- 4) C. Wassilew et al., Physica B 199&200 (1994) 162.
- 5) P. Link et al., J. Phys. Condens. Matter 7 (1995) 373.
- 6) Y. Haga et al., J. Phys. Soc. Jpn. 65 (1996) 3646.
- 7) H. Matsui et al., Physica B 199&200 (1994) 140.
- 8) R. Modler et al., Int. J. Mod. Phys. B 7 (1993) 42.

with the size of about $5 \times 5 \times 1 \text{ mm}^3$ was used in the experiment. In order to reduce the huge absorption of neutrons due to ^{10}B , 98.5% enriched ^{11}B was used as a starting material of the sample. It was set with $[1, -1, 0]$ axis vertical inside the dilution refrigerator cryostat equipped with a superconducting magnet.

We observed magnetic Bragg peaks in phase III, for example $(1/2, 1/4, 1/4)$, which correspond to the magnetic structure described above for the pure material. Their intensities vanish with increasing temperature above about 1 K, indicating that phase IV is actually different from phase III. We have made careful scans along many directions including the principal axes $[100]$, $[110]$ and $[111]$ at 1.3 K to search magnetic response in phase IV. However, there is no indication of magnetic peak in these scans. Thus, it is concluded that phase IV is not a simple one, even if it is magnetic as speculated before. Instead, we found that the intensities of all nuclear Bragg peaks observed so far exhibit unusual increase by 5-10 % just in phase IV. Fig. 2 shows the temperature dependence of the intensity of (100) nuclear Bragg peak as well as that of $(1/2, 1/4, 1/4)$ magnetic Bragg peak. The increased intensities in phase IV return to the level of those in phases I and III by applying a magnetic field of about 0.8 T, which is just the value of the upper boundary of phase IV in the magnetic phase diagram as shown in Fig. 1. This phenomenon is very interesting because a big change of Bragg peak intensities occurs in a very narrow region in the H - T plane without any sign of structure change. One possible explanation is that the extinction effect of the material becomes weak in phase IV. This means that the material may undergo a tiny structural

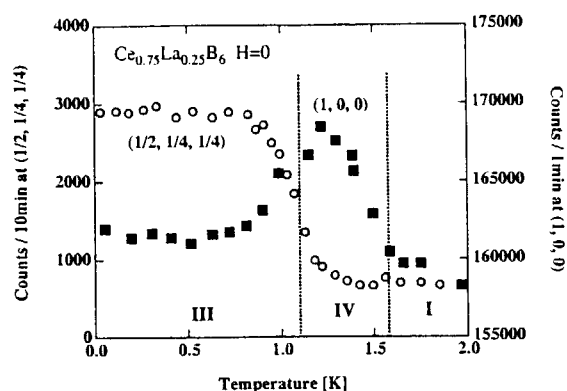


Fig. 2. Temperature dependencies of Bragg peak intensities of $\text{Ce}_{0.75}\text{La}_{0.25}\text{B}_6$.

change in phase IV which is too small to be visible in the present resolution but results in a multi-domain structure giving smaller mosaicity.

Although real origin of above phenomenon is not so clear at this moment, the result of the present experiment strongly suggests that a structural anomaly is important in phase IV of $\text{Ce}_{0.75}\text{La}_{0.25}\text{B}_6$. In order to make the situation clear, more detailed study is necessary.

Reference

- 1) J.M. Effantin et al., J. Magn. Magn. Mater. 47&48(1985)145.
- 2) O. Sakai et al., J. Phys. Soc. Jpn. 66 (1997) 3005.
- 3) M. Hiroi et al., J. Phys. Soc. Jpn. 66 (1997) 1762.
- 4) T. Tayama et al., J. Phys. Soc. Jpn. 66 (1997) 2268.
- 5) O. Suzuki et al., J. Phys. Soc. Jpn. 67 (1998) 4243.

研究テーマ：DyB₆の磁場中磁気構造の研究

表題：10 Tマグネットを用いた磁場中でのDy¹¹B₆の中性子回折

1-2-45

Neutron diffraction study in Dy¹¹B₆ under magnetic fields with 10 T magnet

K. Takahashi, H. Nojiri, Y. Matsuoka¹, N. Metoki¹, S. Kunii² and M. Motokawa

Institute for Materials Research, Tohoku University, Sendai 980-8577, Japan

¹Advanced Science Research Center, JAERI, Tokai 319-1195, Japan

²Department of Physics, Tohoku University, Sendai 980-8578, Japan

DyB₆ is an antiferromagnetic compound with the cubic CaB₆-type structure. The magnetization of a single crystal at 4.2 K shows multistep transitions, and the easy axis of the magnetization is the [111] axis¹⁾. The temperature dependence of the magnetic susceptibility shows two anomalies, one at 26 K and the other at 32 K. Pronounced peaks are also observed at the same temperatures in the specific heat²⁾. The anomaly at higher temperature is due to the structural phase transition in which the structure changes from cubic to rhombohedral symmetry. The other anomaly at 26 K is due to the antiferromagnetic transition and the magnetic structure in the zero field has been found to be complicated by our neutron powder diffraction experiment³⁾.

To investigate magnetic structures in magnetic fields, we have carried out neutron diffraction experiments in high magnetic fields. The experiments were performed on the TAS-2 diffractometer at JAERI by using a 10 T magnet. A single crystal of Dy¹¹B₆ has been made by a crucible-free vertical floating zone method and it is enriched up to 99.5% in ¹¹B in order to decrease neutron absorption by ¹⁰B.

We measured intensities of [11-2] and [1-10] directions as a function of magnetic field at 5 K. The magnetic field, *B* up to 10 T was applied along the [111] axis, since the sample has been divided when it puts on the magnetic field in the direction except for the easy axis. Figure 1 shows the intensities at *B* = 0, 2, 3.1, 4.5, 7, 9, 10 T which were selected to examine each magnetic state of the magnetization. The magnetic structures in each condition below 9 T is under consideration at the present stage including the structure in the zero field.

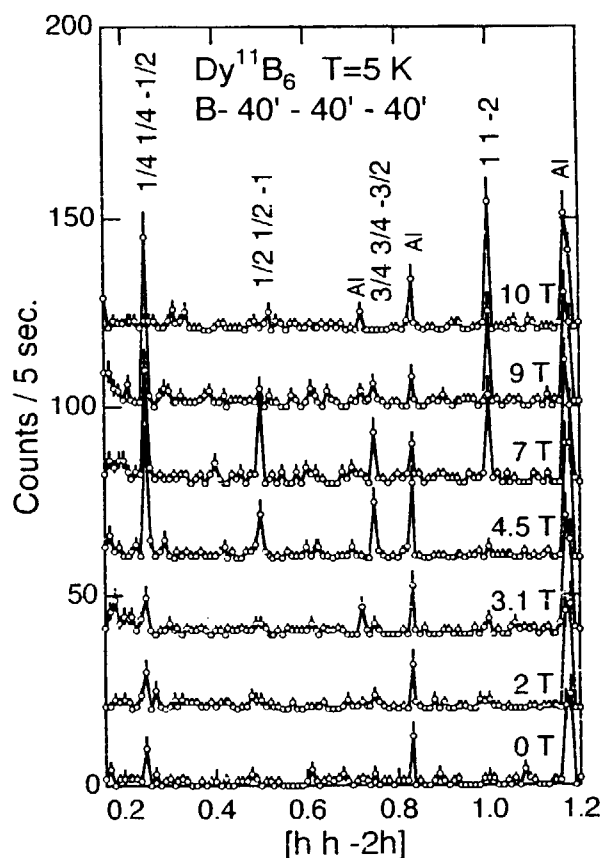


Fig. 1. Bragg peak intensities along [hh-2h] direction in magnetic fields up to 10 T.

References

- 1) S. Kunii, K. Iwashita, T. Matsumura and K. Segawa: *Physica B* **186-188** (1993) 646-648.
- 2) K. Segawa, A. Tomita, K. Iwashita, M. Kasaya, T. Suzuki and S. Kunii: *J. Magn. Magn. Mater.* **104-107** (1992) 1233-1234.
- 3) K. Takahashi, H. Nojiri, K. Ohoyama, M. Ohashi, Y. Yamaguchi, S. Kunii and M. Motokawa: *Physica B* **241-243** (1998) 696-698.

研究テーマ：Ce化合物強相関伝導系における特異な磁気相

表題：混合原子価をもつ Yb_3S_4 の磁気構造研究

1-2-46 Magnetic structure study of mixed valence Yb_3S_4

J.-G. Park, Y.S. Kwon¹, Y. Morii² and M. Kohgi³

Department of Physics, Inha University, Inchon 402-751 Korea

¹ Department of Physics, Sung Kyun Kwan University, Suwon 440-746 Korea

² Advanced Science Research Center, JAERI, Tokai Ibaraki 319-1195 Japan

³ Department of Physics, Tokyo Metropolitan University, Hachioji, Tokyo 192-0364 Japan

Yb_3S_4 forms in the orthorhombic structure with $a=12.90\text{\AA}$, $b=13.00\text{\AA}$ and $c=3.9\text{\AA}$. Although it behaves like a semiconductor with a small gap of 0.4 eV in resistivity data, the electronic specific heat coefficient is as large as $400\text{ mJ/mol}\cdot\text{K}^2$ thus making it a low carrier strongly correlated electron system [1]. According to the heat capacity measurement, it shows a sharp peak at 1.07 K suggesting a transition. It was later corroborated by Mossbauer study of which hyperfine field remains constant up to 0.8 K before disappearing above 1.2 K [2]. According to the Mossbauer study, Yb^{3+} ion is expected to have $1\mu_B$ of spontaneous moment.

In this study, we aimed to determine the magnetic structure that was suggested to exist below 1 K from the heat capacity and Mossbauer results. Since we needed a very low temperature set-up for our study, we decided to take advantage of the newly purchased dilution refrigerator available at TAS-2. Although TAS-2 is good for single crystal works, we originally thought that it is all right for our purpose too since the estimated magnetic moment of Yb_3S_4 is rather large as $1\mu_B$. We have calibrated the

wavelength using standard Si powder sample. Throughout our experiments, we used the wavelength of 2.3702 Å. Since our experiment was cut short because of the problems with the cold source, we succeeded only to measure two full scans at 40 mK and 4 K.

Our main results are shown in figure below. Figure shows difference between data taken at 40 mK and 4 K. As one can see, there is no conceivable change from 4 K to 40 mK in the diffraction data contradicting the previous heat capacity and Mossbauer results. In order to study further magnetic property, we have measured magnetization down to 0.2 K using a homemade extraction magnetometer to find that there is no clear sign of magnetic transition either [3]. (Not shown here)

Therefore we have two different sets of data contradicting to each other. While the heat capacity and Mossbauer measurements show signs of a transition around 1 K, the neutron and magnetization data do not display a magnetic transition at the temperature range of interest at all.

In order to solve the apparent discrepancy, further experiments are necessary. Especially,

原子炉：JRR-3M

装置：TAS-2 (T2-4)

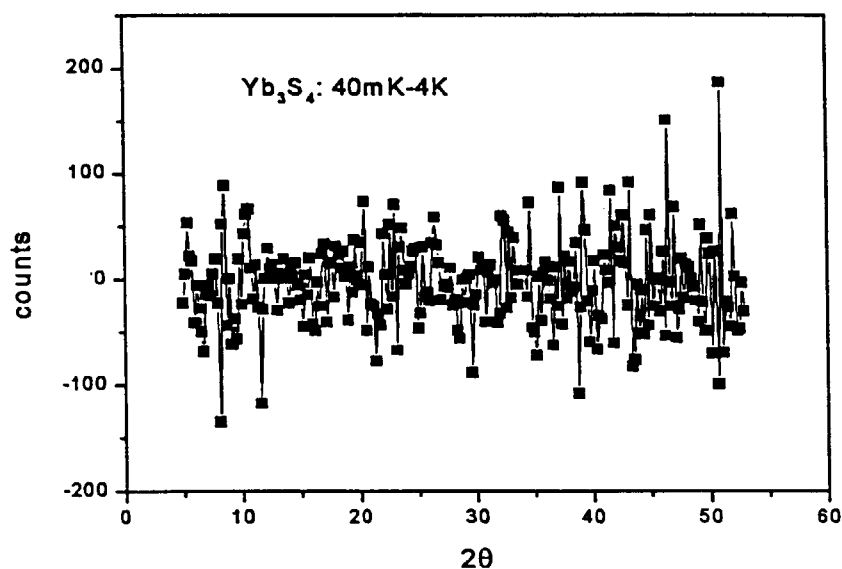
分野：中性子散乱(磁性)

structure study below 1 K using neutron diffraction will be very helpful since there is the possibility that a slight structure change might explain the discrepancy.

[1] Myung-Wha Jung et al., J. Kor. Phys. Soc. **32** (1998) 71.

[2] M.Ram et al., Physica B **259-261** (1999) 271.

[3] C. Paulsen and J.-G. Park (unpublished, 1998) .



原子炉：JRR-3M

装置：TAS-2 (T2-4)

分野：中性子散乱(磁性)

研究課題: $\text{La}_{2-x}\text{Sr}_x\text{CuO}_4$ の格子異常と磁気相関
 標題: $\text{La}_{1.88}\text{Sr}_{0.12}\text{CuO}_4$ の非整合磁気弾性散乱

1-2-47

Neutron Scattering Study of Incommensurate Elastic Magnetic Peaks In $\text{La}_{1.88}\text{Sr}_{0.12}\text{CuO}_4$ [1]

H. Kimura,¹ H. Matsushita,¹ K. Hirota,¹ Y. Endoh,¹ K. Yamada,^{1,4} G. Shirane,² Y. S. Lee,³
 M. A. Kastner,³ and R. J. Birgeneau³

¹Department of Physics, Tohoku University

²Department of Physics, Brookhaven National Laboratory

³Department of Physics, Massachusetts Institute of Technology

⁴Institute for Chemical Research, Kyoto University

Recently, Suzuki *et al.*[2] obtained evidence for incommensurate (IC) magnetic order at low temperature in superconducting $\text{La}_{1.88}\text{Sr}_{0.12}\text{CuO}_4$. We have carried out comprehensive elastic neutron scattering studies of $\text{La}_{1.88}\text{Sr}_{0.12}\text{CuO}_4$ by the HER triple-axis-spectrometer using cold neutron beam to achieve high q and energy resolution. The IC peak was clearly observed at four position of $(\frac{1}{2}-\epsilon, \frac{1}{2}, 0)$, $(\frac{1}{2}, \frac{1}{2}-\epsilon, 0)$. The incommensurability ϵ is essentially identical to that of dynamical spin fluctuations in $\text{La}_{1.88}\text{Sr}_{0.12}\text{CuO}_4$. The line width is very close to resolution limit and the minute analyses convoluted with the instrumental resolution give the intrinsic line width κ in momentum space, which is estimated to be less than 0.005\AA^{-1} . Then the correlation length ξ which corresponds to the inverse of κ can be determined to be more than 200\AA . Furthermore we carried out the scans along several q -direction about one IC peak in order to study static correlations in CuO_2 plane. Then we found that the line width in any direction reaches almost resolution limit. Therefore the static antiferromagnetic correlation extend at quite long-range and is almost isotropic in CuO_2 plane. More surprisingly, as shown in Fig. 1, the T^* coincides with the onset of T_c to within the systematic errors. In addition, we found that weak elastic peaks were observed for $x = 0.10$ with lower T^* than that of $x = 0.12$ while for $x = 0.15$ any elastic scattering is below the detectable limit.

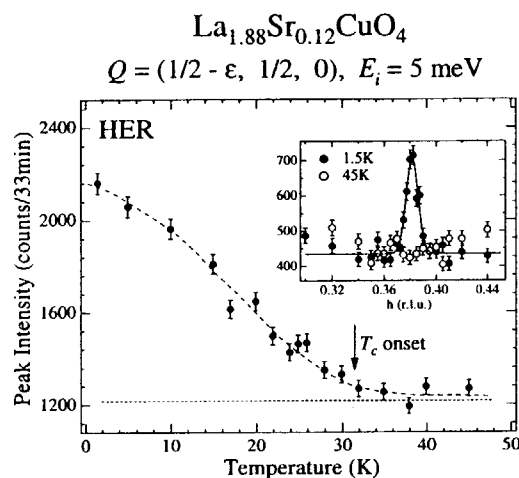


Figure 1: Temperature dependence of the peak intensity at $Q = (\frac{1}{2}-\epsilon, \frac{1}{2}, 0)$ for $\text{La}_{1.88}\text{Sr}_{0.12}\text{CuO}_4$. Short dashed lines in each figure indicate estimated backgrounds. Long dashed lines are guides to the eye. The inset is a scan through the peak position Q below and above T^* .

References

- [1] H. Kimura *et al.*, J. Phys. Chem. Solids, in press.
- [2] T. Suzuki *et al.*, Phys. Rev. B57, R3229 (1998).

研究課題: $\text{La}_{2-x}\text{Sr}_x\text{CuO}_4$ のスピン揺動と超伝導の相関
 標題: $\text{La}_{2-x}\text{Sr}_x\text{CuO}_4$ の低ドーピング領域における磁気弾性散乱

1-2-48

Systematic Neutron Scattering Study of Elastic Magnetic Signals in Lightly Doped $\text{La}_{2-x}\text{Sr}_x\text{CuO}_4$ ($0.03 \leq x \leq 0.06$)[1]

S. Wakimoto,¹ K. Yamada,^{1,5} S. Ueki,¹ G. Shirane,² Y. S. Lee,³ S. H. Lee,⁴ M. A. Kastner,³
 K. Hirota,¹ P. M. Gehring,⁴ Y. Endoh,¹ and R. J. Birgeneau³

¹Department of Physics, Tohoku University

²Department of Physics, Brookhaven National Laboratory

³Department of Physics, Massachusetts Institute of Technology

⁴National Institute of Standards and Technology

⁵Institute for Chemical Research, Kyoto University

In $\text{La}_{2-x}\text{Sr}_x\text{CuO}_4$, Wakimoto *et al.*[2] have established fundamental change of the elastic peaks at the metal-insulator boundary around $x \sim 0.055$; the q -width of the elastic commensurate peak becomes broader with increasing of x in the insulating region and rapidly sharpens in the superconducting region. They also observed new incommensurate elastic peaks for $x = 0.05$, which positions are 45° rotated from those of superconducting samples.

We have carried out further investigations particularly on the elastic incommensurate peaks for $x = 0.06$. Single crystal of $x=0.06$, which size is 6 mm in diameter and 25 mm in length, was grown by an improved travelling-solvent floating-zone method. Neutron-scattering experiments were performed on the HER cold neutron triple-axis spectrometer. We found that the integrated intensity drastically changes across the metal-insulator boundary; the intensity of $x = 0.06$ is 4 times smaller than that of $x = 0.05$ while the intensity in the insulating region stays constant.

References

- [1] S. Wakimoto *et al.*, J. Phys. Chem. Solids, in press.
- [2] S. Wakimoto *et al.*, to be published in Phys. Rev. B.

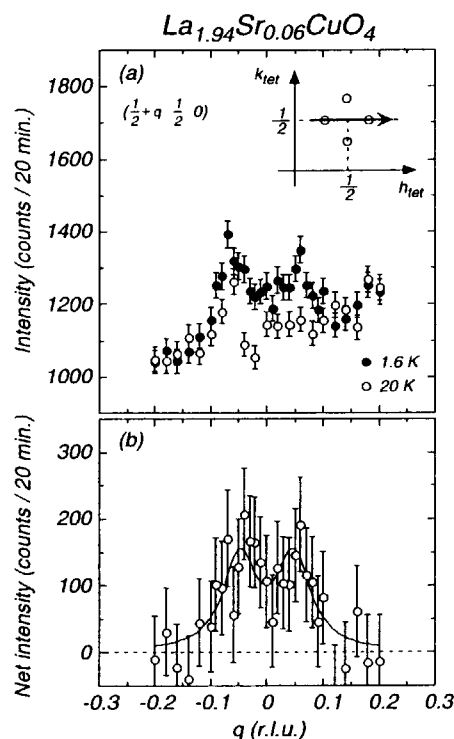


Figure 1: (a) Peak profiles along the scan trajectory shown in the inset figure. Closed circles are data at 1.6 K and open circles are data at 40 K. (b) Net intensity calculated by subtracting the 40 K data from the 1.6 K data. Solid line is fitting result using a double Lorentzian function.

研究テーマ: LiV_2O_5 におけるスピン揺らぎの研究

表題: LiV_2O_5 の高分解能中性子非弾性散乱実験

1-2-49 High Resolution Inelastic Neutron Scattering on LiV_2O_5

Y. Takeo¹, T. Yosihama¹, K. Kakurai^{1,3}, M. Isobe² and Y. Ueda²

¹Neutron Scattering Lab., ISSP, University of Tokyo, Shirakata, Tokai, Japan

²Materials Design and Characterization Lab., ISSP, University of Tokyo, Roppongi, Tokyo, Japan

³CREST, Japan Science and Technology Corporation, Tsukuba, Japan

High resolution inelastic neutron scattering experiment on LiV_2O_5 was performed on the cold neutron triple-axis instrument HER (C1-1) in the guide hall of the JRR3-M. Fixed E_i -mode with $E_i = 4.5 \text{ meV}$ ($k_i = 1.542 \text{ \AA}^{-1}$) and horizontal collimations of open-80'-80' before and after the sample, and after the analyzer, respectively, were chosen. Cooled Be-filter was inserted before the sample to suppress the higher order contaminations.

Figure 1 shows low- T energy scan at a constant $Q = (0, 0.5, -1)$, which belongs to the one dimensional antiferromagnetic zone center plane. In the same Fig. the energy scan at $Q = (0, 0.6, -1)$, slightly away from the zone center, is also shown, which can be regarded as the background of the former scan. At the zone center, low energy excitations down to 0.4 meV can be clearly observed. The strong increase of the background due to the incoherent scattering of Vanadium hinders the access to lower energy transfer regime. We checked the magnetic origin of the inelastic signal by increasing the sample temperature up to 25 K , where the scattering almost disappeared down to the background level.

Figure 2 depicts Q -scans at several constant energy transfers around the antiferromagnetic zone center. Rather sharp peak at $k = 0.5$ can be seen in all the scans. This results indicate a steep spin wave dispersion around the one dimensional antiferromagnetic zone. The solid line indicate resolution convoluted fit results assuming the one dimensional gapless antiferromagnetic spin wave dispersion and the results are consistent with the dispersion relation derived from the higher energy transfer results obtained earlier on the thermal neutron triple axis spectrometer [1].

These results, combined together with the earlier thermal neutron inelastic scattering results clearly show that LiV_2O_5 can be regarded as a $S=1/2$ antiferromagnetic chain system with $J/k_B = (307 \pm 19) \text{ K}$. The interchain exchanges in the double linear chain consisting out of charge ordered V^{4+} ions can be regarded to be much smaller than the above intrachain exchange.

Reference:

[1] Y. Takeo et al., J. Phys. Chem. Solids in press.

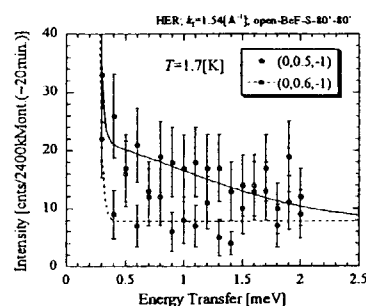


Fig.1: Constant- Q energy scan at $Q=(0,0.5,-1)$ (filled points) and $Q=(0,0.6,-1)$ (open points) at $T=1.7 \text{ K}$.

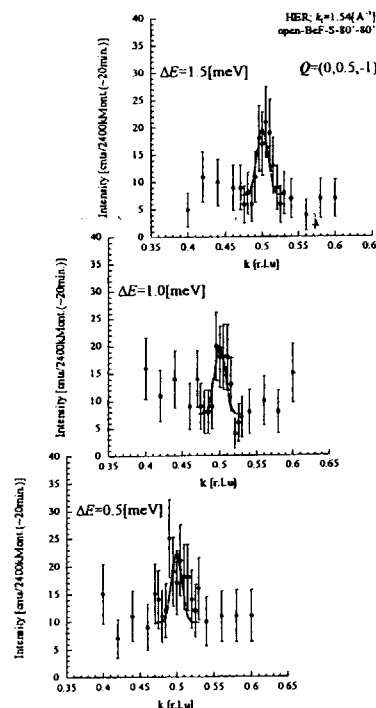


Fig.2: Constant- E momentum scan around $Q=(0,0.5,-1)$ at $T=1.7 \text{ K}$. Solid lines indicate the resolution convoluted fit results (see text).

研究テーマ：反強磁性-非磁性境界付近の重い電子系化合物における反強磁性相関
表題：重い電子系CeRu₂Si₂の磁気相関

1-2-50 Magnetic Fluctuation of the Heavy Fermion CeRu₂Si₂

H. Kadowaki, M. Sato,¹ S. Kawarazaki¹ and Y. Miyako¹

Department of Physics, Tokyo Metropolitan University, Hachioji-shi, Tokyo 192-0397

¹*Department of Earth and Space Science, Osaka University, Toyonaka, Osaka 560-0043*

The magnetic fluctuation of the heavy Fermion CeRu₂Si₂ shows complicated Q-dependence, where intensity maxima appear at $k_1=0.3a^*$, $k_2=0.3(a^*+b^*)$ and $k_3=0.35c^*$, and there is a nearly-constant-intensity ridge between k_1 and k_2 . This Q-dependence of the magnetic excitation has been measured only in the symmetry planes of (h,k,0), (h,h,l) and (h,0,l) [1,2]. One natural question coming out from these observations are whether any other features exist in the other Q-vectors. The present experiment was performed to answer this question by surveying the entire reciprocal space. Since the crystal structure of CeRu₂Si₂ belongs to the ThCr₂Si₂-type, in which magnetic atoms form a body-center-tetragonal Bravais lattice, CeRu₂Si₂ has an advantage that the excitation spectrum should be periodic in the reciprocal space. Thus it is enough to measure the excitation spectrum within an independent part of the first Brillouin zone.

A number of constant E-scans with $E = 1$ meV were carried out on the cold-guide triple-axis spectrometer HER using the horizontally curved analyzer. The result is shown in figure 1 as a three-dimensional (3D) plotting. Although it is not easy to explain all features of the 3D plot by a single view, one can see that the structures related to k_1 , k_2 and k_3 are pronounced, and that there are other minor structure around Z and N points. By using various views, we conclude that no new remarkable intensity peak in Q-space exists.

The magnetic excitation spectrum may be interpreted either as antiferromagnetic correlation from a viewpoint of localized moment, or as particle-hole excitation from a viewpoint of Fermi liquid. This kind discussion has been

made only qualitatively, and few quantitative attempts of analyses have been made. On the basis of the present data and those of reference 2, it is possible and interesting to quantify the discussions. As a preliminary analysis, we tried to analyze the Q-dependence of $\text{Im}(\chi(Q, E=1\text{ meV}))$ from the viewpoint of the localized moment. It is possible to reproduce the complicated Q-dependence of $\text{Im}(\chi(Q, E=1\text{ meV}))$ by using about 40 exchange, RKKY, constants. Further analyses are progressing.

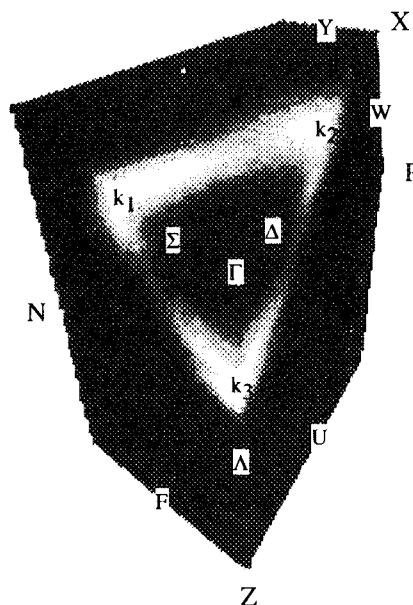


Fig. 1 Three dimensional plot of $\text{Im}(\chi(Q, E=1\text{ meV}))$ in an independent part of the first Brillouin zone. Brighter pixel represents stronger intensity.

References

- [1] L. P. Regnault et al.: Phys. Rev. B **38** (1988) 4481.
- [2] M. Sato et al.: proceedings of ISSP7 (1998)

研究テーマ：近藤格子上的磁気秩序の研究-CeRu₂Si₂とその混晶系を中心として
表題：重い電子系物質CeRu₂Si₂におけるスピン揺らぎ

1-2-51 Spin fluctuation in the heavy fermion compound CeRu₂Si₂

M.Sato M.Miyamura H.Kadowaki^A S.Kawarazaki Y.Miyako

Department of Earth and Space Science, Osaka University, Toyonaka, Osaka 560-0043

^ADepartment of Physics, Tokyo Metropolitan University, Hachioji, Tokyo 192-0397

We have performed inelastic neutron scattering experiments on a paramagnetic heavy fermion compound CeRu₂Si₂. In this compound spin fluctuations which are strongly dependent on the wave number (k) develop below 60K due to the competition between Kondo fluctuation and RKKY interaction. According to previous studies, the amplitude of the fluctuation exhibits three peaks at $k=(0.3,0,0)$ (k_1), $(0.3,0.3,0)$ (k_2) [1] and $(0,0,0.35)$ (k_3) [2]. In these peaks, k_1 and k_3 are the precursors of the static magnetic long range orders caused by substitution of La for Ce[3] or Rh for Ru[4]. We have investigated the k -dependence of the energy spectra of the spin fluctuations in detail over the Brillouin zone. The experiments were performed at HER by using a horizontally focusing analyzer.

All of the energy spectra which we have observed show Lorentzian line shapes as follows.

$$\text{Intensity}(k, \omega) = A \cdot \frac{1}{1 - \exp(-\beta \hbar \omega)} \text{Im} \chi(k, \omega),$$

$$\text{Im} \chi(k, \omega) = \chi(k) \frac{\omega \Gamma(k)}{\omega^2 + \Gamma(k)^2},$$

where $\chi(k)$ is the static staggered susceptibility and $\Gamma(k)$ is the energy width of the energy spectrum equivalent to the relaxation rate of the spin fluctuation. In Fig.1 is shown the k -dependence of $\chi(k)$ and $\Gamma(k)$ from the Γ point to the Brillouin zone boundary along $[100]^*$ and $[001]^*$ at $T=1.5$ K. It can be seen that $\chi(k)$ forms peaks at k_1 and k_3 as mentioned above, where $\Gamma(k)$ exhibits minima. This behavior indicates that the spin fluctuations of k_1 and k_3 are nearly stabilized. Around these points, $\Gamma(k)$ is almost inverse proportion to $\chi(k)$. We should notice the characteristic behavior around the Γ point. Though $\chi(k)$ exhibits no k -dependence with weak intensity around the Γ point, $\Gamma(k)$ decreases as k approaches 0 and exhibits a minimum at the Γ

point ($k=0$). The value of $\Gamma(k=0)$ is smaller than those at k_1 and k_3 . This suggests that the life time of the weak ferromagnetic fluctuation is longer than those of k_1 and k_3 .

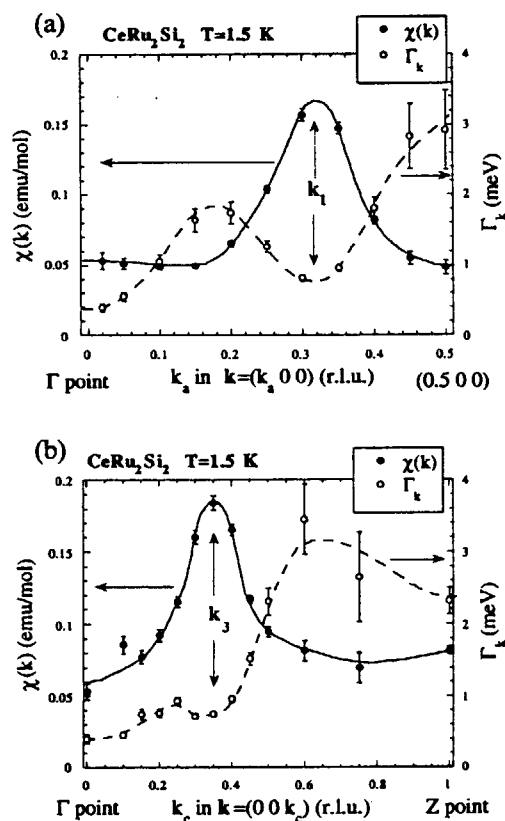


Fig.1 The k -dependence of $\chi(k)$ and $\Gamma(k)$ along $[100]^*$ (a) and $[001]^*$ (b).

Reference

- [1] L. P. Regnault et al. Phys. Rev. B 38(1988) 4481
- [2] M.Sato et al. J. Phys. Chem. Solids accepted
- [3] S.Quezal et al. J. Magn. Magn. Matter. 76&77 (1988) 4-03
- [4] S. Kawarazaki et al. Physica B 206&207 (1995) 298

JRR-3M, HER, 2.Magnetism

研究テーマ 強磁性ヘビーフェルミオンCeCu₂Al_{4-x}の中性子散乱
表題 CeCuAl₃の磁気秩序

1-2-52 Magnetic Ordering of CeCuAl₃

Y. OOHARA, G. MOTOYAMA[†], T. NISHIOKA[†] and M. KONTANI[†]

Neutron Scattering Laboratory, I. S. S. P., University of Tokyo, Tokai, 319-1106

[†]Department of Physics, Nagoya University, Nagoya, 464-08

CeCuAl₃ is a heavy fermion compound of BaNiSn₃ structure.¹⁾ The magnetic ions, Ce³⁺, form the body-centered tetragonal lattice. Many experimental studies suggest that CeCuAl₃ exhibits antiferromagnetic ordering in the low temperature.^{2,3)} To explore the magnetic ordering of CeCuAl₃, we have performed neutron diffraction measurements on the single crystal of CeCuAl₃.

Neutron diffraction measurements were carried out on the ISSP triple-axis spectrometer HER installed at C11 experimental port in JRR-3M in JAERI (Tokai). We used the neutron with $k_i = 1.55 \text{ \AA}^{-1}$ with the collimation open-80'-80' in the triple-axis mode. A monochromatic beam was obtained by the (0 0 2) reflection from pyrolytic graphite. To remove higher order neutrons, we used a Be filter. The sample was cooled with ⁴He cryostat down to 1.5 K.

Figure 1 shows the scan along the ($h h 0$) line. The magnetic peak appears at (0.5 0.5 0). The line width of the magnetic peak is broad along the ($h h 0$). It demonstrates that the magnetic ordering is the short-range order. The line width is also broad along the (0.5 0.5 l) direction. The magnetic intensity is very weak. It indicates that the ordered magnetic moment is small. Figure 2 shows the temperature dependence of the peak intensity at (0.5 0.5 0). With decreasing temperature, the peak intensity increases drastically below $T_N = 4 \text{ K}$.

From the magnetic peak position, one finds that the magnetic ordering in the c -plane is the antiferromagnetic one. It brings about spin frustrations in the body centered-structure. Such frustrations and the Kondo effect suppress the long-range magnetic ordering and reduce the ordered moment.

References

- 1) O. Moze and K.H.J. Buschow: *J. Alloys Comp.* **245** (1996) 112.
- 2) M. Kontani, H. Ido, H. Ando, T. Nishioka and Y. Yamaguchi: *J. Phys. Soc. Jpn.* **63** (1994) 1652.
- 3) G. Motoyama, K. Murase and M. Kontani: *Physics of Strongly Correlated Electron Systems, JJAP Series 11*, p257.

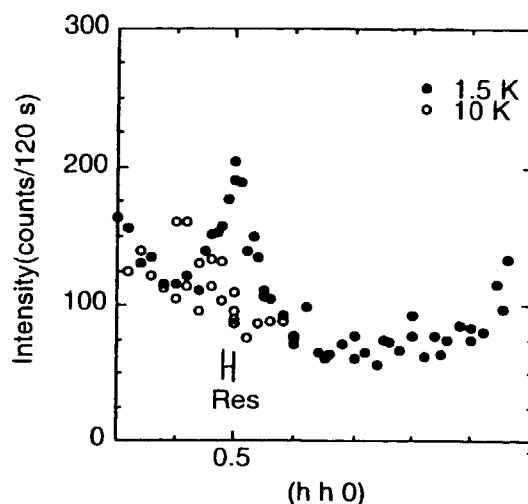


Fig. 1 The scan along ($h h 0$) line.

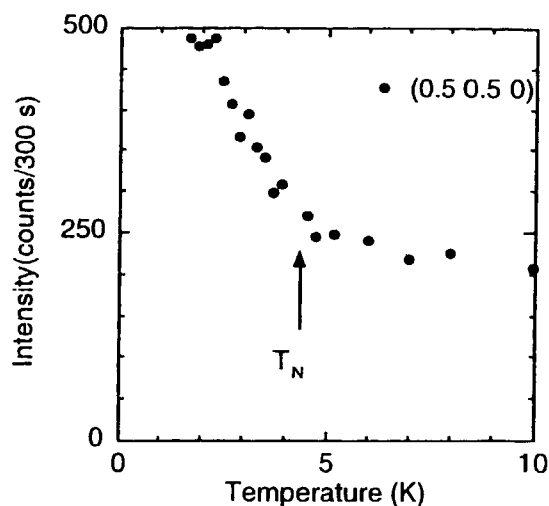


Fig. 2 Temperature dependence of the peak intensity at (0.5 0.5 0).

研究テーマ：中性子散乱による $\text{Li}_2\text{Ge}_7\text{O}_{15}$ の強誘電相転移に関するソフトフォノンの研究

課題：中性子散乱による $\text{Li}_2\text{Ge}_7\text{O}_{15}$ の強誘電相転移の研究

1-2-53 NEUTRON INELASTIC SCATTERING STUDY OF FERROELECTRIC PHASE TRANSITION IN $\text{Li}_2\text{Ge}_7\text{O}_{15}$

Mitsuo Wada Takeda, Yukio Noda¹, Toshihisa Yamaguchi² and Yutaka Iwata³

Shinshu University, ¹Tohoku University, ²Meisei University, ³Kyoto University,

$\text{Li}_2\text{Ge}_7\text{O}_{15}$ undergoes a ferroelectric phase transition at $T_c=283.5\text{K}$. The softening of the optical phonon has been observed by Raman scattering and IR measurements.¹⁻²⁾ On the other hand the dielectric critical slowing-down has been observed by the dielectric dispersion measurements.³⁾ To investigate the mechanism of the phase transition the details of temperature dependence of the dispersion curves of low-lying phonons were measured by the inelastic neutron scattering with 4G and C1-1 spectrometer in JRR-3M at Tokai. Reflections (300) and (500) show most strong temperature dependence. A peak around 1.5meV at 340K which corresponding to the zone center phonon decreases as the temperature decreases, it becomes 0.5meV at 297K, and then the inelastic component disappears into the central component at 288K just above T_c (Fig.1). The temperature dependence of the phonon frequency shows good accordance with that of the B_{1u} soft mode observed by Raman and IR measurements.¹⁻²⁾ The dispersion curves of the lowest-lying phonon along a^* and c^* directions are observed. It is confirmed that the ferroelectric phase transition of $\text{Li}_2\text{Ge}_7\text{O}_{15}$ should be associated with the soft optical phonon at Brillouin zone center. Elastic diffuse scattering is observed below 0.1meV as shown in Figure 2. This implies that there exist a critical phenomenon with the energy lower than 0.1meV.

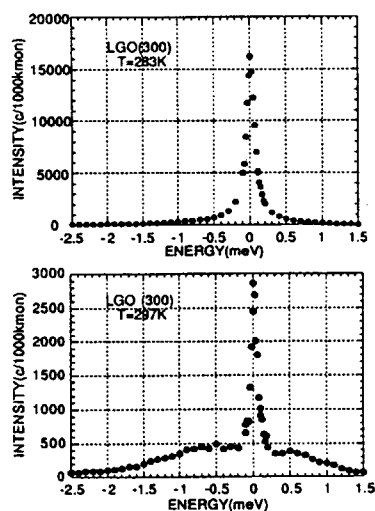


Fig. 1. Temperature dependence of the inelastic peaks around (300) reflection.

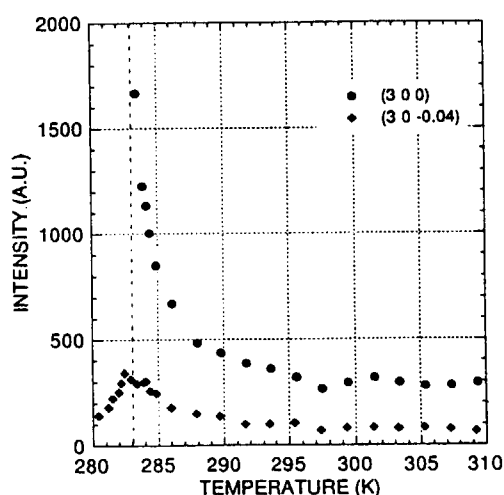


Fig. 1. Temperature dependence of (3 0 0) and (3 0 -0.04)

- 1) M. Wada and Y. Ishibashi; J. Phys. Soc. Jpn., 52 (1983) 193.
- 2) A.A. Volkov, et. al.; J. Phys. Soc. Jpn., 54 (1985) 818.
- 3) M. Horioka, A. Sawada and M. Wada; J. Phys. Soc. Jpn., 58 (1989) 3793.

研究テーマ：CeScSi の粉末中性子回折

表題：CeScSi の粉末中性子回折

1-2-54 Neutron Powder Diffraction Study of CeScSi

M.Yokoyama, M.Kosaka, Y.Uwatoko, M.Ohashi¹, K.Ohoyama², and Y.Yamaguchi²*Department of Physics, Saitama University, 255 Shimo-Okubo, Urawa, 338-8570**Factory of Engineering, Yamagata University, 4-3-16 Jonan, Yonezawa, 992**The Institute for Materials Research, Tohoku University, 2-1-1 Katahira, Sendai, 980-8577*

CeScSi has been reported previously to crystallize the tetragonal La_2Sb -type structure (space group $I4/mmm$) which La atoms occupy the La I site (4c site) and LaII site (4e site). CeScSi shows antiferromagnetic behavior below 28 K [1]. It is thought that Ce atoms occupy the LaII site in CeScSi. The purpose of present study is to clarify the magnetic structure and the atomic positions of Ce. We prepared CeScSi polycrystalline samples by a conventional argon arc technique. A powdered sample was obtained from ingot annealed at 1300°C for a week. The neutron diffraction experiments were carried out using the neutron powder diffractometer (T1-3 HERMES) installed at

JRR-3.

Figure 1 shows the powder neutron diffraction pattern of CeScSi at 2.5 K. We could not observe any peaks except nuclear reflections, though it was reported that CeScSi shows antiferromagnetic behavior. The our result of magnetization measurements using single-crystalline samples seem to indicate canted ferromagnetic behavior with spontaneous magnetization below $T_C = 44$ K. The obtained diffraction pattern was analyzed by Rietveld method using RIETAN-94 [2]. It became clear that Ce atoms occupy the LaII site. The analysis of magnetic structure is now in progress.

[1] P. C. Canfield et al. J. Appl. Phys. 70 (1991) 5992

[2] F. Izumi, "The Rietveld Method," ed. by R. A. Young, Oxford University Press, Oxford (1993), Chap.13

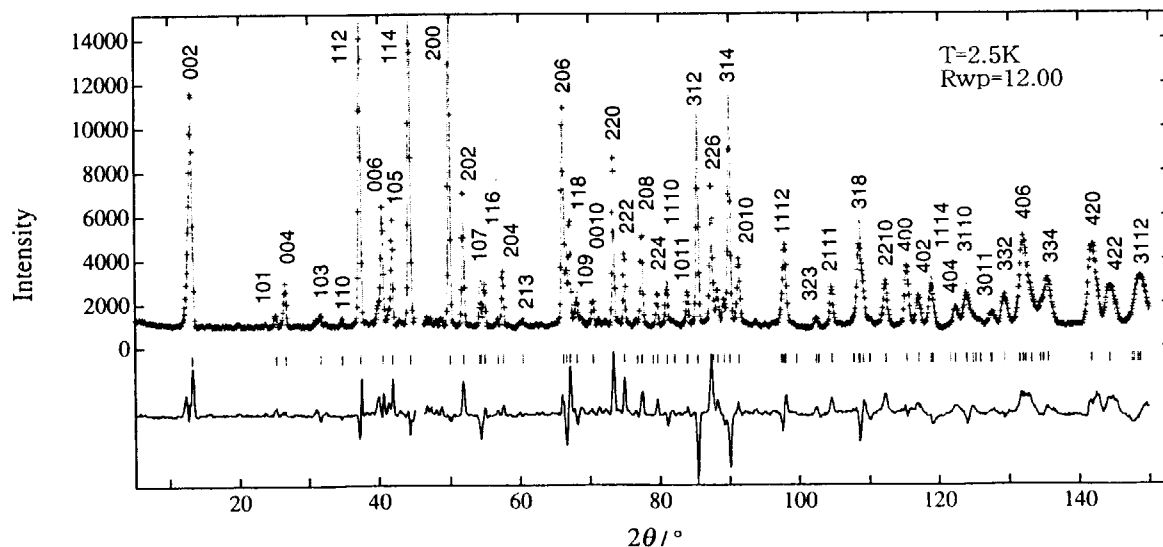


Fig.1 Neutron powder diffraction pattern of CeScSi at 2.5K.

研究テーマ：強相関電子系の中性子散乱の研究

表題：巨大磁気抵抗効果を示す $(\text{La}_{1-x}\text{Tb}_x)_{2/3}\text{Ca}_{1/3}\text{MnO}_3$ の小角散乱

1-2-55 Small-Angle Neutron Scattering Study on CMR effect of $(\text{La}_{1-x}\text{Tb}_x)_{2/3}\text{Ca}_{1/3}\text{MnO}_3$

M. Watahiki^{1,2}, N. Metoki¹, J. Suzuki¹, J. Nie³, Y. Yamada^{1,4} and M. Tachiki^{1,5}

¹Advanced Science Research Center, JAERI, Tokai-mura, Ibaraki 319-1195, Japan

²Japan Science and Technology Corporation, Kawaguchi, Saitama 332-0012, Japan

³Electrotechnical Laboratory, Tsukuba, Ibaraki 305-8568, Japan

⁴Waseda University, Shinjuku-ku, Tokyo 169-8555, Japan

⁵National Research Institute for Metals, Tsukuba, Ibaraki 305-0047, Japan

Much interest is devoted to the manganese perovskites based on the compound RMnO_3 (R : rare earth) since the discovery of colossal magnetoresistance (CMR)¹⁾. Though the pure compound RMnO_3 is a Mott-Hubbard insulator due to the strong correlation of the e_g electrons, the holes introduced into Mn-O planes from the substituting divalent ions for rare earth ions move easily in order to gain kinetic energies. Hwang *et al.* found the CMR in the system of $(\text{La}_{1-x}\text{A}_x)_{0.7}\text{Ca}_{0.3}\text{MnO}_3$ (A : Y, Pr) in which the average ionic radius of the La site $\langle r_A \rangle$ is systematically varied by substituting rare earth ions for La site²⁾. The decrease of $\langle r_A \rangle$ principally reduces electron hopping between Mn sites³⁾. In this paper, we have performed a small-angle neutron scattering (SANS) study in order to investigate a correlation between the CMR and the magnetic correlation in $(\text{La}_{1-x}\text{Tb}_x)_{2/3}\text{Ca}_{1/3}\text{MnO}_3$. The nominal hole concentration is fixed at 1/3, while $\langle r_A \rangle$ is varied by substituting the La ions for the Tb ions. The SANS experiments were carried out with a SANS-J instrument installed at the JRR-3M reactor of JAERI.

Figure 1 (a) and (b) show typical SANS data measured at various temperatures for $x=0.3$ and

0.1, respectively. The scattering crosssections are divided into two components with different q dependence. The scattering crosssections in q region below 0.3 nm^{-1} monotonously increase with decreasing temperature for both samples. The low q component arises from the magnetic scattering from domain structures with the ferromagnetic correlation. The crosssection of the low q component corresponds to a magnetic order parameter. The signal in a higher q region ($0.3 > q \text{ nm}^{-1}$) arises from the short range correlation, most probably due to the dynamical ferromagnetic fluctuation or the static disordering between Mn spins. This high q component shows different temperature dependence for both samples. In the case of $x=0.1$, the scattering crosssection increases with decreasing temperature from 300 K, and then reaches the maximum value near the Curie temperature ($T_C=180 \text{ K}$). Below 150 K this component is rapidly reduced and becomes a almost comparable to a back ground level, resulting from a ferromagnetic long range order. In the case of $x=0.3$, however, the high q component increases monotonously with decreasing temperature.

Figure 2 shows the temperature dependence of

原子炉：JRR-3M

装置：SANS-J(C3-2)

分野：中性子散乱 (磁性)

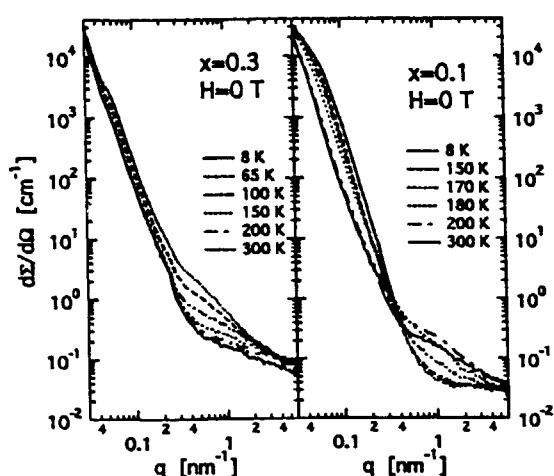


Fig. 1 The SANS crosssections at $H=0$ T for $(\text{La}_{1-x}\text{Tb}_x)_{2/3}\text{Ca}_{1/3}\text{MnO}_3$ with (a) $x=0.3$ and (b) $x=0.1$ respectively.

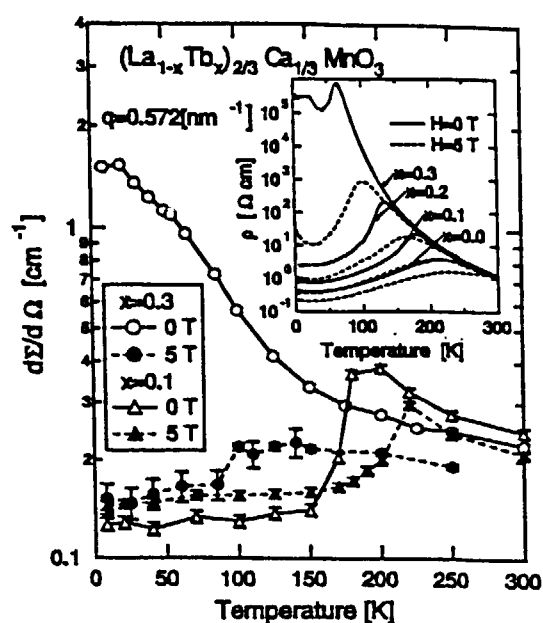


Fig. 2 The temperature dependence of SANS crosssections at $q=0.572 \text{ nm}^{-1}$ at $H=0$ T and 5 T. Inset: The $\rho(T)$ curves for $x=0.0, 0.1, 0.2$, and 0.3 at $H=0$ T and 5 T.

the SANS crosssections obtained at $q=0.572 \text{ nm}^{-1}$. In the case of $x=0.3$, application of an external magnetic field of 5 T suppressed the intensity in whole temperature range. The intensity becomes about one orders of magnitude smaller in the magnetic field below 50 K, where a very large CMR effect by four orders of magnitude is observed. In the case of $x=0.1$, both curves at $H=0$ T and 5 T exhibits cusp like behavior. The temperature of the cusp shifts slightly from 180 K at $H=0$ T to 220 K at $H=5$ T. The inset of Fig. 2 shows the temperature dependence of the resistivity $\rho(T)$ for $(\text{La}_{1-x}\text{Tb}_x)_{2/3}\text{Ca}_{1/3}\text{MnO}_3$ ($x=0.0$ to 0.3) at $H=0$ T and 5 T. It should be noted that the temperature dependence of the high q component is very similar to $\rho(T)$ for both samples. These results indicate that the short range ferromagnetic fluctuation is correlated with the CMR effect. The magnetic correlation length ξ

was estimated by fitting the magnetic scattering component to a Lorentzian-function ($d\Sigma(q)/d\Omega = d\Sigma(q=0)/d\Omega / (1 + (\xi q)^2)$). In the case of $x=0.1$, the ξ takes a maximum value at T_C , 1.44 nm at $H=0$ T and 3.40 nm at $H=5$ T. In the case of $x=0.3$, The value of ξ at $T=8$ K where the CMR appears conspicuously is 2.85 nm at $H=0$ T.

In summary, the $(\text{La}_{1-x}\text{Tb}_x)_{2/3}\text{Ca}_{1/3}\text{MnO}_3$ ($x=0.1, 0.3$) compounds have been studied by SANS measurements. Our data indicates that the short range ferromagnetic fluctuation plays an important role for the CMR effect.

References

- [1] Y. Tokura *et al.*, J. Phys. Soc. Jpn. **63** (1994) 3931-3935.
- [2] H.Y. Hwang *et al.*, Phys. Rev. Lett. **75** (1995) 914-918.
- [3] J.C. Nie *et al.*, **192** (1999) 379-385.

研究テーマ：中性子散乱によるウラン化合物の磁性研究

表題： $\text{U}_3\text{Pd}_{20}\text{Si}_6$ の結晶場励起の観測1-2-56 The Observation of a Crystalline Electric Field Excitation in $\text{U}_3\text{Pd}_{20}\text{Si}_6$ N. Tateiwa, N. Metoki¹, Y. Koike¹, N. Kimura², H. Aoki², and T. Komatsubara

Physics Department, Graduate School of Science, Tohoku University, Sendai 980-8578, Japan

¹Advanced Science Research Center, JAERI, Tokai, Ibaraki 319-1195, Japan²Center for Low Temperature Science, Tohoku University, Sendai 980-8578, Japan

Recently, we have found a new compound $\text{U}_3\text{Pd}_{20}\text{Si}_6$ and reported its magnetic property¹⁾. The crystal structure is an ordered derivative of the Cr_{23}C_6 -type cubic structure with space group $\text{Fm}\bar{3}\text{m}$. The temperature dependence of the susceptibility obeys the Curie-Weiss law above about 50 K with the effective moment $3.30 \mu_B/\text{U}$ and the magnetic entropy reaches $R\ln 3$ per uranium ion at the magnetic transition temperature 19 K. These results suggest that the $5f$ electrons in $\text{U}_3\text{Pd}_{20}\text{Si}_6$ have a localized character. The purpose of this study is to search for a Crystalline Electric Field (CEF) excitation in the inelastic scattering experiments and to confirm a localized character of the $5f$ electrons.

The polycrystal sample of $\text{U}_3\text{Pd}_{20}\text{Si}_6$ were grown by the arc melting method under an Ar gas atmosphere. Neutron scattering experiments were carried out using a triple-axis spectrometer TAS1. The samples were cooled down by the CTI-refrigerator. The incident beam is monochromatized by a vertically bent PG with a Be filter. The collimation was $40^\circ\text{'-}80^\circ\text{'-}40^\circ\text{'-}80^\circ\text{'}$.

Fig. 1 shows the inelastic neutron energy spectrum of $Q=2.2 \text{ \AA}^{-1}$ at 25.2 K and 300 K with the scattering energy fixed at 33.0 meV. The full width at half maximum (FWHM) was 3.20 meV at $dE=0 \text{ meV}$. At 25 K, two peak structures were observed around $dE=13 \text{ meV}$ and 23 meV, which is indicated by arrows. The former is attributed to the phonon excitation because the peak intensity develops with increasing temperature. But the peak intensity of the latter decreased at 300 K suggesting that this peak is a CEF excitation.

Fig. 2 shows the energy spectrum of $Q=2.2 \text{ \AA}^{-1}$ and 5.7 \AA^{-1} at 7 K. The peak intensity around 23 meV decrease with the moment transfer Q being changed from 2.2 \AA^{-1} to 5.7 \AA^{-1} . With these two experiments, it is concluded that the peak around 23 meV is the CEF excitation and the $5f$ electrons in $\text{U}_3\text{Pd}_{20}\text{Si}_6$ have a localized character, which is quite rare in uranium metallic compounds.

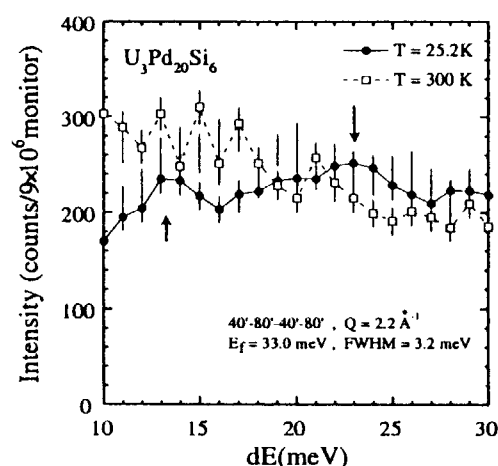


Fig. 1. Inelastic neutron scattering spectrum of $\text{U}_3\text{Pd}_{20}\text{Si}_6$ at 25.2 K and 300 K with the scattering energy fixed at 33.0 meV. Arrows indicate peak positions.

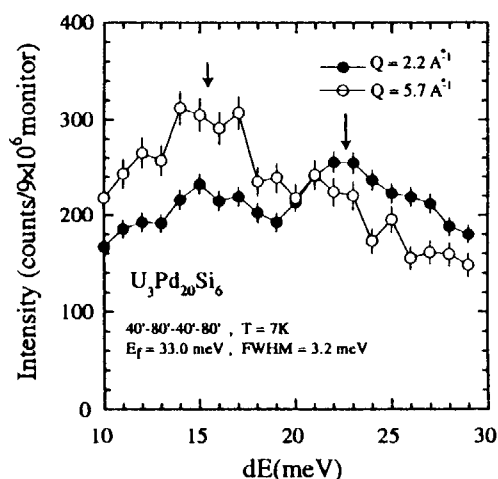


Fig. 2. Inelastic neutron scattering spectrum of $Q=2.2 \text{ \AA}^{-1}$ and 5.7 \AA^{-1} at 7 K. Arrows indicate peak positions.

Reference

- 1) N. Tateiwa, et al., to be published

1. 中性子散乱 3) 超伝導現象

1. Neutron Scattering 3) Superconductivity

This is a blank page.

研究テーマ：高温超伝導体の量子臨界点近傍の磁気励起

表題：YBa₂Cu₃O_{6+y}系高温超伝導体の量子臨界点近傍における中性子散乱研究

1-3-1

Neutron Scattering Study on YBa₂Cu₃O_{6+y} System near the Quantum Critical pointH. Harashina^{1,3}, M. Kanada¹, K. Kodama^{1,3,*}, M. Sato^{1,3}, and K. Kakurai^{2,3}¹ Department of Physics, Division of Material Science, Nagoya University, Furo-cho, Chikusa-ku, Nagoya 464-8602² Neutron Scattering Laboratory, ISSP, The University of Tokyo, Shirakata 106-1, Tokai 319-1195³ CREST, Japan Science and Technology Corporation (JST)

*Present address: Institute for Solid State Physics, The University of Tokyo, 7-22-1 Roppongi, Minato-ku, Tokyo 106

In YBa₂Cu₃O_{6+y} with $T_c \sim 60$ K, a gap-like structure seems to appear in the spectral function of the magnetic excitation $\chi''(q, \omega)$ with decreasing T at around the temperature T_0 , below which various physical properties behave anomalously. This pseudo gap formation has been studied by neutron measurements of the magnetic excitations^{1,2)} and B_{2u} phonons³⁾ in which the O(2) and O(3) atoms within a CuO₂ plane have out-of-phase motions perpendicular to the plane. We report results of further studies on the pseudo gap formation in YBa₂Cu₃O_{6+y} system near the boundary between the superconducting and the antiferromagnetic phases.⁴⁾ Neutron measurements were carried out with ISSP-PONTA spectrometer at JRR-3M at JAERI in Tokai.

Figure 1 shows the energy transfer (E)-dependence of χ'' taken for YBa₂Cu₃O_{6.45} ($T_c \sim 32$ K) at various temperatures. At ~ 250 K a gap-like structure can be

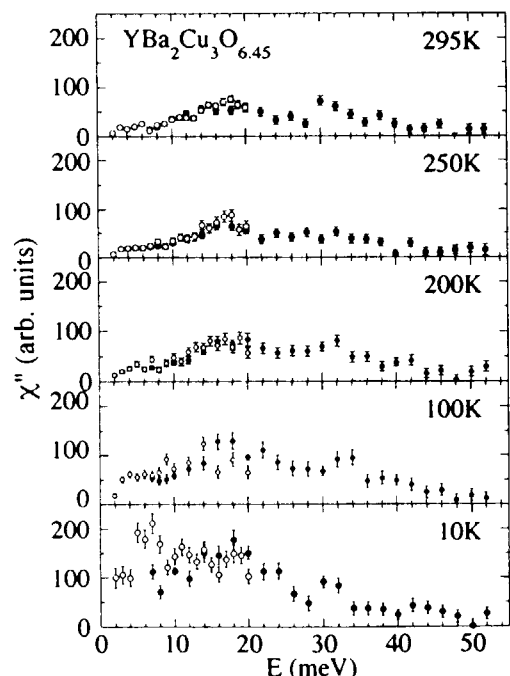


Fig. 1 Spectral functions χ'' for YBa₂Cu₃O_{6.45} are shown against E at several temperatures. Open (closed) circles are data taken by using fixed final energy $E_f = 14.7$ meV (30.5 meV)

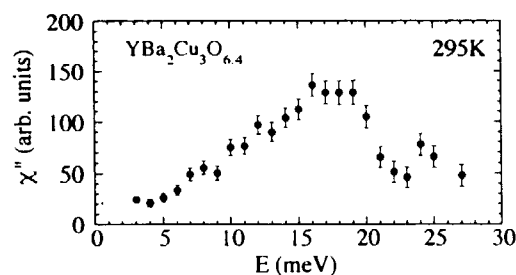


Fig. 2 Spectral function χ'' measured for YBa₂Cu₃O_{6.4} at (3/2, 1/2, -1.7) is shown against E .

observed, while below ~ 100 K spectral weights increase in the low energy region and the gap-like structure disappears. The behavior is very similar to that observed for YBa₂Cu_{2.9}Zn_{0.1}O_{6.75}.²⁾ The similar behavior of χ'' observed in the Zn doped YBCO and the pure YBCO near the M-I phase boundary suggests that the loss of itinerant nature seems to have an important role in the quantum transition from the superconducting state to the Néel ordered one. The electron localization or the randomness effects should be taken into account in the arguments of the hole concentration dependence of the low temperature value of $2\Delta_0$ reported by several experimental results.

Figure 2 shows the E -dependence of χ'' taken at 295 K for YBa₂Cu₃O_{6.4} ($T_c < 20$ K), which is closer to the metal-insulator phase boundary than YBa₂Cu₃O_{6.45}. The χ'' - E curve is slightly concave in the low energy region, which suggests that the singlet correlation persists far above T_{SC} (~ 150 K) where the NMR $1/T_1T$ becomes maximum, possibly to T_0 .

References

- 1) B. J. Sternlieb, M. Sato, S. Shamoto, G. Shirane and J. M. Tranquada, Phys. Rev. B 47 (1993) 5320.
- 2) H. Harashina, S. Shamoto, T. Kiyokura, M. Sato, K. Kakurai and G. Shirane, J Phys. Soc. Jpn. 62 (1993) 4009.
- 3) H. Harashina, K. Kodama, S. Shamoto, M. Sato, K. Kakurai, and M. Nishi, J Phys. Soc. Jpn. 67 (1998) 3216.
- 4) H. Harashina, M. Kanada, H. Sasaki, K. Kodama, M. Sato, S. Shamoto, K. Kakurai, and M. Nishi, J. Phys. Chem. Solids, to be published.

研究テーマ：梯子格子系における超伝導とスピンギャップ

表題：梯子格子系物質； $\text{Sr}_{2.5}\text{Ca}_{11.5}\text{Cu}_{24}\text{O}_{41}$ の圧力下でのスピンギャップ

1-3-2 Neutron Scattering Study of the Pressure Effect on Spin Gap in the Hole-Doped Spin Ladder System $\text{Sr}_{2.5}\text{Ca}_{11.5}\text{Cu}_{24}\text{O}_{41}$

J. AKIMITSU, T. NAGATA, H. FUJINO, M. NISHI¹, K. KAKURAI¹, and S. KATANO²

Department of Physics, Aoyama-Gakuin University, Setagaya-ku, Tokyo 157-8572

¹ *Neutron Scattering Laboratory, ISSP, The University of Tokyo, Tokai, Ibaraki 319-1106*

² *Neutron Scattering Group, Advanced Science Research Center, Japan Atomic Energy Research Institute, Tokai, Ibaraki 319-1195*

The most attractive research for the ladder system is to clarify the relationship between the superconducting and spin gap state. It is well known that $\text{Sr}_{2.5}\text{Ca}_{11.5}\text{Cu}_{24}\text{O}_{41}$ with two leg ladders exhibits superconductivity under pressure.¹⁾ However, the pressure dependence of the magnetic property of this system is not well understood. In this report, the spin gap value and exchange coupling constants in $\text{Sr}_{2.5}\text{Ca}_{11.5}\text{Cu}_{24}\text{O}_{41}$ both at ambient and under high pressure are reported.

Neutron scattering experiments were performed on the triple-axis spectrometers, PONTA and TAS-1, installed at JRR-3M of JAERI in Tokai. The inelastic neutron scattering experiments at TAS-1 were performed with the initial energy (E_i) fixed at 80.5 meV in the constant- Q and in the constant- E methods. In some cases the experiments were performed with the E_i fixed at 30.5 meV on TAS-1, and with the E_f (final energy) fixed at 30.5 meV on PONTA. Pyrolytic graphite (PG) filters were placed before the sample to eliminate the higher harmonics when the energy of 30.5 meV was employed. Collimations were typically set at $40' - 40' - (\text{sample}) - 80' - 80'$. $\text{Sr}_{2.5}\text{Ca}_{11.5}\text{Cu}_{24}\text{O}_{41}$ crystals were placed in an Al can filled with He gas, and then this can was mounted in a conventional cryocooler.

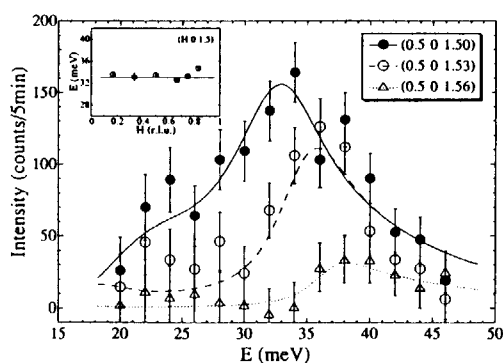


Fig. 1. Inelastic neutron scattering intensities after the subtraction of the background intensity measured in the constant Q scans. The data show the spin excitation at the antiferromagnetic zone center and at the points apart from this zone center. The lines are the results of the convolution with the instrumental resolution. The fits give the spin gap energy of 32.1 ± 0.3 meV and the band maximum of the dispersion of 157.8 ± 17.1 meV.

Figure 1 shows the inelastic neutron scattering intensity at 7K, the difference between the intensity measured at around the antiferromagnetic zone center (0.5 0 1.5) and the background intensity measured at the reciprocal lattice point (0.5 0 1.36) in the constant Q method. A broad but clear peak in the intensity was observed at around 32 meV at the zone center (0.5 0 1.5).

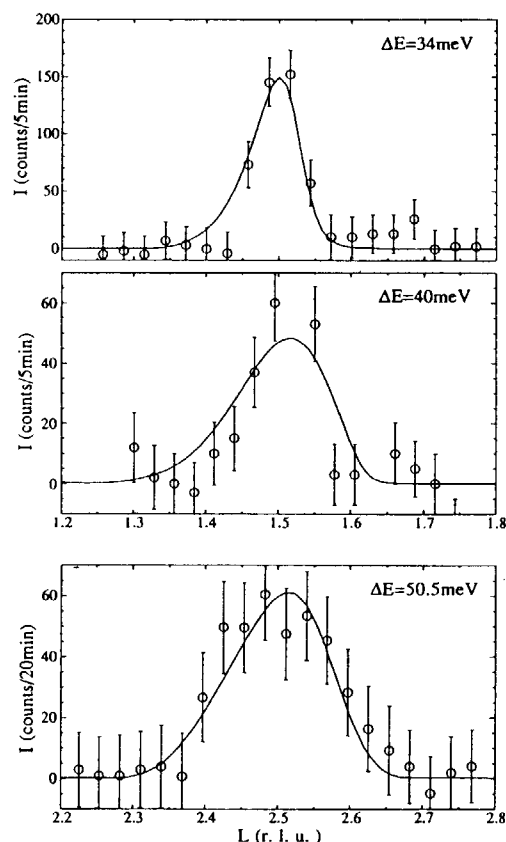


Fig. 2. Inelastic neutron scattering intensities in the constant E scans. The lines are the results of the convolution with instrumental resolution, giving the same energy parameters as in the constant Q scans.

The lines shown for these scans are the results convoluted with the instrumental resolution. The fitting

parameters are the gap energy and the band maximum in the dispersion relation. Here, following the analysis employed by Eccleston *et al.*,²⁾ the dispersion relation was assumed as

$$E^2(Q) = \Delta^2 + A^2 \sin^2(2\pi Q)$$

where Δ is the spin gap and A is the band maximum. (See the Eccleston *et al.*²⁾) As shown in the figure, reasonable fits were obtained for $\Delta = 32.1 \pm 0.3$ meV, and $A = 157.8 \pm 17.1$ meV, thus leading to $J_{//} \sim 90 \pm 15$ meV and $J_{\perp} \sim 65 \pm 15$ meV.

Comparing the spin gap value of the parent material $\text{Sr}_{14}\text{Cu}_{24}\text{O}_{41}$ ($\Delta \sim 32.5$ meV), the spin gap of the doped compound does not change even if Ca is substituted up to 11.5. This result is quite different from the NMR data.^{3,4)}

The inset shows the dispersion curve along the a^* direction. It is clearly shown that there is almost no dispersion along a^* direction.

Figure 2 shows the intensities obtained by the constant E scan. This method is appropriate for the measurements of the steep dispersion. At low energies near 30 meV, as shown in the figure, the scans are peaked at around the antiferromagnetic zone center with a width (FWHM) of ~ 0.06 r.l.u.. The peak broadens to ~ 0.18 r.l.u. at higher energies of about 50 meV and disperses away from the zone center. These roughly indicate that the dispersion is consistent with that obtained in the constant Q method. The solid lines in the figure are the results of the convolution with the instrumental resolution. Reasonable fits are obtained here with the gap energy of 32.1 meV and the band maximum of 157.8 meV as estimated above. Thus, the parameters for the spin excitations were obtained.

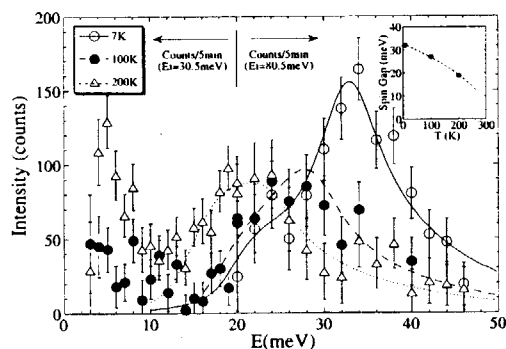


Fig. 3. Intensities as a function of the excitation energy measured at various temperature. The lines are the results of the convolution with the instrumental resolution.

Figure 3 shows the scattering intensities at the antiferromagnetic zone center (0.5 0 1.5) for various temperature. With increasing temperature, the excitation energy decreases; and incoherent scattering increases substantially at low energy. The energy gap plotted against temperature is shown in the inset. The spin gap decreases normally as a function of temperature.

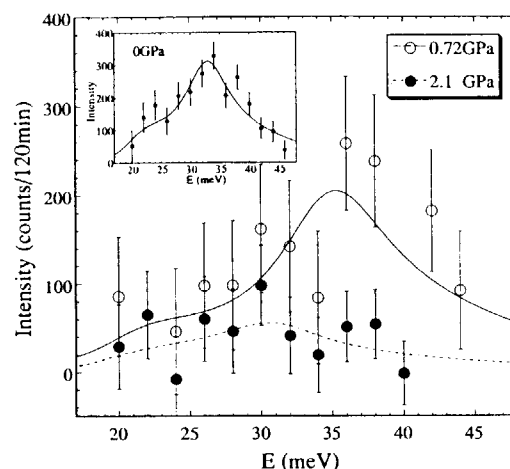


Fig. 4. Pressure dependence of the intensities for the spin gap excitation at the antiferromagnetic zone center (0.5 0 1.5). The lines are the results of the convolution with the instrumental resolution. The inset shows the temperature dependence of the spin gap energy.

Figure 4 shows the spin gap excitations under high pressures. The data at ambient pressure (in the inset) and at 0.72 GPa were normalized by nuclear peak intensities. As shown in the figure, the errors estimated are rather large because of the high background intensities from the pressure cell. Regarding the spin gap energy, however, the gap energy is obtained to be around 30 meV by the fits; that is, even under pressures the spin gap does not change significantly from that of the parent compound. On the other hand, it is clear that the intensity decreases progressively with increasing pressure. This result implies that the number of the electrons which are forming the spin singlet state is decreased under pressures. It is noteworthy that a recent NMR experiment at the pressure of 3.2 GPa demonstrated that the spin gap is vanished, changing to a pseudo-spin gap in the superconducting state.⁵⁾

- 1) T. Nagata, M. Uehara, J. Goto, J. Akimitsu, N. Motoyama, H. Eisaki, S. Uchida, H. Takahashi, T. Nakanishi and N. Môri, *Phys. Rev. Lett.* **81** (1998) 1090.
- 2) R. S. Eccleston, M. Uehara, J. Akimitsu, H. Eisaki, N. Motoyama and S. Uchida, *Phys. Rev. Lett.* **81** (1998) 1702.
- 3) K. Kumagai, S. Tsuji, M. Kato and Y. Koike, *Phys. Rev. Lett.* **78** (1997) 1992.
- 4) K. Magishi, S. Matsumoto, Y. Kitaoka, K. Ishida, K. Asayama, M. Uehara, T. Nagata and J. Akimitsu, *Phys. Rev. B* **57** (1998) 11533.
- 5) H. Mayaffre, P. Auban-Senzier, M. Nardone, D. Jerome, D. Poilblanc, C. Bourbonnais, U. Ammerahl, G. Dhalenne and A. Revcolevschi, *Science* **279**, 345 (1998).

研究テーマ：酸化物高温超伝導物質の構造とダイナミクスの研究
研究表題：超伝導体YBa₂Cu₃O_{7-x}の回折実験の研究

1-3-3 Diffraction Studies in Superconductor YBa₂Cu₃O_{7-x}

A.W. Garrett¹, T. Nishijima¹, M. Arai¹, M. Takahashi², Y. Endoh³, K. Tomimoto⁴, S. Tajima⁴, and Y. Shiohara⁴

¹Institute of Materials Structure Science, KEK, Oho, Tsukuba, 305 Japan

²Department of Physics, Tsukuba Univ., Tsukuba, 305 Japan

³Department of Physics, Tohoku Univ., Aoba, Sendai, 980 Japan

⁴Superconductivity Research Laboratory, ISTEC, Koto-ku, Tokyo, 135 Japan

Recent investigations into the copper oxide superconductors have been greatly influenced by the spin stripe model, in which holes in the CuO₂ plane congregate in periodically spaced domain walls separating antiphase magnetic domains.^{1,2} Evidence for this position comes most clearly from studies of the so-called 1/8 problem in La_{2-x}Ba_xCuO₄,³ in which there is an anomalous suppression of superconductivity when the hole concentration x is near 1/8. Only recently, however, have similar results been observed in the related copper oxide superconductor YBa₂Cu₃O_{7-x}.⁴

Spin stripes will produce magnetic superlattice peaks at the $(\frac{1}{2}\pm\epsilon, \frac{1}{2}, 0)$ position, where ϵ is the inverse of the periodicity of the spin stripes. While these superlattice peaks have been observed,⁵ there should be a corresponding charge ordering peak at the $(1\pm 2\epsilon, 0, 0)$ position that has not been previously reported.

Following initial studies using the KSD spectrometer, we examined a sample of YBa₂Cu₃O_{6.7} using the MRP diffractometer at KEK. The sample was held in an aluminum cylinder, and cooled using a closed cycle refrigerator. The temperature was controlled in a range from 10K to 300K with an accuracy of ± 0.1 K. The crystal was aligned such that the $(1\ 0\ 0)$ direction was observed at $2\theta=30^\circ$, in order to gain sufficient intensity and resolution at the desired wavevector. The crystal was then rotated an addition $\theta = 1.7^\circ$, so that the intensity of the Bragg peak at $(1\ 0\ 0)$ would not overwhelm the superlattice peak.

Figure 1(a) shows the results of this scan at 10K and 300K. Two results are immediately apparent. First, there is a peak at $(1.25\ 0\ 0)$, and that peak is less intense at the greater temperature. This result is consistent with the spin stripe model, with $\epsilon=1/8$. Secondly, there is a larger background contribution at the higher temperature. This increase occurs quite suddenly at 150K, and cannot easily be explained as either thermal diffuse scattering or a phonon contribution. At this time we have no good explanation for this phenomenon.

Figure 1(b) shows the integrated intensity of the peak at the $(1.25\ 0\ 0)$ position. The intensity at all points on the peak was added together, and a linear background subtracted in order to obtain these results. At temperatures below 150K, the intensity is roughly steady at 2×10^{-4} , while above that temperature, the intensity falls to roughly 1×10^{-4} . This would indicate the beginning of the stripe ordering at $T=150$ K.

While theory predicts a similar peak at the $(0.75\ 0\ 0)$ position, this could not be unambiguously resolved. Since the peak intensity should scale roughly with momentum transfer Q^2 , that peak would be only 1/3 the intensity. We were unable to observe this peak during this

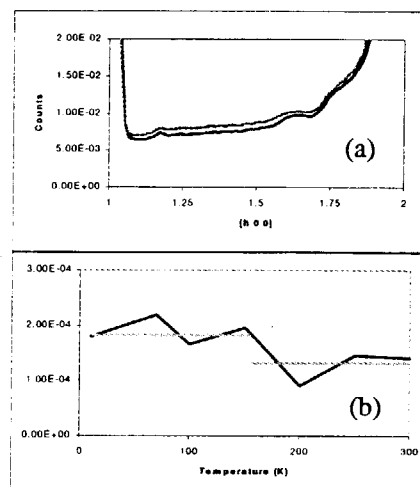


Figure 1 (a) Time of Flight data along the $(1\ 0\ 0)$ direction at $T=10$ K (black line, bottom) and $T=300$ K (gray line, top). (b) Integrated intensity of the $(1.25\ 0\ 0)$ peak, with linear background subtracted. Gray lines are provided as guides to the eye.

experiment.

However, the existence of this peak at the expected position for charge ordering does lend further credence to the spin stripe model. It suggests that this occurs in both La_{2-x}Ba_xCuO₄ and YBa₂Cu₃O_{7-x}, which also suggests it plays a role in the existence of high temperature superconductivity.

References

- 1) J.M. Tranquada *et al.*, Phys. Rev. B **54**, 7489 (1996).
- 2) S. Haas *et al.*, Phys. Rev. B **51**, 5989 (1995).
- 3) J.M. Tranquada *et al.*, Nature **375**, 561 (1995).
- 4) H. Mook *et al.*, cond_mat/9712320
- 5) T. Nishijima, to be published.

研究テーマ：新2次元高温超伝導体 $\text{Li}_x\text{Zr}_{1-y}\text{Hf}_y\text{NCl}$ の構造
 表題：新2次元超伝導体 Na_xHfNCl の構造研究

1-3-4

Structural Study on Novel 2D Superconductor Na_xHfNCl

S. Shamoto, K. Iizawa, M. Yamada, K. Ohoyama†, Y. Yamaguchi† and T. Kajitani

Dept. of Applied Physics, Grad. Sch. of Engineering, Tohoku University, Sendai 980-8579

†Institute for Materials Research, Tohoku University, Sendai 980-8577

The superconductivity on layered nitride $\text{Li}_x(\text{THF})_y\text{HfNCl}$ with $T_c=25.5\text{K}$ has been discovered by S. Yamanaka et al. recently [1]. Similar compound Li_xZrNCl , which is composed of alternate stacking of honeycomb ZrN bilayer and Cl bilayer (Li intercalated YOF-type, $R\bar{3}m$ [2]), is also found to be superconducting with $T_c=15\text{K}$ [3]. A recent LDA band calculation suggests their electronic states have 2D nature [4]. As for the critical temperature, however, it was difficult to understand why T_c of A_xHfNCl (A ; alkali metals) was higher than that of A_xZrNCl in terms of the BCS theory. $5d$ orbital of Hf atom spreads wider than $4d$ orbital of Zr . In addition, Li_xZrNCl has slightly larger in-plane (a -axis) lattice parameter ($3.6016(4)\text{\AA}$ [2]) than that of A_xHfNCl ($3.5892(3)\text{\AA}$). Therefore, the density of states of $5d$ band in Li_xHfNCl may be smaller than that of $4d$ band in Li_xZrNCl . The mass of Hf atom is heavier than that of Zr atom. All these facts contradict with the tendency of the T_c expected by BCS theory. Precise structural study is keenly needed to explain the difference in the T_c between these two layered nitride superconductors.

Neutron diffraction measurement was carried out using the two-axis spectrometer HERMES at T1-3 thermal guide of JAERI-JRR3M in Tokai. The wave length of the incident neutron was 1.8196\AA . The results obtained by neutron diffraction were refined using the Rietveld analysis computer program RIETAN [5].

Fig. 1 shows an observed, calculated, and difference profiles for Na_xHfNCl at $T=4\text{K}$. A small peak from $2\theta=48^\circ$ to 49° was removed in the present analysis, since it was an unknown impurity peak. The refined

parameters are listed in Table. Hf , N and Cl occupation factors were fixed to be 1.0 being consistent with the chemical analysis ($\text{Hf}:\text{N}:\text{Cl}=1.00:1.00:1.00$) [1]. The occupation factor of Na and its isotropic thermal parameter, B_{eq} , were also fixed at the value 0.576 calculated from the ICP value, and 0.4, respectively.

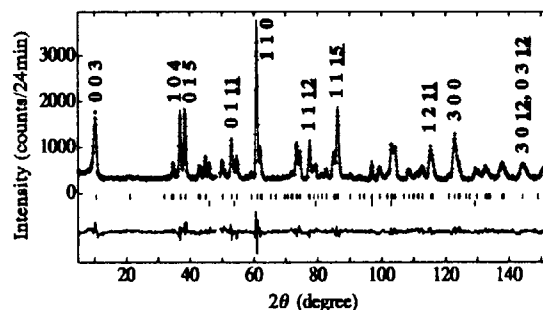


Figure 1 Observed, calculated, and difference profiles of powder neutron diffraction intensities of $\text{Na}_{0.29}\text{HfNCl}$ at 4K including Al sample holder peaks.

Table

Structural parameters of $\text{Na}_{0.29}\text{HfNCl}$ at 4K

$R\bar{3}m$; $a=3.5892(3)\text{\AA}$, $c=29.722(3)\text{\AA}$

atom	site	g	x	y	z	$B_{eq}/\text{\AA}^2$
Hf	6c	1	0	0	0.2083(6)	0.2(3)
N	6c	1	0	0	0.1368(5)	0.4(3)
Cl	6c	1	0	0	0.3944(4)	0.5(4)
Na	3a	0.576	0	0	0	0.4

$R_I=5.19\%$, $R_P=6.67\%$, $R_{wp}=8.38\%$,
 $R_e=4.55\%$

Fig. 2 shows the structure of $\text{Na}_{0.29}\text{HfNCl}$. An electronic conduction is expected mainly in the $\text{Hf } d$ band. In the case

of $\text{Li}_{0.16}\text{ZrNCl}$, ZrN honeycomb lattice is fairly flat, indicating a strong covalence between Zr and N atoms, while HfN honeycomb lattice is zigzag. This difference must be due to the electronegativity in transition metals, *i.e.*, 1.3 for Hf atom and 1.4 for Zr atom. The decrease of covalency between transition metal and nitrogen would lead to the zigzag honeycomb lattice. Alternatively, the increase of electronegativity may result in the shift of transition metals to the center of $3\text{N}+3\text{Cl}$ octahedrons. This change causes some elongation in the interatomic distance between the nearest neighbor transition metal atoms, *i.e.*, from $3.10(1)\text{\AA}$ in Zr-Zr [2] to $3.24(2)\text{\AA}$ in Hf-Hf. The transfer integral between the nearest neighbor transition metal atoms, t_{dd} , can be roughly estimated from the following formula [6],

$$t_{dd} \propto \eta_{dd} r_d^3 / d^5,$$

where η_{dd} is a constant deduced from the d band character, r_d is an effective radius of a transition metal atom, and d is the interatomic distance between the nearest neighbor transition metal atoms. In our comparison between the two isomorphous compounds, η_{dd} must be common. Therefore, we can evaluate the ratio of the transfer integrals of these compounds, *i.e.*, $t_{\text{Hf}}/t_{\text{Zr}} \sim 0.85$, from their interatomic distances, indicating a larger density of states in $\text{Na}_{0.29}\text{HfNCl}$ than that in $\text{Li}_{0.16}\text{ZrNCl}$. Although the enhancement of density of states could increase a screening effect, it is reasonable that the critical temperature of $\text{Na}_{0.29}\text{HfNCl}$ is higher than that of $\text{Li}_{0.16}\text{ZrNCl}$ in the BCS theoretical scheme.

In summary, the structure of Na_xHfNCl ($x=0.29$, $T_c=20\text{K}$) was determined by the powder neutron diffraction. $\text{Na}_{0.29}\text{HfNCl}$ was confirmed to be isomorphous to $\text{Li}_{0.16}\text{ZrNCl}$. The nearest neighbor interatomic distance of Hf-Hf (3.24\AA at 4K) became longer than that of Zr-Zr (3.10\AA at 4K) in $\text{Li}_{0.16}\text{ZrNCl}$. This structural difference could explain the difference between the critical temperature of $\text{Na}_{0.29}\text{HfNCl}$ and that of $\text{Li}_{0.16}\text{ZrNCl}$ by considering their transfer integrals.

Present authors wish to express special thanks to Professor S. Yamanaka for his kind advice in the preparation of samples, Mr. S. Kawano, Mr. S. Watanabe, and Mr. K. Nemoto for their kind technical assistance. The present work is partially supported by the REIMEI Research Resources of Japan Atomic Energy Research Institute.

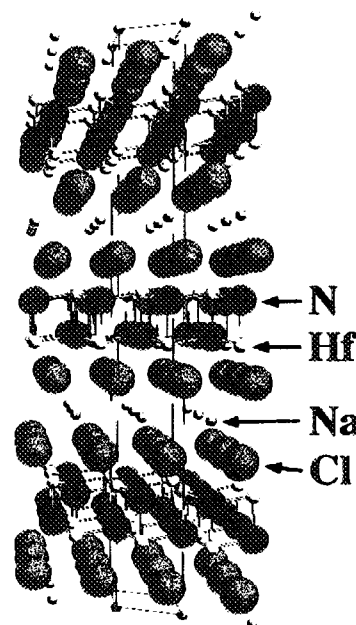


Figure 2 Structure of $\text{Na}_{0.29}\text{HfNCl}$ determined by the present neutron diffraction. Na atoms partially occupy 3a site.

References

- [1] S. Yamanaka, K. Hotehama and H. Kawaji, *Nature* **392**, 580 (1998).
- [2] S. Shamoto, T. Kato, Y. Ono, Y. Miyazaki, K. Ohoyama, M. Ohashi, Y. Yamaguchi and T. Kajitani, *Physica C* **306**, 7 (1998).
- [3] S. Yamanaka, H. Kawaji, K. Hotehama and M. Ohashi, *Adv. Mater.* **8**, 771 (1996).
- [4] I. Hase, Y. Nishihara, *Phys. Rev. B* to be submitted.
- [5] Y.-I. Kim and F. Izumi, *J. Ceram. Soc. Jpn.*, **102**, 401 (1994).
- [6] W. A. Harrison, *Electronic Structure and the Properties of Solids (The Physics of the Chemical Bond)*, W. H. Freeman and Company, San Francisco (1980).

研究テーマ：ウラン化合物における超伝導の研究
表題：URu₂Si₂における磁性と超伝導の相関

1-3-5 Interplay between Magnetism and Superconductivity in URu₂Si₂

T. Honma¹, Y. Haga¹, E. Yamamoto¹, N. Metoki¹, Y. Koike¹, H. Ohkuni² and Y. Onuki^{1,2}

¹Advanced Science Research Center, Japan Atomic Energy Research Institute, Tokai, Naka, Ibaraki 319-1195, Japan

²Graduate School of Science, Osaka University, Toyonaka 560-0043, Japan

Interplay between superconductivity and magnetism is the most important issue for heavy fermion superconductors such as CeCu₂Si₂, UPt₃, UPd₂Al₃, UNi₂Al₃ and URu₂Si₂. Actually the coupling of order parameters has been reported for the first time in UPt₃,¹⁾ then followed by UPd₂Al₃,²⁾ and UNi₂Al₃.^{3,4)} However it has not been reported in URu₂Si₂. URu₂Si₂ is a fascinating compound in which superconductivity coexists with antiferromagnetic ordering. Previous neutron scattering experiments revealed that an antiferromagnetic state with an unusually small magnetic moment 0.04 μ_B/U develops below $T_o = 17.5$ K.⁵⁾ Superconductivity occurs below about 1 K in this ordered state. To shed more light on this phenomenon, we have performed neutron scattering experiments on the magnetic Bragg peak in the temperature range of 200 mK to 30 K.

Neutron scattering experiments were carried out using a cold neutron triple-axis spectrometer, LTAS, installed in the research reactor JRR-3M at the Japan Atomic Energy Research Institute (JAERI). Below T_o , we observed an antiferromagnetic Bragg peak $Q = (1\ 0\ 0)$. We determined the magnitude of the ordered moment $\mu_{ord} \sim 0.02 \mu_B/U$.⁶⁾

Figure 1 shows the temperature dependence of the (1 0 0) magnetic Bragg peak intensity below 20 K for the annealed sample. The

intensity increases slightly below T_o but shows an abrupt increase below 14 K. This result indicates a typical temperature dependence of an order parameter showing a second-order phase transition. The intensity saturates at low temperatures.

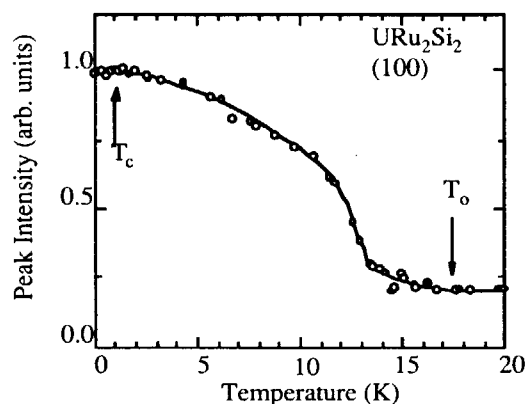


Fig.1 Temperature dependence of the (1 0 0) magnetic Bragg peak intensity below 20K for the annealed sample in URu₂Si₂. The solid line connecting the data is a guideline.

From the neutron data, the magnetic transition temperature is expected to be about 14 K. The difference of the transition temperature of 14 K from the one measured by the specific heat and resistivity $T_o = 17.5$ K is quite unusual. This large deviation cannot be explained as being due to an experimental error of the thermometer.

The specific heat exhibits a sharp peak at T_0 without any significant distribution of the transition. At present we cannot understand the temperature difference. An idea would be the existence of two independent order parameters; a non-magnetic order parameter contributes to T_0 , while the dynamical magnetic order takes place at T_N . Very recently, Mentink *et al.* concluded that the order parameter associated with T_0 is non-magnetic and the tiny moment is only a by-product of this phase transition.⁷⁾

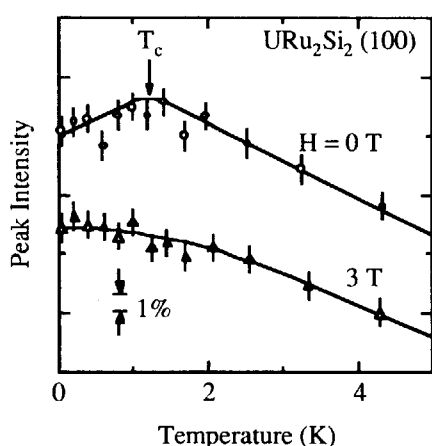


Fig.2 Temperature dependence of the (1 0 0) magnetic Bragg peak intensity under the magnetic fields below 5K in URu_2Si_2 . The solid line connecting the data is a guideline.

In Fig. 2, we show the temperature dependence of the (1 0 0) Bragg intensity around T_c using an enlarged scale.

For $H = 0$, the intensity increases with decreasing temperature above 1 K and shows a peak at about 1 K. The intensity decreases rather steeply below about 1 K. The peak temperature of about 1 K corresponds to the superconducting transition temperature T_c which is determined by specific heat measurements. When superconductivity is destroyed by applying a

magnetic field of 3 T along the [0 0 1] direction, the peak intensity monotonically increases with decreasing temperature and saturates below 1 K. Here we note that the magnetic field of 3 T is larger than the upper critical field of 2.9 T. The steep decrease in the intensity below T_c in zero magnetic field is a new result which was not observed. From the structure factor calculation of URu_2Si_2 , it is clear that this anomaly cannot be explained as due to a redistribution of the magnetic domains. It is thus concluded that the magnetic order parameter is coupled to the superconducting one.

The magnitude of the intensity reduction below T_c in the present experiments is about 1-2% compared to the maximum intensity. This value is approximately the same as in the case of heavy fermion superconductors UPt_3 (reduction rate of 5-10%, an ordered moment of $0.02 \mu_B/\text{U}$), UNi_2Al_3 (3%, $0.2 \mu_B/\text{U}$) and UPd_2Al_3 (1%, $0.85 \mu_B/\text{U}$).¹⁻⁴⁾ The coupling of the order parameters would be a characteristic feature in this system.

References

- 1) G. Aeppli *et al.*, Phys. Rev. Lett. 63 (1989) 676.
- 2) N. Metoki *et al.*, Phys. Rev. Lett. 80 (1998) 5417.
- 3) N. Sato *et al.*, Physica B 230-232 (1997) 367.
- 4) J. G. Lussier *et al.*, Phys. Rev. B 56 (1997) 11749.
- 5) T. E. Mason *et al.*, Phys. Rev. Lett. 65 (1990) 3189.
- 6) T. Honma *et al.*, J. Phys. Soc. Jpn. 68 (1999) 338.
- 7) S. A. M. Mentink *et al.*, Phys. Rev. B 53 (1996) R6014.

研究テーマ：新2次元高温超伝導体 $\text{Li}_x\text{Zr}_{1-y}\text{Hf}_y\text{NCl}$ のフォノン
 表題：新2次元超伝導体 Li_xZrNCl のフォノン

1-3-6 Phonon on Novel 2D Superconductor Li_xZrNCl

S. Shamoto, T. Kato, and T. Kajitani

Dept. of Applied Physics, Grad. Sch. of Engineering, Tohoku University, Sendai 980-8579

The superconductivity on layered nitride Li_xZrNCl with $T_c=15\text{K}$, which is composed of alternate stacking of honeycomb ZrN bilayer and Cl bilayer (Li intercalated YOF-type, $R\bar{3}m$ [1]), has been discovered by S. Yamanaka et al. [2]. Recent band calculations using our structural data reveal 2D nature in electronic states [3,4], an existence of 3-fold nesting condition [3] and zone center A_{1g} phonon frequencies [3], stimulating us to study phonon in the present system.

Neutron scattering measurement was carried out using a TOF-type spectrometer AGNES at C3-1-1 cold guide of JAERI-JRR3M in Tokai.

Fig. 1 shows an observed phonon density of states GPDOS of Li_xZrNCl at room temperature. Arrows are calculated A_{1g} phonon frequencies in ZrNCl by R. Weht et al. [3].

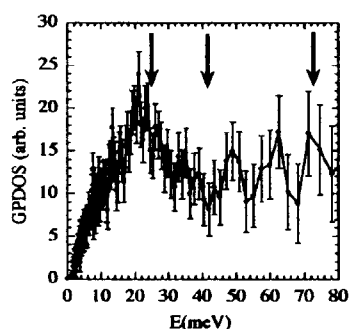


Figure 1 Observed phonon density of states GPDOS of Li_xZrNCl at room temperature.

The highest phonon mode is assigned mainly to nitrogen vibration, while the other modes are related with Zr and Cl motions. In the present study, only the highest mode was observed as a peak.

Fig. 2 shows observed phonon density of states GPDOS of Li_xZrNCl at 16K and 10K,

which are above T_c and below T_c , respectively. A phonon shift was clearly observed from 2.7meV to 2.6meV with decreasing temperature. This phonon behavior can be understood within a frame of ZZ theory [6], since superconducting energy gap, 2Δ , is estimated to be $4.5 k_B T_c$ [5], which corresponds to 5.8 meV.

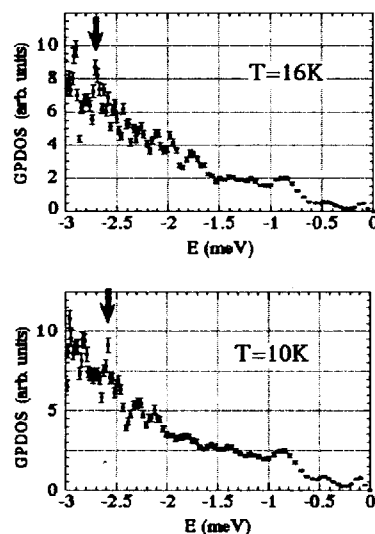


Figure 2 Observed phonon density of states GPDOS of Li_xZrNCl at 16K and 10K.

References

- [1] S. Shamoto, T. Kato, Y. Ono, Y. Miyazaki, K. Ohoyama, M. Ohashi, Y. Yamaguchi and T. Kajitani, *Physica C* **306**, 7 (1998).
- [2] S. Yamanaka, H. Kawaji, K. Hotehama and M. Ohashi, *Adv. Mater.* **8**, 771 (1996).
- [3] R. Weht, A. Filippetti and W. E. Pickett, *Phys. Rev. Lett.*, to be submitted (1999).
- [4] I. Hase and Y. Nishihara, *Phys. Rev. B* to be submitted (1999).
- [5] S. Shamoto, K. Iizawa, et al., *Molecular Crystals and Liquid Crystals*, to be submitted.
- [6] R. Zeyher and G. Zwicknagl, *Z. Phys. B* **28**, 175 (1990).

JRR-3M, AGNES, 3. Superconductivity

研究テーマ：強相関電子系の中性子散乱による研究

表題：中性子小角散乱法を用いたNb単結晶における磁束状態の観察

1-3-7 Observation of Vortex Structure in Nb by Small-Angle Neutron Scattering

S. Miyata, K. Osamura, M. Watahiki¹, and J. Suzuki¹

Department of Materials Science and Engineering, Kyoto University, Kyoto 606-8501, Japan

¹Japan Atomic Energy Research Institute, Tokai, Ibaraki 319-1195, Japan

Since Abrikosov's theoretical analysis of Ginzburg-Landau equation near transition temperature (T_c), study in the mixed state has been progressed mainly about locations of vortices. He showed that a six-fold hexagonal lattice is most stable in the free energy. As London theory also leads to this periodic solution of Abrikosov, the six-fold "Abrikosov" lattice is suggested to be formed not only near T_c but also at low temperatures so far as in a "jellium" model which ignore the crystal structure. Actually, the triangle lattice is observed in a wide range of temperature in many experiments. And due to correlation between vortices and the crystal lattice, distorted triangle lattices or square lattices are also reported in several conditions. For example, in Nb single crystal, completely hexagonal lattice is formed only when external magnetic field is applied parallel to 111 axis which is highest symmetry of all crystal axes. In other directions, distorted triangle lattices are typically observed and square lattice is formed at low temperature when external field is applied parallel to 100 four-fold axis.

These observations were done by decoration method (Bitter technique), Lorentz microscopy, small-angle neutron scattering (SANS), μ SR, STM and so on. Because STM observes the structure of the order parameter, it is complementary to the rest of techniques which observe the magnetic field distribution. Decoration method and Lorentz microscopy can specify the locations of vortices, but they don't have enough resolution to observe the precise magnetic field distribution in the mixed state. On the other hand, SANS and μ SR techniques have enough resolution of the order of angstrom scale, so they can offer the information about the precise field distribution. In SANS experiments, the vortex structure reflects in the form factor which is the envelope of Bragg peaks. We fit the function based on London theory to our experimental data. In the framework of London theory, diameter of a vortex is equal to

the penetration depth from the surface in Meissner state. Taking account of displacement from equilibrium point caused by the thermal fluctuation and/or the static displacement (vortex pinning), a term like as Debye-Waller factor is added to the function. It leads to good agreement with the experimental data. As is expected, the vortex diameter estimated from this fitting doesn't match with penetration depth of Meissner state, because G-L parameter (κ) of Nb is not so large as to be applied to London theory. But apart from whether superconductivity of this material obeys London theory or not, it represents truly at least about a geometrical profile of a vortex. That is, vortices have the structure represented by modified Bessel function of zeroth order, but large shielding supercurrent sharpen the vortex than estimated by London theory.

Reference(s)

- 1) C. Varmazis and Myron Strongin, Phys. Rev. B, **10** (1974) 1885.
- 2) B. W. Maxfield and W. L. McLean, Phys. Rev., **139** (1965) A1515.

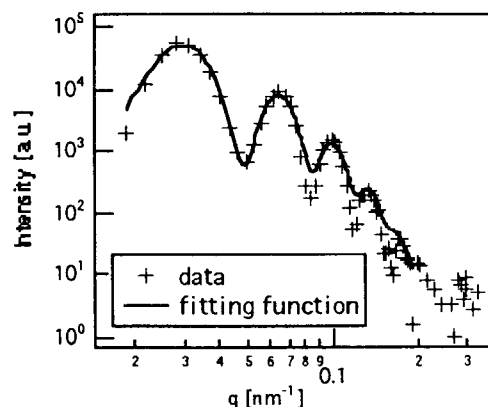


Fig. 1 Fitting result and experimental data.

1. 中性子散乱 4) 非晶質・液体

1. Neutron Scattering 4) Amorphous・Liquid

This is a blank page.

研究テーマ：アモルファス高分子の低エネルギー励起の Q 依存性

表題：干渉性非弾性中性子散乱によるグリセロールガラスの低エネルギー励起

1-4-1 Low-energy Excitations of Glassy Glycerol As Studied by Coherent Inelastic Neutron Scattering

I. Tsukushi, T. Kanaya and K. Kaji

Institute for Chemical Research, Kyoto University, Uji, Kyoto-fu 611-0011, Japan

Low-energy excitations in amorphous materials are poorly understood although extensive studies have been performed by many researchers. In neutron and Raman scattering measurements, the so-called boson peak is commonly observed in amorphous materials at around 2 - 6 meV which corresponds to excess non-Debye heat capacity in a temperature range from 5 to 20 K. The origin is still not clear in spite of many experimental and theoretical efforts. Recently an inelastic X-ray scattering (IXS) technique with high-energy resolution has been developed to study low energy excitation of various amorphous materials [1]. Analysis of the IXS data by a damping harmonic oscillation (DHO) model have revealed a dispersive mode in a low energy region between 2 and 25 meV, and it was insisted that the dispersive mode is an origin of the boson peak. In contrast to this finding, inelastic neutron scattering studies have shown that the boson peak is a localized mode without any dispersion relationship. As far as we know, these contradicted facts are not directly discussed.

The purpose of this study is to examine whether or not the low energy mode in the IXS is identical to that in the INS. For doing experiments along this direction, we have to pay our attention on the facts that the Q range covered by the IXS studies ($0.1 \sim 0.8 \text{ \AA}^{-1}$) is

lower than that of INS studies ($1.0 \sim 3.0 \text{ \AA}^{-1}$) and that the INS studies on the boson peak were mainly performed using incoherent scattering in contrast to coherent scattering of IXS. In this study, therefore, we carried out coherent INS measurements in a Q range as low as possible.

Neutron scattering measurements have been made with a triple axis spectrometer (GP-TAS) in the JRR-3M reactor, Tokai. The Q - and E -ranges were from 0.6 to 6.4 \AA^{-1} and -15 meV to 0 meV, respectively. Glassy material used in the experiment was deuterated glycerol (GLY-d8, $T_g = 185 \text{ K}$ for GLY-h8)).

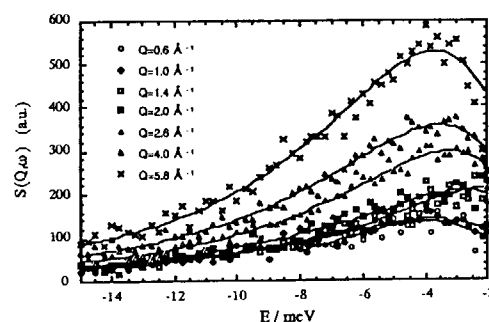


Fig. 1 Dynamic scattering law $S(Q, \omega)$ of deuterated glycerol (GLY-d8) for each Q . The solid lines are the results of fitting by the DHO model.

Figure 1 shows the dynamic scattering law $S(Q, \omega)$ of GLY-d8 at 120 K. A broad low-energy excitation peak (boson peak) was

observed at around -4.5 meV. Its peak position is the same as that of protonated glycerol glass. Following to the IXS studies [1], the observed dynamic scattering laws $S(Q, \omega)$ were fitted to the theoretical one derived from the DHO model, which is given by

$$S(Q, \omega) = m_1(Q) \frac{\omega \Gamma(Q) \Omega(Q)}{[\Omega(Q)^2 - \omega^2]^2 + \Gamma(Q)^2 \omega^2}$$

where $m_1(Q)$, $\Omega(Q)$ and $\Gamma(Q)$ refer to constant, excitation energy and width of the inelastic scattering, respectively.

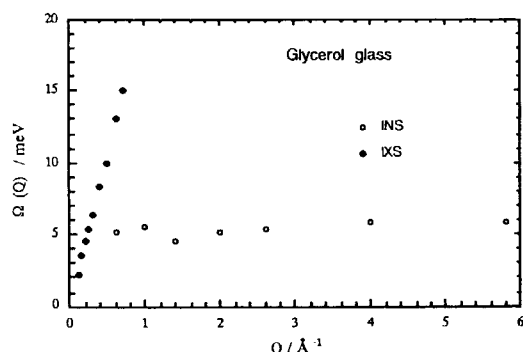


Fig. 2 The Q -dependencies of excitation peak $\Omega(Q)$ derived from fitting to the DHO model. Solid circles present the $\Omega(Q)$ of IXS. Open circles those of INS.

The Q -dependence of the excitation peak $\Omega(Q)$ derived from the DHO model fitting is shown in figure 2. The $\Omega(Q)$ obtained from the INS data (open circles) almost independent of Q . This is in contrast to that of the IXS (solid circles) [1]. This result might suggest that the low energy mode which was observed by IXS is different from that by INS. In other words, there coexist a dispersive mode and a localized mode in the low energy region of glassy glycerol.

In the next step, we analyzed the Q dependence of the inelastic scattering intensity. Generally speaking, coherent inelastic scattering intensity is proportional to Q^2 , static structure factor $S(Q)$ and Debye-Waller factor $\exp(-2W)$ ($2W = \langle u^2 \rangle Q^2$, $\langle u^2 \rangle$ is mean square displacement). Hence, the observed inelastic scattering intensity was scaled by Q^2 , $S(Q)$ and $\exp(-2W)$.

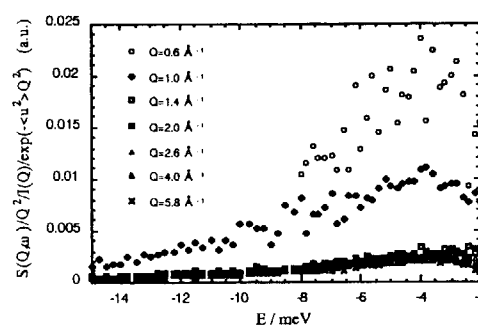


Fig. 3 Energy dependence of $S(Q, \omega)$ divided by Q^2 , $I(Q)$ and $\exp(-\langle u^2 \rangle Q^2)$ for each Q .

Figure 3 presents the energy dependence of the scaled $S(Q, \omega)$. The scaling works very well in a Q range above $Q = 1.4 \text{ \AA}^{-1}$, but excess inelastic scattering intensity is clearly observed at $Q = 1.0 \text{ \AA}^{-1}$ and 0.6 \AA^{-1} . This indicates that some other mode may exist in the low Q region. One plausible mode for the excess inelastic intensity below $Q = 1.0 \text{ \AA}^{-1}$ is the dispersive low energy mode observed in the IXS measurements as expected from Figure 2.

references

- [1] C. Masciovecchio et. al. *Phys. Rev. Lett.* **76**, 3356 (1996), F. Sette et. al. *Science*, **280**, 1550 (1998).

研究課題:液体金属における電子-イオン相関
表題:液体亜鉛の電子-イオン相関

1-4-2 Electron-Ion Correlation in Liquid Zinc by Diffraction Method

S. Takeda, Y. Kawakita, M. Kanehira, S. Yoshioka

Department of Physics, Faculty of Science, Kyushu University, Ropponmatsu Fukuoka 810-8560 JAPAN

Liquid metals can be viewed as a binary mixtures between ions and conduction electrons moving nearly freely through an assembly of ions, and many of their physical properties are linked to the corresponding correlation functions. The aim of this study is to report newly measured structural data of neutron diffraction for liquid Zn and provide the electron-ion correlation around Zn^{2+} ion from the diffraction data.

The samples were sealed in thin quartz tubes of inner diameter 8.0mm with 0.3mm wall thickness under a vacuum.

The neutron scattering measurements were carried out at 470°C, 600°C and 700°C using the powder diffractometer with a multi detector, HERMES, and the used wavelength was 1.83Å. The data at high angle region were combined with those observed by TAS-4G previously.

Figure 1 shows the structure factors of liquid Zn determined by neutron and X-ray diffraction. The structure factor of liquid Zn by X-ray diffraction has an asymmetry around the first peak, while that by neutron diffraction does not. There has been detected a small but the systematic differences are well appreciated. The quantity of $[S_X(Q) - S_N(Q)]$ evaluated from two structure factors is also given in the bottom of Fig. 1.

The electron charge density around an Zn^{2+} ion, $\rho(r)$, and metallic form factor, $f_M(Q)$, are evaluated from these small differences. As shown in the figure, the curve of $\rho(r)$ crosses zero around 1.3Å and a sharp increase toward the center of an ion can be seen less than 0.74Å. Since this value is close to the ionic radius, the accurate spectra of $\rho(Q)$ in the high Q region will be required for the further understanding of the charge distribution in the very small r region less than 0.74Å, which corresponds to the

ionic radius and also near the first maximum position of charge density of an isolated atom. The charge density function in Fig.2 shows that the electron charge screens the ionic charge rather closely contact with the ions and the maximum point exists rather distant at 2.2Å. In case of simple liquid metals as Na, Mg and Al, the electron charge distribution has maximum value around the mid point between the nearest neighbor ions to screen the central ionic charge.¹⁾ The charge distribution of liquid Zn is different from the simple liquid metal case.²⁾

Figure 3 shows the obtained metallic form factor of liquid Zn and it indicates the interesting feature around $2k_F$ region.

References

- 1) S.Takeda, Y.Kawakita, M.Inui, K. Maruyama, S.tamaki and Y.Waseda; J.Non-Cryst.Solids 205-207(1996)365-369.
- 2) S.Takeda, Y.Kawakita, M.Knehir, S.tamaki and Y.Waseda; in print J.Phys. Chem. Solids (1999).

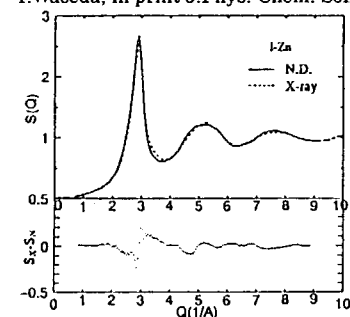


Fig.1
Structure factors
of liquid Zn.

Fig.2 Charge density function $\rho(r)$ of liquid Zn and that of an isolated one.

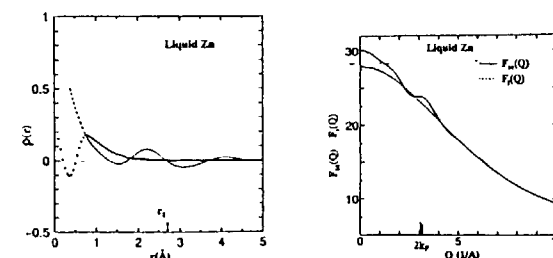


Fig.3 Form factor of liquid (Metallic) Zn and isolated Zn^{2+} .

研究テーマ：droplet マイクロエマルジョンの圧力誘起構造相転移

表題：三元系マイクロエマルジョンにおける構造形成の温度、圧力効果

1-4-3 Temperature and Pressure Effects on Structural Formations in a Ternary Microemulsion

M. Nagao*, H. Seto†, Y. Kawabata† and T. Takeda†

*Institute for Solid State Physics, The University of Tokyo, 106-1 Shirakata, Tokai 319-1106, Japan,

†Faculty of Integrated Arts and Sciences, Hiroshima University, 1-7-1 Kagamiyama,

Higashihiroshima 739-8521, Japan

Small angle neutron scattering (SANS) experiments were carried out in order to investigate temperature and pressure effects on structural formation of a ternary microemulsion composed of AOT (dioctyl sulfosuccinate sodium salt), water and *n*-decane. At the same volume fraction of water and *n*-decane mixed with about 20 vol.% of AOT, its structure is known to be a dense water-in-oil droplet at ambient temperature and pressure. With increasing temperature, the system transforms to a lamellar structure at around 50°C [1, 2]. With increasing pressure, a similar phase transition to the lamellar structure was observed by Nagao and Seto [3]. It was already known that the temperature and the pressure effects on the phase behavior of this system were the same. However, they suggested that the origin of these phase transitions should not be the same.

In order to clarify the difference between the temperature- and the pressure-induced phase transitions, a SANS experiment on the temperature-induced one was performed at SANS-U. The sample was prepared to be $\phi_s=0.224$ with the same volume of water and *n*-decane, where ϕ_s the AOT volume fraction against the total volume. Above $T_s=35.4^\circ\text{C}$

(transition start temperature), the system became two-phase coexistence with the lamellar structure at the lower part of the sample and the microemulsion, which indicates both the possibilities of the droplet and the bicontinuous structures, at the upper part as the case of the pressure [3]. In Fig. 1(a),

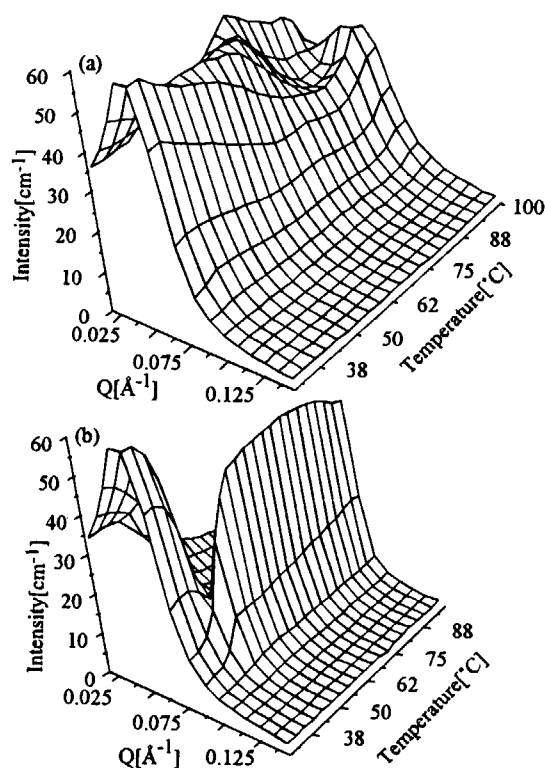


Figure 1: SANS profile obtained from the upper part of the sample (a) and from the lower part (b).

JRR-3M, C1-2 (SANS-U), 4. Amorphous & Liquid

temperature dependence of observed SANS profile from the upper part of the sample is shown and in Fig. 1(b) from the lower part [4]. A broad peak at $Q \sim 0.04 \text{ \AA}^{-1}$ was observed from both the parts at room temperature. With increasing temperature below T_s , the peak shifted to higher Q . Above T_s , the broad peak shifted to the opposite direction and its intensity decreased. At the lower part of the sample, another sharp peak appeared at $Q \sim 0.08 \text{ \AA}^{-1}$ above T_s , which corresponds to the stacking of the lamellae (Fig. 1(b)). On the other hand, no lamellar peak was observed at the upper part of the sample. However, another broad peak appeared at $Q \sim 0.04 \text{ \AA}^{-1}$ at $T = 77.9^\circ\text{C}$ (Fig. 1(a)). This new peak may correspond to the re-entrant microemulsion phase, which has been known to exist at higher temperature [2].

In Fig. 2, the temperature dependence of the mean repeat distance d of both the microemulsion and the lamellar is shown with its pressure dependence [4]. The horizontal axis indicates the normalized temperature (\hat{T}) and pressure (\hat{P}): $\hat{T} = (T - T_s) / |T_s - T_0|$ and $\hat{P} = (P - P_s) / |P_s - P_0|$, where T_0 and P_0 the ambient temperature and pressure, P_s the transition start pressure. The behavior below $\hat{T} = 0$ is the same as that below $\hat{P} = 0$, however, the behavior at the high temperature phase ($\hat{T} > 0$) was different from the high pressure phase ($\hat{P} > 0$). Both the d 's of the microemulsion structure (upper part) and the lamellar structure (lower part) gradually changed with increasing temperature while the d 's stayed constant above the transition finish pressure, P_f . The d of the high temperature

lamellar, d_T , was larger than that of the high pressure lamellar, d_P . The d_T linearly depended on the ϕ_s as Kotlarchyk, Sheu and Capel pointed out [1]. However, d_P did not depend on ϕ_s for $0.209 \leq \phi_s \leq 0.230$ [3]. As described above, a new broad peak appeared above $T = 77.9^\circ\text{C}$ at the upper part of the sample, and simultaneously, the lamellar peak intensity decreased. In the high pressure experiment, such the precursor of the subsequent phase transition was not observed. These evidences indicated that an origin of the pressure-induced phase transition is not driven by the change of the spontaneous curvature of AOT membranes, which is due to the dissociation of counter ions with changing temperature.

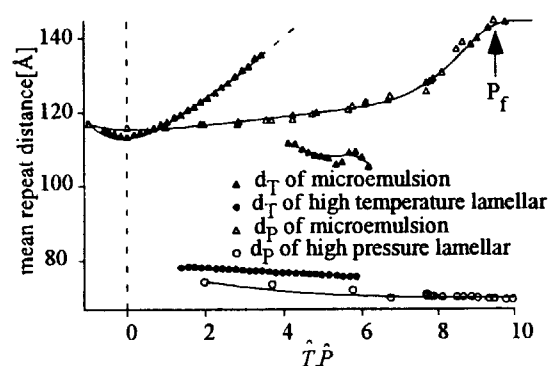


Figure 2: Temperature and pressure dependences of the mean repeat distance.

- [1] M. Kotlarchyk, E. Y. Sheu and M. Capel, *Phys. Rev. A* **46** (1992) 928-939.
- [2] S. H. Chen, S. L. Chang and R. Strey, *J. Chem. Phys.* **93** (1990) 1907-1918.
- [3] M. Nagao and H. Seto, *Phys. Rev. E* **59** (1999) 3169-3176.
- [4] M. Nagao, H. Seto, Y. Kawabata and T. Takeda, submitted to *J. Appl. Cryst.*

研究テーマ：droplet マイクロエマルジョンの圧力誘起構造相転移

表題：三元系マイクロエマルジョンにおける温度、圧力誘起ラメラ構造

1-4-4 Temperature- and Pressure-Induced Lamellar Structure in a Microemulsion System

M. Nagao*, H. Seto†, D. Okuhara‡ and Y. Matsushita‡

*Institute for Solid State Physics, The University of Tokyo, 106-1 Shirakata, Tokai 319-1106, Japan,

†Faculty of Integrated Arts and Sciences, Hiroshima University, 1-7-1 Kagamiyama,

Higashihiroshima 739-8521, Japan

‡Department of Applied Chemistry, School of Engineering, Nagoya University, Furo-cho,

Chikusa-ku, Nagoya 464-8603 Japan

As discussed in a previous article in this issue, a phase transition from a dense water-in-oil droplet to a two-phase coexistence of lamellar and microemulsion structures was induced by temperature and/or pressure in an AOT (dioctyl sulfosuccinate sodium salt) / water / *n*-decane system [1]. Although the static structure at high temperature is similar to that at high pressure, the experimental results suggested that the mechanisms of the temperature- and the pressure-induced phase transitions were not the same. In this report scattering profiles of the high temperature lamellar (HTL) structure and the high pressure lamellar (HPL) were compared in order to clarify the difference between these transitions.

In Fig. 1, SANS profiles observed from the HTL and the HPL for a mixture of $\phi_1=0.215$ with the same volume of water and oil is shown [2], where ϕ_1 the AOT volume fraction against total volume. These profiles were explained by an equation proposed by Nallet *et al.* taking a Helfrich repulsion between membranes into consideration as a stabilization force of the structure [3],

JRR-3M, C1-2 (SANS-U), 4. Amorphous & Liquid

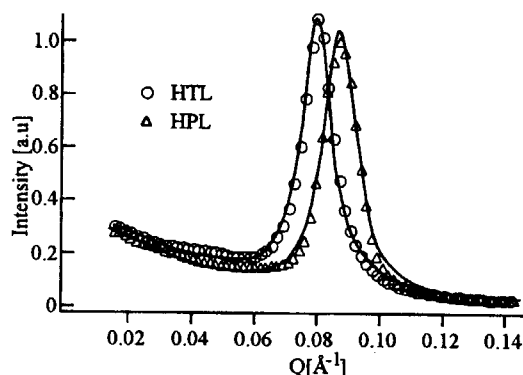


Figure 1: The observed SANS profiles from the HTL at $T=53.2^{\circ}\text{C}$ and $P=0.1\text{MPa}$ and the HPL at $T=24.6^{\circ}\text{C}$ and $P=80\text{MPa}$.

$$I(Q) = \frac{A}{(Q\xi_p)^2 + 1} + \frac{B}{\{(Q - Q_0)\xi_1\}^2 + 1}, \quad (1)$$

where ξ_p , ξ_1 indicate correlation lengths and Q_0 the wave number of a peak position, respectively. The first and the second terms correspond to the scattering from the concentration fluctuation of amphiphile molecules and from the stacking of membranes, respectively. In order to compare the low Q diffuse scattering intensities of the HTL and the HPL, the quasi-Bragg peak amplitudes (B) was

normalized to be unity. In Table 1, obtained fit parameters are shown. This result indicated that the $d_l (=2\pi/Q_0)$ of the HPL was smaller than that of the HTL, and the integrated intensity of the low Q diffuse scattering (the first term of Eq. (1)) of the HPL was also smaller than that of the HTL. Therefore, it could be concluded that the membranes of the HPL are less undulating than that of the HTL.

In Fig. 2, the ϕ_s dependence of the d_l of the HTL (d_{HTL}) and that of the HPL (d_{HPL}) was shown [2]. It clearly showed that the d_{HTL} depended on the ϕ_s , however, the d_{HPL} was almost constant at around 70Å. From these results, the detailed features of the pressure-induced phase and the temperature-induced one are different, i.e., origins of these phase transitions are different.

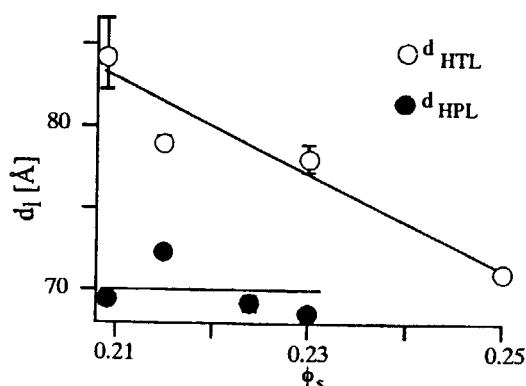


Figure 2: The ϕ_s dependence of the repeat distance d_{HTL} and d_{HPL} .

	A	$\xi_p(\text{\AA})$	$\xi_l(\text{\AA})$	$d_l(\text{\AA})$
HPL	0.33 ± 0.2	27.5 ± 1.8	168 ± 4	72.2 ± 0.3
HTL	0.33 ± 0.1	22.9 ± 1.1	178 ± 4	79.2 ± 0.1

Table 1: Obtained fit parameters of the HPL and the HTL

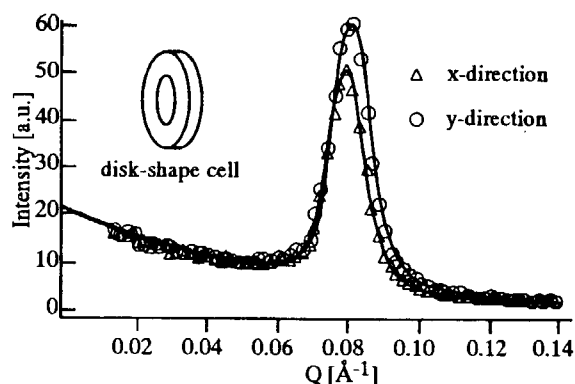


Figure 3: Intersections of the 2 dimensional scattering profiles through the beam center along x- and y-direction observed from the HTL put in a disk-shape cell.

Nagao and Seto have shown an anisotropy of the quasi-Bragg scattering from the HPL [4]. In order to clarify the origin of such the anisotropy, sample cell dependence of the scattering profile from the HTL was investigated, because changing shapes of sample cells in the case of the temperature experiment were easier than that in the case of the pressure. In case that a rectangular quartz cell was used, only an isotropic scattering profile was observed. On the contrary, slight anisotropy of the quasi-Bragg scattering was observed in the case of the disk-shape cell as shown in Fig. 3. The intensity of the quasi-Bragg scattering along y-direction was larger than that along x-direction. Therefore, we concluded that the round shape at the bottom of a sample cell induces the alignment of lamellae.

- [1] M. Nagao, H. Seto, Y. Kawabata and T. Takeda, in this issue.
- [2] M. Nagao, H. Seto, D. Okuhara and Y. Matsushita, *J. Phys. Chem. Solids* in press.
- [3] F. Nallet, D. Roux, S. T. Milner, *J. Phys. France* **51** (1990) 2333-2346.
- [4] M. Nagao and H. Seto, *Phys. Rev. E* **59** (1999) 3169-3176.

研究テーマ：アモルファス合金の過冷却液体状態における構造変化過程の直接観察

表題：バルク合金ガラスのガラス転移点付近の中・長距離構造変化過程の中性子小角散乱によるその場観察

1-4-5

In-situ SANS Measurements on Medium and Long Range Structure Evolution in Bulk Metallic Glass $\text{Ni}_{15}\text{Pt}_{60}\text{P}_{25}$ near Glass Transition

K. Shibata, T. Higuchi, An-Pang Tsai¹, M. Imai² and K. Suzuki

*Institute for Materials Research, Tohoku University,
Katahira 2-1-1, Aoba-ku, Sendai 980-8577*

¹*National Research Institute for Metals, Sengen 1-2-1, Tsukuba 305*

²*Department of Physics, Faculty of Science,
Ochanomizu University, Ohtsuka 2-1-1, Bunkyo-ku, Tokyo 112*

§1. Introduction

There have been found so far several metallic glasses which are very stable even above the glass transition temperature T_g and show a large temperature interval ΔT between the glass transition temperature (T_g) and the crystallization temperature (T_x). Therefore, we can make a bulk metallic glass sample with several millimeters in thickness by simply casting its melt. To investigate the atomic scale mechanism of the stability of bulk metallic glasses, it is essential to measure the isothermal evolution of the structure¹⁾.

In this study, we selected a metal-metalloid bulk metallic glass $\text{Ni}_{15}\text{Pt}_{60}\text{P}_{25}$ alloy because of a large temperature interval $\Delta T = T_x - T_g$ (about 55K) and the facility in preparing the sample with enough thickness up to a few millimeter.

The purpose of this study is to reveal the isothermal evolution of the medium and long range structure in the bulk metallic glass $\text{Ni}_{15}\text{Pt}_{60}\text{P}_{25}$ alloy near the glass transition temperature T_g by the in-situ measurement of small angle neutron scattering.

§2. Experimental

The bulk glass sample of $\text{Ni}_{15}\text{Pt}_{60}\text{P}_{25}$ alloy was prepared by rapidly casting the liquid metal alloy in a mold with 2mm in thickness, 10mm in width and 50mm in deepness.

The samples prepared were characterized by a conventional X-ray diffraction and a differential scanning calorimetry(DSC).

By X-ray diffraction measurement, no evidence was observed for the crystallization of the samples before and after the small angle neutron scattering measurement.

The thermal measurement was performed by using the SEIKO DSC-220 apparatus. The glass transition temperature (T_g) and the crystallization temperature (T_x) were determined $T_g = 488$ K and $T_x = 544$ K respectively with a heating rate of 40 K/min.. We found that the samples could be heated up to at 55 K above T_g before crystallization sets in.

The small angle neutron scattering measurements were performed on the SANS-U spectrometer, which was installed at a cold neutron guide of the research reactor JRR-3M in Japan Atomic Energy Institute (JAERI).

A 2-dimensional neutron counter was located at the position 4m far back from the sample. By using this condition, the small angle neutron scattering intensity $S(Q, t)$ could be measured in the momentum transfer range of $0.008 < Q < 0.08 \text{ \AA}^{-1}$. The sample was heated by two infrared lamps simultaneously from the top and bottom of the sample. When the measurement started the isothermal holding temperature $T_a = 483\text{K}$ was reached within 1 min. from the room temperature. During the measurement, the temperature at the sample was controlled at $T_a = 483\text{K}$ within an accuracy of $\pm 0.1\text{K}$. After heating the sample by infrared lamps for 720 min., the sample was cooled down by a thermal radiation to the

temperature below 373K within 3 min. and then reached to room temperature(20 °C) within 20 min. The measurement was continued for 840 min. and the $S(Q,t)$ data were stored at every 30 min.

§3. Results and Discussions

Figure 1 shows the isothermal evolution of small angle neutron scattering intensity $S(Q,t)$ from the bulk metallic glass $\text{Ni}_{15}\text{Pt}_{60}\text{P}_{25}$ alloy hold isothermally at $T_a=483\text{K}$ for various different holding times. In Fig. 1 the $S(Q,t)$ for every holding time shows a Q^{-4} dependence and no peak structure in the Q -range of $0.008 < Q < 0.05 \text{ \AA}^{-1}$. This means that there is no evidence for any decomposition and any phase separation to occur at least in several nanometer scale in this alloy even after isothermal annealing at $T_a=483\text{K}$ for 720 min..

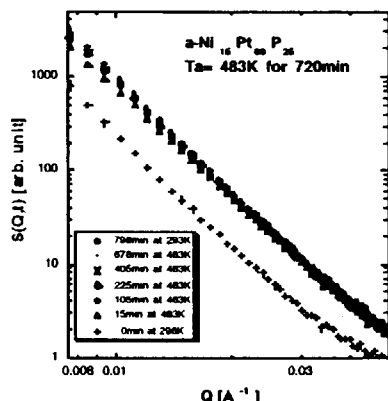


Fig.1. The small angle neutron scattering intensities $S(Q,t)$ from a bulk metallic glass $\text{Ni}_{15}\text{Pt}_{60}\text{P}_{25}$ sample isothermally hold at $T_a=483\text{K}$ for various different times. The $S(Q,t)$ at each holding time shows a Q^{-4} dependence and no peak structure in the Q -range of $0.008 < Q < 0.05 \text{ \AA}^{-1}$.

Figure 2 shows the small angle neutron scattering intensities $S(Q,t)$ as a function of momentum transfer and the holding time at the temperature $T_a=483\text{K}$ below T_g . The $S(Q,t)$ at each momentum transfer Q shows the same isothermal evolution of long range fluctuations as a function of

time and can be scaled in the same curve. The $S(Q,t)$ drastically increases with time in the beginning and then reaches asymptotically to saturated values. Immediately after heating the sample for 720 min., the $S(Q,t)$ suddenly increases about 10% in the all momentum transfer region observed and thereafter keeps constant values within statistical error at room temperature.

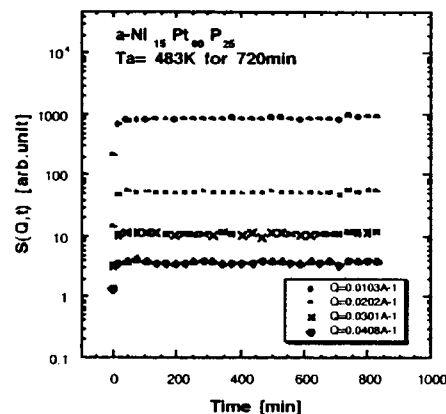


Fig.2. The small angle neutron scattering intensities $S(Q,t)$ as a function of holding time during isothermal annealing at $T_a=483\text{K}$ below T_g at various different momentum transfer values.

The origin of the small-angle intensity is not clear at the present stage in this study. Nevertheless, the increase in the small angle scattering intensity suggests the development of long-range fluctuations just below the glass transition temperature.

It will be necessary for us to investigate the short-range structure derived from the observation of $S(Q,t)$ in the higher Q region, as well as the long-range structure from the small angle scattering. To reveal further the structural properties of this bulk metallic glass around T_g , detailed measurements are in progress.

Reference

- 1). Kaoru. Shibata, Takeshi Higuchi, An-Pang Tsai, Masayuki Imai and Kenji Suzuki
Progress of Theoretical Physics Supplement 126 (1997) 75-78.

研究テーマ：水-プロパノール系におけるクラスター形成とクラスターの内部構造

表題：水-プロパノール系におけるクラスター形成とクラスターの構造

1-4-6

Formation and Structure of Clusters in 1-Propanol-Water Solution

M. Misawa, K. Yoshida¹, H. Munemura¹, Y. Hosokawa¹, K. Maruyama, M. Nagao², M. Imai³

Department of Chemistry, Faculty of Science, Niigata University, Niigata 950-2181, Japan

¹Graduate School of Science and Technology, Niigata University, Niigata 950-2181, Japan

²The Institute of Solid State Science, The University of Tokyo, Tokai 319-1195, Japan

³Department of Physics, Ochanomizu University, Tokyo 112-0012, Japan

Water and 1-propanol mix in any proportion and at any temperature between 0 and 100°C. However, when a small amount of salt such as KCl is added into the solution, the phase separation occurs at a finite temperature range between a lower temperature T_L and an upper one T_H ¹. We examined the structural evolution of concentration fluctuation induced by salt in the solution by means of small-angle neutron scattering.

Figure 1 shows the scattered intensity $I(Q)$ measured by using SANS-U for the $(C_3H_7OD)_1-(D_2O)_5$ solution including about 2mol% KCl in the lower one phase region. The curve (a) is just below the T_L , while the curve (b) is far below the T_L . The $I(Q)$ data in the region of Q greater than 0.03 \AA^{-1} were obtained by using WINK at KEK and are also included in this figure. We carried out the SANS-U measurements for the same solution at various temperatures between 20 and 37°C in the lower one phase region and furthermore between 63 and 76°C in the upper one phase region. All $I(Q)$ curves studied are fitted very well with the scattering function for a fractal structure² given by a correlation function $g(r)=\delta(r)+(A/r^{3-d_f})\exp(-r/\xi)$ with a fractal dimension d_f and a

correlation length ξ . A common fractal dimension of $d_f=1.9$ is obtained despite of the lower and upper one phase regions. Furthermore, the correlation length ξ diverges similarly in both regions. It is concluded that the structural evolution of the concentration fluctuation has a common fractal nature in both the lower and upper one phase regions.

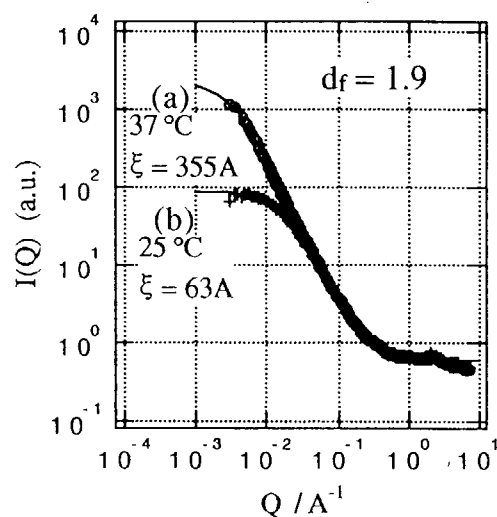


Fig. 1 Small-angle neutron scattering intensity $I(Q)$. Solid curves show fitted results.

1. G. M. Schneider, *Ber. Bunsenges. Physk. Chem.* 1972, **76**, 325.

2. T. Freltoft, K. Kjems and S. K. Sinha, *Phys. Rev.*, 1986, **B33**, 269.

JRR-3M, SANS-U, 4. amorphous & liquid

研究テーマ：液体カルコゲンの中性子小角散乱
表題：液体セレンの中性子小角散乱測定

1-4-7 SANS Measurements of Liquid Se

M. Inui, K. Maruyama¹, Y. Kawakita², S. Takeda², and M. Imai³

*Faculty of Integrated Arts and Sciences, Hiroshima University,
Higashi-Hiroshima 739-8521, Japan*

¹ *Faculty of Science, Niigata University, Niigata 951-2181, Japan*

² *Faculty of Science, Kyushu University, Ropponmatsu, Fukuoka 810-8560, Japan*

³ *Faculty of Science, Ochanomizu University, Tokyo 112-8610, Japan*

Liquid Se is one of typical liquid semi-conductors and it has twofold coordinated chain structure where atoms are covalently bonded. Near the melting temperature, chain molecules in liquid Se are known to consist of 10^4 - 10^5 atoms and the viscosity of liquid Se is large. With increasing temperature, the viscosity decreases while magnetic susceptibility of liquid Se increases. These results together with those of nuclear magnetic resonance measurements suggest that the chain becomes short with increasing temperature. The electrical properties of liquid Se concern with the chain structure. As temperature is raised and the volume is expanded, the electrical conductivity of liquid Se becomes large. It is noteworthy that there appears metallic fluid Se in the supercritical region at high temperature and pressure, where the average chain length is about 10. Inui et al. [1] have carried out small angle x-ray scattering measurements for supercritical fluid Se and observed critical scattering of fluid Se for the first time. Large density fluctuation and very short chain molecules in the supercritical fluid are considered to induce the metallic state.

It is interesting to study the correlation between chains and density fluctuation in liquid Se. Density fluctuations in liquid Se are expected to come from the correlation among many kinds of the chain lengths. Small angle scattering (SAS) is a useful probe of observing density fluctuation in such liquid. We have carried out small angle neutron scattering (SANS) measurements on liquid and amorphous Se [2]. In this work, SANS experiments in smaller wave number region were carried out to investigate the origin of the

cluster formation.

SANS measurements were performed using the spectrometer (SANS-U) of the Institute of Solid State Physics, the University of Tokyo, installed at the beam line of a cold source in JRR-3M. The camera length in this work was 12m and the intensity spectra were measured as a function of a wave number, Q , using a two-dimensional counter at 557K, 660K and 762K. Since the scattering intensity from liquid Se is very small, careful treatment in subtracting the background is necessary. The spectra of the empty cell and the dark counts without neutron beam were measured. The subtraction was carried out on the two-dimensional map and SANS spectra, $I(Q)$, were obtained from integrating the two-dimensional data.

After carrying out the careful analysis, the deduced spectra have largely changed compared with the previous ones [2]. The present results show that the intensity of $I(Q)$ is almost equal to background counts, which means no SANS intensity of liquid Se was observed. The SANS intensity observed in the previous experiments should be an error. This fact may suggest that it was not proper that subtraction was carried out after converting two-dimensional data into one-dimensional spectra.

Reference

- [1] M. Inui, Y. Oh'ishi, I. Nakaso, M. H. kazi and K. Tamura, *J. Non-Cryst. Solids*, (1999) in press.
- [2] M. Inui, S. Takeda, K. Maruyama, Y. Kawakita, S. Tamaki, M. Imai, *Physica B* **213 & 214** (1995) 552.

研究テーマ：3元系マイクロエマルジョンの圧力誘起構造相転移におけるダイナミクス

表題：中性子スピネコー法を用いた3元系両親媒子系複雑液体の温度及び圧力誘起構造相転移におけるダイナミクス

1-4-8 Neutron Spin Echo Studies on Structural Phase Transitions Induced by Temperature and Pressure in a Ternary Complex Fluids involving Amphiphiles

Y.Kawabata*, M.Nagao[†], H.Seto[‡], T.Takeda[‡]

*Graduate School of Bio-Sphere Science, Hiroshima University, [†]Institute for Solid State Physics, The University of Tokyo, 106-1 Shirakata, Tokai 319-1106, [‡]Hiroshima University, Faculty of Integrated Arts and Sciences, Hiroshima University 1-7-1 Kagamiyama, Higashi-Hiroshima 739-8521

A ternary complex fluid involving an ionic amphiphile AOT (dioctyl sulfosuccinate sodium salt) with equal volume fraction of water and oil is known to form a dense water-in-oil droplet structure (RTP phase) at room temperature under ambient pressure. It was reported that a phase transition from the droplet to a lamellar structure occurs with increasing temperature [1]. Recently Nagao *et al* found a similar phase transition occurred with increasing pressure by means of small-angle neutron scattering (SANS) [2]. This experiments also showed that the static features of the high pressure (HP) phases were almost the same as the high temperature (HT) [2, 3]. However, the mechanisms of these phase transitions should be different. In order to clarify the difference of these phase transitions, we investigated dynamic properties of the RTP, HP and HT phases by means of neutron spin echo spectroscopy (NSE).

Intermediate correlation functions $I(Q, t)$ were obtained from NSE experiments. The experiments were performed using the ISSP-NSE at JRR-3M in JAERI, Tokai [4]. The measured momentum transfer Q ranges over $0.04 \leq Q \leq 0.14 [\text{\AA}^{-1}]$ and Fourier time t over $0.15 \leq t \leq 15 [\text{ns}]$. The sample was mixture of 23% of AOT with equal volume fraction of D_2O and n-decane. For the high pressure experiment, a new high pressure cell made of non-magnetic stainless steel was developed,

whose design and performance were the same as the previous one [5]. The experiment was done at 25 °C under 0.1MPa for the RTP, at 40 °C under 0.1MPa for the HT and at 25 °C under 60MPa for the HP.

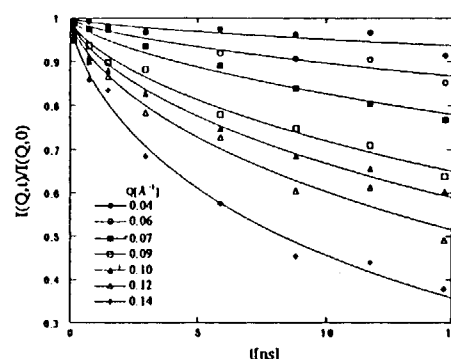


Figure 1: Intermediate correlation function $I(Q, t)$ obtained from the NSE experiments for the RTP. Lines are fitting curves to Eq.(1) with $\beta = 0.67$

Figure 1 shows $I(Q, t)$ obtained from the NSE experiments for the RTP. All $I(Q, t)$ obtained from the NSE experiments could be explained well by a stretched exponential formula as shown in Eq.(1).

$$I(Q, t) = I(Q, 0) \exp[-(\Gamma t)^\beta], \quad (1)$$

where Γ is relaxation rate. The exponent β obtained from the fitting to Eq.(1) was about 0.7. Sheu *et al.* obtained $\beta \sim 0.67$ from the experimental results of quasi-elastic light scattering (QELS) and NSE for the RTP in the same system [6]. Zilman and Granek [7]

derived the stretched exponential relaxation of $I(Q, t)$ shown in Eq.(1) with $\beta = 2/3$ and Γ as follows,

$$\Gamma = [0.025\gamma(k_B T)^{3/2}/\kappa^{1/2}\eta]Q^3, \quad (2)$$

where κ is the bending modulus of the membrane and η the viscosity of the surrounding medium, using a Helfrich bending Hamiltonian in order to describe membrane thermal undulations of sponge and lamellar phases at large Q which is sensitive to single membrane dynamics.

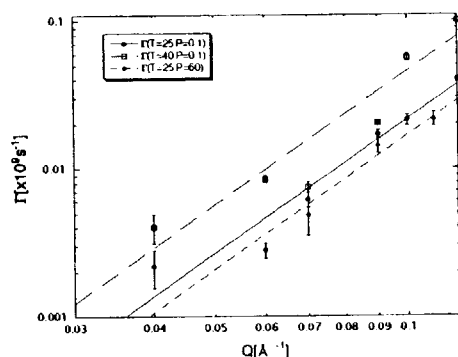


Figure 2: Relaxation rate Γ obtained from the NSE experiments. Lines are fitting one to Eq.(2).

We therefore adopted $\beta = 2/3$ in the fitting. Since the relaxation rate Γ obtained by fitting to Eq.(1) indicated Q^3 proportionality as shown in Fig. 2, we estimated κ using Eq.(2) as shown in Table 1 [8]. κ_{HT} is larger and κ_{HP} smaller than κ_{RTP} . This result indicates that the membranes become flexible with increasing temperature, while they become rigid with increasing pressure.

$\kappa_{RTP} [\times 10^{-20} \text{ J}]$	$\kappa_{HP} [\times 10^{-20} \text{ J}]$	$\kappa_{HT} [\times 10^{-20} \text{ J}]$
1.9	4.1	0.75

Table 1: The bending modulus κ for each phase obtained from the NSE experiments

References

- [1] Chen S.H., Chang S.L. and Strey R., *J.Chem.Phys.*, **93**, 1907-1918 (1990).; Kotlarchyk M., Sheu E. and Capel M., *Phys.Rev.*, **A46**, 928-939 (1992)
- [2] M.Nagao and H.Seto., *Phys Rev.E.*, **59**, 3169-3176 (1999)
- [3] M.Nagao *et al.*, submitted to *J.Phys. Chem.Solids*.
- [4] T.Takeda *et al.*, *J.Phys.Soc.Jpn.*, **65**, Suppl.A 189-194 (1996)
- [5] H.Takeno *et al.*, *Polym.J.*, **29**, 931-939 (1997)
- [6] E.Y.Sheu., S.H.Chen., J.S.Huang and J.C.Sung., *Phys.Rev.A.*, **39**, 5867-5876 (1989)
- [7] A.G.Zilman and R.Granek., *Phys.Rev. Lett.*, **77**, 4788-4791 (1996)
- [8] M.Nagao *et al.*, *Slow Dynamics in Complex Systems*, eds., M.Tokuyama and I.Oppenheim, AIP, New York, P154 (1999) in press

研究課題：両親媒子系複雑液体のスローダイナミクス

表題：中性子スピンエコー法による両親媒子系複雑液体のスローダイナミクス

1-4-9

Neutron Spin Echo Investigation on the Slow Dynamics in Complex Fluids Involving Amphiphiles

T. Takeda, Y. Kawabata, H. Seto, S. K. Ghosh, S. Komura¹, M. Nagao²

Faculty of Integrated Arts and Sciences, Hiroshima University, Higashi-Hiroshima 739-8521

1 Faculty of Science, Ochanomizu University, Ootsuka, Tokyo 112-8610

2 Institute for Solid State Physics, University of Tokyo, Tokai, Naka Ibaraki 319-1106

We have studied slow dynamics in complex fluid systems such as the shape fluctuation of microemulsion droplets, membrane undulation in lipid-bilayers and bicontinuous microemulsions using neutron spin echo (NSE) spectrometer at C2-2 port of JRR-3M, JAERI¹⁾. In order to elucidate the self-assembling mechanisms in complex fluids involving amphiphiles, microscopic parameters like the bending modulus κ on the local scale of the interfacial membrane deduced from dynamical experiments using neutron spin echo (NSE) are important. We present the results of the NSE experiments on the following two systems^{2,3)}; (a) bulk and film contrast samples in the non-ionic surfactant $H(CH_2)_{12}(OCH_2CH_2)_5OH$ ($C_{12}E_5$)/n-octane/ D_2O system at equal volume fraction of octane and water for volume fraction 0.2 of $C_{12}E_5$,

which represents a sequence of low temperature microemulsion(LTM) / lamellar(MTL) / high temperature microemulsion phase(HTM) with increasing temperature, (b) the lipid sample (10wt% dipalmitoylphosphatidylcholine (= DPPC) dispersed in D_2O solutions with 7mM $CaCl_2$) which has the L_α structure with the lamellar repeat distance $d_l = 325 \text{ \AA}$. In the $C_{12}E_5$ /n-octane/ D_2O system, protonated n-octane was used for the bulk contrast samples and deuterated n-octane for the film contrast samples. The LTM and HTM phase have a

bicontinuous structure. The NSE experiments were carried out using MESS at LLB in Saclay as well as the NSE spectrometer at JRR-3M and showed that the performance of the spectrometer at JRR-3M was comparable to that of MESS and that the results obtained using MESS were coherent with that at JRR-3M.

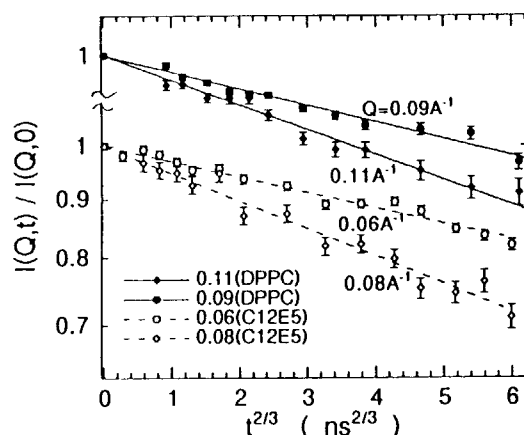


Fig. 1 Intermediate correlation functions $I(Q, t)$ obtained from the NSE experiment in LTM phase of the bulk contrast sample of the $C_{12}E_5$ /n-octane/water system at 21°C (open circles: $Q=0.06\text{\AA}^{-1}$, open diamonds: $Q=0.08\text{\AA}^{-1}$) and the lipid sample (full circles: $Q=0.09\text{\AA}^{-1}$, full diamonds: $Q=0.11\text{\AA}^{-1}$) at 50°C .

As shown in Fig. 1, the intermediate correlation functions $I(Q, t)$ obtained from the NSE experiments were well fitted to the following equation,

$$I(Q, t) = I(Q, 0) \exp[-(\Gamma t)^{2/3}]. \quad (1)$$

Facilities and Instruments

JRR-3M NSE (C2-2)

Research field

4. Amorphous & Liquid

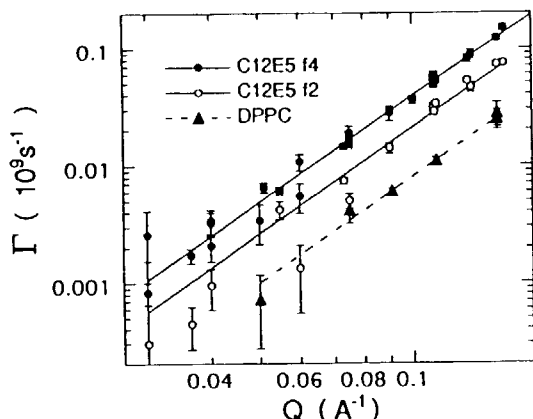


Fig. 2 The dependence of the relaxation rate Γ on Q obtained using the fitting to Eq.(1) in the LTM(open circles) and HTM phase(full circles) of the film contrast sample of the $C_{12}E_5$ /n-octane/water system and the lipid sample (full triangles). The lines are fitting curves to Eq.(2).

The relaxation rate Γ obtained from the fitting to Eq.(1) increased as Q^3 as shown in Fig. 2. These results support the theory presented by Zilman and Granek⁴⁾. They used the Helfrich bending free energy to describe membrane undulations in sponge and lamellar phases and predicted a relaxation of Eq.(1), where

$$\Gamma = 0.025\gamma (k_B T / \kappa)^{1/2} (k_B T / \eta) Q^3. \quad (2)$$

Here, κ is the bending modulus of the membrane and η the viscosity of the surrounding medium. Figure 3 shows κ estimated in the $C_{12}E_5$ / n-octane / water system using Eq.(2), where we put $\gamma = 1$ and used 3 times the value of average solvent viscosities η_{solvent} for η taking the local dissipation at the membrane into consideration. κ decreases monotonously with increasing temperature independently of the mesoscopic structure and the scattering contrast. κ in 10 wt% DPPC - D_2O with $CaCl_2$ of 7 mM at 50 °C was estimated to be

$5.8 \times 10^{-20} \text{ J}$ using the similar procedure and $\eta = 4 \eta_{\text{solvent}}$.

References

1. T. Takeda , H. Seto, S. Komura, S. K. Ghosh, M. Nagao, J. Matsuba, H. Kobayashi, T. Ebisawa, S. Tasaki, C. M. E. Zeyen, Y. Ito, S. Takahashi, H. Yoshizawa: J. Phys. Soc. Jpn. 65 Suppl.A, 189-194 (1996).
2. T. Takeda, Y. Kawabata, H. Seto, S. Komura, S. K. Ghosh and M. Nagao: Slow Dynamics in Complex Systems, eds. M. Tokuyama and I. Oppenheim, AIP, New York, 1999, p.148.
3. T. Takeda, Y. Kawabata, H. Seto, S. Komura, S. K. Ghosh, M. Nagao, D. Okuhara : J. Phys. Chem. Solids (1999) in press.
4. A. G. Zilman and R. Granek: Phys. Rev. Letters 77, 4788-4791 (1996).

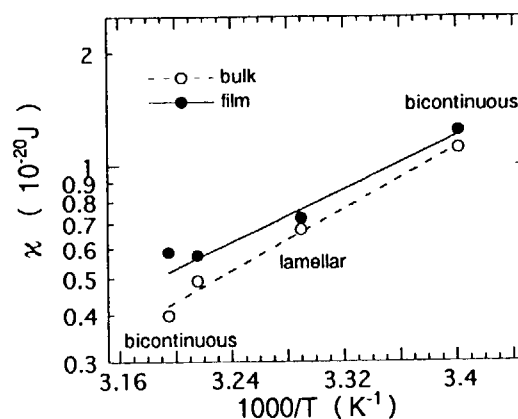


Fig.3 The dependence of bending modulus κ of the membrane on the temperature T obtained from NSE experiments of the bulk(open circles) and film sample(full circles) in the $C_{12}E_5$ / n-octane / water system. The lines which are a guide for the eye are fitting curves to an exponential function $\kappa = a \exp(- b/T)$, where a and b are constant .

研究テーマ：多価アミン-多価アルコール二成分系におけるボゾンピークの組成依存性
表題：多価アミン-多価アルコール二成分系におけるボゾンピーク強度の組成依存性

1-4-10

Composition Dependence of Boson Peak Intensity in Polyamine-Polyalcohol Binary Mixture

K. Takeda, K. Harabe[†], O. Yamamuro[†], I. Tsukushi^{‡,*} and T. Kanaya[‡]

Dept. of Chemistry, Naruto Univ. of Education, Naruto, Tokushima 772-8502 Japan

[†]Dept. of Chemistry, Grad. Sch. of Science, Osaka Univ., Toyonaka, Osaka 560-0043 Japan

[‡]Inst. for Chemical Research, Kyoto Univ., Uji, Kyoto 611-0011 Japan

The boson peak, which is observed at 2-5 meV in most of amorphous materials, has been studied in many ways. Although some theoretical models have been proposed, its origin still remains open to question. We have studied^{1,2)} on the boson peaks of some simple molecular glasses. Their peak energy and intensity can be explained by assuming cluster-like structure in the glass and the libration of the cluster in strained and disordered fields.

On the other hand, it is reported that polyamine-polyalcohol mixture shows a maximum in the composition dependence of glass transition temperature T_g .³⁾ This phenomenon was explained as a result of the increase in the number of hydrogen bond per unit volume on mixing. Therefore, the study on the boson peak of polyamine-polyalcohol mixture enables us to examine the effect of the hydrogen-bond density on the boson peak, giving a significant information on the origin of the boson peak. We have measured the inelastic neutron scattering spectra and heat capacities of several binary mixtures between 1,2-propanediamine (12PDA) and 1,3-propanediol (13PDO).

The inelastic neutron scattering data were collected at around 103 K by a pulsed cold neutron scattering spectrometer AGNES of Institute for Solid State Physics, the University of

Tokyo. It is installed on C3-beamline of JRR-3M at Tokai. The heat capacity measurements were carried out with an adiabatic calorimeter of Osaka University.

In Figure 1, the dynamic structure factor $S(Q, E)$ and heat capacity C_p divided by cubic temperature T^3 are plotted against energy transfer ΔE and temperature T , respectively. The plotted $S(Q, E)$ is the average of the data with different momentum transfers over 1.7-2.6 Å⁻¹; $Q_{av} = 2.1$ Å⁻¹. The peaks in both quantities

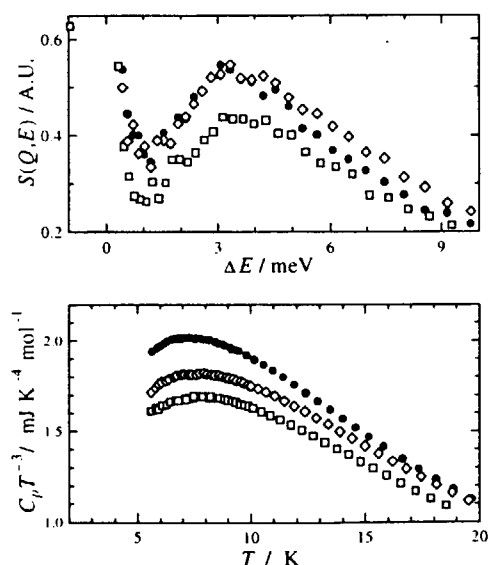


Figure 1. Dynamic structure factors (upper) and heat capacities divided by T^3 (lower) of (12PDA)_x(13PDO)_{1-x} system for $x = 0.1$ (●), 0.5 (□) and 0.9 (◇).

are attributed to the boson peak. In the upper part of Figure 2, peak intensities I_{\max} of $S(Q,E)$ and maximum values of $C_p T^3$ are plotted as functions of x . The intensity of boson peak shows a clear minimum in the intermediate concentration region for both quantities. The peak energy of $S(Q,E)$ and peak temperature of $C_p T^3$ are plotted in the lower part of Figure 2. The peak energy may have a maximum in the intermediate concentration region though it is not clear for the heat capacity data. The tendency that I_{\max} decrease as the E_{\max} increase is consistent with that obtained for some alcoholic glasses⁴⁾.

If the development of hydrogen bond structure causes the magnification of the cluster in the glass, the total degrees of freedom for the libration should decrease because each cluster has 3 degrees of freedom for the libration. Thus the decrease of the boson peak intensity observed in the INS spectra and heat capacity data is explained as the decrease of the number of oscillators responsible for the boson peak.

References

1. O. Yamamuro *et al.*, *J. Chem. Phys.*, **105**, 732 (1996).

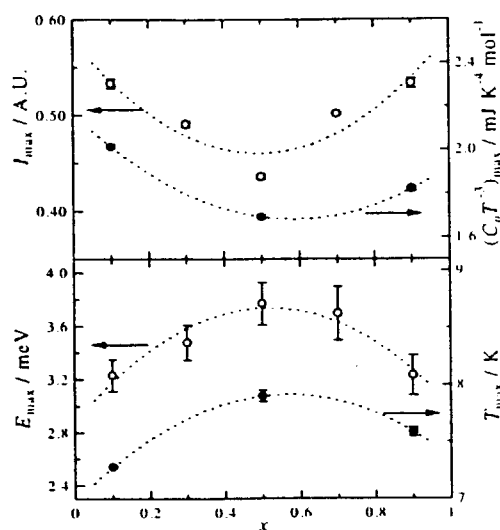


Figure 2. Maximum values of $S(Q,E)$ and $C_p T^3$ (upper), and energy value E_{\max} at maxima of $S(Q,E)$ and temperature T_{\max} at the peak in $C_p T^3$ (lower) for $(12\text{PDA})_x(13\text{PDO})_{1-x}$. The dotted lines are guide for the eyes.

2. O. Yamamuro *et al.*, *J. Chem. Phys.*, **106**, 2997 (1997).
3. K. Takeda, *et al.*, *J. Phys. Chem.*, **103**, 3457 (1999).
4. O. Yamamuro *et al.*, *ISSP Activity Report*, **5**, 177 (1998).

*Present address: Department of Physics, Chiba Institute of Technology, Narashino, Chiba 275-0023, Japan.

研究テーマ：部分的重水素置換によるアルコールガラスのボゾンピークの研究
 表題：部分的に重水素置換したアルコールガラスのボゾンピーク

1-4-11 Boson Peaks in Partially-deuterated Alcohol Glasses

O. Yamamuro, K. Harabe, I. Tsukushi ^{1,*}, T. Kanaya ¹, and T. Matsuo

*Department of Chemistry, Graduate School of Science, Osaka University,
 1-1 Machikaneyama-cho, Toyonaka, Osaka 560-0043, Japan*

¹ Institute for Chemical Research, Kyoto University, Uji, Kyoto 611-0011, Japan

Introduction

A broad excitation peak is observed at 2—5 meV in Raman and neutron scattering spectra of amorphous solids. This peak is usually called "boson peak" from the temperature dependence of the peak intensity. It is of interest that this phenomenon is universal for any kinds of amorphous materials with different structures and interparticle interactions, e.g., for network glasses, molecular (van der Waals) glasses, and polymer glasses. The origin and the microscopic mechanism of the boson peak have not been explained with sufficient generality though a number of studies have been done in the last 20—30 years [1].

Hydrogen-bond glasses are important for the study of the boson peak because they are structurally intermediate between covalent-bond network glasses and molecular glasses. Last year, we reported on the boson peaks of several mono- and polyalcohol glasses [2-4]. The most interesting result was that the boson peak intensity decreases and the peak energy increases as the number of carbon atoms bonded with hydrogen-bonding oxygen increases.

In the present study, we have measured inelastic neutron scattering (INS) of fully and partially deuterated propanol ($T_g = 98$ K) and glycerol ($T_g = 185$ K). The samples studied were as follows: propanol- d_8 ($CD_3CD_2CD_2OD$), propanol- d_7 ($CD_3CD_2CD_2OH$), propanol- d_1 ($CH_3CH_2CH_2OD$), glycerol- d_8 [$(CD_2(OD)CD(OD)CD_2OD)$], glycerol- d_3 [$CH_2(OD)CH(OD)CH_2OD$], glycerol- d_5 [$CD_2(OH)CD(OH)CD_2OH$]. Since the incoherent scattering from hydrogen atoms is dominant for these samples, one can separately see the density of vibrational states associated with hydrogen-bonding part or non-hydrogen-bonding part.

Experimental

INS experiments were performed with a direct geometry chopper-type TOF spectrometer AGNES (C3-1-1) installed at the cold neutron source of JRR-3M (Tokai, Japan) [5]. The wavelength of the incident neutron

(selected by PG(002) monochromators) was 4.22 \AA (4.59 meV). The energy resolution was 0.1 meV and the energy window was < 30 meV. In our experiment, 61 ^3He tube counters were installed at $2\theta = 70\text{--}130^\circ$ with the step of 1° . This counter arrangement covers the scattering vector Q region of $1.7\text{--}2.6 \text{ \AA}^{-1}$ for elastic scattering.

All of the samples (purity: ca. 99 %) were purchased from CDN isotope and used without purification. The liquid samples were confined in a concentric double-cylinder aluminum can (35 mm in height, 14.5 mm in outer diameter of the outer cylinder, 12 mm in outer diameter of the inner cylinder, 0.25 mm in thickness of both cylinders) using an indium gasket. The thickness of the sample was selected in the range 0.5—2 mm to adjust the transmission of neutron beam to about 75—80 %. Propanol and glycerol samples were measured at 94 K and 180 K, respectively. These temperatures are a few Kelvin lower than the respective glass transition temperatures. The duration of the measurement was 20—30 h for each sample.

The raw scattering data, neutron counts (I) against time-of-flight (t_f), were processed into the dynamic structure factor $S(Q, E)$ by correcting for the effects of the background, counter efficiency, Jacobian dt_f/dE , etc. in the standard way.

Results and Discussion

Figures 1 and 2 show the $S(Q, E)$ of propanol and glycerol glasses, respectively. The data of fully protonated samples are also plotted for comparison. All of the data from different counters were summed up to improve counting statistics; the average Q value for elastic scattering was 2.0 \AA^{-1} . The data were scaled by dividing the integrated intensity for each sample. A boson peak appeared in all of the samples. The peak energy was ca. 2 meV for propanol and ca. 3.5 meV for glycerol. It is very interesting that the $S(Q, E)$ curves of the four different samples coincide with each other for both propanol and glycerol. The present result indicates that the hydrogen-bonding and non-hydrogen-bonding (alkyl)

parts contribute to the boson peak cooperatively. It was found to be a wrong model that the libration of alkyl group is the origin of the boson peak.

Recently a generalized model for the boson peak was proposed by Nakayama [6]. This model, which is called the broken-network model, assumes one dimensional main chains and side chains randomly attached to the main chain. The force constant between the adjacent particles inside the main chain is larger than that between the adjacent main- and side-chain particles. The number of the main-chain particles is larger than that of the side-chain particles. Lattice dynamics calculation showed the occurrence of strongly localized vibration corresponding to the boson peak as the collective anti-phase vibration of the main- and side chain particles.

If the hydrogen-bond network of alcohol glasses is regarded as the main chains and the non-hydrogen-bonding part (alkyl group) the side chain, the present results for partially deuterated propanols and glycerols agree neatly with the broken-network model. The substance dependence of the boson peak energy and intensity, which was described in Introduction, also agreed with the tendency predicted by the broken-network model [4].

References

- [1] For example; U. Buchenau, in *Dynamics of Disordered Materials*, edited by D. Richter, A. J. Dianoux, W. Petry, J. Teixeira (Springer, Berlin, 1989).
- [2] O. Yamamuro, K. Harabe, K. Takeda, I. Tsukushi, T. Kanaya and T. Matsuo, ISSP Activity Report 5, 177 (1998).
- [3] O. Yamamuro, Proceedings of International Workshop on JHF Science (JHF98) (KEK Proceedings 98-5), Vol. III, 160 (1998).
- [4] O. Yamamuro, K. Harabe, K. Takeda, I. Tsukushi, T. Kanaya and T. Matsuo, *J. Chem. Phys.*, submitted.
- [5] T. Kajitani, K. Shibata, S. Ikeda, M. Kohgi, H. Yoshizawa, K. Nemoto, K. Suzuki, *Physica B* **213&214**, 872 (1995).
- [6] T. Nakayama and N. Seto, *J. Phys.: Cond. Matter* **10**, L41 (1998).

* Present address: Department of Physics, Chiba Institute of Technology, Narashino, Chiba 275-0023, Japan.

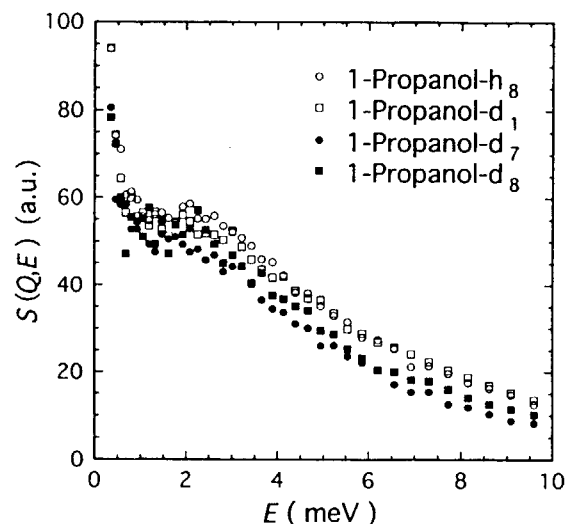


Fig. 1 $S(Q,E)$ spectra of partially deuterated propanol glass measured at 94 K. The average Q value for elastic scattering is 2.0 \AA^{-1} .

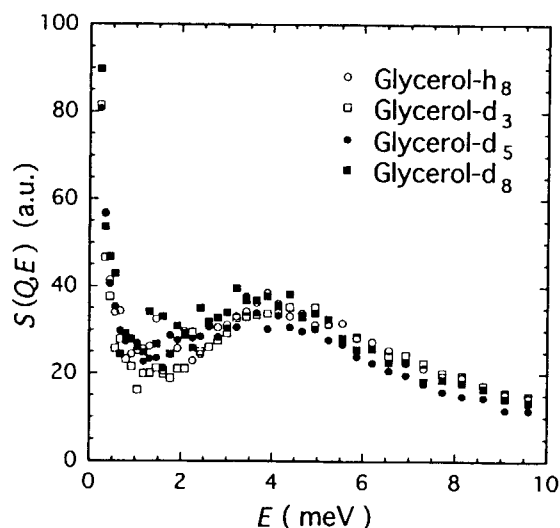


Fig. 2 $S(Q,E)$ spectra of partially deuterated glycerol glass measured at 94 K. The average Q value for elastic scattering is 2.0 \AA^{-1} .

研究テーマ：水-プロパノール系におけるクラスター分散に果たす溶媒水の構造化と添加塩効果

表題：水-プロパノール溶液中のクラスター分散に対する添加塩効果の動的側面

1-4-12

Dynamical Aspects for Salt Effect on the Distribution of Clusters in 1-Propanol-Water Solution

M. Misawa, K. Yoshida¹, H. Munemura¹, Y. Hosokawa¹, K. Maruyama and T. Kajitani²

Department of Chemistry, Faculty of Science, Niigata University, Niigata 950-2181, Japan

¹Graduate School of Science and Technology, Niigata University, Niigata 950-2181, Japan

²Graduate School of engineering, Tohoku University, Sendai 980-8579, Japan

The water and 1-propanol mix in any proportion at any temperature between 0 to 100°C. However, by the addition of small amount of salt, the solution separates into two liquid phases in some limited temperature range between lower- and upper- phase separation temperatures [1]. We intended to study the microscopic origin of this phase separation phenomenon, especially a role of salt.

We carried out quasi elastic neutron scattering (QES) measurements by using AGNES spectrometer on the solutions of a composition of $(\text{H}_2\text{O})_5 - (\text{C}_3\text{D}_7\text{OH})_1$ with KCl [HPK] and without KCl [HP2]. For reference, we measured also the spectra on pure water (H_2O) and $(\text{H}_2\text{O})_{37} - (\text{C}_3\text{D}_7\text{OH})_3$ solution [HP1].

Figure 1 shows the QES spectra measured at 25°C in the lower one phase region. The addition of 1-propanol molecules into water makes the FWHM of the QES spectra narrower significantly, suggesting the suppress of the motion of H_2O molecules in the 1-propanol solution.

The QES spectra were analyzed by using a jump diffusion model [2] in which two characteristic times are important

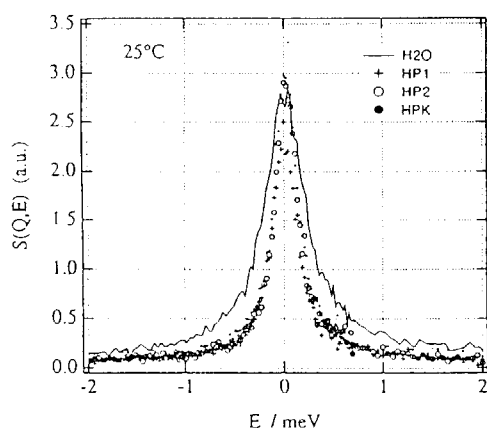


Fig. 1. QES spectra measured at 25°C and $Q=1.22 \text{ \AA}^{-1}$ for 4 samples (see text).

parameters: a mean resident time τ_0 for a jump diffusion and a relaxation time τ_1 associated with rotational diffusion. A typical example of the fit to the QES spectra based on the above model are given in Fig. 2. The values of τ_0 estimated at 25°C is 1.0 ps for pure water, 2.2 ps for the 1-propanol solution without KCl, and 2.0 ps for the solution with KCl. These results imply that the motion of H_2O molecules in the H_2O -1-propanol solution is much suppressed compared to pure water, while this suppression seems to be recovered in part by the addition of KCl. The change in motion of H_2O molecules induced by small amount of KCl may be responsible to the phase separation in this system.

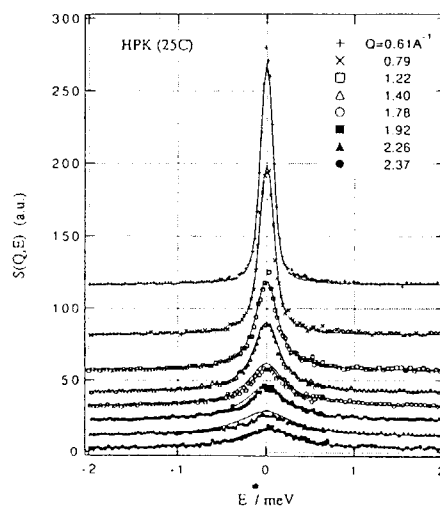


Fig. 2. Comparison of fitted and observed $S(Q,E)$ for the solution with KCl [HPK].

References

1. G.M.Schneider, Ber. Bunsenges. Physk. Chem. 76, 325 (1972).
- 2 J. Teixeira, M. C. Bellissent-Funel, S. H. Chen and A. J. Dianoux, Phys. Rev. A31, 1913 (1985).

研究テーマ 非弾性中性子散乱法によるオレイン酸の分子委運動の研究
表題 配向オレイン酸結晶の中性子非干渉性非弾性散乱

1-4-13 NEUTRON INCOHERENT INELASTIC SCATTERING OF ORIENTED OLEIC ACID CRYSTAL

Tomoyuki YOKOYAMA, Norio ACHIWA and Masao SUZUKI⁴

Department of Physics, Kyushu University, Fukuoka, 8128581, Japan

⁴Nippon Oil and Fat Co.ltd., Amagasaki, Hyogo, 580, Japan

1 INTRODUCTION

The neutron incoherent inelastic scattering of oriented polyethylene along chain compound shows anisotropic phonon modes[1]. Oleic acid, a typical finite polymethylene compound whose internal molecular vibration were reported by Kobayashi et al. by using infrared absorption and Raman scattering [2].

Oleic acid molecular crystal consists of a couple of finite polymethylene chains connected by ethylene double bond carbons; molecular formula is $\text{CH}_3(\text{CH}_2)_7\text{CH}=\text{CH}(\text{CH}_2)_7\text{COOH}$. Above a melting point it shows liquid crystal phase. On cooling at the rate of 1-2°C per hour, a crystallization from liquid crystal to α crystal phase occurs at 286K, and a transition from α phase to γ phase at 270K. The α phase crystal is melted and kept at 13-14°C, then the α phase transforms to β phase.

In the β crystal, the chain molecules align along the c-axis. Then, it is expected anisotropic phonon modes such as an accordion mode and a twisting mode for the finite chain. In order to investigate such anisotropic low energy molecular motional modes, we have performed the neutron incoherent inelastic scattering experiment of the orientated oleic acid crystal. It is important to investigate the lowest excitation of molecular accordion mode in a molecular crystal of finite chain, since it easily couples with lattice modes which are related to the phase transitions such as crystal phase to liquid crystal phase.

2 EXPERIMENTS

In order to get an oriented crystal, a field cooling technique was adopted for ferrofluid solution of oleic acid. The ferrofluid was prepared by solvating 1 weight percent of oleic acid covered-magnetite(Fe_3O_4) particle to ultra pure oleic acid liquid(99.9 %, supplied by M.Suzuki on Nippon Oil and Fat Co.ltd.). Since the neuron total scattering length of magnetite particle is very weak comparing with that of hydrogen atoms of oleic acid, and even magnetite particle concentration is small, so the effect of the scattering from magnetite can be ignored. A strong magnetic field tends to align the magnetic particles along the magnetic field in liquid crystal phase. Then the sample was cooled down below the melting point, 286K of oleic acid, under applied magnetic field 0.6T. The solvent oleic acid is crystallized as β phase with the direction of the hydrocarbon chain perpendicular to the applied field but in the horizontal plane. In this experiment the magnetic field was applied in the horizontal scattering plane of neutron.

The inelastic incoherent neutron spectra of the oriented oleic acid crystal were measured with time-of-flight neutron spectrometer AGNES with an incident neutron energy 4.59meV, installed at the cold neutron guide, C3-1-1, in JRR-3M[3]. 61 detectors of the spectrometer cover the angle region from 25° to 130°. The sample was contained in a cylindrical aluminium tube of diameter 15mm. The sample had been cooled down to 276K on the goniometer in the applied magnetic field. After the magnetic field cooling in the horizontal scattering plane, the solid oriented sample can be freely rotated in the plane. The spectra

were measured at 276K along four different directions angled 45 degrees, step by step. In the time-of-flight experiment the direction of scattering vector varied according to the time channel of each counter. So the direction dependence of phonon scattering function is obtained by summing up the data in the range of 10 degrees of each Q direction.

3 RESULTS

Figure 1 shows the anisotropic phonon scattering function, which is normalized as follows for the neutron energy gain case,

$$G(Q, \omega) = \frac{4\pi m_n}{Q^2 \hbar^2} \frac{\omega}{e^{2W(Q)} n(\omega)} S(Q, \omega) \quad (1)$$

This shows anisotropic phonon contribution to the phonon density of state.

Molecular formula of oleic acid is $\text{CH}_3(\text{CH}_2)_7\text{CH}=\text{CH}(\text{CH}_2)_7\text{COOH}$ and it makes dimer in the crystal. The crystal constants of β phase is $a=9.3\text{\AA}$ $b=5.5\text{\AA}$ $c=35.3\text{\AA}$ $\alpha=87.9^\circ$ $\beta=82.8^\circ$ $\gamma=86.2^\circ$. The c-axis is approximately parallel to the molecular chain.

A 4meV peak which only appears along the c-axis might corresponds to the zone boundary phonon mode of which corresponds to the Van der Waals interaction between dimers along the c-axis.

8meV and 16meV peaks appear only in the phonon scattering parallel to the c-axis but don't in the perpendicular direction. Raman spectra of accordion modes of various polymethylenes were observed by Schaufele et al.[4]. For 18 and 36 carbon atoms of polymethylene chains, the mode energies are about 16meV and 8 meV, respectively, which are inversely proportional to the number of carbon atoms. So the 8meV and 16meV peaks correspond to the one dimer accordion mode and one molecule accordion mode, respectively. At the zone boundaries, one dimer accordion, one molecule accordion modes are that of four molecules, two molecules and one molecule along the c-axis, respectively. So the 4meV mode is assigned to be the zone boundary lattice mode. This hierarchical structure is correspond to the oleic acid crystal structure along the c-axis.

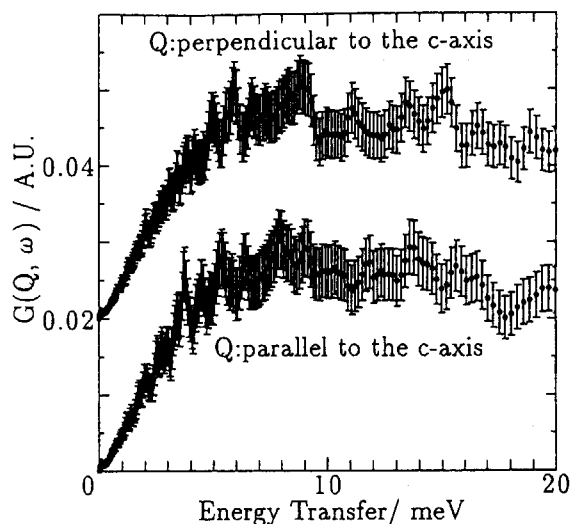


Figure 1: Anisotropic phonon scattering function by crystalline oleic acid at 276K for the scattering Q vector parallel and perpendicular to the chain axis c.

4 CONCLUSIONS

Inelastic incoherent neutron scattering of the orientated oleic acid crystal which was get by a field cooling of ferrofluid state have been measured at 276K. The anisotropic phonon scattering function of finite polymethylene chains in the crystal were observed in this experiment. At these zone boundaries, one dimer accordion and one molecule accordion modes were observed in 4meV, 8meV and 16meV with Q parallel to the c-axis.

REFERENCES

1. Jobic H, J.Chem.Phys. **76**, 2693(1982).
2. Kobayashi M., Kaneko F., Sato K. and Suzuki M., J.Phys.Chem. **90**, 6371(1986).
3. Kajitani T., Shibata K., Ikeda S., Kohgi M., Yoshizawa H., Nemoto K. and Suzuki K., Physica **B213&214**, 872(1995).
4. Schaufele R.F. and Shimanouchi T., J.Chem.Phys. **47**, 3605(1967).

研究テーマ：永久圧縮石英ガラスの低エネルギーダイナミックスの研究

表題：圧縮石英ガラスの低エネルギーダイナミックスの密度依存性

1-4-14

Density dependence of low energy dynamics of densified vitreous silica

Y.Inamura¹, M.Arai¹, O.Yamamuro², A.Inaba², N.Kitamura³, T.Otomo¹, T.Matsuo² and S.M.Bennington⁴, A.C.Hannon⁴

¹Institute of Materials Structure Science, KEK, 1-1 Oho, Tsukuba 305, Japan

²Chemistry Dept., Osaka Univ., 1-1 Machikaneyama, Toyonaka, Osaka 560, Japan

³Government Industrial Research Institute of Osaka, 1-8-31 Midorigaoka, Ikeda, Japan

⁴Rutherford Appleton Laboratory, Chilton, Didcot, Oxon OX11 0QX, UK

Introduction

Low energy dynamics of intermediate range structure (IMRS) is likely responsible for the universal thermodynamic properties of non-crystalline system[1]. Hence, we have modified IMRS of vitreous silica artificially by densification in order to investigate the effects on the thermodynamic properties from the modified structure. We reported the detailed results on the structural and evolution in dynamics[2], which showed a large upward shift of the Boson Peak on densification observed by RAMAN scattering. However, RAMAN scattering does not often give a realistic intensity evolution because of the unknown phonon-photon coupling factor. Hence, we have conducted neutron inelastic scattering studies as well as specific heat (Cp) measurements to elucidate a relation between the evolution of low energy dynamics including Boson peak and low temperature thermodynamics in the absolute value basis.

Experimental

The prepared samples are normal and densified SiO₂ glasses, whose densities are 2.20 g/cc and 2.63±0.03 g/cc. The inelastic neutron scattering experiment was performed on the AGNES spectrometer in JRR-3M facility at the Japan Atomic Energy Research Institute and the MARI spectrometer in the ISIS facility at the Rutherford Appleton Laboratory, UK. For studies in lower energy range, we also used the LAM80ET spectrometer in KENS facility at the High Energy Accelerator Research Organization, Japan. The heat capacity of the densified SiO₂ was measured by using a standard intermittent heating method at Osaka university.

Results

Figure 1 shows the dynamic structure factor S(Q,E), which was obtained by integrating in a Q range from 1Å⁻¹ to 7Å⁻¹. Boson peaks of the normal and densified sample exist at 5meV and 10meV respectively. The intensity drastically decreased on

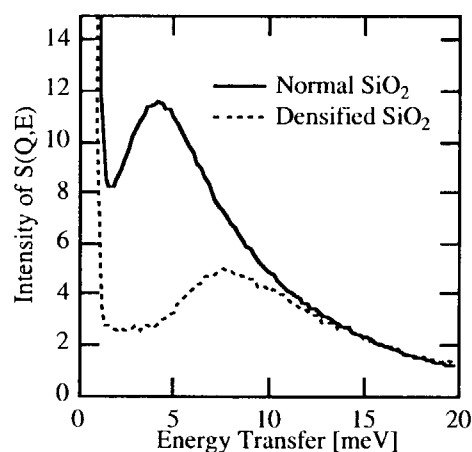


Fig.1. S(Q,E) integrated a Q range from 1 to 7 Å⁻¹ of the normal and densified SiO₂

densification in the low energy region, while the intensities above 12 meV did not show any significant change. Figure 2 shows the vibrational density of states (VDOS) around the Boson peak. The data below 1.2 meV was derived from the measurement on LAM80ET. In the region below 1.2 meV, the ratio of the intensity between the VDOS's of two samples does not have an ambiguity, however, the absolute value was not estimated by the measurement. Therefore, in order to estimate the absolute value of the VDOS below 1.2 meV, Cp was calculated from VDOS by adjusting a constant factor to be multiplied to the VDOS below 1.2 meV until having a reasonable agreement with the observed Cp. Here, the VDOS between 1.2 and 2.0 meV was taken an interpolated value and a constant value below 0.2 meV. The same factor was used to calculate the Cp of the densified sample. In Fig. 3 the observed Cp and calculated one are depicted together with the observed Cp. The observed Cp of the normal SiO₂ are taken from early studies[4]. It is obvious that the decrease in Cp of densified sample is induced from the small change of VDOS around boson peak, which is about 0.5% of the whole VDOS.

Discussion

It has been clarified in the present work that the evolution of the vibrational density of states is not a simple shift on densification as observed by RAMAN scattering[5], which was explained as a phonon scattering by local density fluctuation[6], but it is a suppression of the states in the low energy region. The shift is a result of the suppression. In the structural study we found that a void space shrinks by densification with keeping the tetrahedron structure [2]. Of course the bond angle between SiO_4 units becomes smaller by about 5 degree for the highest density, however, this structural change mainly causes a downward shift of the highest energy mode at 130

meV[3]. Hence, it is natural to consider that the large suppression of the low energy dynamics is related to the shrinkage of the void space[7]. Soft mode in the void space has plausibly been suppressed by its shrinkage, i.e. a constraint for freedom of the soft mode in void space increases by densification. This explanation is consistent with a recent theoretical work on Boson peak by Nakayama[8].

The density of states below 0.5 meV seems to saturate to a value as shown in the inset of Fig.2. Hence, C_p was calculated using the neutron data by assuming a constant density of states by extending the observed value below the minimum energy of 0.2 meV as mentioned in the previous section. In Fig.3 preliminary calculations of C_p for the normal and densified glasses, reasonably reproduces the observed C_p very well. Here we note that the constant value below 0.2 meV is about 6.0×10^{-6} [1/(meV·SiO₂-unit)] for normal sample, which is about one-seventh of the reported results [9]. The ratio between the density of states of the normal and the highest density sample is depicted. It is about 2.0 in the very low energy range, makes a weak hump at about 4 meV near the Boson-peak energy, and gradually becomes unity at about 12 meV. According to the soft potential model, the density of states of the Boson peak is proportional to that of two level system[10], and extends up to a certain energy about 12 meV for vitreous silica [9]. The present results seems to be satisfying these scenario. However, because of a contrary argument from systematic studies[11], we should make a further detailed investigation before making a conclusion.

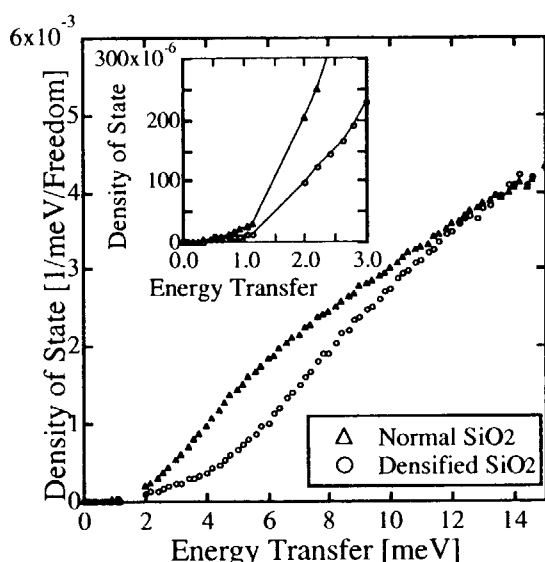


Fig.2. The VDOS for normal and densified SiO₂ in the low-energy region.

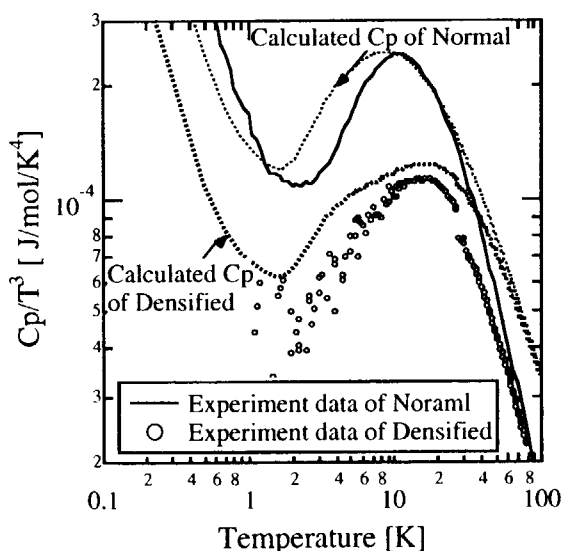


Fig.3. The observed and calculated specific heat for the normal and densified SiO₂

References

- [1] Pohl and Zeller, Phys. Rev. B5 (1971) 2029
- [2] Y.Inamura et al., Physica B 241-243 (1998) 903
- [3] Hiramatsu et. al., Physica B 219-220 (1996) 287
- [4] M.A. Ramos et al., Phys. Stat. Sol. 135 (1993) 477
- [5] S.Sugai and A.Onodera, Phys. Rev. Lett., 77 (1996) 4210
- [6] A.P.Sokolov et al., Phys. Rev. Lett. 69 (1992) 1540
- [7] S.R.Elliott, Phys. Rev. Lett., 67 (1991) 711
- [8] T.Nakayama, Phys. Rev. Lett. 80 (1998) 1244
- [9] U.Buchenau, et al., Phys. Rev. B43 (1991) 5939
- [10] P.W.Anderson et al., Phil. Mag. 25 (1972) 1, W.A.Philips, J.Low Temp. Phys. 7 (1972) 351
- [11] A.P.Sokolov et al., Phys. Rev. Lett. 78 (1997) 2405
- [12] T. Nakayama, J. Phys. : Condens. Matter 10 (1998) L41-L47
- [13] W.A. Philips, J. Low Temp. Phys. 7 (1972) 351

1. 中性子散乱 5) 材料科学

1. Neutron Scattering 5) Material Science

This is a blank page.

研究テーマ: 蛍石関連固溶体の構造変化

表題: 高温中性子回折による ZrO_2 -13mol% $\text{YO}_{1.5}$ における正方-立方相転移のその場観察

1-5-1

In Situ Observations of the Tetragonal-Cubic Phase Transition in the ZrO_2 -13mol% $\text{YO}_{1.5}$ Using High Temperature Neutron Diffraction

Y.Hatoyama, T.Oketani, M.Yashima, Y.Yamaguchi¹, K.Ohoyama¹

Department of Materials Science and Engineering, Interdisciplinary Graduate School of Science and Engineering, Tokyo Institute of Technology, 4259, Nagatsuta-cho, Midori, Yokohama, 226-8502, Japan.

¹Institute for Materials Research, Tohoku University, Katahira, Aoba, Sendai, 980-8577, Japan.

Zirconia ceramics as ZrO_2 - $\text{YO}_{1.5}$ have superior mechanical, electrical, thermal and optical properties. These properties closely have connection with crystal structure. Therefore, many researchers have investigated crystal structures and phase transitions of zirconia ceramics. In zirconia ceramics, the study of diffusionless cubic-tetragonal phase transition is the key to understand structural changes and phase diagram.^{1,2} The cubic-to-tetragonal phase transition is believed to be induced by oxygen displacement. Yashima et al. reported the compositional dependence of oxygen displacement through neutron diffraction study at room temperature. However, there is no detailed knowledge on the temperature dependence of the oxygen displacement, that is of vital importance for the mechanism of this transition. Aldebert and Traverse³ studied this phase transition using neutron powder diffraction and investigated the temperature dependence of lattice parameters and oxygen atomic coordinate z . Yokota⁴ reported in situ

observations of the tetragonal-cubic phase transition using high-temperature neutron diffraction in ZrO_2 - $x\text{mol}\%\text{YO}_{1.5}$ ($x=12$ and 14). In this study, in situ observations of the tetragonal-cubic phase transition are performed using high-temperature neutron diffraction for ZrO_2 -13mol% $\text{YO}_{1.5}$.

A compositionally homogeneous ZrO_2 -13mol% $\text{YO}_{1.5}$ sample was prepared by a polymerized complex method.⁵ Neutron-diffraction measurements were performed using a neutron diffractometer KSD at JRR-3M research reactor of Japan Atomic Energy Research Institute. Neutron diffraction profile was in situ measured in air keeping the sample at a constant temperature in the range of 24°C to 1550°C where the sample was heated using a new furnace for neutron-diffraction measurements.⁴ Neutron wavelength used here was 1.53 \AA . To estimate the oxygen atomic coordinate, profiles of 111 and 112 reflections were measured by a step-scan technique. The atomic coordinate z of oxygen was estimated

JRR-3M, KSD, 5. Materials Science

by following equation¹:

$$z = \frac{1}{4} - \frac{1}{4\pi} \sin^{-1} \left(\frac{b_c}{b_a} \sqrt{\frac{I(102) \cdot L(101)}{I(101) \cdot L(102)}} \right)$$

where $b_c, b_a, I(hkl)$, and $L(hkl)$ denote the average neutron scattering lengths of cation and anion containing vacancies, the integrated intensity of hkl reflection and the Lorentz factor.

Figure 1 shows temperature dependence of 112 peak profile of ZrO_2 -13mol% $\text{YO}_{1.5}$. In neutron diffraction measurements, the intensity of 112 peak, forbidden for cubic phase, decreased from 24°C to 1484°C with increasing in temperature and seemed to disappear between 1484°C and 1556°C. This disappearance indicates that the tetragonal-cubic phase transition occurred at $1520 \pm 36^\circ\text{C}$. Figure 2 shows the relationship between temperature and oxygen atomic coordinate z in ZrO_2 -13mol% $\text{YO}_{1.5}$. Oxygen atomic coordinate z approached the cubic value 0.25 with increasing in temperature.

Acknowledgements

We would like to express our thanks to Prof. M.Yoshimura, M.Kakihana and Dr. O.Yokota for experimental support in preparation of the sample.

References

1. M.Yashima, S.Sasaki, M.Kakihana, Y.Yamaguchi, H.Arashi and M.Yoshimura, *Acta Crystallogr. B* 50, 663-672 (1994).
2. M.Yashima, S.Sasaki, Y.Yamaguchi, M.Kakihana, M.Yoshimura and T.Mori, *Applied Physics Letters*, 72, 182-184

(1998).

3. P.Aldebert and J.P.Traverse, *J.Am.Ceram.Soc.*, 68, 34-40 (1985).
4. O.Yokota, Ph D. Thesis, Tokyo Institute of Technology, (1998).
5. M.Yashima, K.Ohtake, M.Kakihana and M.Yoshimura, *J.Am.Ceram.Soc.*, 77, 2773-2776 (1994); O.Yokota, M.Yashima, M.Kakihana, A.Shimofuku and M.Yoshimura, *J.Am.Ceram.Soc.* 82 in press (1999).

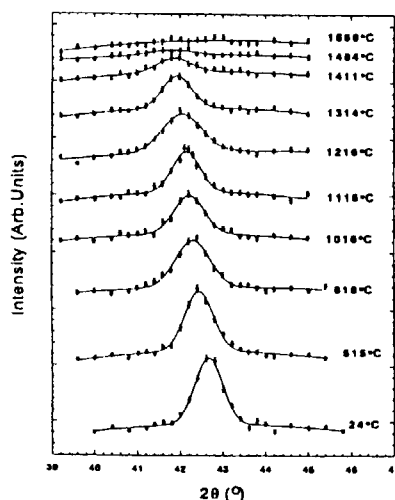


Fig.1 Temperature dependence of 112 peak profile of ZrO_2 -13mol% $\text{YO}_{1.5}$.

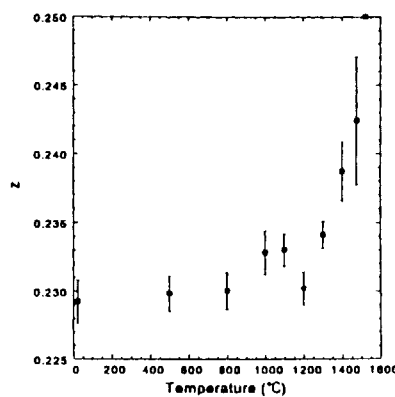


Fig.2 Relationship between temperature and oxygen atomic coordinate z in ZrO_2 -13mol% $\text{YO}_{1.5}$.

研究課題：中性子粉末回折用高温電気炉の開発

表題：高温における材料の構造変化のその場観察：空气中1550°Cで得たデータのリートベルト解析

1-5-2

***In Situ* Observations of the Structural Changes in Materials at High Temperatures: Rietveld Refinements of Data Obtained at 1550°C in Air**

M. Yashima, T. Oketani, O. Yokota, Y. Hatoyama, R. Ali, T. Nogami, S. Utsumi, H. Sugawara, M. Ohashi^{1,2}, K. Ohoyama¹, and Y. Yamaguchi¹

Department of Materials Science and Engineering, Interdisciplinary Graduate School of Science and Engineering, Tokyo Institute of Technology, 4259, Nagatsuta-cho, Midori, Yokohama, 226-8502, Japan.

¹*Institute for Materials Research, Tohoku University, Katahira, Aoba, Sendai, 980-8577, Japan.*

²*Present address: Yamagata University.*

Structural investigation at high temperatures is of vital importance for materials science and engineering, physics, chemistry and geoscience. In materials science, *in situ* measurements of structures at high temperatures can improve (1) the understanding of the structure-property correlation, (2) optimization and understanding of practical use of materials, (3) optimization and understanding of materials processing. Neutron diffraction is a powerful tool for studies of crystal structures of materials containing elements of very dissimilar atomic number or neighboring elements in the Periodic Table. This technique is useful to analyze the thermal motion and disorder because of (1) the lack of electronic interference and of (2) neutron form factor independent of scattering angle. Neutron diffraction at nonambient temperatures has an added advantage over X-ray study: The low absorption of the sample-environment apparatus itself is less damaging to the data quality. Nevertheless, there have been no available high-temperature furnace for neutron-diffraction study above 1000°C in Japan. Therefore, we have constructed a new high-temperature furnace for neutron-diffraction research at HERMES (T1-3) and at KSD (T1-2) at the research reactor JRR-3M, in JAERI. In the present report we describe the design of the new furnace and some of the results obtained by it.

We have designed and fabricated a new electric furnace for neutron diffraction measurements in air at high temperatures up to 1864 K (1591°C). The instrument has been designed as effectively as possible to maximize the neutron-diffraction intensity as well as to suppress the background level and neutron-diffraction intensity from outside the sample. This furnace was also designed to have both a

temperature homogeneity and ease for use. The procedure was as follows:

1. The furnace uses MoSi₂ heaters. The MoSi₂ heater has some advantages: (1) MoSi₂ heater can be used in air, (2) little degradation during usage in air and relatively long lifetime in air comparing with SiC heaters, (3) MoSi₂ heater can make a furnace with a temperature homogeneity comparing with the mirror furnace. (4) No low-temperature degradation occurs which is often seen for the LaCrO₃ heaters.
2. Relatively large samples can be used to increase the neutron scattering intensities. It is advantageous also for the alignment of the furnace.
3. This furnace is not so large that it could be moved by hand on the goniometer stage of HERMES and KSD in JRR-3M, Japan Atomic Energy Research Institute (JAERI).
4. The furnace is made of two parts: upper and lower parts. Thus, the sample can quickly be exchanged without the need for further alignment of the furnace.
5. The body of the furnace was made from aluminum and alumina walls, which enables both ease of manufacturing and the excellent penetration of neutrons. Aluminum wall was used to shield the detector with collimators from the thermal emission. Aluminum wall is as thin as 0.5 mm to avoid any significant absorption and the diameter is as large as 530 mm to keep as low as possible spurious scattering from the walls that might enter the detector. Walls made of porous alumina refractories were also used both to improve the temperature homogeneity of the sample and to protect the aluminum wall against the high

Reactor: (JRR-3M)

Facility: (HERMES (T1-3), KSD(T1-2))

Field: (materials)

temperatures. The alumina wall is as thin as 15 mm to avoid any significant absorption and the diameter is as large as 250 mm to keep as low as possible spurious scattering from the walls that might enter the detector. It should be noted that except for these walls, no part of the furnace is in the path of neutrons from the sample.

6. The part between the furnace and the goniometer-stage was cooled by water, to keep the goniometer at room temperature.

We show two results below. Figure 1 shows the Rietveld pattern of zirconia ceramics obtained at 1550°C at KSD (T1-2 site), where a computer program written by Izumi was used. The reliability factors were $R_{wp} = 12.62\%$, $R_p = 9.53\%$, and $RI = 5.23\%$. Goodness of fit S was 1.12. Figure 2 shows the Rietveld pattern of HERMES (T1-3). The reliability factors were $R_{wp} = 9.97\%$, $R_p = 7.35\%$, and $RI =$

5.68 %. Goodness of fit S was 1.88. It should be noted that no significant peaks from heaters, refractories and sample holder are observed as shown in Figs. 1 and 2. Therefore we can investigate weak reflection peaks and diffuse scattering from samples. Furthermore Rietveld refinements were successfully performed for some samples in the wide range of temperature (300 K-1823 K: 25°C-1550°C) Using this furnace, we have been studying temperature dependence of crystal structures of various materials.

We would like to express our thanks to Mr. S. Hotta (Tokyo-Motoyama-Shokai) and Mr. K. Nemoto (Tohoku University) for the experimental assistance.

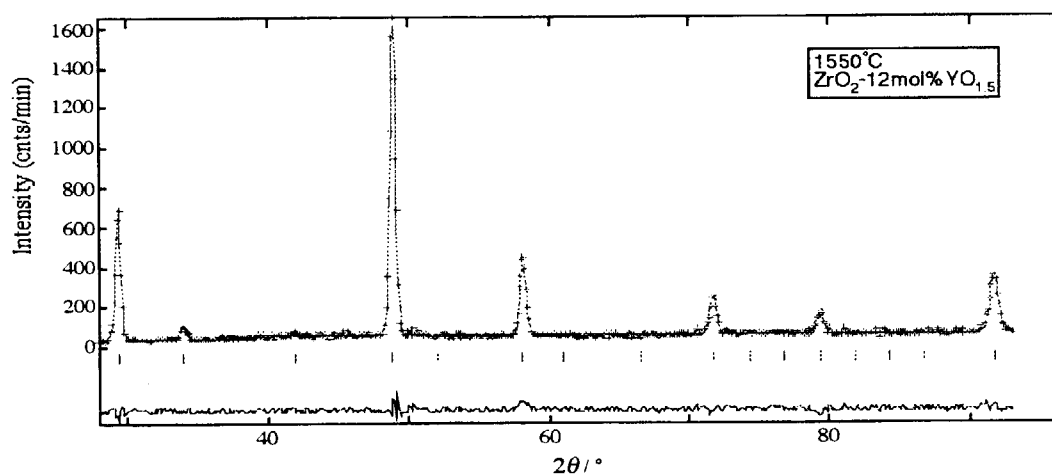


Fig. 1 Rietveld pattern for neutron diffraction data measured at 1550°C at KSD (T1-2).

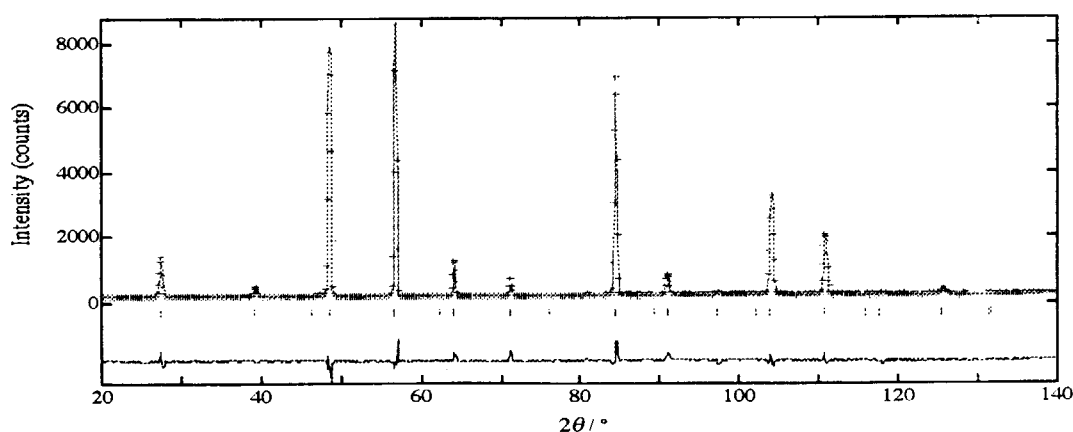


Fig. 2 Rietveld pattern of neutron diffraction data measured at 1550°C using HERMES (T1-3).

研究テーマ：TiCoN_xSn の中性子回折

表題：CoTiSn 窒化生成物の中性子回折による研究

1-5-3 Neutron Diffraction Study on Nitrogenation of CoTiSn

G. Nakamoto, T. Nobata, M. Kurisu, Y. Makihara¹, Y. Andoh², S. Kawano³ and M. Ohashi⁴

*Japan Advanced Institute of Science and Technology,
Tatsunokuchi, Ishikawa 923-1292, Japan*

¹*Physics Department, Kyushu Kyoritsu University, Kitakyushu 807-8585, Japan*

²*Faculty of Education, Tottori University, Tottori 680-8551, Japan*

³*Research Reactor Institute, Kyoto University, Kumatori, Osaka 590-0494, Japan*

⁴*Faculty of Engineering, Yamagata University, Yonezawa 992-8510, Japan*

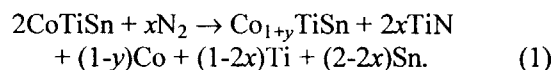
CoTiSn is a ferromagnetic Heusler compound with the MgAgAs-type structure. This crystal structure has four interpenetrating fcc sublattices with a vacancy site. It has been revealed that the magnetic properties of the compound are strongly improved by nitrogenation. Both saturation magnetic moment and the Curie temperature are almost doubled to those of Co₂TiSn with the Cu₂MnAl-type structure where Co atoms fully occupy a vacancy site of the MgAgAs-type structure.

In the present study, we have performed the neutron diffraction measurement on gas-phase nitrogenation products (GPNP) of CoTiSn by using HERMES in order to identify the nitrogenation process of CoTiSn.

Polycrystalline sample was prepared by arc melting the stoichiometric amounts of constituent elements in pure Ar atmosphere. Nitrogenation was performed on the pulverized sample of CoTiSn in N₂ atmosphere. The amount of absorbed nitrogen atoms in GPNP was estimated by the increase of sample mass during nitrogenation process. The sample containing $x=0.45$ nitrogen atoms per a CoTiSn formula was obtained and used for the measurement.

Figure 1 shows the neutron diffraction pattern and the result of the Rietvelt analysis of GPNP of CoTiSn at 20 K. It is confirmed that all the diffraction peaks are indexed as the mixture of Co₂TiSn, TiN and Sn. The Rietvelt analysis indicates that GPNP consists of Co₂TiSn, TiN and Sn in the ratio of 1 : 0.88 : 0.79. In this analysis, R_{wp} and $S(=R_{wp}/R_e)$

factors are 6.99 and 2.46, respectively. Therefore, we propose the following possible nitrogenation process for CoTiSn:



Traces of Co and Ti metals have been not observed in the diffraction pattern. In the case of $x=0.5$ and $y=1$, eq. (1) is given by



The ratio of three components in GPNP obtained by the present analysis is in good accordance with that in eq. (2). Thus we conclude that GPNP of CoTiSn is composed of equivalent molar Co₂TiSn, TiN and Sn.

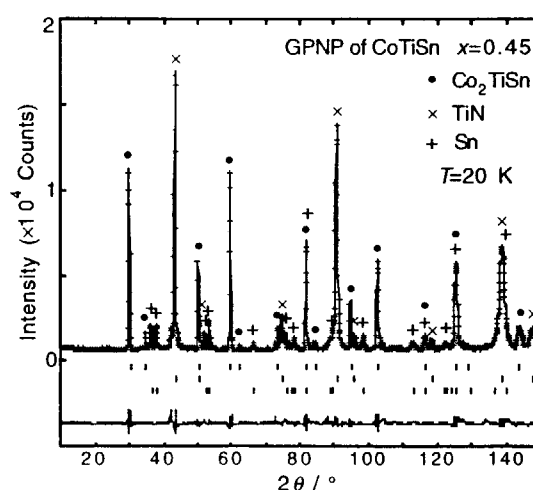


Figure 1 Neutron diffraction pattern and the result of the Rietvelt analysis of gas-phase nitrogenation products (GPNP) of CoTiSn at 20 K.

研究課題：ペロブスカイト関連化合物の構造変化
表題：高温中性子回折によるCaTiO₃ペロブスカイトの研究

1-5-4 High-temperature neutron diffraction study of CaTiO₃ perovskite

R. Ali, M. Yashima, T. Oketani, T. Nogami, H. Sugawara, K. Ohoyama¹, and Y. Yamaguchi¹

Department of Materials Science and Engineering, Interdisciplinary Graduate School of Science and Engineering, Tokyo Institute of Technology, 4259, Nagatsuta-cho, Midori, Yokohama, 226-8502, Japan.

¹Institute for Materials Research, Tohoku University, Katahira, Aoba, Sendai, 980-8577, Japan.

CaTiO₃ is a model compound for the Earth's most abundant mineral, (Mg,Fe)SiO₃ and has an orthorhombic perovskite structure at room temperature. High-temperature X-ray diffraction studies on CaTiO₃ have been carried out by several researchers and reported the phase transitions from orthorhombic structure via an intermediate to cubic phase. Vogt *et al.*¹ performed high-temperature neutron diffraction experiments, however showed no evidence for the intermediate phase. We report here the phase transitions and the evidence for the intermediate phase through high-temperature neutron diffraction.

Neutron diffraction measurements were performed in the temperature range from 23°C to 1447°C using the powder diffractometer HERMES installed at JRR-3M in JAERI. The measurements were done in air under atmospheric pressure. The neutron wave length was 1.8196 Å and the diffraction patterns were recorded over the 2θ range from 20.0 to 152.0 in step width 0.1°.

As shown in Fig. 1, the orthorhombic 120 and 210 peaks were not observed at 1299°C, indicating an intermediate structure. Further 121,103 and 211 peaks of the intermediate phase did not exist at 1447°C, showing the cubic symmetry. The orthorhombic-to-intermediate phase transition occurred at 1225 (±25) °C on heating, and the inverse transformation temperature was 1238 (±13) °C on cooling. These temperatures agreed well, suggesting that this transition is of the second order. On the other hand, the intermediate-to-cubic phase transition occurred at 1361 (±13) °C on heating, and the inverse transformation temperature was 1363

(±13) °C on cooling. These temperatures agreed well, suggesting that this transition is also of the second order. The Rietveld analyses of high-temperature data are now in progress. The present neutron-diffraction study has indicated that CaTiO₃ has an intermediate phase between orthorhombic and cubic phases. On the other hand, in the previous high-temperature neutron diffraction study, Vogt *et al.*¹ reported no intermediate phase.

References

- 1) T.Vogt and W.W. Schmahl, *Europhys. Lett.* **24**, 281-285 (1993).

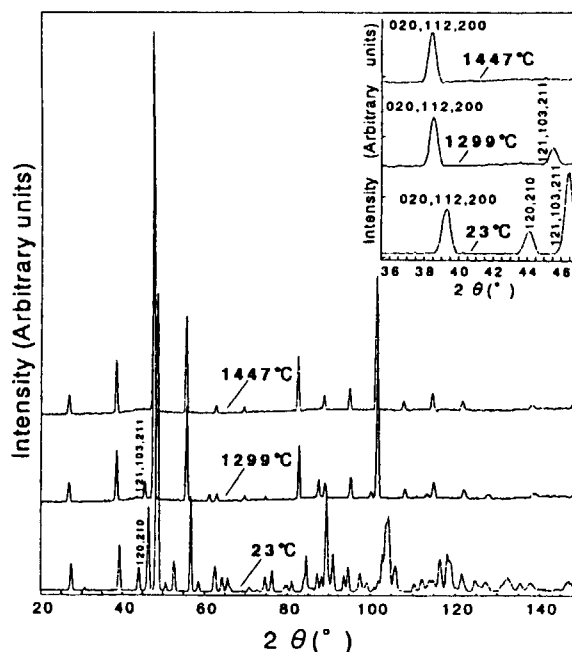


Fig.1. Neutron diffraction patterns of orthorhombic, intermediate and cubic CaTiO₃ observed at 23°C, 1299°C and 1447°C, respectively.

Reactor: (JRR-3M)

Facility: (HERMES(T1-3))

Field: (materials)

研究テーマ：(La,Sr) $n+1$ MnO $3n+1$ のスピンの電荷ダイナミクス
表題：層状マンガン酸化物のスピバルブMR

1-5-5 Spin-valve MR in (La_{0.9}Nd_{0.1})_{1.4}Sr_{1.6}Mn₂O₇

Y. Moritomo^{A,B}, K. Ohoyama^C and M. Ohashi^C

^A Center for Integrated Research in Science and Engineering,
Nagoya University, Nagoya 464-8601, Japan

^B PRESTO, JST, Japan

^C Institute for Material Research, Tohoku University, Sendai 980-77, Japan

Manganese oxide with cubic perovskite structure has stimulated interest because of their magnetoresistive (MR) properties; they exhibit extremely large change in resistance in respond to applied magnetic field. But for technological applications to magnetic memory or switching device to be viable, great improvements are needed in the field sensitivity.

Single crystals of (La_{0.9}Nd_{0.1})_{1.4}Sr_{1.6}Mn₂O₇ were grown by the floating-zone method at a feeding speed of 14 mm/h. Powder X-ray diffraction measurements at room temperature and Reitveld analysis indicate that the crystals were nearly single phase. The neutron powder profiles were obtained with Kinken powder diffractometer for high efficiency and high resolution measurements, HERMES, installed at the JRR-3M reactor in Japan Atomic Energy Research Institute, Tokai, Japan. Neutrons with wave length 1.819Å were obtained by the (331) reflection of Ge monochromator, and a combination of 12'-∞-Sample-22' collimator. Melt-grown crystal ingots were crushed into fine powder and were sealed in a vanadium capsule with helium gas, and mounted at the cold head of the closed-cycle He-gas refrigerator.

In Fig.1 are shown powder patterns at $z=0.1$ together with results of Rietveld refinements (Fat-Rietan); upper panel is for 100 K ($\geq T_N=60$ K) and lower panel is for 15 K ($\leq T_N$). The obtained magnetic structure at 15 K is of a layered-type with magnetic moment of $3.3 \pm 0.05 \mu_B$ along the c -axis. The exchange coupling is ferromagnetic within the bi-layer but antiferromagnetic between the neighboring bi-layers. The effective transfer integral t_{eff} in the double-exchange system is expressed as:

$$t_{eff} = t_0 \cdot \cos(\theta/2), \quad (1)$$

where t_0 and θ are bare transfer integral and relative angle of the adjacent t_{2g} -spins. Then, the e_g -carriers can not hop into the adjacent bi-layers in the layered antiferromagnetic state ($t_{eff} \sim 0$ if $\theta \sim \pi$; shut state of the spin-valve).

Figure 2 shows magnetic field dependence of out-of-plane component of resistivity ρ_c (upper panel) and magnetization M_c (lower panel) for (La_{0.9}Nd_{0.1})_{1.4}Sr_{1.6}Mn₂O₇ at various temperature. The CCP-MR shows a switching behavior near below the critical magnetic field for the antiferromagnetic-ferromagnetic transition (see also the magnetization curves in the lower panel). For example, at 5 K the CPP resistance decreases from 14 Ω cm down to 4 Ω cm at $H \sim 0.5$ T (in the field-increasing run), and

then becomes nearly field-independent. The MR ratio defined by $\rho_c(0)/\rho_c(H)$ is $\sim 120\%$ at $H=0.3$ T at 5 K. The ratio further increases up to $\sim 250\%$ ($H=0.3$ T) at 40 K on approaching to T_N ($= 60$ K).

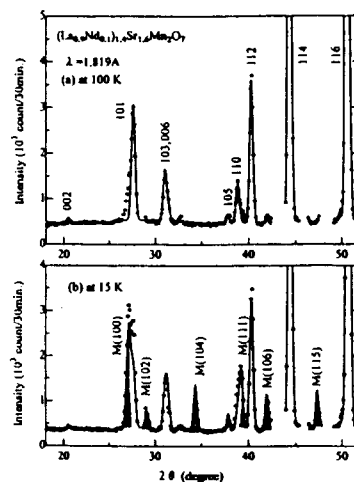


FIG. 1. Neutron powder profiles at 100 K ($\geq T_N$; upper panel) and 15 K ($\leq T_N$; lower panel). Shaded areas indicate magnetic reflections, which are indexed in the $I4/mmm$ setting. Solid curve is results of the Rietveld refinement ($R_{wp}=10.17$ at 100 K and $R_{wp}=9.34$ at 15 K).

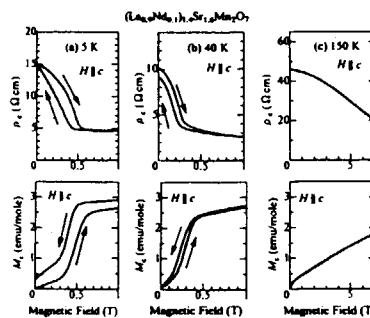


FIG. 2. The current-perpendicular-to-plane magnetoresistance (CPP-MR; upper panel) and corresponding magnetization curve (lower panel) at various temperature. The magnetic field was applied perpendicular to the MnO₂-sheet ($H \parallel c$).

研究テーマ：リエントラント液晶の構造

表題：リエントラント液晶の構造

1-5-6 Structure of a Reentrant Liquid Crystal

O. Oishi, S. Miyajima, M. Nagao¹, and M. Imai¹*Institute for Molecular Science, Myodaiji, Okazaki 444-8585, Japan*¹*Neutron Scattering Laboratory, The Institute for Solid State Physics, The University of Tokyo, Shirakata, Tokai, Naka, Ibaraki, 319-11, Japan*

When conventional liquid loses its isotropic (I) symmetry and assumes uniaxial orientational order, the nematic (N) liquid crystalline state is formed. The smectic A (SA) state is characterized by its one-dimensional translational order in addition to the nematic order. It is therefore natural that the phase transition sequence be I-N-SA on lowering the temperature. However, the present compound, CBOBP (4-cyanobenzoyl-oxy-[4-octylbenzoyloxy]-*p*-phenylene), exhibits a transition sequence, I-N-SAd-N-SA1 (doubly reentrant sequence) on lowering the temperature. The second N phase is called reentrant nematic (RN), and the SAd to RN transition means that 1-D translational lattice *melts* on lowering the temperature. Due to this peculiarity, the nature of this transition sequence has been one of the interesting topics in recent liquid crystal research [1].

We made neutron diffraction study to clarify the structure of the liquid crystalline phases and hence to clarify the microscopic mechanism of this phenomenon. For this purpose a compound with perdeuterated chain,

CBOBP-d17 was prepared. SANS-U instrument was used at an wavelength of 7.0 Å with a velocity selector.

Figure 1 shows the intensity of the smectic primary peak. What is striking is that the peak intensity was very small in SAd phase; smaller than those in N or RN phases, and therefore the reentrant *melting* seems to accompany *increase* in peak intensity. This revealed highly disordered chain structure in the SAd mesophase, in accordance with the deuterium NMR study [1].

[1] S. Miyajima and T. Hosokawa, Phys. Rev. B, 52, 4060 (1995).

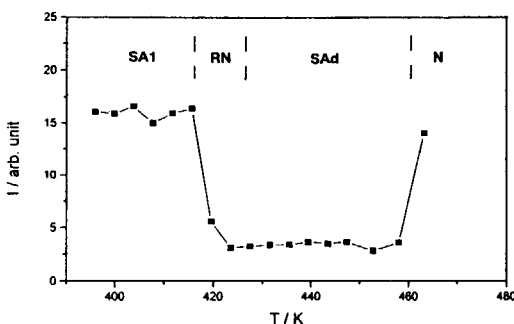


Figure 1. Intensity I of the smectic primary peak as a function of temperature in CBOBP-d17.

1. 中性子散乱 6) 高分子

1. Neutron Scattering 6) Polymer

This is a blank page.

研究テーマ：高分子多成分系の静的階層構造の研究
 標 題：牛血清アルブミンゲルのPNO研究2

1-6-1 PNO Study on Bovine Serum Albumin Gels 2

Y. IZUMI, K. SOMA, K. AIZAWA¹, S. KOIZUMI¹ AND H. TOMIMITSU¹

Graduate School of Science and Engineering, Yamagata University, Yonezawa, Yamagata 992-8510

¹Advanced Science Research Center, JAERI, Tokai, Ibaraki 319-1195

In a previous review¹⁾, we reported the structure of bovine serum albumin (BSA) gel revealed by PNO measurements. The previous results are summarized as follows. The transparent BSA gel (C_p , the concentration of BSA, 15wt% and no added salt) gave too very small excess intensity to detect, indicating a structure with a very small contrast or very small junction point. On the other hand, the opaque gel ($C_p = 15\text{wt}\%$ and C_s , the concentration of NaCl, 0.2mol NaCl) gave a clear difference between the intensity of the gel and that of the solvent. The analysis of the excess intensity indicated the value of 3.1 ± 0.05 as the fractal dimension. This value was previously considered as mass fractals but should be regarded as surface fractals, as a result, the surface of the junction zone is maximally rough. Furthermore, the structure of the opaque gels, i.e., the size of the junction zone and the size distribution strongly depend on the gelation temperature.

In present work, we intended to investigate the effect of added NaCl to the structure of opaque gels. The measurements have been carried out by PNO spectrometer. The details of measurements and the analysis are described elsewhere²⁾. Four gels with different C_s (0.05, 0.1, 0.2, and 0.3M NaCl) were prepared by heating during 5min at 90°C.

Fig. 1 shows the excess scattering curves $I(q)$, radially averaged, in a double log presentation. The Porod behavior of $I(q) \propto q^{-4}$ is observed for the gel prepared at 0.05M NaCl. On the other hand, the behavior of $I(q) \propto q^{-3}$ is observed for the gels prepared at 0.1-0.3M

NaCl. This crossover between the exponents indicates a change in the surface structure of the gels. The exponent value of -4 indicates the smooth surface of the junction zones, while the exponent value of -3 indicates the maximally rough surface. The crossover occurs at a concentration between 0.05M and 0.10M NaCl. The results indicate that the PNO technique is very useful to characterize the surface structure and the size of the junction zone of micron order in gels.

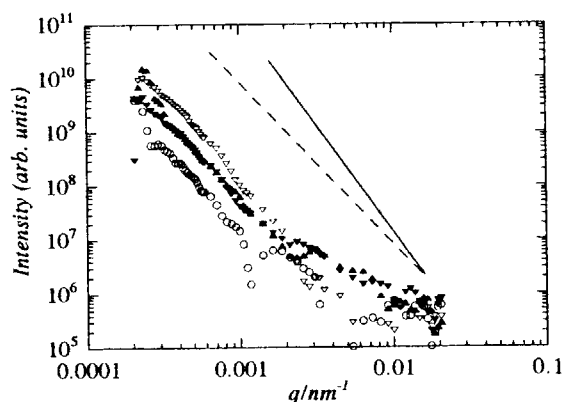


Fig. 1. Log-log plot of intensity vs. q for four gels. ∇ (0.05M NaCl), \circ (0.1M NaCl), \blacktriangledown (0.2M NaCl), \blacktriangle (0.3M NaCl). The straight and broken lines indicate the slopes of -4 and -3, respectively.

References

- 1) Y. Izumi, K. Soma, K. Aizawa, S. Koizumi, and H. Tomimitsu, JAERI-Rev. 99-003, p.27(1999).
- 2) K. Aizawa & H. Tomimitsu, Physica B 213&214(1995)884-886.

研究テーマ：高分子の結晶構造とダイナミックス

表題：ポリ-p-フェニレンベンゾビスオキサゾールの中性子構造解析

1-6-2 Neutron Structure Analysis of Poly(p-phenylene Benzobisoxazole)

Yasuhiro Takahashi

Department of Macromolecular Science, Faculty of Science,
Osaka University, Toyonaka, Osaka 560, Japan

In a previous paper,¹ the disordered structure of poly(p-phenylene benzobisoxazole) (PBO) was reported, where one molecule passes through a monoclinic unit cell with parameters, $a = 5.651 \text{ \AA}$, $b = 3.570 \text{ \AA}$, c (fiber period) = 6.03 \AA , $\gamma = 101.4^\circ$. In the present study, neutron crystal structure analyses of PBO were carried out for the equatorial intensity data measured at 17, 100, 200, and 295K.

Neutron diffraction measurements were carried out by a powder diffractometer (HERMES) equipped with JRR-3M installed by the Japan Atomic Energy Research Institute using $\lambda = 1.8196 \text{ \AA}$. Numbers of observed reflections on the equator at 17, 100, 200 and 295K are 11, 11, 12, and 12, respectively.

The constrained least-squares refinements² were carried out by using the bond lengths and bond angles reported by Fratini et al.³ R-factors reduced to 9.85, 9.47, 13.14, and 12.08 % for 17, 100, 200, 295K, respectively. In Fig. 1, the temperature

dependences of unit cell parameters are shown and in Fig.

2, the half-widths of the reflections, 100, 010, $\bar{1}10$. The half-widths are independent of the temperature. This shows that the crystallite size and lattice distortion are independent of the temperature. In Fig.3, the crystal structure projected on the ab-plane at 295K is shown. In Fig. 4, the internal rotation angle τ is shown. PBO molecule assumes the planar structure when τ is 180° . PBO molecule deviates about 20° from the planar structure.

References

1. Y. Takahashi, T. Sato, H. Tadokoro, and Y. Tanaka, *J. Polym. Sci. Polym. Phys. Ed.* **11**, 233 (1973).
2. Y. Takahashi, *Rep. Progr. Polym. Phys. Jpn.*, **41**, 363 (1998).
3. A. V. Fratini, P. G. Lenhert, T. J. Resch, and W. W. Adams, *Mat. Res. Soc. Symp. Proc.* **134**, 431 (1989).

JRR-3M, HERMES, polymer

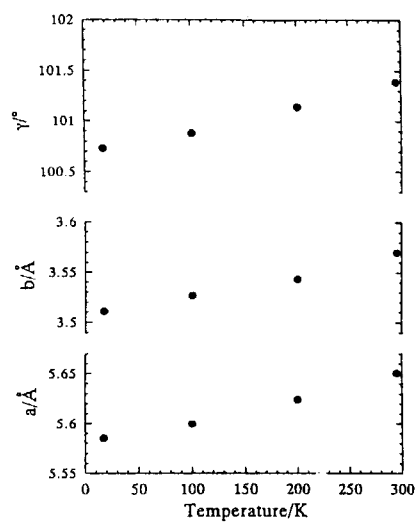


Fig. 1 Temperature dependences of unit cell parameters.

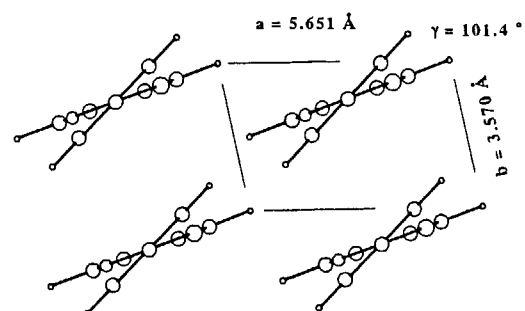
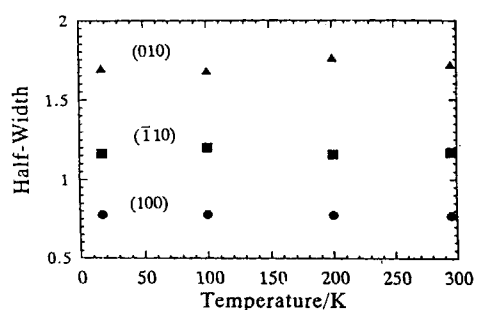
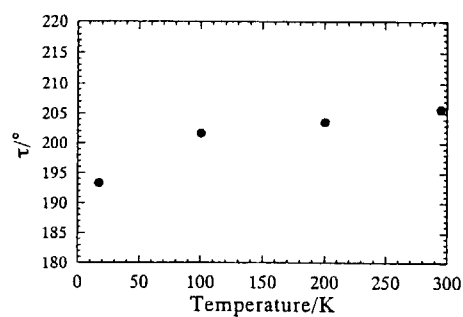
Fig. 3 . Crystal structure of poly(*p*-phenylene benzobisoxazole) at 295 K.

Fig. 2 Temperature dependences of half-width of reflections 100, 010, and 110.

Fig. 4 Temperature dependence of the internal rotation angle τ .

研究テーマ：非晶高分子のダイナミクス

表題：置換ポリアセチレンの局所運動とガス透過性

1-6-3 Local Mobility of Substituted Polyacetylenes and Its Relationship with Gas Permeability

T. Kanaya[†], M. Teraguchi[‡], T. Masuda[‡] and K. Kaji[†][†] Institute for Chemical Research, Kyoto University, Uji, Kyoto-fu 611-0011[‡] Department of Polymer Chemistry, Kyoto University, Kyoto 606-8501

Substituted polyacetylenes generally exhibit relatively high gas permeability among all the existing polymers [1]. Among them, poly[1-(trimethylsilyl)-1-propyne] [poly(TMSP)] and poly[1-phenyl-2-(*p*-trimethylsilylphenyl)-acetylene] [poly(*p*-Me₃SiDPA)] show extremely high permeability to various gases. However, gas permeability of poly[1-phenyl-2-(*p*-triisopropylsilylphenyl)acetylene] [poly(*p*-iPr₃SiDPA)] is much smaller than those of the above two polymers, which is rather unexpected. A possibility is that, if the round-shaped substituent is too large, its mobility is low, which leads to low permeability. In this work, therefore, the local mobility of three polymers was studied by means of a quasielastic neutron scattering (QENS) technique to confirm if the relatively low permeability of poly(*p*-iPr₃SiDPA) is caused by its low mobility.

QENS measurements were performed with HER spectrometer at a beam port C1-1 with a fixed scattered wavenumber of $k_f = 1.25 \text{ \AA}^{-1}$ using a horizontal focusing analyzer.

Fig. 1 shows $S(Q, \omega)$ of three polymers which were fitted to a Lorentzian function to evaluate the relaxation rate of local motion Γ and the mobile fraction f_m . The results of fits are shown in Fig. 1 as solid curves. As a measure of the local mobility we took local flux $\Gamma \times f_m$ which is a product of the relaxation rate Γ and mobile fraction f_m . In Fig. 2 the local flux is plotted against the carbon dioxide

permeability coefficient P_{CO_2} for the three polymers. The larger the CO₂ permeability coefficient, the larger the local flux. It is concluded that the local mobility is an important factor to determine the gas permeability in substituted polyacetylenes.

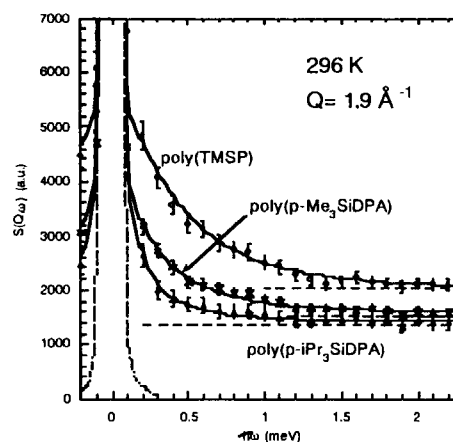


Figure 1. $S(Q, \omega)$ of poly(TMSP), poly(*p*-Me₃SiDPA) and poly(*p*-iPr₃SiDPA). The solid curves are the results of fits with a Lorentzian function. The dashed lines represent the inelastic contributions.

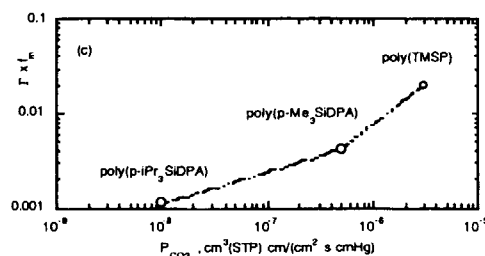


Figure 2. Local flux $\Gamma \times f_m$ as a function of CO₂ permeability coefficient P_{CO_2} .

[1] M. Teraguchi and T. Masuda, *J. Polym. Sci., A Polym. Chem.*, **36**, 2721 (1998) and references herein.

研究テーマ：界面活性剤・水系のモルフォロジー転移
 表題：Gyroidドメインのコarsening過程における弾性効果

1-6-4 Elasticity Effects on Coarsening of Gyroid Domain

M. Imai¹, K. Nakaya¹, and T. Kato²

¹Department of Physics, Ochanomizu University, Bunkyo, Tokyo 112-0012, Japan

²Faculty of Science, Tokyo Metropolitan University, Hachioji, Tokyo 192-03, Japan

Surfactant solutions and block copolymers show a variety of ordered mesophases. Typical examples are one dimensional cylinders, two dimensional lamellae and gyroid structure having three dimensional bicontinuous cubic lattice with $Ia3d$ symmetry. These ordered morphologies composed of amphiphilic molecules have large internal degrees of freedom and this "soft" nature brings unique features which are hardly observed in "hard" materials. In this study we investigate the coarsening process of the gyroid phase of a nonionic surfactant system using time resolved small angle neutron scattering (SANS) and small angle neutron Laue diffraction (SANLD) techniques. The time evolution of SANS

patterns shows anomalous coarsening of the gyroid domains. The observed Laue spot from a gyroid domain becomes elongated along the radial direction with the elapse of time and at a certain time the elongated spot is split into two spots (Fig. 1). The results can be interpreted as follows. During the coarsening process, mismatch of the lattice orientation at the domain boundary brings strong stress to the gyroid domain resulting in the distortion of the domain. The stored stress in the domain finally brings splitting of the gyroid domain. The elastic and fragile nature of the gyroid domains composed of the "soft matter" is responsible to the anomalous coarsening.

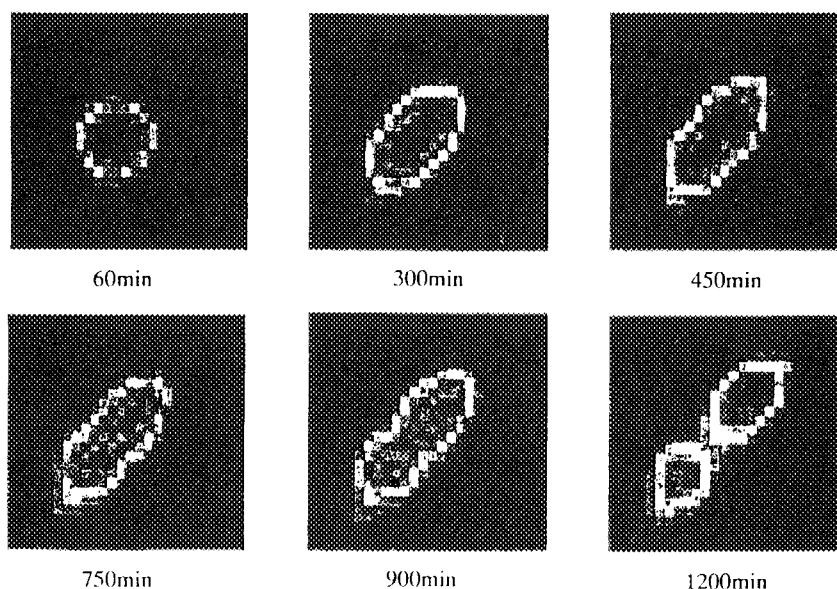


Fig. 1 Time evolution of Laue spot during coarsening process of gyroid domain

JRR-3M, SANS-U, 6 Polymer

研究テーマ：ブロック共重合体のマイクロドメインの流動配向化とそのヒステリシスの検討
 表題：スチレン-2ビニルピリジンブロック共重合体のマイクロドメイン構造に対する流動の影響

1-6-5

FLOW EFFECTS ON MICRODOMAIN STRUCTURE OF POLY(STYRENE-*b*-2-VINYLPYRIDINE) SOLUTIONS

Y. Takahashi*, M. Noda, K. Matsuoka, T. Murayama

*Center for Integrated Research in Science and Engineering, and Graduate School of Eng., Nagoya Univ., Nagoya 464-8603 Japan

Flow effects on the lamellar structure of a symmetric poly(styrene-*d*₈-*b*-2-vinylpyridine), DP20 ($M_w=3.6 \times 10^5$, $M_w/M_n=1.08$, $\phi_{PS}=0.53$) in a common good solvent, α -chloronaphthalene near the order-disorder transition (ODT) were studied by small angle neutron scattering under steady shear flow (flow-SANS) at 30 °C for 14.0 and 12.5 wt% solution (ODT: 12 wt% at 30 °C)¹⁾. Flow-SANS were performed with the SANS-U spectrometer at the ISSP, The University of Tokyo in JRR-3M at Tokai, Japan by using a couette type flow cell.

Anisotropic scattering peaks were observed in the vertical direction under the flow for both solutions. When the flow was stopped, the anisotropy disappeared instantaneously for 12.5 wt% solution, while it remain unchanged for rather a long time for 14.0 wt% solution.

Figure 1 shows plots of the peak intensity ratios, $I(q^*)_y/I(q^*)_x$ vs. shear rate $\dot{\gamma}$ for the two solutions. Here, *y* and *x* denote vertical and horizontal (flow) directions. The data for 14.0 wt% solution increase with increase of $\dot{\gamma}$ up to say 10^2 s⁻¹, while the data for 12.5 wt% at the

lowest $\dot{\gamma}$ have very small value and tend to be constant at around 10 at the higher $\dot{\gamma}$.

From above results, we conclude that the lamellae of DP20 solutions are oriented by the flow as their normals are preferentially aligned along the vorticity direction, though the degree of alignment differ with concentration. The structure of 12.5 wt% solution is hardly oriented at low $\dot{\gamma}$. The detail of this study will published in Proceedings of ISSP7.

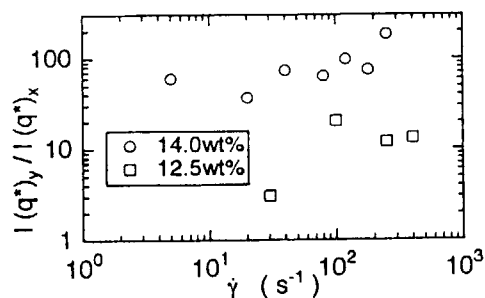


Fig. 1 Plots of $I(q^*)_y/I(q^*)_x$ vs. $\dot{\gamma}$ for the two solutions.

Reference

1. Takahashi Y., Kitade S., Noda M., Ochiai N., Noda I., Imai M., and Matsushita Y., Polym. J. 30, 388 (1998).

研究テーマ：ループ状の相図を有するブロック共重合体の相転移に関する研究

表題：ループ状の相図を有するブロック共重合体の相転移

1-6-6 Phase Transition in Block Copolymers with a Looped Phase Diagram

T. Hashimoto, T. Hashimoto, H. Hasegawa, M. Takenaka,
M. Sawamoto, M. Nagao¹ and M. Imai¹

Department of Polymer Chemistry, Graduate School of Engineering,
Kyoto University, Sakyo-ku, Kyoto, 606-8501 Japan

¹ Neutron Scattering Laboratory, The Institute for Solid State Physics,
The University of Tokyo, Shirakata, Tokai, Naka, Ibaraki, 319-11 Japan

Phase behavior of a deuterated polystyrene-*block*-poly(vinyl methyl ether) diblock copolymer (DPS-PVME, $M_n = 5.0 \times 10^4$, $M_w/M_n = 1.18$, DPS/PVME=61/49) was investigated by small-angle neutron scattering (SANS) and transmission electron microscopy (TEM). The sample preparation has been reported elsewhere.² It was found that this sample also stayed in the disordered state at all temperatures between room temperature and 460 K. Therefore, the DPS-PVME sample was subjected to water vapor at room temperature because it was known that moisture significantly decreased the miscibility between DPS and PVME. The uptake of water before the SANS measurements was 44 wt%.

Figure 1 shows the SANS profiles obtained at 424 K for two DPS-PVME samples: one was dry and the other wet. The scattering profile of the dry sample showed no significant peak suggesting the disordered state. In contrast, the wet sample exhibits the peaks at $q = 1.25 \times 10^{-1}$ and $2.5 \times 10^{-1} \text{ nm}^{-1}$, suggesting the microphase separation into the lamellar structure with ca. 50 nm spacing. This was confirmed by the TEM micrograph of the RuO_4 -stained ultrathin section obtained from the wet sample after cooling down from 424 K, exhibiting a lamellar structure as shown in Figure 2. It is considered that RuO_4 stained the interfaces

between DPS and PVME dark. Then the lamellar spacing obtained by TEM is ca 50 nm in good agreement with the SANS result.

References

- 1) T. Hashimoto et al., *Macromolecules*, **30**, 6819 (1997).

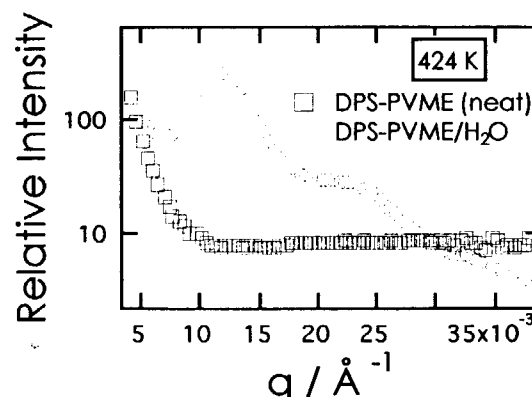


Figure 1 Effect of moisture on the SANS profiles of the DPS-PVME diblock copolymer at 424K.

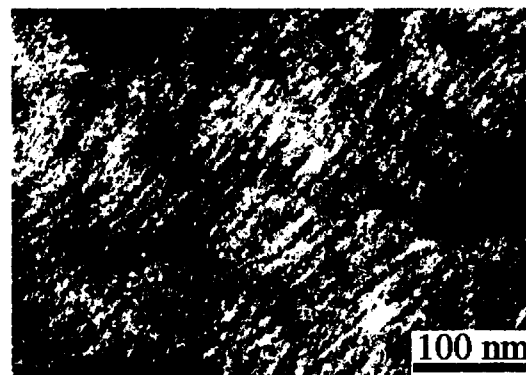


Figure 2 Electron micrograph of the DPS-PVME diblock copolymer annealed at 424K under the presence of moisture.

研究テーマ：弱荷電ゲルの体積相転移の動力学に関する研究

表題：弱荷電ゲルの体積相転移の動力学に関する研究

1-6-7 Kinetics of Volume Phase Transition in Poly(N-isopropylacrylamide-co-acrylic acid) Gels

M. Shibayama and H. Hirose

*Department of Polymer Science and Engineering, Kyoto Institute of Technology,
Matsugasaki, Sakyo-ku, Kyoto 606-8585, Japan*

The shrinking/swelling behavior across the volume phase transition temperature, T_c , has been investigated for cylindrical gels made of poly(N-isopropylacrylamide-co-acrylic acid) (NIPA/AAC). The NIPA/AAC gel shrank at $T_c = 43^\circ\text{C}$ by quasistatic heating. On the other hand, the gel underwent a shrinking transition at a lower temperature, i.e., $T_c \approx 40^\circ\text{C}$, when a temperature jump was applied to the gel from 20°C . More interestingly, the shrinking process consisted of three stages; (i) a uniform shrinking stage where the gel diameter, d , decreases exponentially, (ii) a plateau stage where the gel shrinks further from both ends of the cylinder while the middle (swollen) part remains in swollen state, and (iii) a collapsing stage where the middle part of the gel shrinks linearly with time. This sequential process was found to be characteristic of weakly charged gels with a large aspect ratio. This interesting shrinking behavior was discussed by comparing the results of swelling kinetics. In the case of NIPA homopolymer gel, the shrinking process was strongly decelerated due to phase separation, while the swelling process was well reproduced by the TF theory.

Experimental Section

Samples Poly(N-isopropylacrylamide-co-acrylic acid) (NIPA/AAC) copolymer gels were prepared by redox polymerization. NIPA monomer was purified by recrystallization. An aqueous solution of a monomer mixture of NIPA (668 mM) and acrylic acid (AAC; 32 mM) was polymerized in the presence of N,N'-methylenebisacrylamide (BIS; cross-linker; 8.62 mM) in a micropipette of 471 μm -diameter at 20°C . Thus prepared gel was cut to a cylindrical piece of 5 mm long and washed with an

excess amount of distilled water.

Swelling Degree measurement The sample was immersed in a thermostatted chamber filled with distilled water. The degree of swelling was measured by monitoring the diameter of the cylindrical gel, d , via an inverted microscope (TMD300, Nikon, Japan) coupled with an image processor (Algas 2000, Hamamatsu Photonics, Japan).

Small-angle Neutron Scattering

Small-angle Neutron Scattering (SANS) experiments were carried out at the Research Reactor of the Institute of Solid State Physics, the University of Tokyo, located at the Japan Atomic Energy Laboratories, Tokai, Japan. Two types of NIPA/AAC gels having different sample dimensions were employed. One was a one-piece gel of disk shape with the dimension of 4 mm thick and 25 mm in diameter, and the other was a smashed gel with a 500 μm sieve. In both cases, the gel samples were sealed in a quartz cell and thermostatted at the desired temperature.

Results and Discussion

Figure 1 shows the comparison of the variations of d/d_0 for quasistatic heating (filled circles) and T-jump processes (open circles) for NIPA/AAC gels, where d_0 is the gel diameter at preparation. In the case of quasistatic heating, the gel remains in a swollen state until 43°C , and then suddenly shrinks to the shrunken state as shown by filled circles. Note that it took 60 h to reach the shrunken state. On the other hand, a T-jump resulted in a steep decrease in d/d_0 , followed by a plateau region. It should be noted here that there is a significant difference in d/d_0 between the two processes, although both of d/d_0 's eventually reach the same value (i.e., $d/d_0 \approx 0.5$). This provides much insight into the

shrinking mechanism of weakly charged gels. Now, we ask ourselves (i) why the charged gels have the intermediate size during the T-jump and (ii) why the value of d/d_0 is larger for the case of the quasistatic heating than that for the T-jump. In order to answer these questions, we carried out a SANS experiment.

Figure 2 shows a comparison of SANS intensity curves of smashed gels (in equilibrium) and of one-piece gels after T-jump to 40 °C. The smashed gels can easily attain its thermodynamic equilibrium by temperature change compared with the one-piece gel because the size of individual gels is on the order of submillimeters. By T-jump, the scattered intensity, $I(q)$, increased with time and a scattering peak appeared at $q = 0.014 \text{ \AA}^{-1}$. The intensity rise was confirmed to saturate at $t > 16 \text{ min}$. On the other hand, it took several hours for the one-piece gel of this thickness (4 mm) to reach equilibrium because this is a diffusion-limited process. This figure indicates that the microdomain structure with characteristic spacing of $2\pi/q \approx 450 \text{ \AA}$ is further developed in the smashed gels than in the one-piece gel.

We propose a mechanism for the shrinking process of NIPA/AAC gels. By quasistatic heating, a gel has enough time to adjust to a new equilibrium whenever temperature is changed. Above the so-called Θ temperature of NIPA gels, i.e., ca. 34 °C, hydrophilic regions around the charged AAC segments are formed in the gel. This is a kind of microphase separation. The hydrophilic regions retain the swollen state until the attractive interaction (hydrophobic demixing) dominates the repulsive interaction (electrostatic interaction and/or Donnan potential). This is why the gel keeps a larger value of d/d_0 until 43 °C before shrinking to the shrunken state. Contrary to this, a T-jump does not allow the gel to form such region, resulting in a less

swollen state (at the plateau region). This is why the gel treated by quasistatic heating has a larger swelling ratio than the T-jumped gel in the plateau region.

The details of the experiment and the discussion are given elsewhere.¹

References

1. M. Shibayama and H. Hirose, *Macromolecules*, **31**, 5336 (1998).

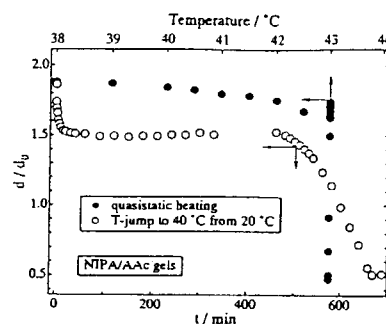


Fig. 1 Comparison of the variations of d/d_0 of NIPA/AAC weakly charged gels for the quasistatic heating (solid circles) and the T-jump processes (open circles).

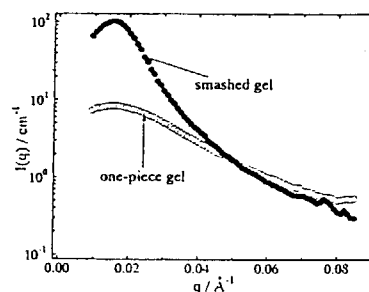


Fig. 2 SANS intensity profiles of NIPA/AAC gels after T-jump; smashed gel (in equilibrium; solid circles) and one-piece gel (kinetically frozen; open circles) observed at $t = 16 \text{ min}$ after T-jump.

研究テーマ：帯型高分子のミクロ相分離構造中の分子形態と界面

表題：ラメラ状ミクロ相分離構造中のグラフト鎖の分子形態

1-6-8 Conformation of a Graft Polymer Chain in Lamellar Microphase-Separated Structure

N. Torikai, J. Suzuki,¹ J. Watanabe,² and Y. Matsushita³

Neutron Science Laboratory, KEK, 1-1 Oho, Tsukuba, Ibaraki 305-0801, JAPAN

¹Neutron Scattering Laboratory, ISSP, The University of Tokyo, Tokai, Ibaraki 319-0801, JAPAN

²Fuji Film Corporation, Minami-Ashigara, Kanagawa, 250-0123 JAPAN

³School of Engineering, Nagoya University, Furo-cho, Chikusa-ku, Nagoya 464-8603, JAPAN

ABB graft copolymer has a peculiar structural feature that its A- and two B-chains are connected at one junction point so that its chain distribution is asymmetric at domain boundary in microphase-separated structure, while AB diblock copolymer shows symmetric chain distribution. It was clarified in our previous work that ABB graft copolymer shows different composition dependence of morphology from that of AB diblock copolymer due to its asymmetric chain distribution. In this work, we investigated the conformation of A-graft chain of ABB graft copolymer in alternating lamellar structure by small-angle neutron scattering (SANS) measurement.

Samples used are a poly(2-vinylpyridine-*g*-styrene-*h*_g) (SPP) having the molecular weight, M , of 327×10^3 and the volume fraction of styrene graft chain, ϕ_s , of 0.56, and its counterpart (DPP) with deuterated styrene graft chain having $M=324 \times 10^3$ and $\phi_s=0.43$. They were mixed at the ratio of SPP/DPP=87.0/13.0 in weight so as to equalize coherent scattering length densities of polystyrene and poly(2-vinylpyridine). A film specimen for SANS was prepared by solvent-casting from dilute THF solution, and annealed at 150 °C in vacuum for a week. It was confirmed by small-angle x-ray scattering that lamellar structure was formed parallel to film surface with high orientation. SANS measurement was performed on SANS-U spectrometer of ISSP, the University of Tokyo, installed at JRR-3M reactor. The wavelength, λ , of neutrons was 7 Å, and the distance between sample and detector was 12 m. Scattering intensities were observed at through view geometry, in which incident neutron beam is irradiated along the direction perpendicular to film surface.

Diffraction peaks from lamellar structure was not observed in scattering intensity profile at the through view, though the profile is not shown here. It was assumed that the scattering intensity profile without diffraction peaks consists of only single-chain scattering from styrene graft chain. Thus, the radius of gyration, $R_{g,z}$, of styrene graft chain along the direction parallel to lamellar interface was evaluated from the scattering intensities at the through view according to the modified Guinier's approximation

$$I(q)=I(0)\exp(-q^2R_{g,z}^2)$$

where q is the scattering vector. Figure 1 shows the Guinier plots of scattering intensities, in which the upper limit of the Guinier range defined as $q^2R_{g,z}^2 < 1.3^2/3$ is indicated by the vertical broken line. The value of $R_{g,z}$ of styrene graft chain was evaluated to be 5.42nm. This value is slightly larger than that of styrene block chain of SP diblock copolymer, 5.12nm, calculated from the empirical relationship obtained for SP diblock copolymers

$$R_{g,z}=0.0289M_s^{0.43} \text{ (nm)}$$

using the weight-averaged molecular weight, 169×10^3 , of styrene graft chain for M_s .

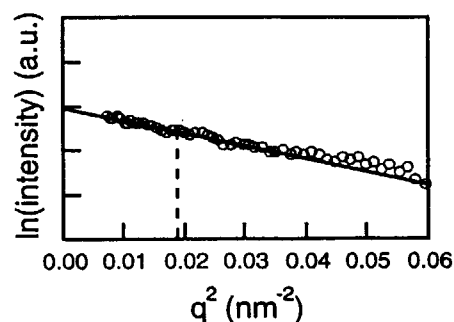


Figure 1 Guinier plots of scattering intensities at the through view for SPP graft copolymer.

JRR-3M, SANS-U, 6.Polymers

研究テーマ：両親媒性環境下におけるポリペプチド鎖の構造解析

表題：ドデシル硫酸ナトリウム存在下の蛋白質ポリペプチド鎖の分子形態

1-6-9 Chain Conformation of a Protein Polypeptide in the Presence of Sodium Dodecyl Sulfate

Y. Watanabe, I. Tanaka¹, M. Imai², Y. Sano, and N. Niimura¹

National Food Research Institute, Tsukuba, Ibaraki 305-8642, Japan

¹Advanced Science Research Center, JAERI, Tokai, Ibaraki 319-1195, Japan

²Faculty of Science, Ochanomizu University, Bunkyo, Tokyo 112-0012, Japan

Sodium dodecyl sulfate (SDS) -polyacrylamide gel electrophoresis is used for estimating the relative molecular weight of a protein polypeptide in biochemistry. The method has arisen from a series of empirical observation, so that its detailed physical basis is not yet fully understood. The high level of binding of the charged detergent and the constant binding ratio will generally "swamp out" the intrinsic charge contribution of most proteins, so that an approximately constant negative charge per unit mass will be obtained. All polypeptides also appear to have a similar shape when SDS is bound, generally considered as elongated particles, with a constant diameter and a length proportional to the number of amino acid residues in the polypeptide chain. The exact nature of the protein-SDS complex is not known; none of the models proposed is entirely consistent with the many experimental observations.

In this study, as a first approach, the perdeuterated dodecyl sulfate in neutron scattering experiments was used to determine the configuration of the protein-polypeptide derived from reduced carboxymethylated bovine serum albumin in the complex.

Small-angle neutron scattering experiments were performed with the SANS-U spectrometer of the University of Tokyo in JRR-3M reactor of Japan

Atomic Energy Research Institute (Tokai). Sample-to-detector distance and wavelength were 1m and 7 Å, respectively.

Figure 1 shows the Kratky plot for a typical scattering pattern of reduced carboxymethylated bovine serum albumin in perdeuterated dodecyl sulfate. The scattering of the protein polypeptide in the complex was obtained in the D₂O buffer solution that matches approximately the scattering length density of perdeuterated dodecyl sulfate. From the transition Q value, that is 0.12, the protein polypeptide chain in the complex is found to be a wormlike chain with a persistence length of about 16 Å.

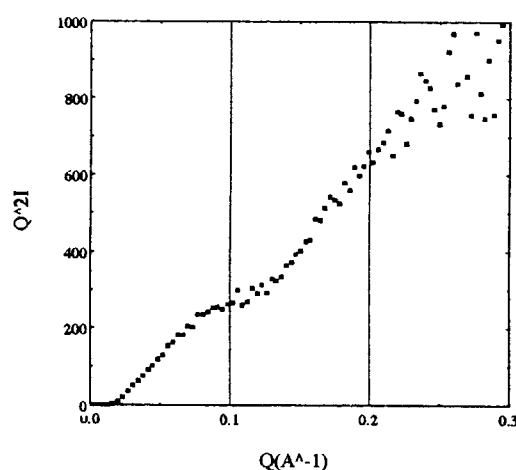


Figure 1 the Kratkey plot of the protein polypeptide chain in dodecyl sulfate.

研究テーマ：多糖/水系の高次構造形成と機能発現
表題：ジェランガム/水系のゾルーゲル転移の構造研究

1-6-10

Structural Studies of Sol-Gel Transition of Gellan Gum in Water

Y. Izumi, Y. Jinbo, K. Soma, S. Saito, M. Nagao¹, M. Hashimoto¹
and T. Takahashi¹

Graduate School of Science and Engineering, Yamagata University, Yonezawa,
Yamagata 992-8510 Japan

¹Institute for Solid State Physics, University of Tokyo, Roppongi, Tokyo 106, Japan

Physico-chemical studies show that gellan gum forms a thermoreversible gel upon cooling and suggest that the junction zones of the gels arise from the association and possibly crystallization of sections of the polymer chain. Although many studies have been performed to reveal the structure and mechanism, its gelling mechanism is not yet fully understood.

The present work aims to specify the gelling characteristics and the gel structures of gellan gum in aqueous solutions by means of SANS-U and ULS. The sample of sodium-salt-type gellan gum was used. The inorganic ions were contained as Na⁺:2.59%, K⁺:0.009%, Ca²⁺:0.02% and Mg²⁺:0.001%. The number average and weight average molecular weights were 5.7×10^4 and 9.47×10^4 , respectively. The samples were prepared in the absence of added salts.

The neutron scattering experiments were performed with the ISSP C1-2 SANS-U and C1-3 ULS spectrometers installed at JRR-3M reactor of JAERI (Tokai). The SANS-U data were obtained at 25°, 35° and 55°C while the ULS data were obtained at 30°C.

Figure 1 shows the SANS-U profiles at 6wt% of gellan gum. As can be seen, a peak has appeared at around $q_m = 0.075 \text{ \AA}^{-1}$ at 25°C. At 35°C, this peak becomes sharper and the second peak has appeared at around $q_m = 0.15 \text{ \AA}^{-1}$. Noting that these q_m values are in a simple ratio of 1:2, the ordered structures in the gels are lamellae and the junction zone is formed by such a lamellar stack. At 55°C, these peaks almost disappear. The results suggest that the interaction forming these lamellae is due to the hydrogen bonding between hydroxyl groups contained in the chemical structure of gellan gum.

Figure 2 shows the excess ULS curve of gellan gum gel in a double log presentation. As can be seen, a power-law decay is observed. After the slit collimation, we obtain 2.60 as the fractal dimension. As this value is closer to the dimension 2.5, it is suggested that the gelation proceeds according to the diffusion limited aggregation mechanism.

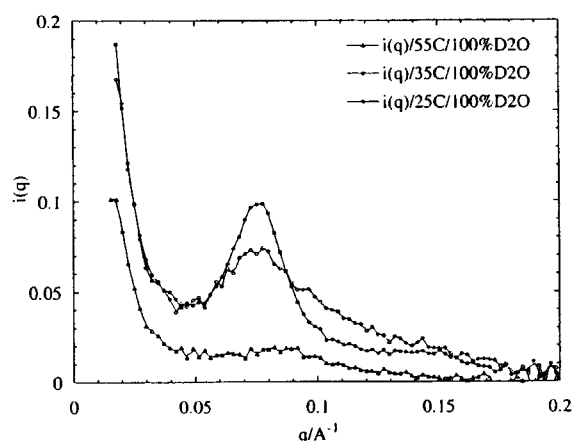


Fig. 1. SANS-U profiles for the gellan gum in D₂O at 6wt%: ○(25°C); ●(35°C); △(55°C).

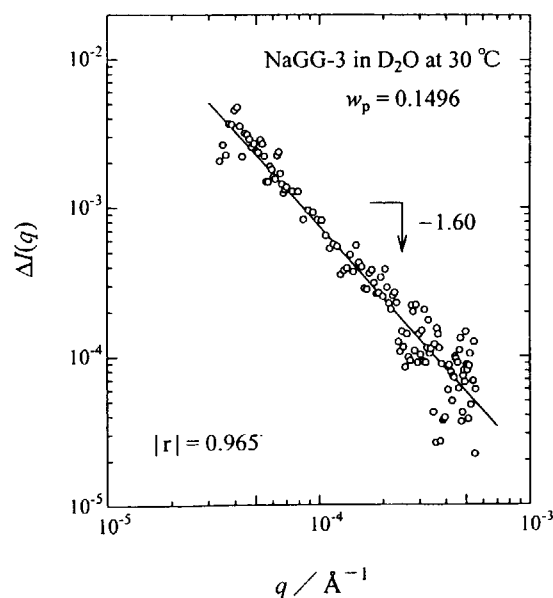


Fig. 2. Excess ULS profile for gellan gum gel at the concentration of 15wt%.

研究テーマ：重水素化ポリブタジエン/ポリイソプレン混合系の相溶性におよぼす圧力効果のミクロ構造依存性

表題：高分子の相溶性に関する圧力効果のミクロ構造依存性

1-6-11 Microstructure Dependence of Pressure Effects on Polymer Miscibility

H. Hasegawa, M. Takenaka, T. Hashimoto,
M. Nagao¹ and M. Imai¹

Department of Polymer Chemistry, Graduate School of Engineering,
Kyoto University, Sakyo-ku, Kyoto, 606-8501 Japan

¹ Neutron Scattering Laboratory, The Institute for Solid State Physics,
The University of Tokyo, Shirakata, Tokai, Naka, Ibaraki, 319-1106 Japan

Introduction Pressure dependencies of the miscibility of polydienes were investigated by small-angle neutron scattering (SANS) directing our attention to their microstructures. Deuterated polybutadiene (DPB) and polyisoprene (HPI) can take plural microstructures as shown in Table I, and the percentage of each microstructure in the polymer molecule depends on the synthetic method.

Experiment SANS-U ($\lambda=7.0\text{\AA}$, SDD=4.0m or 8.0m) equipped with the high-pressure cell¹⁾ was used. The scattering data were obtained for two deuterated polybutadiene-*block*-polyisoprene diblock copolymers (DPB-HPI) with different microstructures and molecular weights: B-11 (94.8% 1,4 for both DPB and HPI, $M_n=4.9\times 10^5$) and B-12 (45.8 and 27.6% 1,4 for DPB and HPI, respectively, $M_n=7.0\times 10^4$) as a function of temperature and pressure.

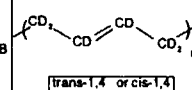
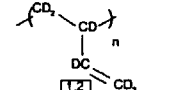
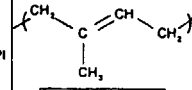
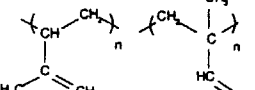
Results Under atmospheric pressure, the two block copolymers exhibited quite different phase behavior. Both samples were in disordered state at room temperature. The miscibility of B-11 decreased significantly with increasing temperature (resulting in a large increase in the scattering intensity) and underwent ordering transition, exhibiting lower critical order-disorder transition temperature (LCODTT)-type phase behavior. On the

other hand, the temperature dependence of the scattering intensity of B-12 was very small but decreased slightly with increasing temperature indicating upper critical order-disorder transition temperature (UCODTT)-type phase behavior. The pressure dependence of the scattering from the two samples was also very different. The miscibility of B-11 increased dramatically with increasing pressure, indicating upper critical order-disorder transition pressure (UCODTP)-type phase behavior. In contrast, the scattering intensity of B-12 slightly increased with increasing pressure, indicating lower critical order-disorder transition pressure (LCODTP)-type phase behavior. Thus, it was found that temperature and pressure affect the miscibility in an opposite manner.

References

- 1) H. Takeno et al., *Polymer J.*, **29**, 931 (1997).

Table I Possible microstructures for DPB and HPI

	1,4	vinyl
DPB		
HPI		

JRR-3M, SANS-U, 6. Polymer

研究テーマ：両親媒性ポリマーの水及び有機選択溶媒中における会合体形成挙動

表題：両親媒性ポリマーの水及び有機選択溶媒中における会合体形成挙動

1-6-12 Aggregation Behavior of Amphiphilic Polymers in Water and Organic Selective Solvents

Hideki Matsuoka, Minoru Nakano, Makoto Kubota, Masaki Deguchi,
Yusuke Yamamoto, and Hitoshi Yamaoka,

Department of Polymer Chemistry, Kyoto University, Kyoto 606-8501, Japan

Block copolymers self-assemble in selective solvents to form micelles consisting of an inner core composed of solely insoluble segments and outer shell of soluble segments swollen by the solvent. Although many studies have been reported on conventional hydrocarbon block polymers, little is known about organometallic block polymers. Recently, we have studied the aggregation of amphiphilic carbosilane block copolymer composed of poly(1,1-diethylsilacyclobutane) (PSB) and poly(2-hydroxyethyl methacrylate) in methanol and toluene solutions by a small-angle X-ray scattering.¹ Here, we examined the micellar structure formed by amphiphilic block copolymers composed of PSB and poly(2,3-dihydroxypropyl methacrylate) (PDHMA) (Fig. 1) in aqueous solution by a small-angle neutron scattering.

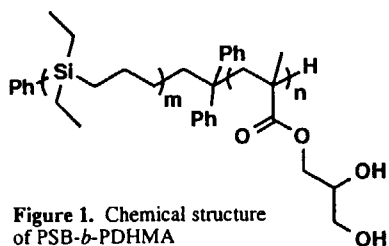


Figure 1. Chemical structure of PSB-*b*-PDHMA

Figure 2 shows SANS profiles in D₂O. Strong scattering at small angle region indicated the existence of aggregates. The scattering curve of polymer A was well reproduced by the theoretical curves of a core-

shell spherical model. On the other hand, scattering intensity of polymer B was proportional to $1/q$ at small angle regions ($q < 0.01$), indicating the formation of rod-like micelles. It is thought that a block polymer having low molar fraction of hydrophobic segment (PSB) formed spherical micelle, whereas a polymer having high molar fraction of PSB formed anisotropic micelle. The analogous tendency has been observed in the case of amphiphilic vinyl ether block copolymers.²

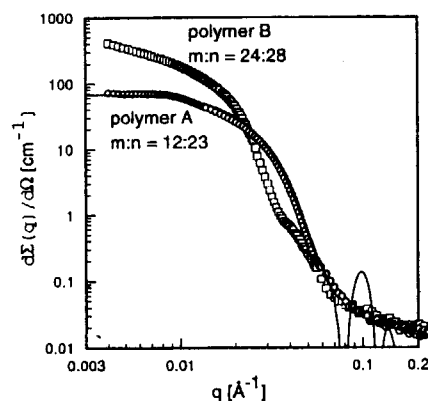


Figure 2. SANS profiles of 1.0 v% PSB-*b*-PDHMA aqueous solution. Solid line is theoretical curve for core-shell sphere ($R_c = 62 \text{ \AA}$, $R_s = 120 \text{ \AA}$, $N_{agg} = 320$).

References

- 1) Nakano, M.; Deguchi, M.; Matsumoto, K.; Matsuoka, H.; Yamaoka, H. *Macromolecules*, submitted.
- 2) Nakano, M.; Matsuoka, H.; Yamaoka, H.; Poppe, A.; Richter, D. *Physica B* **1998**, 241-243, 1038.

JRR-3M, SANS-U, 6. polymer

研究テーマ：高分子濃厚溶液の濃度揺らぎとセグメント運動の関係

表題：ポリ酢酸ビニル濃厚溶液のセグメント運動に対する濃度揺らぎの効果

1-6-13

Effect of Concentration Fluctuation on Segmental Motions in Concentrated Solutions of Polyvinylacetate

M. Nakazawa, O. Urakawa, and K. Adachi

*Department of Macromolecular Science, Graduate School of Science,
Osaka University, Toyonaka, Osaka 560-0043 Japan*

In our recent dielectric studies for concentrated solutions of poly(vinyl acetate) (PVAc) in toluene (Tol), we found that the dielectric relaxation spectrum for the segmental mode process of PVAc broadened strongly. One of the origin for the distribution of relaxation times may be attributed to local heterogeneity present in the solutions. In order to examine this possibility, and also to determine the average length scale of the heterogeneity, we investigated small angle neutron scattering for concentrated PVAc/Tol solutions.

Polyvinylacetate (PVAc) with molecular weight of 200,000 was purified by reprecipitation from methanol solution in water. Deuterated toluene C_7D_8 used as the solvent was obtained from Wako Pure Chemicals Co. Measurements of small angle neutron scattering (SANS) were performed by using SANS-U at Japan Atomic Energy Research Institute, Tokai, Japan. The q -range employed was from 0.007 \AA^{-1} to 0.04 \AA^{-1} . Intensities due to incoherent scattering and scattering from quartz cell were corrected by using the SANS data for 30 and 40 wt% solutions of the monomer (vinylacetate) in C_7D_8 .

Results for 30 wt% solutions are shown in Fig.1. The most characteristic feature of SANS profile is that a steep increase of the scattering intensity I is seen in the range $q < 0.01$. This indicates the existence of inhomogeneity of long length scale. The intensity increases with decreasing temperature indicating the amplitude of the concentration fluctuation increases

with decreasing temperature. This result is in harmony with the dielectric data, *i.e.*, the dielectric relaxation spectra broaden with decreasing temperature. Similar results were also obtained for 40 wt% solutions. The length scale of the concentration fluctuation was estimated from the Ornstein-Zernike plot to be ca 30nm.

One may anticipate from this feature that PVAc solution is gel-like. However it is noted that the solution is transparent and a viscous liquid at least in the range above 265 K. Therefore the inhomogeneity observed for PVAc solution is not due to crosslink points. At present we cannot explain this peculiar behavior.

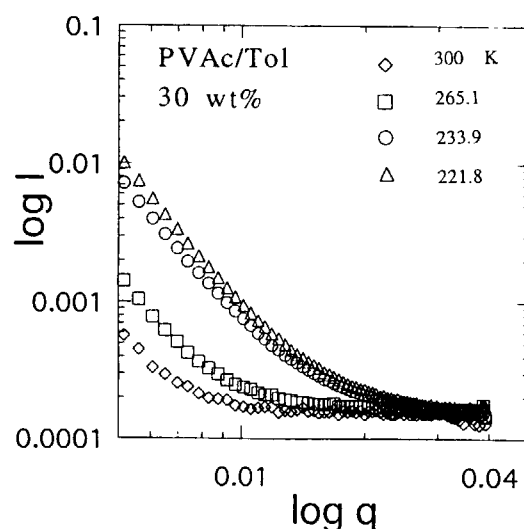


Fig.1 q dependence of the logarithm of scattering intensity I .

研究テーマ:セルロース粒子におけるフラクタル構造の研究
表題:微細結晶性セルロースの大規模構造

1-6-14 Large Scale Structure of Microcrystalline Cellulose in Aqueous Suspension

M. Sugiyama^a, K. Hara^b, N. Hiramatsu^c and H. Iijima^d

^aDepartment of Chemistry and Physics of Condensed Matter, Graduate School, Kyushu University, Fukuoka, 812-8581 Japan

^bInstitute of Environmental Systems, Kyushu University, Fukuoka, 812-8581 Japan

^cDepartment of Applied Physics, Fukuoka University, Fukuoka, 814-0180, Japan

^dChemical Technology Department IV, Asahi Chemical Industry Co., Ltd., Nobeoka, Miyazaki 882-0847, Japan

A microcrystalline cellulose (MCC), which has been recently developed by Asahi Chemical Industry Co., Ltd., is a fine particle with the average size of 3 μm . We revealed that in the scale range between 10 and 100 nm this new material has a fractal structure with the dimension of 2.2 using a small angle neutron scattering method¹. And then we are interested in the maximum limit of this fractal structure and an inter-particle correlation in an aqueous suspension of MCC since the unique property of this new material is that its aqueous suspension exhibits almost temperature-independent viscosity between 20 and 80°C².

In order to clarify the large scale structure, we performed the ultra small-angle neutron scattering experiment with ULS (US-ANS) spectrometers installed at JRR-3M in the Japan Atomic Energy Research Institute, Tokai, Japan. A deuterated aqueous suspension of a specially prepared microcrystalline cellulose, of which MCC concentration was 4.0 wt%, was supplied by Asahi Chemical Industry Co., Ltd, Japan.

Figure 1 shows the USANS profiles of the deuterated aqueous suspension of MCC particles in the double-logarithmic scale. The q dependence of the scattered intensity obeyed the power law with the index of -1.3. It has been known that an observed index is added one into a true index because of the smearing effect by the shape of the incident beam profile (length \times width=2 \times 1 cm²) in the ULS spectrometer³. Therefore, the fractal dimension in this q -range is about 2.3, which is almost same with the dimension observed in

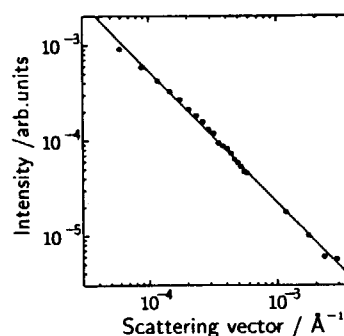


Fig. 1. Double-logarithmic plots of the US-ANS of the deuterated aqueous suspension of MCC particles at room temperature.

higher q -range previously¹. In Fig. 1, the smallest q value ($\sim 6 \times 10^{-5} \text{ \AA}^{-1}$) corresponds to 10 μm in a real space. This is larger than the average size of the MCC particle of 3 μm . Therefore, the aggregation could occur in this concentration (4wt%). In addition, there is no peak indicating the ordering of the microcrystalline cellulose particles. This also indicates that there is no ordered structure between the aggregated units.

1. M. Sugiyama, K. Hara, N. Hiramatsu and H. Iijima: Jpn. J. Appl. Phys. **37** (1998) L404.
2. E. Kamata: New Food Industry, **36** (1994) 59 (in Japanese).
3. Y. Izumi, A. Uchida, H. Nogami, K. Kajiwar, H. Urakawa, Y. Yuguchi, M. Hashimoto and T. Takahashi: Activity Rep. Neutron Scattering Res., **4** (1997) 205.

JRR3M, ULS, 6 Polymer

研究テーマ：ABC 型三成分ブロック共重合体の界面構造

表題：バルク高分子を試料とする中性子反射率測定へのコントラスト・マッチング法の応用

1-6-15 Application of Contrast-Matching Technique to Neutron Reflectivity Study on Bulk Polymer System

N. Torikai, Y. Matsushita,¹ K. Soyama,² N. Metoki,² and Y. Morii²

Neutron Science Laboratory, KEK, 1-1 Oho, Tsukuba, Ibaraki 305-0801

¹ School of Engineering, Nagoya University, Furo-cho, Chikusa-ku, Nagoya 464-8603

² Japan Atomic Energy Research Institute, Tokai, Naka-gun, Ibaraki 319-1195

In the preceding study, we have investigated interfacial structures of isoprene-styrene- d_8 -2-vinylpyridine (IDP) triblock copolymers with lamellar microdomains by using neutron reflectivity (NR) measurement. However, there exist two kinds of interfaces, i.e., I/D and D/P, in microphase-separated structures of IDP triblock copolymers, so that it is difficult to determine the exact structure from their reflectivity profiles uniquely. In principle, it is possible to eliminate the contribution of interfacial structure to reflectivity profile by matching scattering length densities, b/v , between two phases at the interface. Thus, we checked the applicability of contrast-matching technique to NR measurement on bulk polymer system by using styrene-2-vinylpyridine diblock copolymer, which has been well characterized by small-angle neutron scattering (SANS).

Samples used are a styrene- h_8 -2-vinylpyridine (SP) diblock copolymer and its counterpart (DP) with deuterated styrene block chain. Their molecular weights are about 6.5×10^4 and the volume fractions of styrene block chain are 0.50. It has been confirmed that both diblock copolymers form lamellar structures in bulk. Also, it was clarified by our previous SANS work¹⁾ that their optimum blend ratio for satisfying contrast-matching condition between styrene and 2-vinylpyridine is DP/SP=10.5/89.5% in weight. Thus, DP and SP were blended at that optimum ratio determined by SANS. Thin film specimens for NR were prepared by spin-coating from p-dioxane solutions on silicon wafers, and then were annealed at 150 °C in vacuum for one week. NR measurement was performed on the triple-axis

spectrometer (LTAS) of JAERI using neutrons with the wavelength, λ , of 6.2 Å. Specular reflection was observed as a function of neutron momentum transfer, q ($=4\pi\sin\theta/\lambda$), along the direction perpendicular to film surface.

Fig.1 compares specular reflectivity profiles for DP and its blend with SP. The critical q value of total reflection for DP/SP blend is apparently lower than that for DP indicating that average b/v value of DP/SP is lower than that of DP. Also, DP shows the Bragg peaks from lamellar structure, which is preferentially oriented along the direction parallel to the film surface, but DP/SP blend does not show them. These results imply that contrast-matching technique is applicable to NR on bulk polymer. In the next step, IDP/ISP blend whose (b/v) 's of styrene and 2-vinylpyridine are designed to be matched, should be investigated.

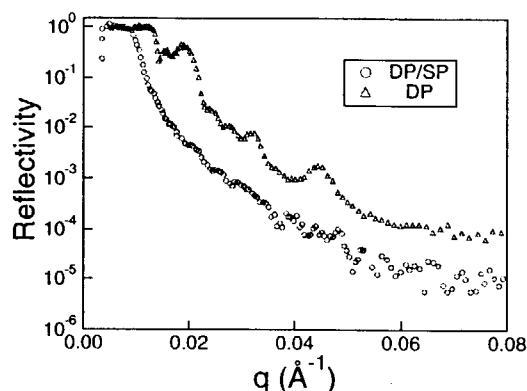


Fig.1 Comparison of specular reflectivity profiles for DP and its blend with SP.

Reference

- 1) Y. Matsushita et al., *Macromolecules* 21 (1988) 1802-1806.

研究テーマ：中性子スピネコー法による両親媒性高分子ミセルの動的挙動の定量的評価
 表題：中性子スピネコー法による両親媒性高分子ミセルの動的挙動の定量的評価

1-6-16 Neutron Spin-echo Study of the Dynamic Behavior of Amphiphilic Diblock Copolymer Micelles in Aqueous Solution.

Y. Yamamoto,[#]H. Matsuoka, H. Yamaoka

Department of Polymer Chemistry, Kyoto University, Kyoto 606-8501, Japan

Amphiphilic polymers, sometimes called polymer surfactants, are a class of macromolecules that consist of hydrophobic and hydrophilic segments connected by a covalent bond. The coexistence of these two kinds of segment in a single polymer chain is expected to produce very interesting characteristics, such as a surface activity, and micellization. The structure and dynamics of these micelles in aqueous solution have been attracting keen attentions for physical chemists and biochemists. The importance of the study on amphiphilic polymer micellization in aqueous systems is absolutely obvious if one take what happens in biological systems into account.

The structural study on micelle geometry in aqueous media is systematically performed by some researchers. Next interest is dynamics of micelle structure. A dynamic light scattering (DLS) is now common and conventional technique to evaluate dynamics in a system, but the dimension of the structure of the system is limited to large scale region because of the limitation of Q range covered. So we use Neutron Spin-Echo(NSE) technique. Since NSE technique can give us an information of dynamics in the length scale of polymers, this technique should be quite useful to study the dynamics of polymer micelle.

In this study, a systematic NSE study has been carried out for diblock copolymer micelle in aqueous solution to estimate dynamic properties existing in this system.

The amphiphilic polymer used is a diblock copolymer of poly-2-hydroxyvinylether as a hydrophilic segment and poly-n-butylvinylether as a hydrophobic segment (N496). The degree of polymerization of each segments are 49 and 6, respectively.

Figure 1 shows the time correlation function obtained by NSE experiments for N496 5wt% D_2O solution at various scattering vector Q . The time-correlation functions obtained were well

fitted by double exponential function and the fast and slow modes could be separately estimated. The slow mode showed an excellent linearity in $\Gamma-Q^2$ plot. From its slope, a translational diffusion coefficient was estimated. The hydrodynamic radius(R_h) obtained by Einstein-Stoke equation was consistent with the value which was estimated by DLS. Hence, this slow mode reflects the translational diffusion of polymer micelle in aqueous solution.

On the other hand, the fast mode was found to be a major factor at larger scattering angle regions, in which SANS curve showed Porod behavior. From this fact, the fast mode should be an internal motion of the polymer micelle. We believe that the origin of the fast mode is the corona dynamics, more detailed analysis should be necessary to clarify this point completely. A comparison with theoretical prediction is now in consideration.

By systematic NSE experiments, two dynamic modes, the fast and slow modes, were found for amphiphilic diblock copolymer micelle in aqueous solution. It was clearly confirmed that NSE is very powerful tool to study dynamics which can not be covered by DLS technique for its spatial dimension and time-order.

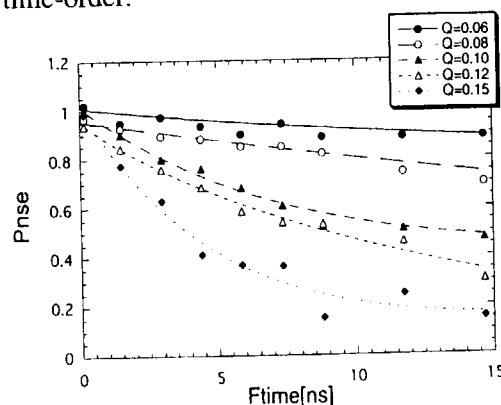


Fig.1 The time correlation function obtained by NSE for N496 micelles in aqueous solution. Conc.=5wt% temp=21°C. The lines are the best fit curves by double exponential function.

研究テーマ：PVAゲルの構造とダイナミクス

表題：PVAゲルの中性子スピンエコー研究

1-6-17 Neutron Spin Echo Studies on PVA gels

T. Kanaya, K. Kaji, Y. Kawabata², M. Nagao¹, H. Seto² T. Takeda²*Institute for Chemical Research, Kyoto University**Institute for Solid State Physics, University of Tokyo¹**Faculty of Integrated Arts and Science, Hiroshima University²*

Neutron spin echo (NSE) measurements have been performed on poly(vinyl alcohol) (PVA) gels in a mixture of deuterated dimethyl sulfoxide (DMSO-d₆) and D₂O with volume ration 60/40 to elucidate dynamics of the crosslinking points. The previous wide and small angle neutron scattering studies [1] have revealed that the crosslinking points of the PVA gel are crystallites and the size has been estimated to be about 70 Å in radius under an assumption of sphere shape of a crystallite.

NSE measurements were carried out on NSE spectrometer at a beam port (C2-2) of JRR-3M reactor. Using neutron wavelength 7.7 Å, we can cover a Fourier time rang from 0.08 to 15 ns. A homogenized PVA solution

at 100 °C was quenched to 25 °C to stand for 24 h to gel and the measurements were made at 25 °C.

Fig. 1 shows the SANS intensities of the PVA gel in a Q range of 0.01 to 0.2 Å⁻¹ measured by NSE and SANS-U spectrometers, showing a good agreement. It is noted that the intensity decreases according to a power law $Q^{-4 \pm 0.2}$, the so-called Porod's law. This Porod's law has been assigned to the smooth surface of crystallites (crosslinking points) [1]. The present NSE measurements were performed in the Porod's region at $Q = 0.03, 0.07$ and 0.10 Å⁻¹, suggesting that we mainly observed the motions of crosslinking points of crystallites.

Normalized intermediate scattering functions $I(Q,t)/I(Q,0)$ of the PVA gel are shown in Fig. 2 at $Q = 0.03, 0.07$ and 0.1 Å⁻¹.

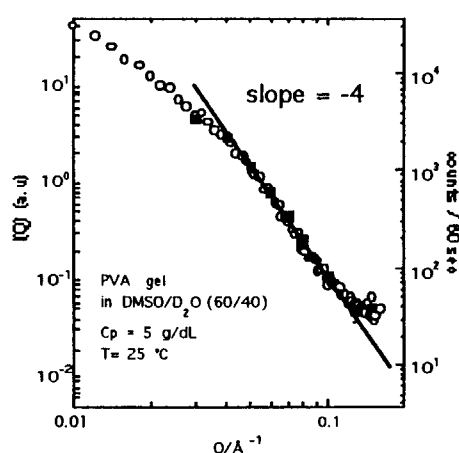


Fig. 1. SANS intensities of PVA gels measured with NSE (■) and SANS-U (○) spectrometer.

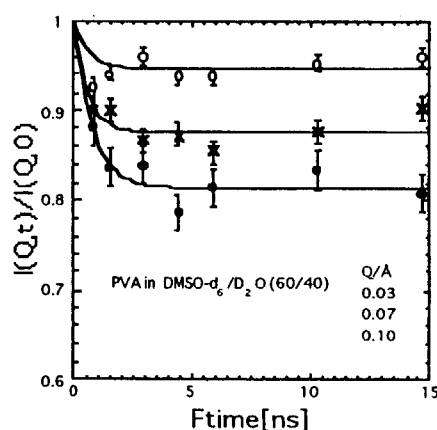


Fig. 2. Normalized intermediate scattering function $I(Q,t)/I(Q,0)$ of PVA gel.

$I(Q,t)/I(Q,0)$ shows a very rapid decay in the time region shorter than about 2 ns while it is almost constant in the time region longer than about 2 ns. It is obvious that the crosslinking points are involved in the PVA network, implying that large scale motions are extremely suppressed. A possible motion of the crosslinking point is restricted in a finite space near its equilibrium position. $I(Q,t)/I(Q,0)$ of such restricted motion is generally expressed by

$$\begin{aligned} I(Q,t)/I(Q,0) \\ = A_0(Q) + [1 - A_0(Q)]F(Q,t) \end{aligned} \quad (1)$$

where $A_0(Q)$ is a non-decaying component which is an elastic one in a frequency domain, and $F(Q,t)$ is a generalized decay function. In the Rouse model, for example, it is given by [2,3]

$$F(Q,t) = \exp[-Q^2(W\sigma^4 t / 9\pi)^{1/2}] \quad (2)$$

where $W\sigma^4$ is the Rouse parameter. If we assume that the probability to find a crosslinking point at a distance r from its equilibrium position is described by a Gaussian function, $A_0(Q)$ is approximately expressed by

$$A_0(Q) = \exp[-l^2 Q^2 / 3] \quad (3)$$

where l^2 is a mean square displacement. Assuming a Debye type decay function for $F(Q,t)$ we fitted eq. (1) to the observed decay curve and the results are shown by solid curves in Fig. 2. The agreement is good. The decay rate is so fast that we could not estimate the exact value. What we can

state at present is that it is shorter than 0.7 ns.

Logarithm of $A_0(Q)$ evaluated in the fit is plotted in Fig. 3 as a function of Q^2 and was fitted with eq. (3) to find the mean square displacement l^2 of 67 \AA^2 . This result means that the crosslinking points (crystallites) are fluctuating in a thermal cloud of 8.2 \AA at around its equilibrium position (see Fig. 4).

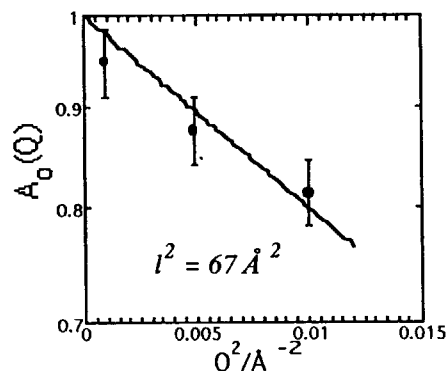


Fig. 3. Q^2 dependence of non-decaying component $A_0(Q)$.

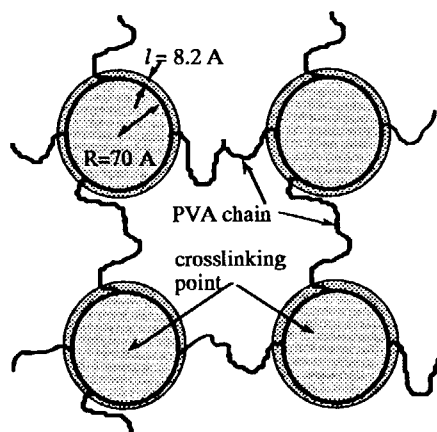


Fig. 4. Schematic sketch of motion of crosslinking points (crystallite) in PVA gel. Shadow shows a fluctuation region.

- 1) T. Kanaya, M. Ohkura, K. Kaji, M. Furusaka, M. Misawa, *Macromolecules*, 1994, **24**, 5609.
- 2) P. G. de Gennes, *Physics*, **3**, 37 (1967).
- 3) R. Oeser, B. Ewen, D. Richter and B. Farago, *Phys. Rev. Lett.*, **60**, 1041 (1988).

研究テーマ：低分子量アモルファスポリスチレンのガラス転移温度以下でのダイナミクス
 表題：準弾性中性子散乱で見たガラス転移近傍におけるアモルファスポリスチレンの高分子効果

1-6-18

Polymerization Effects of Amorphous Polystyrene by Quasi Elastic Neutron Scattering near T_g

I. Tsukushi, T. Kanaya and K. Kaji

Institute for Chemical Research, Kyoto University, Uji, Kyoto-fu 611-0011, Japan

Amorphous solid has many characteristic features which are not found in crystal. Fast process is one of such universal features in amorphous solid. It is observed in neutron scattering as excess quasielastic scattering over Bose-Einstein population factor and appears above near glass transition temperature T_g . The microscopic origin of the fast process is still not clear in spite of many experimental and theoretical efforts. In this study, we have measured the incoherent neutron scattering of polystyrene and styrene trimer by a time of flight (TOF) spectrometer, AGNES, at JRR-3M, Tokai. The energy resolution (HWHM) of AGNES is 70 μeV . Polystyrene and styrene trimer are composed of a same monomer except its polymerization. The investigation of the effect of polymerization on fast process may give a hint to the microscopic origin of its phenomena.

Figure 1 shows the temperature dependencies of elastic intensity for polystyrene and styrene trimer at $Q = 2.6 \text{ \AA}^{-1}$. The intensity is evaluated from integration from -0.24 meV to 0.22 meV and normalized by the intensity at lowest temperature to compare both compounds. The intensity for both polystyrene and styrene trimer decrease linearly with increasing temperature below 200 K. This indicates that a harmonic approximation for atomic vibration is valid in

this temperature and time (\sim resolution) range. Above 200 K, the elastic intensity deviate from linear decreasing for both samples. This tendency has already pointed out for polystyrene [1]. It seems that its deviation is due to fast process. Although T_g of styrene trimer (= 223 K) is 150 K lower than that of polystyrene (= 373 K), the onset temperature of fast process is not so different. It may suggest that the origin of fast process is local motion without effect of connectivity.

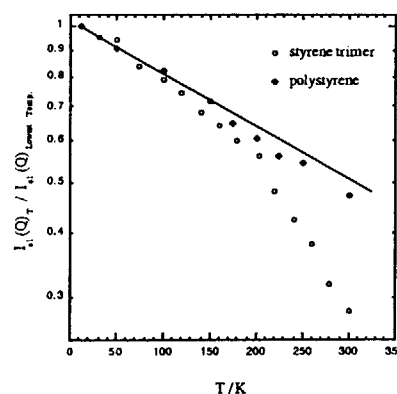


Fig. 1 Temperature dependence of elastic intensity for styrene trimer (open circles) and polystyrene (closed circles). The solid line is a guide for eye.

Reference

- [1] T. Kanaya et. al. *J. Chem. Phys.* **104** (1996) 3841.

研究テーマ: 中性子反射率法による固・液界面における両親媒性高分子の形態とその集合状態の解析

表題: 中性子反射率法による固・液界面における両親媒性高分子の形態とその集合状態の解析

1-6-19 Determination of the Density Profile of Amphiphilic Polymer Adsorbed at Solid/Liquid Interface by Neutron Reflectometry

H. Endo, K. Kago, R. Yoshitome, K. Matsumoto, H. Matsuoka, H. Yamaoka
Department of Polymer Chemistry, Kyoto University, Kyoto 606-8501, JAPAN

Polymer surface and interface play important roles in various phenomena such as adsorption, adhesion etc.

Polyethylene glycol (PEG) adsorbs to the glass surface from the aqueous solution irreversibly. This is due to a hydrogen bonding between the hydroxyl group of the glass and the PEG segment.

To investigate the structure of PEG layer formed at the solid/liquid interface, neutron reflectometry (NR) was carried out. NR technique gives us information about thickness of layers, surface and interface roughness with very high resolution (angstrom order) by *in situ* experiment.

In the previous studies, the formation of the adsorbed layer of PEG was observed by NR at the quartz/PEG solution (solvent: D₂O) and silicon/PEG solution interfaces. The clearer interference fringes were observed in the NR profile for the silicon/PEG solution system. It means that the uniform layer was formed on the silicon surface.

In this study, NR measurements were carried out for the silicon/PEG solution system. In order to make thicker layer, higher molecular weights of PEG were used.

A single-crystal, optically flat silicon slab was used as a substrate in order to achieve acceptable transmission. The solution of 1wt% of polymer in D₂O was introduced into the gap between the silicon block and the Teflon base. The samples of different molecular weights ($M_w=2k, 24k, 250k, M_w/M_n \leq 1.1$) were used. The measurement was started more than two hours after the solution was packed into the cell.

The NR measurements were performed at

JRR-3, MINE, 6. Polymers

JRR-3 MINE. The wavelength of incident neutron beam was 12.6 Å.

NR profiles are shown in Figure 1. The reflectivity is nearly unity below the critical angle (θ_c , about 0.8°). At θ_c , the critical edge can be seen clearly. From these phenomena, reflection was occurred perfectly at the silicon/PEG solution interface.

Above θ_c , no difference can be observed between the profiles for different molecular weights; the reflectivity decreased monotonically with the increase of the angle.

It is thought that PEG was not adsorbed to the silicon surface, because the NR profile of the silicon/PEG solution interface was almost the same as that for the silicon/D₂O interface.

The reason can be guessed that the silicon surface used in this study was smooth, so PEG could not adsorb easily, and that the oxidation of the silicon surface affected the adsorption.

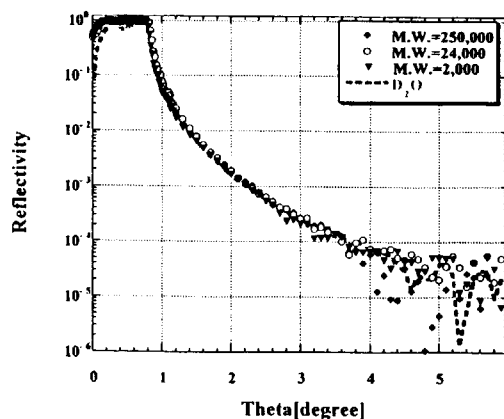


Figure 1. NR profiles for silicon/PEG solution interface.

研究テーマ：高分子多成分系のパターン形成に関する研究

表題：高分子混合系のガラス転移温度近傍における濃度揺らぎの置換基効果

1-6-20 Effects of bulky side group on thermal concentration fluctuations near the glass transition temperature of polymer blends

Hiroyuki Takeno, Satoshi Koizumi¹ and Takeji Hashimoto

Kyoto University, Kyoto, 606-8501, Japan

¹Japan Atomic Energy Research Institute, Tokai, Ibaraki 319-11, Japan

Recently, we have investigated thermal concentration fluctuations (TCF) in the single-phase state for various miscible polymer blends in a wide temperature region from far above the glass transition temperature (T_g) to below the T_g by means of small-angle neutron scattering (SANS). Consequently, for blends of deuterated polystyrene (dPS) and poly (vinyl methylether) (PVME) which is unique in having a large difference ($\Delta T_g = 127$ K) in the T_g of each component, the scattering intensity in the small q was found to be more suppressed than that predicted from de Gennes' theoretical scattering formula, near the T_g of the blend.¹⁾ For such blends, reciprocal zero angle scattering intensity $S(0)^{-1}$ can be divided into three regimes as functions of reciprocal temperature T^{-1} : (i) in the temperature regime far above the T_g which is free from vitrification of polymers, $S(0)^{-1}$ linearly increases with increase of T^{-1} , (ii) $S(0)^{-1}$ deviates upwards from the linear dependence on T^{-1} near the T_g , i.e., $S(0)$ is more suppressed than that predicted from the linear dependence, (iii) $S(0)^{-1}$ shows almost no temperature change due to the freezing below the T_g . On the other hand, for the blend of deuterated polybutadiene (dPB) and protonated polybutadiene (hPB), and that of dPB and polyisoprene (PI) which have almost no difference in the T_g of each component ($\Delta T_g = 4$ K and 29 K for dPB/hPB blend and dPB/PI blend, respectively), suppression of $S(0)$ was not observed near the T_g . We speculated such suppression of $S(0)$ might be caused by the fact that the component with a higher T_g has bulky side groups and consequently their

rotational entropy made a significant contribution to suppression of TCF with a large wavelength.¹⁾ In the case of dPS/PVME blend, the component with a higher T_g , i.e., dPS has bulky benzene rings as side groups.

In this study, we aim to investigate the effects of bulky side groups on anomalous suppression of thermal concentration fluctuations near the T_g for polymer blends with a large difference in the T_g of each component. The polymer blend investigated is a blend of dPS and tetramethyl polycarbonate (TMPC). Though this blend has a large difference ($\Delta T_g = \text{ca. } 100$ K) in the T_g of each component, TMPC with a higher T_g does not have any bulky side group. Fig. 1 shows $S(0)^{-1}$ vs. T^{-1} for dPS/TMPC = 28.9/71.1 (wt%/wt%). As shown in Fig. 1, though upward deviation of $S(0)^{-1}$ from linear relation of $S(0)^{-1}$ and T^{-1} was very slightly observed near the T_g , it is much smaller than that for dPS/PVME. Thus, suppression of the $S(0)$ near the T_g is predicted to be significantly affected by bulkiness of side group for the component with a higher T_g .

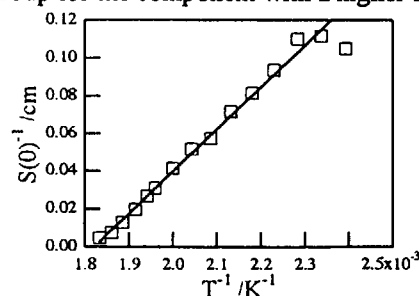


Fig. 1 $S(0)^{-1}$ vs. T^{-1} for dPS/TMPC = 28.9/71.1. reference

1) H. Takeno et al. *Macromolecules*, 29, 2440 (1996)

研究テーマ：ポリエチレンD/Hブレンド試料におけるD鎖とH鎖の凝集状態：延伸に伴う変化の追跡
 表題：重水素化および水素化ポリエチレンブレンドの1軸延伸試料における分子鎖凝集構造

1-6-21 Aggregation Structure of Chains in Uniaxially-Oriented Polyethylene Blends of Deuterated and Hydrogenous Species

Kohji Tashiro¹, Rieko Tanaka¹ and Satoshi Koizumi²

¹ Graduate School of Science, Osaka University, Toyonaka, Osaka 560-0043, Japan

² Japan Atomic Energy Research Institute, Tokai, Ibaraki 319-11, Japan

In order to clarify the spatial distribution of molecular chains in a crystalline lamella and the stacking structure of these lamellae in the bulk polymer sample, a utilization of the blend between the deuterated and hydrogenous species is one of the most useful methods. In such a case of polyethylene (PE) blends between the D and H species, for example, we have always to take into consideration the problem of phase segregation of the D and H species. But we found that some special blends of deuterated high-density PE (DHDPE) with the hydrogenous linear-low-density PE (LLDPE(2)) of ca. 17 ethyl branchings show almost perfect cocrystallization phenomenon even when the sample is cooled slowly from the melt. On the other hand, in the case of the PE blend samples consisted of DHDPE and LLDPE(3) with ca. 43 ethyl branchings, the D species crystallizes at first at higher temperature to form the lamellar stacking structure and then at lower temperature the H species forms the lamellae in-between the stacked lamellae of the D species. In this way, depending on the type of chains, the blend samples change their bulk structure and the crystallization behavior quite sensitively [1-3].

We have now another question for these D/H blend samples. What happens when the polyethylene blends are stretched to give the uniaxially-oriented samples? We measured

the small-angle X-ray scattering (SAXS) and the small-angle neutron scattering (SANS) for these samples. At the same time, by carrying out these measurements as functions of temperature, the different behavior will be expected depending on the type of the blend sample showing the cocrystallization phenomenon or phase segregation phenomenon. In this report, we will describe some preliminary experimental results about the temperature dependence of the SANS patterns taken for the uniaxially-oriented polyethylene blend samples of DHDPE/LLDPE(2) and DHDPE/LLDPE(3).

(1) Blend Samples of DHDPE/LLDPE(2)

The blend sample was prepared by mixing the D and H species into the boiling p-xylene and quenched into methanol at room temperature. This sample was melted and quenched into liquid nitrogen temperature and then was drawn about the 5 times the original length at ca. 110°C. The SANS patterns taken for the uniaxially-oriented samples show the meridional scatterings along the draw axis. Depending on the D/H ratio, the estimated long spacing as well as the relative intensity were changed continuously. As already reported [1-3], this continuous shift of the long spacing corresponds well to the continuous change of the lamellar thickness due to the continuous change

in the spatial distribution of the D and H chain stems in the lamellae.

(2) Blend Samples of DHDPE/LLDPE(3)

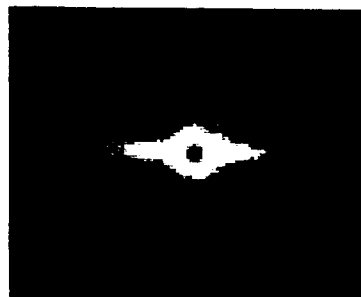
The uniaxially-oriented blend sample of D/H 50/50 content was prepared under the similar condition with the above-mentioned DHDPE/LLDPE(2) case and was set into the heating cell and the 2-dimensional SANS pattern was measured by heating the sample step by step. As shown in Figure 1, the meridional scattering was difficult to detect at room temperature. By heating the sample above 110°C, the meridional scattering increased the intensity and shifted toward the lower scattering angle. The temperature dependence of the SANS profiles traced along the meridional direction is shown in Figure 2. According to the DSC data [1-3], in this temperature region the lamellae of the H species are melted at first and only the lamellae of the D species are remained. This large morphological change might be intimately related with the observed remarkable change in the SANS pattern. At higher temperature the D lamellae were also melted and the patterns disappeared.

We are now analyzing these data quantitatively to investigate the change in the aggregation structure of lamellae consisted of D and/or H species in more details.

References

- [1] K. Tashiro et al., *Macromolecules* **25**, 1801 (1992); **25**, 1809 (1992); **27**, 1221 (1994); **27**, 1228 (1994); **27**, 1234 (1994); **27**, 1240 (1994); **28**, 8477 (1995); **28**, 8484 (1995).
- [2] K. Tashiro, *Acta Polymerica*, **46**, 100 (1995).
- [3] S. Sasaki et al., *Polym. J.*, in press.

25°C



125°C

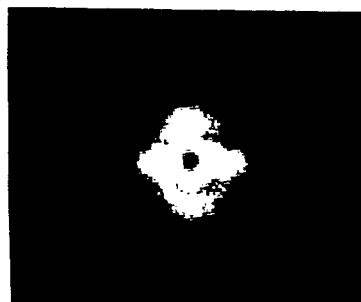


Figure 1 Temperature dependence of the 2-dimensional SANS patterns taken for the uniaxially-oriented samples of DHDPE/LLDPE(3) blend.

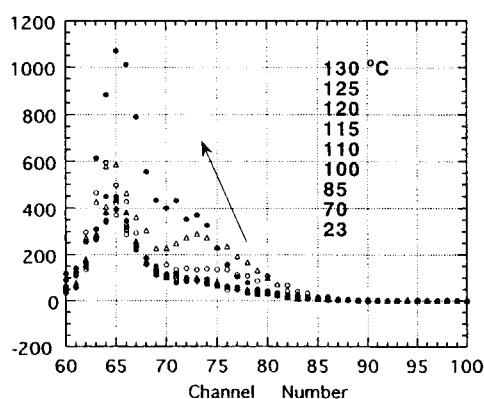


Figure 2. Temperature dependence of the meridional profile of the SANS pattern taken for the DHDPE/LLDPE(3) samples.

This is a blank page.

1. 中性子散乱 7) 生物学

1. Neutron Scattering 7) Biology

This is a blank page.

研究テーマ：コバロキシム錯体結晶の光異性化反応における水素移動

表題：コバロキシム錯体における 2-1 光異性化反応

1-7-1 2-1 photoisomerization of a Cobaloxime Complex

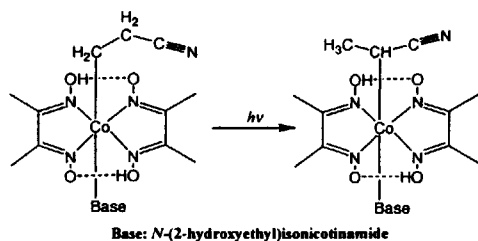
Hiroyuki Imura, Takashi Ohhara, Yuji Ohashi, Ichiro Tanaka,¹ and Nobuo Niimura¹

Department of Chemistry, Tokyo Institute of Technology, Meguro-ku, Tokyo 152-8551

¹Advanced Science Research Center, Japan Atomic Energy Research Institute, Tokai, Ibaraki 319-1195

It was found that the 2-cyanoethyl group bonded to the cobalt atom in some cobaloxime complexes is isomerized to the 1-cyanoethyl group (as shown in the Scheme) on exposure to visible light in the solid state.¹⁾ Many attempts were made to observe the 2-1 isomerization with retention of the single crystal form. When the axial base ligand is *N*-(2-hydroxyethyl)isonicotinamide [hei], the structures before and after the irradiation analyzed by X-rays showed that more than 70% of the 2-cyanoethyl group were isomerized to the 1-cyanoethyl group without destroying the crystallinity.²⁾ The produced 1-cyanoethyl group takes one enantiomeric structure at one site.

In order to make clear the questions how the hydrogen atom transferred to the neighboring atom and why only one enantiomer was produced at one site in photoisomerization, the complex of (2-cyanoethyl-*d*^α,*d*^α)[hei]cobaloxime (**1**) was prepared. To reduce the background, the hydrogen atoms of cobaloxime moiety were replaced with the deuterium atoms in the preparation. A crystal with dimensions 3.5 x 1.5 x 0.5 mm was irradiated with a xenon lamp for 10 days and the crystal structure was analyzed by neutron diffraction at JAERI.



Scheme

Figure 1 shows the molecular structures before irradiation and after 10 days exposure. One of the deuterium atom bonded to the 1-position of the 2-cyanoethyl group keeps the original position, whereas another one was transferred to the 2-position, the methyl carbon. The process of the deuterium atom transfer is proposed in Figure 2.

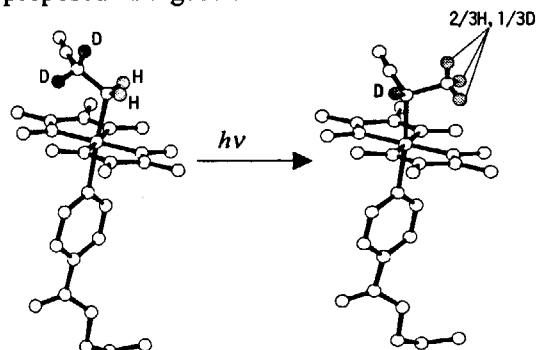


Fig. 1 Molecular structures of **1** before and after irradiation.

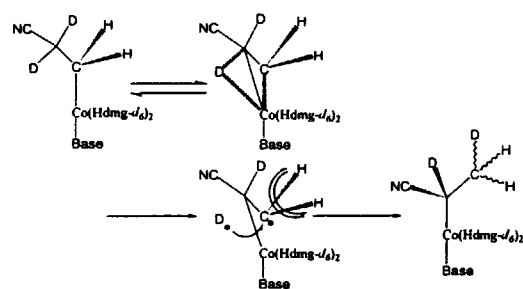


Fig. 2 The proposed process of the deuterium atom transfer in photoisomerization.

References

- [1] Y. Ohgo and S. Takeuchi, *J. Chem. Soc., Chem. Commun.* 21 (1985).
- [2] T. Yoshimiya, Master Thesis, Tokyo Institute of Technology, 1996.

研究テーマ：中性子回折による生体物質の構造研究

表題：pH 4.9 で作成したニワトリ卵白リゾチーム単結晶の中性子回折のデータ収集

1-7-2

Data Collection of Neutron Diffraction from a Single Crystal of Hen Egg-White Lysozyme at pH 4.9

S. Fujiwara, Y. Yonezawa¹, S. Kumazawa, Y. Haga, Y. Minezaki, I. Tanaka, and N. Niimura

Japan Atomic Energy Research Institute, Tokai, Ibaraki 319-1195

¹Tsukuba College of Technology, Tsukuba, Ibaraki 305-08211

Neutron crystallography can locate positions of hydrogen atoms in and around a protein. Hydrogen atoms play important roles in various aspects of functions of the proteins and in stability of the proteins. We have started measuring neutron diffraction of a single crystal of hen egg-white lysozyme grown in D₂O at pH 4.9. This is the first step of the project which explore the protonation of amino acid residues in the protein at various pH. Since pH dependence of charge distribution of the protein may have important effects on thermodynamic characterization of the proteins, it is important to study the pH dependence of protonation of amino acid residues in the protein, in order to elucidate the relationship between structural data and thermodynamic data.

The quality of the crystal used for the measurements had been checked, and the strategy of the efficient measurements had been optimized¹⁾. The space group of the crystals was P4₃2₁2, and the cell parameters were a=b=7.91nm and c=3.66nm. We have used the neutron diffractometer BIX-II for collecting data. The oscillation method of 0.4 degrees has been employed. Exposure time was 11 hours per frame. Diffraction spots of at least 0.2 nm resolution were observed.

We had scheduled that the measurements would have finished within this fiscal year (1998). However, because of the unexpected

shut-down of the reactor JRR-3M from August 1998 to March 1999, we could not finish the data collection. So far, the crystal was rotated 40.8 degrees. The crystal should be rotated about 90 degrees, so the measurements will be continued to the next year (1999).

We analyzed the data obtained so far with DENZO and SCALEPACK²⁾. This program suite was originally written for X-ray diffraction measurements. With some adjustments of the parameters in these program suite, indexing of the diffraction spots and calculation of the integrated intensities from neutron diffraction measurements were properly done. With 0.2 nm resolution, total of 17849 reflections has been observed during these measurements. The number of independent reflections ($>1\sigma$) was 4945. After the measurements will be completed, the structure analysis using these data will be started.

References

- 1) S. Fujiwara et al.: JAERI Review 99-003 (1999) 13.
- 2) Z. Otwinowski and W. Minor: Methods Enzym. 276 (1997) 307-326.

研究テーマ： リン脂質膜構造形成においてコレステロール分子の果たす役割に関する研究
 表題： リン脂質膜構造形成においてコレステロール分子の果たす役割に関する研究

1-7-3

Study on Cholesterol's Roles of a Structure Formation in Phospholipid Membranes

T. Adachi[#], H. Takahashi, M. Imai^{*} and I. Hatta

Department of Applied Physics, Nagoya University, Chikusa, Nagoya 464-8603, Japan

**Institute for Solid State Physics, University of Tokyo, Tokai, Naka, Ibaraki 319-1195, Japan*

[#]Institute of Materials Structure Science, High Energy Accelerator Research Organization, Tsukuba, Ibaraki 305-0801, Japan

A ripple phase is well known in phospholipid systems, especially in dipalmitoylphosphatidylcholine (DPPC). The ripple structure exhibits a periodic undulation of a bilayer, but its detailed structure has not yet been determined. Incorporation of cholesterol into a phospholipid bilayer affects the nature of the bilayer. It has been reported that the periodic spacing of the ripple structure increases as cholesterol concentrations rise. Although several explanations of this mechanism have been proposed, it has still not elucidated. The most important point to understand the cholesterol effect on the ripple structure is to determine the distribution of cholesterol in the bilayers. Thus, in order to make clear the cholesterol distribution in the ripple structure, small angle neutron diffraction experiments were performed on a DPPC-cholesterol system.

We investigated the DPPC bilayers containing 0, 5, 10 and 15 mol% cholesterol. We used pure DPPC-d75 and DPPC-d75/-d0 5:1 mixture as DPPC.

A reflection intensity from ripple structure was stronger on pure DPPC-d75 systems than DPPC-d75/-d0 mixture. It

suggests that cholesterol could make complex with DPPC molecules. The detailed analysis is now in progress.

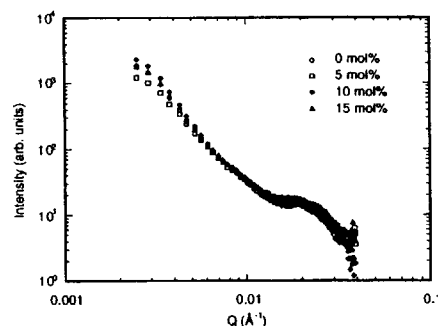


Figure 1 Small angle scattering profile of DPPC-d75 systems.

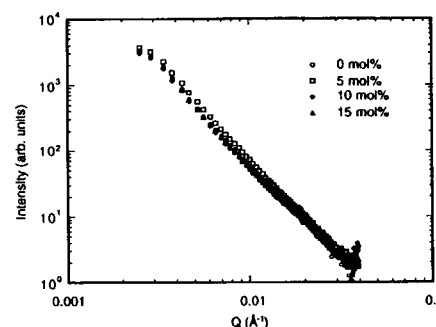


Figure 2 Small angle scattering profile of DPPC-d75/-d0 systems.

研究テーマ：ムコ多糖蛋白質複合体の超分子内部構造

表題：中性子散乱によるプロテオグリカンの構造研究

1-7-4 Structural Study of a Proteoglycan by Neutron Scattering

Y. Watanabe, Y. Sano, I. Tanaka¹ and N. Niimura¹

National Food Research Institute, Tsukuba, Ibaraki 305-8642, Japan

¹Advanced Science Research Center, JAERI, Tokai, Ibaraki 319-1195, Japan

Proteoglycans are extreme examples of glycosylated proteins. The bulk of their structure is usually the large amount of carbohydrate that is attached to the polypeptide chain at very many sites. The carbohydrates consequently dominate the physical and biological properties of proteoglycans. In our project, small-angle neutron scattering methods were used to characterize the structure of a proteoglycan molecule under physiological conditions.

Samples were prepared and purified from shark-fin cartilage and finally soluble in 100 % D₂O containing 10 mM sodium phosphate buffer, pH 7. Small-angle neutron scattering experiments were performed with the SANS-U spectrometer of the University of Tokyo in JRR-3M reactor of Japan Atomic Energy Research Institute (Tokai). Sample-to-detector distance and wavelength were 12m and 7 Å, respectively. Multiple samples were mounted on a sample changer at 25°C.

In the previous study, the average radius of gyration in 100% D₂O was found to be 250 ± 15 Å without concentration dependence ranging from 8 to 20 mg/ml. The contrast matching point was estimated to be 47% D₂O. The Stuhmann plots indicated that the protein is the core of the proteoglycan molecule with symmetrical distribution of neutron scattering density.

In the further analysis of the neutron scattering patterns of the proteoglycan, the preliminary information of its overall shape was obtained as shown in Figure 1. The results indicate that the proteoglycan molecule in a solution can be described to a first approximation by a simple elongated ellipsoid with a main axial ratio about 1:1:120. The detail further investigations are in progress to obtain the interior structure of the shark-fin cartilage proteoglycan.

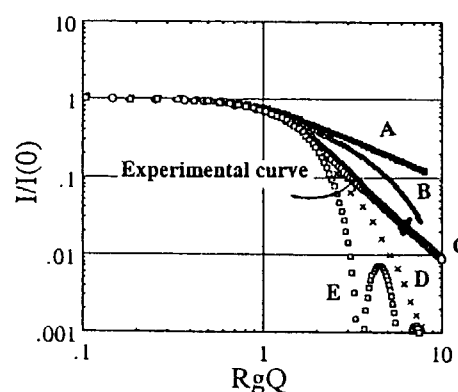


Figure 1 Comparison of the experimental scattering curve with theoretical curves of some models in a log-log plot. An experimental curve was obtained in D₂O buffer. Simple models were cylinders ($h=100r$ (A) and $h=10r$ (B)), ellipsoids of revolution of the axial ratio (1:1:120)(C) and 1:1:3 (D)), and a sphere (E), respectively.

研究テーマ：中性子溶液散乱による原核生物核様体構造の研究

表題：DNA結合蛋白質HUのコントラスト変調法を用いた中性子小角散乱による研究

1-7-5 A Small-Angle Neutron Scattering Study on the DNA-Binding Protein HU Using Contrast Variation Method

S. Fujiwara, Y. Yonezawa¹, and M. Nagao²

Advanced Science Research Center, Japan Atomic Energy Research Institute, Tokai, Ibaraki 319-1195, Japan

¹*Tsukuba College of Technology, Tsukuba, Ibaraki 305-0821, Japan*

²*Neutron Scattering Laboratory, The Institute for Solid State Physics, The University of Tokyo, Tokai, Ibaraki 319-1196, Japan*

In bacteria, DNA molecule is condensed into the complex nucleoprotein structure, nucleoid. One of the major component of the nucleoid is the protein HU. It has been shown that this protein plays an important role not only in the condensation of the bacterial DNA but also in a variety of DNA metabolic events such as replication, transcription, and site-specific recombination. Understanding how the long DNA molecule is condensed in the HU-DNA complex should give valuable insight into the molecular mechanism of these events. As a first step towards understanding the structure of the HU-DNA complex, we characterized the low resolution structure of HU in solution with small-angle neutron scattering method.

HU dimers, which are structural units of this protein, were expressed in *E. coli*, purified, and suspended in 10 mM imidazole (pH 7.0), 50 mM NaCl in 0%, 20%, 80%, and 100% D₂O. The concentration of HU in each solution was 23 mg/ml. Small-angle neutron scattering experiments on these HU solutions were done with the SANS-U spectrometer in the guide hall of the reactor JRR-3M. A wavelength (λ) of 7.0 Å was used with a fractional spread ($\Delta\lambda/\lambda$) of 10%. A sample-to-detector distance was 200 cm. The temperature of the samples was kept at 7°C.

The Guinier analysis of the scattering curves yields the radius of gyration (R_g) and

JRR-3M, SANS-U, 7. Biology

the extrapolated scattering intensity at zero scattering angle ($I(0)$). The $I(0)$ and R_g values at each contrast were obtained by this analysis. From the contrast dependence of the square root of $I(0)$, the contrast matching point of HU was determined to be 41.1% D₂O. Molecular weight estimation from the $I(0)$ value indicated that most HU molecules are in a form of tetramers at the concentration of 23 mg/ml. Figure 1 shows the Sturmann plot of the R_g values of the HU tetramer at various contrast. Approximation of the contrast dependence of R_g by a quadratic curve indicates that there is rather significant fluctuation of scattering-length density in the HU tetramer, that the distribution of the scattering-length density is not isotropic, and that the higher density region is near the outer surface of the tetramer.

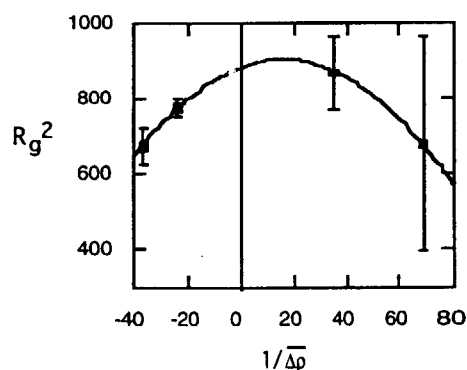


Figure 1 Sturmann plot (the square of the radius of gyration vs. the reciprocal of the contrast) of the HU tetramer.

研究テーマ：大腸菌外膜蛋白質OmpAの構造変化ならびに両親媒性分子との相互作用の研究
表題：オクチルグルコシド存在下で可溶化された大腸菌外膜蛋白質OmpAの構造

1-7-6

Gross Structure of *Escherichia coli* Outer Membrane Protein, OmpA Solubilized in the Presence of Octylglucoside

K.Kameyama, M.Sato¹, S.Ohnishi², and M.Nagao³

Faculty of Engineering, Gifu University, Yanagido, Gifu, 501-1193 Japan

¹ Graduate School of Integrated Science, Yokohama City University

² Department of Biochemistry and Biophysics, University of Rochester, 601 Elmwood Ave. Box 712, Rochester, NY, USA

³ Neutron Scattering Laboratory, The Institute for Solid State Physics, The University of Tokyo, Shirakata, Tokai, Naka, Ibaraki, 319-1106

Gross structure of a complex formed between OmpA from *Escherichia coli* outer membrane and a nonionic surfactant, *n*-octyl- β -glucoside (OG) was investigated by small angle neutron scattering (SANS) using the contrast variation method.

The membrane protein was solubilized from the envelope fraction of a strain of *E.coli* K-12, TNE001 which lacks OmpF and OmpC, and purified by the use of size exclusion and hydroxyapatite chromatographies in the presence of sodium dodecyl sulfate. The purified protein was equilibrated against 50mM Na-phosphate buffer (pH 6.9) containing 22mM of OG and concentrated. A couple of aliquots of the solution were dialysed against the buffer with the same composition as above (0 % D₂O), and against that prepared with heavy water (100 % D₂O), respectively. OmpA solutions with D₂O/H₂O ratios, 10% and 40% were prepared by mixing the dialysates in appropriate ratios. SANS measurements were carried out by the use of the SANS-U instrument installed at the C1-2 beam port of JAERI JRR-3M reactor. Scattering intensity was collected as a function of momentum transfer, q ($= 4\pi \sin \theta / \lambda$, where 2θ and λ are scattering angle and de Broglie wavelength of neutron, respectively). The wavelength of neutron was selected to be 7Å with a sample-to-detector distance, 4000 mm, to cover the q range between 0.005 and 0.1 Å⁻¹. Raw data sets were normalized for the thickness of the sample cell and corrected for transmission.

In the above range of q , linear Guinier plots

were obtained for determination of mean square radius of gyration, r_g , except for the sample with 40% D₂O. The results are shown in Table 1.

Table 1. SANS results for OmpA-octylglucoside complex

D ₂ O/H ₂ O ratio	c_{protein} (mg/ml)	$\Delta I(0)$ (count)	$r_g(\text{\AA})$
0 %	5.2	28.6	35.8
10 %	5.2	13.7	30.5
40 %	5.1	(5)	—
100 %	4.0	270	25.2

The mean neutron scattering length density, $\bar{\rho}$, for the complex was determined to be $1.21 \times 10^{10} \text{ cm}^{-2}$. This value lower than those for simple proteins (around $1.8 \times 10^{10} \text{ cm}^{-2}$) implies that 0.99 g of OG is bound to 1g of OmpA, provided by the calculated value of $\bar{\rho}$ for the surfactant, $0.694 \times 10^{10} \text{ cm}^{-2}$. The above results can be analyzed according to the Stuhrmann plot,

$$r_g^2(\Delta\rho) = a\Delta\rho^{-2} + b\Delta\rho^{-1} + r_v^2$$

where $\Delta\rho$ is the difference in ρ between the complex and solvent. The r_v , the r_g of the particle shape for the complex, was estimated to be 31.2Å. The plot gave a non-zero negative value for a . This result strongly suggests that the surfactant moiety in the complex distributes asymmetrically on the surface of the membrane protein, and significant portion of the protein scarcely binds the surfactant.

研究課題：糖脂質（ガングリオシド）凝集系の水和構造と熱可逆相転移
表題：ガングリオシドミセル構造の温度依存性

1-7-7 Temperature Dependence of Ganglioside Micellar Structure

M. Hirai,¹ H. Iwase,¹ T. Hayakawa,¹ S. Arai,¹ S. Mitsuya,¹ and Y. Matsushita.²

¹ Department of Physics, Gunma University, Maebashi 371, Japan.

² Institute for Solid State Physics, University of Tokyo, Tokai 106-1, Japan.

1. Introduction

Gangliosides, most abundant sialoglycosphingolipids in nerve cells, have been clarified by many investigators to participate in various cell surface events such as self-organization of tissues, immune response and cell differentiation through the molecular recognition depending on a numerous variety of ganglioside structures. It is essentially important for understanding physiological functions of gangliosides to elucidate physicochemical characteristics of gangliosides. By using neutron and SR-X-ray scattering techniques and calorimetry, we have been studying the structural phase behavior of ganglioside aggregates depending on solvent conditions [1] and the binding specificity of gangliosides with proteins depending on both oligosaccharide chain and protein surface modification. By using SR-SAXS and a shell-modeling analysis, we found that the hydrophilic portions of ganglioside molecules composed of oligosaccharide chains sensitively change the conformations depending on temperature with accompanying intensive occlusion-and-extrusion of water in hydrophilic portion of ganglioside micelle.

To confirm the above transition, we have studied the thermal structural transition of ganglioside micelle by using the solvent contrast variation method of small-angle neutron scattering since neutrons are very sensitive for detecting a change of hydration.

2. Experimental

Ganglioside used for the present

experiments was monosialoganglioside (GM1) from bovine brain purchased from Sigma Chemical Co., Ltd. The samples used for the scattering experiments were prepared by dissolving the ganglioside lyophilized powder of 0.5 % w/v in 50 mM Hepes buffer at pH 7. We prepared four different Hepes buffer solvents with different D₂O/H₂O ratios (100, 80, 60, 0 % v/v D₂O).

SANS experiments were performed by using a SANS spectrometer installed at the C1-2 port of the cold-neutron beam line in the research reactor JRR-3M of the Japan Atomic Energy Research Institute (JAERI), Tokai, Japan. The wavelength used was 7.0 Å and the sample-to-detector distance was 150 cm. The temperature of the samples was varied from 10 to 50 °C. The exposure time was varied depending on D₂O/H₂O ratios. To estimate a radius of gyration R_g we used the Glatter's method as follows.

$$R_g^2 = \frac{\int_0^{D_{\max}} p(r)r^2 dr}{2 \int_0^{D_{\max}} p(r) dr} \quad (1)$$

where $p(r)$ is the distance distribution function. The $p(r)$ function was calculated by the Fourier transform of the scattering curve $I(q)$ as

$$p(r) = \frac{2}{\pi} \int_0^{\infty} r q I(q) \sin(rq) dq \quad (2)$$

where q is the magnitude of scattering vector, D_{\max} is the maximum dimension of the particle estimated from the condition $p(r) = 0$ for $r > D_{\max}$. The zero-angle scattering intensity $I(0)$ was estimated by using the Guinier equation $I(q) = I(0) \exp(-q^2 R_g^2 / 3)$ for the scattering curve $I(q)$ in the small q range of 0.025 Å⁻¹ to 0.035 Å⁻¹.

3. Results and discussion

Fig. 1 shows the temperature dependence of the scattering curve $I(q)$ of 0.5 % w/v G_{M1} ganglioside micellar solutions in four different solvents (100 %, 80 %, 60 % and 0% v/v D_2O Hepes buffer at pH 7.0) at different temperatures, where (a) and (b) correspond to at 10 °C and at 50 °C, respectively. According to the simple linear relation between $[I(0)]^{1/2}$ and x where $I(0)$ the zero-angle scattering intensity, x the volume percentage of D_2O in water), we determined the contrast matching point ρ_m from the condition satisfying $[I(0)]^{1/2} = 0$. With elevating temperature the ρ_m value varies from 26.9 % D_2O at 10 °C to 24.4 % D_2O at 50 °C. In Figure 2 the square of the radii of gyration R_g , obtained from the $p(r)$ function using Eqs. 1 and 2, are plotted against $1/\Delta\rho$ ($\Delta\rho$ contrast, so-called Stuhrmann plot). For a monodispersion containing spherical particles the positive slope of Stuhrmann plots indicates that the solute particle is composed of a high-density shell surrounding a low-density core, which corresponds to the present case. Thus, the change of the slope from ~ 5.5 to ~ 7.5 in Fig. 2 clearly shows that the thermal structural change of the G_{M1} ganglioside micelle accompanies the change of the intramicellar scattering density distribution, namely the dehydration of the oligosaccharide chain portion of the micelle since the hydration of this portion reduces the difference between the scattering densities of the hydrophilic shell and the hydrophobic core regions of the micelle. The present results strongly support our previous results [1].

References

1. M. Hirai et al., *Biophys. J.* 70, 1761 (1996); *J. Phys. Chem.* 100, 11675 (1996); *Thermochim. Acta* 308, 93 (1998); *J. Chem. Soc. Faraday Trans.* 92, 4533 (1996); *Biophys. J.* 74,

3010 (1998); *J. Phys. Chem. B* 102, 3062 (1998).

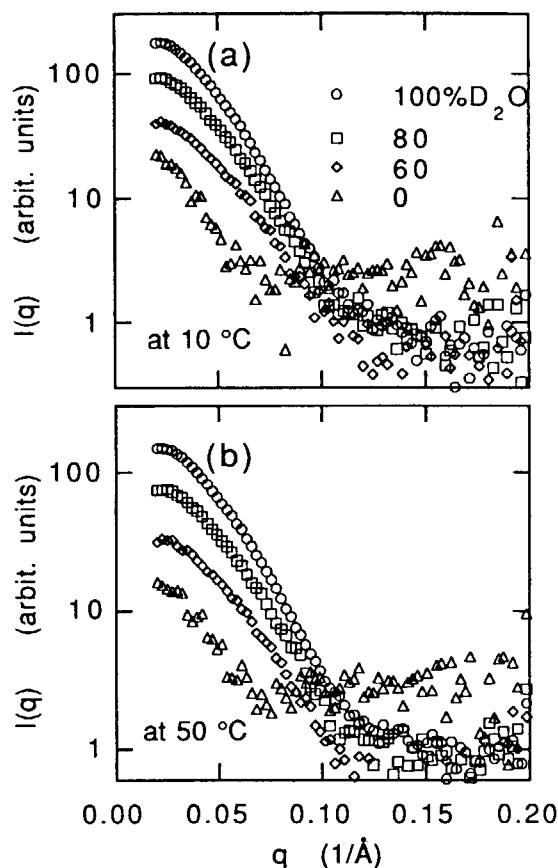


Figure 1. Temperature dependence of G_{M1} ganglioside micellar solutions at different contrast.

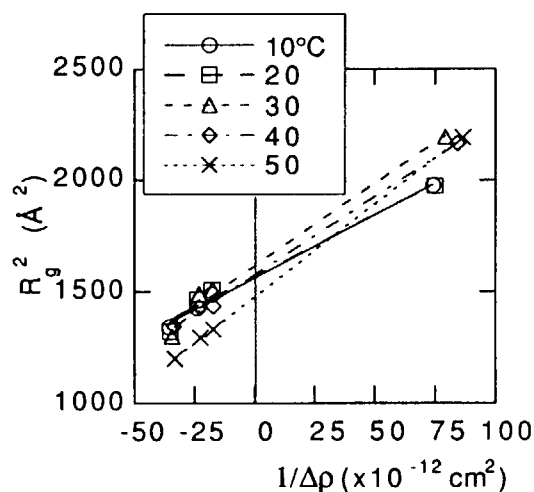


Figure 2. Variation of the slope of the Stuhrmann plots depending on temperature.

1. 中性子散乱 8) 基礎物理学・中性子光学

1. Neutron Scattering 8) Fundamental Physics Neutron Optics

This is a blank page.

研究テーマ：精密中性子光学実験の基礎と応用の研究

標 題：改3号炉PNOにおける中性子干渉計実験

1-8-1 Neutron Interferometry at PNO in JRR-3M

Hiroshi Tomimitsu, Yuji Hasegawa¹ and Kazuya Aizawa

Advanced Science Research Center, JAERI, Tokai, Ibaraki, 319-1102 Japan

¹Faculty of Engineering, Tokyo University, Hongo, Bunkyo, Tokyo, Japan

1. Measurement of Neutron Scattering Lengths by LLL-type Interferometer

As the neutron scattering lengths of elements or isotopes are very important as the basic quantity, many values measured by various methods have been tabulated[1]. Data on several isotopes are, however, still lacking and some of them can be determined in a more accurate way.

We determined the accurate value of gallium isotopes, ⁶⁹Ga and ⁷¹Ga, with the interferometry at the PNO-apparatus. An LLL-type Si interferometer was used with the beam-collimator of 30min. of arc., the wavelength of 0.15123nm and the cross section of the neutron beam was restricted to 2mm in width and 4mm in height. Because of their small amount, the specimens were set so as to receive the transmitted-beam only behind the 1'st reflecting plate of the interferometer.

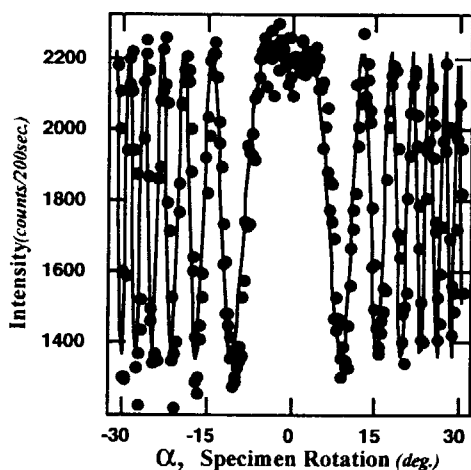


Fig.1 Example of the Intensity Oscillation of ⁶⁹Ga

Fig.1 shows the typical example of the measured oscillation curves of ⁶⁹Ga, with the least square fits on the experimental data. Experimental data were analyzed following the

equation;

$$I = A \cos(B / \cos(\omega + C) + D) + E, \dots (1)$$

where the parameters mean as following;

ω : the amount of specimen rotation from the original angular position,

A: apparent amplitude of the intensity-oscillation,

C: amount of the angular mis-setting from the ideal origin of the specimen,

D: intrinsic phase term of the interferometer, and

E: apparent back-ground part in the intensity-oscillation including all of the imperfectness of the experimental condition, respectively, and

B: this includes all of the physical meanings as

$$B = -N\lambda tb, \dots (2)$$

with N =atomic density of the specimen,

λ =wavelength of the neutron used,

t =thickness of the specimen, and

b = the coherent scattering length to be determined.

We obtained the B 's for the Eq.(2), after reducing the effect of the glass cell and the air. Further, by taking the effect of the impurities, the effect of the isotopic mutual contamination and the uncertainties into account., we finally concluded the b -values for the isotopes as follows[2]:

$$\begin{aligned} b &= 8.053 \pm 0.013 \text{ fm} && \text{for } ^{69}\text{Ga}, \text{ and} \\ b &= 6.170 \pm 0.011 \text{ fm} && \text{for } ^{71}\text{Ga}, \end{aligned}$$

respectively.

The former is larger by about 2% and the latter is less by about 4% compared with the tabulated values[1], respectively. On the other hand, the values of the high purity aluminum, niobium and natural gallium, which were also measured as the standard specimens in the present experiment, were almost the same as the known values.

2. Preparation of the Double LL-Type Interferometry

It seems very important to realize a large working area for the space to put gaseous samples or magnetic elements and other dynamical equipments, in order to extend the applicability of the neutron interferometry. As one of most actual and powerful solution for the requirement, we are trying the system of double LL-type interferometer, as shown in Fig.2, where 1'st and 2'nd LL's are set and typical beam paths are shown. In the figure, D means the separation of the first and second reflected

beams by the 1'st LL block, and L the length between 1'st and 2'nd LL blocks.

In the present trial, two LL blocks were made by modifying a large scale "imperfect" LLL-type interferometer, the distance between two reflecting beams being around 4cm with 220 reflection of 0.15nm wavelength.

Fig.3 shows an example of the characterization of the LL-system, with an Al phase shifter of 3-mm thickness, with the distance of around 50cm between the 1'st and 2'nd LL blocks. The visibility of around 2.6% should be much more improved.

Further investigations are in progress.

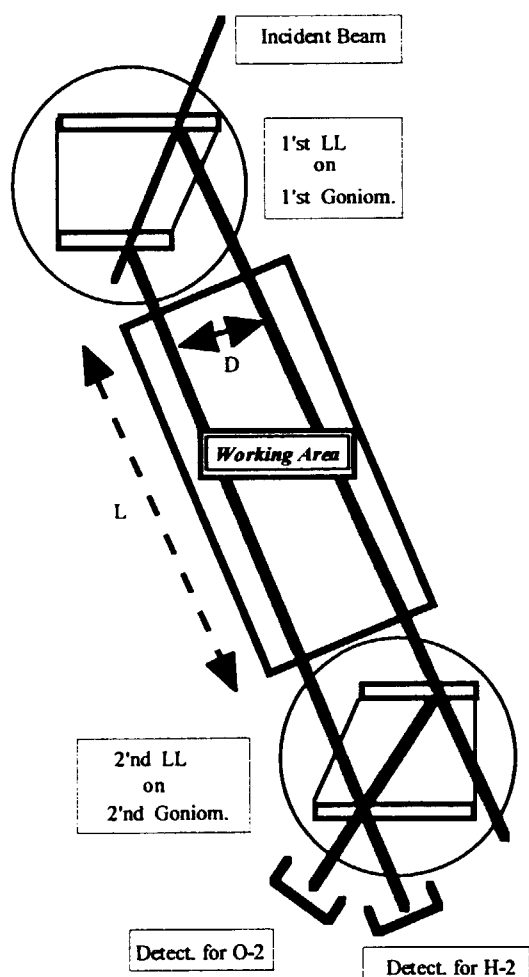


Fig.2 Schematic draw of the double LL-system.

D means the beam separation between first and second reflected beams, L the distance between 1'st and 2'nd LL blocks.

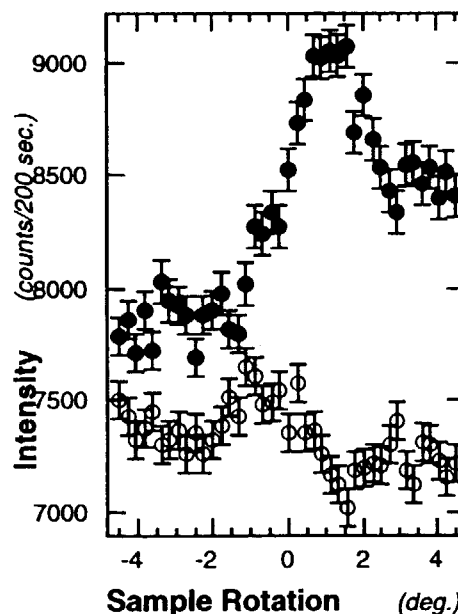


Fig.3 Example of the characterization of the present LL-system, with an Al phase shifter of 3-mm thickness, 220 reflection with 0.15nm wavelength. Open circles mean the intensity oscillation of O-2 wave, while black ones the H-2 wave. They seem to be oscillating rather complementary.

References

- 1) L.Koester, H.Rauch and E.Seymann: Atomic Data and Nuclear Data Tables 49(1991) 65.
- 2) H.Tomimitsu, Y.Hasegawa, K.Aizawa and S.Kikuta: Nucl. Instr. and Meth. in Phys. Res. A420(1999) 453.

研究テーマ: 中性子ラーモア回転によるパーマロイ単結晶の動力学回折
表題: 中性子ラーモア回転によるパーマロイ単結晶の動力学回折

1-8-2 Observation of Dynamical Diffraction Phase due to Neutron Spin Precession through Ferromagnetic Crystal of Permalloy

N. Achiwa, G. Shirozu, S. Tasaki¹, M. Hino¹, T. Ebisawa¹ and T. Kawai¹, K. Kakurai² and M. Shiga³

Department of Physics, Kyushu University, Hakozaki, Fukuoka 812-8581, Japan

¹*Research Reactor Institute, Kyoto University, Kumatori, Osaka 590-0494, Japan*

²*Neutron Scattering Laboratory, ISSP, University of Tokyo, Tokai, Ibaraki 319-11, Japan*

³*Graduate School of Engineering, Kyoto University, Kyoto 606-01, Japan*

1¹ INTRODUCTION

We have, for the first time, observed neutron spin precession due to a dynamical diffraction effect through a pair of ferromagnetic crystals of Permalloy across a Bragg condition of (002) by means of neutron spin echo and phase echo principles. In spite of imperfect crystal, the shift of Larmor precession is enhanced in the rocking curve of the transmitted beams at the magnetic Bragg condition. What was observed is longer dwelling phase of \uparrow spin neutron wave function due to the multiple reflection process of O-wave at Bragg reflection against the rather freely passing opposite spin wave function.

Recently we reported Larmor Precession of neutron spin due to dynamical diffraction effect through magnetic multilayer of permalloy (Fe₅₅Ni₄₅:55Å) (abbreviated as PA)-Ti(54Å)15 bilayers[1][2], PA-Ge-PA Fabry-Perot magnetic thin film resonator[3], and helical magnetic crystal of holmium [4], using a forward diffraction (transmission) neutron spin echo technique. For these magnetic films, the shift of spin precession oscillating sinusoidally as a function of the incident angle at Bragg condition or Fabry-Perot resonating condition was well reproduced by a calculated phase difference between \uparrow and \downarrow spin wave function of neutron through one dimensional periodic potentials for each spin directions. The shift of the Larmor precession is considerably enhanced in the rocking curve of the transmitted beams near a magnetic Bragg condition or at Fabry-Perot bound states. But the spin precession through the helical magnetic crystal showed only delayed side phase shift at (000) \pm magnetic Bragg condition. This may be disappearance of the first order extinction effects due to the mosaic crystal and what was observed is a longer dwelling phase of \uparrow (or \downarrow) neutron wave-function against the freely passing opposite spin wave function, due to the multiple Bragg reflection process of O-wave at Bragg condition.

In spite of theoretical predictions of the phase shift of a neutron spin precession due to dynamical diffraction by a perfect ferromagnetic crystal at the Bragg

reflection[5], it is not so easy to observe it, because, not only difficult to get perfect magnetic crystal but also difficult to avoid the dephasing of Larmor precession due to a wavelength distribution, beam divergence and inhomogeneity of magnetic induction through a large magnetic induction of ferromagnetic crystals. We have overcome these difficulties by adopting neutron spin echo and phase echo principles to observe neutron spin precession of O-wave through ferromagnetic crystal at Bragg condition due to dynamical diffraction effect even to use non-perfect mosaic crystal. The extra spin precession of transmitted O-wave through ferromagnetic crystal at Bragg condition comes from the difference of Fourier potentials $V_{hkl\pm}$ for \uparrow and \downarrow spin neutron as follows.

$$V_{hkl\pm} = \frac{2\pi\hbar^2 N}{m} F_{hkl}(b \pm p) \quad (1)$$

where N is the number of unit cell/cm³, F_{hkl} the structure factor, b and p the coherent nuclear and magnetic scattering length, respectively.

2 EXPERIMENTALS

The two thin single crystals of permalloy (Fe₄₀Ni₆₀, lattice constant $a=3.576\text{\AA}$) with the thickness of 450 μm were cut as square plate parallel to the (110) plane and the (100) plane inclines 45° to the surface so as to be the direction of the (200) Bragg reflection ($2\theta = 90^\circ$, for neutron wavelength 2.528Å) within this thin crystal plane when the neutrons are incident perpendicular to this plane. The experimental setup to observe a spin precession through a pair of ferromagnetic single crystal of PA across a Bragg condition should keep both the spin echo and the phase echo conditions. The spin echo-phase echo setup was build up on the NSE spectrometer PONTA at JRR-3M with a neutron wavelength 2.528Å. The thin plate of single crystals are saturated in the ferromagnetic flux circuits which are inserted in the first and the second precession field of neutron spin echo spectrometer with non-adiabatic spin flipper as shown in Fig. 1. The measurement of the spin precession was carried out under the conditions of spin echo and phase echo

¹JRR-3M, PONTA, 8, Neutron Optics

so as to prevent dephasing of Larmor precession by wavelength distribution and beam divergence. When Larmor precessing neutrons are incident perpendicular to the pair of magnetized crystal plane, both crystals satisfy the (200) Bragg condition for the \uparrow spin component of the precessing neutron. Then the multiply reflected \uparrow spin with the Bragg angle of 90° in the thin crystal get extra phase shift and after the transmission as the O-waves they couple with \downarrow spin component again starting Larmor precession. If the π spin flipper works after a neutron passes through the first crystal, the second crystal cancels the extra Larmor precession due to the Bragg condition. The extra Larmor precession due to the Bragg condition can be extracted if the shift of the spin echo signal is obtained as a function of rocking angle of the second crystal, which is the deviation angle from the Bragg condition.

3 RESULTS AND DISCUSSIONS

Since the visibility of the spin echo signal around Bragg condition indicates the coherency of the transmitted neutron of coupled \uparrow and \downarrow spin, it shows minimum at the Bragg condition against rocking angle where the intensity of the transmitted O-waves of \uparrow spin become minimum due to the Bragg reflection. The shift of the spin echo signal gives a basis precession phase just at the Bragg condition of the both crystals. In the small rocking angle region of the second crystal around the Bragg condition, $\omega = 0$ in Fig. 1, the precession shift seems at first to decrease with plus and minus deviating angle from the Bragg condition and increases again for the further angle deviations. This increase of precession shift with the further deviation angles is due to longer path length of Larmor precessing neutrons through the crystal. The precession decreases against small angle deviation from the Bragg condition indicates that a multiply reflected O-wave of \uparrow spin spends longer phase time in the crystal while that of \downarrow spin goes through the crystal without multiple Bragg reflection. This result seems similar phenomena which was observed in the extra Larmor precession through helical mosaic single crystal of holmium[4]. Though we cannot directly observe the oscillating dynamical phase for the perfect crystal across the Bragg condition, we succeeded in observing the delayed spin precession shift Δ due to the multiple Bragg reflection of O-wave for \uparrow spin neutron among different crystallite parallel with each other.

$$\Delta = \frac{V_{hkl+} - V_{hkl-}}{V_{hkl+}} \delta l_m \frac{2\pi}{\lambda} \quad (2)$$

where δl_m is the sum of the extra wave path length for \uparrow spin neutron during the multiple Bragg reflection

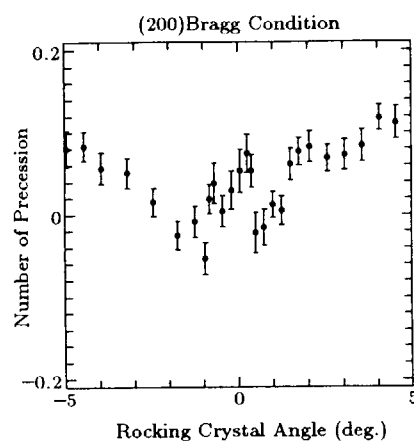


Figure 1: Number of extra spin precession as a function of rocking crystal angle around (200) Bragg condition.

of O-wave through the ferromagnetic crystal. The delayed precession shift may correspond to longer dwelling time of \uparrow spin neutron.

In this experiment, though the effects of beam divergence is not yet extrapolated to zero limit, and even the crystal is mosaic one, the \uparrow and \downarrow neutrons always only couple with their parallel component after multiple Bragg reflection of \uparrow spin O-wave. This is a new principle to observe dynamical diffraction phase by spin precession using even imperfect crystal.

This work was supported by a Grant-in-Aid for Science and Culture of Japan under the program number 10440122.

References

- [1] Achiwa N., Hino M., Tasaki S., Ebisawa T., Akiyoshi T. and Kawai T., J. Phys. Soc. Jpn. **65**, Suppl. A 183(1996).
- [2] Achiwa N., Hino M., Tasaki S., Ebisawa T., Akiyoshi T. and Kawai T., Physica B **241-243**, 1068(1998).
- [3] Hino M., Achiwa N., Tasaki S., Ebisawa T., Akiyoshi T. and Kawai T., Physica B **241-243**, 1083(1998).
- [4] Achiwa N., Hino M., Kakurai K. and Kawano S., Physica B **241-243**, 1204(1998).
- [5] Guigay J.P. and Schlenker M., J. Mag.Mag.Mat. **14** 340(1979).

研究テーマ：コヒーレント中性子ビームによる非弾性散乱の研究

表題：チャンネルカット結晶のロッキングカーブのテールに現れる散乱の裏面反射の影響

1-8-3 Influence of rear face reflections on scattering appearing in the tail of the rocking curve of channel-cut crystals

M. Hashimoto, K. Sumitani, S. Nakatani, T. Takahashi

*The Institute for Solid State Physics, The University of Tokyo,
Roppongi, Minato-ku, Tokyo, 106-8666 Japan*

Channel-cut crystals made of perfect crystal such as silicon and germanium are used for monochromator and analyzer of neutrons in the measurement requiring high angular resolution. This is because they provide tailless beam. For instance, they are used in high resolution measurements in angle and energy using the triple crystal arrangement. Thus we carried out the experiment on inelastic scattering at the beam line C1-3 of JRR-3M. However, in our experiences the rocking curves observed without sample in the double crystal arrangement show deviations from the calculated curves based on the dynamical theory at the tail parts. Those deviations appearing at the tail parts do not give any significant disturbance in usual measurements, so that special attention has not been paid to the discrepancy. But they give crucial influence on the high resolution measurements in angle and energy using the triple crystal arrangement at the extremely small scattering angle comparable to the Darwin width. In this study we found that the main cause of the extra scatterings appearing in the tail parts of the rocking curve is attributed to rear face reflection of neutrons by simulations based on the dynamical theory, as shown dotted line in Fig.1.[1] Furthermore we discussed designs of

channel-cut crystals to reduce such scattering. By using such channel-cut crystal the measurements with higher resolution will be performed. However the cause of the extra scattering of the rocking curve appearing at the region of larger $|W|$ is not yet understand.

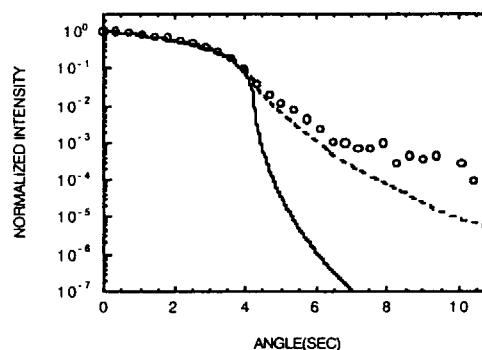


Fig1: Circles mean the observed intensity for five-bounce Si 111 channel-cut crystals in the (+,-) parallel setting. Solid line is calculated based on the Darwin curve and broken line is calculated by taking into account the back surface reflections.

[1] M.Hahshimoto,T.Takahashi; ISSP7'98

研究テーマ: シリコン単結晶とラーモア歳差回転を用いた $\uparrow\downarrow$ スピン中性子の横方向干渉性の測定
表題: スピンスプリッターによる $\uparrow\downarrow$ スピン中性子の横方向干渉性の測定

1-8-4 Measurement of transverse coherent separation of spin precessing neutron using spin splitters

M.Hino, T.Ebisawa, S.Tasaki, Y.Otake¹, H.Tahata², M.Hashimoto³, T.Takahashi³, N.Achiwa⁴

Research Reactor Institute, Kyoto University, Osaka, 590-0494, Japan

¹The Institute of Physical and Chemical Research(RIKEN), Mikazuki, Hyogo, 679-5143, Japan

²Department of Nuclear Engineering, Kyoto University, Kyoto, 606-8501, Japan

³Institute for Solid State Physics, Roppongi, Minato-ku, Tokyo, 106-8666, Japan

⁴Department of Physics, Kyushu University, Fukuoka, 812-8581, Japan

Let us consider Larmor precessing neutron reflected by a pair of spin splitters as shown in Fig.1. The spin splitter consists of a magnetic layer on top, followed by a gap layer and a nonmagnetic layer[1, 2]. At the incident angle θ , as shown in Fig.1(a), the transverse separation with the $(+, -)$ arrangement is canceled out. On the other hand the separation with $(+, +)$ arrangement, as shown in Fig.1(b), the transverse separation is doubled. The transverse coherency of \uparrow and \downarrow spin neutron waves can be estimated from loss of visibility of the spin precession as a function of the gap thickness. When the \uparrow and \downarrow spin neutron waves propagate parallel to each other as shown in Fig.1, we can estimate a maximum transverse coherent separation.

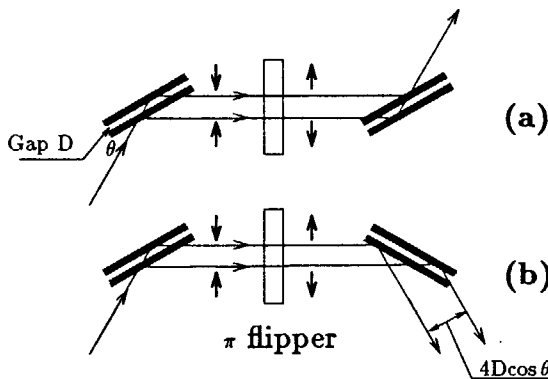


Figure 1: Schematic view of transverse separation and convergence of \uparrow and \downarrow spin neutron wave by a pair of spin splitters with (a) $(+, -)$ and (b) $(+, +)$ arrangements.

The first experiment has been performed with the neutron spin interferometer installed at MINE at JRR-3M in JAERI. We observed transverse coherent separation of a neutron with wavelength of 12.6\AA ($\delta\lambda/\lambda = 3.5$). The experiments, however, did not show convincing the existence of an intrinsic maximum coherent separation of a neutron. Therefore we have installed a neutron spin interferometer at ULS in JAERI in order to use better monochromatic incident neutron beam reflected from Si-perfect crystal.

JRR-3M, MINE, 8, Fundamental Physics & Neutron Optics

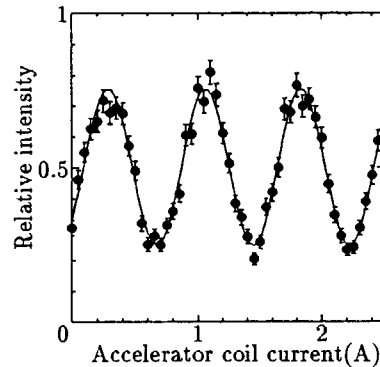


Figure 2: Typical NSE signals reflected by a pair of multilayer spin splitter with $(+, -)$ configuration, in the spin interferometer in ULS.

ULS provides the cold neutron beam with a wavelength of 4.73\AA ($\delta\lambda/\lambda = 1.1\%$). The strength of guide magnetic field was 0.86 mT and the divergent angle of incident beam was 2.3 mrad . The polarizer and analyzer which consist of Supersendust ($\text{Fe}_{58}\text{Ni}_{32}\text{Si}_6\text{Al}_4$; 9nm)/germanium(Ge ; 8nm) [30bilayers] has been used to magnetically saturate in the lower magnetic field. Figure 2 shows the NSE signal of \uparrow and \downarrow spin neutron waves reflected by a pair of the spin splitters for the gap thickness of $0.2\text{ }\mu\text{m}$ with $(+, -)$ arrangement shown in Fig.1(a). The visibility of NSE signal is estimated to be 0.51 . Since the incident divergent angle was not small, the visibility was not so good for precise measurement of the coherent separation. Even then, this result shows the feasibility of the measurement of the transverse coherent separation.

References

- [1] H.Funahashi, T.Ebisawa, T.Haseyama, M.Hino M, A.Masaike, Y.Otake, T.Tabaru, S.Tasaki, Phys. Rev. A54, 649(1996)
- [2] T.Ebisawa, S.Tasaki, T.Kawai, M.Hino, N.Achiwa, Y.Otake, H.Funahashi, D.Yamazaki, and T.Akiyoshi, Phys. Rev. A57, 4720(1998)

研究テーマ: ラーモア回転による中性子波束のスピン干渉
 表題: スピン回転による多連結ファブリペロー磁気膜での中性子束縛状態の測定

1-8-5 Larmor precession of bounded neutron spin in multiply coupled magnetic Fabry-Perot film

N. Achiwa, M. Hino¹, S. Tasaki¹, T. Ebisawa¹, T. Kawai¹, D. Yamazaki², G. Shirozu

Department of Physics, Kyushu University, Fukuoka, 812-8581, Japan

¹Research Reactor Institute, Kyoto University, Osaka, 590-0494, Japan

²Department of Nuclear Engineering, Kyoto University, Kyoto, 606-8501, Japan

Quasibound states of neutron were observed for the first time with ultracold neutron by Steyerl and co-workers[1] and Mázza estimated neutron lifetime in quasibound states[2]. However, we measured Larmor precession angles of neutron spins transmitted through double-hump or triple-hump potential barriers for \uparrow spin neutrons[3] including the tunneling region. Recently, Hino reported precise measurement of tunneling phase shift through ferromagnetic thin films of permalloy using Larmor precession [4].

This time, we have connected multiply coupled magnetic potentials created by a sequence (permalloy $\text{Fe}_{55}\text{Ni}_{45}$ (PA)-Ge) n -PA films deposited on flat silicon wafer. Here an \uparrow spin neutron wave feels multiply coupled bound state potential wells and a \downarrow one feels almost a small rectangular potential. These multilayers are called multiple Fabry-Perot magnetic thin film resonator, and the layer thickness of each films was measured by a quartz crystal oscillator during deposition. The measured thicknesses of permalloy $_{45}(\text{Fe}_{55}\text{Ni}_{45})$ films for $n=10$ were 200Å and the thicknesses of all germanium films were 400Å.

By inserting the multiple Fabry-Perot resonator into the second spin precession field of a neutron spin interferometer(NSI)[5] installed at the cold neutron guide tube(C3-1-2) of the JRR-3M reactor at JAERI, we could observe quasibound states of \uparrow spin neutron in the Fabry-Perot resonator using Larmor precession, which is shown by the shift of neutron spin echo(NSE) signals. In this experiment, the NSI is considered as a miniature of a transverse NSE instrument, and the wavelength resolution and the divergent angle are $12.6\text{Å}\pm 0.44\text{Å}$ (FWHM) and $0.7\times 10^{-3}\text{rad}$, respectively.

As shown in Fig. 1, the number of Larmor precession versus the incident angles show sinusoidal oscillations and the oscillation is well reproduced by the theoretical phase difference of \uparrow and \downarrow spin neutron wave functions calcu-

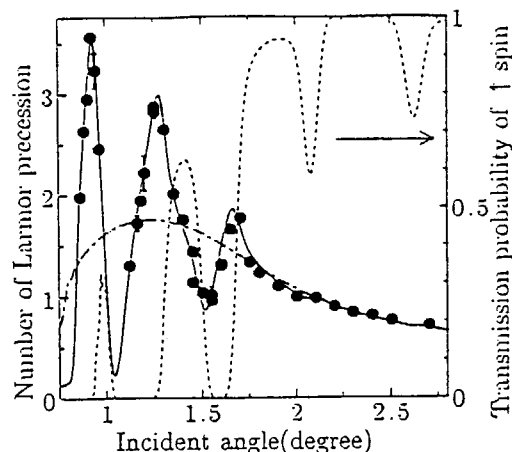


Figure 1: The number of precessions(closed circles and solid line) and transmission probability(broken line) of \uparrow spin neutron through the multiple (PA-Ge) 10 -PA Fabry-Perot resonator as a function of incident angle.

lated with one-dimensional Schrödinger equation for multiply coupled potential barriers. The smaller the incident angles, the bigger the amplitude of sinusoidal oscillations are. The sinusoidal amplitude of the number of Larmor precession seems proportional to the number of coupled quantum wells, though the transmission probability seems to be constant.

References

- [1] A.Steyerl, T.Ebisawa, K.A.Steinhauser and M.Utsuro, Z. Phys. B. 41(1981)283.
- [2] M.Maaza, B.Pardo, J.P.Chauvineau, A.Raynal, A.Menelle, F.Bridou, Phys. Lett. A223(1996)145.
- [3] M. Hino, N. Achiwa S.Tasaki, T. Ebisawa, T. Kawai and T. Akiyoshi, Physica B241-243(1998) 1083.
- [4] M. Hino, N. Achiwa S.Tasaki, T. Ebisawa, T. Kawai and T. Akiyoshi, Phys. Rev. A59(1999) 2261.
- [5] T. Ebisawa, H. Funahashi, S.Tasaki, Y.Otake, T. Kawai, M. Hino, N. Achiwa and T. Akiyoshi, J. Neutron Research vol 4, 157(1996).

¹JRR-3M, MINE, 8, Neutron Optics

研究テーマ:中性子ラーモア歳差回転によるトンネル時間とラーモア時計の研究
表題:吸収の強い磁気膜を透過する中性子のスピン回転

1-8-6 Measurement of spin precession angle of neutron transmitted through magnetic thin film with absorption

M. Hino, S. Tasaki, T. Ebisawa, T. Kawai, N. Achiwa¹, D. Yamazaki²

Research Reactor Institute, Kyoto University, Osaka, 590-0494, Japan

¹Department of Physics, Kyushu University, Fukuoka, 812-8581, Japan

²Department of Nuclear Engineering, Kyoto University, Kyoto, 606-8501, Japan

Recently, we have succeeded in measuring spin precession angles of neutrons tunneling and non-tunneling through Permalloy45 ($\text{Fe}_{55}\text{Ni}_{45}$) ferromagnetic film as a function of incident angles[1]. The spin precession angle is well reproduced by the theoretical phase difference of \uparrow and \downarrow spin neutron wave functions based on one-dimensional Schrödinger equation using optical potential model[2]. In this report, we present spin precession angle and transmission probability of neutron through PA/Gd magnetic thin film for non-tunneling case, where the PA/Gd film consists of Permalloy45($\text{Fe}_{55}\text{Ni}_{45}$ and gadolinium atoms, the total thickness is 1100Å and the ratio of PA and Gd is 10:1. The film were evaporated on a polished silicon wafer in an applied magnetic field of 14mT in order to saturate the magnetic film under lower magnetic field. Here we assume that the value of potential barrier in the magnetic absorber is represented as $V = V_{\text{nuc}} \pm \mu B + iV_{\text{ab}}$ for \uparrow and \downarrow spin, respectively, where V_{nuc} , V_{ab} and μB is the average coherent nuclear potential, absorption one, magnetic one, respectively[3].

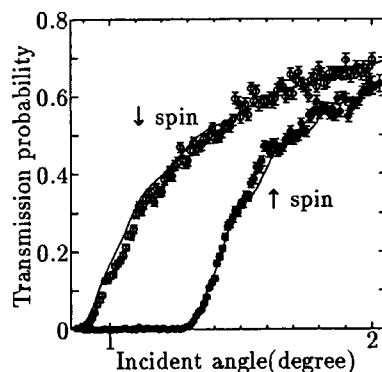


Figure 1: Transmission probabilities of \uparrow (●) and \downarrow (○) spin neutron transmitted through the PA/Gd film.

As shown in Fig.1, the experimental transmission probabilities of \uparrow and \downarrow spin neutrons are well reproduced by the theoretical lines. The theoretical lines are calculated from one-

JRR-3M, MINE, 8, Fundamental Physics & Neutron Optics

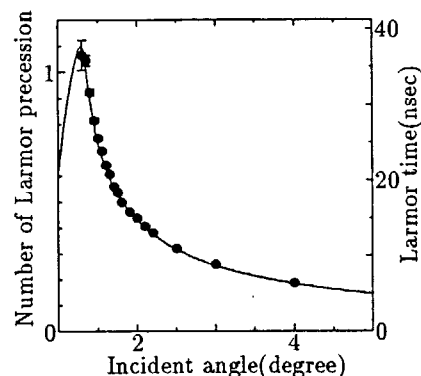


Figure 2: The shift of NSE signals through the PA/Gd film.

dimensional Schrödinger equation using the optical potential barrier with absorption including effects of the incident wavelength distribution.

The angles of additional spin precession are directly observed as a shift of neutron spin echo(NSE) signals by inserting the film in one of the Larmor precession fields of a transverse NSE spectrometer. As shown in Fig.2, the additional spin precession angles were well reproduced by the relative phase difference between \uparrow and \downarrow spin neutron wave functions which were derived with solving one-dimensional Schrödinger equation for the optical potential with absorption. From these results, it is clear that the optical potential model with absorption is acceptable for non-tunneling case.

References

- [1] M. Hino, N. Achiwa, S. Tasaki, T. Ebisawa, T. Kawai, T. Akiyoshi and D. Yamazaki, Phys. Rev. A59, 2261(1999).
- [2] S. Yamada, T. Ebisawa, N. Achiwa, T. Akiyoshi and S. Okamoto, Annu. Rep. Res. Reactor Inst. Kyoto Univ., 11, 8(1978).
- [3] T. Ebisawa, T. Akiyoshi, N. Achiwa, S. Yamada and S. Okamoto, Annu. Rep. Res. Reactor Inst. Kyoto Univ., 14, 10(1981).

研究課題: 冷中性子スピン干渉計の開発とその応用
表題: RF flipper による冷中性子スピン干渉を用いた分光法の開発

1-8-7 Modified Spin Echo Method Using Cold Neutron Spin Interferometry with RF Flippers

T. Ebisawa, D. Yamazaki¹, M. Hino, T. Kawai, S. Tasaki, N. Achiwa² and Y. Otake³

Research Reactor Institute Kyoto University
Department of Nuclear Engineering Kyoto University¹
Department of Physics, Kyushu University²
SPRING The Institute of Physical and Chemical Research³

We have been developing a modified spin echo method using a cold neutron spin interferometry with radio frequency flippers (RF flipper)[1], which is similar to Mieser spectrometer[2]. A basic system of the modified method is shown in Fig.1[3]. The guide coil supplies a uniform low magnetic field of a few Gauss to the whole system. The low field is enough to avoid neutron depolarization and saturate the magnetization of the magnetic mirrors of the polarizer and analyzer we developed[4]. The first and second RF flippers with high frequency are operated as $\pi/2$ flipper and π flipper, respectively. The third flipper with low frequency functions as $\pi/2$ flipper.

We consider the case of the following conditions as regards the magnetic fields of the system,

$$B_{z,1} = B_{z,2} = B_z \gg B_{z,3} = B_g \quad (2)$$

where $B_{z,i}$ are the magnetic field in z axis of the i th RF flipper and B_g the guide field, respectively.

The polarized neutron is split into the two spin eigenstates with energy difference with $\hbar\omega_z$ by the first RF $\pi/2$ -flippers. The spin state and energy difference of these partial waves are reversed by the second RF π -flippers. The third $\pi/2$ -flipper superposes them in the $\uparrow\uparrow$ and $\downarrow\downarrow$ spin states. The analyzer mirror reflects the pair of the $\uparrow\uparrow$ spin states and the phase difference between them is measured by the neutron intensity. The above behaviors of the partial waves are illustrated in Fig.1(b).

The phase difference Φ_t at the detector is calculated as a function of detection time of the neutron t , neglecting B_g for B_z , [1, 3]

$$\Phi_t = \omega_z t + k_z(L_1 - L_2 - L_3) \quad (3)$$

$$= \omega_z t + \left\{ \omega_z \frac{(L_1 - L_2 - L_3)}{v} \right\} \quad (4)$$

$$t = t_0 + t_1 + t_2 + t_3 \quad (5)$$

where t_0 is the time which the neutron is incident on the first RF $\pi/2$ -flipper, k_z the wave number difference between the two spin components given by ω_z/v , L_1 the length between the first and second RF flippers, L_2 the length between the second RF flipper and the sample, L_3 the length between the sample and the detector, and t_i is the neutron flight time given by L_i/v .

The phase shift given by the first term of Eq.(3) oscillate as a function of the neutron detection time with frequency ω_z . The second term is a dispersive phase difference caused by the momentum difference. Measuring a time spectrum, we can obtain a neutron intensity with time dependent oscillation from the first term. On the other hand, the second term induces a dispersive phase shift depending on the velocity resolution of the incident neutron, which is in quite analogous situation to Larmor precession. Accordingly, in order to observe an interference

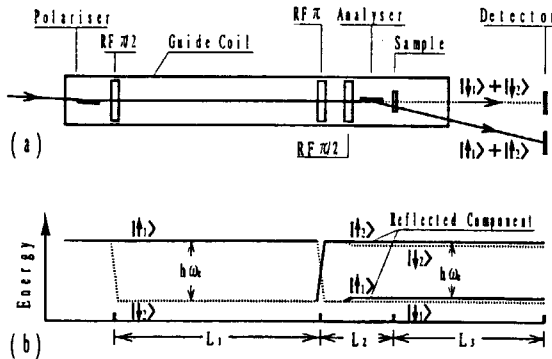


Figure 1: (a) An arrangement of a modified neutron spin echo method using cold neutron spin interferometer with RF flippers. (b) Illustration of splitting and superposing of a polarized neutron.

Assuming the resonance condition for the RF flipper and expressing the oscillating field as $B_x \sin \omega_z t$, the frequency of the oscillating field, ω_z is given by the magnetic field applied to the RF flipper B_z ,

$$\hbar\omega_z = 2\mu B_z \quad (1)$$

where μ is the neutron magnetic moment.

JRR-3M, MINE, 8, Fundamental Physics

pattern varying with the neutron detection time, the following condition is required, [1, 2, 3] respectively. They are given by,

$$L_1 - L_2 - L_3 = 0 \quad (6)$$

Then the phase difference is given by as a function of the neutron flight time t ,

$$\Phi_t = \omega_z t \quad (7)$$

Figure 2 shows a time spectra measured for a frequency of 200 KHz and $L_1 = L_2 + L_3 = 80\text{cm}$. This visibility of the time spectra disappeared for a deviation of the detector position from the best position owing to the second term of Eq(2).

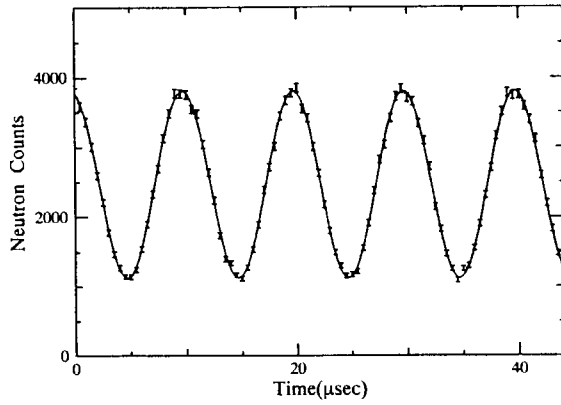


Figure 2: Time spectra measured for a frequency of 100 KHz.

Change of neutron velocity by the inelastic scattering with the sample gives rise to a change $\Delta\Phi$ of the phase difference given by Eq.(3), which can be calculated,

$$\Delta\Phi = \omega_z \Delta t_3 - \Delta k_z L_3 \quad (8)$$

$$\Delta t_3 = t_3 \frac{\Delta v}{v} \quad (9)$$

$$\Delta k_z = \omega_z \frac{\Delta v}{v^2} \quad (10)$$

where Δv , Δt_3 and Δk_z are the change of the neutron velocity, the neutron flight time and the wave number, respectively, after the scattering. Phase shift at a same detection time ($\Delta t_3=0$) changes by the second term in Eq.(8). Thus the neutron velocity change after the scattering is related to the change of the phase shift $\Delta\Phi$ as follows;

$$\Delta\Phi = -\omega_z L_3 \frac{\Delta v}{v^2} \quad (11)$$

$$= -\omega \tau_{nse} \quad (12)$$

ω and τ_{nse} are the energy transfer corresponding to the velocity change and the spin echo time,

$$\omega = \frac{m}{\hbar} v \Delta v \quad (13)$$

$$\tau_{nse} = \frac{\hbar \omega_z L_3}{m v^3} \quad (14)$$

These discussions show that this spectroscopy is similar to conventional spin echo method in spite of different spin interferometry. The typical characteristics of this system as a spin echo method can be evaluated from these equations and is shown in Table 1.

Table 1: Energy resolution and τ_{nse} of a modified spin echo method using RF flippers as a function of neutron wavelength for three frequencies of the time interference, assuming $L_3 = 1\text{m}$. The energy resolution corresponds to phase shift of 2π .

wavelength(Å)	6	12	24
Frequency : 10KHz			
energy resolution(μeV)	2100	267	33
$\tau_{nse}(\text{nsec})$	0.002	0.016	0.12
Frequency : 100 KHz			
energy resolution (μeV)	210	26.7	3.3
$\tau_{nse}(\text{nsec})$	0.019	0.155	1.24
Frequency : 1 MHz			
energy resolution(μeV)	21.4	2.67	0.33
$\tau_{nse}(\text{nsec})$	0.194	1.55	12.4

References

- [1] D.Yamazaki, T.Ebisawa, T.Kawai, S.Tasaki, M.Hino, T.Akiyoshi, N.Achiwa, Physica B 241-243(1998)186-188.
- [2] W.Besenböck, P.Hank, M.Köppe, R.Gähler, T.Keller, R.Golub, J. Phys. Soc. Jpn. 65 Suppl.A (1996) 215.
- [3] T.Ebisawa, S.Tasaki, M.Hino, T.Kawai, Y.Iwata, D.Yamazaki, N.Achiwa, Y.Otake, T.Kanaya, K.Soyama, Journal of Physics and Chemistry of Solids (1999) in press.
- [4] D.Yamazaki, et al.. to be published.

1. 中性子散乱 9) 装 置

1. Neutron Scattering 9) Instrument

This is a blank page.

研究テーマ：(1) 生体物質の中性子回折による研究

表題：生体高分子用中性子イメージングプレート付き改良中性子回折計

1-9-1 An Upgraded Neutron Diffractometer (BIX-III) for Macromolecules with a Neutron Imaging Plate

I. Tanaka, K. Kurihara, T. Chatake, Y. Nishimura, Y. Haga, Y. Minezaki, S. Fujiwara, S. Kumazawa¹, Y. Yonezawa², N. Niimura, R. Bau³, A. Suzuki⁴, E. Otani⁴

Advanced Science Research Center, JAERI, Tokai, Ibaraki 319-1195, Japan

¹ Neutron Scattering Laboratory (KENS), KEK, Tsukuba, Ibaraki 305-0801, Japan

² Tsukuba College of Technology, Tsukuba, Ibaraki 305-0821, Japan

³ Dep. of Chemistry., Univ. of Southern California, Los Angeles, CA 90089, USA

⁴ Faculty of Science, Tohoku Univ., Sendai, Miyagi 980-8578, Japan

An upgraded diffractometer¹⁾ with a neutron imaging plate (NIP)²⁾ dedicated to protein crystallography (Fig.1) has been constructed at JRR-3M. Thanks to the NIP for covering large scanning area, upgraded elastically bent perfect Si monochromator³⁾ and shifting of the sample position to upstream for shielding effectively against neutrons and γ -rays⁴⁾, finally we obtained an improvement factor of 40 in comparison to different aspects of an old diffractometer BIX-I⁵⁾ (table 1). Till now we have already taken data for several challenging samples and succeeded as in Fig.2-4. All experiments were carried out using $\lambda = 2.35 \text{ \AA}$.

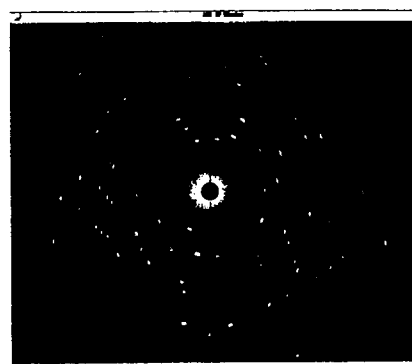


Fig.2 Diffraction pattern of HEW-Lysozyme in D_2O . The sample size was $2.0 \times 2.0 \times 3.5 \text{ mm}^3$, the exposure time was about 15 hrs, and still. About 2 \AA spots could be observed.

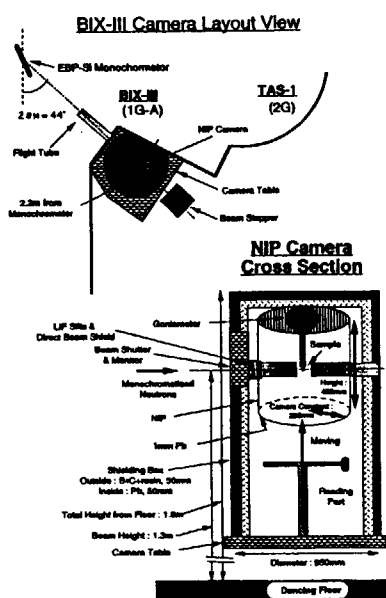


Fig. 1 Schematic view of BIX-III.

References

- [1] I. Tanaka, K. Kurihara, Y. Haga, Y. Minezaki, S. Fujiwara, S. Kumazawa, and N. Niimura, *J. Phys. & Chem. Solids* (1999), in press.
- [2] Niimura N., Karasawa Y., Tanaka I., Miyahara J., Takahashi K., Saito H., Koizumi S., and Hidaka M., *Nucl. Instr. Meth. A* **349**, (1994) 521.
- [3] I. Tanaka, N. Niimura & P. Mikula, *J. Appl. Cryst.*, **32** (1999), 525.
- [4] Haga Y., Kumazawa S., and Niimura N., *J. Appl. Cryst.*, (1999), in press.
- [5] Tanaka I., Minezaki Y., Harada K., and Niimura N., *Physica B* **241-243** (1998) 227.

Table 1 : Current specifications of BIX-III and BIX-I; geometrical comparisons (a) and practical crystallographic comparisons (b).

(a)

Parameter	BIX-III	BIX-I
Monochromator (M.)	EBP-Si(111) / (311)	EBP-Si(111) / (220)
M. Dim. [mm]	W250 x H40 x T10	W250 x H40 x T5
Wavelength [Å]	2.35 / 1.23	1.73 / 1.06
M. to Sample Dist.	2250mm	3100mm
Camera Constant	200mm	600mm
Detector	Neutron Imaging Plate (cylindrical)	2 Gas Proportional Counters [flat]
Detector Shielding	B ₄ C+resin=T50mm, Pb=T50mm(with 1mm thick Pb cover)	B ₄ C+resin=T20-110mm

(b)

Parameter	BIX-III	BIX-I	Gains
Intensity at Sample Position [10^6 n/cm ² /sec]	6 / -	3 / 1	2.0
Maximum Cell Const.[Å]	90 / 50	90 / 50	-
Solid Angle (4π [rad]=1)	0.595	0.028	21.5
d-min[Å]	1.2 / 0.6	1.5 / 0.8	-
Total Gains			43

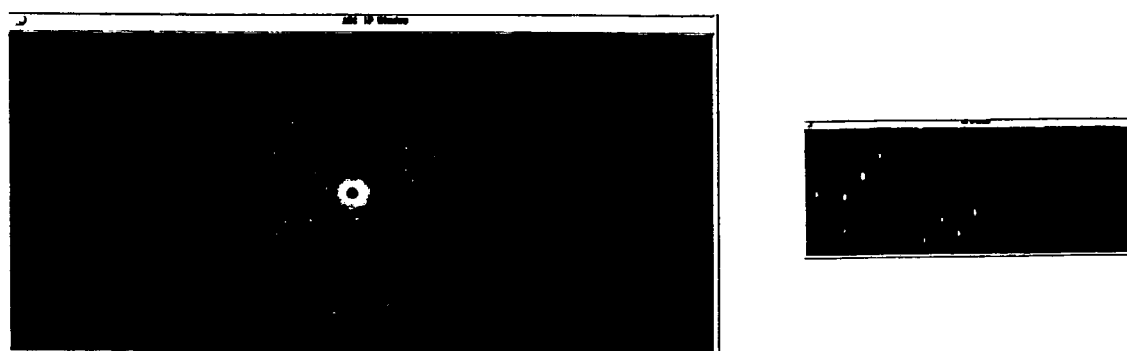
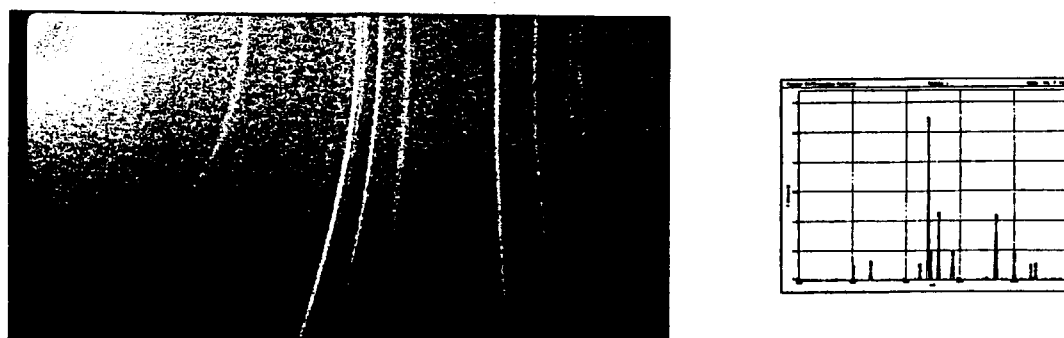
Fig.3 Diffraction pattern of Rubredoxin in D₂O. The sample size was 2.5x2.0x1.0 mm cube, the exposure time was about 23 hrs, and 0.4 deg oscillation. The minimum d-spacing spot was 1.6 Å.

Fig.4 Powder diffraction pattern of a kind of minerals. The sample size was 1mm cube, the exposure time was about 11 hrs, and the image was read by a reader of Fuji Co. Ltd.

原子炉 : JRR-3M

装置 : BIX-III(1GA)

分野 : (7) 装置

研究テーマ：高圧下での結晶構造・相変態の研究
表題：中性子散乱用ミニチュア高圧セル

1-9-2 Miniature High Pressure Cell for Neutron Scattering

A. Onodera, F. Amita¹, Y. Ishii² and Y. Morii²

School of Engineering Science, Osaka University, Toyonaka, Osaka 560-8531, Japan

¹School of Science, Kyoto University, Kyoto 606-8502, Japan

²Japan Atomic Energy Research Institute, Tokai, Ibaraki 319-1106, Japan

There has been a growing interest in the study of physics of pressurized condensed matters by means of neutron scattering. Magnetic scattering, for instance, can now be carried out at pressures greater than 10 GPa on conditions that the sample under study is as small as 0.1 mm³, it is enriched, and supermirror is installed along the beam incidence. It should be noted that the state of the art of high-pressure technique does not allow simultaneous attainment of both high pressure and large volume.

A prerequisite to generate pressures higher than about 3 GPa is the employment of opposed anvil design. With the opposed anvil, however, the sample volume is very small. Enlarging the volume within this system is to prepare a hollow space on top of the anvil. Along this line, we have developed hollowed anvils made of sapphire, sintered alumina, and tool steel.

Figure 1 shows sketch of the hollowed anvil. When two anvils are set opposed, a space whose shape is a flying saucer is achieved. A gasket holding the sample to be studied is placed into this space.

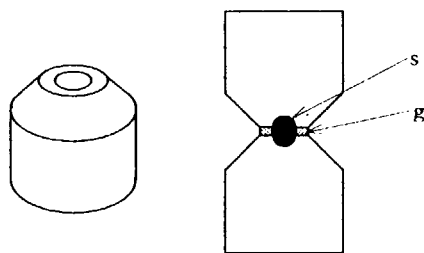


Fig. 1. Hollowed anvil (s:sample, g:gasket).

The pressure generated with the anvils was calibrated by the changes in the electrical resistance of HgSe and HgTe. Figure 2 shows typical examples of the resistance measurements with the steel or sintered alumina anvils using polyethylene as the gasket, demonstrating that pressures exceeding 2.5 GPa is attained.

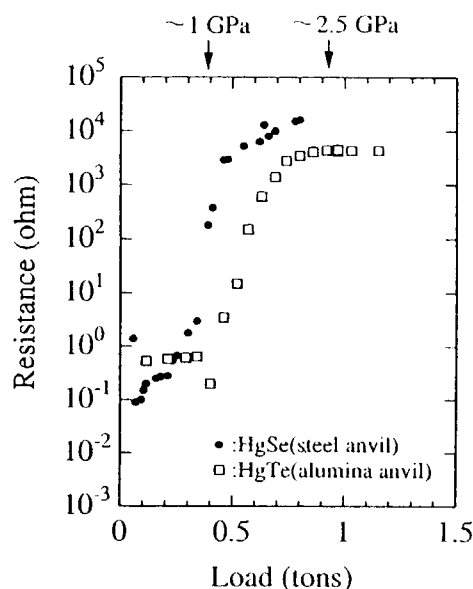


Fig. 2. Electrical resistance of HgSe and HgTe.

The pressure can be locked by use of a miniature device as shown in Fig. 3. The device is 90 mm in height and 70 mm in width. An angle of 148° is available for neutron scattering.

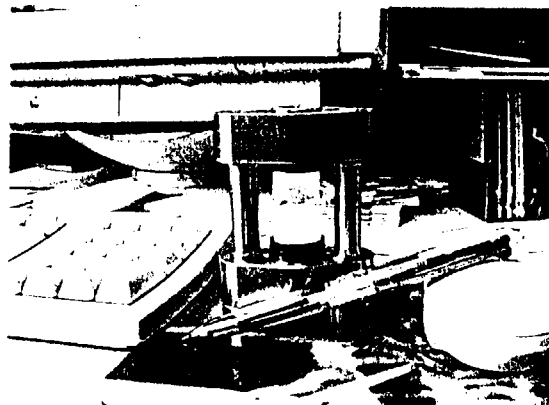


Fig. 3. Miniature device holding anvils.

研究テーマ：研究炉利用高度化の技術開発

表題：中性子散乱実験用多重極限条件発生装置の性能試験

1-9-3 Performance Test of a System for Simultaneously Generating Triple Extreme Conditions for Neutron Scattering Experiments III

A. Moriai, S. Ichimura, A. Ohtomo, S. Kawano¹, A. Onodera²

Department of Research Reactor, JAERI, Tokai, Naka, Ibaraki, 319-1195, Japan

¹Research Reactor Institute, Kyoto University, Kumatori, Sennan, Osaka, 590-0451, Japan²School of Engineering Science, Osaka University, Toyonaka, Osaka, 560-8531, Japan

As previously reviewed, we have newly developed a cryomagnet system with a high pressure cell¹⁾ which can simultaneously controlling three extreme conditions such as low temperature- T , high magnetic field- H and high pressure- P . Now we have carrying out some tests to demonstrate the performance of the system by neutron scattering experiments. In the test, magnetic transition of the compound TbNi_2Si_2 , which undergoes multi-step metamagnetic transition involving six long modulated structures in the c -axis magnetization process up to 5T at 4.2K²⁾, have been observed under three extreme conditions. In our previous study under $P=0.7\text{GPa}$ at $T=1.7\text{K}$ in $H=0\sim 5\text{T}$ ³⁾, we reported that the pressure effects on the field induced structures of the compound were found above $H=4.0\text{T}$. The present issue represents the result of the study for an additional pressure up to 1.2GPa.

Neutron diffraction patterns were collected in the a^*-b^* reciprocal plane using the TAS-2 at JRR-3M of JAERI. The spectrometer was set up to be 2-axis mode with an incident wavelength of 2.44\AA . The sample set-up is the same way as described in Ref.3).

Figure 1 gives the representation of the magnetic Bragg peaks in the a^*-b^* reciprocal plane at 1.7K under 0.0GPa, 0.7GPa and 1.2GPa. In the external field of 3.3T, no significant differences in magnetic structures exhibit between under 0.0GPa and under 0.7GPa, while for the phase at 1.2GPa the peaks related to the wave vectors $\mathbf{Q}=(1/2\pm\tau, 1/2\mp\tau, 0)$ with $\tau=0.000, 0.125$ no longer appear along the $\langle 1-10 \rangle$ line. This magnetic phase at $P=1.2\text{GPa}$ under $H=3.3\text{T}$ can be described as the same vectors with the

phase at $P=1.2\text{GPa}$ under $H=3.3\text{T}$ ³⁾. Thus an additional pressure 1.2GPa causes the great change of the magnetic structure in lower field.

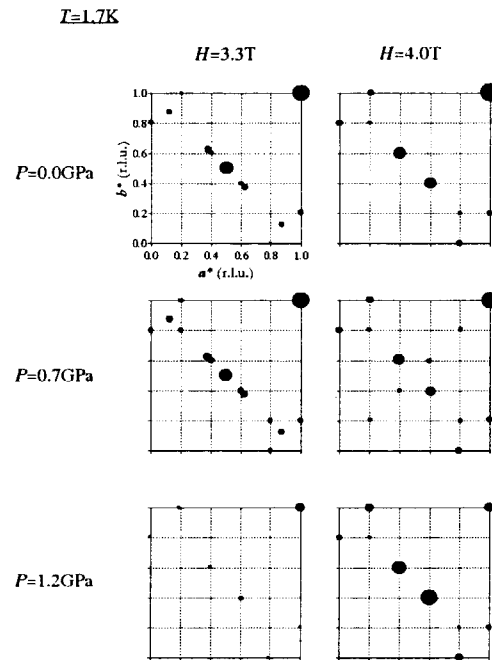


Fig. 1 Schematic representation of the magnetic Bragg peaks in the a^*-b^* reciprocal plane at 1.7K under 0.0GPa, 0.7GPa and 1.2GPa.

References

- 1) S. Kawano *et al.* Physica B 241-243 (1998) 145-147
- 2) H. Fujii, T. Shigeoka, J. Magn. Magn. Mat. 90&91 (1990) 115-120
- 3) S. Kawano *et al.* Physica B 241-243 (1998) 657-659
- 4) J. A. Blanco *et al.* J. Magn. Magn. Mat. 97 (1997) 4-1

研究テーマ： 中性子スピネコー分光器 (IMT)

表題： 改3号炉C2-2中性子スピネコー分光器の改良

1-9-4 Improvement of Neutron Spin Echo Spectrometer at C2-2 of JRR-3M

T. Takeda, H. Seto, Y. Kawabata, S. Satoh¹, M. Furusaka¹, M. Nagao², H. Yoshizawa²

Faculty of Integrated Arts and Sciences, Hiroshima University, Higashi-Hiroshima 739-8521

1 KENS, KEK, Tsukuba, Ibaraki 1305-0801, Japan

2 Institute for Solid State Physics, University of Tokyo, Tokai, Naka Ibaraki 319-1106

We have been improving a neutron spin echo spectrometer(NSE) at C2-2 cold neutron guide port of JRR-3M, JAERI¹⁻³⁾. In order to measure the scattered neutrons efficiently, we replaced the spiral coils with wider area one. The spiral coils for the beam cross section of $S = 50\phi\text{mm}$ were set at both the entrance and the exit side of the first precession coil and also at the entrance side of the second precession coil, and the coil for $S = 70\phi\text{mm}$ at the exit side of the second precession coil for the general users at present. We also installed a new detector system with an assembly of 8 (which will be increased to 16 in the future) one-dimensional position sensitive detectors(1D-PSDs) of 1/2 inch in diameter and 60 cm long. Each 1D-PSD is set vertically in parallel. The PSD is made by Reuter Stokes specified as RS-P4-0424-206. We can observe each NSE signal, that has a different spin precession phase corresponding to the different field integrals, by means of the PSD which specifies the different divergent neutron paths. Therefore, the use of PSD loosens the condition of the homogeneity of the field integral D . Thus, we can use the scattered neutrons with large angular divergences for the NSE experiment using the PSD. Especially, in this NSE spectrometer, the detector system

with an assembly of PSDs is very effective to upgrade the performance by specifying each particular neutron path, since the magnetic substance of other instruments disturbs the precession field and causes the deviation of the field integral from the axial symmetry which cannot be corrected for by the spiral coils.

In the preliminary NSE experiment using the new detector system, the neutron intensity observed at the detector increased 9 times the old detector system when the beam collimation at the entrance of the first precession coil and at the sample position was $30\phi\text{mm}$ and the collimation at the exit of the second precession coil was $70\phi\text{mm}$.

References

1. T. Takeda, S. Komura, S. Seto, M. Nagai, H. Kobayashi, E. Yokoi, C.M.E Zeyen, T. Ebisawa, S. Tasaki, Y. Ito, S. Takahashi and H. Yoshizawa : Nucl. Instr. and Methods in Phys. Research, A364 (1995) 186.
2. T.Takeda, H. Seto, S. Komura, S. K. Ghosh, M. Nagao, J. Matsuba, H. Kobayashi, T. Ebisawa, S. Tasaki, C. M. E. Zeyen, Y. Ito, S. Takahashi, H. Yoshizawa; J. Phys. Soc. Jpn. 65 Suppl.A (1996) 189.
3. T. Takeda, H. Seto, Y. Kawabata, D. Okuhara, T. Krist, C. M.E. Zeyen, I. S. Anderson, P. Hfgfhj, M. Nagao, H. Yoshizawa, S. Komura, T. Ebisawa, S. Tasaki and M. Monkenbusch: J. Phys. Chem. Solids (1999) in press.

研究テーマ：薄板基板上の多層膜の中性子反射率測定
表題：レプリカスーパーミラーの製作と中性子反射率

1-9-5 Production and Neutron Reflectivity of Replica Supermirrors

Y. Kawabata¹, M. Suzuki², S. Tasaki¹ and K. Somemiya³

¹ Research Reactor Institute, Kyoto University, Kumatori, Osaka 590-0494, Japan

² Japan Atomic Energy Research Institute, Tokai, Naka, Ibaraki 319-1195, Japan

³ Faculty of Engineering, Kyoto University, Sakyo-ku, Kyoto, Japan

Placing a neutron guide tube very near the cold neutron source in a reactor core or an accelerator target system allows one to extract more very low energy neutrons. However, this requires that the guide tube should be extremely radiation resistant. Neutron mirrors enduring a hard environment are essential for VCN extraction. Therefore, we developed a metal-based neutron supermirror to be used in high radiation environments. As a new technique of very low energy neutron transportation, it is demonstrated that a replica supermirror can be produced. They were fabricated as follows. A conventional (Ni-Ti) supermirror is deposited onto a float glass substrate and Cu is electroplated on top of the mirror. The glass is then removed, leaving the replica supermirror on the copper.

The surface precision of the fabricated replica mirrors was measured by optical methods. The values of surface roughness (peak to valley) of two samples were 22 and 200 nm, respectively, and the arithmetic mean values of the roughness (R_a) were 1.3 and 2.0 nm. These values show that the surface of the replica mirrors is almost as good as that of float glass.

The neutron reflectivity of a replica supermirror was measured by cold neutrons. The reflectivities of a replica supermirror, a supermirror on a glass plate and a nickel mirror are shown in the figure. The calculated reflectivity of the deposited layers is also shown. The wavelength in the figure is the neutron wave component perpendicular to the mirror surface. The measured results show the possibility to realize a good replica supermirror.

The roughness of replica supermirrors is very good, but the flatness is not so good because of the thinness of the base metal. It is important to support it correctly to keep it flat for the practical use. This measurement shows it possible. As the critical angle of the VCN on the supermirror is much larger than the order of the flatness, the effect of surface flatness will be relatively small for VCN extraction.

References

[1] Y. Kawabata et al., Nucl. Instru. and Meth. in Phys. Res. A420(1999)213-217.

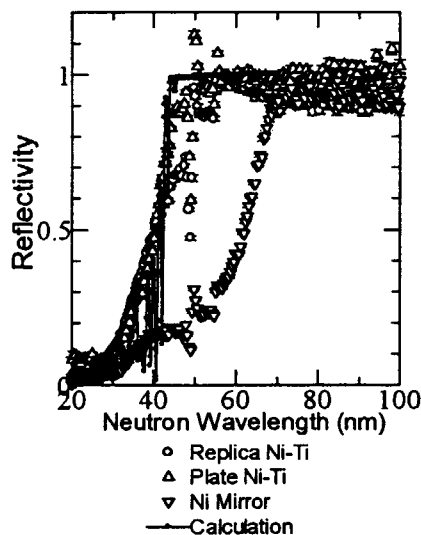


Figure Neutron reflectivity of a replica supermirror, a supermirror on a glass base and a nickel mirror.

JRR-3M, MINE, 9.Instrumentations

研究課題: 低磁場制御冷中性子偏極バルサーの開発
表題: 低磁場制御 Permalloy/Ge 磁気鏡のヒステリシス・ループ

1-9-6 Hysteresis Loop of the Permalloy/Ge magnetic mirror working under low external magnetic field

T.Kawai, M.Hino, S.Tasaki, T.Ebisawa, Y.Otake¹ and N.Achiwa²
Research Reactor Institute Kyoto University

¹Spring8 The Institute of Physical and Chemical Research¹ Physics Department, Kyushu University²

The magnetic neutron devices for cold neutron optics are required to satisfy the following conditions: (1) the stray fields from the magnetic devices should be small enough not to give magnetic effects to the nearby devices, (2) they should control the neutron spin states easily and precisely. In order to fulfill these conditions, a magnetic neutron mirror must be magnetized to saturation under a very low external magnetic field. A multilayer magnetic neutron mirror placed in the pulsed magnetic field is called a cold neutron pulser and produces the pulsed polarized neutrons. We have developed the Permalloy(Fe₅₅Ni₄₅)/Ge multilayer (PGM) magnetic mirror working as a cold neutron pulser in the pulsing magnetic field of 15 gauss [1]. This magnetic mirror is used also as a polarizer working under low external field of several gauss and a device generating stationary magnetic optical potential for studying spin interference phenomena. Such a magnetic mirror allow us to set the neutron optical instrument compactly in a restricted space.

When the magnetic mirror is used as a high-frequency (HF) cold neutron pulser generating dynamic optical potentials, an external magnetic field for magnetizing to saturation need to be as low as possible. We measured the coercive force of the PGM magnetic mirror for developing HF cold neutron pulser.

The PGM ((Permalloy: 90 Å / Ge: 80 Å) × 20 (layers)) mirror is fabricated by vacuum evaporation onto Si wafer (75 mm in diam. and 3 mm in thickness) in a magnetic field of about 130 gauss. The evaporating rate is about 1 Å/s. The hysteresis loop was measured using the cold neutron spin interferometer installed at the C3-1-2 of JRR-3M which supplies 12.6 Å neutrons with FWHM band width of 3.5%. The polarizer, π flipper and the analyzer (PGM sample mirror) are set in the guide field of about 9 gauss. The strength and direction of the external magnetic field for the PGM mirror is controlled using additional coil.

The reflectivity is shown in Fig. 1 and the measuring hysteresis loop in Fig. 2. The calculated reflectivity shown by the solid line assumes 1.6 T for the saturation induction of the mirror. The coercive force was 15 gauss. The PGM magnetic mirror could be used as a neutron pulser under the low-external magnetic field of 15 gauss. However the HF cold neutron pulser for investigating non-stationary spin interference phenomena might require a cold neutron pulser working under much lower external field.

The Supersendust (Fe₅₈Ni₃₂Si₆Al₄) magnetic mirror of which coercive force is 5 gauss has been developed [2]. So we are now developing the HF cold neutron pulser using these magnetic mirror. The range of frequency is expected to be 1 MHz.

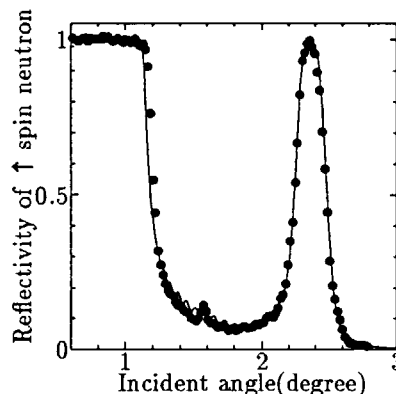


Figure 1: The measured reflectivity of the Permalloy/Ge multilayer magnetic mirror. The calculated reflectivity is shown by the solid line.

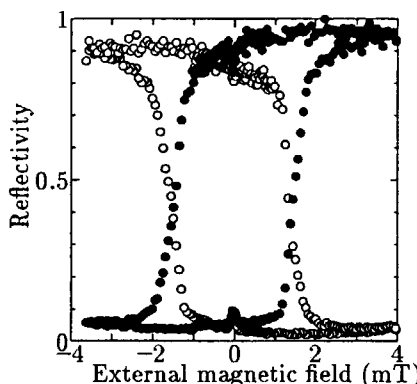


Figure 2: The measured hysteresis loop of the Permalloy/Ge multilayer magnetic mirror. The closed circle (●) is for ↑ spin component and open circle (○) for ↓ spin component.

References

- [1] T.Kawai, T.Ebisawa, S.Tasaki, M.Hino, D.Yamazaki, H.Tahata, T.Akiyoshi, Y.Matsumoto, N.Achiwa and Y.Otake, *Physica B*, 241-243 (1998) 133.
- [2] M.Hino, T.Kawai, T.Ebisawa, S.Tasaki, N.Achiwa, *Physica B* (1999), in press.

研究テーマ：高性能多層膜ミラーの開発

表題：イオンポリッシュ法による多層膜中性子ミラーの高反射率化

1-9-7 Enhancement of reflectivity of multilayer neutron mirrors by ion polishing

K.Soyama, W.Ishiyama¹ and K.Murakami¹

Japan Atomic Energy Research Institute, Tokai, Naka, Ibaraki 319-11

¹ Nikon Corporation, Nishi-ohi, Shinagawa, Tokyo 140

Multilayer neutron mirrors are now widely used at many neutron sources for neutron control devices. A multilayer with smaller d -spacing is desirable to lead greater angles of reflection for most applications. One of the most important problems in producing the small d -spacing multilayers is the reduction of the interface roughness which becomes larger with the number of bilayers deposited.

We have applied ion polishing in combination with ion beam sputtering deposition to smoothen the layer. We have carried out the investigation on Ni/Ti multilayers from the viewpoint of the ion polishing time, ion acceleration energy and incident angle, in order to optimize the Ar⁺ ion beam parameters.

Ni/Ti multilayers ($d=120\text{\AA}$, $N=10$ bilayer) with either Ni layers or Ti layers ion-polished were deposited. The ion polishing was applied immediately after the deposition of a layer to smoothen the layer. The condition of the sputtering deposition were fixed for all multilayer mirrors, on the other hand, conditions of the ion polishing were scanned. The d -spacing and interfacial roughness of multilayers were evaluated with X-ray grazing angle reflectivity measurements, which were performed in a θ - 2θ mode between 0° and 10° using Cu K α radiation ($\lambda=1.54\text{\AA}$). The measured reflectivity was fitted with the reflectivity which is calculated using the Fresnel's formulae and the interface roughness considered in terms of the Debye-Waller factor σ , assuming the optical parameters of the

material in bulk.

In the study of optimization of the Ar⁺ ion polishing time, the evaluated interface roughness σ of the multilayers are shown in Fig.1, which illustrates the ion polishings (in all cases) to be very effective for the reduction of σ . In case of ion-polished Ni layers, σ value of 6.5\AA without ion-polishing decreases to a minimum value of 3.5\AA by an ion polishing of 69 sec. On the other hand, a constant reduction of σ value of 4.5\AA was observed over every polishing time in cases of ion-polished Ti layers.

It was observed that the neutron reflectivity and the interface roughness of multilayers are clearly improved and the best condition of the ion polishing have been determined.

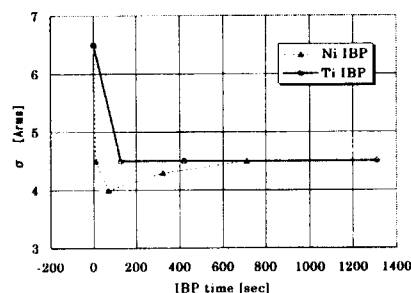


Fig.1 Evaluated interface roughness σ of the multilayers for various ion polishing times.

References

- [1] K.Soyama *et al.*: ICANS-XIV, ANL-98/33 Vol.I(1998)132
- [2] K.Soyama *et al.*: J. of Phys. and Chem. of Solid in press

研究テーマ：多層膜による中性子反射率・透過率の測定
 表題：多層膜による特徴的な非鏡面干渉性反射の測定と解析

1-9-8 Preliminary measurement of neutron reflectivity and transmissivity from a multilayer mirror

S.Tasaki

Research Reactor Institute Kyoto University

Interface roughness is one of the main cause of reduction of neutron reflectivity and transmissivity from multilayer mirrors. Usually reflectivity reduction due to the interface roughness is taken into account to the calculated reflectivity by multiplying the ideal reflectivity by a Debye-Waller type reduction factor. The calculation is based on a model that reflected wave is scattered by the interface roughness. This model gives us the result that the sum of the reflectivity and the transmissivity becomes less than unity at the Bragg angle. On the other hand, there is another explanation for the reduction of reflectivity that the optical potential which neutrons 'see' in the multilayer is effectively lowered due to the roughness and/or density reduction of the evaporated materials. This latter model gives us that the sum of neutron reflectivity and transmissivity is unity except for the absorption and incoherent scattering by the materials.

In this study, we made measurements on reflectivity and transmissivity of neutron from a multilayer mirror,

The multilayer, fabricated using the vacuum evaporation in Research Reactor Institute Kyoto University[1], consists of Ni and Ti with d -spacing of 100Å, and the number of layers of 100. The multilayer is evaporated on a 130mm×60mm×0.6mm-Si wafer. The measurements were performed with the neutron reflectometer installed at C2-1 beam port of JRR-3M reactor in Japan Atomic Energy Research Institute.

For the transmissivity data, absorption by the Si substrate should be corrected by the factor

$$f = \exp \left(\frac{\sigma_a}{\lambda_0} \lambda N_{\text{Si}} \frac{T}{\sin \theta} \right), \quad (1)$$

where $\sigma_a (= 0.145\text{b})$, $N_{\text{Si}} (= 5.0175 \times 10^{22}/\text{cm}^3)$, $T (= 0.6\text{mm})$ are absorption cross section, atomic number density of Si, and the thickness of the substrate. $\lambda_0 (= 1.79\text{Å})$ is the neutron wavelength at which absorption cross section is given by σ_a . $\lambda (= 6\text{Å})$ and θ are neutron wavelength and incident angle of neutron to the substrate.

The results are shown in Fig.1. The transmissivity T in the figure is Si absorption corrected. In the ordinal roughness scattering model, the sum ($R+T$) should be less than unity at the Bragg position ($\theta \approx 1.1\text{deg}$) and very close to unity else where. The figure shows, however, that there is no such reduction of the sum around Bragg condition. This result implies that neutrons 'see' mean structure of the multilayer and the scattering induced by the roughness is very weak.

In the last comment, we hope that mirror holding system and beam collimation system of the reflectometer will be improved. They were rather rough for the precise reflectometry.

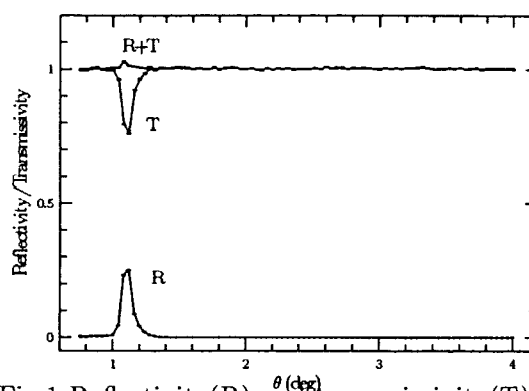


Fig.1 Reflectivity(R) and transmissivity(T) and their sum(R+T) from a Ni/Ti multilayer. The sum is very close to the unity at the Bragg peak.

References

- [1] S.Tasaki, T.Ebisawa, T.Akiyoshi, T.Kawai, and S.Okamoto, *Nucl. Inst. Meth. Phys. Res.*, A355 (1995) 501

This is a blank page.

1. 中性子散乱 10) その他

1. Neutron Scattering 10) Etc

This is a blank page.

研究テーマ：構造材料の残留応力と疲労損傷の評価

表題：残留応力測定に関するVAMAS TWA20のプロジェクト

1-10-1 VAMAS TWA20 Project Measurement of Residual Stresses

Keisuke TANAKA, Yoshiaki AKINITWA, Makoto HAYASHI¹
Shinobu OHKIDO¹, Nobuaki MINAKAWA², and Yukio MORII²

Nagoya University, Nagoya 464-8603, Japan

¹Hitach Ltd., Ibaragi, 300-0013, Japan

²Japan Atomic Energy Research Institute, Tokai, Ibaragi 319-1195, Japan

Versailles Project on Advanced Materials and Standards (VAMAS) is an international project for the standardization of advanced materials. TWA 20 was started in 1995 by G. A. Webster, Imperial College, London, in order to standardize the measurement of residual stress. It has the following four objectives: (1) To establish accurate and reliable procedures for making non-destructive residual stress measurements in crystalline materials by neutron diffraction. (2) To make measurements on single phase and multiphase materials containing residual stresses which have been introduced by a variety of fabrication techniques and in-service loads. (3) To conduct inter-laboratory comparisons to determine the extent to which reproducible results can be obtained. (4) To assemble the necessary technical information for the preparation of a suitable standard for the non-destructive measurement of residual stress by neutron diffraction. Five task groups are working to achieve the objectives. Task group 4 deals with the round robin specimens. Four specimens are now being circulated. They are ring-and-plug aluminum assembly, composite of alumina and silicon carbide, shot-peened nickel super alloy, and welded steel sample.

We started the measurement of residual stress by neutron diffraction at JRR-3M, JAERI in 1992. Dr. M. Ono, KURRI, attended the first meeting of TWA 20 to the fourth, and we became active members of TWA 20 from the third meeting in 1997. Now JAERI takes the responsibility for the project of TWA 20 in Japan.

We joined the group of round robin measurements of two kinds of samples: ring-and-plug aluminum alloy and composite. The

distribution of the residual strains in radial, hoop, and axial directions were measured by RESA (RESidual Stress Analyze equipment) across the assembly of shrink-fit ring and plug. The residual stresses in three directions were computed from the measured strains by using diffraction elastic constants which were determined in a separate experiments with loading device installed in RESA. The measured distribution of residual stress agreed well with computational prediction by the finite element method [1].

The round robin composite sample is α -alumina (Al_2O_3) mixed with 25 vol. % of silicon carbide (SiC) which is 95% hexagonal. The sample is a disk with a diameter of 20mm and a thickness of 3mm. The lattice constants of each phase is obtained from the measurements of monolithic samples. The mean strain in Al_2O_3 determined by 113 and 116 diffractions was tensile, and that in SiC by 102 and 110 diffractions was compressive. TAS 2 was used for the composite measurement. Since the thermal expansion coefficient is larger for Al_2O_3 (8.5×10^{-6}) than for SiC (3.3×10^{-6}), the thermal residual strain is tensile in Al_2O_3 and compressive in SiC. The experimental results agree at least qualitatively with the prediction. The magnitude of measured residual strains, however, are smaller than the predictions. The influences of the gage volume and positioning on the measured phase strain need to be studied in the future.

References

- [1] S. Okido, M. Hayashi, K. Tanaka, Y. Akinawa, N. Minagawa, and Y. Morii, Proc. 7th Iner. Conf. Nuclear Engng, ICONE, Tokyo, 1999

原子炉：JRR-3M

装置：RESA(T2-1), TAS2(T2-4)

分野：中性子散乱 (工業材料)

研究テーマ：構造材料の残留応力と疲労損傷の評価

表題： $\text{Al}_2\text{O}_3/\text{SiC}$ および $\text{Al}_2\text{O}_3/\text{ZrO}_2$ 複合材料の残留応力測定

1-10-2 Measurement of Residual Stress in $\text{Al}_2\text{O}_3/\text{SiC}$ and $\text{Al}_2\text{O}_3/\text{ZrO}_2$ Composites

Keisuke TANAKA, Yoshiaki AKINIWA,
Noriaki MINAKAWA¹, and Yukio MORII¹

Nagoya University, Nagoya 464-8603, Japan

¹Japan Atomic Energy Research Institute, Tokai, Ibaragi 319, Japan

Discontinuously reinforced ceramics matrix composites have some advantages such as high fracture toughness and strength. Since the coefficients of thermal expansion of the filler is different from that of matrix, residual stresses are induced. The residual stresses affect the mechanical properties. Evaluation of residual stress is very important to develop the composites.

The neutron and X-ray diffraction methods can detect separately the stress in each constituent phase of the composite. The neutron diffraction methods was used to measure the phase stresses in composite ceramics of zirconia mixed with various volume fractions of alumina ($\text{ZrO}_2/\text{Al}_2\text{O}_3$) and alumina mixed with silicon carbide ($\text{Al}_2\text{O}_3/\text{SiC}$). The measured phase stresses were compared with the results measured by X-ray diffraction methods.

The experimental materials used were composite ceramics of zirconia mixed with various volume fractions of alumina ($\text{ZrO}_2/\alpha\text{-Al}_2\text{O}_3$) and alumina mixed with silicon carbide ($\alpha\text{-Al}_2\text{O}_3/\beta\text{-SiC}$). For the composite of $\text{ZrO}_2/\text{Al}_2\text{O}_3$, volume fraction of alumina is 0, 27.6, 50.4, 69.6, 85.9 and 100%. The materials were hipped at 1450°C for 1hr under 98MPa in Ar gas. The composite has equiaxed grains for both phases. Coefficient of thermal expansion of monolithic ceramics is 10.9×10^{-6} and 8.5×10^{-6} for ZrO_2 and $\alpha\text{-Al}_2\text{O}_3$, respectively. For the composite of $\alpha\text{-Al}_2\text{O}_3/\beta\text{-SiC}$, volume fraction of silicon carbide is 0, 3, 7, 14, 26 and 100%. The materials were hipped under 40MPa. The temperature was determined at 1300 to 1900°C to obtain the maximum flexural strength. Coefficient of thermal expansion of monolithic $\beta\text{-SiC}$ is 4.7×10^{-6} .

The neutron residual stress measurement was performed for Al_2O_3 113, Al_2O_3 116, Al_2O_3 300,

ZrO_2 202, ZrO_2 222, ZrO_2 400, SiC 111, SiC 220, and SiC 311 with the RESA (REsidual Stress Analyze equipment) at JAERI. The wave length used was 2.0995 Å. The strain was calculated on the basis of the lattice spacing of monolithic ZrO_2 , monolithic Al_2O_3 and SiC powder.

The X-ray diffractions from Al_2O_3 146 by $\text{Cu-K}\alpha$ and ZrO_2 133 by $\text{Cr-K}\alpha$ radiation were used for X-ray stress measurement in $\text{ZrO}_2/\text{Al}_2\text{O}_3$ composite. On the other hand, Al_2O_3 2.1.10 by $\text{Fe-K}\alpha$ radiation was used in $\text{Al}_2\text{O}_3/\text{SiC}$ composite. The stress was evaluated by the $2\theta - \sin^2\psi$ method. Stress constant calculated by Kröner's model from the elastic constants of single crystals is -1206 and -666 MPa/deg for Al_2O_3 146 and Al_2O_3 2.1.10, respectively. For the case of ZrO_2 133, stress constant of -277 was measured from monolithic ceramics.

For $\text{ZrO}_2/\text{Al}_2\text{O}_3$ composites, the residual stress in Al_2O_3 phase measured by the neutron method was compression, and decreased linearly with the Al_2O_3 volume fraction. On the other hand, the tensile residual stress was observed in the ZrO_2 phase, and increased linearly with the Al_2O_3 volume fraction. For $\text{Al}_2\text{O}_3/\text{SiC}$ composites, the residual stress in SiC phase was also compression, and decreased linearly with the SiC volume fraction. For both composites, the change of the residual stress with volume fraction is similar to that obtained by X-ray method.

References

- [1] K. Tanaka, M. Matsui, R. Shikata and T. Nishikawa, J. Soc. Mat. Sci. Japan, Vol. 41, No. 464 (1992), 593.
- [2] J. Otsuka, S. Iio, Y. Tajima, M. Watanabe, K. Tanaka, J. Ceramic Soc. Japan, Vol. 102, No. 1 (1994), 29.

研究テーマ：工業材料の残留応力と疲労損傷の評価

表題：直径 40mm の鋼丸棒の残留ひずみの測定（Ⅱ）

1-10-3 Residual Strain Measurements of a Round Steel Bar with a diameter of 40 mm (Ⅱ)

K. INOUE, T. HORIKAWA, H. NAKAMURA, N. MINAKAWA,¹ Y. MORII,¹ N. KEDA¹ and R. UDONO²

Fac. Sci. & Tech. Ryukoku Univ. Seto, Otsu 520-2194, Japan

¹*Japan Atomic Energy Research Institute, Tokai-Mura, Ibaraki 319-1195, Japan*

²*Dep. Materials Sci. Eng. Ibaraki Univ. Hitachi, Ibaraki 310-0033, Japan*

By neutron diffraction, we have measured the diametrical dependence of the three dimensional strain on an annular circular notch root of a fatigued S15C steel round bar. The diameter of the notch root was 40 mm and the factor of stress concentration, α , was 1.05. It was annealed at 700°C for 2 hours and cooled down to room temperature in a furnace to exclude the strain caused by machining. The 7.5 Hz alternating load fatigue test with a stress ratio of -1 was done. The stress amplitude was 203 MPa and the repetition was 2.1×10^5 cycles. As this repetition number is about 60% of the fatigue life, the occurrence of stress redistribution on the notch root is expected because of the repetition of the plastic deformation at the sample surface.

The residual stress analyzer RESA of JRR-3M was used. The wave length of the neutron beam was 2.0996 Å. For the measurements of lattice spacing of (110) planes of radial and hoop directions, the bar was set up, where $2 \times 15 \text{ mm}^2$ slits were used for incident and reflected beams. For the axial direction, the bar was reclined, where both $2 \times 8 \text{ mm}^2$ slits were used.

In Fig. 1, the observed (110) peak from the axial plane at a position of 16 mm from the center of the notch root and its Gauss fitting are shown. For figure (a), it took 180 s to obtain one measuring point and for figure (b), it took 1800 s. Because of the attenuation of the neutron beam intensity due to the long path length in the material, which is about 70 mm for an axial plane, the data points scatter widely for 180 s measuring time. But, those are much improved statistically for 1800 s measuring time. In Fig. 2, the diametrical dependence of the strain for three directions at a 1 mm step is shown. The empty marks were obtained with 180 s measuring time. The black circles correspond to 1800 s measuring time. The axial strain with 1800 s measuring time was obtained at only 10 positions, because of limited

machine time of 5 days. But, from these improved data represented by black circles, we see that for the axial direction the strain is tensile near the surface of the bar, then it becomes compressive as approaching to the center of the notch root and again changes to tensile near the center of the notch root. This phenomenon is consistent with that observed in case of 8 mm ϕ notch root of a fatigued S55C steel round bar.¹⁾

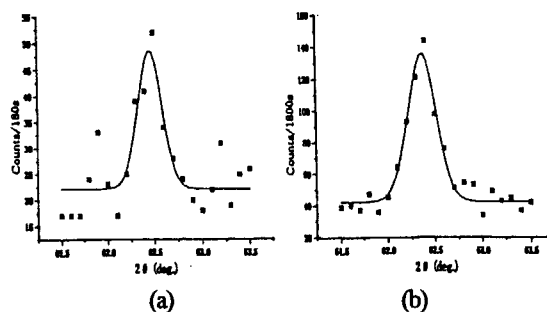


Fig. 1 (110) reflection from the axial plane at a position of 16 mm from the center of the notch root

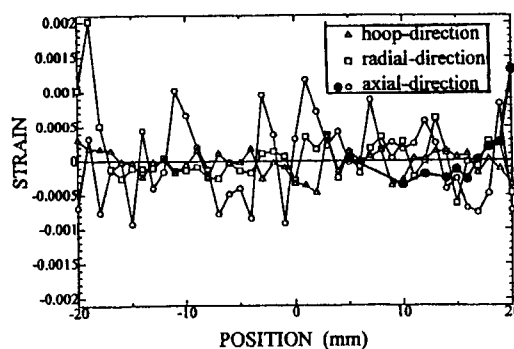


Fig. 2 Diametrical dependence of each strain

Reference

- 1) K. INOUE et al., Jpn. J. Appl. Phys. 37(1998)5680.

研究テーマ：中性子イメージングプレートを用いた中性子応力測定による内部残留応力分布
状態の非破壊測定法に関する研究
表題：中性子イメージングプレートを用いた中性子応力測定

1-10-4 Neutron Stress Measurement using Neutron Imaging Plate

T.Sasaki, N.Niimura¹, Y.Morii¹, N.Minakawa¹, Y.Tsuchiya¹, Y.Yoshioka², Y.Hirose and S.Takago

Kanazawa University, Kanazawa, Ishikawa 920-1192, Japan

¹Japan Atomic Energy Research Institute, Tokai, Ibaraki 319-1195, Japan

²Musashi Institute of Technology, Setagaya Tokyo, 158-8557, Japan

Neutron has an ability to penetrate material much deeper than x-ray, so that the method of neutron stress measurement is given attention as a tool for nondestructive measurement of internal stress profile in industrial materials. An imaging plate was developed recently as an area detector for neutron experiment, and is expected to be utilized to the stress measurement. So, this study was performed to develop the method for determining stress in polycrystalline materials with the neutron diffraction using the neutron imaging plate.

In this study, a fundamental investigation with a x-ray imaging plate was also performed. The neutron experiment was made using the reactor named JRR3M at Japan Atomic Energy Research Institute to determine stress in steel under tensile load.

A brief outline of the principle of the neutron stress measurement is as follows; From Debye-Scherrer ring detected with IP, strain can be obtained through the image processing and Bragg's equation. Then stress is calculated based on the elasticity. This method has been studied using the x-ray imaging plate, and was showed to be practical

The specimen used for the neutron experiment was steel with a thickness of 2 mm. Mean grain size of the specimen was 10 μ m. Main neutron diffraction conditions were as follows; wave length of neutron is 0.209 nm, diffraction is Fe 211 for the specimen and Cu 311 for standard material (Cu plate), incident angle of neutron beam is 24 deg, diameter of neutron beam is 1 mm, exposure time is 60 min for both the specimen and Cu plate. Applied strain to the specimen is 0, 400 and 800 ($\times 10^{-6}$) respectively.

Fig 1 shows change in Debye-Scherrer ring due to the thickness of the specimen, in case that the incident angle of neutron beam is $\psi_0=0$ deg. Fig 2 shows the similar one as Fig 1 without the incident angle $\psi_0=45$ deg.

Fig 3 shows neutron Debye-Scherrer ring in applied strain of 800×10^{-6} . There are two rings which diffracted from the specimen (Fe 211 diffraction, outer ring) and the Cu plate (311 diffraction, inner ring). The reason why the left part of Fe ring is broken off is due to Gd painting on the tensile loading equipment which shut off the neutron beam. The diffraction image data were analyzed on the computer and diffraction profile in the direction of the radius of the ring were calculated for the whole ring,

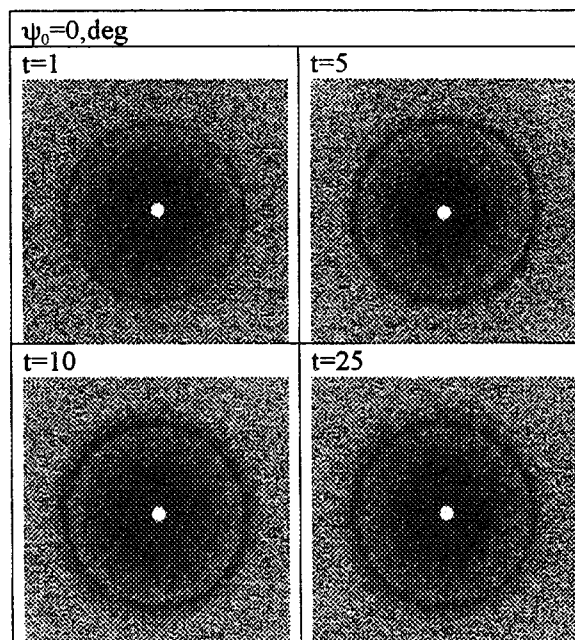


Fig.1 Change in Debye-Scherrer rings due to thickness of material. (incident angle $\psi_0=0$, deg)

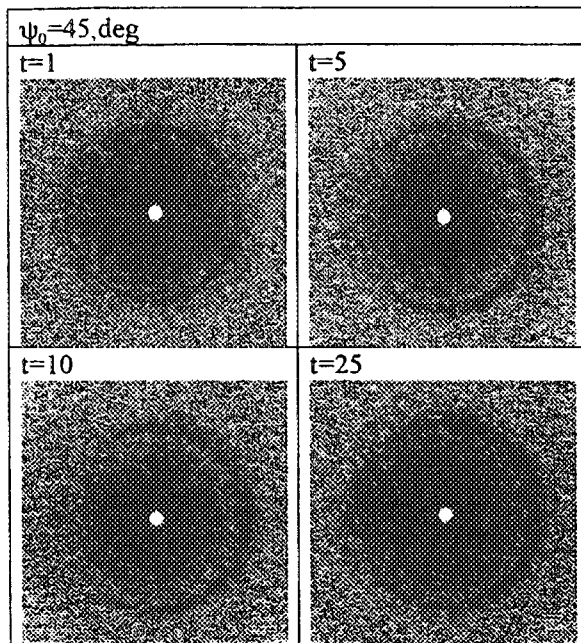


Fig.2 Change in Debye-Scherrer ring due to thickness of material. (incident angle $\psi_0=45, \text{deg}$)

from which the radii of the ring and the strain were determined. Finally, the stress was calculated according to the $\cos \alpha$ method. Fig 4 shows stress which were obtained from the specimen through the procedure mentioned above. The figure shows mean stress of two measurements as a function of applied strain. A line in the figure indicates the theoretical relation which was calculated with applied strain and Young's modulus. It is seen that the stress obtained by the present method agrees well to the theoretical value. The result shows that it is possible to determine mean stress in the material with neutron diffraction using a neutron imaging plate.

Though the experiment was performed in the case of uniaxial and uniform stress distribution along the cross section of the specimen, most materials have generally multi-axial stress state as well as nonlinear depth profile. It is necessary to clear these problems at the next stage. In x-ray range, however, these are already investigated and some approaches are proposed.

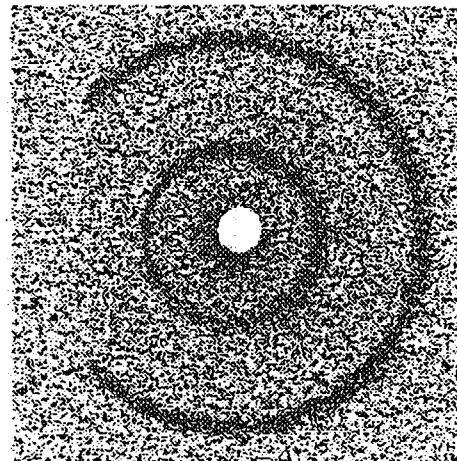


Fig.3 Debye-Scherrer rings in case of applied strain is 800×10^{-6}

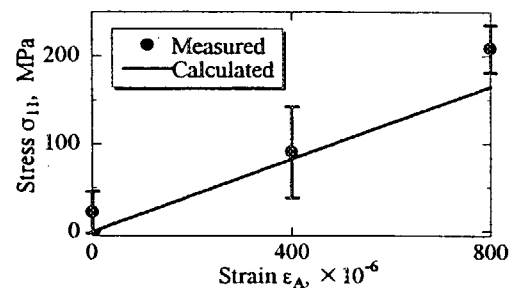


Fig.4 Result of stress measurement and comparison to theoretical value

References

- [1] T. Sasaki and Y. Hirose, J. Soc. Mat. Sci., Japan, vol.44, No.504 (1995) 1138-1143.
- [2] T. Sasaki and Y. Hirose, Trans. Japan Soc. Mech. Eng., vol.61, No.590, A, (1995) 2288-2295.
- [3] T. Sasaki, Y. Hirose and S. Yasukawa, Trans. Japan Soc. Mech. Eng., vol.63, No.607, A, (1997) 533-541.

This is a blank page.

2. 中性子ラジオグラフィ

2. Neutron Radiography

This is a blank page.

研究テーマ：中性子ラジオグラフィによる沸騰二相流のボイド率計測

表題：中性子ラジオグラフィ高速度撮像法による瞬間および時間平均ボイド率の計測

2-1 中性子ラジオグラフィ高速度撮像法による瞬間および時間平均ボイド率の計測

呉田 昌俊、秋本 肇

日本原子力研究所

エネルギーシステム研究部

熱流体研究グループ

本研究では、中性子ラジオグラフィ (NRG) を用いて狭い流路内を流れる熱的に非平衡な沸騰流 (サブクール沸騰流) を高時間分解能で可視化し、瞬間ボイド率分布および時間平均ボイド率分布を計測している¹⁾²⁾。狭間隙流路内サブクール沸騰流のボイド率は、核融合炉機器等高熱流束機器開発と関連して重要な熱工学因子である。しかし従来のボイド率計測法では計測が困難であり、本中性子ラジオグラフィ実験により初めて瞬間および時間平均ボイド率の計測が可能となった。

本実験は、JRR-3M 熱中性子ラジオグラフィ実験施設 (TNRF-2) を利用した。試験部は矩形流路 (流路間隙が 3mm および 5mm、加熱長 100mm、流路幅 30mm、加熱幅 20mm) であり、作動流体である水が流路内を垂直上昇するように設置した。加熱は加熱部片面から直接通電により行い、サブクール沸騰時の NRG 画像を、約 1 msec の時間分解能で記録した。

図 1 にサブクール沸騰流の瞬間ボイド率分布の時間変化を示す。瞬間ボイド率の時間変化情報を得たことにより、(1) サブクール気泡の瞬時物理量が定量的に計測でき、また (2) 周期的な流動変動が生じていることがわかった。図 1 条件での流動の変動周期は約 10 msec であり、時間平均ボイド率を得るためには 1 秒以上の時間平均化が必要であることがわかった。図 2 に時間平均ボイド率分布の熱流束変化を示す。図 2 中の加熱部出口に注目すると、低熱流束では鞍型分布、高熱流束では中央ピーク分布に変化している様子がわかる。この変化は、加熱面両脇で発生したサブクール気泡が流路中心線上で合体し中央ピークに変化する流動様式を示している。本実験では熱流束以外に、質量流量、入口水温、流路間隙をパラメータとしてボイド率分布を詳細に計測し、ボイド率データベースを

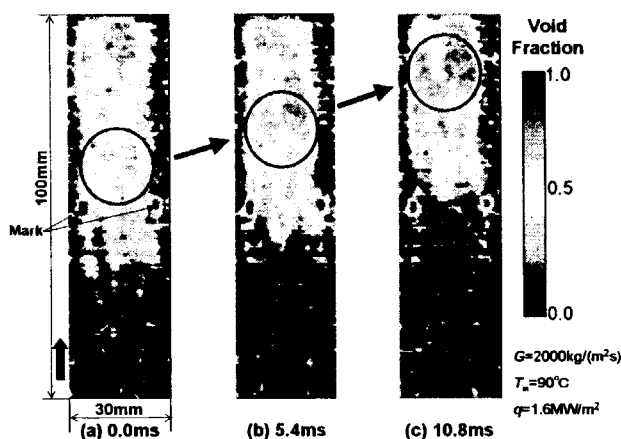


図 1 瞬間ボイド率分布の時間変化

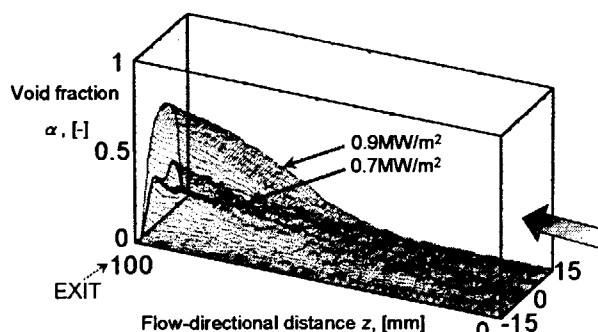


図 2 時間平均ボイド率分布の熱流束変化

作成した。なお本実験のボイド率計測誤差は 10% 以内と見積もられる。現在、得られたボイド率データを用いて、ボイド率予測モデル、および限界熱流束モデルの検討を行っている。

参考文献

- 1) 呉田昌俊、松林政仁、秋本肇、JAERI-Research 99-023.
- 2) M. Kureta et al., Proc. Two-Phase Flow Modelling and Experimentation 1999, 1509-1514.

研究テーマ：原子炉シビアアクシデント時の熔融炉心冷却に関する基礎研究
表題：熔融燃料／冷却材相互作用の可視化実験

2-2 熔融金属中に落下する水ジェット挙動の可視化

柴本泰照、 中村秀夫、 安濃田良成
日本原子力研究所 東海研究所 原子炉安全工学部

原子炉シビアアクシデント時の熔融燃料の冷却過程において、冷却材との相互作用 (MFCI) の解明は重要な課題となっている。この際、液体中に注入される水ジェットの挙動について、沸騰を伴う両者の相互作用について論じた研究は限られている。本報では、中性子ラジオグラフィ (NRG) による可視化観察を中心に、両者の混合過程における観察結果を概略的に報告する¹²⁾。

試験部は半径 85mm の扁平形扁平容器で、中心軸上部には水ジェット注入するためにノズルが設置されている。実験は、低融点合金 Pb-Bi (比重 10.05) をあらかじめ満たしたところに、流速約 9.0m/s (径 6mm) の水をジェット状に注入し、両者の相互作用を NRG により観察した。水 (室温) と熔融金属の接触温度が 450K (Run.1) と 650K (Run.2) の二つのパラメータについて行い、これは、本実験条件における均質核生成温度 (594K) を境界とした二種類の沸騰状態の比較を意味する。撮像系には、高速減衰のイメージインテンシファイアを用いた高速のビデオ撮影 (1125f/s) を採用し、沸騰を伴う高速現象に対応した。

水ジェット注入時の NRG 画像を図 1 に示す。上下段がそれぞれ、Run.1 と 2 に対応する。Run.1 では、顕著な沸騰が見られず、水ジェットとメルトの境界

で形成される cavity 内に水が蓄積されていく様子が観察された。これに対し Run.2 では、落下後 60ms 付近で蓄積内部より顕著な沸騰が生じ、生成された蒸気泡が上方に吹き抜けた。この蒸気流が後続のジェット先端部を分散することで侵入を阻害し、蒸気の吹き抜けによって、メルトプール内に熔融金属を巻き込まない開口部が形成された。後続のジェットは、約 80ms から cavity 内への蓄積を再開し、さらに 120ms 付近で、メルトとの接触面において 2 番目の主要な蒸気泡が現れ、水-メルト境界面上に沿って上昇する様子が観察された。

MFCI の混合挙動を理解するために重要なパラメータとして、ジェット侵入時のメルト内での広がりがある。ここでは、水相部 (黒い部分) を対象画像として、侵入深さと侵入幅を画像処理により計測した (図 3)。垂直および水平軸上に投影した長さを X, Y とし (図 2)、侵入深さ (D) と侵入幅 (W) を次式により求めた。

$$D = Y - L_i \quad (L_i: \text{メルト初期液位}),$$

$$W = A/Y \quad (A: \text{水相部の面積}).$$

時間 0s は図 1 と同様ジェットがメルト表面に到達した時間を示しており、縦軸はジェット径 (D_j) で規格化した値である。約 9m/s でメルト表面に到達したジェットは、約 1m/s に減速されてメルト内に侵

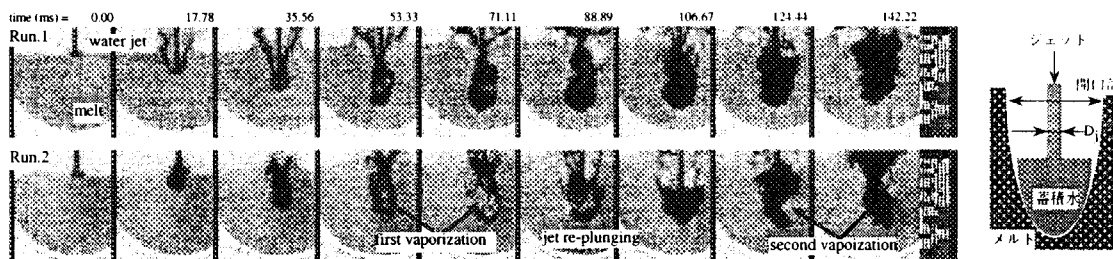


図 1 水ジェット侵入時の NRG 撮影結果

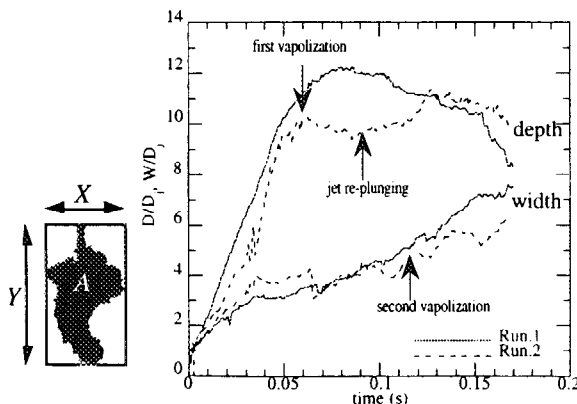


図 2 記号

図 3: ジェットの侵入深さおよび侵入幅

入していき、両実験とも、初期の侵入速度はほぼ同じ速度であった。その後 Run.2 では沸騰により 60ms 付近で侵入が停滞し、さらに、80ms より再び侵入を開始する。一方、侵入幅は水の蓄積とともに増加していくが、横方向の広がりについては両者に顕著な差が認められなかった。これは、生成された蒸気は主に上方に吹き抜けて cavity 内に停留しないためと考えられる。今後、より高温条件でのデータの蓄積とともに、伝熱特性の定量評価を行う予定である。

参考文献

- 1) Park, et al.: ICONE-7254 (1999)
- 2) 柴本ら、「日本原子力学会 99 春の年会」111

研究テーマ：中性子ビーム利用技術に関する開発研究
表題：中性子ラジオグラフィ技術の開発研究

2-3 中性子ラジオグラフィ技術の開発研究

松林 政仁

日本原子力研究所 東海研究所 中性子科学研究センター

本研究では、原研と高エネルギー加速器研究機構の統合計画として進められている核破碎中性子源において利用しうる中性子ラジオグラフィ撮像系の開発を行っている。本年度は10 μm 台の解像度を目標とした高空間分解能撮像系及び1 msを切る時間分解能を目標とした高時間分解能撮像系の特性測定実験を予定していたが、原子炉の計画外停止により高空間分解能撮像系のみについて実験を行った。また、蛍光コンバータを使用する撮像系において問題となる中性子照射の積算による蛍光コンバータの発光輝度低下についても実測を行った。

1) 高空間分解能撮像系

これまで開発を行ってきた蛍光コンバータと冷却型Charge Coupled Device (CCD)カメラを光学レンズで接続する撮像系では空間分解能は蛍光コンバータにより主に決定されていた。このため薄型の(塗布量が少ない)蛍光コンバータを開発し高空間分解能を達成した¹⁾が、同時に蛍光材の塗布量が減少したことに伴う発光量の低下も確認された。²⁾ 発光量の低下は露光時間を長くするだけでなく、照射に起因して画像上に発生するノイズも増加させる。さらにレンズを用いて蛍光コンバータ上の画像をCCDチップ上に拡大撮影する場合撮影視野が小さくなる程、蛍光をカメラへ伝達する過程における損失が増加することから、これに代わる光学接続方法としてFiber Optic Plate (FOP)上に蛍光材を直接塗布しカメラに直接接続する撮像システムの開発を開始した。蛍光材は $\text{Gd}_2\text{O}_2\text{S}(\text{Tb})$ を50 μm 厚FOPに塗布して使用した。

本システムを用いてTNR-2でリチウム電池CR1/3N(外径10mmの円柱状)を撮影例した結果をFig. 1に示す。撮影は蛍光面に対して電池の負極底面が密着するレイアウトで行った。正極材

(MnO_2)と負極材(Lithium metal)がロール状に巻かれている様子が確認できる。特にFig. 1では正極材と負極材の間に存在するセパレータまでも確認できるのに対し、同じ電池を冷却型CCDカメラを用いて撮影した場合では確認が困難であった。定量的に表現するには、Cd製 knife edgeを用いたEdge Spread Functionの測定が必要であるが、解像度が従来のシステムより高いことは本画像により確認できた。

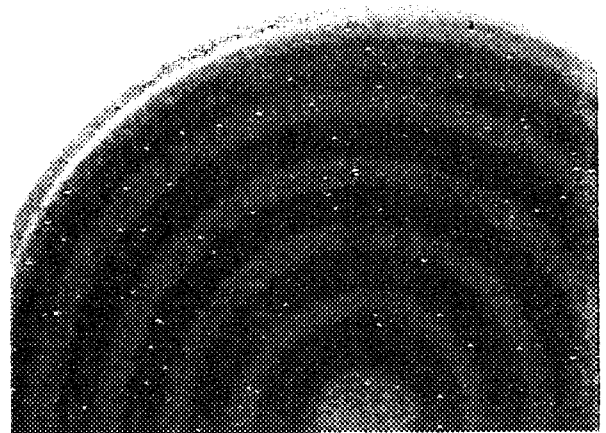


Fig. 1 Captured neutron image of Lithium battery (CR1/3N)

蛍光材面と接触しているCCDチップは直接中性子ビームに曝されるため白点状のノイズが多数画像上に観察された。Fig. 2に試料なしで撮影した映像信号(NSTC)の1水平走査線分をオシロスコープで観察した結果として示す。蛍光による映像信号が黒レベルより少し高い程度であるのに対し、ノイズ信号はその10倍にも達している。ノイズの原因としては、 γ 線が考えられるが、ビーム中の γ 線によるものかシンチレータ(Gd)からの即発 γ 線によるものかを同定する必要がある。

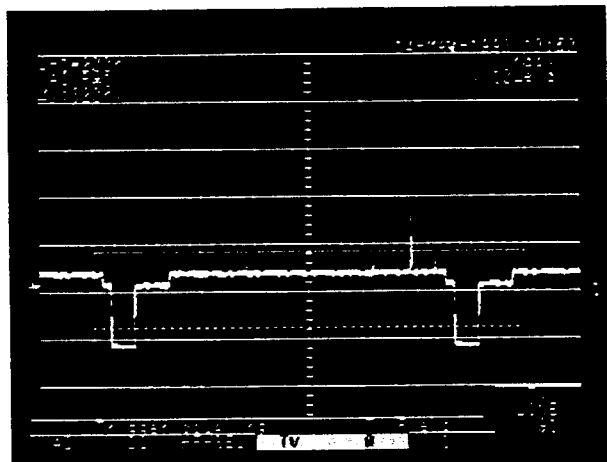


Fig. 2 One horizontal line of video signal with shot noises

次年度以降は蛍光体塗布量に対する空間分解能と感度の変化を実験により測定し最適値を決定する予定である。

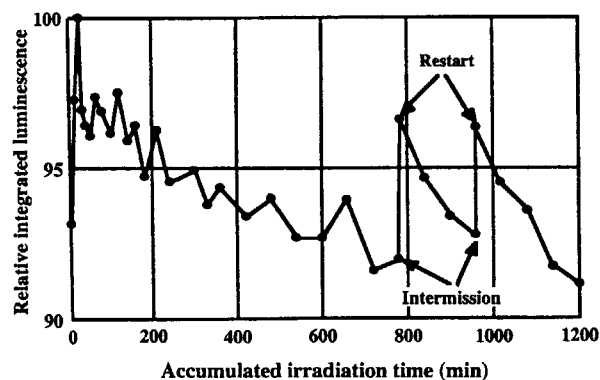
2) 蛍光コンバータ照射試験³⁾

JRR-3M中性子ラジオグラフィ装置では電子撮像法用の蛍光コンバータとして化成オプトニクス社製NRコンバータ(${}^6\text{LiF}:\text{ZnS}(\text{Ag})$)を使用しているが、中性子照射が進むにつれカラーリング及び発光輝度の低下が確認されていた。通常、実験毎に試料なしでの撮影を行いシェーディング補正を行っているが、実験時間内の発光輝度の低下が無視できない場合はデータ補正が困難となる。特に中性子ビームを照射しながら1時間程連続して撮影を行うComputed tomography(CT)の場合は1枚のシェーディングデータを共通で使うことから問題が生じる。

NRコンバータの発光輝度と中性子照射量の関係を得るため、TNRF-2でNRコンバータに積算で20時間中性子照射を行いながら発光スペクトルの測定を行った。測定には浜松ホトニクス製PMA11を使用した。測定結果をFig. 3に示す。測定可能範囲(300-800 nm)内の積分強度は20時間経過後においても10%程度の低下となっている(Fig. 3a)のに対し、ZnS(Ag)の発光ピークである450 nm付近の積分強度は65%以下にまで落ちていること(Fig. 3b)が分かる。各時間毎の発光スペクトルの観察により、ピーク強度の低下に伴う新たな長波長側の発光ピーク(670 nm)出現が原因であると考えられる。本結果は発光強度の低下がスペクトルの変形を伴って起きていることを示し

ており、受光感度の異なる撮像系では影響の程度も異なる。現在使用されている撮像系では、Silicon Intensifier Target (SIT)管カメラが500 nm、冷却型CCDカメラが750 nmに感度のピークを持っているため、中性子照射に伴う蛍光コンバータの発光輝度低下はSIT管カメラの方が大きく、冷却型CCDカメラでは長波長側のピーク出現により主ピークの輝度低下の影響は小さい。今後冷却型CCDカメラを用いた実験の増加が予想されることから詳細なデータの蓄積が不可欠となる。

a)



b)

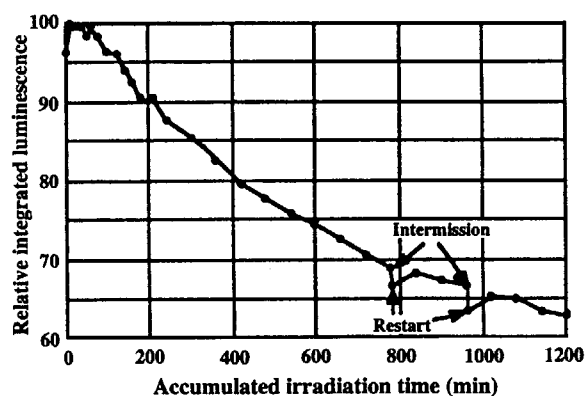


Fig. 3 Dependency of integrated luminescence on accumulated irradiation time. a) 300-800 nm, b) 350-550 nm.

参考文献

- 1) A. Tsuruno et al., Proc. 2nd Int. Topical Meeting on Neutron Radiography System Design and Characterization(Rikkyo, 1995) p.288.
- 2) M. Matsubayashi et al., WCNR5, DGZfP, 1997, p.275.
- 3) 松林政仁、海老谷益志, KURRI-KR-27, P9-15, 1999.

2-4 JRR-3MM冷中性子を利用するラジオグラフィ高度化技術の開発と応用研究

Development and Application of Advanced Neutron Radiography Techniques Using JRR-3M Cold and Thermal Neutron beams

名古屋大学 工学研究科

玉置昌義、久木田豊、辻 義之、親松和浩、大久保興平、小田将広、
本田真彦、八木貴広、舟橋隆之、西口 蔵、増永優作、土田浩司

日本原子力研究所 研究炉部

松林政仁

はじめに

従来の中性子ラジオグラフィは、被験体の定性的検査技術としての応用がほとんどであり、被験体内部の物質組成分布の定量解析を行う手段としては技術的に不十分であった。それは、主として、散乱中性子とガンマ線の影響により直達中性子のみによる中性子ラジオグラフィを行うことが困難であったからである。また、線源の整備といった問題から応用例の限られていた冷中性子ラジオグラフィは、冷中性子エネルギー領域（数 meV 程度）での中性子全断面積が物質ごとに特徴的な変化を示すことから、新たな応用分野を開く可能性がある。そこで、本研究では、散乱中性子及びガンマ線の影響を除去することで中性子ラジオグラフィ技術による定量解析精度を高めること、定量解析する上での冷中性子ラジオグラフィ固有の問題を解決することを目的とし、さらに、冷中性子ラジオグラフィの応用性の拡張について実験的に検討した。

具体的には、JRR-3M CNRFの冷中性子ビームを利用するラジオグラフィ（CNR）の高度化技術の開発を目指して、フィルム法確立、イメージングプレート技術のNR技術への展開、PCD・CCD冷却型固体撮像素子の利用による広ダイナミックデジタルラジオグラフィの開発などの基礎実験を実施した。以下に概要をまとめる。

(1) フィルム法による直達中性子ラジオグラフィ法の確立

中性子ラジオグラフィの定量解析性及びその高度化を論じるためには、物質と相互作用することなく透過した直達中性子の透過率を正しく評価できていなければならない。従来の中性子ラジオグラフィでは、散乱中性子やガンマ線の影響が重なり、直達中性子のみでの透過率を正しく評価することができなかった。そこで、これらの影響を除去し、直達中性子のみによる中性子ラジオグラフィを行うために、散乱中性子除去用マルチチャンネル（MC）コリメータ及びガンマ線カブリ評価用の二枚フィルム法を開発し、これらを組み合わせた手法の有効性を実験的に検証した。

MC コリメータは、中性子吸収体を内面に塗布した小口径コリメータを束ねたものである。コリメータの軸方向を中性子ビーム方向と一致させて設置することにより、角度成分を持つ散乱中性子を吸収・除去する。二枚フィルム法では、撮像にX線フィルムを二枚使用する。二枚のフィルムのうちの一枚から通常の（ガンマ線のカブリを含む）撮像結果を、もう一枚からガンマ線のみでの撮像結果を得ることにより、ガンマ線カブリを評価・除去することができる。本法を用いることにより、中性子ラジオグラフィにおける散乱中性子及びガンマ線の影響を無視しうる程度まで除去することができ、直達中性子透過率0.03程度までの測定を可能にした。本法は、定量的な解析のみならず、画像のコントラストを向上させるという点で、定性的な観察及び可視化においても有用である。さらに、熱中性子エネルギー近傍で全断面積が変化する鉛の中性子透過率と透過厚さの関係は、その他の物質とは異なり、単純な指数関数で

JRR3M 7R

熱中性子ラジオグラフィ装置

中性子画像工学

JRR3M C2-3

冷中性子ラジオグラフィ装置

中性子画像工学

近似することが困難であった。これは、中性子減衰係数が透過厚さと共に変化することを示しており、単純な指数関数に基づく定量解析法の限界を示すものである。

直達中性子のみによる中性子ラジオグラフィ技術を確立した上で、冷中性子ラジオグラフィにおいて減衰係数が透過厚さ依存性を持つ場合の中性子透過曲線を記述する関数を提案した。この減衰係数の透過厚さ依存性は、冷中性子CTにおいては、定量解析における誤差の要因となるため、補正する必要がある。しかし、その透過厚さ依存性から、その元となる物質の全断面積のエネルギー依存性や中性子ビームのスペクトルの非単色性、非一様性の情報を抽出できる可能性があることを明らかにした。この解析法をさらに拡張することにより、中性子ラジオグラフィ技術によって、ビームスペクトルや、物質の全断面積のエネルギー依存性、それに影響する物質の結晶性等のマクロな構造についての情報を取得することが可能となり、中性子ラジオグラフィの応用範囲がさらに拡大することが期待される。

成果の公表

1) Tamaki, M., Oda, M., Takahashi, K., Tanimoto, W. and Funahashi, T.,

"Study on neutron imaging techniques and processings for developing quantitative neutron radiography"

Nucl. Instr. Meth., A377, pp. 102-106 (1996)

2) Oda, M., Tamaki, M., Takahashi, K. and Tasaka, K.,

"Removal of scattered neutrons in thermal neutron radiography using a multichannel collimator"

Nucl. Instr. Meth., A379, pp. 323-329 (1996)

3) Oda, M., Tamaki, M., Tsuruno, A., Yoneda, K. and Kobayashi, H.,

"Transmittance measurements of cold neutrons for some materials by means of neutron radiography"

Nucl. Instr. Meth., A377, pp. 72-75 (1996)

4) 小田将広、玉置昌義、松林政仁、森線千鶴夫

"冷中性子計算機断層撮影の定量性におけるビームスペクトルの影響"

日本原子力学会誌、39、pp. 647-656 (1997)

5) Oda, M., Tamaki, M., Matsubayashi, M. and Kobayashi, H.,

"Dependence of Attenuation Coefficient on Penetrating Path Length in Cold Neutron Radiography",

Proc. 5th World Conference on Neutron Radiography, ed. C. O. Fischer (DGZfP, Berlin, 1997) 199-205.

6) 小田将広 (学位論文)

"冷中性子ラジオグラフィ技術の定量解析性向上に関する基礎研究"

課程博士論文 (1997. 11、名古屋大学)。

(2) IPによるQNRの確立

イメージングプレート技術のNR応用への展開の基礎実験を実施した。

1) ハニカムコリメータとイメージングプレートを組み合わせて用いるNR法を中心に、散乱中性子線除去効果評価のための特性測定を行った。ラジオグラフィ像を撮り、画像処理原理の検証のために各種の画像処理法を実施し、散乱線除去効果に関する情報と定量性向上に関する解析をした。また、ハニカムコリメータによる散乱線影響除去とともにγ線除去を行える方法を考案・実施し、定量性向上を試験した。

2) IPのγ線カブリという問題解決を、ジスプロシウムによる転写法をX線用IPに施すことにより広いダイナミックレンジを有効に活用できることを確認するための実験をした。

3) γ線不感化処理可能なIPとして、ジスプロシウム入りIPを考案し、開発のための試作をした。試作IPを用いて、中性子照射・撮像直後、画像消去処理によりγ線カブリ像を一度消去し、つづいて冷暗所において放射化したジスプロシウムによるIPの感光を2時間程度行い、IPリーダーで読み取る方法を試験した。

4) 中性子ラジオグラフィの被写体には金属をはじめとする結晶性固体が多く、冷中性子を用いるときには、被写体の結晶性に由来するブラッグ・カットオフ散乱を起こし、興味ある情報を含む冷中性子ラジオグラフィ像を得る。冷中性子ビームを用いて、

鉛、ベリリウム、黒鉛をフィルターに用いてフィルム法・Dy-I P転写法で冷中性子スペクトルシフトに関する実験を行った。

以上の研究を実施したことにより新しい知見を得た。

1) ハニカムコリメータを用いる中性子散乱線除去法によるラジオグラフィの定量性向上をI P法で検証できた。

2) ジスプロシウムを用いる転写法にX線I Pが優れた性能を示すことを明らかに出来た。ダイナミックレンジをフィルム法より大きく広げることができた。

3) ジスプロシウム入りイメージングプレートの開発により、 γ 線カブリの影響のない定量的NR画像取得の可能性を示せた。特許申請をおこなった。

4) フィルム直接法・Dy-I P間接法により、冷中性子中性子ラジオグラフィのスペクトルシフト効果を確認し、CNRCTの定量性確保の手法を確立した。シミュレーション計算でその実効性を検証した。また、熱中性子ラジオグラフィでも鉛はスペクトルシフトをおこすことが実験的に確認できた。

成果の公表

1) Tamaki, M., Oda, M. and Tsuruno, A.,

"Film Imaging and Processing Techniques for Quantitative Neutron Radiography",

Proc. 5th World Conference on Neutron Radiography, ed. C.O. Fischer (DGZfP, Berlin, 1997) 391-398.

2) M. Tamaki (Invited Talk)

"Imaging plates, Converters and Neutron energies for developing quantitative neutron radiography,"

Presented at 6th World Conference on Neutron Radiography, (Osaka, 1999. 5. 17-21).

3) Y. Masunaga, M. Tamaki, O. Nishiguchi, K. Yoneda, Y. Kukita,

"Characterization of imaging plates for quantitative neutron radiography,"

Presented at 6th World Conference on Neutron Radiography, (Osaka, 1999. 5. 17-21).

4) O. Nishiguchi, M. Tamaki, M. Oda, M. Matsubayashi, Y. Kukita,

"Application of imaging plates for quantitative thermal and cold neutron radiography,"

Presented at 6th World Conference on Neutron Radiography, (Osaka, 1999. 5. 17-21).

5) M. Tamaki, Y. Masunaga, K. Tuchida, S. Taguchi, K. Yoshii, S. Fujine, H. Kobayashi,

"Applications of imaging plate for fast and epi-thermal neutron radiography,"

Presented at 6th World Conference on Neutron Radiography, (Osaka, 1999. 5. 17-21).

6) M. Tamaki, O. Nishiguchi, Y. Masunaga, S. Tazaki, S. Iwai, Y. Kukita,

"Diminishing procedure of gamma-ray fogging using new type imaging plate for advanced quantitative neutron radiography,"

Presented at 6th World Conference on Neutron Radiography, (Osaka, 1999. 5. 17-21).

7) 西口 蔵、玉置昌義、小田将広、久木田豊、松林政仁、

"イメージングプレートを用いた高感度間接法中性子ラジオグラフィ(2)"、

日本原子力学会、1997年秋の大会(沖縄)、A64.

8) 玉置昌義、西口 蔵、舟橋隆之、田崎誠二、江藤雅弘、

" γ 線不感処理イメージングプレート中性子ラジオグラフィ法"、

日本原子力学会、1997年秋の大会(沖縄)、A65.

9) 玉置昌義、岩井定彦、鎌石恵子、田崎誠二、

"中性子画像変換方法"、

特願平9-190530.

(3) 定量的ラジオグラフィ技術の応用

確立したQNR技術の応用に関する研究をおこなった。

1) PCDの持つ広ダイナミックレンジを活用するために、ハニカムコリメータによる散乱中性子線除去とともに、 γ 線カブリの評価法に関する基礎実験を進めた。また、散乱中性子、 γ 線カブリ、ハニカムコリメータの効果についてモンテカルロシミュレーションを行った。これによってPCDによる定量的デジタルラジオグラフィの確立をした。 γ 線カブ

りの評価法が確立できた。ハニカム性能のモンテカルロシミュレーションを可能にした。今後の新しいコリメータが設計可能となった。

2) 屈曲型サーモサイフンの熱伝達特性に及ぼす作動流体の動的挙動を研究するために、高速度中性子テレビジョンを用いて、サーモサイフン内の対向2相流を可視化し、その画像データをボイド率分布の形で表現し、その時空間相関解析研究を行った。高速度中性子テレビジョンを利用してヒートパイプ内の対向2相流を実時間撮像し、画像処理によりボイド率分布に変換する基礎技術を確立した。さらにこの実時間ボイド率分布データを使って、時間・空間相関解析により、流体の移動速度、流動様式、対向流振動周波数、移動経路などの可視化・定量化を可能にした。

3) 気・液・固3相共存の液体ボンド球充填型模擬燃料中の液体挙動を研究するため、冷却型CCDカメラを用いたNRCT実験を行い、合わせて開発したCTプログラムを用いて可視化・解析をすすめた。小球充填床中の気液共存系の冷却型CCDによる可視化を行い、CT用データ取得のためにNR撮像し、CT再構成により、100 μ 程度の分解能で3次元CT像を得ることができた。

成果の公表

1) Santos, B., Tamaki, M., Oda, M., Honda, M. and Ikeda, Y.,

"Neutron Radiography with a one-dimensional image sensor having a high linearity range"

Nucl. Instr. Meth., A377, pp. 133-136 (1996)

2) Tamaki, M., Hara, Sh., Kondoh, I., Yoneda, K., Tsuruno, A. and Kobayashi, H.,

"Visualization and Analysis of forced diffusion of hydrogen in palladium by electrotransport",

Nucl. Instr. Meth., A377, pp. 166-169 (1996)

3) Y. Tsuji, S. Matsueda, M. Oda, M. Matsuda, T. Yagi, M. Tamaki, M. Matsubayashi and S. Fujine,

"Visualization and correlation analysis of counter-current two-phase flow in a thermosyphon by neutron radiography",

Nucl. Instr. Meth., A377, pp. 148-152 (1996)

4) T. Funahashi, M. Tamaki, M. Oda, S. Somyoy,

M. Matsubayashi,

"Application of neutron computed tomography for liquid film measurement in simulated liquid-bonded sphere-packed nuclear fuel element",

Presented at 6th World Conference on Neutron Radiography (Osaka, 1999. 5. 17-21).

(4) 今後の計画

以上のようにこの3年間で大きな成果が得られたと確信するとともに、本研究計画最終の第3年度目に当たった平成10年度のJRR-3Mの故障に伴って実施できなかったイメージングプレートに関するより深い研究、さらにCCD・高速度テレビにおける定量性の確保という課題、スペクトルシフトの物理的取り扱い方の展開方向、高速度テレビにおける中性子束不足の課題など以下に示すような今後解決すべき問題も多く残された。平成11年度以降の新計画の研究課題として引き続き追求することとした。

1) イメージングプレートを用いる広ダイナミックレンジ中性子ラジオグラフィ実験を中心に進める。また、フィルム法、新旧イメージングプレート法およびCCD法を用いるNR技術開発の成果の実験的に評価を行い、応用の視点からそれぞれについて最適化の方向を総合的にまとめる。

2) 中性子束向上に関する冷中性子のキャピラリー導管特性研究のための予備実験に着手し、新研究テーマの発掘を進める。さらにシステムの性能向上と最適化に向けた周辺機器とソフトの整備検討を行う。

3) イメージングプレートおよびCCDの特性を生かした応用研究を結晶性固体構造解析、金属中水素空間分析、充填層気液二相解析、燃料非破壊検査等の視点から試行する。

2-5 JRR-3M 冷・熱中性子を用いたラジオグラフィ技術の高度化(II) —高温融体と冷却材の混合の可視化に関する研究—

Development of Advanced Neutron Radiography Techniques Using Thermal and Cold Neutrons from JRR-3M
— Visualization Study on Molten Metal-Water Interaction —

京都大学原子炉実験所 三島嘉一郎、日引 俊、齊藤泰司
日本原子力研究所 杉本 純、森山清史、松林政仁

K. Mishima, T. Hibiki, Y. Saito, *Research Reactor Institute, Kyoto University*

J. Sugimoto, K. Moriyama, M. Matsubayashi, *Tokai Establishment, Japan Atomic Energy Research Institute*

1. 研究の目的と意義

本研究は、これまでに開発した中性子ラジオグラフィ高速度撮像技術と熱中性子ラジオグラフィ画像の定量化法（ Σ -スケールリング法）とを応用して原子炉シビアアクシデント時の熱流動現象の基礎的過程を調べるとともに、更なる技術革新を目指して熱中性子ラジオグラフィの技術的課題を明らかにしようとするものである。

原子炉のシビアアクシデント時には、熔融炉心と冷却材との相互作用により水蒸気爆発が発生することが懸念され、もしもこれが起これば事故の影響が著しく拡大する恐れがあるため、これについての研究が精力的に進められている。水蒸気爆発では、高温の熔融炉心が安定な蒸気膜に覆われた状態で冷却材の中に分散する初期粗混合過程、トリガリング過程を経て、爆発的な蒸気発生と、これに伴う圧力波の発生が起こることが知られている。このとき、初期粗混合過程における冷却材中での熔融炉心や蒸気の分散状態は、水蒸気爆発の初期条件となり、その結果として起こる水蒸気爆発の発生確率や爆発のエネルギーがこれに依存するため、水蒸気爆発の重要な素過程と考えられている。

初期粗混合過程における冷却材中での熔融炉心や蒸気の分散状態を精度よく予測するためには、この過程を高温熔融金属と水を用いた模擬実験などにより詳細に把握しておく必要がある。現象の理解のためには可視化が最も確実な方法

であるが、可視化の手段として光学的な方法を用いた場合、蒸気と水との界面における乱反射のため、蒸気泡で覆われた熔融金属の挙動を詳細に観察することが困難である。そこで本研究では、界面での反射の影響を受けない中性子ラジオグラフィ法を用いて、水中に落下させた高温熔融金属の挙動を可視化する方法を採用した。そして画像処理により、粗混合過程における蒸気膜崩壊に至るまでの高温熔融金属と水との相互作用の挙動を可視化し、その特性を把握することとした。また、複雑な熔融金属粒子のまわりの伝熱現象をより詳細に調べるために、熔融金属粒子を単純な体系である加熱剛体球により模擬し、これと冷却水との相互作用を可視化する実験も実施した。

2. 研究の方法

(1) 研究方法の概要

熔融炉心を模擬した熔融金属（ウズメタル）を水中に落下させて、熔融金属の液塊やジェットの分裂と分散、冷却水との混合状態を熱中性子ラジオグラフィ高速度撮像法により可視化・観察した。加熱剛体球の実験では、同様の装置により熔融金属のかわりに高温に加熱した剛体球を水中に落下させ、剛体球周りの蒸気泡の様子を可視化した。

可視化には、JRR-3Mの熱中性子ラジオグラフィ設備を用い、画像処理技術を用いて、

JRR-3M 7R(TNRF2)、中性子ラジオグラフィ装置、熱流体工学

蒸気泡や高温溶融金属の液滴やジェットの分裂挙動、冷却水との混合状態の動態を可視化観察した。また、加熱剛体球の実験では、剛体球周りのボイド率分布を測定した。

(2) 年次計画

年次計画は、平成8年度に、

- ① 実験手法の検討
- ② 実験装置の設計、製作
- ③ 溶融金属と水との相互作用予備実験、

平成9年度に、

- ④ 溶融金属と水との相互作用実験
- ⑤ 画像処理技術の改良
- ⑥ 加熱剛体球と水との相互作用実験

平成10年度に、

- ⑦ 画像処理による加熱剛体球周りの蒸気ボイド率分布の測定
- ⑧ 実験結果の解析

を実施するという計画である。これにしたがって、実験の実施状況を以下に述べる。

平成8年度には、中性子ラジオグラフィ高速度撮像法を検討し、この方法による溶融金属-水混合状態の可視化の可能性を確かめる実験を行った。中性子源として日本原子力研究所 JRR-3M 熱中性子ラジオグラフィ設備を利用した。シンチレータには残光時間の短い⁶LiF/ZnSを用い、撮像系には、高感度の画像増幅器を取り付けた高速度ビデオ（最高撮像速度毎秒 1000 コマ）を用いた。この方法により、溶融金属と軽水あるいは重水を適当に組み合わせれば、溶融金属-水混合状態において溶融金属と水、気泡との間の識別が可能であることが確認できた。

平成9年度には、この方法を使い、重水プール中に 650 °C まで加熱・溶融したウッズメタルをジェット状や滴状に落下させ、ジェットや液滴の分裂や微粒化の様子を可視化した。その結果、水と気泡、溶融金属の滴あるいはジェットの挙動、微粒化したときの溶融金属の微粒子の雲などの識別が可能であった。微粒化が起こる位置を見ると、水面でのインパクトの瞬間に起こる場合と、ジェット状に落下させた場合では細長いジェットの途中で起こる場合もあった。

これらの現象は、画像処理により特長をより明確にとらえることができた。そして溶融金属の落下の形態を細かく観察し、それと実験後回収されたデブリの形状・粒径との関連を調べた。

気泡については、溶融金属が水中に落下するさいに巻き込んだカバーガスと沸騰による蒸気泡の両方が観察されたものと推測されるが、両者の識別は困難であった。また、溶融金属の周囲の薄い蒸気膜及びジェット分裂後の微粒子の1つ1つは画像の空間分解能の制限と中性子強度の揺らぎによる画像輝度のちらつきのために識別が困難であった。また、溶融金属まわりのボイド率計測に関しては定量性に問題があることが懸念されたため、加熱剛体球を用いた実験を行うこととした。

平成10年度には単一の加熱剛体球を水中に落下させる実験を行う計画であったが、JRR-3Mの計画外停止のために予定されていた実験の一部のみしか実施できなかった。しかしながら、これまでの実験により得られた画像を処理することにより、加熱剛体球周りに発生するボイド率分布を計測し、加熱剛体球から冷却水への伝熱量を推測する解析を行った。

(4) 実験方法

中性子ラジオグラフィ高速度撮像法

Fig.1 に中性子ラジオグラフィによる高速度撮像系のブロックダイアグラムを示す。

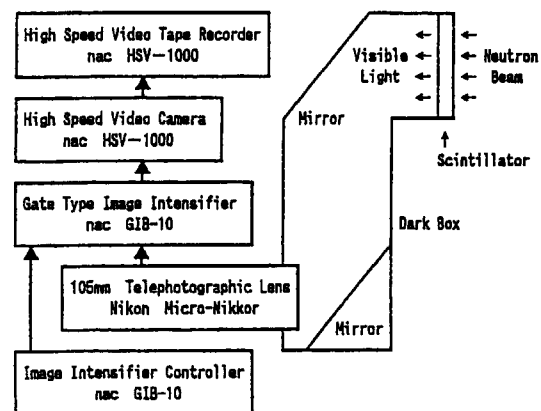


Fig.1 Block diagram of the imaging system for high-frame-rate NR.

中性子ラジオグラフィによる高速度撮影を行うためには $10^8 \text{ n/cm}^2 \text{ s}$ 程度の高中性子束が必要であるが、現在、我が国では、このような熱中性子源としては、日本原子力研究所 JRR-3M の熱中性子ラジオグラフィ設備のみであり、ここではこれを利用した。

速い現象を撮影するため、コンバータ/シンチレータは発光量が大きく、解像度がよく、しかも残光時間の短い特性が要求される。このような要求を満たすものとして、ここでは、 $^6\text{LiF/ZnS:Ag}$ シンチレータ（化成オプトニクス NR コンバータ）を採用した。このシンチレータは、ガドリニウム金属シンチレータに比べると解像度は 90% であるが、感度は 100 倍大きい。また、残光時間が $20 \sim 46 \mu\text{s}$ という短い値であり、これは毎秒 10,000 \sim 25,000 コマの撮像速度に対応し、現時点では最適の特性を有している。

撮像装置として用いられる高速度ビデオについては、撮像速度の観点からは、毎秒数千コマの高速度撮像の可能なデジタルメモリ方式の高速度ビデオが有利であるが、メモリ容量の制約から録画時間が 1 秒程度、長くて数秒しかなく、ある程度長い時間（例えば 1 分間以上）現象を録画する必要があるため、アナログ録画方式を選択した。ここでは、最高撮像速度毎秒 1000 コマの高速度ビデオ nac-HSV-1000 を選んだ。このシステムでは、標準録画時間 180 分の VHS カセットを用いれば、約 21 分間の録画が可能である。この撮像系は、ロータリシャッターを組み込んでいて、シャッター速度は $1/10,000$ 、相対感度は 50(ISO) である。解像度は 350×480 画素である。

微弱な可視光の画像を高速度ビデオで撮像可能にするため、高速度ビデオに画像増幅器（浜松ホトニクス GIB-M2P）を取り付けた。この画像増幅器は、2 段のマイクロチャンネルプレート (MCP) を取り付けゲインを拡大した。MCP 1 枚で、ゲインは 100,000 倍であり、2 枚では、ある程度で飽和するが、100,000 倍以上のゲインである。この画像増幅器は回路でゲートを開閉し、シャッター機能を持たせてある。このゲート開放時間は、100ns から連続開放まで段階的に可変

である。また、解像度は 23 line-pairs/mm である。

実験装置

実験装置は、Fig.2 に示すように、低融点金属を加熱・融解する加熱炉と重水を満たした試験部により構成される。加熱炉は最高 1kW の出力の電気炉であり、これにより熔融金属を約 650°C まで昇温できる。加熱炉の下部には熔融金属落下用の弁を設け、熔融金属が所定の温度になったときにこれを開き、熔融金属を落下させた。ジェットの連続落下と断続的な滴下が可能なように弁機構はソレノイド弁方式を採用した。熔融金属が落下するノズルの内径は 4mm とした。

試験部は肉厚 10mm のアルミニウム製矩形容器であり、内法は、高さ 400mm、幅 100mm、厚さ（中性子ビームの進行方向）30mm とした。高さ 200mm、厚さは 50mm の試験部も製作したが、予備実験の結果より、熔融金属粒子が水中落下中にほぼ凝固するためには 200mm の高さでは足りず、また、厚さを 50mm にすれば重水による中性子の減衰が大きすぎて、画像に十分な輝度が得られないことが分かったために、前述のような寸法を選んだ。

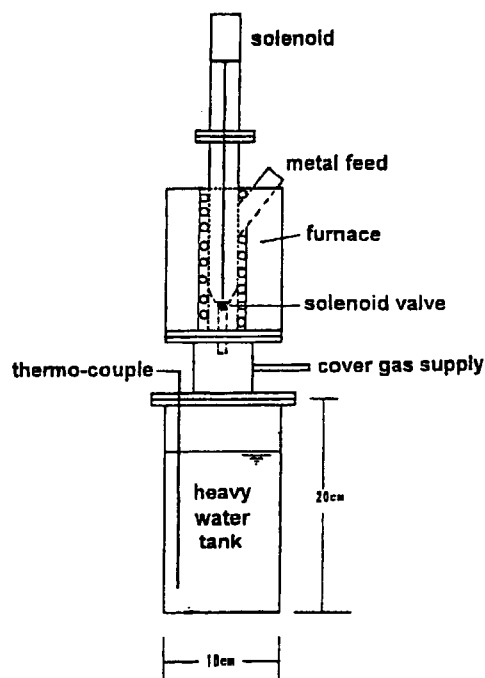


Fig.2 Test rig for the molten metal-water interaction experiment.

Table 1 Summary of experimental conditions and the results.

RUN No.	Metal		Water		Result (Atm: atomization)
	Material	Temp. [°C]	H ₂ O or D ₂ O	Temp. [°C]	
0	Wood's metal	100?	H ₂ O	20?	no Atm: disc- or donut-shaped droplets
1	Pb-Bi	638	H ₂ O	15	Atm: irregular fragments + powder
2	Wood's metal	298?	H ₂ O	15	Atm: smooth surface fragments + powder
3	Wood's metal	330?	H ₂ O	16	Atm: smooth surface fragments + powder
4	Wood's metal	300	D ₂ O	22	no Atm: deformed droplets
5	Wood's metal	650	D ₂ O	22	no Atm: deformed droplets
6	Wood's metal	560	D ₂ O	19	no Atm: deformed droplets + small spherical particles
7	Wood's metal	650	D ₂ O	10	Atm: deformed droplets + powder
8	Wood's metal	640	D ₂ O	14	Atm: fractal-like fragments + powder
9	Wood's metal	560	D ₂ O	?	Atm?: irregular fragments + small particles

この実験では、低沸点液プール中に少量の溶融金属を落としその挙動を見ることが目的であったため、溶融金属が黒く、低沸点液がやや暗く、蒸気泡が明るく写るような溶融金属と低沸点液の組み合わせを選んだ。すなわち、溶融金属として中性子吸収断面積の大きいカドミウムを含んだウッズメタル（成分比は、スズ 12.50%、ビスマス 50.00%、カドミウム 12.50%、鉛 25.00%）を、低沸点液として重水を用いた。重水を用いたのは、軽水に比べて中性子に対する巨視的断面積が約 1/10 であるので、水の層が厚くても明るく写ることが予想されたためである。

以上の実験では溶融金属の落下はソレノイド弁方式によったため、溶融金属を 1 滴ずつあるいは連続的にジェット状に落下させることができる。滴下させた場合、1 滴の直径は数ミリメートル、ウッズメタルの量はおよそ 5~10g である。落下前のウッズメタルの温度は 300°C~650°C、重水温度は 10~22°C に設定し、溶融金属落下後は重水温度が 20~36°C に上昇した。ジェット状に落下させた場合、ジェットの流速は、連続画像の移動距離から測定すると 1.4m/s、自由落下として計算すると 1.7m/s であった。また、

ジェットの直径は 1.7mm~2.2mm であった。

加熱剛体球の実験でも Fig.2 と同様の試験部を用いた。剛体球はステンレス鋼製であり、直径が 6, 9, 12mm の 3 種類を用い、これらを 600°C~1000°C まで加熱して、重水中に落下させた。

3. 実験結果

(1) 溶融金属実験

Table 1 に溶融金属落下実験の実験条件を示す。Photo 1 に 22°C の重水に 650°C の溶融ウッズメタルの塊を落下させたとき (RUN5) の 14ms ごとの連続画像を示す。時間は、左上から下に、次に右上から下に進んでいる。この場合、水蒸気爆発は起こらず、最初の溶融金属塊が水面に突入した際にカバーガスを巻き込み、液面に井戸形の穴を形成しているのが分かる。後続の液塊は、この穴の中を抵抗なく進み、先行する液塊に追いついている。液塊は、この窪みの底の気液界面付近に集まり、穴を押し広げながら進行するが、このとき既に幾つかの分裂片に分かれているものと思われる。そして、最後は、穴の気液界面と溶融金属とは分かれ、穴の界面は上昇し、溶融金属は水中を落下する。実験後回

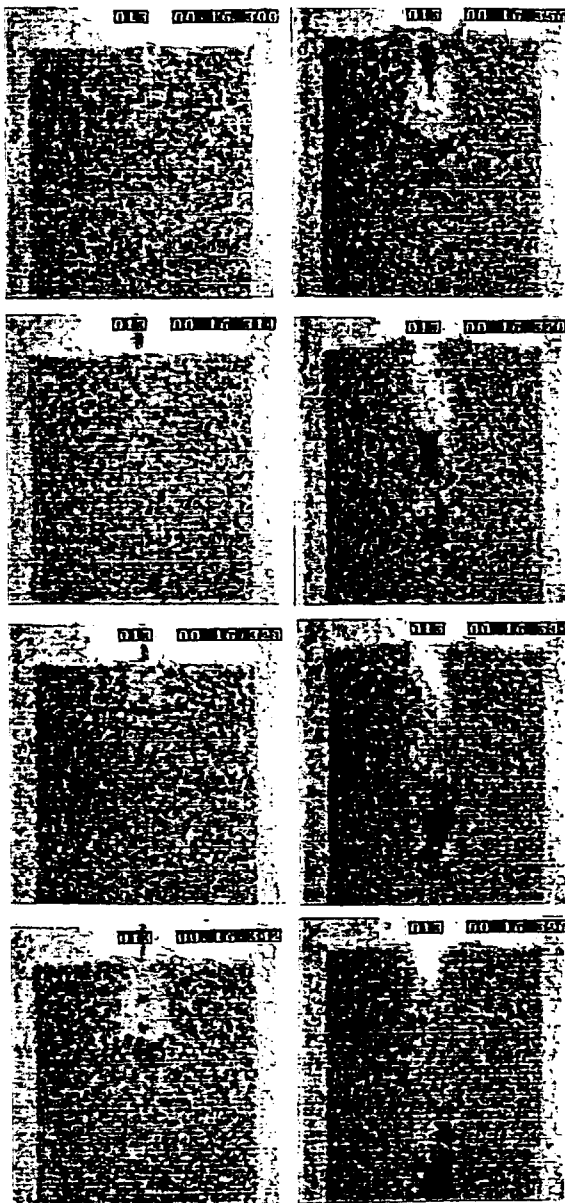


Photo 1. Gas entrainment due to the impact by a molten metal drop (RUN5).

収されたデブリは比較的大きな球形に近い粒子となっており、粉末状の微粒子は見られない。

Photo 2 は、640 ° C に加熱した熔融ウッドメタルを 14 ° C の重水にジェット状に落下させたとき (RUN8) の 4ms ごとの連続画像である。時間は左上から下へ、次に右上から下に進んでいる。ジェットは水面をあまり乱さずに貫通しているが、水面下約 5cm のところで切れている。水面直下のジェットを見ると、時刻 254ms (写

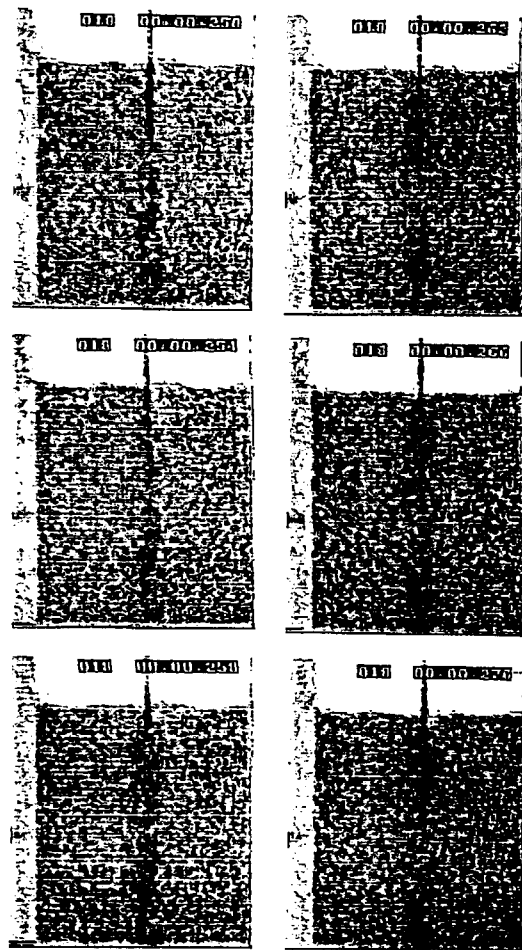


Photo 2. Molten metal jet penetrating into heavy water pool (RUN8).

真左上から 3 枚目) 以後の写真で金属塊が雲のように見えるのは小さな水蒸気爆発のためと思われる。このとき回収されたデブリは、角の丸いものや細長いもの、フラクタル図形のように複雑にちぎれた形状をしたものなど様々で、大きさも大小さまざまである。少量ではあるが熔融金属の微粒化した粒子や粉末が混じっている。

Photo 3 には Photo 2 の原画像を二値化処理した画像を示す。この写真で、熔融金属ジェットは黒く重水は白く写っている。また水面近傍の水平の黒い線は、初期の水面からの揺動部分である。一般に原画像には中性子の揺らぎなどに起因するノイズが含まれているため、これをそのまま二値化した場合、画像中の個々の黒点が熔融金属の粒子に対応するとは限らない。通常の画像処理におけるノイズ除去や画像のダイナ

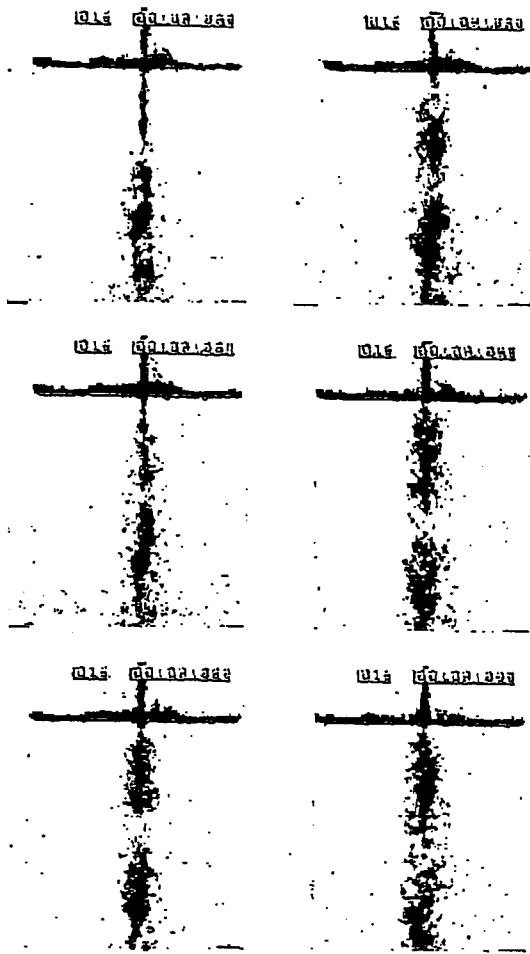


Photo 3. Binary value transformation of Photo 2.

ミックレンジと二値化のしきい値の調節によりある程度はこのノイズを除去できる。Photo 2 では、連続画像から明らかなノイズと思われる黒点は除去してある。このような二値化によりジェットの大まかな特徴はよく捉えられている。また、この画像処理における1画素の幅は0.2mm程度であり、一方、微粒化により生成される微粒子は数ミクロン～数十ミクロンのオーダーであるので、個々の微粒子の可視化は困難であり、微粒子の集合としての粒子雲として観察するのが妥当であろう。気泡に関しては、二値化した場合、気泡は消されてしまい、背景に隠れてしまう。従って、二値化のみでは熔融金属周りの気泡の可視化は困難である。

Photo 4 には、熔融金属塊の落下による水面からのカバーガスの巻き込みの様子の原画像と二値化と輪郭強調処理を組み合わせ得られた画



a. Original image b. Processed image

Photo 4. Images of molten metal and bubbles obtained by combining the binary-value transformation and the Laplacian filter, and their original images.

像を示す。ただし、二値化画像にはノイズ除去及び8近傍平均操作を行った。この画像処理法によれば、熔融金属周りの気泡の輪郭が明確に捉えられており、現象の理解に有効であると考えられる。ただし、より詳細に見れば熔融金属の微粒化の画像処理と同じ議論で、個々の小さな気泡のように見えるものはノイズの可能性もあるので、この方法を物理量の計測に利用する場合、その定量性について吟味する必要がある。しかしながら、この方法により、液面の揺動の様子や、気泡の巻き込みによる液面の窪みの様子、熔融金属塊の分裂、液面の窪み内を進む熔融金属塊の分裂そして気泡と熔融金属の分裂片との分離の様子が明らかに捉えられている。

Photo 5 には熔融金属ジェットを水中に落下させた瞬間のジェット及びジェット周りの気泡の

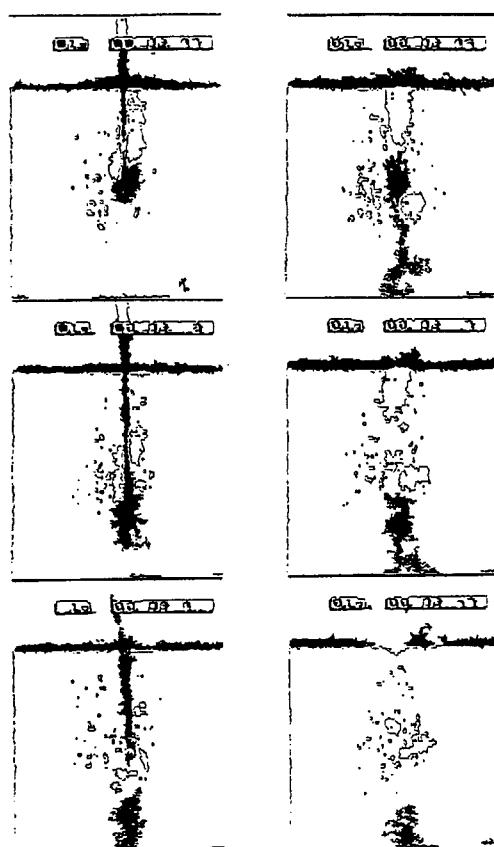


Photo 5. Break-up of a jet delineated by combining the binary-value transformation and the Laplacian filter.

分布を、Photo 4 と同じ手法により処理した画像で示したものがある。この方法により、ジェットの分裂や気泡挙動を類型化して表し、現象の理解を助けることが可能である。

(2) 加熱剛体球実験

Photo 6 に 1000°C に加熱した直径 12mm のステンレス鋼球を重水中に落下させたときの 8ms 毎の連続画像を示す。撮像速度は毎秒 500 コマである。この場合、時間は左上から下に進行している。この画像では分かり難いが、動画の観察より時刻 0ms において剛体球は重水面の直上に達し、20ms 後には画像外に去っていることが分かる。加熱剛体球が水中を進行するにつれてガス（カバーガスと水蒸気の混合ガスと考えられる）の穴が成長しているが、剛体球がこのガス穴を去った後にも成長は続く。このことは、

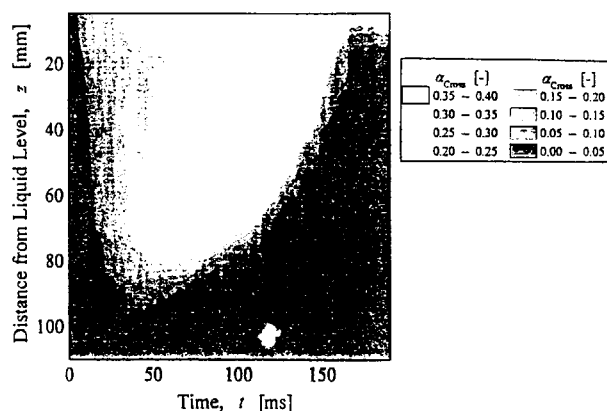


Fig.3 Contour map of cross-sectional average void fraction against the distance from the liquid surface and passage time.

加熱剛体球から周りの水への熱輸送は極めて急速に起こり、時刻 20ms 以後でもガス穴が成長していることは、加熱剛体球周りの水のスーパーヒートあるいはガス圧の上昇など、熱的非平衡状態の可能性を示唆している。時刻 32ms から 64ms の間では、ガス穴の先端の位置はほとんど変化せず、ガス穴の直径が増加している。その後、ガス穴は収縮を始めている。

Fig.3 は、Photo 5 に示した場合について、試験部の断面平均ボイド率を水面からの距離および時間の関数として表したものである。この場合、断面平均ボイド率は各位置における中心から左右に 38mm の幅で、奥行き 30mm の水平面内におけるボイド率である。ボイド率 0.05 に対応する等高線の勾配は、ほぼガス穴の先端の進行速度に一致しており、速度は最初下向きで、後に上向きに転じている。時刻が 0ms から 20ms の間では、速度は 5.3m/s であり、これは 1.5m の距離の自由落下の速度 5.4m/s にほぼ等しい。すなわち、時刻 0ms から 20ms の間では、ガス穴の先端は剛体球の運動に連れて成長し、その短い間に剛体球の熱量が大量に周囲の水に伝えられ、周囲の水はスーパーヒートされると考えられる。このためにガス穴は、剛体球がガス穴を去った後にも成長を続ける。しかし、さらに時間が進むと、緩和現象の終結に伴いガス穴は収縮を始める。ガス穴のボイド率の最大値およびその位置は剛体球の大きさと初期温度に比例して増加する。したがって、ガスの成分は大部分水蒸気

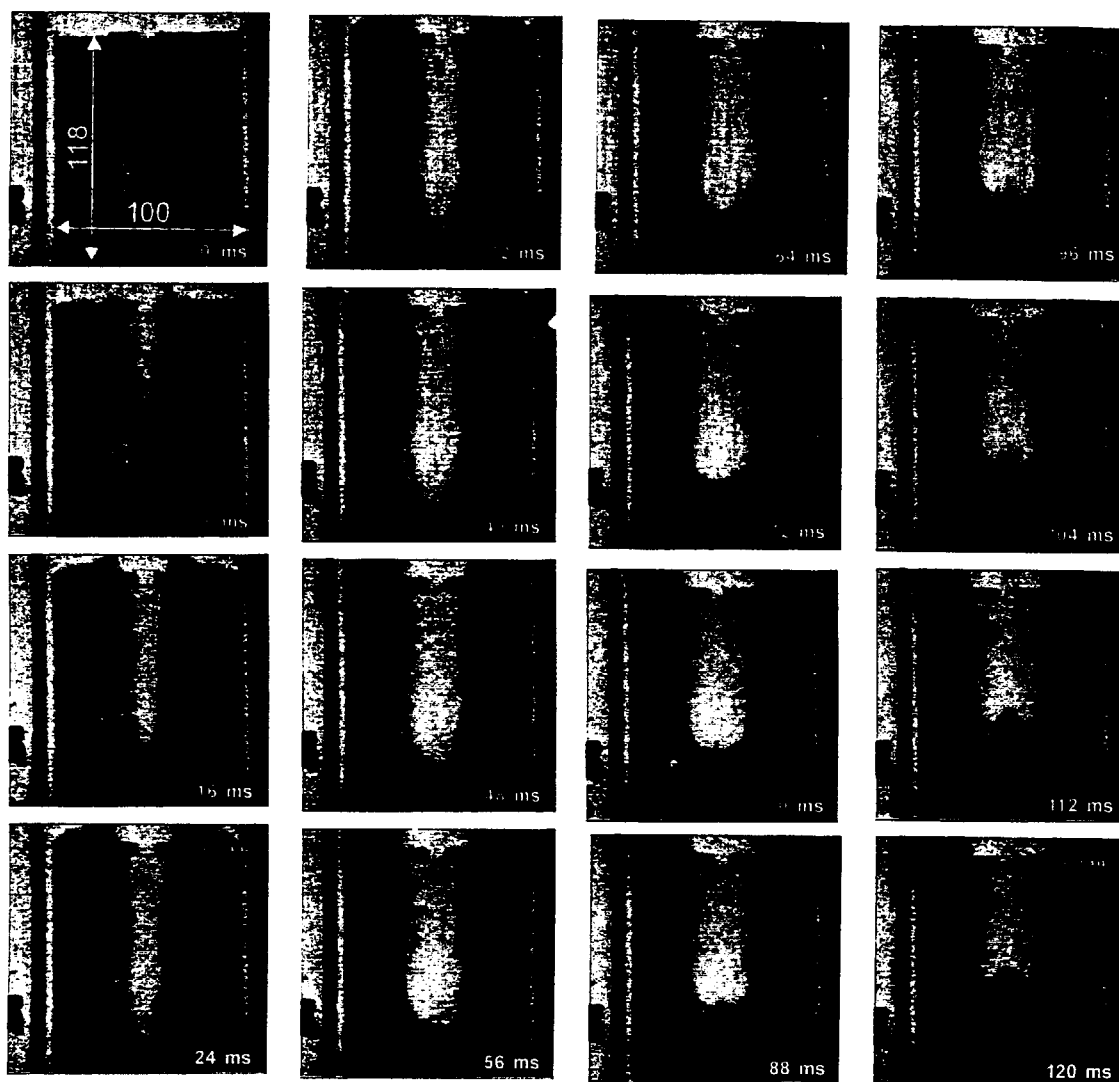


Photo 6. Consecutive images of hot stainless-steel particle and heavy water interaction (recording speed: 500fps; frame interval: 8ms; initial particle temperature: 1000 °C; particle diameter: 12mm).

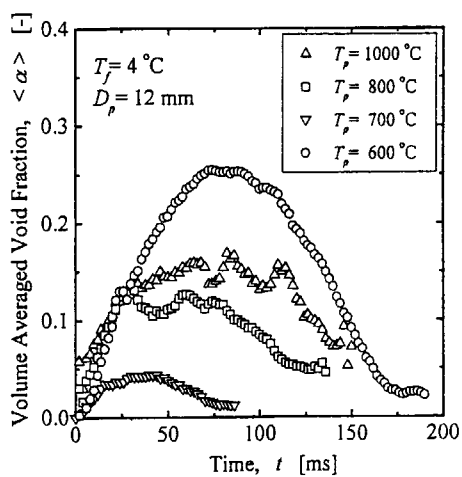


Fig.4 Temporal variation of volume average void fraction with the particle temperature as a parameter.

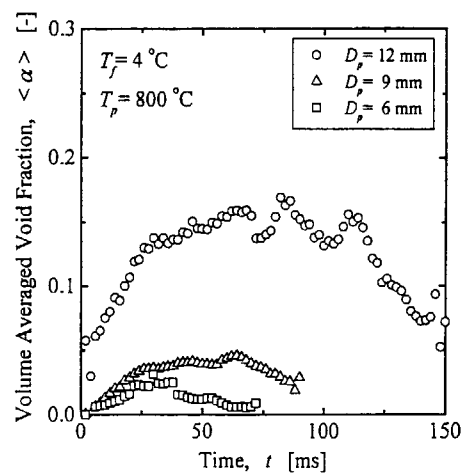


Fig.5 Temporal variation of volume average void fraction with the particle size as a parameter.

であり、これにカバーガスが混じっていることが推測される。

Fig.4 は、直径 12mm の剛体球の初期温度を変化させた場合の体積平均ボイド率の時間変化を示している。このように、体積平均ボイド率は初期温度に比例して大きくなる。また、時間変化を見ると、初期温度が 600°C ~ 800°C のとき、2つのピークが見られる。このピークの位置は 10~20ms であり、剛体球がカス穴を離れる時間と対応している。したがって、第1のピークは剛体球という熱源がなくなったことによるものと考えられる。第2のピークの位置は、剛体球の初期温度が 600、700、 800°C のとき、それぞれ 40、60、80、90ms である。これは先に述べた緩和現象の終結に対応している。

Fig.5 は、初期温度を 800°C に維持し、剛体球の直径を変えた場合の体積平均ボイド率の時間変化である。この結果によれば、発生蒸気量は、剛体球に蓄積された熱量、すなわち剛体球の大きさ、初期温度および熱容量におよそ比例している。

4. 結果の評価

溶融ウッドメタルを重水中に落下させ、その挙動を中性子ラジオグラフィにより可視化した。定常熱中性子束 $1.5 \times 10^8 \text{n/cm}^2/\text{s}$ のもと、これまでに開発した中性子ラジオグラフィ高速度撮像法により毎秒 500 コマの撮像速度で現象を撮影した結果、水中に落下した溶融金属と発生する水蒸気あるいは液面において巻き込まれるカバーガス及び液面の揺動の様子が観察できた。また、得られた画像を処理することにより、水中に落下した溶融金属のジェットあるいは液塊、分裂片と蒸気泡、水との界面を識別できた。局所的な水蒸気爆発が起こった実験では、個々の微粒子の識別は困難であったが、水蒸気爆発の発生地点に微粒子の雲が観察された。

加熱剛体球の落下実験では、剛体球の周りのボイド率のデータを得ることができ、これにより加熱剛体球と周囲の液との間の過渡的な熱伝達についておよそではあるが定量的な情報が得られた。

これらの結果より、粗混合過程における溶融金属と水蒸気の分布状態の観察及び剛体球周りのボイド率などの物理量の計測に、中性子ラジオグラフィ高速度撮像法を用いた方法が有効であることが明らかとなった。

この方法の限界としては、溶融金属の周囲の薄い蒸気膜及びジェット分裂後の微粒子は、画像の空間分解能の制限と中性子強度の揺らぎによる画像輝度のちらつきのために識別が困難であることが分かった。また、加熱剛体球の周りのボイド率の計測は可能であるが、複雑な形状をしている溶融金属まわりのボイド率計測に関しては定量化は困難であった。

5. 成果の公表

本研究により得られた成果の一部あるいは全部を、国際会議あるいは雑誌に公表したものは以下のとおりである。

- (1) K. Mishima, T. Hibiki, Y. Saito, H. Nakamura, Y. Kukita, "Visualization study of molten metal-water interaction by using neutron radiography," Proc. Workshop on Severe Accident Research in Japan, SARJ-96, Oct. 28-30, 1996, Tokyo, Japan.
- (2) K. Mishima and T. Hibiki, "Development of high-frame rate neutron radiography and quantitative measurement method for multiphase flow research," Proc. OECD/CSNI Specialist Meeting on Advanced Instrumentation and Measurement Techniques, March 17-20, 1997, Santa Barbara, USA.
- (3) K. Mishima, T. Hibiki, Y. Saito, A. Yamamoto, K. Moriyama and J. Sugimoto, "Visualization study of molten metal-water interaction by using neutron radiography," Proc. International Seminar on Vapor Explosion and Explosive Eruptions, May 22-24, 1997, Sendai, Japan, 101-109.
- (4) K. Mishima, T. Hibiki, Y. Saito, K. Moriyama and J. Sugimoto, "Visualization study on hot particle-water interaction by using neutron radiography," Proc. Workshop on Severe Accident Research in Japan, SARJ-98, Nov. 4-6, 1998, Tokyo, Japan.
- (5) Y. Saito, K. Mishima, T. Hibiki, A. Yamamoto, J.

- Sugimoto and K. Moriyama, "Application of high-frame-rate neutron radiography to steam explosion research," Nucl. Instr. Meth. Phys. Res. A424 (1999) 142-147.
- (6) Y. Saito, T. Hibiki, K. Mishima, K. Moriyama and J. Sugimoto, "Visualization study on hot particle-water interaction by using neutron radiography," Proc. Two-Phase Flow Modelling and Experimentation, May 23-25, 1999, Pisa, Italy.
- (7) K. Mishima, T. Hibiki, Y. saito, J. Sugimoto and K. Moriyama, "Visualization study of molten metal-water interaction by using neutron radiography," Nucl. Eng. Design 189 (1999) 391-403.

2.1 ファイバ・オプティクス・シンチレータ

今回、中性子透過画像－光学画像変換に従来用いられている蛍光コンバータの代わりにファイバのコアに Gd をドープしたファイバ・オプティクス・シンチレータを用いる。今回使用するファイバ・オプティクス・シンチレータは高強度 X 線ラジオグラフィ用として米国で開発されたもので、Gd/Tb を用いていることから熱中性子ラジオグラフィに対しても有効であると考え、今回適用を試みた。ファイバ構造の中性子検出器を用いることにより、ファイバがライトガイドとして働くことから励起光を空間分解能を劣化させることなく出力面に導くことが出来る。このことは、中性子の検出効率を向上させたい場合に中性子捕獲部を厚く設計できることとなり検出効率の向上に有利である。

中性子検出には一般に、捕獲材として ${}^6\text{Li}$ と ${}^{157}\text{Gd}$ が使用されるが、それぞれ表 2.1 のような特徴がある。Gd は熱中性子に対する吸収断面積が Li に比べて大きく、熱中性子を効率的に捕獲する事が出来る。しかしながら、蛍光体を励起させるエネルギーが Li の (T, α) 反応に比べて非常に小さいため出力される光子数は Li 系に比べ小さいものとなる。参考として両捕獲材を蛍光コンバータとして使用した場合の発生光子数の比較を表 2.2 示す。

表 2.1 Gd と Li の熱中性子に対する特性

捕獲材	反 応
Gd 系	${}^{157}\text{Gd} + n \rightarrow {}^{158}\text{Gd} + e \text{ (70 keV)}$
Li 系	${}^6\text{Li} + n \rightarrow \text{T} + \alpha + 4.97\text{MeV}$

表 2.2 ${}^6\text{LiF/ZnS (Ag)}$ と $\text{Gd}_2\text{O}_3\text{/Tb}$ の蛍光体による発生光子数

捕獲物質/蛍光体	発光波長
${}^6\text{LiF/ZnS (Ag)}$	450 nm
$\text{Gd}_2\text{O}_3\text{/Tb}$	550 nm

ところで、空間分解能を考えた場合、Li 型の変換機構は蛍光体に作用するエネルギーが大きいた

め、エネルギーの拡散に伴う発光領域の拡大があると考えられ、反応エネルギーの低い Gd 型の変換機構の方が有利であると考えられる。そこで、今回は Gd を中性子捕獲材とした変換機構を採用することとする。ファイバ・オプティクス・シンチレータの概略図を図 2-2 に示す。

今回使用する FOP シンチレータの特性

- ・コア: $\text{Gd}_2\text{S}_3\text{O/Tb SO}_4$
- ・クラッド : 石英ガラス

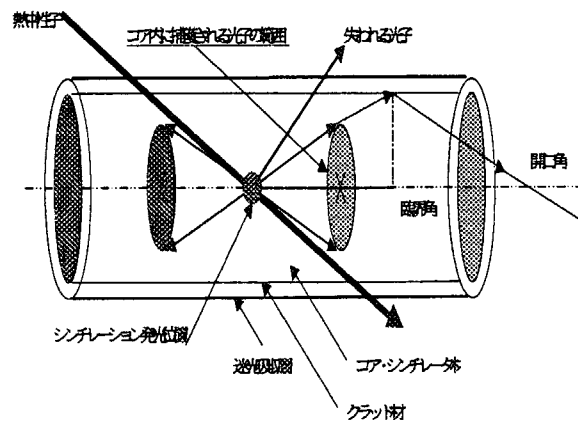


図 2-2 ファイバ・オプティクス・シンチレータ

2.2 イメージファイバ

シンチレータからの励起光をカメラの対物レンズにより撮像する方法では、シンチレータ出力面での光の拡散により検出光子数は約 $1/1000$ になってしまう。そこで、今回、FOP シンチレータからの励起光をイメージファイバにより撮像素子表面に結合する方法を採用した。

イメージファイバは、光学特性に優れたファイバ素線を束ねて 2 次元画像の伝達を行うもので、従来のレンズによる光学画像伝達より損失が極めて少ないという特徴を持つ。これは入射面より入射した光がファイバコアを全反射しながら伝達するためであり、このことから光学的散乱による解像度の劣化も少ない。今回の様な低照度場での高精細撮像を行う場合の光学画像伝達の方法として最適なものである。

イメージファイバの特性：

- ・ファイバ素線径 : $24\ \mu\text{m}$
- ・イメージファイバ端面径 : $6.4\ \text{mm}$
- ・コア屈折率 : 1.58
- ・クラッド屈折率 : 1.48
- ・開口比 : $\text{NA}=0.55$
- ・解像度 : $41.6\ \mu\text{m}$

3. 実験装置

図3-1に今回使用する撮像システムの構成図を示す。

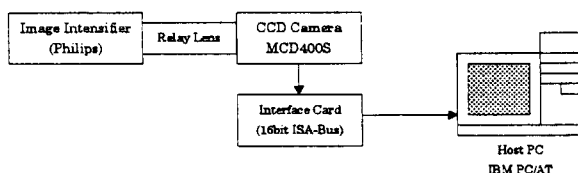


図3-1 撮像システム

撮像システムはカメラヘッド、コントロール・インターフェイス、ホスト・パソコンからなり、露光時間のセット等カメラの設定はホストコンピュータからインターフェイス・カードを介して任意に行うことが出来る。また、CCDからの映像信号はアナログ信号でインターフェイスカードに送られ、オン・ボードADCによりデジタル信号に変換された後、ISAバスを介してIBM PC/AT互換機に転送される。ホストコンピュータにより取得画像表示、暗電流、シェーディング、積算処理を行い、データをストレージすることが可能となっている。

3.1 カメラ、コントロールインターフェイス部

シンチレータで得られる極低照度の透過画像をカメラで測定可能な照度まで増幅するためイメージ・インテンシファイア(I.I.)を使用する。今回用いるI.I.はPhilips社製XX1380(解像度:51LP/mmゲイン:22000倍)である。

イメージ・インテンシファイアにより増幅された

透過画像はリレーレンズを介してCCDカメラで撮像する。

今回使用するカメラはSpectra Source Instruments社製冷却型CCDカメラ:MCD400Sで、カメラヘッドとコントロール用コンピュータ・インターフェイス・カードより構成され、ホストコンピュータであるIBM PC/AT互換機でコントロールを行う。CCDカメラの基本仕様を表3-1に示す。

表3-1 CCDカメラヘッドの仕様

画素	336[pixels] × 243[pixels]
画素サイズ	10 × 10[μm]
有功受光サイズ	3.3 × 2.4[mm^2]
ADC Resolution	16
読み出し速度	100[kilo Pixel/sec]

3.2 実験フィールド

実験は、JRR-3Mが長期間停止したため、立教大学原子力研究所所有のTRIGA-II研究炉において実験を行った。立教大学原子炉照射場の特性を表3-2に示す。

表3-2 立教大原子炉照射場特性

中性子源	TRIGA-II
熱中性子束	$3.2 \times 10^6 [\text{n}/\text{cm}^2 \cdot \text{sec}]$
L/D	79.9
照射野	$\phi 200 [\text{mm}]$
出力	100 [kW]

4. 実験結果と評価

4.1 Cdステップ撮像

今回採用したGd/TbタイプFOPシンチレータの熱中性子に対する特性を取得するためにCdステップによる熱中性子ラジオグラフィ撮像実験を行った。Cdの厚さを100 μm 、200 μm 、300 μm 、500 μm 、1mm、2mmと変化させた。

この実験より得られたCdの厚さと熱中性子の透過率をまとめたものを図4-1に示す。

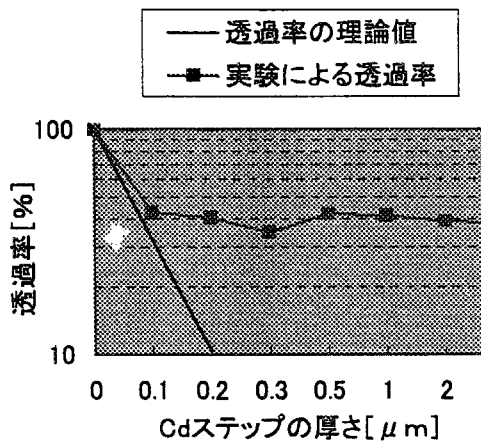


図4-1 Cdステップの透過率

図4-1より、Cdプレートの厚さが厚くなるに従って、理論値との開きが大きくなっている。これにより透過画像のコントラストが低下していることが分かる。これはCdが γ 線に対しても感度を持つ為、Cdに熱中性子が照射された時に発生する即発 γ 、原子炉からのビーム及び照射場に存在する γ 線、熱外中性子による影響であると考えられる。このことより、今回用いたFOPシンチレータは熱中性子に対して有効であることが分かったが、 γ 線、熱外中性子にも十分な感度を持っているため、熱中性子ラジオグラフィを行う場合には γ 線、熱外中性子強度の低いフィールドが適していると考ええる。

4.2 Cdホールによる熱中性子ラジオグラフィ

次に、解像度評価を行うために厚さ $250\mu\text{m}$ のCd板に 0.5mm の穴を開けたオブジェクトを作成し、熱中性子ラジオグラフィによる撮像実験を行った。オブジェクトは厚さ $250\mu\text{m}$ のCd板に直径 0.5mm の穴を複数個あけたものである。オブジェクトを図4-2に示す。

また、中性子ラジオグラフィによって得られた画像を図4-3に示す。

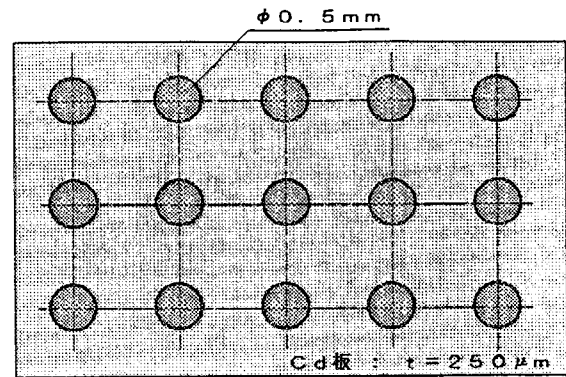


図4-2 オブジェクト

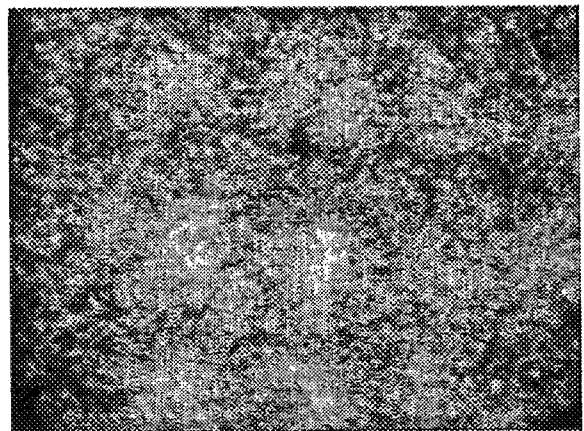


図4-3 透過像

図4-3は取得したオブジェクトデータにシェーディング、暗電流処理を行ったものである。露光時間は撮像実験により 0.6 秒と決定した。撮像視野は $3.0\text{mm} \times 4.1\text{mm}$ である。今回、原子炉の運転サイクルと時間的關係から十分な実験時間が確保できなかったため、今回フレーム積算撮像は出来なかった。

図4-3は辛うじてオブジェクトのホールが確認出来る程度であり、解像度についての評価は難しい。これは極低照度であるために、照射熱中性子の粒子性があらわれているものとする。更に、FOPシンチレータが γ 線や熱外中性子にも十分な感度を持つてしまうことから、オブジェクトに中性子が照射されることによって発生する即発 γ 線、原子炉ビーム

中の熱外中性子及び γ 線の影響、原子炉ビーム照射口のL/Dが十分に大きな値では無いため、原子炉からのビームの散乱成分、FOPシンチレータへの放射線の斜入力の影響が大きいものとする。

これらの実験の結果から、Gdが冷中性子にも十分な捕獲効率を持つことを考慮すると、微細構造のラジオグラフィ撮像を目的とした場合、実験フィールドとしてはL/Dが十分大きく、ビームの散乱成分が極めて少ない日本原子力研究所東海研究所 JRR-3Mの冷中性子ポートを使用したフィールド等が適していると考えられる。今回、露光時間0.6秒での撮像を行ったが、実験フィールドとして日本原子力研究所東海研究所 JRR-3M 熱中性子ラジオグラフィフィールド:TNRF2(熱中性子束 1.5×10^8 [n/cm²·sec])を用いた場合、フレーム周期1/30秒での動画の取得も可能であるとする。これは、TNRF2では熱中性子束が今回用いた立教炉の約46倍となるため、フレーム毎の露光時間を計算すると今回の約1.6倍の露光時間に相当するためである。

5. 今後の方針

今回実験に使用した Spectra Source Instruments MCD400S CCD Camera はアマチュア天文用に作られた物であり、露光時間にばらつきがあり定量的測定には適していない。

そこで、撮像システムの計測の定量性を向上させるために新たに CCD を用いた撮像システムを設計製作している。CCD に THOMSON-CSF 社製画素開口率100%のフルフレーム型 CCD を採用し、ベルチエ素子による電子冷却を行い CCD の暗連流成分を抑制し、検出効率を重視したカメラとしている。また、画像収集装置には CCD のリセットノイズを除去するためにダブル・サンプリング処理、取得画像の非同期ノイズを低減させる為にフレーム積算処理機構を積載したシステムを設計している。

2-7 植物試料の中性子ラジオグラフィ Neutron Radiography of Plant Sample

中西友子・古川純・松林政仁¹

Tomoko M. Nakanishi, Jun Furukawa and Masahito Matsubayashi

東京大学大学院農学生命科学研究科

¹ 日本原子力研究所東海研究所中性子科学研究センター

Graduate School of Agricultural and Life Sciences,

The University of Toiyo

¹ Center for Neutron Science, Tokai Establishment,

Japan Atomic Energy Research Institute

1. 目的と意義

生きている植物における情報伝達に水が大きく関与していると予想されるが、まだそれを調べる手法は未発達である。現時点では、試料の大きさ、分解能などの点から中性子ラジオグラフィが水分動態を調べるための最も優れた手法であるため、本手法を用いて植物体および植物-土壌系の活動を調べることを目的に実験を進めた。また、X線フィルム法では、種子や樹木の小口材における水分の吸収ならびに乾燥過程の可視化も行うことができたので、合わせて報告する。

土壌中、根から1mm以内は根圏と呼ばれ、根からの分泌物とや微生物数が多いことから特別な環境が形成されているが、まだ根圏における水分動態の実測値は報告されていない。根圏における水分動態は根の活動そのものを反映していることから、本研究ではダイズ根の根圏の水分量の変化を中性子ラジオグラフィにより求めることを目的とした。

また、従来行ってきたX線フィルム法を発展させ、中性子線によるCT像を得る試みも検討し始めた。従来のX線フィルム法とは異なり、水分の立体分布を可視化する試みである。土壌中に育成

している根および周辺土壌のCT像を得ることが最終目的であるが、予備実験として、カーネーションの花を用いてCT像を構築する試みを行った。

2. 根-土壌系

まず、根の活動については、根から1mm以内の土壌中の水分動態の中性子ラジオグラフィ像を解析した。根圏における水分動態は根の活動そのものを反映していることから、本研究ではダイズ根の根圏の水分量の変化を中性子ラジオグラフィ像から求めた。また、中性子ラジオグラフィでは、水分動態のみならず根の形態変化もトレースすることができるため、形態変化と土壌水分動態とを合わせて根の活動を解析した。

吸水性ポリマー中にバナジウムを吸収させ、土壌に添加してダイズを育成させたところ、根の生育の形態変化は6日目まで認められなかったものの、根から1mm以内の、根に沿った土壌中の水分量は、2日目から変化が示されず、根の活動が低下していることが示された。

また、薄箱中に育成させたダイズの根は、形態的な変化が認められない早い時期(2日後)から水分吸収能が土壌環境の変化により低下するこ

とが判った。現在、中性子ラジオグラフィによる根周辺の経時的な水分量の変化をもとに、根活動度のシミュレーションモデルを組み立てて検討を行っている最中である。

ハツカダイコンを用いた土壌改良材の評価では、主に根の形態変化をトレースすることにより行った。化学修飾したパルプ廃材（クラフトリグニン）を土壌に添加したところ、アルミニウムの害が軽減されることが示された。この結果は、土壌中のアルミニウムによる根の生育阻害を廃材パルプを原料とした土壌改良材を利用することにより軽減できる可能性を示したものである。なお、土壌中の可溶化したアルミニウムは、酸性土壌における植物生育阻害の最大要因の一つである。また、中性子ラジオグラフィによる根の形態をトレースして根長を求めたところ、従来の格子法と良く一致することが示された。

3. スギ小口材の乾燥過程

スギは同じ種でも生育環境により心材部の水分量が異なり、製材上での大きな問題となっており、心材部の水分量が異なる小口材を用いて、乾燥過程における水分量の変化を調べた。その結果、心材部の水分量が多い小口材は、心材部の水分量が少ない試料と比較して水分が乾燥しにくいことが画像処理により確かめられた。

4. 種子の水分吸収

アサガオ、トウモロコシ、イネ、ムギおよびソラマメの種子を用い、種子の水分吸収過程を2時間ごとに中性子ラジオグラフィにより調べたところ、種子中のどの部分から水分が吸収されるかが判った。なお、水分吸収が早い種子ほど発芽率が高かった。

5. カーネーションのCT像

これまでのX線フィルムを使用する方式とは異なり、CCDカメラおよび原子力研究所の松林氏らが開発した蛍光コンバータ測定系を用いた。

試料は1度ずつ回転させながら180枚の画像をコンピュータに取り込み、これらの像から花のCT像を得た。さらに、これらのCT像を垂直方向に積み重ねることにより（200枚/cm）、カーネーションの3次元中性子ラジオグラフィ像を得ることができた。得られたカーネーションの花のCT像から、乾燥処理を施した場合、特に子房周辺の水分量が減少することが判った。

6. 評価および今後の方針

中性子線による水のイメージングは他の手法と比較して、試料の大きさの制限がないこと、および分解能が非常に高いことが特徴である。本研究により、中性子ラジオグラフィ法が生きている植物試料の水分動態を調べるためには最も優れた手法であることが、根、花の中性子ラジオグラフィ像などから示された。

しかし、まだ画像解析手法に多々の問題を抱えており、特にCT像におけるCT値と水分値との換算方法、高分解能化などが今後の課題として残されている。

植物中の水の非破壊イメージングを行っている研究は現在世界中に存在していないため、本研究をさらに発展させることにより、生きている植物の活動の新しい知見が得られると予想される。

研究発表

(1) 学会誌等

1. K.Saito, T.M.Nakanishi, M.Matsubayashi and G.Meshitsuka : Development of New Lignin Derivatives as Soil Conditioning Agents by Radical Sulfonation and Alkaline-Oxygen Treatment.

Mokuzai Gakkaishi43(8), 669-677 1997

2. T.M.Nakanishi, A.Tsuruno and M.Matsubayashi : Water Movement in Plant. Proc. of Fifth World Conference on Neutron

- Radiography, C.O.Fischer, J.Stade and W.Bock (Eds.) DGZfp (Deutsche Gesellschaft für Zertörungsfreie Prüfung E.V.) Publisher 716-719 1997
3. T.M.Nakanishi and M.Matsubayashi : Water Imaging of Seeds by Neutron Beam. Bioimages 5(2), 45-48 1997
 4. T.M.Nakanishi and M.Matsubayashi : Nondestructive Water Imaging by Neutron Beam Analysis in Living Plants. J.Plant Phys. 151, 442-445 1997
 5. T.M.Nakanishi, K.Okano, I.Karakama, T.Ishihara and M.Matsubayashi : Three Dimensional Imaging of Moisture in Wood Disk by Neutron Beam During Drying Process. Holzforschung, 52, 673-676 1998
 6. T.M.Nakanishi, J.Furukawa and M.Matsubayashi : A Preliminary Study of CT Imaging of Water in Carnation Flower. Nucl. Instr. Meth. Phys. Res. A424, 136-141 1999
 7. J.Furukawa, T.M.Nakanishi and M.Matsubayashi : Neutron Radiography of the Root Growing in Soil with Vanadium. Nucl. Instr. Meth. Phys. Res. A424, 116-121 1999
 8. T.M.Nakanishi, I.Karakama, T.Sakura and M. Matsubayashi : Moisture Imaging of a Camphor Tree by Neutron Beam. Radioisotopes, 47, 387-391 1998
 9. T.M.Nakanishi, J.Furukawa and M.Matsubayashi : CT Imaging of Water in Root-Soil System by Neutron Beam. Soil Phys. Conditions and Plant Growth, Japan, in press
(2) 口頭発表
 1. K.Saito, K.Takami, T.Nakanishi, M.Matsubayashi, G.Meshitsuka : Development of New Lignin Derivatives as Soil-Conditioning Agents by Radical Sulfonation and Alkaline-oxygen Treatment. International Chemical Congress of Pacific Basin Societies, Honolulu, Hawaii, Dec.17-22 1995
 2. 斎藤、高見、中西、松林、飯塚 : リグニン系土壌改良剤の開発 (4) 中性子ラジオグラフィによる根の伸長成長の評価 第46回日本木材学会大会、熊本 Apr. 3-5 1996
 3. T.M.Nakanishi, A.Tsuruno and M.Matsubayashi : Water Movement in Plant Sample. Proc. of Fifth World Conference on Neutron Radiography, Berlin, 1996
 4. T.M.Nakanishi, J.Furukawa and M.Matsubayashi : CT Imaging of Water in Carnation Flower 3rd International Topical Meeting on Neutron Radiography, Lucerne, Switzerland, 1998
 5. J.Furukawa, T.M.Nakanishi and M.Matsubayashi : Neutron Radiography of the Root Growing in Soil with Vanadium. 3rd International Topical Meeting on Neutron Radiography, Lucerne, Switzerland, 1998
 6. J.Furukawa, T.M.Nakanishi and M.Matsubayashi : CT Imaging of Soybean Root Imbedded in Soil by Neutron Beam. Proc. of Six World Conference on Neutron Radiography, Osaka, 1999
 7. 古川、中西、松林 : バナジウム (V) 存在下における根近傍の水分動態の解析-中性子線を用いた根-土壌系の経時的な立体像の構築- 平成11年日本土壌肥料学会年次大会 7月、1999

3. 即発ガンマ線分析

3. Prompt Gamma-ray Analysis

This is a blank page.

研究テーマ：畜産および水産研究における原子炉中性子即発ガンマ線分析法の利用

表題：中性子即発ガンマ線分析法による畜産および水産関係試料中のホウ素およびケイ素の定量

3-1 中性子即発ガンマ線分析法による畜産および水産関係試料中のホウ素およびケイ素の定量

宮本進, 塩本明弘¹, 西村宏一, 米沢伸四郎², 松江秀明², 安達武雄², 星三千男²

農林水産省畜産試験場

¹ 農林水産省遠洋水産研究所

² 日本原子力研究所

1. 目的

畜産および水産研究分野においては、近年、分析対象とする環境および生体中の元素、成分が増加し、さらに対象とする試料の形状も多様化している。高感度で迅速かつ簡便な分析法の導入が望まれている。本研究では、即発ガンマ線分析法(PGA)を畜産および水産試料に適用し、家畜体内における元素の動態および海洋における植物プランクトンのホウ素の取り込み機構を明らかにし、畜産および水産における生産性の向上を図ることを目的とし、日本原子力研究所で開発、所有しているJRR-3Mの中性子ガイドビームを利用した中性子即発ガンマ線分析装置を利用して実験を行った。

今までに、即発ガンマ線分析法による植物、動物及び海洋性試料中の元素分析法の基礎データを得るため、感度の高いホウ素(B)を対象元素として、国際標準試料(植物、動物)を用い、測定時における試料形状、試料量、Bの測定限界等について検討すると共に、畜産関連試料中のB等の測定をPGAにより行った。また、海洋試料中のケイ素(Si)等の測定法についても検討した。

2. 試験研究の概要

畜産関連では、羊3頭にルーサンハイキューブ(1,100g/日/頭)とB添加水(ホウ酸ナトリウム:Bとして100ppm)を18日間給与し、この間に得られた血液(血漿)、尿および実験終了後得られた臓器(肝臓、腎臓、筋肉等)を供試試料とした(B投与区(T))。なお、対照区(C)の羊2頭(B非添加水を給与)から得られた試料についても同様に処理した。

各試料は、血漿および尿については1mlをテフロン製容器に入れ、プランクトン、糞は乾燥後、臓器は凍結乾燥後粉末とし錠剤成形器を用いてペレ

ット状に成形(直径:13mm、重量:0.3g程度)PEPフィルム(厚さ25μm)で二重に溶着した。試料はPTFE製保持具の中央にPTFE製糸で固定し、原研JRR-3M熱中性子ガイドビームに設置された即発ガンマ線分析装置を用い、ヘリウムふんい気中でガンマ線スペクトル測定を行った(測定時間1,000から18,000秒/試料)。ホウ素の検量線は、スズ板にHBO₃標準溶液を滴下乾固した試料、血漿あるいは尿にホウ素を添加した試料を用い478 keVのホウ素のピークの面積を求める方法により作成した。

血漿(図1)、尿および糞中のB濃度はB添加水給与開始後急上昇し、5日目頃からほぼ一定レベルとなった。18日間B添加水を給与した後、屠殺して得られた臓器中のB濃度は、対照区のそれよりも明らかに高かった(肝臓:22.9ppm(T), 2.2ppm(C), 腎臓:57.3ppm(T), 4.6ppm(C))。また、量的には羊の体内に入ったBの大部分は尿、次いで糞を経由して体外に排泄され(表1)、臓器では肝臓に多く蓄積された。これらの結果から、飲水中のBは家畜(羊)に速やかに吸収され血漿および尿中のBレベルは上昇し、臓器に蓄積されることが明らかになった。

代表的な沿岸性の海産珪藻であるSkeletonema costatumを室内で培養し、このプランクトンの細胞数の変化とホウ素量の変化の関係について検討した。試料はよく乾燥させた後に即発ガンマ線分析に供した。

Skeletonema costatumは、温度18℃、明暗12時間周期、光の強さは8000lux、栄養塩添加海水培地(f/2型)を用いて100mlのポリカーボネイト製の三角フラスコ中で11日間培養した。毎日午後1時ごろに試水5mlをニュークリポアフィルターにてろ過して、即発ガンマ線分析に供した。培養したSkeletonema costatumの細胞数の経時変化をみると、

原子炉: JRR-3M 装置: 即発γ線分析装置 分野: 即発γ線分析(農・水産物)

培養後3日目から5日目の間に細胞数が顕著に増加し始め、5日目に細胞数が最大に達した(図2)。5日以降、細胞数に顕著な増加はみられなかった。培養して1-2日が誘導期、3-5日が対数期、5-8日が定常期に相当した。また、この時のニュークリポアフィルター上に集められたホウ素すなわち懸濁態ホウ素の量の変化をみると、細胞数の変化とほぼ同じ挙動がみられた(図2)。ケイ素では検出感度の点から困難であるが、ホウ素を用いれば *Skeletonema costatum* の増加を追跡することがで

きる事が明らかとなった。

参考文献

- 1) 第34回理工学における同位元素発表会 講演要旨集、(1997) PP. 92
- 2) 第35回理工学における同位元素発表会 講演要旨集、(1998) PP. 168
- 3) 平成9年度国立機関原子力試験研究成果報告書、第38集、(1999)84-1~4, 85-1~4

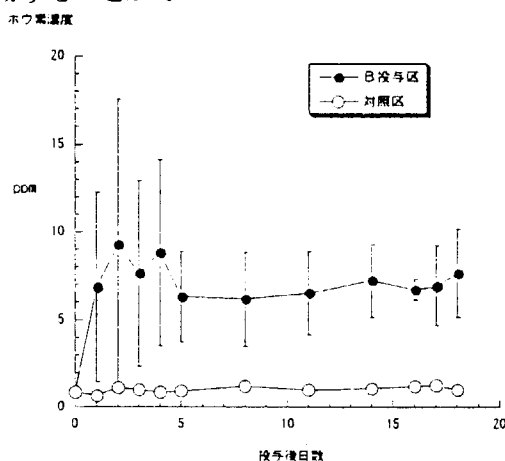


図1 ホウ素濃度(血漿) B投与区の値は平均値±S. D. (n=3)
対照区の値は平均値

表1 羊におけるホウ素の出納

	摂取量 (I)	排泄量 (E)			E / I
		尿	糞	合計	
	mg/day	mg/day	mg/day	mg/day	%
対照区	53(53, 53)	27(28, 27)	15(15, 14)	42(43, 41)	79.2(81.1, 77.4)
B投与区	573±124	453±74	83±23	536±92	94.2±4.6

摂取量と排泄量の値はB投与開始後16~18日間の平均値
B投与区の値は平均値±S. D. (n=3)

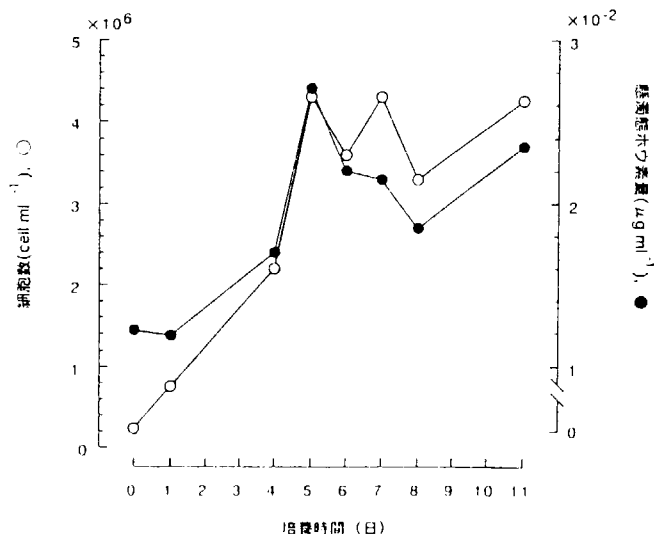


図2 培養した *Skeletonema costatum* の細胞数と懸濁態ホウ素量の経時変化

研究テーマ：原子力関連物質の分析化学

表 題：中性子即発 γ 線分析の研究

3-2 中性子即発 γ 線分析の研究

米沢伸四郎、松江秀明

物質科学研究部 分析センター

1. はじめに

報告者らはこれまでに JRR-3M の冷及び熱中性子ビームを使用する中性子即発 γ 線分析法 (PGA) を開発し、各種分野の試料分析に応用してきた。本年度は、熱中性子ビーム (第 1 サイクル) と冷中性子ビーム (第 2~4 サイクル) を使用し、1) k_0 法による多元素定量、2) 極微量ホウ素の定量、3) ^{56}Co 及び ^{66}Ga の γ 線放出率測定、4) 大学及び国立研究所との協力研究及び共同研究を実施した。

2. k_0 法による多元素定量

内標準法に基づいた k_0 法は、比較標準試料を使用しないで多元素を簡単に定量できることから、NAA の定量法として注目されている。近年ハンガリー同位体研究所 (IKI) 及び米国 NIST において PGA への k_0 法の適用が試みられている。PGA に k_0 法を適用することにより、比較標準試料を使用しないで多元素を正確に定量でき、さらに得られた k_0 値は他の施設にも共用することができる。

PGA で分析対象となることの多い 26 元素について k_0 係数を測定した。対象元素は塩化物をそのままか、あるいは酸化物等と塩化アンモニウムとを混合して調製した試料を用い、冷及び熱中性子ビームで即発 γ 線スペクトルを測定した。正確な k_0 係数を測定する上で Ge 検出器の γ 線検出効率の校正が重要である。検出効率は標準線源と中性子照射によって作成した γ 線源 (^{24}Na , ^{46}Sc , ^{56}Mn , ^{75}Se , $^{110\text{m}}\text{Ag}$) 及び即発 γ 線測定 ($\text{C}(\text{n},\gamma)$, $\text{N}(\text{n},\gamma)$,

$\text{Cl}(\text{n},\gamma)$) により得られた γ 線 (59 ~ 10829 keV) を用いて求めた。その結果、冷及び熱中性子においてそれぞれ、2.4%, 2.3% 以内の誤差で検出効率曲線が得られた。今年度は、冷中性子ビームで 26 元素、熱中性子ビームで 18 元素の $k_{0,\text{Cl}}$ 値を 3% 以下の測定誤差で求めることができた。冷及び熱中性子ビームにおける $k_{0,\text{Cl}}$ 値は、Cd, Sm 等の比較的 low 中性子エネルギー領域に大きな中性子吸収断面積を持つ元素を除き、ほとんどの元素において 3% 以内で一致した。また、JRR-3M の冷及び熱中性子ビームの $k_{0,\text{Cl}}$ 値は同じ熱中性子ガイドビームによる IKI の $k_{0,\text{Cl}}$ 値と 15 元素中 9 元素が 3% 以内で一致した。更に、本定量法の正確さを評価するために River Sediment (NIST SRM 1645) 及び Coal Fly Ash (NIST SRM 1633a) 標準物質の分析を行った結果、それぞれの認証値に対して 6% 以下の正確さで定量することができることを確認した。

3. 微量ホウ素の定量

B は PGA で最も高感度な元素の一つであり、他の分析法で問題となる汚染や飛散による損失の影響を受けることなく、ppb 以上の B を正確に定量することができる。また、B は中性子吸収断面積が大きいことから、原子が材料中の不純物として最も嫌われる元素の一つであり、その許容される濃度は低く定められている。このようなことから本年度は原子炉材料として使われるステンレス鋼中の 1.1 ~ 22 ppm のホウ素の定量を行った。

4. ^{56}Co , ^{66}Ga の γ 線放出率の測定

^{56}Co (半減期 78.8 d)及び ^{66}Ga (半減期 9.4 h)は、放射性核種としては例外的に 3 MeV 以上の高エネルギー γ 線を放出するが、正確な放出率は求められていない。広いエネルギー範囲にわたって γ 線の検出効率が正確に求められている JRR-3M の即発 γ 線分析装置でその γ 線スペクトル測定をすることにより、 γ 線放出率を正確に求めることができる。このようなことから、タンデム加速器を使用し、 $^{56}\text{Fe}(p,n)^{56}\text{Co}$ 及び $^{66}\text{Zn}(p,n)^{66}\text{Ga}$ 反応で生成した、 ^{56}Co と ^{66}Ga の γ 線放出率の測定を行った。

5. 協力及び共同研究

JRR-3M の即発 γ 線分析装置を使用し、大学との協力研究(8 件)及び国立研究所(1 件)を実施した。協力研究としては、PGA 法による高エネルギー荷電粒子の物質中での挙動の研究(大同工業大学工学部)、固体環境試料および地球化学的試料の即発ガンマ線分析(東京大学大学院)、植物試料中のホウ素の分析(東京大学大学院)、中性子ガイドビームを用いた中性子吸収反応の核・放射化学への応用(熊本大学工学部)、即発 γ 線分析の大型試料への適用(東京都立大学大学院)、隕石試料の即発 γ 線分析(東京都立大学大学院)、電気めっきスラッジの PGA 分析(東京都立大学理学部)、X 線・低エネルギー γ 線検出による即発 γ 線分析(武蔵大学人文学部)、の研究を行った。また、共同研究としては、農林水産研究における原子炉中性子即発 γ 線分析の利用に関する研究(農林水産省 畜産試験所、遠洋水産研究所)を行った。

6. 成果の公表

1. C. Yonezawa, H. Matsue, T. Adachi, M. Hoshi, E. Tachikawa, P. P. Povinec, S. W. Fowler, M. S. Baxter, "Neutron-induced prompt γ -ray analysis of Gulf marine environmental samples", Extended Synopses of International Symposium on Marine Pollution, IAEA, p.296 (1998).
2. 松江秀明、米沢仲四郎:「中性子即発 γ 線分析法における k_0 法の適用」、第 42 回放射化学討論会予稿集、p.37 (1998)
3. C. Yonezawa, "Prompt γ -ray analysis using cold and thermal guided neutron beam at JAERI", Proceedings of International Conference on Nuclear Analytical Material in the Life Sciences, in press, Humana, (1999).
4. C. Yonezawa, H. Matsue, "Usefulness of prompt gamma-ray analysis with guided neutron beams comparing to neutron activation analysis", J. Radioanal. Nucl. Chem., in press (1999).
5. H. Matsue, C. Yonezawa, " k_0 Standardization approach in neutron-induced prompt gamma-ray analysis at JAERI", J. Radioanal. Nucl. Chem., in press (1999).
6. C. Yonezawa, P. P. Ruska, H. Matsue, M. Magara T. Adachi "Determination of boron in Japanese geochemical reference samples by neutron-induced prompt γ -ray analysis", J. Radioanal Nucl. Chem., 239, 571 (1999).

Nuclear and Radiochemical Applications of Neutron Absorption
 Reactions at the Neutron Beam Guides of JRR-3M (II):
 Developement of the Precise Measurement Method for Energy
 of Neutron Capture Prompt Gamma-Ray - Photpeak profile
 3-3 中性子ビームガイドを用いた中性子吸収反応の核・放射化学への応用 (II) :
 即発ガンマ線エネルギー精密測定法の開発-光電ピーク形状

KISHIKAWA, Toshiaki and UEMURA, Jitsuya,
 Kumamoto University Faculty of Engineering
 YONEZAWA, Chushiro

JAERI

熊本大学工学部 岸川俊明, 上村実也
 原研物質科学研究部 米沢仲四郎

Abstract

This paper describes effect of base profile for precise measurement of photon energy in prompt gamma-ray analysis (PGA). The base profile has been examined in the vicinity of full energy (FE), single escape and double escape peaks. Major origins of step-wise base profiles are single and double escape events for triple photon annihilation and single and double Compton escape events for double photon annihilation in the detector in addition to general events for the FE peak. A formula has been proposed for the quantitative characterization of the base profile.

1. Introduction

Deviation of photon energy values between data obtained by photon spectrometry, i.e., the prompt-gamma ray analysis (PGA) and the decay gamma-ray analysis with Ge or Ge(Li) detectors, and those obtained by crystal diffraction spectrometry, has led that the "conventional" method of energy calibration for the photon spectrometry is not adequate to the precise energy assignment. A "new" method has solved this problem by introducing the concept of an instrument function, which is the transfer function between an input signal-shape function, as summarized in ref. 1.

General relationship of the input signal-shape function $E(E,x)$, the instrument function $I(x)$ and the output (measured) signal-shape function $M(E,x)$ can be described as follows based on convolution nature of these functions:

$$M(E,x) = \int I(x) H(E,x-u) du = I(x) * H(E,x) \quad (1)$$

where x is the channel number appeared in the spectrometer and the symbol $*$ indicates the convolution integral. Equation (1) implies that if the input signal-shape function is the delta function, then the output (measured) signal-shape indicates the same shape as the instrument functional shape. If the input signal-shape function is, on the other hand, the step function, then the output (measured) signal-shape shows the sigmoid shape. Detailed description of the instrument function can be seen elsewhere [1].

The instrument function is different from the normal distribution (ND) due to distortion caused by the random losses of charge carriers in a Ge detector. The instrument function is a probability density distribution function in which the ND function is convoluted by the random escape probability density distribution (REPDED). The ND folded in the instrument function never appears in the spectrum, though it is the key function in the peak shape analysis. General

prospects of the instrument function are as follows: (1) precise measurement of incident photon energy, because of the centroid of ND being the energy reflecting parameter, and (2) precise measurement of photopeak intensity, because of an integration of the instrument function multiplied by the frequency (i.e., the count rate) giving the intensity of photopeak.

For these prospects, however, it is indispensable to examine the feasibility of base profile subtraction from overall photopeak profile. Commonly used, pre-base profile subtraction methods for spectral analysis are insufficient for the precise measurement of both the photon energy and intensity. The general profile of a measured, full energy (FE) photopeak is an overall function of the individual input-signal shape functions convoluted with the instrument function:

$$\begin{aligned} (\text{FE peak profile}) &= (\text{Fe peak shape}) \\ &+ (\text{base profile}) \\ &= (\text{FE peak shape}) \\ &+ (\text{SAS} + \text{LE} + \text{RS} + \text{CO shapes}) \end{aligned}$$

where SAS is the small angle scattering, LE is the edge loss, RS is the random summing and CO is the continuum (which is the shape due to photons coming from sources and Compton events produced by the more energetic photons). Schematic diagram of the FE peak profile is shown in Reference 3. By the method of pre-base subtraction, definite quantity of the base components is remained in the subtracted photopeak shape which cause one of origins of the deviation of the precise energy, as well as the uncertainty of precise photopeak counts. Therefore, non-base subtraction method [3] for the spectral analysis is the promising way of parameter estimation to obtain the centroid of ND. The key signal shapes are those of the single escape (SE) peak and the double escape (DE) peak, besides the FE peak shape, for the precise energy measurement by the PGA with photon energy higher than 1.02 MeV, because the energy difference of both the FE and SE and the SE and DE are 0.511 MeV and that of the FE and DE is 1.02 MeV.

However, the profiles of the SE and the DE are both completely different from that of the FE, as shown in Fig. 1. While the base profile of the FE indicates a step-down profile, that of the SE seems to show no step-wise profile and that of the DE, a step-up profile. The goal of the peak shape analysis (with prompt as well as decay and transition photons) [1] is, essentially, to estimate the parameters of the instrument function. This paper aims at describing interaction events in the Ge detector, formulating the relative energy spectrum functions of the base components in the vicinity of both the SE and the DE for either- analytical shape parameter estimation or Monte Carlo simulation of the spectral response.

2. Theoretical

2.1. Gamma-ray interactions in the detector

Here, we consider higher energy photon with energy $E > 1.022$ MeV. Major processes in the detector are the photoelectric absorption process, the Compton scattering process and the pair production process.

The input signal function for the full energy photopeak has the delta functional distribution function which is resulted from the following three processes: (1) the direct photoelectric absorption, (2) the photoelectric absorption of Compton scattered photon with diffused Compton electron in the detector, and (3) the photoelectric absorption of annihilation photons generated from pair creation partner of a positron with diffused, counter pair of an electron.

The input signal function for the Compton electron can be given by the probability density distribution function with E_c being the Compton electron energy. The differential cross section of Compton scattering is given by the Klein-Nishina equation.

The pair production occurs in the detector, if E is higher than twice of the electron rest mass energy ($= 1.022$ MeV).

2.2 Interaction of positron in a medium

When an energetic positron (create by the pair production) transmits in an appropriate medium, then it loses its kinetic energy by successive collisions with orbital electrons. Finally the positron forms a positron-electron pair. Then it undergoes either the double-photon annihilation (DPA) or the triple-photon annihilation (TPA). If the positron-electron pair forms a positronium, the DPA or the TPA is allowed according to the state being singlet or triplet. Ore and Powell [2] derived the energy spectrum function of the TPA based on the QED (quantum electrodynamics) theory with E_{3A} being the TPA photon energy.

The TPA relative energy spectrum is a continuously rising distribution in the energy range from zero to E_e ($E_e = 0.511$ MeV), because of the multiple character of the three-photon process.

2.3. Escape events of annihilation photon(s) from the detector

In the case of DPA the single escape peak (SE/2A) and the double escape peak (DE/2A) appears at energy of respectively, $E_{SE/2A} = E - E_{2A}$ and $E_{DE/2A} = E - 2E_{2A}$. Both the relative energy spectrum functions of SE/2A and DE/2A processes, i.e., $P_{SE/2A}(E_{SE/2A})$ and $P_{DE/2A}(E_{DE/2A})$, respectively, are in the form of delta function, because both the incident photon and annihilation photon are monoenergetic.

In the escape event with the TPA process, on the other hand, there are three types of escape processes: the single escape with energy $E_{1/3A}$, the double escape with energy $E_{3A,1} + E_{3A,2}$ and the triple escape with energy $E_{3A,1} + E_{3A,2} + E_{3A,3} = E_{TE/3A} = 2E_e$ where suffixes 3A,1, 3A,2 and 3A,3 are the first, the second and the third TPA photons, respectively. Figure 2 shows schematic diagrams of relevant photon interactions with the TPA in the detector. The relative energy spectra for the TPA escape processes are rather complicated as follows:

(1) Relative energy spectrum function of single escape for the TPA process (SE/3A):

In the case of single photon escape as a result of event coming after positron-electron pair creation, the two TPA photons undergo the photoelectric absorption. The photoelectrons marked 3A,2 and 3A,3 in Fig. 2(A) generates charge carriers in the detector to give the input signal function. As three body nature of TPA process, the absorbed photon energy has continuous energy spectrum with the detected energy:

$$\begin{aligned} E_{\text{detec}} &= E - 2E_e + E_{D/3A} \\ &= E - 2E_e + E_{3A,2} + E_{3A,3} \end{aligned} \quad (3)$$

where $E_{D/3A}$ is the sum energy of the second (3A,2) and third (3A,3) TPA photons.

According to the well known probability theory, on the other hand, if two probability variables have linear combination and two probability density distribution functions with those of the variables independent each other, then the overall function of these two functions can be obtained by the convolution integration of these functions. Therefore we obtain the relative energy spectrum function of single escape for the TPA, $P_{SE/3A}(E_{\text{detec}})$:

$$P_{SE/3A}(E_{\text{detec}}) = P_{3A,2}(E_{3A,2}) * P_{3A,3}(E_{3A,3}) \quad (4)$$

(2) Relative energy spectrum function of double escape for the TPA process (DE/3A):

Contrary to the case (1) in the previous paragraph, the double escape for the TPA process undergoes photoelectric absorption with the single TPA photon. Therefore, the shape of relative energy spectrum function is identical with that TPA probability density function:

$$\begin{aligned} P_{DE/3A}(E_{\text{detec}}) &\approx P_{S/3A}(E_{S/3A}) \\ &\approx P_{3A}(E_{3A}) \end{aligned} \quad (5)$$

with $E_{\text{detec}} = E - 2E_e + E_{3A}$, where $E_{S/3A}$ is the energy of absorbed TPA photon in the detector.

(3) Relative energy spectrum function of triple escape

for the TPA process (DE/3A):

Since the sum energy of the triple escape photons for the TPA is the same quantity as that of the double escape photons for the DPA, the observed energy is:

$$E_{\text{detec}} = E - E_{TE/3A} = E - 2E_e \quad (6)$$

and, therefore, the shape of relative energy spectrum function, $P_{TE/3A}(E_{\text{detec}})$ is identical with that of double escape signal of the DPA.

Figure 3 shows the relative energy spectrum functions of single, double and triple escape for the TPA process.

2.4. Compton escape events with double photon annihilation in the detector

Since the Compton scattering happens for the annihilation radiation as a result of interaction of annihilation photon with the detector material, escape events of the scattered annihilation photon takes place in the detector. In the DPA process there are three types of escape events concerning the Compton scattering.

- (1) Relative energy spectrum function of single Compton escape and single annihilation absorption with the DPA (SCE/SA/2A):

In this process a Compton scattered DPA photon escapes from the detector while the counter part of DPA photon undergoes the photoelectric absorption. So we obtain the relative energy spectrum function:

$$P_{SCE/SA/2A}(E_{\text{detec}}) \text{ with } E_{\text{detec}} = E + E_e + E_c.$$

- (2) Relative energy spectrum function (if single Compton escape and single annihilation escape with the DPA (SCE/SE/2A):

In this process a Compton scattered DPA photon escapes from the detector while the counter part of DPA photon also escapes from the detector. So we obtain the relative energy spectrum function $P_{SCE/SE/2A}(E_{\text{detec}})$ with $E_{\text{detec}} = E + 2E_e + E_c$.

- (3) Relative energy spectrum function of double

Compton escape with the DPA (DCE/2A):

In this process, a similar probability relation to the former section (1) can be established, since these two Compton processes are independent each other. Therefore we obtain the folded relative energy spectrum function as:

$$P_{DCE/2A}(E_{\text{detec}}) = P_{C,1}(E_{CZA,1}) * P_{C,2}(E_{CZA,2}) \quad (7)$$

with $E_{\text{detec}} = E - 2E_e + E_{CZA,1} + E_{CZA,2}$.

- (4) Compton escape with the TPA photons:

Similarly the Compton escape with the TPA photons happen with the TPA photon. The relative energy spectrum of both single and double Compton escape with the TPA are complicated, because the relative energy spectrum of single and double escape for the TPA processes, respectively, $P_{SE/3A}(E_{\text{detec}})$ and $P_{DE/3A}(E_{\text{detec}})$, have continuous spectrum. We omit to consider these events, here. Figures 4 and 5 shows, respectively, the interactions events of γ -rays and the relative energy spectrum function with these processes SCE/SA/2A, SCE/SE/2A and DCE/2A in the detector.

3. Experimental

PGA measurements were performed at the JRR-3M thermal (port T1-4-1) and cold (port C2-3-2) neutron beam guides in Tokai Establishment, JAERI. The PGA system

consist of a closed-end high purity (HP) germanium detector (HPGe) surrounded by bismuth-germanium oxide (BGO) scintillation crystals and a multi mode-operation spectrometer. A precision pulser, BNC PB-4 was used for non-proportionality correction.

4. Results and discussion

General input signal function, $H(E_{\text{detec}})$, of the corresponding relative energy spectrum function, $P(\text{detec})$, described in the previous subsections can be given by introducing frequency term n to the relative energy spectrum function:

$$H(E_{\text{detec}}) = n P(E_{\text{detec}}) \quad (8)$$

Overall input signal function for the detection events described in the former sections (3) and (4) are the summation of all the individual input signal functions:

$$\begin{aligned} H_{\text{sum}}(E_{\text{detec}}) = & n_{\text{FE}} P_{\text{FE}}(E_{\text{detec}}) + n_{\text{DE}} P_{\text{SE}}(E_{\text{detec}}) \\ & + n_{\text{DE}} P_{\text{DE}}(E_{\text{detec}}) + n_{\text{SCE/SA/ZA}} P_{\text{SCE/SA/ZA}}(E_{\text{detec}}) \\ & + n_{\text{SCE/SE/ZA}} P_{\text{SCE/SE/ZA}}(E_{\text{detec}}) \\ & + n_{\text{SE/3A}} P_{\text{SE/3A}}(E_{\text{detec}}) + n_{\text{DE/3A}} P_{\text{DE/3A}}(E_{\text{detec}}) \\ & + n_{\text{TE/3A}} P_{\text{TE/3A}}(E_{\text{detec}}) \end{aligned} \quad (9)$$

where n 's are the frequency term (i.e., the count rate) or individual processes. Ore and Powell [2] derived the cross section ratio of the DPA to TPA being $s\text{DPA}/s\text{TPA}=1/370$ for free positron-electrons annihilation. However, if the annihilation undergoes via positronium formation, then the fraction of TPA depends on physicochemical nature of the material (i.e., Ge of the HPGe detector in operation). Therefore the n 's should be treated as estimation variables when the output peaks for FE, SE and DE are subjected for the parameter estimation. Typical example of a heaping up pattern of the overall input signal function with appropriate n 's values ($n = 1$ for every n) for the single mode operation of the Ge/BGO detectors is shown in Fig. 6. All of the FE, SE and DE peaks accompany the SAS, the LE, the RS and the CO shapes in their vicinity as quoted in the introducing section. Therefore we have to add up these terms for the practical cases. Even if we take these shapes into account, the partial spectrum of input signal functions remarkably demonstrates the step-wise base profiles around the FE and DE peak regions, and the non-step wise base profile around the SE peak region. According to the instrument function, the distortion of ND is caused by the trapping event of charge carriers forming the REPDED. That is, the position reflecting energy is not the position of peak maximum, namely, the peak position x [channel, but the centroid x_c Of the ND. If the peak position of energy E (keV), the $x_p(E)$ is proportional \sim energy then the quantity $x_p(E) c_w/E$ must be unity [i.e. = 1, with c_w being the channel width in units of (keV/channel)]. If the peak position, on the

other hand, is not the energy reflecting position, then the quantity would be $x_p(E) c_w/E = 1 + \delta_{\text{peak}}(E)$ where $\delta_{\text{peak}}(E) (\neq 0)$ is the deviation indicating term (which is [to be the peak index). The variation of the peak position with energy has been remarkably demonstrated by the $^{56}\text{Fe}(n, \gamma)$ prompt photons. Therefore, the energy differences of $E_{\text{SE}} - E_{\text{FE}}$, $E_{\text{DE}} - E_{\text{SE}}$ or $E_{\text{DE}} - E_{\text{FE}}$ should be, adjusted for the centroid of ND convoluted in the instrument function. The energy differences of annihilation photons are, essentially, the self containing, intrinsic measure of energy in every samples. For this reason, the formulation of base profile provides strong tool for the de-convolution of Eq. (1) in the measurement of photon energy.

5. Conclusion

This work clearly demonstrates the importance of formulating input base-shape signal functions in the vicinity of full-energy, single-escape and double-escape peaks, particularly when they are subjected for the precise energy analysis. The result of this study demonstrate that major origins of the base profiles are (1) the escape of photons for the triple photon annihilation, (2) the escape of Compton scattered photons for the double photon annihilation and (3) the escape of Compton scattered photons for the triple photon annihilation.

References

- [1] T. Kishikawa, K. Nishimura, S. Noguchi, Nucl. Instrum. Meth. A353 (1994) 285.
- [2] A. Ore, J.L. Powell, Phys. Rev., 75 (1949) 1696.

Publications

- [1] T. Kishikawa, S. Noguchi, C. Yonezawa, H. Matsue, A. Nakamura, H. Sawahata "Photopeak profile of full energy and escape peaks in neutron capture prompt-gamma ray spectra", J. Radioanal. Nucl. Chemistry,

215 (1997) 211-217.

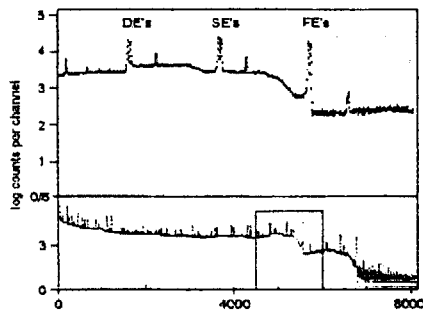


Fig. 1. Typical example of neutron capture gamma-ray spectra obtained by activation of natural iron plate at the single mode operation of BGO/Ge spectrometer installed at the JRR-3M neutron beam guide hall. Doublet peaks of 7631- and 7645-keV Fe capture gamma-rays are shown; FE: full energy peak, SE: single escape peak, DE: double escape peak

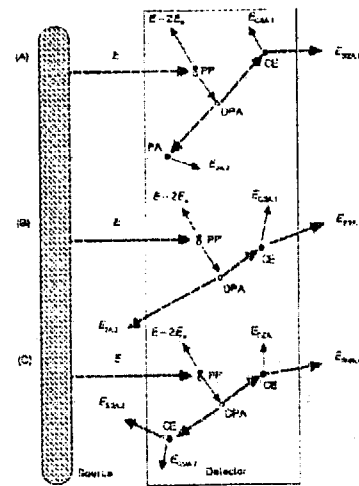


Fig. 4. Escape of photons after the double photon annihilation (DPA) in the Ge detector, (A) single Compton escape - single photoelectric absorption of DPA, (B) single Compton effect - singles escape of DPA, (C) double Compton escape of DPA, PP: pair production, PA: photoelectric absorption

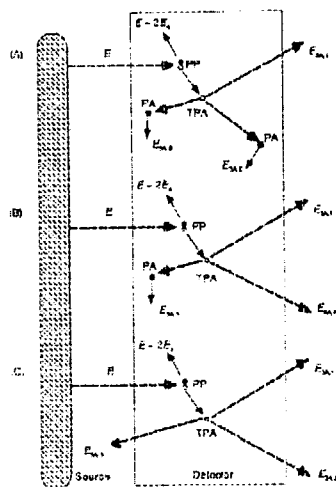


Fig. 2. Escape of photons after the triple photon annihilation (TPA) in the Ge detector. (A) single photon escape of TPA, (B) double photon escape of TPA, (C) triple photon escape of TPA, PP: pair production, PA: photoelectric absorption

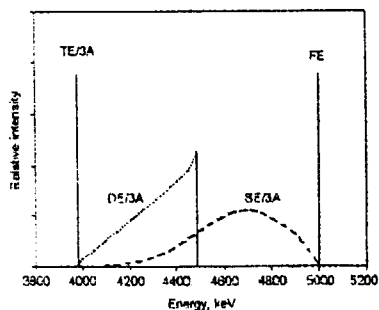


Fig. 3. Energy spectra of triple photon annihilation (TPA) in a Ge detector. TE/3A: triple escape of TPA. FE: full energy peak of photon energy 5000 keV, DE/3A: double escape of TPA, SE/3A: single escape of TPA

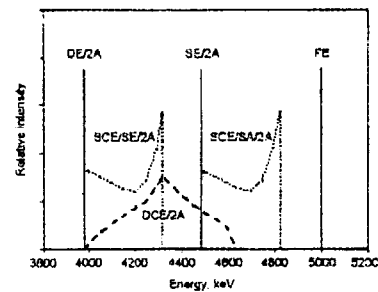


Fig. 5. Energy spectra of double photon annihilation (DPA) in a Ge detector, DE/2A: double escape of DPA, SE/2A: single escape of DPA, FE: full energy peak of photon energy 5000 keV, SCE/SE/2A: single Compton escape with single escape of DPA, SCE/SA/2A: single Compton escape with single absorption of DPA, DCE/2A: double Compton escape of DPA

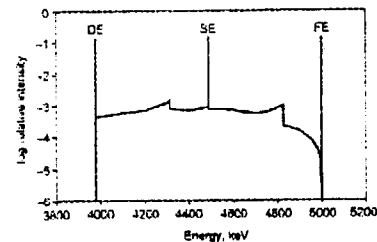


Fig. 6. Calculated overall input signal function with appropriate k's-values ($= 1$ for every k) of the BGO/Ge spectrometer at the single mode operation. Accompanying SAS, LE, RS and CO for the FE, SE and DE peaks, together with the Compton spectrum of FE are not considered (see text). The photon energy is 5000 keV

4. 放射化分析

4. Neutron Activation Analysis

This is a blank page.

研究テーマ：ラジオアイソトープ技術者の養成

表 題：実習 放射化分析

4-1 貝殻中の銅・ナトリウムの放射化分析

上 沖 寛

国際原子力総合技術センター（東京研修センター）

本研究は、RI技術者の養成を目的とする研修コースの中で実習教科として行うものである。本報告では、平成10年度の研究炉をもちいた成果として、国内原子力技術および放射線利用に関係する人材養成を行った基礎課程、およびアジア・太平洋地域開発途上国の原子力分野人材養成への国際援助としてJICAと協力して行った原子力基礎技術コースにおいての実習教科としての放射化分析について報告する。

原子力の基礎として中性子核反応の理論や応用を理解させることは重要である。放射化分析の実際を経験させることはこれらの知識の理解を深めるのに大変重要であり、結果としてガンマ線スペクトル解析による放射能測定法および非密封RIの安全取扱法を習得させることになる。

平成10年度は基礎課程とJICA原子力基礎技術コースの中で5回の放射化分析実習を行った。分析試料は海水産の大アサリであり、炭酸カルシウムをマトリックスにして微量元素を含有する。分析目的核種は、放射化生成核種のガンマ線スペクトルで主成分となるナトリウム24、放射化生成物が

陽電子壊変を伴い陽電子消滅ピークを主要放射線ピークとする銅64である。照射条件は研究炉の気送管で2～5分間照射とし、ナトリウムと銅の標準試料と共に大アサリ貝殻の照射を5回行った。

銅の分析：

銅64の陽電子消滅放射線は、他の放射化生成核種からの高エネルギーガンマ線や宇宙線が物質にもたらす電子対生成による放射線と同一放射線であるから、銅64分析には化学分離を必要とした。簡単な銅の化学分離法として金属亜鉛により銅イオンを還元させて銅の沈殿分離を行った。この化学分離の操作は、30分間の所要時間で0.1 ppm Cu濃度に対して5%の精度で分析された。本実習は、生成核種を同定および定量することにより核反応の理解を深め、RI実験における放射線被曝に対する工夫、除染、サーベイ等の一連の安全取扱いの基礎を習得させるものとして有効であった。本実験による研修生の被曝線量は、線源が 10^5 Bq位に対し最大1 μ Sv程度であった。

原子炉：JRR-3M

装置：気送管 分野：放射化分析（環境）

研究テーマ：農林生態系におけるハロゲン元素の動態

表 題：世界の土壌・植物系におけるハロゲン元素の含量レベルと動態の解明

4-2 ロシア国 東・中央シベリア高緯度地域の土壌

結田康一¹⁾、松浦陽次郎²⁾

1) 農業環境技術研究所

2) 森林総研北海道支所

ハロゲン元素（ヨウ素、臭素、塩素）の環境での易動性は大きく、動植物での欠乏・過剰・汚染問題が生じやすい。

本研究では、これらの元素の高感度・高精度分析法である化学分離操作を伴う放射化分析法を用いて、世界各地の土壌・植物系における含量・分布と動態を明らかにする。その中で特に気候や地形条件、土壌や植物の種類、土地利用・農業活動等人為的作用との関連を解析する。

前年度はタンザニア国キリマンジャロ州と日本国北海道・九州の土壌を対象にしたが、本報では、東・中央シベリア地方の土壌を対象とした。

対象土壌と分析法：北緯 62°～71°の北極域に近い寒冷（平均気温 -9.2℃～-15.0℃）、小雨（年平均降水量 177～317mm）の東・中央シベリア地方の 4 地域（図 1）より、24 地点、180 点（層位）の土壌試料を採取して、放射化分析法でヨウ素、臭素および塩素を分析した。

結果：ヨウ素と臭素の含量は地点差、土壌差、層位間差も大きいがこれまでの最も低い土壌のグループに属し、ヤクーツクのカラマツ林下の E 層ではヨウ素 0.09、臭素 0.34mgkg⁻¹ の低い値を示した。塩素は 4.3mgkg⁻¹ と低い値を示す事例もあったが、

平均的にはやや低いレベルに留まっていた（表 1:ヤクーツク-2）。これは、降水量が少ないことから供給量の少なさや植生の貧弱さによる植物による吸収・集積効果の小ささ、凍結効果による融解期の溶脱などが原因と考えられる。ヨウ素、臭素、塩素の極低濃度の溶脱層が存在する場合、永久凍土層のやや上部にかなり高濃度の層が存在し、夏期融解水による溶脱が示唆された（ヤクーツク-1,2）。2) 地形的に降水量以上の水が集まる又は通過する地点・地層（傾面下部、くぼ地、池近くなど水浸透による供給がある地点）では、3 ハロゲン元素とも高レベルになる傾向を示した。蒸発量が降水量を上回る気候条件下にあり池の縁より 9m の湿地帯（ヤクーツク-3）では、表層の A または O 層に、ヨウ素 22、臭素 112、塩素 1556mgkg⁻¹ と世界の平均的レベルを遙かに越える高濃度を示した。3) 地表面上の有機物層や有機質土壌（Histosol）では 3 ハロゲン元素とも高い（特に塩素）傾向を示し（コリマ低地-2 他）、植物による吸収・集積効果が示された。

参考文献

1) 日本土壌肥料学会（北海道大会）で発表予定, 1999.7.30

原子炉：JRR-3M 装置：気送管 分野：放射化分析（環境、農・水産物）

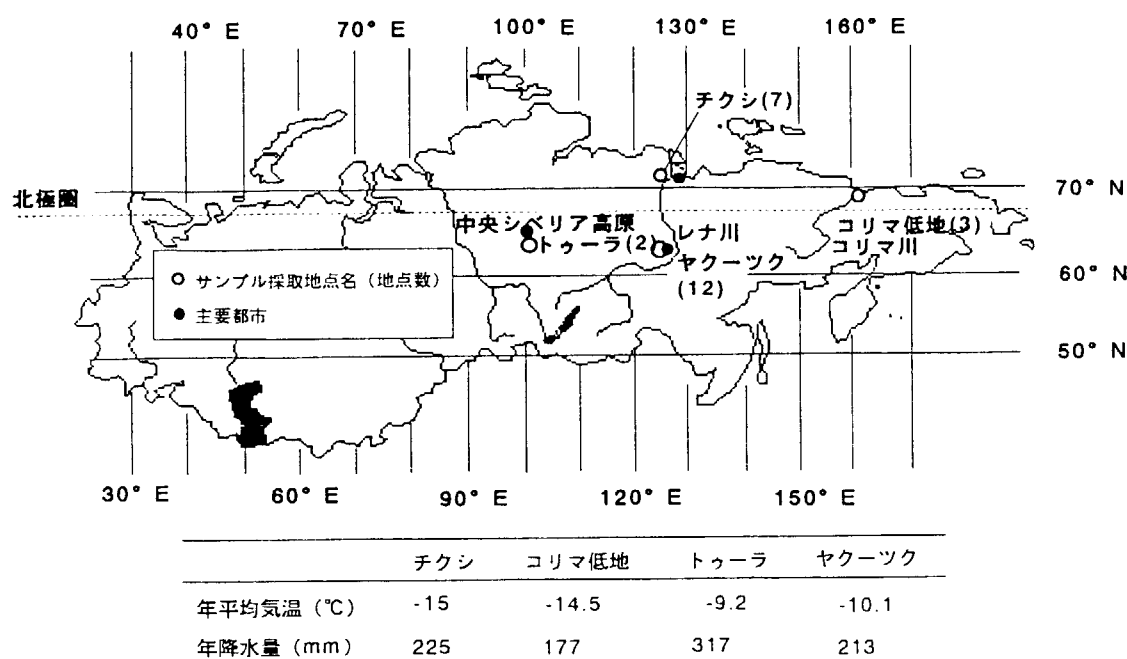


図1 東・中央シベリア高緯度地域の土壌採取地点

表1 土壌層位別ヨウ素、臭素および塩素含量 (代表事例)

ハロゲン元素 mgkg ⁻¹							ハロゲン元素 mgkg ⁻¹						
地点	層位	深度 (cm)	土性	ヨウ素	臭素	塩素	地点	層位	深度 (cm)	土性	ヨウ素	臭素	塩素
ヤクーツク (62°) -1	O	4 ~ 0		1.1	7.7	118	トゥーラ (64°)	O	3 ~ 0		0.78	3.1	59
(レナ川中流域)	A	0 ~ 6	S	0.73	1.2	13	(中央シベリア高原)	A	0 ~ 7	L	1.2	2.4	50
[スバスカヤバイト実験林: カラマツ林]	B	6 ~ 64	S	0.38	1.1	3.4	{トゥーラ実験林: カラマツ林}	AB	7 ~ 23	L	0.91	2.2	48
傾面 (5°) 中央部	Bh ₁	64 ~ 96	SL	4.1	6.6	15.6	緩やかな傾斜地の上部	B	23 ~ 77	CL	0.83	2.8	58
<Gelic Cambisol>	Bh ₂	96 ~ 110	SCL	1.5	40.1	23.7	<Gelic Cambisol>		(77cm以下永久凍土層)				
(110cm以下永久凍土層)													
ヤクーツク (62°) -2	O	8 ~ 0		0.95	12.3	109	コリマ低地 (68°) -1	O	3 ~ 0		1.8	6.4	106
(レナ川中流域)	A	0 ~ 4	LS	0.45	1.6	11	(コリマ川下流域)	AB	0 ~ 5	CL	1.5	4.2	47
[スバスカヤバイト実験林: カラマツ林]	E ⁺	4 ~ 52	S	0.09	0.34	4.7	森林 (森林ツンドラ)	Bg	5 ~ 32	CL	0.91	1.5	30
平原 (緩やかな傾斜地下部)	Bh ₁	52 ~ 91	LS	1.6	7.1	12	緩やかな傾斜地の上部	Bl	32 ~	CL	1.0	2.8	38
<Gelic Cambisol>	Bw	91 ~ 100	SL	7.9	20	27	<Gelic Gleysol>		(永久凍土層)				
(115cm以下永久凍土層)	Bh ₂	100 ~ 115	SL	0.63	2.0	13							
ヤクーツク (62°) -3	O	2 ~ 0		4.7	80	1556	コリマ低地 (68°) -2	O	2 ~ 0		3.6	11	231
(レナ川中流域)	A	0 ~ 23	L	22	112	192	(コリマ川下流域)	H ₁	0 ~ 10	未分解	5.3	18	295
[アラス試験地: 草地 (沼地帯)]	AB	23 ~ 41	L	20	74	61	森林 (森林ツンドラ)	H ₂₋₃	10 ~ 33	有機物層	13	23	255
池の縁より9m, 沼地帯	Bh	41 ~ 60	CL	16	59	73	緩やかな傾斜地の中央部	H ₄	33 ~		15	19	200
<Gelic Cambisol>	BH(g)	60 ~ 72	L	7.7	25	68	<Gelic Histosol>		(永久凍土層)				
or	Bw	72 ~ 80	SdL	1.4	7.0	34							
<Gelic Solonchets>	Bl	80 ~	C	2.2	7.0	71	チクシ (71°)	O	4 ~ 0		1.0	7.1	120
(永久凍土層)							(レナ川下流域)	A	0 ~ 5	CL	1.1	6.9	49
							ツンドラ	AB	5 ~ 21	CL	1.0	4.5	24
							平坦面	B	21 ~ 41	L	0.76	1.5	18
							<Gelic Regosol>	Bl	41 ~	CL	0.59	1.5	18
							(永久凍土層)						

*溶脱層 FAO (1997) Guideline for Soil Profile description (2nd ed.)

* 溶脱層 FAO (1997) Guideline for Soil Profile description (2nd ed.)

原子炉: JRR-3M

装置: 気送管

分野: 放射化分析 (環境、農・水産物)

研究テーマ：新アクチバブルトレーサーをマーカーとした家畜消化管内容物移動の解析手法の開発
表題：サマリウム、ランタン等をマーカーとした家畜消化管内容物移動の解析

4-3 サマリウム、ランタン等をマーカーとした家畜消化管内容物移動の解析

松本光人, 宮本進, 山岸規昭

農林水産省畜産試験場

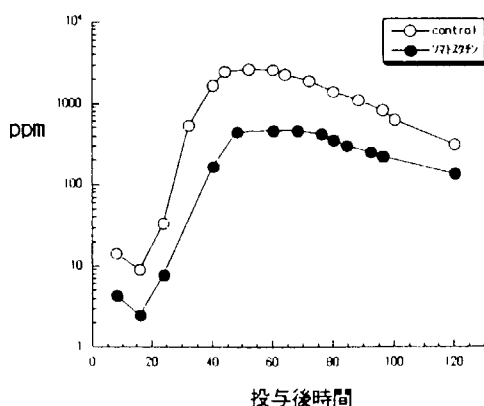
1. 目的

家畜の飼養管理の集約化・技術の高度化にともなって、多くの解決すべき問題が研究ニーズとして提起されているが、特に乳牛の糖質代謝が泌乳初期の生産性を高める意味で注目されている。さらに、分娩のストレスにより、泌乳初期では第一胃をはじめとする消化管の機能の回復が十分ではなく、採食性の低下などが生じ、生産性を圧迫している。そのため、摂取された飼料の消化管内での移動を定量的に把握すること、及びその基礎となる標識物質（マーカー）の探索が重要な課題になってくる。本課題では、消化管内の物質移動を知るためのマーカーとして、種々の新しいアクチバブルトレーサーの利用を図り、家畜の第一胃発酵、糖質および微量元素の代謝機構を解明する。

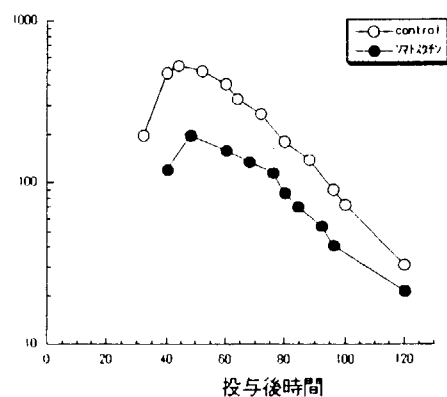
平成10年度は、標識物質（マーカー）としてサマリウム（Sm）、ランタン（La）を用い、山羊（去勢雄、体重45Kg）における飼料の消化管内移動について検討した。

2. 試験研究の概要

日本ザーネン種山羊4頭にSmで標識した牧乾草、Laで標識した濃厚飼料（各400g/日/頭）を給与し、ソマトスタチン（成長ホルモン放出抑制因子）を連続注入し消化管運動に及ぼす影響をみる試験を行った（ソマトスタチン注入区：ソマトスタチン、対照区：control）。試験期間中に得られた糞試料を原研東海研究所の原子炉（JRR-3M）を用いて、熱中性子照射を行った。照射時間は3分間とし、ゲルマニウム半導体検出器およびマルチチャンネル波高分析機によりSm、Laの測定を行った。Sm、La標識飼料を給与した山羊から得られた糞中のSm、La濃度の放射化分析による結果（一部）を第1図、第2図に示した。ソマトスタチン（成長ホルモン放出抑制因子）が家畜の消化管運動に及ぼす影響については、試料中のSm、Laの分析がほぼ終了したので、データ解析終了後、検討する。



第1図 牧乾草に標識したSmの
山羊糞中の濃度（山羊No. 4）



第2図 濃厚飼料に標識したLaの
山羊糞中の濃度（山羊No. 4）

原子炉：JRR-3M 装置：気送管 分野：放射化分析（農・水産物）

研究テーマ：伊豆小笠原弧背弧域における火成活動および熱水活動に関する研究

表題：伊豆小笠原弧背弧地域における深成岩と斑岩銅鉱床型熱水活動

4-4 伊豆小笠原弧背弧地域における深成岩と斑岩銅鉱床型熱水活動

— 海洋性島弧におけるトーナライトと斑岩銅鉱床 —

石塚 治・湯浅 真人・宇都浩三・石井輝秋¹・A.G. Hochstaedter²

地質調査所 つくば市東 1-1-3

¹ 東京大学海洋研究所

² Monterey Peninsula College

伊豆小笠原弧背弧域の海山の一つである万治海山では、この地域では唯一トーナライト質の深成岩及びそれに伴って斑岩銅鉱床型の熱水活動が存在していたことを示す熱水変質岩が確認されている。ここでは、深成岩類を含む火成岩類及び斑岩銅鉱床型熱水活動の特徴を報告し、それらの成因の関連等を検討する。

伊豆小笠原弧は、その地形的特徴に基づき、東から火山フロント地域、活動的背弧リフト盆地、背弧海丘帯、背弧海山列の4つの地域に区分できる。このうち背弧海山列では、四国海盆拡大終了直前の約17 Ma ごろから火成活動が始まり、約3 Maに背弧海丘帯でリフティングが開始するまで継続していたことが明らかになっている。背弧海山列の火山岩は、おもに安山岩が主体で、これに玄武岩及びデイサイトが伴う。背弧海山列の玄武岩質溶岩は、火山フロントの溶岩に比べて液相濃集元素に富み、E-MORB に似た Nb/Zr 比を示す。

万治海山は、底経東西約10km、南北約7.5km、比高約1200mの背弧海山列上の海山で火山フロントの西約100kmに位置する。山頂の水深は約700mで、直径約2kmの平坦面からなり、東斜面からは円礫を含む礫岩も採取されていることから、かつて海面上で侵食されたと考えられる。この海山では、トーナライトポーフリー、トーナライト、ガプロといった深成岩類及び安山岩～流紋岩を主体とする溶岩が採取されている。溶岩の化学的特徴は他の背弧海山列上の海山の溶岩と類似しており、火山フロントの石に比べてアルカリや他の液相濃集元素に富んでいる。一方トーナライト質深成岩は、主に石英、斜長石、角閃石からなり、カリ長石や黒雲母を含まない。カリウムに乏しいトーナライトの化学組成を持ち、フィリピン海プレート上の島弧由来と考えられる他地域のカコウ岩質深成岩類と類似している。一方微量元素組成のMORB規格化パターンは、一部変質による影響を除けば、当海山の溶岩のものに近い。深成岩類の

成因として、1) この海山での安山岩～流紋岩質溶岩を噴出した火成活動により生成された、すなわち固結したマグマだまりが露出したもの、2) 伊豆小笠原弧の中部地殻にその存在の可能性が指摘されているトーナライト、すなわち島弧の地殻構成物質として深部に存在する岩体が、構造運動等により上昇露出したもの、3) 古島弧が四国海盆拡大以前に侵食を受けて深成岩類が露出、侵食されて形成された礫岩層が露出している、といった可能性が考えられる。レーザ加熱⁴⁰Ar/³⁹Ar年代測定の結果、溶岩について7.7-6.3 Ma、深成岩について7.0-6.3 Maの年代値が得られ、深成岩及び溶岩の活動はほぼ同時期であり、一連の火成活動の産物であることが明らかになった。従って成因は1) であると考えられる。

一方万治海山において採取された熱水変質岩は、以下の特徴において斑岩銅鉱床における変質岩と極めて類似している。1) 変質鉱物の組合せが、斑岩銅鉱床におけるカリ変質帯及びプロビライト化変質帯の岩石に相当する。2) 石英-磁鉄鉱脈のストックワークの存在。3) 銅鉱化作用の存在。4) 高温(約600°C)、高塩濃度(約63%)の熱水をトラップした流体包有物の存在。5) トーナライトポーフリーの存在。他の時期の火成活動が万治海山でおきていた証拠はないので、ポーフリーの形成を含む約7 Maの火成活動に伴って斑岩銅鉱床型熱水活動がおきたと考えられる。斑岩銅鉱床と同様、万治海山でもトーナライト質深成岩の固結に伴って発生した揮発性元素を含む高温の流体、およびマグマからの熱により熱水系が形成されたと考えられる。

万治海山では、火山体深部で形成されたはずのトーナライト質深成岩及び斑岩銅鉱床が同時期の溶岩とはほぼ同位置で採取されている。海洋性島弧でのトーナライト質深成岩の起源及び露出過程、また背弧雁行海山列の成因を明らかにする上で、重要な制約が得られる地域と考えられる。

原子炉：JRR-4 装置：T-パイプ 分野：放射化分析(地球化学)

研究テーマ：核融合炉用低放射化構造材料の開発

表題：SiC 繊維(Hi-Nicalon Type S)の不純物定量分析

4-5 SiC 繊維(Hi-Nicalon Type S)の不純物定量分析

井川直樹、田口富嗣、山田禮司、武田道夫¹

日本原子力研究所・物質科学研究部材料照射解析研究グループ

¹ 日本カーボン株式会社

SiC 繊維強化 SiC 複合材料は、低誘導放射能特性や高温安定性などから、有望な核融合炉用構造材料として注目されている。マトリックス強化用の SiC 繊維材料には、一般に Hi-Nicalon が使用されているが、さらに高温安定性に優れた Hi-Nicalon Type S(Type S)が開発された。本研究では、Type S の製造プロセスに関して、放射化の原因となる不純物の混入過程を解明し、これを基にさらに優れた低放射化材料を実現するため、Type S とその中間工程品中の金属不純物の定量分析を行った。

日本カーボン(株)製、SiC 繊維(Hi-Nicalon Type S)及びその繊維作製時における中間工程品について、核融合炉環境下での放射化に関して特に問題となる金属不純物の定量分析を、原研 JRR-4 において中性子照射した後、 γ 線スペクトル解析法により行った(中性子放射化分析法)。また、得られた放射化分析結果をもとに、IRACM コードを用いて核融合炉環境下における繊維の放射化の評価を行った。

図 1 に放射化分析結果を示す。今回分析を行った主要な金属不純物量は工程を経るに従って、ほぼ単調に増加する傾向を示し、特に各工程における著しい不純物量の増加はみられなかった。この単調な増加傾向は、各工程における有機物等の分解・脱離または繊維の緻密化等を考慮すると、原料であるポリカルボシラン(PCS)中に元々存在していた金属不純物が繊維中に濃縮されていった可能性が高いと考えられる。従って、繊維の高純度化のためには PCS の高純度化を進めることが極めて有効であることが分かった。

この Type S SiC 繊維を核融合炉環境下で使用した場合の、炉停止後の Type S の表面線

量当量率変化の計算結果を図 2 に示す。表面線量当量率は、Na 不純物による影響が特に大きいことが分かり、低放射化 SiC 繊維の開発には、Na の濃度の低減が有効であることが明らかとなった。

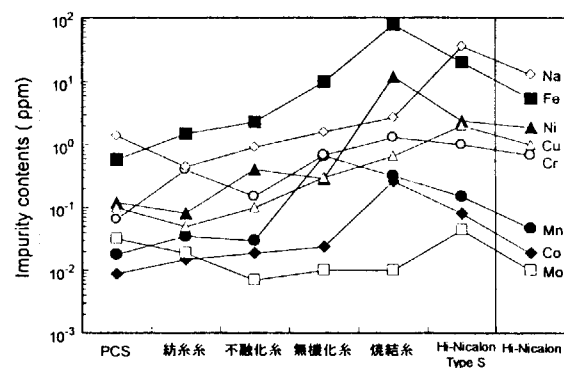


図 1 SiC 繊維(Hi-Nicalon Type S)および中間工程品の主な金属不純物濃度

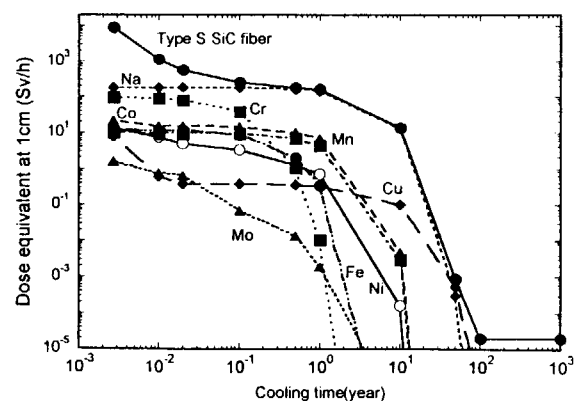


図 2 IRACM によって計算した核融合炉環境下の SiC 繊維(Hi-Nicalon Type S)の表面線量当量率における主な金属不純物の寄与

研究テーマ：多重ガンマ線スペクトルの分析科学への応用

表題：多重ガンマ線測定装置の中性子放射化分析への応用

4-6 多重ガンマ線測定装置の中性子放射化分析への応用

初川雄一、早川岳人¹、篠原伸夫、大島真澄

物質科学研究部原子核科学研究グループ

¹光量子科学センター自由電子レーザー研究グループ

核構造研究において顕著な成果を収めている多重ガンマ線測定装置（クリスタルボール）を分析化学、特に中性子放射化分析法に応用して岩石試料中の微量元素の検出を試みた。一般に地質学的試料の中性子放射化分析では主要成分からの放射線が強く微量成分の検出には化学分離などが必要であるが、クリスタルボールによって得られた2次元スペクトルにより非破壊で微量成分の検出に成功した。

多重ガンマ線測定装置の優れた検出感度は加速器を用いたインビーム実験での原子核構造研究において顕著に発揮されている。インビーム実験では大きな分岐を有するガンマ線の中から極微少なガンマ線に分岐を検出することにより極限状態の原子核に関する情報を得ることが可能となり超変形や高励起状態の研究に活用されている。この検出感度の高さに着目して中性子放射化分析に応用することを試みた。実験は地質調査所から配布¹⁾され微量成分の定量がなされている標準岩石試料JB-1a（玄武岩）とJP-1（かんらん石）を用いて行った。原研原子炉JRR-4気送管で標準岩石試料約100mgを10分間照射した後に多重ガンマ線測定装置GEMINI²⁾を用いてガンマ線測定を行った。多重ガンマ線測定装置GEMINI

Iは12組のBGO結晶によるアンチコンプトンサプレッサーを装備したゲルマニウム検出器から成っており、得られたガンマ線の同時事象は磁気テープ上に記録される。地質学的試料の中性子放射化分析では主要成分であるナトリウムやマンガンから生成される²⁴Na（半減期14.95h）や⁵⁶Mn（半減期2.57h）からのガンマ線が支配的であり微量成分からのガンマ線を測定するためには、これら核種からの影響を減ずるため化学分離を行ったり妨害核種の崩壊を待ってから長半減期の核種の測定を行うわざを得ないが、本研究では照射試料を非破壊で測定して微量成分の検出を試みた。得られたコインシデンススペクトルを図-1に示す。

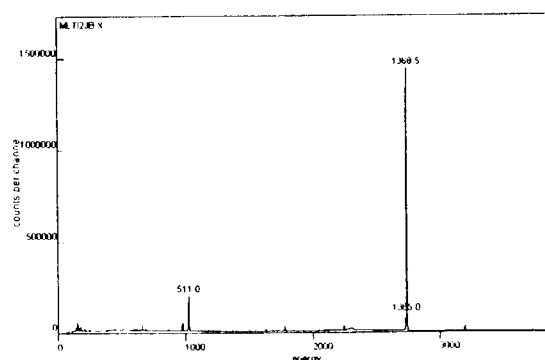


図-1 標準岩石試料JB-1aのガンマ線コ
インシデンススペクトル

原子炉：JRR-4 装置：気送管 分野：放射化分析（その他）

図-1より観測されたガンマ線の中でほとんどは ^{24}Na （半減期14.95h）から発せられた1368keVのガンマ線である事がわかる。この得られた2次元マトリクスから γ - γ のコインシデンスを取り出し解析を行った結果2種類の標準岩石資料JB-1aおよびJP-1試料中に合計27元素を検出することができた。検出された元素はK, Sc, Ca, Fe, Ni, Co, Ga, As, Br, Ba, Cs, La, Ce, Eu, Sm, Gd, Tb, Yb, Lu, Hf, Ta, W, Bi, Th(Pa), U(Np), Na, Mnである。この内UとThは娘核種のNpとPaを経由してそれぞれ観察された事を示す。臭素については

^{82}Br （図-2）を測定することができたが、JB-1aおよびJP-1では今までに臭素の含有量について報告されていなかった。また検出された元素の中ではJP-1中のEuがもっとも微量な成分でありその含有量はわずか4ppbであった。（図-3）

文献

- 1) N. Imai, et al., *Geochemical Journal* **29**, 91(1995).
- 2) K. Furuno, et al., *Nucl. Instr. and Meth. A* **421** 211(1999).

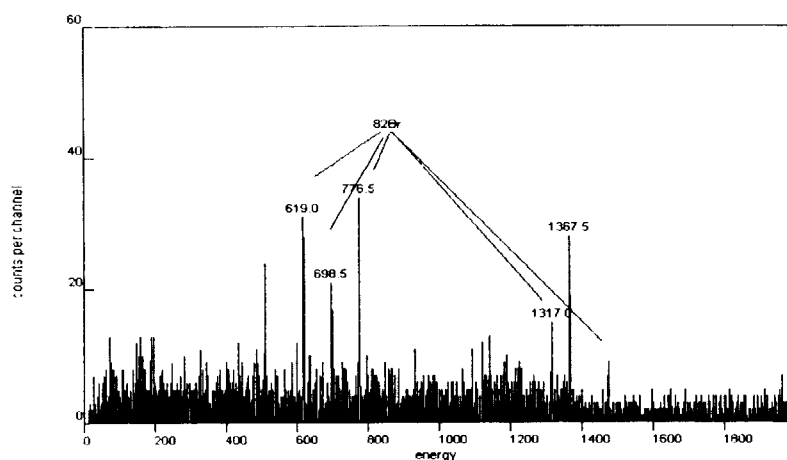


図-2

JB-1a試料の554keVのゲートスペクトル。 ^{82}Br から発せられた1317, 619, 698, 776keVのガンマ線がコインシデンスしている。

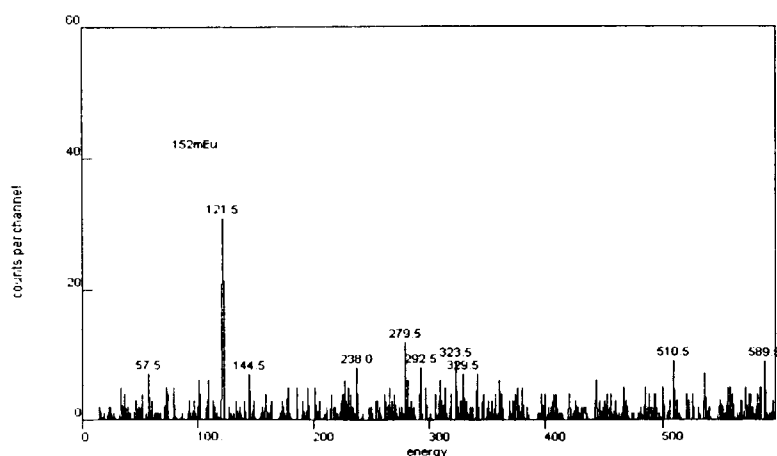


図-3

JP-1試料の842keVのゲートスペクトル。 $^{152\text{m}}\text{Eu}$ から発せられる122keVのガンマ線とコインシデンスしている。JP-1中のEuの含有量はわずか4ppbである。

4-7 植物試料の元素分析

Element Analysis of Plant Sample

中西友子・古川純・片岡達彦

Tomoko M. Nakanishi, Jun Furukawa and Tatsuhiko Kataoka

東京大学大学院農学生命科学研究科

¹日本原子力研究所東海研究所中性子科学研究センター

Graduate School of Agricultural and Life Sciences,

The University of Tokyo

1. 研究目的と意義

本研究では、植物中の元素を放射化分析により求めた。目的としては次の三つが挙げられる。

(1) アルミニウムの定量

世界の耕作可能地の 40% を占める酸性土壌では、植物の生育は可溶化したアルミニウムにより著しく阻害されることが知られているが、まだそのメカニズムはよく判っていない。そこで、我々は、高感度で植物中のアルミニウムを検出できるルモガリオン染色法を開発した。その染色法の感度ならびに染色方法の開発においてアルミニウムの定量が必要であったため、放射化分析を行った。なお、放射化分析は立教炉を用いても可能であるが、P から生成される ^{28}Al の量をできる限り抑えるため、Cd 比が 400 である、JRR-3M の気送管を用いた。

(2) 植物による元素のリサイクルシステムの解明

植物-土壌系において元素はリサイクルされ植物に利用されている。環境インパクトを知るためには、どのように元素がリサイクルされているかを知る必要がある。我々は、まず、アサガオを用い、次にダイズを用いて、発根から枯れるまでの植物のライフサイクル

における元素量を全ての組織で調べ、植物の活動モデルを構築することを試みた。膨大な植物試料を分析しなければならないため、まだ、実験は途中であるが今までに得られた結果を報告する。放射化分析は、短時間放射化分析は Al の定量が可能な日本原子力研究所で行い、長時間放射化については立教炉を用いた。

(3) ブラジル東北部の半乾燥地における土壌および植物中の元素分析

ブラジル東北部の半乾燥地を殆ど占めて生育しているカーチンガ樹種ならびにその生育土壌をサンプリングしたので、これらの試料中の元素分析を放射化分析により求め、土壌ならびに樹木の性質、樹種の有効利用などについての考察を行った。

2. 方法

(1) ルモガリオン染色法の開発

アルミニウム処理を施したダイズ幼植物の根を切り取り、固定後、スライサーにて 100 ミクロンの厚さに切りとり、ルモガリオンにて染色を行った。洗浄液、固定液、染色後のルモガリオン溶液および根中のアルミニウム濃度を放射化分析により求めた。試料は日本原子力研究所 JRR-3M 気送管 (PN3) にて 5

秒間照射し、 γ 線スペクトロメトリーによりアルミニウムの定量を行った。

(2) 植物による元素のリサイクルシステムの解明

植物組織中の元素動態は、N、P、Kを除いてまだ殆ど知られていない。植物は土壌から栄養を吸収し、枯れると微生物の分解によりまた次の世代の栄養となる。ダイナミックな元素循環系を解明するために、植物の全ての生育ステージにおいて、全ての組織中の元素量を放射化分析により求めた。植物試料は、アサガオおよびダイズを用いた。アサガオでは、発根後、0, 4, 6, 13, 18, 23, 56, 61 および 78 日後の植物体を 5~10 個体採取し、根、各茎、葉、花などの全ての組織を切りとり、60℃、一晩乾燥させた。次にこれらの試料をビニル袋に封入し、(1)と同様に放射化分析を行った。12の生育時期、約100個体の各々の組織について元素分析を行った。ダイズ試料もアサガオの場合と同様、各生育ステージにおける各組織についての元素分析を行った。

(3) ブラジル東北部の半乾燥地における土壌および植物中の元素分析

カーチンガ樹種7種類について、地上部ならびに地上1mにおける幹、各土壌層における根ならびに土壌をサンプリングした。幹は、中心に向かって数試料を切りだし、土壌は数十mgをビニル袋に封入し、放射化分析を行った。

3. 結果及び考察

(1) ルモガリオン染色法の開発

ルモガリオン染色法は、新しい染色法であるため、染色過程において固定された根から、どの過程でどの程度のAlが溶出するかがポイントであった。固定液、染色液などの組成を

変化させ、各段階の溶液中へのAl溶出量をできる限り低くなる条件を求めた。その結果、根の固定の際のみに約10%のアルミニウムが溶出される条件を見つけることができた。

(2) 植物による元素のリサイクルシステムの解明

非破壊状態で、Na、Mg、Al、Cl、K、Ca、Sc、V、Cr、Mn、Fe、Co、Zn、Brならびに希土類元素数種を定量することができた。ライフサイクル中、これらの元素は根-地上部間の関門以外にも、葉と葉柄、花柄と花などの間に一定の濃度関門を形成して分布していることが示された。環境問題で着目されている、AlとVは殆どが根のみに存在し、KおよびClは、葉-葉柄において濃度差が大きく、その傾向は全ライフサイクルにおいて一定であった。Mnは、蒸散流に従った濃度分布を示し、古い葉ほど濃度が高かった。Ca濃度は幼植物期に蓄積され、花芽形成に伴い上部へ移動した。また、実では、種柄、種皮に重金属は蓄積され、種子内にはほとんど蓄積されないことが判った。

ダイズを用いた元素分析は、Na、Mg、K、Mnの結果まで得られており、遷移元素については、これから分析を行う予定である。現在まで得られた結果では、吸収された元素が全てまた次世代の植物により利用されると仮定すると、最もリサイクルにおいて不足する元素はKであり、約3世代目にはK欠乏となることが示された。

(3) ブラジル東北部の半乾燥地における土壌および植物中の元素分析

放射化分析の結果、Na、Mg、Al、Cl、K、Ca、Sc、V、Cr、Mn、Fe、Co、Zn、Brならびに希土類元素数種を定量することができた。土壌試料では、殆どの遷移元素は深度が深く

なるに従い、高い濃度を示した。土壌から根への元素分配はMgやCoでは高く、根から幹への分配はVが最も高かった。カーチンガ樹木では希土類元素濃度は根が高く、土壌中の濃度との差は小さかった。根中の希土類元素濃度はAlやSc濃度との相関が幹中や土壌中の相関よりも高いことが示された。

4. 今後の方針

まだ、ダイズについては、ライフサイクルにおける元素分析が終了していないため、まず、残った元素分析を行う。その後、これまで得られた結果を踏まえ、ダイズにおける元素のリサイクルシステムのモデルを構築し、元素循環のシュミレーションを行う。また、土壌中にV、Alなどの元素量が増加した系について、同様な実験を行い、どのように植物の元素吸収活性が変化するか、また、活性の変化量によって、環境インパクトの推定が可能かについて調べる予定である。

ルモガリオン染色法はほぼ確立したので、本法開発のためのAl定量については終了する。これからは、この手法を用いて、組織内および細胞内におけるAl分布を確認しながら組織、細胞に取り込まれるAlの定量のため放射化分析を行っていききたい。また、異なる化学形態のAlがどのように根の生育を阻害するかについても研究を進めていきたい。

ブラジルにてサンプリングした試料の放射化分析は終了した。

研究発表

1. T.M.Nakanishi, J.Takahashi and H.Yagi : Partition of Transition Elements between Soil and Caatinger Wood Grown in North-East Brazil Determined by Neutron

Activation Analysis.

J.Radioanal.Nucl.Chem.,Letters 214(6), 517-527 1996

2. T.M.Nakanishi, J.Takahashi and H.Yagi : Rare Earth Element, Al, and Sc Partition between Soil and Caatinger Wood Grown in North-East Brazil by Instrumental Neutron Activation Analysis. Biological Trace Element Research 60, 163-174 1997

3. T.Kataoka, M.Mori, T.M.Nakanishi, S.Matsumoto and A.Uchiumi : Highly Sensitive Analytical Method for Aluminum Movement in Soybean Root through Lumogallion Staining. J.Plant Res.110, 305-309 1997

4. T.Kataoka, H.Iikura and T.M.Nakanishi : Aluminum Distribution and Viability of Plant Root and Cultured Cells.

Plant nutrition-for sustainable food production and environment. 427-431 1997

5. T.M.Nakanishi and M.Tamada : Kinetics of Element Profile Pattern during Life Cycle Stage of Morning-Glory. J.Radioanal. Nucl. Chem., 239(3), 489-494 1999

6. T.M.Nakanishi and M.Tamada : Kinetics of Transition Element Profile during the Life Cycle of Morning-Glory.

Proc. of Tenth International Conference on Modern Trends in Activation Analysis. Bethesda, USA 1999

7. J.Furukawa and T.M.Nakanishi : A Study of Nutrient Recycling System in Plant-Soil System using Neutron Activation

Analysis.

ibid, 1999

8. T.M.Nakanishi, S.Ueoka and
J.Furukawa : A Simulation of an
Environmental Effect to a Soybean Plant
Derived from the Kinetics of Ca and Mg
throughout the Generation.

Proc. of the 45th Conference on Bioassay,
Analytical & Environmental Radiochemistry,
Washington DC 1999

9. S.Ueoka, J.Furukawa and
T.M.Nakanishi : An Effect of Al and V on an
Element Uptake Manner in a Soybean Plant.

ibid 1999

4-8 放射化分析による海藻由来の含ハロゲン化合物の生合成研究

Biosynthetic Study of Halogenated Compounds from Marine Algae
by Activation Analysis鈴木 稔^a、中野 智^a、高橋 義宣^a、野矢 洋一^b、大西 俊之^b^a北海道大学大学院地球環境科学研究科、^b北海道大学アイソトープ総合センター

1. はじめに

紅藻フジマツモ科ソゾ属(*Laurencia*)の海藻は、多種多様な含臭素有機化合物を生産していることで知られている^{1,2)}。しかし、これら含ハロゲン代謝産物の生理的役割や生合成機構などについては不明の部分が多い。そこで生合成機構を解明するために、先に私達は⁸²Brをトレーサーに用いる方法を検討した。その結果、ソゾ由来の臭素化合物に中性子を照射して⁸²Br化合物へ直接変換し、生成した⁸²Br化合物を薄層クロマトグラフィーで展開した後に、薄層板をイメージングプレート法と発色剤法で検出できることを明らかにした。さらに、放射化した臭化物イオン(⁸²Br⁻)存在下で各種ソゾの培養を行い、24時間後には⁸²Br⁻が含臭素二次代謝産物へとり込まれることおよび暗所での培養では含臭素化合物の生成速度が遅くなることが判明した^{3,4)}。

本研究課題(平成9年度~10年度)では、⁸²Br⁻を用いて経時変化による含臭素代謝産物の生成量の測定と新種のソゾが含臭素化合物を生合成しているかどうかを⁸²Br⁻の取り込み実験によって確かめた後に、このソゾの大量培養、抽出、分離を行い、数種の含臭素化合物の同定と構造決定を行った。

2. 経時変化による含臭素化合物の生成量

放射化した臭化ナトリウム($\text{Na}^{+82}\text{Br}^{-}$)を人工海水ASP₁₂NATに加え培地とした。ウラボゾの"laureatin race"と"laurencin race"⁵⁾を腰高シャーレ中15℃、明条件下で各設定時間(1、2、4、6、8時間)まで培養した。

培養後、海藻をとり出して水分をかるく除去し、

メタノールで抽出した。メタノールを濃縮後エーテルと水で分配し、エーテル層をTLC上にスポットして展開した。展開後、薄層板をイメージングプレートに3日間露光した。さらにその後、リンモリブデン酸で発色させた。コントロールとしては、放射化していないNaBrを添加した培地中15℃、明条件下で培養した。それらの結果をTable 1およびTable 2に示した。

"laurencin race"では、1時間後にすでに含臭素化合物の生成が見られ時間の経過とともに蓄積していることが示された。"laureatin race"の主要な代謝産物であるlaureatin(1)とisolaureatin(2)⁶⁾は約3:2の割合で生成されており、これは天然の海藻からの両化合物の収率とほぼ一致していた。

一方、"laurencin race"でも、1時間後にすでに含臭素化合物の生成が見られ時間の経過とともに蓄積していることが示された。"laurencin race"の主要な代謝産物のlaurencin(4)とdeacetylalaurencin(5)⁷⁾は約1:1の割合で生成されていた。しかし、天然の海藻からの両化合物の収率は約4:1であるので、放射化分析の結果と異なっていた。

3. ⁸²Br⁻存在下での新種のソゾの培養

沖縄県備瀬崎で採集された新種のソゾ(*Laurencia* sp.)は、大量の採集が困難な種のために今までに成分分析は行われておらず含ハロゲン化合物を生産しているかどうか不明であった。そこで、この海藻(培養株)が含臭素化合物を生合成しているかどうかを放射化した臭素原子を用いて調べた。

放射化した臭化ナトリウム($\text{Na}^{+82}\text{Br}^{-}$)を人工海水のASP₁₂NATに加え培地とした。新種のソゾを腰高

研究施設・装置

JRR-4(気送管)、JRR-3(気送管)(東海原研)

研究分野

海洋天然物化学、代謝化学、放射化分析

Table 1. ^{82}Br -存在下で培養したウラソゾ ("laureatin race") のメタノール抽出物における臭素化合物の放射活性値

Compound	PSL ^{*1}				
	1h	2h	4h	6h	8h
10-bromo- α -chamigrene (3)	37.9	86.9	106.7	109.9	244.5
(bromophenols) ^{*2}	148.7	473.8	492.1	914.2	1845.4
isolaureatin (2)	35.2	46.9	65.2	72.4	96.5
laureatin (1)	40.5	80.6	81.7	109.0	173.3
unknown	32.8	59.3	137.5	85.4	271.7

^{*1} PSLは放射線量に比例するイメージングプレート法で使用する単位。

表の数値はバックグランド (1.213 PSL/mm²) を引いた値。

^{*2} bromophenol類であることが示唆されたが未同定。

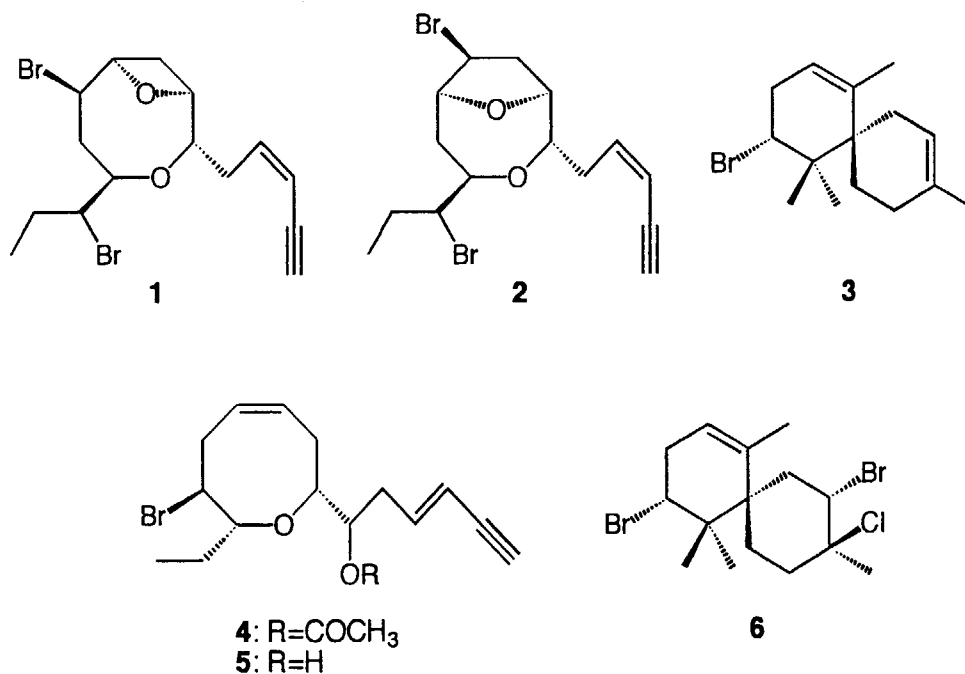
Table 2. ^{82}Br -存在下で培養したウラソゾ ("laurencin race") のメタノール抽出物における臭素化合物の放射活性値

Compound	PSL ^{*1}				
	1h	2h	4h	6h	8h
2,10-dibromo-3-chloro- α -chamigrene (6)	0	0	11.8	20.8	45.5
(bromophenols) ^{*2}	63.8	70.7	93.9	144.4	362.2
laurencin (4)	34.5	56.1	64.5	68.0	172.2
deacetylalaurencin (5)	43.1	39.6	46.6	49.1	203.6

^{*1} PSLは放射線量に比例するイメージングプレート法で使用する単位。

表の数値はバックグランド (1.376 PSL/mm²) を引いた値。

^{*2} bromophenol類であることが示唆されたが未同定。



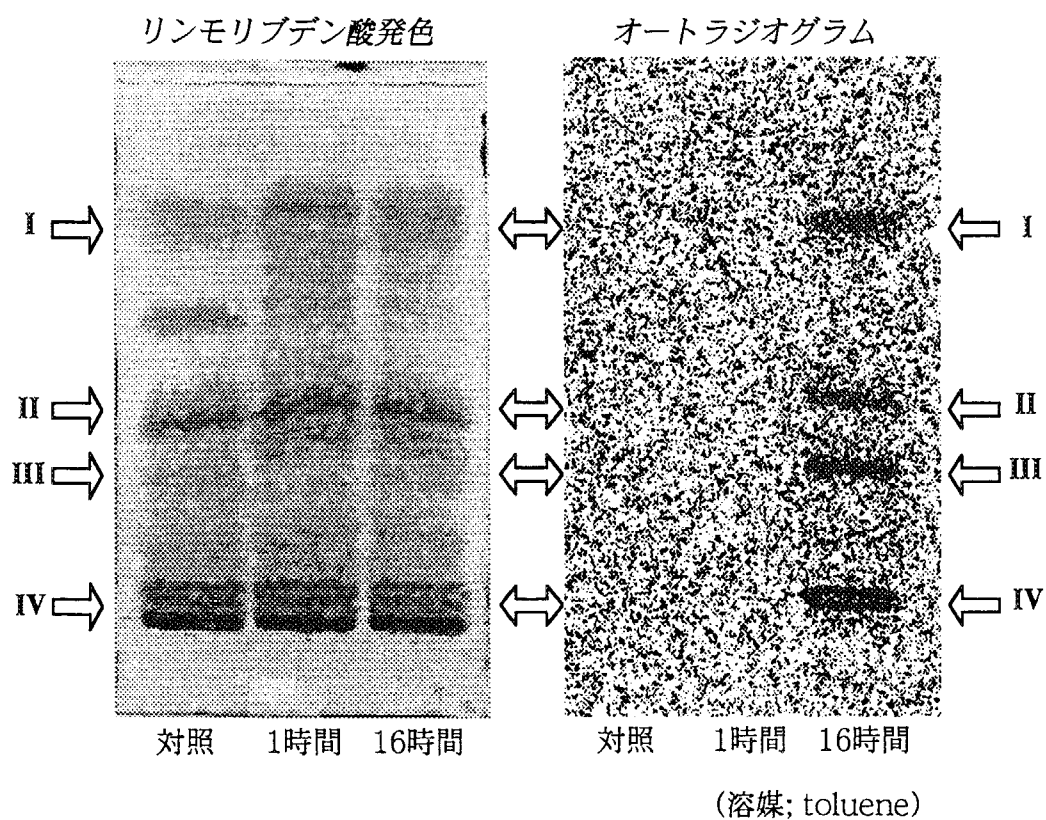
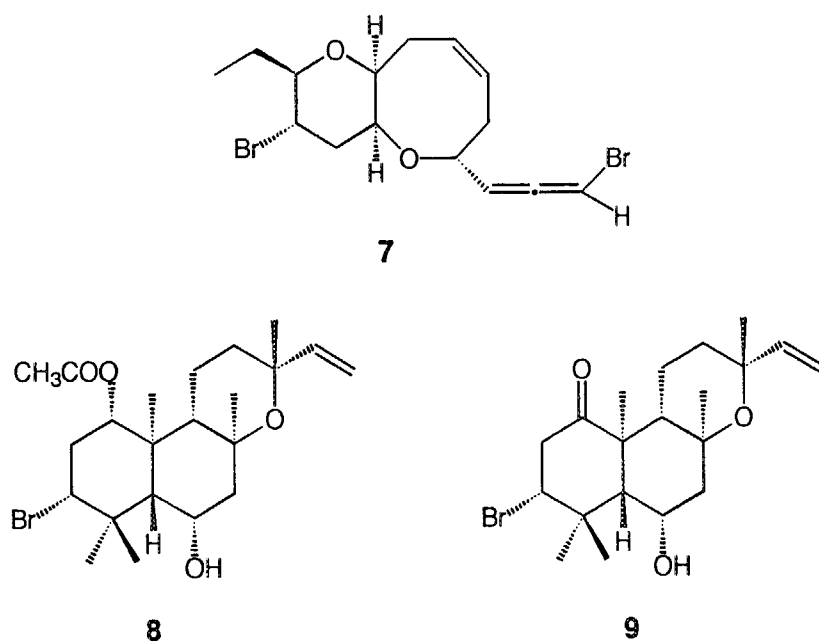


Fig. 1. ^{82}Br -存在下で培養した *Laurencia* sp. のメタノール抽出物の薄層クロマトグラム



シャーレ中15℃、明条件下で1時間と16時間培養した。

培養後、海藻をとり出して前述のように処理して薄層板をイメージングプレートに3日間露光した。さらにその後、リンモリブデン酸で発色させた。コントロールとしては、放射化していないNaBrを添加した培地中で同様な条件下で培養した。結果をFig. 1に示した。

Fig. 1から明らかなように4ヶ所 (I, II, III, IV) に ^{82}Br 化合物の生成が確認できた。

4. 新種のソゾが生産する含臭素代謝産物の構造

新種のソゾが含臭素化合物を生合成していることが判明したので、次に成分分析を行った。

大量培養した海藻 (22g) をメタノールに浸漬した。メタノールを減圧濃縮後エーテルと水で分配し、エーテル層から抽出物 (290mg) を得た。

Fig. 1に示した放射化分析の結果を指標にして、この抽出物をシリカゲルカラムクロマトグラフィーおよび分取薄層クロマトグラフィーで分離した。

構造決定は、各種スペクトルデータ (^1H -NMR, ^{13}C -NMR, 2D-NMR, Massなど) を解析して行った。

Fig. 1のIに相当する化合物は、以前いろいろなソゾから分離されている既知化合物の2,10-dibromo-3-chloro- α -chamigrene(6)と同定した⁸⁻¹⁰⁾。また、IIに相当する化合物は、以前フランス産の*Laurencia miclocladia*から分離されている既知化合物のmiclocladallene(7)と同定した¹¹⁾。しかし、IIIに相当する化合物は、含有量が少ないために同定不可能であった。

次に、IVに相当する化合物は、薄層クロマトグラフィー上ではワンスポットを示したが、NMRスペクトルでは2種の化合物の混合物であることが分かった。これらの混合物は高速液体クロマトグラフィーでもさらなる分離は不可能であった。しかし、幸いなことに分別結晶法によって分離することができた。熱ヘキサンで分別結晶を行い、不溶部から化合物(8)が、可溶部から化合物(9)が得られた。

化合物(8) $[\alpha]_{\text{D}} +28.0^\circ$ (c 0.27; CHCl_3), mp 183-184℃ は、高分解能マスペクトルから分子式 $\text{C}_{22}\text{H}_{35}\text{BrO}_4$ を有することが明らかとなった。

一方、化合物(9) $[\alpha]_{\text{D}} -120^\circ$ (c 0.08; CHCl_3) は、高分解能マスペクトルで分子式 $\text{C}_{20}\text{H}_{31}\text{BrO}_3$ を有することが分かった。

二つの化合物の平面構造式は、二次元NMRスペクトル (^1H - ^1H COSY, HSQC, HMBC) を詳細に解析することによって決定した。また、相対立体配置は、NOEスペクトルから8式および9式に示すように決定した。

すなわち、化合物(8)は、1-acetoxy-3-bromo-6-hydroxy-8,13-epoxylabd-14-eneであり、化合物(9)は、3-bromo-6-hydroxy-8,13-epoxylabd-14-en-1-oneである¹²⁾。

化合物(8)および化合物(9)の構造の確認と絶対配置の決定は、化合物(8)のX線結晶解析によって行った。8の絶対配置は、1S,3R,5S,6S,8S,9S,10S,13Rであり、9の絶対配置は、3R,5S,6S,8S,9S,10S,13Rである。

5. 今後の研究

これまでの研究においてイメージングプレート法による ^{82}Br 有機化合物の分析が有効であることが分かったので、今後さらに紅藻ソゾが生産する含臭素代謝産物の生合成プロセスを解明したい。特に、含臭素化合物の生成にはプロモベルオキシダーゼ(BPO)の関与が考えられているが、含臭素化合物の代謝には他の酵素の関与も必要なのかどうかについても検討したい。

謝辞

本研究の実施にあたり、中性子線の照射と照射試料の郵送でご協力をいただいた澤幡浩之博士、川手稔博士をはじめ大学共同利用解放研究室のスタッフの皆様に感謝いたします。

参考文献

- 1) 黒澤悦郎, 鈴木稔 (1983). "紅藻ソゾ(*Laurencia*)の代謝産物", 化学と生物, 21, 23-32.
- 2) K. L. Erickson (1983). "Constituents of *Laurencia*" in "Marine Natural Products; Chemical and Biological Perspectives", P. J. Scheuer ed., Vol. 5, pp 131-257, Academic Press, New York.

3) 鈴木稔, 野矢洋一, 大西俊之 (1997). "放射化による含臭素化合物の海洋生物内の代謝の研究", 原研施設利用共同研究成果報告書 (平成8年度), pp 63-65.

4) M. Suzuki, Y. Takahashi, S. Nakano, Y. Noya and T. Ohnishi, in preparation.

5) T. Abe, M. Masuda, T. Suzuki and M. Suzuki (1999). "Chemical races in the red alga *Laurencia nipponica* (Rhodomelaceae, Ceramiales)", *Phycol. Research*, **47**, 87-95.

6) T. Irie, M. Izawa and E. Kurosawa (1970). "Laureatin and isolaureatin, constituents of *Laurencia nipponica* Yamada", *Tetrahedron*, **26**, 851-870.

7) T. Irie, M. Suzuki and T. Masamune (1968). "Laurencin, a constituent of *Laurencia glandulifera* Kützinger", *Tetrahedron*, **24**, 4193-4205.

8) B. M. Howard and W. Fenical (1975). "Structures and chemistry of two new halogen-containing chamigrene derivatives from *Laurencia*", *Tetrahedron Lett.*, 1687-1690.

9) M. Suzuki, A. Furusaki and E. Kurosawa (1979). "The absolute configurations of halogenated chamigrene derivatives from the marine alga, *Laurencia glandulifera* Kützinger", *Tetrahedron*, **35**, 823-831.

10) Y. Takahashi, M. Suzuki, T. Abe and M. Masuda (1999). "Japonenyne, halogenated C₁₅ acetogenins from *Laurencia japonensis*", *Phytochemistry*, **50**, 799-803.

11) D. J. Kennedy, I. A. Selby, H. J. Cowe, P. J. Cox and R. H. Thomson (1984). "Bromoallenes from the alga *Laurencia microcladia*", *J. Chem. Soc. Chem. Commun.*, 153-155.

12) M. Suzuki, S. Nakano, Y. Takahashi, H. Takahashi, Y. Noya, T. Ohnishi, T. Abe and M. Masuda, in preparation.

6. 成果の公表

鈴木稔, 中野智, 高橋義宣, 阿部剛史, 増田道夫, 野矢洋一, 大西俊之 (1998). 「海藻由来のハロゲン化合物の生合成研究」日本化学会北海道支部1998年夏季研究発表会 (7月26日, 釧路).

中野智 (1999). 「海藻由来のハロゲン化合物の生合成研究」北海道大学大学院地球環境科学研究科修士論文 (3月).

Development of synthetic multi-element reference material with pseudo-biological matrix and its application

4-9 (生物体類似多元素合成標準物質の開発と応用)

Y. Iwata and A. Nakamura

Department of Chemistry, College of Education, Akita University

(秋田大学教育学部)

Abstract

A new type of synthetic multi-element reference material (SyRM) with pseudo-biological matrix was prepared by co-polymerization reaction of homogenate aqueous solution of acrylamide and acrylic acid containing known amount of the elements. SyRM has the excellent homogeneity and the quantitative retention of major and trace elements. Elemental composition can simulate the biological samples to be analyzed. SyRM can be used for same purpose of conventional certified reference material with high accuracy and precision. SyRM was applied as a comparative standard for non-destructive photon and α -particle activation analysis. Selective preconcentration methods combined with NAA were proposed and the SyRM containing some fifty elements with known amounts was prepared. In order to evaluate of the reliability of present methods, 3d transition elements and rare earth elements in the SyRM were determined. It was clearly observed that these methods have good accuracy and precision in trace analysis for biological materials by comparing analytical results with the original contents in the SyRM. The SyRM supported multi-element analysis of marine macro-algae as comparative standards and quality assurance of analytical techniques, and then 35 elements could be determined.

Introduction

Analytical standards are indispensable to the calibration of apparatus and the evaluation of the accuracy and precision of analytical techniques. Several organizations have been making certified reference materials (CRM) of biological material and many kinds of standard materials have been prepared and issued, however utilities of such CRM, *i. e.* number of certified element, reliability of certified value and kind of CRM are limited. These CRM are prepared from biological materials and the certified value for each element is given by actual analysis. Several types of the synthetic reference materials have been introduced, for example, phenol-formaldehyde resin^{1,2}, gelatin^{3,4}, and silica^{5,6} but accuracy and homogeneity of elements doped in these matrix materials were not examined in detail. In addition, there was no synthetic

reference material having a variable range in concentrations of major, minor and trace elements.

We proposed a new type of synthetic multi-element reference material (SyRM) with polyacrylate-acrylamide gel matrix^{7,8}. SyRM was applied as a comparative standard for non-destructive activation analysis⁹⁻¹¹ and also was applied for the evaluation of the accuracy and precision of analytical techniques^{12,13}. In this paper, characteristics and utilities of SyRM for activation analysis are summarized, and results of activation analyses, which were supported by SyRM, to marine macro-algae are also shown.

Experimental

Preparation of SyRM

A recommended procedure is outlined in Fig. 1. To an aqueous solution containing 10 g of acrylamide and/or acrylic acid together with 0.5 g of *N,N'*-methylenebisacrylamide as a linking agent was added citric acid. The molar concentration of citric acid was adjusted to be ten times the sum of the molar concentrations of transition elements and Al. A known amount of a multi-element standard solution were added. After the addition of 2 ml of 5% *N,N,N',N'*-tetramethylethylenediamine solution as a stimulator, the pH was adjusted to 3.4–4.7 with 1 M aqueous ammonia or 1 M nitric acid, then the volume of the solution was made up to 96 ml. After deaeration, 2 ml of 0.5% ammonium sulphite solution and 2 ml of 2.5% ammonium peroxodisulphate solution were added and the mixture was kept under reduced pressure. We had been used sodium hydrogen sulphite in previous papers^{8, 10–13}. In order to make metal-free matrix, ammonium sulphite was used. After complete gelification (ca. 12 h), the gel was broken into small pieces and lyophilized for 48 h. The SyRM was

dried for 4 h at 85°C just before use.

Results and Discussion

Characteristics of SyRM

Easy preparation and handling The well known gelification reaction for poly-acrylamide gel, often used for the electrophoresis, was modified for SyRM. About 13 g of SyRM could be obtained by the present procedure with one day for mixing solutions and gelification, three days for lyophilization. We prepared standard solutions of elements by dissolving high purity metals, oxides, halides and carbonates in nitric acid or pure water because we often need to control the concentration of Cl accurately. When the exact Cl determination is unnecessary, commercial standard solutions for AAS and ICP based on hydrochloric acid are also acceptable.

SyRM looks like powdered milk and is easy to make a pellet which is suitable for activation analysis. SyRM is more stable for heating and radiation than ordinary biological materials. No decomposition of SyRM stored more than 10 years in an ordinary refrigerator at 4°C was observed. On the other hand, it is decomposed

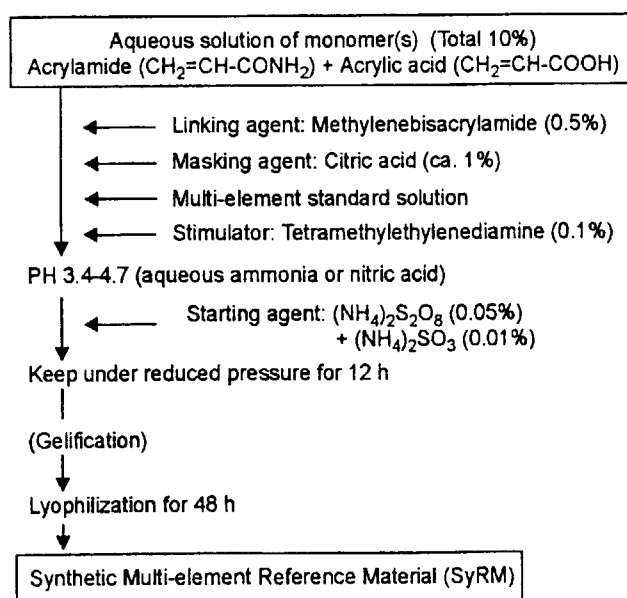


Fig. 1. Preparation of synthetic multi-element reference material: Numerical values in parentheses show the concentration (in % w/v) of each reagent just before gelification

easily by dry ashing at 500°C or wet digestion with $\text{HNO}_3\text{-H}_2\text{O}_2$.

Excellent homogeneity and quantitative recovery of added elements The homogeneity and recovery of added elements such as Na, Cr, Mn, Zn, As, Se and I in SyRM were ascertained by using corresponding radiotracers (Na-22 , Cr-51 , Mn-54 , Zn-64 , As-74 , Se-75 , I-126)^{7,8}. In the preparation of SyRM, each radiotracer was added to standard solution. After an ordinary lyophilization, the radioactivity of 200-500 mg portions of SyRM was measured. The homogeneity and recovery were calculated from specific activities (cps/mg SyRM) and comparing with the initial radioactivity, respectively. The relative standard deviation (RSD) of specific activities of 5-14 portions taken arbitrarily from the prepared SyRM were 0.4-1.1% for all radiotracers. The recovery for each element was 98-102%. The retention during the air drying for As, Se and I, which have been recognized as volatile elements, are examined. No loss of these elements was

observed on the air drying at 85°C for 6h. The same is practically true for a very trace level of 10ng/g Hg labeled by Hg-197^8 . Homogeneity of smaller portions (of 100 mg) was also examined for Se as an example, where an RSD value of 1.1% was observed for ten portions. In ordinary CRM made by biological materials, the minimum sampling size is 250-500 mg and the certified values for trace elements are given with several or more than ten percent of uncertainty^{14, 15}. For SyRM, the elemental contents can be accurately calculated from the dry weight and the quantities of added elements, since the elements, including volatile trace elements, added initially are quantitatively and homogeneously retained.

Variability of regulation for matrix, elements and its content Contents of N and O in SyRM can be regulated simply by changing the mixing ratio of two monomers, acrylamide ($\text{CH}_2=\text{CH-CONH}_2$) and acrylic acid ($\text{CH}_2=\text{CH-COOH}$). The matrix composition of SyRM in the region of high weight ratio of acrylic acid is quite

Table 1. Elemental composition of SyRM for a comparative standard to α particle activation analysis (A) and SyRM to evaluate rare earth determination by NAA after separation (B)

Element	mg/g		Element	$\mu\text{g/g}$ B	ng/g	
	A	B			B	
H	45	61	V	5.49	Sc	13.4
C	395	369	Cr	0.908	Y	26.0
N	9.2	32	Mn	21.1	La	666
O	253	481	Fe	86.6	Ce	1090
			Co	0.0201	Pr	228
Na	31.7	0.141	Ni	0.524	Nd	1070
Mg	10.1	5.65	Cu	17.1	Sm	936
Al	—	0.0852	Zn	29.2	Eu	481
P	3.24	0.997	As	1.11	Gd	644
S	1.2	2.36	Br	7.22	Tb	92.0
Cl	114	0.394	Sr	95.7	Dy	559
K	126	17.6	Cd	0.0349	Ho	62.6
Ca	9.38	30.8	Cs	0.103	Er	55.8
			Hg	0.0553	Tm	37.6
I	2.19	0.00165	Pb	14.1	Yb	82.7
					Lu	13.5
					U	40.3

A: Matrix and major elements similar to marine macro-algae.

B: Containing all rare earth elements in matrix and coexistent elements similar to NIST Citrus Leaves.

similar to that of the botanical samples which are O rich, and in the region of weight ratio of 50-100% of acrylamide is similar to that of the muscle, liver or blood sample from animals.

Elemental composition of 2 kinds of SyRM are shown in Table 1. Their matrix are based on 100% of acrylic acid as monomer. The elemental composition of SyRM A and SyRM B are similar to that of dried marine macro-alga and leaves of fruit trees, respectively. SyRM A includes 8 major elements because it was prepared for a comparative standard for non-destructive α -particle activation analysis for P, Cl, K and Ca¹¹. It has simple component, however, it contains high concentrations of inorganic elements (total 30%). Content of total salts in marine plant is richest in biological materials. SyRM could be simulated such a salt rich sample. SyRM B includes all rare earth with similar matrix and coexistent elements to NIST SRM 1572 Citrus Leaves in order to evaluate of the reliability of rare earth determination by NAA after separation by coprecipitation¹³. There is no CRM of biological material having certified values for all rare earth and even up-to-date CRMs have less than 30 certified values for elements¹⁵. SyRM B contains known amounts of 41 elements in a pseudo-botanical matrix. Variability for matrix composition, kinds and concentrations of elements in SyRM is satisfactory to many type of analytical methods and biological sample to be analyzed.

Utility of SyRM

Because of similar or superior characteristics, SyRM can be used for same purpose of conventional CRM with high accuracy and precision. We have been interested in the elemental abundance of marine macro-algae. There is a CRM made by marine macro-alga, however, it has certified values only for 5 minor elements and 11 trace elements¹⁶. We used SyRM for multi-element analysis of marine macro-algae, and analytical methods and results for 35 elements are summarized in Table 2.

Use as comparative standard for activation analysis SyRM was applied as a comparative standard for non-destructive photon¹⁰ and α -particle activation analysis¹¹. We prepared SyRM contains known amount of interesting elements with major coexistent elements in similar matrix to the alga sample. The SyRM and dried alga samples were compressed to a cylindrical pellet with a diameter of 10mm. The SyRM and alga samples were irradiated simultaneously by bremsstrahlung of 30 MeV electron from a LINAC or 18 MeV of α -particles from a cyclotron. γ -Rays from the SyRM and alga samples were measured at same geometry. For α -particle and also other charged particle activation analysis, similarity of the elemental composition of analytical samples and comparative standard is important because the range of incident charged particles is highly influenced by elemental composition of target. Comparing Table 1 and 2, it is found that the composition of matrix, major and minor elements are closely similar to each other. Hence, no special correction was needed due to the difference in the range of α -particle. Coupling the two kinds of non-destructive activation analysis using the SyRM, 9 kinds of alkali metals, alkali earth metals and halogens, and P and As could be determined with good reproducibility.

Use for evaluation of accuracy and precision of analytical technique CRM are indispensable for the evaluation of analytical techniques, especially in trace analysis combined with chemical separation. We applied the SyRM to pre-separation NAA for some 3d transition elements¹² and rare earth elements¹³. It is well known that NAA has excellent sensitivity for those elements, however, a non-destructive γ -ray spectrometry cannot be often performed in the case of biological samples. This problem is serious for marine macro-alga sample because it contains only $\mu\text{g/g}$ levels of 3d transition elements and ng/g levels of rare earth elements. In addition, the measurement of nuclides of such trace elements is remarkably interfered by very strong back-ground activity, which are induced from large amounts of alkali

metals and halogens. Hence chemical separation methods for those elements are inevitable to obtain reliable results.

The SyRM was digested with $\text{HNO}_3\text{-H}_2\text{O}_2$. V, Mn, Fe, Co, Cu and Ni were separated by diethyldithiocarbamate extraction from digested solution of the SyRM into benzene phase. In order to irradiation by a reactor, metal complexes were collected directly with a polystyrene foam produced by lyophilization of the benzene extract after an addition of polystyrene. The foam was pelletized and subjected to NAA. Quantitative recoveries of 6 elements for the separation and collection steps were ascertained by using corresponding radiotracers. The precision of the technique is demonstrated by RSD for three determinations of the SyRM. The accuracy is verified by relative error shown by comparing analytical results and original content of the SyRM. The precision and accuracy (RSD : 4-6%, Error : 1-8% for each element) were satisfactory, then the technique was applied to marine

macro-algae samples.

Rare earth elements in the digested solution of the SyRM were separated by coprecipitation caused by substoichiometric precipitation of calcium oxalate. Calcium oxalate containing rare earth elements was subjected to NAA. Quantitative recovery had been checked by radiotracers and the reliability of this technique was appreciated by three determinations of the SyRM. It was found that this technique had high precision (RSD: 1-5%) and good accuracy (Error: $\pm 0.1\text{-}5\%$), then it was also applied to marine macro-algae samples and determined 12 elements¹⁷.

Use as calibration standard for AAS SyRM can be used as calibration standard for AAS because it is easy to dissolve by wet ashing. We used the SyRM for such a purpose to Graphite furnace Zeeman AAS analysis of Ni and Cr in marine macro-algae.

Table 2. Multi-element analysis of marine macro-algae* supported by SyRM

Element	mg/g	Element	$\mu\text{g/g}$	Element	ng/g
H	49	V	2.53 ± 0.14	La	42.2 ± 0.2
C	346	Cr	0.125 ± 0.003	Ce	145 ± 2
N	19	Mn	5.61 ± 0.2	Pr	9.88 ± 0.49
		Fe	19.4 ± 1.6	Nd	17.4 ± 0.5
Na	34.8 ± 1.3	Co	0.0718 ± 0.001	Sm	4.01 ± 0.15
Mg	9.67 ± 0.4	Ni	0.195 ± 0.005	Eu	1.43 ± 0.01
P	1.53 ± 0.2	Cu	0.66 ± 0.08	Tb	0.673 ± 0.013
S	7.56 ± 0.1	Zn	17 ± 0.2	Dy	5.84 ± 0.27
Cl	122 ± 4	As	58 ± 1.3	Ho	0.67 ± 0.051
K	137 ± 47	Br	1000 ± 60	Er	4.52 ± 0.31
Ca	12.2 ± 0.4	Rb	45.5 ± 2.2	Yb	6.88 ± 0.07
		Sr	629 ± 36	Lu	1.38 ± 0.06
		I	4460 ± 170		

Based on dry weight, $n = 3$.

* *Laminaria religiosa*, Sampling, 30 July 1984. Onagawa bay, Miyagi Pref. Japan.

Methods of analysis:

Photon activation analysis by 30 MeV bremsstrahlung from a LINAC: Na, Mg, Cl, Ca, As, Br, Rb, Sr, I.

Alpha-activation analysis by 18 MeV α from a cyclotron: P, Cl, K, Ca.

NAA after extraction and polystyrene foam collection: V, Mn, Fe, Co, Cu, Zn.

NAA after coprecipitation by calcium oxalate: rare earth elements.

Graphite furnace Zeeman AAS: Cr, Ni.

Substoichiometric isotope dilution analysis: S.

Organic microanalysis: C, H, N.

Conclusion

This synthetic standard is an artificially synthetic polymer-type standard, and, of course, does not have absolutely the same chemical form and structure as the natural biological materials. But considering the above advantages and utilities, this new type of reference material can be more effectively used not only for activation analysis but also for spectrophotometric analysis such as AAS or ICP.

References

1. L. M. MOSULISHVILI, M. A. KOLOMITSEV, V. YU. DUNDUA, N. I. SHOMIA, O. A. DANILOVA, J. Radioanal. Chem., 26 (1975) 175.
2. D. I. LEYPUNSKYS, V. I. DRYNKIN, B. V. BELENKY, M. A. KOLOMITSEV, V. YU. DUNDUA, N. V. PACHULIA, J. Radioanal. Chem., 26 (1975) 293.
3. D. H. ANDERSON, J. J. MURPHY, W. W. WHITE, Anal. Chem., 44 (1972) 2099.
4. D. H. ANDERSON, J. J. MURPHY, W. W. WHITE, Anal. Chem., 48 (1976) 116.
5. J. W. MICHELL, L. D. BLITZER, T. Y. KOMETANI, T. GILIS, L. CLARK Jr., J. Radioanal. Chem., 39(1977)335.
6. A. R. DATE, Analyst, 103 (1978) 84.
7. K. MASUMOTO, N. SUZUKI, Radiochem. Radioanal. Lett., 42(1980) 99.
8. N. SUZUKI, Y. IWATA, H. IMURA, Anal. Sci. 2(1986)335.
9. K. KUDO, N. SUZUKI, J. Radioanal Nucl. Chem., 88(1985)75.
10. N. SUZUKI, Y. IWATA, Appl. Organomet. Chem., 4 (1990) 287.
11. Y. IWATA, H. NAITOH, N. SUZUKI, J. Radioanal. Nucl. Chem., 159 (1992)121.
12. N. SUZUKI, Y. IWATA, H. IMURA, Intern. J. Environ. Anal. Chem., 30 (1987) 289.
13. Y. IWATA, N. SUZUKI, Anal. Chim. Acta, 259 (1992)159.
14. Y. MURAMATU, R.M. PARR, Survey of Currently Available Reference Materials for Use in Connection with the Determination of Trace Elements in Biological and Environmental materials, IAEA/RL/128, IAEA, Vienna, 1985.
15. NIST Standard Reference Materials Catalog 199. 6, NIST Special Publication 260, National Institute of Standards and Technology, Gaithersburg, MD, 1995.
16. NIES Certified Reference Material No. 9 "Sargasso", National Institute for Environmental Studies, Ibaraki, JAPAN 1988.
17. Y. IWATA, H. IMURA, N. SUZUKI, J. Radioanal. Nucl. Chem., 172 (1993)305.

Publication

Advantages of Synthetic Multi-Element Reference Material with Pseudo-Biological Matrix in Activation Analysis, Y. Iwata and N. Suzuki, J. Radioanal. Nucl. Chem., 233 (1998)49.

4-10 宇宙物質の中性子放射化分析(2)

Neutron activation analysis of the extraterrestrial materials

海老原充、尾寄大真、孔屏、内野智功、箕輪はるか、S. K. Latif、

石井友子、日高洋、大浦泰嗣、G. W. Kallemeyn、中原弘道、

M. Ebihara, H. Ozaki, P. Kong, T. Uchino, H. Minowa, S. K. Latif,

T. Ishii, Y. Oura, G. W. Kallemeyn, H. Nakahara

東京都立大学大学院理学研究科

Graduate School of Science, Tokyo Metropolitan University

米田成一

S. Yoneda

国立科学博物館理工学研究部

Department of Science and Engineering, National Science Museum

1 はじめに

平成8年度から10年度にかけて、標記課題で原研施設を利用した共同研究を行った。この間に行った研究は2つに分類できる。1つは宇宙物質としていくつかの異なる種類の隕石について、その微量元素含有量を中性子放射化分析で分析し、その元素存在をに基づいて、それらの隕石が形成された太陽系初期の物質の進化について考察する研究である。もう一つは、今後の宇宙探査計画に沿った、いわば予備的研究である。本報告書ではこの2番目の成果についてまとめる。上に挙げた2つの研究はその発展を期して平成11年度からの共同研究にも引き継がれている。

21世紀は人類が積極的に宇宙空間に出ていく時代となることは間違いあるまい。これは、今世紀から21世紀の初頭にかけて、宇宙探査計画が目白押しであることから容易にうなずける。順調な経済力をバックに、アメリカでは小型惑星探査計画、いわゆるディスカバリー計画が軌道に乗っており、ヨーロッパでもEC共同体として宇宙探査に積極的である。日本でも、経済力に陰りがあるものの、21世紀は宇宙の時代であるとの認識では世界と共通であり、高度な科学技術に裏打

ちされて、独自の宇宙探査計画がたてられており、そのいくつかはすでに実施されている。

アメリカのディスカバリー計画の一つで、すでに実施が決まっているものの一つに「Genesis Mission」がある。このMission計画は、2001年1月に打ち上げが予定されている探査計画で、2003年8月に地球に試料を持ち帰る予定である。この探査計画で持ち帰られる地球外物質は、太陽風である。太陽風は太陽から常に放出されているプラズマ粒子で、主に陽子(プロトン)からなる。Genesis Missionでは太陽風を約2年間捕集し、地球に持ち帰る予定である。地球に持ち帰られた太陽風試料は、主に元素と同位体の分析に用いられる。

太陽風の元素組成は太陽の元素組成にほぼ等しいと考えられている。太陽系の元素組成は惑星科学や地球科学の分野における最も基本的な数値である。その値はほとんどの元素で隕石の化学分析によって求められている。隕石は太陽系が形成されたときに一緒に固体物質として形成されたもので、その後の変化をほとんど受けていないことから、元素組成的にも形成当時の情報を内包していると考えられるからである。

研究施設と装置名

JRR-3M

研究分野

宇宙化学

しかし、その妥当性を検証することは非常に難しい。太陽系の質量が集中する太陽の組成がわかれば、その組成を太陽系の組成として採用するのが最も妥当である。太陽の組成を求めるには地上からの分光観測に多く依存するが、現在の測定技術では太陽の元素組成を精度良く計することは非常に難しい。Genesis Mission はこのような状況のもとで、太陽の組成を直接分析することによって、精度良い元素組成を求めようとするものである。同 Mission では、元素組成の他、太陽の同位体組成を直接求めることも計画の大きな柱になっている。

Genesis Mission で太陽風を捕獲して、その元素組成を求める場合、感度の高い分析方法を用いる必要がある。また、できるだけ多くの元素が分析できることが望まれる。さらに、繰り返し分析するだけの試料の量が得られないので、一度の分析で確実にデータが得られなければならない。このような条件を満たす方法として、中性子放射化分析法の採用が決まった。本研究では、実際の分析に先立って、太陽風を捕集するために用いられる捕集板の材質の評価と、分析法の適用性の確認を行った。

2 実験

2.1 試料

太陽風の捕集を行うには純物質で、不純物ができるだけ含まれていない材質が望ましい。放射化分析で分析することを考えて、実際の Mission では金属ケイ素を用いる。本研究では搭載候補として、アメリカの半導体メーカー、MEMC 社と Unisil 社から提供されている2種類の高純度ケイ素金属試料を用いた。ケイ素試料は直径 19 mm、高さ 21 mm (重量: 約 13.6 g) のシリンダー状に成形されたものを用いた。

2.2 照射

試料と、比較標準に用いるアルミ箔とともに石英管に封入し、日本原子力研究所 3 号炉 (JRR-3M) で 25 日間中性子照射した。

2.3 照射後の処理

表面に付着している不純物を除くためと、表面から内部にかけてどのような元素組成の変化があるのかを調べるために、材質の溶出実験を行っ

た。溶出はアルコールで表面を洗浄した後、MEMC 社製品についてはフッ酸と硝酸の混酸で、Unisil 社製品についてはフッ酸と過酸化水素水の混合溶液で、変化の様子を見ながら数秒から数時間に渡って溶出操作を繰り返した。フッ酸と過酸化水素での溶出では数時間の接触でも 0.1 % 以下の質量の減少しかなく、最終的には Unisil 製の製品に関してもフッ酸と硝酸の混酸で溶出を行った。

酸による溶出によって、MEMC 社製のケイ素では 3.3%、Unisil 社製のケイ素では 1.75% の質量欠損があった。溶出によって溶解する元素が一部電着する可能性があり、以下の操作に進む前にこのような不純物も除く目的で、表面を紙ヤスリで研磨した。その結果、両試料で初めの質量に比べて 4.5 % 減少した。

2.4 セレンと希土類元素の放射化学的分離

高純度ケイ素金属中のセレンと希土類元素の不純物量を求めるために、放射化学的分離操作を行った。実験の概略は以下の通りである。上記の研磨後の高純度ケイ素をテフロンピーカーにとり、セレンと希土類元素の一定量を担体として加え、さらに鉄を保持担体として加えて、硝酸とフッ酸の混酸で溶解した。溶液を乾固し、塩酸で溶解し、水で適度に希釈後、溶液を遠心分離して沈殿と上澄みに分離した。沈殿は主に希土類元素のフッ化物であり、放射化学的に精製して γ 線測定用試料とした。上澄みに亜硫酸ガスを通じてセレンを金属セレンに還元して回収し、 γ 線測定用試料とした。

3 結果と考察

3.1 高純度金属ケイ素中の不純物の定量

ヤスリで研磨した後のケイ素試料を都立大学・RI 研究施設 (TMU-RIRL) において γ 線測定を行った。用いた検出器は ORTEC 社製ゲルマニウム検出器 (相対効率 30%、エネルギー分解能 1.9 keV) で、1 試料あたり約 1 週間測定した。Table 1 は γ 線ピークから同定された核種、計数率、およびその核種を生じる元素の含有量を示す。定量値を得るために、ケイ素試料と一緒に照射したアルミ箔中に含まれる鉄とコバルトの含有量と生成した ^{59}Fe 、 ^{60}Co の生成放射能から中性子フ

ルエンスを求めた。シリンダー上のケイ素試料と、ディスク状のアルミ箔の計数効率、適当な放射性核種の既知量を同一形状の容器にとり、 γ 線測定して求めた。計算の過程において、照射中の熱中性子以外の寄与と γ 線測定の際の試料による吸収は無視した。誤差は計数誤差で、1 σ の値である。

3. 2 試料中のセレン、希土類元素の定量

2つのケイ素試料から放射化学的に分離・生成したセレンと希土類元素試料を TMU-RIRL で測定したが、予想されるエネルギー位置にピークは認められなかった。そこで、バックグラウンドが TMU-RIRL に比べて約2桁低い、金沢大学低エネルギー放射能測定施設 (KU-LLRL) のゲルマニウム半導体検出器で測定したところ、同様にピークはどの元素に関しても認められなかった。そこで、測定された γ 線強度からそれぞれの元素の上限値を計算した。結果を Table 2 に示す。希土類元素の中では、半減期を考慮して、 ^{153}Gd 、 ^{152}Eu 、 ^{160}Tb の3つの核種について検討した。上限値は対応するピークでの半値幅の2倍をピーク領域とし、そのバックグラウンドの計数誤差の3倍とした。また、KU-LLRL の測定器によるシリンダー状試料の検出効率も、適当な放射性核種を用いて求めた。

3. 3 Genesis Mission 搭載試料としての妥当性

本研究で分析対象とした試料を太陽風の捕集板として衛星に取り付けた場合の性能について評価を加えた。太陽風を捕集する条件として以下の仮定を設ける；

- ①太陽数のケイ素板への打ち込まれる深さ：100 nm
- ②太陽風の捕集期間：2 年
- ③太陽風の水素のフラックス： 3×10^8 atom/cm² s
- ④太陽風の相対元素存在度：太陽系の元素存在度 (Anders and Grevesse, 1989)

太陽風を捕集後、深さ 100 nm までのケイ素試料を用いて分析するものと仮定し、単位面積あたりの不純物含有量と実際に捕集されると期待される量を Table 3 に比べた。表から明らかなように、ガドリニウムを除いてどちらの高純度ケイ素の

不純物含有量も捕集推定量に比べて2桁以上低い値である。従って、実際に高純度ケイ素に捕集されるセレン、ユーロピウム、テルビウムを定量する際には、どちらの高純度ケイ素を用いた場合でも不純物が定量値に及ぼす影響は非常に小さいといえる。

実際に分析して、定量値を出す場合には測定場のバックグラウンド条件を含めた測定装置の性能を考慮する必要がある。Table 4 は TMU-RIRL と KU-LLRL の検出器の検出限界 (Bq) と太陽風を捕集して中性子照射したときの推定誘導放射能 (Bg/cm²) を比較したものである。推定誘導放射能は、太陽風を2年間捕集し、中性子照射を JRR-3M で25日間行い、1半減期冷却した時の値を示した。定量値を得るためには照射後の生成放射能が検出限界より大きくなる必要があり、KU-LLRL で測定を実施すれば、セレン、ユーロピウム、テルビウム、ガドリニウムを定量するのにそれぞれ 18 cm²、82 cm²、630 cm²、7600 cm² 以上の面積の試料が最低必要となる。現実的には一枚の捕集板は約 5000 cm² 程度であり、ここで検討している4元素ではガドリニウムを除いた元素の定量が可能であると見込まれる。

4 補足説明-なぜセレンと希土類元素を測定するか？

上記の研究では、セレンと希土類元素の定量の可能性を検討した。その理由は以下の通りである。

太陽系の元素存在度は、現在ではごく一部の元素を除いて CI コンドライトの化学分析値を用いて推定されている。その値の妥当性は (i) 分光観測から求めた太陽の元素組成値との比較、(ii) いわゆる Suess plot のうち、奇数質量数核種の存在度の変化、から推定される。(i) の場合、太陽光球の分光データの精度が良くないので、その値を用いて隕石の分析値の妥当性を判断することは本来不可能である。(ii) については、奇数の質量数の存在度がどの程度なめらかに変化するか、をもって隕石から得られた値の妥当性を考察するが、太陽系の元素組成がなめらかに変化することの理論的裏付けはない。現在最も妥当な太陽系の元素存在度として利用されている Anders and Grevesse (1989) の推定値をよく調べると、

^{75}As - ^{77}Se - ^{79}Br の領域でセレンの存在度が予想値よりも低い値をとり、さらに希土類元素の領域で ^{149}Sm - ^{151}Eu - ^{153}Eu - ^{155}Gd の変化においてユーロピウムが両隣の元素より高い値を示す。これらの値が太陽系本来の値であるか、あるいは CI コンドライトの特異的な問題なのかは、CI コンドライトのコンドライトグループ中にしめる位置や、さらに隕石を用いて描いてきた原始太陽系像を再検討する必要があるかどうかを議論するところにまで波及する問題である。

研究成果 (発表論文)

(原研炉を利用して得られた成果で、1996 年から 1998 年までに発表したもの)

1. M. Ebihara (1996) Solar and solar system abundances of the elements. J. Royal Soc. West. Australia 79, 51-57.
2. M. Ebihara and T. Miura (1996) Chemical characteristics of Cretaceous, Tertiary and their boundary layers at Gubbio, Italy. Geochim. Cosmochim. Acta 60, 5133-5144.
3. M. Ebihara, P. Kong and K. Shinotsuka (1997) Chemical composition of Y-793605, a Martian lherzolite. Antarct. Meteorite Res. 10, 83-94.

Table 1. Impurities in Si metals determined by INAA

Element	Nuclide (Energy, keV) ^a	Counting rate ^b (cps)	Content (g/g Si)
<i>MEMC</i>			
Sb	^{124}Sb (602.7)	$(1.98 \pm 0.12) \times 10^{-3}$	$(2.8 \pm 0.2) \times 10^{-14}$
Ag	^{110}Ag (657.8)	$(4.08 \pm 0.12) \times 10^{-3}$	$(7.6 \pm 0.5) \times 10^{-15}$
Zn	^{66}Zn (1115.5)	$(4.66 \pm 0.15) \times 10^{-3}$	$(1.9 \pm 0.1) \times 10^{-12}$
Co	^{60}Co (1332.5)	$(1.84 \pm 0.13) \times 10^{-3}$	$(3.0 \pm 0.3) \times 10^{-14}$
<i>Unisil</i>			
Sb	^{124}Sb (602.7)	$(1.89 \pm 0.19) \times 10^{-3}$	$(3.1 \pm 0.4) \times 10^{-14}$
Ag	^{110}Ag (657.8)	$(2.69 \pm 0.16) \times 10^{-3}$	$(5.3 \pm 0.4) \times 10^{-15}$
Co	^{60}Co (1332.5)	$(7.66 \pm 0.21) \times 10^{-3}$	$(1.3 \pm 0.1) \times 10^{-14}$

^aGamma-ray energy in parentheses is used for calculation.

^bCounting time: ~4 d. An error is due to counting statistics (1 σ).

Table 2. Upper limits of counting rates^a and corresponding contents for Se and some REE

Element	Nuclide (Energy, keV)	Counting rate (cps)	Content (g/g Si)
<i>MEMC</i>			
Se	^{75}Se (264.7)	$<1.7 \times 10^{-4}$	$<6.1 \times 10^{-14}$
Gd	^{153}Gd (97.4)	$<1.0 \times 10^{-4}$	$<5.6 \times 10^{-14}$
Eu	^{152}Eu (344.3)	$<1.1 \times 10^{-4}$	$<2.0 \times 10^{-16}$
Tb	^{160}Tb (879.4)	$<6.8 \times 10^{-5}$	$<6.5 \times 10^{-15}$
<i>Unisil</i>			
Se	^{75}Se (264.7)	$<1.8 \times 10^{-4}$	$<6.5 \times 10^{-14}$
Gd	^{153}Gd (97.4)	$<8.8 \times 10^{-5}$	$<5.1 \times 10^{-14}$
Eu	^{152}Eu (344.3)	$<8.3 \times 10^{-5}$	$<1.6 \times 10^{-16}$
Tb	^{160}Tb (879.4)	$<5.4 \times 10^{-5}$	$<5.4 \times 10^{-15}$

^aAt Ogoya facility of Kanazawa Univ., referred as KU-LLRL in the text.

Table 3. Comparison of impurities in silicon metals and estimated amounts of elements in the solar wind corrected by Si panel

Element	MEMC-Si (g/cm ² · 100 nm)	Unisil-Si (g/cm ² · 100 nm)	Estimated amount ^a (g/cm ²)
Se	$<1.4 \times 10^{-18}$	$<1.5 \times 10^{-18}$	6×10^{-15}
Gd	$<1.3 \times 10^{-18}$	$<1.2 \times 10^{-18}$	6×10^{-17}
Eu	$<4.8 \times 10^{-21}$	$<3.8 \times 10^{-21}$	2×10^{-17}
Tb	$<1.5 \times 10^{-19}$	$<1.3 \times 10^{-19}$	1×10^{-17}

^aSee text for details.

Table 4. Comparison of detection limits at TMU and KU counting facilities and estimated activities for Se and some REE nuclides

Nuclide	Energy (keV)	Detection limit ^a (Bq)		Estimated activity ^b (Bq/cm ²)
		TMU-RIRL	KU-LLRL	
⁷⁵ Se	264.7	<0.285	<0.00777	4.4×10^{-4}
¹⁵³ Gd	97.4	<0.548	<0.0282	3.7×10^{-5}
¹⁵² Eu	344.3	<1.38	<0.0165	2.0×10^{-4}
¹⁶⁰ Tb	879.4	<0.961	<0.0196	3.1×10^{-5}

^aCalculated from background count at corresponding energy. TMU-RIRL=Tokyo Metropolitan University, Radioisotope Research Laboratory. KU-LLRL=Kanazawa University, Low Level Radioactivity Laboratory.

^bCalculated activity assuming 25 d irradiation at JRR-3M and one half-life cooling. See text for details.

4-11 放射化分析支援システムの検証試験

東京大学 原子力研究総合センター 伊藤 泰男、澤幡 浩之
日本原子力研究所 東海研究所 桜井 文雄、大友 昭敏、笹島 文雄

放射化分析支援システムは、放射化分析の経験が少ない利用者でも、簡便かつより正確に分析試料の多元素同時分析を行えるように分析作業を支援するためのものである。本研究では、大学開放研究室に結集する放射化分析の専門家・利用者と原研研究炉部とが協力して整備している k_0 標準化放射化分析支援システムの検証を、標準環境試料の分析を行ってその精度、正確さを確認することによって行う。 k_0 標準化放射化分析システムでは JRR-3M, JRR-4 の代表的な照射場のパラメータを決定し、また大学開放研究室所有の測定器・原研所有の測定器の幾つかについて校正を行い、利用者は任意の組み合わせを選定できるように整備される予定であるが、1998年度は JRR-3M の計画外停止があったために、JRR-3M の照射場パラメータ決定の作業は今後に残されることになった。ここでは JRR-4 の k_0 法放射化分析の整備・検証について報告する。

Evaluation of the k_0 Standardization Neutron Activation Analysis System

Ito Yasuo, SAWAHATA Hiroyuki (RCNST, The Univ. of Tokyo)

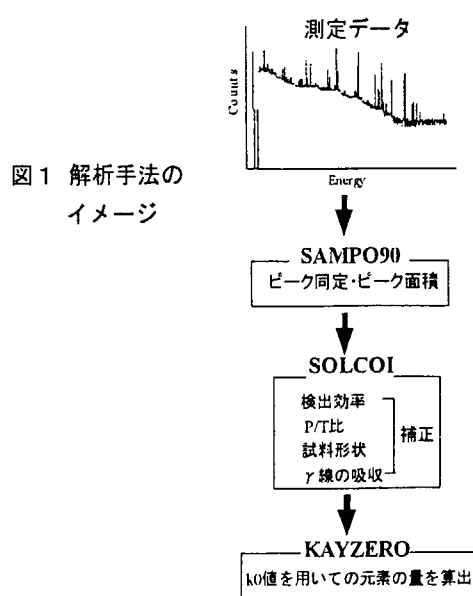
SAKURAI Fumio, OOTOMO Akitoshi, SASAJIMA Fumio (Tokai, JAERI)

A system to support the users of neutron activation analysis is being constructed using the k_0 standardization method that has been developed recently. This will make it possible to obtain highly accurate analytical results without much professional knowledge and experience. In the current system, determination of the parameters of the irradiation field and precise calibration of Ge solid state detectors are necessary. The former has to be done for all the irradiation fields of JRR-3M and JRR-4 that are going to be used in activation analysis, and the latter has to be done for several detectors belonging to KAIHOKEN (the Inter-University Laboratory) or to JAERI. This enables the users choose any combination of irradiation field and detector. Most of these works have been performed, excepting for some of the irradiation field of JRR-3M.

1. はじめに

開発しているシステム(図1参照)は、データとり込みやスペクトルの核種同定・ピーク面積の決定などを行う「SAMPO 90」、検出器の同時計数補正や試料の立体角計算などを行う「SOLCOI」及び金標準試料の測定値をもとに k_0 値を介して全ての核種の量を計算し元素の濃度算出を行う「KAYZERO」という三つのソフトウェアの構成から成り立っている。 k_0 標準化法は従来の比較分析法のように各元素毎に標準試料を準備する必要がないため、格段の簡素化が可能となる。

k_0 標準化法を用いた NAA は、国内ではまだ広く利用されていない分析方法である。このため大学開放研究室でこれを整備して共同利用することは研究炉利用の高度化と一層の活性化に大きな意味を持つ。



JRR-4 気送管、I-, S-パイプ、
JRR-3M 気送管、HR-1,2

放射化分析

2. 解析手法

近年、ヨーロッパを中心に盛んに利用されている手法として k_0 法による放射化分析がある。この方法は、Simonits, De Corte, 他によって開発されているもので、シングルコンパレータ法のコンパレータ係数 k 値から照射場及び測定器に依存する係数を分離し、汎用性のある複合核定数として評価された k_0 値を用いて多元素同時分析を行う

ものである。この特徴としては、分析元素毎の比較標準試料を必要としないで、簡便かつ正確な分析が行えることである。元素濃度 ρ_a (mg/g) は、次式により計算される。

$$\rho_a = \frac{A_{sp,a}}{A_{sp,m}} \cdot \frac{1}{k_{0,m}(a)} \cdot \frac{G_{th,m} \cdot f + G_{e,m} \cdot Q_{0,m}(\alpha)}{G_{th,a} \cdot f + G_{e,a} \cdot Q_{0,a}(\alpha)} \cdot \frac{\epsilon_{p,m}}{\epsilon_{p,a}} \cdot 10^6$$

ここで、

A_{sp} : 比放射能、 $A_{sp} = (N_p/t_c) / \text{SDCW}$

(N_p : ネットエリア、 t_c : 計測時間、

S : 飽和係数、 D : 減衰補正、

C : 測定中の減衰補正、 W : 試料重量

G : 自己遮蔽補正係数

Q_0 : 共鳴積分と放射化断面積の比 (I_0/σ_0)

f : 熱中性子束と熱外中性子束の比 (f_{th}/ϕ_e)

α : 熱外中性子スペクトルの $1/E$ からのずれを示す係数

ϵ_p : Ge 検出器の検出効率

k_0 : k_0 係数

添字 th, e : 熱中性子、熱外中性子

添字 m, a : 中性子モニタ元素、目的元素とする。

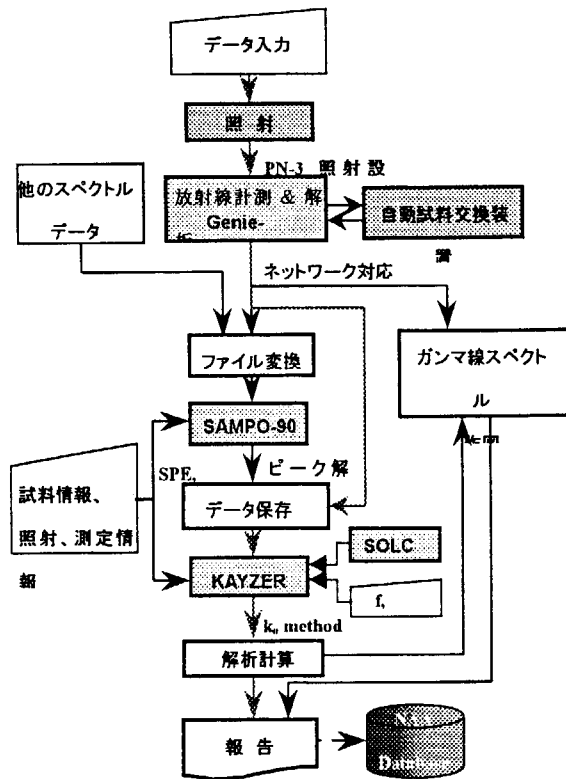


図 2

放射化分析支援システムのフローチャート

3. 照射場パラメータの決定

照射場のパラメータは、中性子スペクトルを補正するための係数で、熱中性子と熱外中性子の比 (f)、 $1/E$ 分布からのずれ (α) で表される。このパラメータ (f, α) は照射場固有の定数なので、利用者がその都度決定するのではなく、施設側で予め測定しておけば共通に使うことが出来る。ただし、経時的な変化があり得るので、このパラメータは時々点検測定して管理することが必要がある。

この測定は、熱中性子領域と熱外中性子領域で中性子吸収断面積の異なる 2 つの核種の放射化を測定することによって行われる。SOLCOI ソフトウェアでサポートされている、bare triple 法では、Au と Zr をモニターとして一緒に照射し、Au-98/Nb-97m/Zr-95 の放射化を測定する。この方法によって得られた照射場パラメータを表 1 に示す。

表 1 照射場のパラメータ

Reactor	Channel	f	Alpha	Fc
JRR-3M	HR-1	0.1757	33.5105	696246.72
	HR-2	0.1569	41.3171	556855.79
	PN-1	0.3759	38.2714	327500.60
	PN-2	0.3647	50.5323	247763.77
	PN-3	0.5798	175.5754	578631.24
JRR-4	T-pipc	0.2352	92.469	82049.46
	PN	0.2364	92.880	57640.64
	S-pipc	0.2431	93.321	87134.23

4. 検出器の校正

k_0 法によって正確な分析値を得るためには、検出器の校正を厳密に行うことが重要である。Ge検出器の校正として、ピーク対トータル比、計数効率があるが、ソフトウェアSOLCOIでは任意の試料位置での検出効率や吸収補正などを行うので、検出器形状図3に示すような結晶のサイズ、空乏層領域の大きさ、dead layerの厚さ、結晶とキャップの距離、キャップの材質と厚さ)が厳密に分かっている必要がある。

ピーク対トータル比と計数効率は、放射能が正しく校正された標準線源を用いた測定結果をSOLCOIに入力する。SOLCOIは検出器形状の情報に基づいてモンテカルロ計算して計数効率を計算するが、この計算結果が測定結果と一致するように、dead layerの厚さなどの値をガイdnチューニングする。このような検出器校正は、施設側において一度行っておけば良いので、利用者はこの面倒な作業を行うことを免れる。

ピーク対トータル比及び計数効率の測定結果をそれぞれ図4、5に示す。

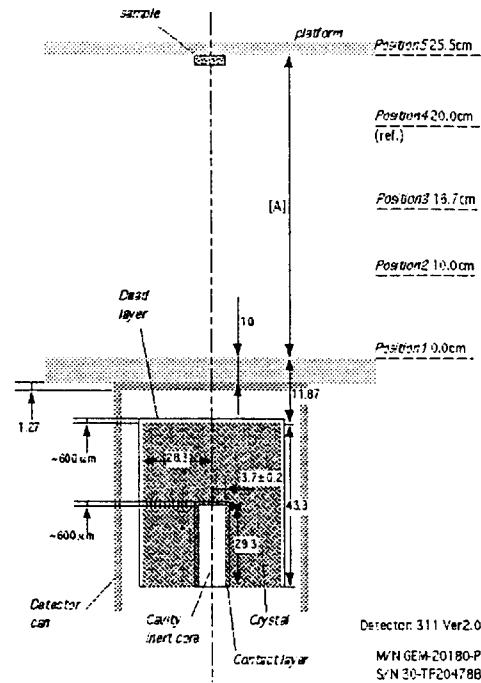


図3 SOLCOIに与える検出器形状の情報

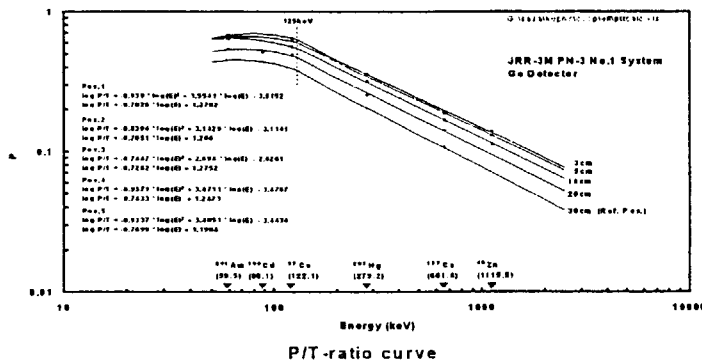
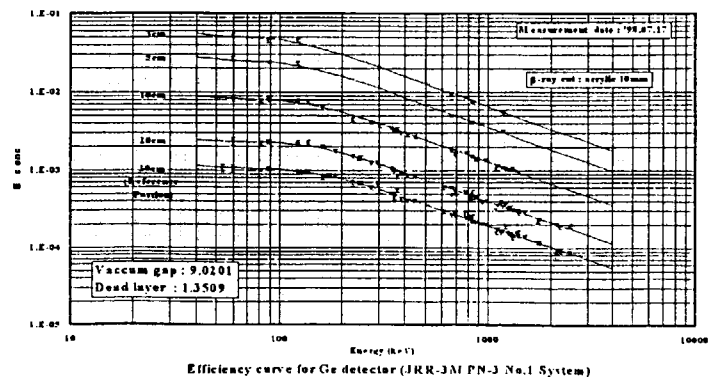


図4

ピーク対トータル比の測定結果

図5

ガンマ線検出効率の
測定結果



5. R I の製造

5. Production of Radio Isotopes

This is a blank page.

研究テーマ：R I の製造技術の開発

表 題：ガドリニウム造影剤の体内分布を高感度で検出

5-1 ガドリニウム造影剤の残留分布を高感度で検出 — 原子炉で放射化し画像で見る新手法を開発 —

小林勝利、本石章司、照沼久寿男、今橋強
羽鳥晶子¹、重松昭世¹

日本原子力研究所 アイソトープ開発室

¹ (株) 生体科学研究所

磁気共鳴断層撮影(MRI)用、ガドリニウム(Gd)造影剤は、脳や脊髄などの血管や病巣部分をまわりの正常組織より明瞭に映し出すために開発された薬剤である。わが国では 1988 年に使用が開始され、広く一般に利用されている。Gd 単体では有害性があるが、たとえば、Gd-DTPA (ガドリニウム-ジエチレントリアミン五酢酸；化学式 $C_{14}H_{20}GdN_5O_{10}$) という化合物にすることにより、通常大部分は尿中に排泄され、体内の蓄積も僅かであるとされていた。最近、厚生省の緊急安全性情報で、まれに、ショックやアレルギー反応などの副作用を起こすことが発表された。

従来の確認方法は、放射性 ^{153}Gd (半減期：242 日) を使った造影剤を初めから投与するので、放射性物質を使うことによる施設の管理や取り扱いが面倒になる。

新手法は、造影剤 (Gd-DTPA キレート化合物) をラットに静脈内投与後、常法により経時的に全身マクロオートラジオグラフ(ARG)用試料を作製した。また、主要組織および排泄物も試料として用い、未投与群(コントロール)を対照試料として、すべて乾燥後ポリエチレン袋に封入した。

試料を原研の原子炉(JRR-3M：熱中性子束：約 $5 \times 10^{13} \text{ cm}^{-2} \cdot \text{sec}^{-1}$) で 15 分間照射した。生成した ^{153}Gd の放射能は、約 1 週間経過後、高純度ゲルマニウム(Ge)検出器を用い、2 本の γ 線 (97、103 keV) により定量した。

ここで、天然の Gd (Gd-152 の存在比：0.2%) の存在比を 30% まで高めた安定濃縮同位体で合成した造影剤を用いることにより、ガンマ線検出器で測定した際の検出感度を 150 倍に上昇させた。放射化した試料から出る放射線を蛍光物質を塗布したプレートに露出して分布を求めるオートラジオグラフィ法で、試料中の残留

分布を二次元的放射線画像(イメージングプレート像)として鮮明にとらえることができた。

ARG は富士バイオイメージングシステム(BAS-2000)を用いた。生体成分も放射化され、主として骨組織中の ^{32}P (半減期：14.28 日) や ^{45}Ca (半減期：165 日) からの β 線の影響を受ける。そこで、 ^{153}Gd が長半減期であることを利用し、 ^{32}P などが充分減衰するまで待つとともに、 ^{45}Ca はアルミニウム箔で遮蔽し、 ^{153}Gd のみを画像化する工夫をした。

今回開発した方法は、非放射性の薬剤を用いるため、試料の調製が容易で通常の実験室で扱えることから Gd に限らず、幅広い応用が期待できる。また、動物試験および臨床試験における血液、血漿、尿などの試料から、体内吸収および排泄の動態についての情報を得ることも可能であり、両結果の相関性について知見を得る価値は高いものと考ええる。

参考文献

- 1) 小林勝利、羽鳥晶子：“ガドリニウム造影剤の体内残留を高感度で検出”，Isotope News, 12-14(1998年2月号)
- 2) Akiko Hatori, Akiyo Shigematsu, Katsutoshi Kobayashi, Shoji Motoishi, Kusuo Terunuma, Tsuyoshi Imahashi, and Keiji Mori：“A novel autoradiography technique: Neutron activated whole body autoradiography”, The Society for whole body autoradiography, Ann Arbor, Michigan (1997)

原子炉：JRR-3M 装置：気送管 分野：R I の製造 (アクチバブル・トレーサ用)

研究テーマ：非定常放出に対するガスモニタ校正法の開発

表 題：放射性ガスモニタの校正法の比較

5-2 放射性ガスモニタの校正法の比較

大石哲也、吉田 真
保健物理部線量計測課

これまで、放射性ガスモニタの新たな校正方法として放射性ガスの短時間注入による手法（パルス注入校正法）を提案し、その妥当性の検証を行った¹⁾。パルス注入校正法を Fig.1 に示す。本手法は、放射能既知のガスをパルス注入することによりガスモニタの応答関数を決定し、ガスモニタ出力から流入放射能を直接評価する方法である。パルス注入校正法は、濃度が一定な定常放出、過渡変化の大きな非定常放出のいずれにも適用することが可能である。一般的に、原子炉施設等における放射線管理で使用されるガスモニタの校正は、Fig.2 に示す閉ループ校正法で実施されている。この校正法は、閉ループ内へ導入した放射性ガスの放射能濃度を基準電離箱により決定し、ガスモニタ出力と放射能濃度との換算係数を決定する手法である。現状では、過渡変化の大きな放出に対しても閉ループ校正法が適用されている。そこで、両者の方法で検出器が異なる3種のガスモニタを校正し、それぞれの校正結果を比較検討した。

実験には、 β 線用ガスモニタとして電離箱型及びプラスチックシンチレーション型を、 γ 線用ガスモニタとして NaI(Tl)シンチレーション型を用いた。また、原子炉施設等の管理上重要なガス状の核種を考慮し、 β 線用として ^{85}Kr を、 γ 線用として ^{41}Ar をそれぞれ校正ガスとして使用した。はじめに、各ガスモニタに対して閉ループ校正を実施し、放射能濃度とガスモ

ニタの出力電流又は計数率との換算係数 ($\text{Bq}/\text{cm}^3/\text{A}$ 又は $\text{Bq}/\text{cm}^3 \cdot \text{s}$) を求めた。つぎに、パルス注入校正を実施した。パルス注入校正法は換算係数ではなく応答関数を決定する校正法であり、校正時におけるガスモニタ出力及びそのサンプリング容器内の放射能濃度は時間経過とともに変化する。そこで、閉ループ校正法の換算係数と比較するために、パルス注入校正法における平均出力と平均放射能濃度を求め、それらの換算関係（以下、換算係数）を決定した。ガスモニタの平均出力は出力のピーク面積をその出力が生じている時間（以下、ピーク時間）で除して求め、平均放射能濃度は流入放射能をピーク時間と流量率との積で除して求めた。流量率が 10、15L/min におけるパルス注入校正及び閉ループ校正の換算係数の比較結果は 5%以内で一致し、今回使用した流量率、サンプリング容器の体積等の条件においてはパルス注入校正法と閉ループ校正法のどちらでも同じ校正結果を与えることがわかった。以上により、パルス注入校正法を定常放出に適用できることが実証されるとともに、現状の校正手法である閉ループ校正法の妥当性も検証された。

参考文献

- 1)大石哲也、吉田 真：RADIOISOTOPES, Vol.48, No.1, (1999), 23-31,

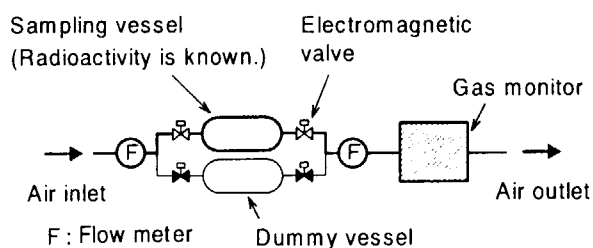


Fig.1 Calibration of gas monitor by pulse-like injection of radioactive gases.

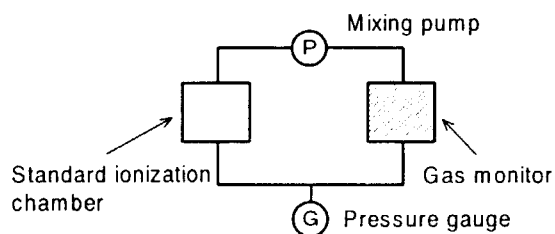


Fig.2 Calibration of gas monitor by closed loop.

6. 原子炉材料照射試験

6. Irradiation Test of Reactor Materials

This is a blank page.

研究課題：原子力用機能性材料の研究開発
表題：酸化リチウム単結晶からのヘリウム放出挙動

6-1 Helium Release from Neutron-Irradiated Li_2O Single Crystals

Daiju Yamaki, Takaaki Tanifuji and Kenji Noda

Japan Atomic Energy Research Institute, Tokai-mura, Ibaraki, Japan.

For all Li_2O single crystal specimens irradiated with thermal neutrons, the helium release curves in the constant heating rate tests show only one broad peak in the range of 1100-1300K. It suggests that the helium release process from Li_2O single crystals irradiated with thermal neutrons consists of only one process. The helium release processes from Li_2O single crystal are thought to consist of the bulk diffusion and surface processes by analogy from the tritium release processes. However, the surface process can be neglected, since helium atom is inert for Li_2O and sweep gas components. Thus, only the bulk diffusion process was into account.

In the previous study, the helium release behavior from Li_2O sintered pellets was investigated. In the helium release curves from the Li_2O sintered pellets, four kinds of peaks were observed as shown in fig. 1. From the dependencies of the temperature of the peak on the grain diameter, bulk density and the thermal neutron fluence, and the activation energies of the peaks, it is considered that the helium migration process for peak A in fig.1 is the diffusion process along the grain boundary, that for peak B is the bulk diffusion process, and those for peak C and D are the diffusion process with trapping at closed pores in the grains, although the reason has not been clarified why the two peaks C and D appear for the trapping process.

Figure 2 shows the grain diameter dependence of the temperature of the peak B in fig. 1 which is considered to be the peak of the bulk diffusion process, and the crystal diameter dependence of the temperature of the peak from single crystal irradiated with thermal neutrons. It is clearly shown that the temperature of both the peaks shows the similar dependence on the grain and crystal diameters. It is suggested that the migration process for peak B in the helium release curves of Li_2O sintered pellets and for the peak in that of Li_2O single crystal are the same process, that is, the diffusion process in

the bulk.

Figure 3 shows the relationship between the thermal neutron fluence and the temperature of the peak in the helium release curves from Li_2O single crystals irradiated with thermal neutrons. It indicates that the temperature of the peak increases with the thermal neutron fluence. For example, the temperature of the peak for 150-297 μm specimen irradiated to 2×10^{17} n/cm² of thermal neutrons was 1134 K, and that for same diameter specimens irradiated to 2×10^{19} n/cm² of thermal neutrons was 1304 K. From the relationship between the temperature of the peak and the grain or crystal diameter shown in fig. 2, the peak temperature of 1304 K for 150-297 μm specimen irradiated to 2×10^{19} n/cm² of thermal neutron is calculated to be equal to the 3080 μm crystal diameter specimen irradiated to 2×10^{17} n/cm² of thermal neutrons. It means that the apparent helium diffusion path for the 150-297 μm specimen irradiated to 2×10^{19} n/cm² thermal neutrons is about fourteen times of that for the specimen irradiated with 2×10^{17} n/cm² thermal neutrons. It seems to indicate that the helium diffusing in the Li_2O crystal is trapped at defects introduced in the crystals by the energetic helium and tritium generated by the reaction of ${}^6\text{Li}(n, \alpha){}^3\text{H}$. Radiation damage studies performed so far showed that F⁺ centers (an oxygen vacancy trapping an electron), F-aggregate centers, Li colloidal centers, etc. introduced by irradiation. Although such irradiation defects are annealed out at the temperatures lower than 900 K, the irradiation effects on the peaks are still observed above 900 K, as shown in fig. 3. Thus, the irradiation defects as the trapping sites are considered not to be the above-mentioned irradiation defects such as F⁺ centers and Li colloidal centers but some defect clusters such as dislocation loops etc. which are not completely annealed out even at 1400K.

Conclusion

Helium release behavior in post-irradiation heating tests was investigated for Li_2O single crystals which had been irradiated with thermal neutrons in JRR-4 and JRR-2. It is clarified that the helium release curves from JRR-4 and JRR-2 specimens consist of only one broad peak. From the dependence of the peak temperature on the neutron fluence and the crystal diameter, and the comparison with the results obtained for sintered pellets, it is considered that the helium generated in the specimen is released through the process of bulk diffusion with trapping by irradiation defects such as some defect clusters.

References

- [1] D. Yamaki, T. Tanifuji and K. Noda, J. Nucl. Mater. 258-263 (1998) 549-554.

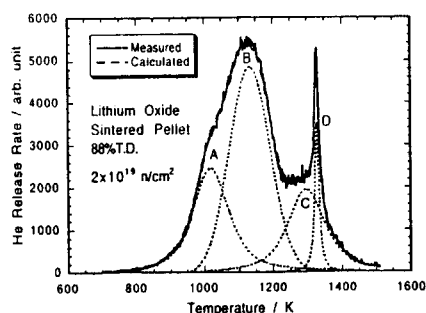


Figure 1. The typical helium release curves from sintered Li_2O irradiated with thermal neutrons.

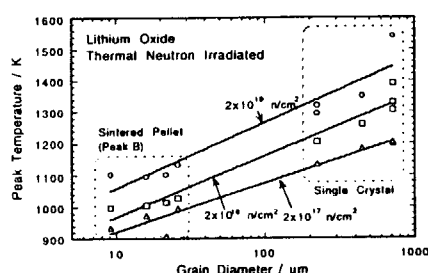


Figure 2. The grain diameter dependence of the temperature of the peak B in fig.1 and that of the peak in the helium release from Li_2O single crystal irradiated with thermal neutrons.

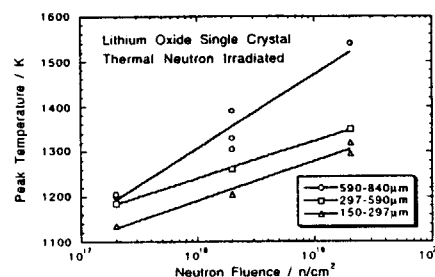


Figure 3. The relationship between the thermal neutron fluence and the temperature of the peaks in the helium release curves from Li_2O single crystals irradiated with thermal neutrons.

7. その他

7. Etc

This is a blank page.

研究テーマ：LiAlの電気的性質の中性子照射効果の研究II

表 題：LiAlの電気的性質の中性子照射効果の研究II

7-1 LiAlの電気的性質の中性子照射効果の研究II

須貝宏行、矢萩正人¹、浜中廣見²、内山周²、栗山一男²

日本原子力研究所研究炉部アイソトープ開発室・茨城県那珂郡東海村

¹ 青森大学工学部・青森県青森市幸畑

² 法政大学工学部・東京都小金井市梶野町

1. はじめに

金属間化合物 β -LiAl (Li組成48-54 at.%) は、トリチウム製造試験用のターゲット材料^{1, 2)} ($^6\text{Li} (n, \alpha) ^3\text{H}$ 反応による) や電力貯蔵用電池開発における電極材料として用いられてきた。しかし、最大3.6 at.%もの原子空孔を含む特異な格子欠陥構造やその電気伝導機構は明らかでなかった。そこで、本研究は、未照射および中性子照射した β -LiAlの格子欠陥構造を明らかにし、 β -LiAl中のトリチウムやLiの拡散と格子欠陥の関係を解明することを目的とする。

2. これまでの研究経過

β -LiAlは、Li原子とAl原子がそれぞれダイヤモンド副格子を組むNaTi型構造という独特な結晶構造を有する。また、 β -LiAlは半金属的なバンド構造をもち、主なキャリアはホールであり、その電気伝導は β 相内に存在する格子欠陥によるキャリアの散乱に大きく影響される。^{3, 4)} そこで、我々は、極めて大きな反応断面積をもつ、熱中子と ^6Li の核反応を利用して、 β -LiAlの格子欠陥構造に乱れを与え、電気抵抗率測定から、 β -LiAl中の格子欠陥によるキャリアの散乱機構を明らかにした。²⁾ この研究の過程で、 β -LiAl中に存在する3種類の構造欠陥(Li原子空孔、Al格子点の置換Li原子、これら2つの点欠陥が隣り合う格子点に存在する複合欠陥)の濃度²⁾を決定した。これらの欠陥のうちLi原子空孔が、トリチウムやLiの拡散に大きな影響をおよぼすことが明らかになってきた。さらに、Li組成が50 at.%付近の β - $^6\text{LiAl}$ を中性子照射したところ、約50%抵抗率が減少するとともに、抵抗率の温度依存性に、90 K付近で大きな不連続が現われた。^{2, 5)} これまで、未照射試料ではLi組成48 at.%付近で、抵抗率の温度依存性90 K付近で大きな不連続⁶⁾(Li原子空孔の規則-不規則変態に起因する)が

観測されていたが、中性子照射試料で観測されたのは初めてである。これは、 $^6\text{Li} (n, \alpha) ^3\text{H}$ 反応にともなう放射線損傷とその反応熱により、複合欠陥^{2, 5)}中のLi原子空孔を経路としたLi原子の移動がおり、 β - $^6\text{LiAl}$ のLi組成が50 at.%付近から48 at.%付近になったためと考えられる。

3. 本年度の進捗状況

本年度は、 β -LiAlと同じLi系Ia IIIb金属間化合物に属する β -LiGa (Li組成44-54 at.%) についても β - $^6\text{LiGa}$ 結晶を作製し、実験が進行中である。 β -LiGaにも抵抗率の温度依存性に大きな不連続が存在するが、その温度は230 K⁷⁾で、 β -LiAlの場合の90 Kよりも高温である。この原因は、Li原子空孔数の違いによると考えられている。同様の結晶構造をもつ β -LiAlと β -LiGaの実験結果の比較により、 β -LiAl中のLi原子の移動のメカニズム等が格子欠陥構造との関係でより明らかになるとと思われる。

参考文献

- 1) H. Sugai, M. Tanase, and M. Yahagi, J. Nucl. Mater., **151** (1998) 254.
- 2) H. Sugai, M. Tanase, M. Yahagi, T. Ashida, H. Hamanaka, K. Kuriyama, and K. Iwamura, Phys. Rev. **B 52** (1995) 4050.
- 3) K. Kuriyama, T. Kamijoh, and T. Nozaki, Phys. Rev. **B 21** (1980) 4887.
- 4) M. Yahagi, Phys. Rev. **B 24** (1981) 7401.
- 5) 矢萩, 須貝, 棚瀬, 浜中, 栗山, 日本物理学会 1996 年秋の分科会講演概要集, 3aN-7.
- 6) K. Kuriyama, Takashi Kato, Tomoharu Kato, H. Sugai, H. Maeta, and M. Yahagi, Phys. Rev. **B 52** (1995) 3020.
- 7) K. Kuriyama, H. Hamanaka, S. Kaidou, and M. Yahagi, Phys. Rev. **B 54** (1996) 6015.

原子炉: JRR-4 装置: Dパイプ, Tパイプ

分野: その他(材料科学、放射線損傷)

7-2 黒曜石のフィッション・トラック年代測定値の標準化

—とくに Au・Zr モニターによる放射化反応率測定を試み

Standardization of obsidian fission-track ages

—an attempt to estimate activation rate with Zr and Au monitors

鈴木達郎

鹿児島大学教育学部

Tatsuo Suzuki

Faculty of Education, Kagoshima University

1. はじめに

フィッション・トラック年代測定(FTD)に適した地質試料としては、ジルコンやアパタイトなどの鉱物や黒曜石などの火山ガラスがある。ジルコンやアパタイトなどでは他の方法による正確な年代測定値の知られた年代標準試料が提案され、ゼータ法(Hurford and Green, 1983)によって比較的規格化されたデータが出されるようになってきている。他方黒曜石などのガラス試料においては地質学分野でも多くの興味ある適用があるが、広く頒布されている標準試料が今のところない。そのため具体的な年代測定値を得る方法がなく、近年ではガラスの年代測定を試みても報告例も少なくなっている。しかし黒曜石などのガラス試料においては、年代標準試料によるゼータ較正法の確立を求めるのは必ずしも有効ではないのではないと思われる。なぜならガラスの年代標準試料それ自体のアニーリング補正も必要があろうし、一般に若い試料の多い黒曜石など火山ガラス試料では自発トラック密度が低く、目的試料と標準試料両方の低密度のトラック計数によって誤差を拡大する可能性があるからである。

ガラス中のトラックは熱的補正を要することはがあるが、トラックの計数そのものは微小な結晶鉱物に比べてより容易で安定したデータを得やすい。従って黒曜石のフィッション・トラック年代測定値の標準化においては、比較法であるゼータ法ではなく U-235 の核分裂反応率の絶対値算出もおこなう必要があると

考えられる。

このような観点から、フィッション・トラック測定のための通常熱中性子照射においても放射化反応率からより正確な核分裂反応率の絶対値算出を検討している。中性子フルエンス測定というより核分裂反応率の直接算出の観点からのモニターガラス確立の検討とガラス中のトラックの熱補正の検討である。フィッション・トラック年代測定では、カドミ比 3.5 以上の照射場を使用することが勧告されている(Hurford, 1990)ので、日本原子力研究所東海研究所の研究炉の照射場では JRR-3M 炉の PN1・PN2 のみが FTD として利用可能な照射場である。しかしまだこの照射場での照射利用回数も少なく今後繰り返して検討を重ねる必要があるが、現在までに得られているデータをもとに今後の見通しを含めてここに報告する。

2. Au・Zr モニターによる照射場の特性

5N Au (レアメタリック社製)および 4N75 ZrO₂ (JMC 社製)をコーニング研究所製の標準ガラスに加えてモニターとしてガラス試料の照射に使用した。これは FTD として利用可能な照射場で試料の U-235 の誘導核分裂トラックによるカドミウム比を測定するのは実用的でないの、金とジルコニウムの放射化反応率から熱中性子束・カドミウム比及び α 値を De Corte et al. (1981) に従って計算し、U-235 の誘導核分裂反応率を推定しようとするものである。Fig.1 は F-Basic

研究施設名: JRR-3M,

研究分野: フィッショントラック地質年代学

R1571 (JRR3M PN2)
Irradiation = 0.5000 min T(i) = 1998/ 2/ 10

1 place of decimals

I = -9	Alpha = -0.90000	Z = -41416.03906
I = -8	Alpha = -0.80000	Z = -18437.22070
I = -7	Alpha = -0.70000	Z = -8329.80957
I = -6	Alpha = -0.60000	Z = -3823.50122
I = -5	Alpha = -0.50000	Z = -1782.87878
I = -4	Alpha = -0.40000	Z = -842.77753
I = -3	Alpha = -0.30000	Z = -401.79266
I = -2	Alpha = -0.20000	Z = -191.24640
I = -1	Alpha = -0.10000	Z = -89.13836
I = 0	Alpha = 0.00000	Z = -39.05173
I = 1	Alpha = 0.10000	Z = -14.38086
I = 2	Alpha = 0.20000	Z = -2.32354
I = 3	Alpha = 0.30000	Z = 3.40230

2 places of decimals

I = 0	Alpha = 0.20000	Z = -2.32354
I = 1	Alpha = 0.21000	Z = -1.53531
I = 2	Alpha = 0.22000	Z = -0.80394
I = 3	Alpha = 0.23000	Z = -0.12569
I = 4	Alpha = 0.24000	Z = 0.50236

3 places of decimals

I = 0	Alpha = 0.23000	Z = -0.12569
I = 1	Alpha = 0.23100	Z = -0.06065
I = 2	Alpha = 0.23200	Z = 0.00390

4 places of decimals

I = 0	Alpha = 0.23100	Z = -0.06065
I = 1	Alpha = 0.23110	Z = -0.05417
I = 2	Alpha = 0.23120	Z = -0.04770
I = 3	Alpha = 0.23130	Z = -0.04123
I = 4	Alpha = 0.23140	Z = -0.03477
I = 5	Alpha = 0.23150	Z = -0.02831
I = 6	Alpha = 0.23160	Z = -0.02186
I = 7	Alpha = 0.23170	Z = -0.01541
I = 8	Alpha = 0.23180	Z = -0.00897
I = 9	Alpha = 0.23190	Z = -0.00253

5 places of decimals

I = 0	Alpha = 0.23130	Z = -0.00253
I = 1	Alpha = 0.23191	Z = -0.00188
I = 2	Alpha = 0.23192	Z = -0.00124
I = 3	Alpha = 0.23193	Z = -0.00060
I = 4	Alpha = 0.23194	Z = 0.00004

R1571 (JRR3M PN2)
Irradiation = 0.5000 min T(i) = 1998/ 2/ 10

k(0)[ZR-96 : 743.729keV] = 1.33911E-05
k(0)[ZR-94 : 724.199keV] = 9.33094E-05
k(0)[ZR-94 : 756.729keV] = 1.15079E-04
k(0)[AU-197 : 411.805keV] = 1.00000E+00

I(0)[ZR-96] = 1.372
I(0)[ZR-94] = 0.048
I(0)[AU-197] = 1044.681

a = 2.74039
b = 2.92046
Alpha(0) = -0.17009

Alpha = 0.23193

f = 107.354

Cd Ratio [ZR-96] = 2.712
Cd Ratio [ZR-94] = 122.154
Cd Ratio [AU-197] = 11.292

Fig. 1. An output example for α and Cd calculation with Au and Zr monitors

(Win95/98 対応)によって書かれた α 値・カドミウム比計算プログラムによる出力例である。この計算値は厚さ 1 mm のカドミウム容器を用いた実測値 (Table 1) にかなり近い。

Table 1. Cd ratio at PN2, JRR-3M

Nuclide	Cd ratio	R. R. Date
Au-197	14.84 \pm 0.54	98/2
Zr-94	70.39	98/2
Zr-96	2.74	98/2

3. モニターガラスの較正

コーニング研究所作成の標準ガラス CN1・CN5 をフィッション・トラックのモニターとして使用した。CN5 のウラン含有量を 12.17ppm (Bellemans et al. (1995) とするとき、トラック計数データの比から推定される JR1・JR2 などの黒曜石のウラン含有量 Table 2 に示した。そ

Table 2. U-content determination of obsidians by fission track analysis

Rock Name (Locality)	Uranium(ppm)
JR-1 (Wada Pass)	8.82 \pm 0.08
JR-2 (Ibid.)	12.25
Nitto (Kagoshima Pref.)	6.28
Ushihana (Ibid.)	2.36
Mifune (Ibid.)	2.62
Nagatani (Ibid.)	2.61

の結果は放射化分析のデータと良く一致している。このことはガラス中の核分裂片トラックの有効飛程が試料によってあまり変わらないこと、トラック計数では安定したデータが得られることから、有効飛程の標準値を定めることによりモニターガラスのトラック密度から核分裂反応率を推定する試み (鈴木, 1992) が可能であることを示している。

Au の熱中性子束 (スペクトル未補正) に対応する CN5 の誘導トラック密度の 1 例を Table 3 に示した。

Table 3. Thermal neutron flux (Conventional) and induced track density of CN5 dosimeter glass

$\phi_{th}(Au) = (3.729 \pm 0.051) \times 10^{13} / \text{cm}^2$
$\rho_i(CN5) = (1.620 \pm 0.044) \times 10^5 / \text{cm}^2$

4. 等温プラトー (ITP) 法によるアニーリング補正

ガラス試料では U-238 の自発核分裂片トラック (化石トラック) が地質学的な時間のなかでフェイディングをおこしていることが多いので、これを補正する必要がある。中性子を照射した試料と未照射試料とを同時に一定時間加熱し誘導核分裂片トラックの不安定部分を消去し、自発/誘導トラック長が一致したときの自発/誘導トラック密度比から年代値を

算出するプラトー法が近年発展してきている。Fig. 2 は JR1 の 151℃での等温プラトー (ITP) 法によるアニーリング特性の 1 例を示したものである。ガラスの FTD ではこのように外部ディテクターを用いずに自発/誘導トラックともに試料そのものから計測することが求められるので、鉱物試料で一般に用いられる年代標準試料を用いたゼータ法は必ずしも必要でなくいことになる。

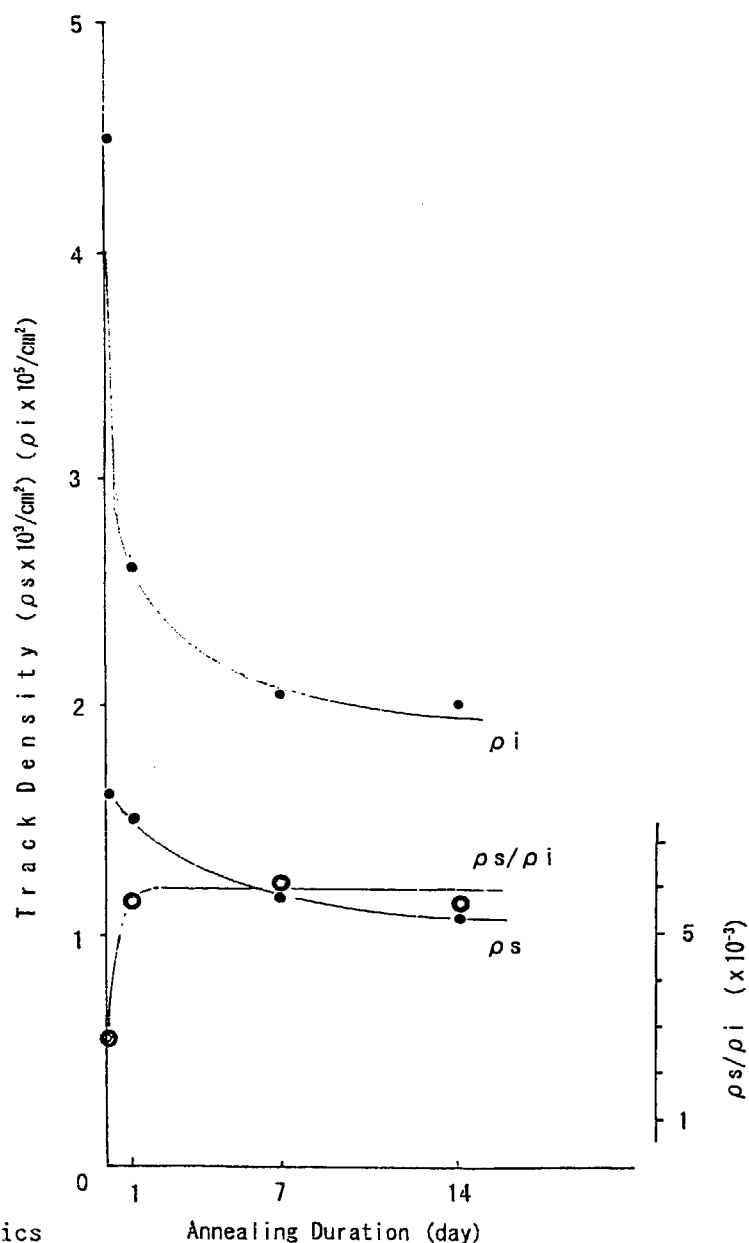


Fig. 2.
Annealing characteristics
of JR-1 obsidian

5. まとめ

Au・Zr モニターにより照射場の特性を推定するための計算プログラムを整備し、Au・Zr モニターの放射化による Au・Zr のカドミウム比を求めた。この計算値は Au・Zr モニターとカドミウム容器を用いて得た実測値と比較的良く一致しているといえるが、単独で使用しても信頼できる値を得られるようにするためにはなお慎重な測定を多数繰り返す必要がある。

今後さらに検討を繰り返し、照射場での試料照射時の中性子スペクトルを考慮したフィッション・トラック測定用のモニターガラスにおける U-235 核分裂反応率を推定すること、またモニターガラスの核分裂片トラックの有効飛跡長を標準化することで、黒曜石などガラス試料のフィッション・トラック年代測定値の標準化を確立したい。

6. 謝辞

JR1 の 等温プラトー法によるアニーリング実験はメルボルンのラトロブ大学地球科学教室滞在中に行った。A. J. W. Gleadow 教授・B. Khon 博士はじめ

フィッショントラック研究グループ及び同教室スタッフに謝意を表す。また標準ガラスを提供されたコーニング研究所の H. W. H. Schreurs 博士・JR1 原岩試料を提供された元地質調査所の安藤 厚博士に謝意を表す。

7. 引用文献

- Bellemans, F. et al. (1995): Radiat. Meas., 24, 153-160.
 De Corte, F. et al. (1981): Jour. Radioanal. Chem., 62, 209-255.
 Hurford, A. J. (1990): Chem. Geol., 80, 171-178.
 Hurford, A. J. and Green, P. F. (1983): Isot. Geosci., 1, 285-317.
 鈴木達郎(1992): 放射線, 18, 16-24.

8. 成果の発表

- 鈴木達郎(1998): 国内研究用原子炉の照射場の特性からみたフィッション・トラック年代測定と放射化分析. 日本地質学会西日本支部会報. No. 112, p. 3-4.

Recoil Effect in Water-Soluble Macrocyclic Metal Complex Systems (Continued) (In the Case of Water-Soluble Metal Phthalocyanine Systems)

Hitoshi Shoji

Department of Chemistry, University of Tsukuba

7-3 水溶性大環状金属錯体系における反跳効果 (続) (水溶性金属フタロシアニン系について)

莊司 準

筑波大学化学系

【Introduction】 Macrocyclic metal complex compounds such as metal porphyrins or metal phthalocyanines provide us with very suitable systems for the study of recoil phenomena because of their strong resistance for irradiations due to the π -electron resonance of cyclic structures. Recently hydrophilic groups have been introduced to the ring structure, for example a carboxylate, sulfonate and N-methylpyridyl group and so forth. As the result more kinds of variations can be expected in the combination of a central metal atom and a ligand. Moreover even a complex ion associate could be obtained in some cases. In addition their high water-solubility has made the wet chemical separation remarkably easier after the irradiation than in the previous case without hydrophilic groups in the structure. The typical example is the case of metal phthalocyanines. Although metal phthalocyanine is very stable against high radiation dose and it shows us pure recoil effect clearly without the interfere due to radiation decomposition, we had no suitable solvent for the wet chemical treatment after the irradiation other than conc. sulfuric acid, even in the case of which, there were severe time and temperature restrictions for its usage (keeping

as the solution within 3 min or so at ice-cooled temperature, for example).

As for the irradiated water-soluble metal phthalocyanine, dissolution in water is very easy and prompt, and ion exchange technique is applicable for the separation of ionic products, which remarkably shortened the time for the chemical treatment. If the labelled bare metal ions could be obtained with high specific activity using these water-soluble metal complexes, it must be a great merit for the simple and easy production of a radio tracer, especially in the field of radiopharmaceutical chemistry.

In this study triammonium hydrogen copperphthalocyaninetetrasulfonate and its homologue of cobalt (II) as a central metal atom were taken for the investigation. The chemical structure is shown in Fig. 1.

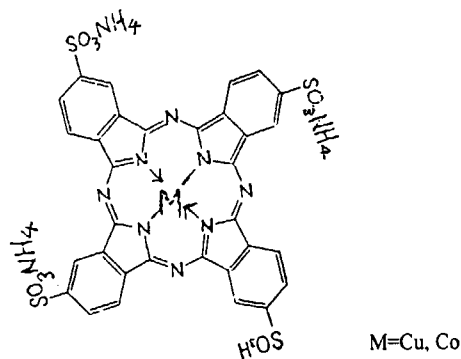


Fig. 1. Chemical Structure of the Complex Used.

【Experimental】 1) Sample Preparation The preparation of the complexes were carried out according to Fukada¹⁾. In the case of copper complex 4-sulfophthalic acid tri-ammonium salt, highly pure copper metal powder and urea were mixed with water and the mixture was gradually heated to 230 °C. Deep blue vigorous crude product was dissolved in hydrochloric acid and the solution was concentrated. A saturated solution of ammonium chloride was added and the solution was warmed. Then blue black precipitate was salted out. This salt was resalted out from conc. ammonium chloride in 1M Hydrochloric acid. The fine crystal obtained was treated with hot ethanol several times. Coexisting ammonium chloride was removed by sublimation at 170-190°C.

In the case of the cobalt complex cobalt(II)acetate tetrahydrate was used as the starting material instead of cobalt metal powder and the preparation procedure was almost similar to the copper complex case.

The samples were confirmed by elemental analysis and absorption spectra in uv-visible region.

2) Irradiation Samples were irradiated in the pneumatic tube of JRR-3M Reactor of JAERI at Tokai for 2-3 min at dry ice temperature. Sometimes they were also irradiated in the incore tube of TRIGA MARK II Reactor at Rikkyo University for 2 hr at the same temperature as the comparison.

3) Chemical Separation After the irradiation the samples were stored at dry ice temperature until the time of wet chemical separation. The samples were dissolved in water without containing carriers, because the measurement of enrichment factor was one of the purposes of

this investigation. In almost all the cases the sample was dissolved almost instantaneously. An aliquot of the sample solution was taken and added to the column of anion exchanger (Dowex-1, X8, NO₃-form, 100-200 Mesh). The elution was done with water until the volume of the effluent attained to almost 40ml, which was more than 2 times of that from the another cation exchanger column. Another aliquot was taken into the column of cation exchanger (Dowex-50, X8, NH₄-form, 100-200 Mesh). The effluent was collected until the blue color disappeared completely from the effluent. The volume to that point was less than 15 ml in all the cases. The volume of the untreated solution and two kinds of the effluent was adjusted to the same using water. The γ -spectrum of each fraction was measured under the constant geometrical condition for the detector.

4) Measurement of Activity The γ -spectra of fractions prepared were measured by a pure Ge detector connected to a computer system and analysed. The peak area concerned in γ -spectra was calculated by a computer.

5) Measurement of Enrichment Factor The enrichment factor of ⁶⁴Cu in cation fraction was measured using ICP equipment after the activity of ⁶⁴Cu decayed out while that of ⁶⁰Co was measured spectrophotometrically with 1-nitroso-2-naphthol as the coloring reagent.

【Result and Discussion】 As for the attaching position of sulfonate group 4 kinds of different combinations can be thought, each of which corresponds to each geometrical isomer both in the copper and cobalt complex cases. However, no difference due to such possible isomers was observed in column chromatography with ion exchangers and

sailica gel, which showed very little difference in chemical behaviour among the isomers and which implies the mixture of these isomers was treated in this study.

The wet chemical separation was very simple and clear, which was far easier than ordinary metal phthalocyanines without hydrophilic group. In this case metal phthalocyaninetetrasulfonate anions were retained very tightly in a short deep colored band at the top of the anion exchanger column and the effluent containing bare labelled cations was completely colorless. From the cation exchanger column deep colored metal phthalocyaninetetrasulfonate anions appeared very soon and was eluted out almost in passing freely.

Radiochemical yields of bare metal ions (η) and retention (R) were calculated for ^{64}Cu and ^{60}Co , respectively, which are shown in Table 1, as well as the enrichment factor (E) for cationic fractions.

Table. 1 Results of wet chemical separation.

Nuclide	η (%)	R (%)	E
^{64}Cu	95.7 ± 0.7	3.2 ± 1.8	~ 15
^{60}Co	94.0 ± 3.2	2.6 ± 0.2	~ 4

Statistics represent standard deviations from the repetition.

The sum of η and R was less than 100%. The main reason was thought that a small amount of cationic species eluted out later.

These retention values are a little smaller than those for α — form Cu- and Co-phthalocyanine, 4.5 ± 0.2 and 3.0 ± 0.1 (%), respectively, reported by Kujirai et al²⁾, which implies the little effect of introduction of sulfonate group to the π -electron resonance

structure. In contrast to the present case the water-soluble metal porphyrin showed much higher retention in general, which sometimes exceeded 50%. Therefore water-soluble metal porphyrins are not suitable for the production of labelled metal ion tracer.

The enrichment factor for cationic species was small, considering the typical common case of pure hot-atom effect. If the E value depends only on the radiolytic decomposition of the target material, it attains to almost 20% in Co complex and 7% in Cu complex, though these values seems to be too large as the compound having very stable metal phthalocyanine structure. There might be some problems in the preparation of the samples such as the remaining of free metal or metal ions to be introduced to the central position of the complex. At the beginning of this study much higher enrichment factor or $^{64}\text{Cu}^{2+}$ and $^{60}\text{Co}^{2+}$ of much higher specific activity were expected, the simple and easy production of which, would give advantages to radiopharmaceutical region. One of the proposals to prevent radiolytic decomposition of this kind of complex compounds is thought to be the partial substitution of H atoms by Cl. The copper phthalocyanine derivative in which all the hydrogen atoms are substituted by chlorine atoms (commercially it is called phthalocyanine Green) is extremely resistant to the radiation but no suitable solvent has been found for it. So as the compromise between these characters, partial chlorination of water-soluble metal phthalocyanine is taken into consideration.

In this study simple production of labelled metal cations using water-soluble metal phthalocyanine to be highly resistant to

radiation was initially thought to obtain ^{186}Re and ^{188}Re of high specific activity. Accelerators have no advantages for their production, because of low reaction cross section and the problems of biproducts. However, the actual use of them is very much expected in the field of nuclear medicine for their duplicate roles of γ -emitting detection tracer for diagnoses and of β -source for radiotherapy. Many times of trial have been done but pure water-soluble rhenium phthalocyanine target has not been obtained, though the trial is still continued.

Another application of water-soluble metal phthalocyanine was tried. It was to use them as the material for preparation of very thin molecular film to observe irradiation effect microscopically by the use of an electron microscope with very high resolution. In some lucky case the molecular structure was reported in constituent atomic level using metal phthalocyanine derivatives. Although water-soluble metal phthalocyanine was suitable for very thin film using its diluted aqueous solution, it was very easily decomposed under the electron beam in a high resolution electron microscope. Instead of them much more tough phthalocyanine Green (above-mentioned all chlorinated Cu-phthalocyanine) is now being tested. Even using it, it needs special technique newly developed and some luck to distinguish irradiation damage previously received in a reactor or a ^{60}Co -facility from damage by energetic electrons of the electron microscope itself.

378 and 1141(1953).

- 2) O.Kujirai, N. Ikeda, Radiochem. Radioanal. Letters, Vol. 15, 67(1973).

Publications

- 1) H. Shoji, "Some Specific Features of the Recoil Behaviour of Central Metal Atoms in the Solid System of Water-Soluble Metalloporphyrin Ion Associates," Res. Report of Lab. of Nucl. Sci., Tohoku Univ. Vol. 29, 57(1996).
- 2) H. Shoji, "Correlation of Some Recoil Features in the Water-Soluble Metalloporphyrin Ion Associate Solid System with Structural Factors," J. Radioanal. Nucl. Chem., Vol. 239, 191(1999).

References

- 1) N. Fukada, Nihon Kagaku Zasshi, Vol. 75,

7-4 石英中の酸素空格子生成: 内部 α 粒子照射による効果 及び γ 線の線量率効果

Formation of oxygen vacancies in quartz: the radiation effect given by internal α particles and the dose rate dependence of external γ rays

大阪大学大学院理学研究科宇宙地球科学専攻* 豊田 新

Shin Toyoda, Department of Earth and Space Science, Graduate School of Science,
Osaka University*

(*現在の所属 岡山理科大学理学部応用物理学科)

(*present affiliation: Department of Applied Physics, Faculty of Science, Okayama University of Science)

1. 目的

ESR (電子スピン共鳴) 年代測定法は、サンゴや貝殻、化石の歯、骨に適用され、最近約200万年間の第四紀の年代測定法として発展し、応用分野が拡大してきた(Ikaya, 1993)。石英は地球表面において最も普遍的に見られる鉱物の1つであるが、これを用いて、断層運動、テフラ(火山噴出物)、堆積物、フリントなどの年代測定が行われてきた(Ikaya, 1993)。年代測定範囲が約200万年に限られるのは、ESRで検出できる常磁性格子欠陥としての準安定な状態の寿命のためであるが、最近になって、酸素空格子に関連した常磁性格子欠陥である E'_1 中心の信号強度が、花崗岩中の石英で、年代と相関があることが示された(Odom and Rink, 1989)。

一方、筆者らは E'_1 中心の生成と消滅の基礎的な研究から、 E'_1 中心の信号強度はその前駆体である反磁性の状態も含めた酸素空格子量全体に関連していることを明らかにした(Toyoda and Ikaya, 1991)。また、この前駆体である酸素空格子は他のESR信号に比べて熱的に非常に安定であり、室温に置かれていれば、地球史全体の年代にわたって安定であることを示した(Toyoda and Ikaya, 1991)。年代既知の花崗岩試料について石英中の酸素空格子量を E'_1 中心に変換して(Toyoda and Ikaya, 1991)計測したところ、やはり年代と相関があることがわかった(Toyoda et al., 1992, 1994)。

しかし、この酸素空格子を用いて年代測定を行うためには、自然において石英中の酸素空格子の生成過程を明らかにしなくてはならない。Rink and Odom (1991)は石英のマトリックス中に極微量に含まれるU, Thの壊変の際の α 反跳によって作られると考えた。しかし、筆者らは石英の外部の他の鉱物中の放射性核種からの β 及び γ 線によって生成されたと考え、 γ 線照射によって生成される酸素空格子量を調べたところ、年代と放射性核種の量から推定される被曝線量に対して生成されると考えられる酸素空格子量が、自然に石英中に存在する酸素空格子量とほぼ合うことを見出した(Toyoda et al., 1996)。

本研究では、次の2点を明らかにすることを目的にした。

(1) Rink and Odom (1991)では、計算コードTRIM (Ziegler, 1989)に基づいて α 反跳核種による酸素空格子の生成を推定した。ここでは石英内部から α 粒子を石英に照射し、生成する酸素空格子量を調べることで、TRIMによる計算の妥当性を評価する。

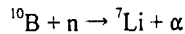
(2) Toyoda et al., (1996)において行った γ 線照射の線量率は、自然放射線の線量率の 10^0 - 10^{11} 倍程度であった。酸素空格子生成の γ 線線量率依存性を調べることによって、ここで用いた線量率が自然放射線を模擬するのに適切であったかどうかを評価する。

γ 線照射施設・Co-60照射施設(東海研究所)、原子炉・JRR-3(東海研究所)、照射効果

2. 内部起源 α 線によって生成する酸素空格子

(1) 実験方法

ホウ素を含む石英を合成し、熱中性子を照射することによって、



の核反応によって石英中に生成する酸素空格子量を ESR によって定量する。

ホウ素を含む石英及びホウ素を含まない純粋石英（結晶）は日本電波工業に依頼して水熱合成法によって合成した。ホウ素を含む石英については、熱中性子即発 γ 線分析によってドーブされたホウ素量を定量した。次にこれらの試料 100mg 及び 53mg をとり、 1×10^{16} 個/cm² の熱中性子を照射して上記核反応を起こさせた。300°C 15 分加熱して酸素空格子を常磁性の E_1' 中心に変換して (Toyoda et al., 1992) これを ESR 測定装置 (JEOL, RE-3X) で定量し、この量を酸素空格子量とした。測定条件は、マイクロ波出力 0.01 mW、磁場変調 100kHz、磁場変調幅 0.1mT、測定磁場範囲 $g=2.001$ 付近 5 mT、掃引速度、時定数は信号強度によってそれぞれ、8分または16分、0.3秒または1秒とした。

(2) 結果と考察

ホウ素をドーブした石英中に含まれるホウ素含有量は、熱中性子即発 γ 線分析の結果、1.5ppm であった。

ESR 測定によって E_1' 中心の信号が観測され、その信号強度から、生成した酸素空格子濃度を計算した。その結果は表 1 の通りである。ホウ素を含まない純粋石英にも酸素空格子が生成したが、これは、熱中性子照射の時に同時に照射される速中性子及び γ 線によって生じたものであると考えられる。従って、熱中性子のみの効果は、ホウ素

をドーブした石英に生成した酸素空格子量と、純粋石英に生成した酸素空格子量との差で与えられ、その値は、 1.0×10^{14} 個/g となった。

計算コード TRIM による計算の結果、上記核反応 1 回あたりに生成する酸素空格子数は、 α 粒子によって 47 個、Li 粒子によって 106 個、合計 153 個となった。これをもとに今回の実験条件の下で生成する酸素空格子数を計算すると、表 1 に示されるように、 1.0×10^{14} 個/g となった。

このように、実験結果と理論計算による結果とが、偶然かもしれないがきわめてよく一致した。熱中性子のフルーエンスを変えるなどして、確認の実験がさらに必要であるが、よく一致しているとすれば、計算コード TRIM による計算が実際に生成する酸素空格子を正確に与えること、また、300°C 15 分加熱して酸素空格子を常磁性の E_1' 中心に変換する方法 (Toyoda et al., 1992) によって、石英中の酸素空格子全部の量が定量できることをも示していると考えられる。

さらに、これは、Rink and Odom (1991) の、計算コード TRIM に基づく、 α 反跳核種による酸素空格子の生成量が正しいということを意味するであろう。つまり、ppb オーダーの U, Th が石英のマトリックス中に一様に分布していれば、観測される酸素空格子量が α 反跳核種によって生成したとして説明できることになる。そうであれば、次の課題は、U, Th が石英のマトリックス中に一様に分布しているかどうか、インクルージョンなどの中に濃集していたりしないかどうかを調べることとなる。

表1 ホウ素をドーブした石英に熱中性子を照射して生成した酸素空格子

	質量 (mg)	ホウ素含有量 (ppm)	生成した酸素空 格子量 (g^{-1})	計算による酸素空 格子量 (g^{-1})
ホウ素をドーブした石英	53	1.5	3.5×10^{14}	1.0×10^{14}
高純度石英	100	—	2.5×10^{14}	0
差			1.0×10^{14}	1.0×10^{14}

3. γ 線によって生成する酸素空格子の線量率依存性

(1) 実験方法

岡山県産万成花崗岩 (granitic) 及びアメリカ合衆国ニューメキシコ州のバイアスカルデラ付近のテフラ (volcanic) から抽出した石英の粉末 (100-250 μ m) を準備し、600 $^{\circ}$ Cで30分加熱してすべての酸素空格子を消去した。各々の試料を100mgずつ6試料に分け、それらに γ 線照射を行った。照射は日本原子力研究所東海研究所のCo-60 γ 線照射施設を使用した。試料をアルミ箔で栓をした直径5mm長さ約1cmのパイレックスのガラス管に入れ、それをさらに直径10mmのパイレックスのガラス管に入れた。さらにそれを肉厚1mmの直径18mmの両端に栓をしたアルミ管に入れて照射した。線量率をそれぞれ、105, 160, 250, 320, 430, 590 C/kg \cdot hとして、照射時間を変えて6試料とも 7×10^4 C/kgの照射をした。300 $^{\circ}$ C15分加熱して酸素空格子を常磁性の E_1' 中心に変換して (Toyoda et al., 1992) これをESR測定装置 (JEOL, RE-1X) で定量し、この量を酸素空格子量とした。測定条件は上記と同様である。

(2) 結果と考察

結果を図1に示す。両方の試料ともごく小さい線量率依存性が観測された。この線量率の範囲で

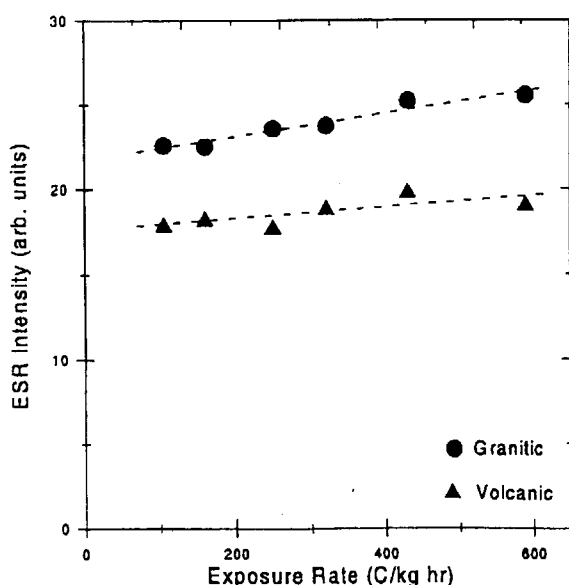


図1 酸素空格子生成量の γ 線線量率依存性

信号強度は10%程度しか変化しないことがわかった。このデータを直線に当てはめてよいかどうかは問題であるが、自然放射線の線量率まで外挿しても線量率依存性が非常に大きな問題になることはないと考えられる。

花崗岩に含まれる石英の酸素空格子量からESRを用いて年代を求めようとするとき、もしその酸素空格子が石英外部の鉱物中の放射性核種からの β 線及び γ 線であるならば、通常のESR年代測定の際に行うように、人為 γ 線照射でその生成を模擬して、その傾向を外挿することにより被曝線量を求めることが可能になる。その際の照射についての線量率依存性は、根本的にその方法が無意味になるほど大きくはない。しかし、10%以内の精度で正確に年代を求めようとするときには、考慮しなくてはならないファクターであるといえる。

4. 成果発表

Toyoda, S. and Hattori, W. (submitted) Formation and decay of the E_1' center and of its precursor, Appl. Radiat. Isot.

豊田新・池谷元伺 γ 線による石英の酸素空格子の生成 研究会・放射線検出器とその応用 1998年1月21-23日 高エネルギー加速器研究機構

Toyoda, S., Hattori, W., and Ikeya, M., Formation and decay of the E_1' center and of its precursor. International Conference on Biodosimetry and 5th International Symposium on ESR Dosimetry and Applications, June, 22-26, 1998, Medical Radiological Research Center of Russian Academy of Medical Sciences, Obninsk, Russia.

豊田新 石英中の E_1' 中心の生成過程と年代測定への応用 第14回ESR応用計測研究発表会 1998年11月21日 大阪大学 豊中

謝辞

石英を合成して試料を提供いただいた日本電波工業の加賀見氏に、また石英中のホウ素の定

量をしていただいた日本原子力研究所米沢氏に深く感謝いたします。

引用文献

- Ikeya, M. (1993) New Applications of Electron Spin Resonance, Dating, Dosimetry and Microscopy, World Scientific, Singapore.
- Odom, A. L. and Rink, W. J. (1989) Natural accumulation of Shottky-Frenkel defects: Implications for a quartz geochronometer, *Geology*, 17, 55-58.
- Rink, W. J. and Odom, A. L. (1991) Natural alpha recoil particle radiation and ionizing radiation sensitivities in quartz detected with EPR: implications for geochronometry, *Nucl. Tracks Radiat. Meas.*, 18, 163-173.
- Toyoda, S. and Ikeya, M. (1991) Thermal stabilities of paramagnetic defect and impurity centers in quartz: Basis for ESR dating of thermal history, *Geochem. J.* 25, 437-445.
- Toyoda, S., Ikeya, M., Morikawa, J., and Nagatomo, T. (1992) Enhancement of oxygen vacancies in quartz by natural external β and γ ray dose: a possible ESR Geochronometer of Ma-Ga range, *Geochem. J.* 26, 111-115.
- Toyoda, S. and Ikeya, M. (1994) Formation of oxygen vacancies in quartz and its application to dating, *Quatern. Geochronol.* 13, 607-609.
- Toyoda, S., Rink, W. J., Schwarcz, H. P., and Ikeya, M. (1996) Formation of E_1' precursors in quartz: applications to dating and dosimetry, *Appl. Radiat. Isot.*, 47, 1393-1398.
- Ziegler, J. F. (1989) Software - TRIM version 5.0 IBM Research (unpublished).

謝 辞

本報告書の発刊にあたり、多くの皆様から多大なご協力を頂きました。編集に際し、ご協力頂いた、研究炉部長海江田圭右氏、研究炉部次長高柳政二氏、研究炉部次長高橋秀武氏、研究炉利用課本田由里恵さん、また本報告書の査読を頂いたJRR-4管理課長桜井文雄氏に深く感謝致します。

付 録 (1)

Appendix (1)

This is a blank page.

付 録(1)

成果報告論文・参考文献一覧

No.	成果報告論文及び参考文献	頁
1-1-1	[1]A.C.Momin,E.B.Mirza and M.D.Matherws,J.Mat.Sci.Lett.,10(1991)1246. [2]S.A.Howard,J.Yau and H.U.Anderson,J.Am.Ceram.Soc.75(1991)1685. [3]T.Hashimoto,N.Matsushita,Y.Murakami,N.Kojima,K.Yoshida,H.Tagawa, M.Dokiya and T.Kikegawa,Solid State Communication 108(1998)691.	59
1-1-2	[1]R.W.Whatmore and A.M.Glazer,J Phys.C12,1505(1979). [2]H.Fujishita and S.Hoshino,J Phys.Soc.Jpn.53,226(1984). [3]E.Sawaguchi,J Phys.Soc.Jpn.7,110(1952). [4]F.Jona,G.Shirane and R.Pepinsky,Phys.Rev.97,1584(1955). [5]D.L.Corker,A.M.Glazer,J.Dec,K.Roleder and R.W.Whatmore,Acta Cryst.B53, 135(1997). [6]H.Fujishita,Y.Shiozaki,N.Achiwa and E.Sawaguchi,J Phys.Soc.Jpn.51,3583 (1982). [7]H.Fujishita and S.Katano,J Phys.Soc.Jpn.66(1997)3484.	60
1-1-3	[1]M.Sakata and M.Sato:Acta Cryst.A46(1990)263-270. [2]S.Kumazawa et al.:JAERI NSL Report April 1995-March 1996,99. [3]M.Takata et al.:Nature 377(1995)46-49. [4]F.Izumi et al.:Proc.Int.School on Powder Diffraction,Allied Publishers,New Delhi(1998)pp.24-36. [5]M.Sakata et al.:J.Appl.Cryst.26(1993)159-165.	62
1-1-4	[1]M.Sakata and M.Sato:Acta Cryst.A46(1990)263-270. [2]S.Kumazawa et al.:JAERI NSL Report April 1995-March 1996,99. [3]M.Takata et al.:Nature 377(1995)46-49. [4]M.Sakata et al.:J.Appl.Cryst.26(1993)159-165.	63
1-1-5	[1]T.Furubayashi,T.Matsumoto,T.Hagino and S.Nagata,J.Phys.Soc.Jpn.63,3333 (1994).	64
1-1-7	[1]K.Aizawa,H.Tomimitsu,H.Tamaki and A.Yoshinari:(PROGRESS REPORT ON NEUTRON SCATTERING RESEARCH,April 1,1996-March 31),1997, 54. [2]K.Aizawa,H.Tomimitsu,H.Tamaki and A.Yoshinari:(PROGRESS REPORT ON NEUTRON SCATTERING RESEARCH,April 1,1997-March 31),1998, 93.	66
1-1-8	[1]T.Suzuki:Jpn.J.Appl.Phys.Series 8(1993)267. [2]see for example,M.Kohgi et al.:J.Phys.Soc.Jpn.65(1996)Suppl.B99. [3]T.Chattopadhyay et al.:Phys.Rev.B49(1994)15096. [4]K.Iwasa et al.:Physica B259-261(1999)285. [5]T.Kasuya and T.Suzuki:J.Phys.Soc.Jpn.61(1992)2628. [6]K.Iwasa et al.:unpublished. [7]N.Wakabayashi and A.Furrer:Phys.Rev.B13(1976)4343.	67

1-1-9	<p>[1] A. Ochiai et al.: J. Phys. Soc. Jpn. 59(1990)4129.</p> <p>[2] M. Kohgi et al.: Physica B 230-232(1997)638; K. Iwasa et al.: unpublished.</p> <p>[3] M. Kohgi et al.: Phys. Rev. B 56(1997)R11388.</p> <p>[4] T. Goto et al.: Physica B 230-232(1997)702.</p> <p>[5] A. Ochiai et al.: Physica B 186-188(1993)437.</p> <p>[6] H. A. Mook and R. M. Nicklow: Phys. Rev. B 20(1979)1656; H. A. Mook and F. Holtzberg: Valence Fluctuations in Solids (North Holland, 1981) p.113.</p>	68
1-1-12	<p>[1] H. Yamauchi, H. Onodera, K. Ohoyama, T. Onimaru, M. Kosaka, M. Ohashi, Y. Yamaguchi, J. Phys. Soc. Jpn 68(1999) in press.</p> <p>[2] J. Bauer and J. Debuigne: C. A. Acad. Sci. Ser. C 274(1972)1271.</p> <p>[3] P. K. Smith and P. W. Gilles, J. Inorg. Nucl. Chem 29(1967)375.</p> <p>[4] T. Onimaru, H. Onodera, K. Ohoyama, H. Yamauchi, Y. Yamaguchi, J. Phys. Soc. Jpn 66(1999) in press.</p>	72
1-1-13	<p>[1] P. J. Webster, K. R. A. Ziebeck, S. L. Town and M. S. Peak: Philos. Mag. 49(1984) 295.</p> <p>[2] F. Izumi, The Rietveld Method, ed. R. A. Young (Oxford Univ. Press, Oxford, 1993) Chap. 13.</p>	74
1-1-14	<p>[1] T. Suzuki et al., Phys. Rev. B 57, R3229(1998).</p> <p>[2] Fukase et al., Jpn. J. Appl. Phys. Series 7, 213(1992).</p> <p>[3] T. Goto et al., J. Phys. Soc. Jpn. 66, 2870(1997).</p> <p>[4] S. Katano et al., Proc. of 4th Int. Symposium on Advanced Physical Fields: Quantum Phenomena in Advanced Materials at High Magnetic Fields, 315 (1999).</p>	76
1-1-15	<p>[1] J. K. Furdyna: J. Appl. Phys. 64(1988)R29.</p> <p>[2] T. M. Giebultowicz: J. Appl. Phys. 67(1990)5096.</p> <p>[3] Y. Ono et al.: J. Phys. Chem. Solids, in press.</p>	77
1-2-4	<p>[1] M. Uehara, T. Nagata, J. Akimitsu, H. Takahashi, N. Mori, and K. Kinoshita, J. Phys. Soc. Jpn. 65, 2764(1996).</p> <p>[2] S. Katano, T. Nagata, J. Akimitsu, M. Nishi, and K. Kakurai, Phys. Rev. Lett. 82, 636 (1999).</p> <p>[3] T. Nagata, H. Fujino, J. Akimitsu, M. Nishi, K. Kakurai, S. Katano, M. Hiroi, M. Sera, and N. Kobayashi (submitted).</p> <p>[4] A. Onodera, Y. Nakai, N. Kunitomi, O. A. Pringle, H. G. Smith, R. M. Nicklow, R. M. Moon, F. Amita, and N. Yamamoto, Jpn. J. Appl. Phys. 26, 152(1987).</p> <p>[5] T. Nagata, M. Uehara, J. Goto, J. Akimitsu, N. Motoyama, H. Eisaki, S. Uchida, H. Takahashi, T. Nakanishi, and N. Mori, Phys. Rev. Lett. 81, 1090(1998).</p>	84
1-2-5	<p>[1] see for example, T. Takabatake, F. Iga, T. Yoshino, Y. Echizen, K. Katoh, K. Kobayashi, M. Higa, N. Shimizu, Y. Bando, G. Nakamoto, H. Fujii, K. Izawa, T. Suzuki, T. Fujita, M. Sera, M. Hiroi, K. Maezawa, S. Mock, H. v. Löhneysen, A. Brückl, K. Neumaier, K. Andres, J. Magn. Magn. Mater. 177-181(1998)277.</p> <p>[2] F. Iga, N. Shimizu, T. Takabatake, J. Magn. Magn. Mater. 177-181(1998)337.</p>	86

1-2-6	<p>[1] M. Kohgi, T. Osakabe, K. Iwasa, J. M. Mignot, I. N. Goncharenko, Y. Okayama, H. Takahashi, N. Mori, Y. Haga, and T. Suzuki, J. Phys. Soc. Jpn. 65(1996)supple. B, p. 99.</p> <p>[2] T. Osakabe, M. Kohgi, K. Iwasa, N. Nakajima, J. M. Mignot, I. N. Goncharenko, Y. Okayama, H. Takahashi, N. Mori, Y. Haga, and T. Suzuki, Physica B 230-232 (1997)645.</p> <p>[3] M. Kohgi, T. Osakabe, K. Iwasa, J. M. Mignot, I. N. Goncharenko, P. Link, Y. Okayama, H. Takahashi, N. Mori, Y. Haga, and T. Suzuki, Rev. High Pressure Sci. Technol., 7(1998)221.</p> <p>[4] Y. Okayama, Y. Ohara, S. Mitsuda, H. Takahashi, H. Yoshizawa, T. Osakabe, M. Kohgi, Y. Haga, T. Suzuki and N. Mori, Physica B 186-188(1993)531.</p> <p>[5] H. Takahashi and T. Kasuya, J. Phys. C, Solid State Phys. 18(1985)2697, 2709, 2721, 2731, 2745 and 2755.</p> <p>[6] Y. Haga, Ph.D. thesis, Tohoku University (1995).</p> <p>[7] N. Takeda, Y. S. Kwon, Y. Haga, N. Sato, T. Suzuki and T. Komatsubara, Physica B 186-188(1993)153.</p> <p>[8] T. Osakabe, M. Kohgi, K. Iwasa, K. Kakurai, J. M. Mignot, I. N. Goncharenko, Y. Okayama, H. Takahashi, N. Mori, M. Kubota, H. Yoshizawa, Y. Haga and T. Suzuki, JJAP Series 11p.123.</p> <p>[9] see for example, T. Kasuya, Y. Haga Y. Haga and T. Suzuki, J. Alloys Compounds 219(1995)290.</p>	87
1-2-7	<p>[1] Ramirez, A. P., B. Batlogg, and E. Bucher, 1987, J. Appl. Phys. 61, 3189.</p> <p>[2] Troc, R. and V. H. Tran, 1988, J. Magn. Magn. Mater. 73, 389.</p> <p>[3] Buschow, K. H. J., E. Brück, R. G. van Wierst, F. R. de Boer, L. Havela, V. Sechovsky, P. Nozar, E. Sugiura, M. Ono, M. Date, and A. Yamagishi, 1990, J. Appl. Phys. 67, 5215.</p> <p>[4] Tran, V. H., F. Bouree, G. Andre, R. Troc, Solid State Comm. 98(1996)111.</p>	89
1-2-8	<p>[1] K. Nakajima, and Y. Endoh: J. Phys. Soc. Jpn. 67(1998)1552.</p> <p>[2] S. Sugai et al.: J. Phys. Soc. Jpn. 67(1998)2992.</p> <p>[3] M. Saitoh and H. Fukuyama: J. Phys. Soc. Jpn. 66(1997)3259.</p> <p>[4] S. Yamamoto et al.: J. Phys. Soc. Jpn. 67(1998)3711.</p> <p>[5] I. Korenblit Europhys. Lett. 46, 82(1999).</p>	90
1-2-9	[1] H. Ikeda, K. Iwasa and K. H. Andersen: J. Phys. Soc. Jpn. 62(1993)3832.	92
1-2-10	[1] B. Fåk et al., J. Magn. Magn. Mater., 154(1996)339.	94
1-2-13	<p>[1] S. Itoh et al., Phys. Rev. Lett. 74, 2375(1995).</p> <p>[2] S. Itoh et al., Physica B 241-243, 546(1998).</p> <p>[3] G. Reiter and A. Sjölander, Phys. Rev. Lett. 39, 1047(1977).</p> <p>[4] S. Yamamoto, Phys. Rev. Lett. 75, 3348(1995).</p> <p>[5] N. Hatano and M. Suzuki, J. Phys. Soc. Jpn. 62, 1346(1993).</p> <p>[6] J. Deisz et al., Phys. Rev. B 48, 10227(1993).</p>	97

1-2-14	<p>[1] K. Magishi, S. Matsumoto, Y. Kitaoka, K. Ishida, K. Asayama, M. Uehara, T. Nagata and J. Akimitsu, Phys. Rev. B 57(1998)11533.</p> <p>[2] S. Katano, T. Nagata, J. Akimitsu, M. Nishi and K. Kakurai, Phys. Rev. Lett. 82 (1999)636.</p> <p>[3] T. Nagata, H. Fujino, J. Akimitsu, M. Nishi, K. Kakurai, S. Katano, M. Hiroi, M. Sera and N. Kobayashi, J. Phys. Soc. Jpn. (in press).</p> <p>[4] S. Ohsugi, K. Magishi, S. Matsumoto, Y. Kitaoka, T. Nagata and J. Akimitsu, Phys. Rev. Lett. (in press).</p> <p>[5] J. Akimitsu and Y. Ito, J. Phys. Soc. Jpn. 40(1976)1621.</p> <p>[6] Y. Gotoh, (private communication).</p> <p>[7] T. Nagata, M. Uehara, J. Goto, J. Akimitsu, N. Motoyama, H. Eisaki, S. Uchida, H. Takahashi, T. Nakanishi and N. Mori, Phys. Rev. Lett. 81(1998)1090.</p>	99
1-2-15	<p>[1] M. Matsuda et al., Phys. Rev. B 59, (1999)1060-1067.</p> <p>[2] B. Leuenberger et al., Phys. Rev. B 30, (1984)6300-6307.</p> <p>[3] R. S. Eccleston et al., Phys. Rev. Lett. 81, (1998)1702-1705.</p> <p>[4] L. P. Regnault et al., Phys. Rev. B 59, (1999)1055-1059.</p>	101
1-2-16	<p>[1] A. V. Andreev, K. P. Belov, A. V. Deryagin, Z. A. KaZei, R. Z. Leivitin, A. Menovski. Yu. F. Porov and V. I. Silant'ev, Zh. Exsp. Teor. Fiz. 75(1978)2351: Sov. Phys. JETP, 48(1978)1187.</p> <p>[2] Y. Kuroiwa, M. Kohgi, T. Osakabe, N. Sato and Y. Onuki: Proceedings of the Fifth International Symposium on Advanced Nuclear Energy Research, JAERI-M 93-228(1993)314.</p> <p>[3] Y. Oniki, S. W. Yun, I. Umehara, K. Satoh, F. Fukuhara, H. Sato, S. Takayanagi, M. Shikama and A. Ochiai, J. Phys. Soc. Jpn., 60(1991)2127.</p>	102
1-2-17	<p>[1] J. Takeda et al., J. Phys. Soc. Jpn., 64(1995)2550.</p> <p>[2] Y. Yasui et al., J. Phys. Soc. Jpn., 65(1996)2757.</p> <p>[3] Y. Yasui et al., J. Phys. Soc. Jpn., 66(1997)3194.</p> <p>[4] S. Shamoto et al., J. Phys. Soc. Jpn., 66(1997)1138.</p> <p>[5] H. Sasaki et al., J. Phys. Soc. Jpn., 66(1997)3975.</p>	104
1-2-18	<p>[1] H. Fujioka et al., J. Phys. Chem. Solids, in press.</p> <p>[2] M. C. Martin et al., Phys. Rev. B 53(1996)R14285.</p>	106
1-2-19	<p>[1] S. Nakamura, T. Goto, S. Kunii, K. Iwashita and A. Tamaki: J. Phys. Soc. Jpn., 63 (1994)623.</p> <p>[2] S. Kunii: unpublished.</p> <p>[3] K. Takahashi and S. Kunii: J. Sol. Stat. Chem., 133(1997)198.</p>	107
1-2-21	<p>[1] T. Tsutaoka, et al., J. Magn. Magn. Mater. 167(1997)249.</p> <p>[2] X. Xun, et al., Physica B 241-243(1998)742.</p>	109
1-2-22	[1] E. Matsuoka et al. Physica B 259-261(1999)112.	110
1-2-23	[1] E. Matsuoka et al. Physica B 259-261(1999)112.	111
1-2-24	<p>[1] Y. Andoh, M. Kurisu, S. Kawano and I. Oguro, J. Magn. Magn. Mater. 140-144 (1998)1063.</p> <p>[2] Y. Andoh, M. Kurisu, G. Nakamoto, T. Nobata, S. Nakamura, Y. Makihara, and S. Kawano, Activity Report on Neutron Scattering Research 5(1998)124.</p>	112

1-2-25	[1]K.Motoya and Y.Muraoka:J.Phys.Soc.Jpn.62(1993)2819. [2]K.Motoya,S.Kubota and S.M.Shapiro:J.Magn.Magn.Mater.140-144(1995)75. [3]K.Motoya,K.Nakaguchi and S.Kubota:J.Phys.Soc.Jpn.68 No-7(in press).	113
1-2-26	[1]A.Murakami and Y.Tsunoda submitted to the Phys.Rev.B.	114
1-2-27	[1]A.Ito,S.Morimoto,Y.Someya,Y.Syono and H.Takei,J.Phys.Soc.Jpn.51(1982)3173. [2]Q.J.Harris,Q.Feng,Y.S.Lee,R.J.Birgeneau and A.Ito,Phys.Rev.Lett.78(1997)346. [3]A.Ito,C.Uchikosi,A.Fukaya,S.Morimoto,K.Nakajima, and K.Kakurai,J.Phys.Chem.Solid(1999)in press.	115
1-2-28	[1]W.Bao,C.Broholm,S.A.Carter,T.F.Rosenbaum,G.Aeppli,S.F.Trevino,P.Metcaf,J.M.Honig and J.Spalek: Phys.Rev.Letters 71(1993)766. [2]W.Bao,C.Broholm,J.M.Honig,P.Metcaf and S.F.Trevino,Phys.Rev.B 54(1966)3726. [3]K.Nakayama and T.Moriya:J.Phys.Soc.Jpn.56(1987)2918.	117
1-2-30	[1]S.Kunii,K.Iwashita,T.Matsumura,K.Segawa,186-188(1993)646.	119
1-2-31	[1]K.Takahashi and S.Kunii:J.Sol.Stat.Chem.,133(1997)198. [2]S.Nakamura,T.Goto,S.Kunii,K.Iwashita and A.Tamaki:J.Phys.Soc.Jpn.,63(1994)623.	120
1-2-32	[1]K.Pierre,A.P.Murani,R.M.Galere,J.Phys.F Metal Phys.11(1981)679. [2]Y.Uwatoko,H.Fujii,M.Nishi,K.Motoya,Y.Ito,Solid State Comm.72(1989)941.	121
1-2-34	[1]H.Taguchi,T.Takeishi,K.Suwa,K.Masuzawa and Y.Minachi:Proceedings of the Seventh International Conference on Ferrites(ICF7),C1-311(Bordeaux, 1997). [2]F.Izumi:The Rietveld Method(Oxford University Press,Oxford,1993)Chap.13.	123
1-2-35	[1]Y.Hattori et al.,J.Phys.Condens.Matter,6(1994)8035. [2]O.D.MacMasters et al.,J.Less-Common.Met.,45(1976)275.	124
1-2-36	[1]Y.Mizuno et al.,Phys.Rev.B 57,(1998)5326-5335. [2]M.Matsuda and K.Katsumata,J.Magn.Magn.Mater.177-181,(1998)683-684. [3]M.Matsuda,K.Ohoyama, and M.Ohashi,J.Phys.Soc.Jpn.68,(1999)269-272.	125
1-2-37	[1]R.Sugi,T.Shimomura,M.Matoba,S.Matsuzaka,S.Fujii,N.Hagiwara and S.Anzai.Phys.Stat.Sol (b) 189(1995)K65. [2]A.I.Kapliencko,B.N.Leonov and V.V.Chekin,Soviet Phys.Solid,State 12(1970)3030.	126
1-2-38	[1]M.Goto,K.Takagi,T.Kamimori and H.Tange;Proceeding of the 2nd International Symposium on Physics of Magnetic Materials.(1992,Beijing, China,International Academic Publications)P.508. [2]M.Goto,T.Kamimori,H.Tange,K.Kitao,S.Tomiyoshi,K.Ohoyama and Y.Yamaguchi;J.Magn.Magn.Mater.,140-144(1995)277.	127

1-2-39	[1]J.K.Furdyna,J.Appl.Phys.64(1988)R29. [2]Y.Ono et al.,J.Phys.Chem.Solids,in press. [3]T.M.Holden et al.,Phys.Rev.B26(1982)5074. [4]J.M.Cowley:J.Appl.Phys.21(1950)24.	128
1-2-40	[1]M.Kubota et al.,J.Phys.Chem.Solid,in press. [2]Y.Moritomo et al.,Nature(London)380 141(1996).	129
1-2-41	[1]A.Oyamada,A.Isobe,H.Kitazawa,A.Ochiai,T.Suzuki and T.Kasuya:J.Phys.Soc.Jpn.62(1993)1750. [2]W.N.Stassen,M.Sato and L.D.Calvar:Acta Cryst.B26(1970)1534. [3]K.Ohoyama,H.Hayashi,H.Onodera,M.Ohashi,Y.Yamaguchi,A.Oyamada,M.Kohgi,T.Suzuki,J.Phys.Chem.Solids in press.	130
1-2-42	[1]F.Izumi,H.Asano,H.Murata and N.Watanabe:J.Appl.Crystallogr.20(1987)411. [2]A.Urushibara,Y.Moritomo,T.Arima,A.Asamitsu,G.Kido and Y.Tokura:Phys.Rev.B51(1995)14103.	131
1-2-43	[1]C.Geibel et al.,Z.Phys.B84(1994)1. [2]N.Sato et al.,Phys.B53(1996)14043. [3]R.Caspary et al.,Phys.Rev.Lett.71(1993)2146. [4]C.Wassilew et al.,Physica B 199&200(1994)162. [5]P.Link et al.,J.Phys.Condens.Matter 7(1995)373. [6]Y.Haga et al.,J.Phys.Soc.Jpn.65(1996)3646. [7]H.Matsui et al.,Physica B199&200(1994)140. [8]R.Modler et al.,Int.J.Mod.Phys.B7(1993)42.	133
1-2-44	[1]J.M.Effantin et al.,J.Magn.Magn.Mater.47&48(1985)145. [2]O.Sakai et al.,J.Phys.Soc.Jpn.66(1997)3005. [3]M.Hiroi et al.,J.Phys.Soc.Jpn.66(1997)1762. [4]T.Tayama et al.,J.Phys.Soc.Jpn.66(1997)2268. [5]O.Suzuki et al.,J.Phys.Soc.Jpn.67(1998)4243.	135
1-2-45	[1]S.Kunii,K.Iwashita,T.Matsumura and K.Segawa:Physica B 186-188(1993)646-648. [2]K.Segawa,A.Tomita,K.Iwashita,M.Kasaya,T.Suzuki and S.Kunii:J.Magn.Magn.Mater.104-107(1992)1233-1234. [3]K.Takahashi,H.Nojiri,K.Ohoyama,M.Ohashi,Y.Yamaguchi,S.Kunii and M.Motokawa:Physica B 241-243(1998)696-698.	137
1-2-46	[1]Myung-Wha Jung et al.,J.Kor.Phy.Soc.32(1998)71. [2]M.Ram et al.,Physica B 259-261(1999)271. [3]C.Paulsen and J.-G.Park(unpublished,1998).	138
1-2-47	[1]H.Kimura et al.,J.Phys.Chem.Solids,in press. [2]T.Suzuki et al.,Phys.Rev.B57,R3229(1998).	140
1-2-48	[1]S.Wakimoto et al.,J.Phys.Chem.Solids,in press. [2]S.Wakimoto et al.,to be published in Phys.Rev.B.	141
1-2-49	[1]Y.Takeo et al.,J.Phys.Chem.Solids,in press.	142

1-2-50	[1]L.P.Regnauld et al.,Phys.Rev.B 38(1988)4481. [2]M.Sato et al.,proceedings of ISSP7(1998).	143
1-2-51	[1]L.P.Regnauld et al.,Phys.Rev.B 38(1988)4481. [2]M.Sato et al.,J.Phys.Chem.Solids accepted. [3]S.Quenzel et al.,J.Magn.Magn.Matter.76&77(1988)403 [4]S.Kawarazaki et al.Physica B 206&207(1995)298	144
1-2-52	[1]O.Moze and K.H.J.Buschow:J.Alloys Comp.245(1996)112. [2]M.Kontani,H.Ido,H.Ando,T.Nishioka and Y.Yamaguchi:J.Phys.Soc.Jpn.63 (1994)1652. [3]G.Motoyama,K.Murase and M.Kontani:Physics of Strongly Correlated Electron Systems,JIAP Series 11,p257.	145
1-2-53	[1]M.Wada and Y.Ishibashi;J.Phys.Soc.Jpn.,52(1983)193. [2]A.A.Volkov,et al.;J.Phys.Soc.Jpn.,54(1985)818. [3]M.Horioka,A.Sawada and M.Wada;J.Phys.Soc.Jpn.,58(1989)3793.	146
1-2-54	[1]P.C.Canfield et al.J.Appl.Phys.70(1991)5992. [2]F.Izumi,"The Rietveld Method,"ed.by R.A.Young,Oxford University Press, Oxford(1993),Chap.13.	147
1-2-55	[1]Y.Tokura et al.,J.Phys.Soc.Jpn.63(1994)3931-3935. [2]H.Y.Hwanget al.,Phys.Rev.Lett.75(1995)914-918. [3]J.C.Nie et al.,192(1999)379-385.	148
1-2-56	[1]N.Tateiwa,et al.,to be published.	150
1-3-1	[1]B.J.Sternlieb,M.Sato,S.Shamoto,G.Shirane and J.M.Tranquada,Phys.Rev.B47 (1993)5320. [2]H.Harashina,S.Shamoto,T.Kiyokura,M.Sato,K.Kakurai and G.Shirane,J.Phys. Soc.Jpn.62(1993)4009. [3]H.Harashina,K.Kodama,S.Shamoto,M.Sato,K.Kakurai and M.Nishi,J.Phys. Soc.Jpn.67(1998)3216. [4]H.Harashina,M.Kanada,H.Sasaki,K.Kodama,M.Sato,S.Shamoto,K.Kakurai and M.Nishi,J.Phys.Chem.Solids,to be published.	153
1-3-2	[1]T.Nagata,M.Uehara,J.Goto,J.Akimitsu,N.Motoyama,H.Eisaki,S.Uchida, H.Takahashi,T.Nakanishi and N.Mori,Phys.Rev.Lett.81(1998)1090. [2]R.S.Eccleston,M.Uehara,J.Akimitsu,H.Eisaki,N.Motoyama and S.Uchida, Phys.Rev.Lett.81(1998)1702. [3]K.Kumagai,S.Tsuji,M.Kato and Y.Koike,Phys.Rev.Lett.78(1997)1992. [4]K.Magishi,S.Matsumoto,Y.Kitaoka,K.Ishida,K.Asayama,M.Uehara,T.Nagata and J.Akimitsu,Phys.Rev. B 57(1998)11533. [5]H.Mayaffre,P.Auban-Senzier,M.Nardone,D.Jerome,D.Poilblanc, C.Bourbonnais,U.Ammerahl,G.Dhalenne and A.Revcolevschi,Science 279, 345(1998).	154

1-3-3	<p>[1]J.M.Tranquada et al.,Phys.Rev.B 54,7489(1996).</p> <p>[2]S.Haas et al.,Phys.Rev.B 51,5989(1995).</p> <p>[3]J.M.Tranquada et al.,Nature 375,561(1995).</p> <p>[4]H.Mook et al.,cond_mat/9712320.</p> <p>[5]T.Nishijima,to be published.</p>	156
1-3-4	<p>[1]S.Yamanaka,K.Hotehama and H.Kawaji,Nature 392,580(1998).</p> <p>[2]S.Shimoto,T.Kato,Y.Ono,Y.Miyazaki,K.Ohoyama,M.Ohashi,Y.Yamaguchi and T.Kajitani,Physica C 306,7(1998).</p> <p>[3]S.Yamanaka,H.Kawaji,K.Hotehama and M.Ohashi,Adv.Mater.8,771(1996).</p> <p>[4]I.Hase,Y.Nishihara,Phys.Rev.B to be submitted.</p> <p>[5]Y.-I.Kim and F.Izumi,J.Ceram.Soc.Jpn.,102,401(1994).</p> <p>[6]W.A.Harrison,Electronic Structure and the Properties of Solids (The Physics of the Chemical Bond), W.H.Freeman and Company,San francisco(1980).</p>	157
1-3-5	<p>[1]G.Aeppli et al.,Phys.Rev.Lett.63(1989)676.</p> <p>[2]N.Metoki et al.,Phys.Rev.Lett.80(1998)5417.</p> <p>[3]N.Sato et al.,Physica B 230-232(1997)367.</p> <p>[4]J.G.Lussier et al.,Phys.Rev.B56(1997)11749.</p> <p>[5]T.E.Mason et al.,Phys.Rev.Lett.65(1990)3189.</p> <p>[6]T.Honma et al.,J.Phys.Soc.Jpn.68(1999)338.</p> <p>[7]S.A.M.Mentink et al.,Phys.Rev.B53(1996)R6014.</p>	159
1-3-6	<p>[1]S.Shamoto,T.Kato,Y.Ono,Y.MInezaki,K.Ohoyama,M.Ohashi,Y.Yamaguchi and T.Kajitani,Physica C 306,7(1998).</p> <p>[2]S.Yamanaka,H.Kawaji,K.Hotehama and M.Ohashi,Adv.Mater.8,771(1996).</p> <p>[3]R.Weht,A.Filippetti and W.E.Pickett,Phys.Rev.Lett,to be submitted(1999).</p> <p>[4]I.Hase and Y.Nishihara,Phys.Rev.B to be submitted(1999).</p> <p>[5]S.Shamoto,K.Iizawa et al.,Molecular Crystals and Liquid Crystals,to be submitted.</p> <p>[6]R.Zeyher and G.Zwickyagl,Z.Phys.B28,175(1990).</p>	161
1-3-7	<p>[1]C.Varmazis and Myron Strongin,Phys.Rev.B,10(1974)1855.</p> <p>[2]B.W.Maxfield and W.L.McLean,Phys.Rev.,139(1965)A1515.</p>	162
1-4-1	<p>[1]C.Masciovecchio et al.Phys.Rev.Lett.76,3356(1996),F.Sette et. al.Science, 280,1550(1998).</p>	165
1-4-2	<p>[1]S.Takeda,Y.Kawakita,M.Inui,K.Maruyama,S.Tamaki and Y.Waseda;J.Non-Cryst.Solids 205-207(1996)365-369.</p> <p>[2]S.Takeda,Y.Kawakita,M.Knehira,S.Tamaki and Y.Waseda;in print J.Phys. Chem.Solids(1999).</p>	167
1-4-3	<p>[1]M.Kotlarchyk,E.Y.Sheu and M.Capel,Phys.Rev.A46(1992)928-939.</p> <p>[2]S.H.Chen,S.L.Chang and R.Strey,J.Chem.Phys.93(1990)1907-1918.</p> <p>[3]M.Nagao and H.Seto,Phys.Rev.E59(1999)3169-3176.</p> <p>[4]M.Nagao,H.Seto,Y.Kawabata and T.Takeda,submitted to J.Appl.Cryst.</p>	168
1-4-4	<p>[1]M.Nagao,H.Seto,Y.Kawabata and T.Takeda,in this issue.</p> <p>[2]M.Nagao,H.Seto,D.Okuhara and Y.Matsushita,J.Phys.Chem.Solids in press.</p> <p>[3]F.Nallet,D.Roux,S.T.Milner,J.Phys.France 51(1990)2333-2346.</p> <p>[4]M.Nagao and H.Seto,Phys.Rev.E59(1999)3169-3176.</p>	170

1-4-5	[1]Kaoru Shibata,Takeshi Higuchi,An-Pang-Tsai,Masayuki Imai and Kenji Suzuki Progress of Theoretical Physics Supplement 126(1997)75-78.	172
1-4-6	[1]G.M.Schneider,Ber.Bunsenges.Physk.Chem.1972,76,325. [2]T.Freltoft,K.Kjems and S.K.Shnha,Phys.Rev.,1986,B33,269.	174
1-4-7	[1]M.Inui,Y.Ohishi,I.Nakaso,M.H.kazi and K.Tamura,J.Non-Cryst.Solids,(1999) in press. [2]M.Inui,S.Takeda,K.Maruyama,Y.Kawakita,S.Tamaki,M.Imai,Physica B 213& 214(1995)552.	175
1-4-8	[1]Chen S.H.,Chang S.L. and Strey R.,J.Chem.Phys.,93,1907-1918(1990).; Kotlarchyk M.,Sheu E. and Capel M.,Phys.Rev.,A46,928-939(1992). [2]M.Nagao and H.Seto,Phys.Rev.E59(1999)3169-3176. [3]M.Nagao et al.,submitted to J.Phys.Chem.Solids. [4]T.Takeda et al.,J.Phys.Soc.Jpn.,65,Suppl.A 189-194(1996) [5]H.Takeno et al.,Polym.J.,29,931-939(1997). [6]E.Y.Sheu.,S.H.Chen.,J.S.Huang and J.C.Sung.,Phys.Rev.A.,39,5867-5876 (1989). [7]A.G.Zilman and R.Granek.,Phys.Rev.Lett.,77,4788-4791(1996). [8]M.Nagao et al.,Slow Dynamics in Complex Systems,eds.,M.Tokuyama and I.Oppenheim,AIP,New York,P154(1999) in press.	176
1-4-9	[1]T.Takeda,H.Seto,S.Komura,S.K.Ghosh,M.Nagao,J.Matsuba,H.Kobayashi, T.Ebisawa,S.Tasaki,C.M.E.Zeyen,Y.Ito,S.Takahashi,H.Yoshizawa:J.Phys.Soc. Jpn.65 Suppl.A,189-194(1996). [2]T.Takeda,Y.Kawabata,H.Seto,S.Komura,S.K.Ghosh and M.Nagao:Slow Dynamics in Complex Systems,eds.,M.Tokuyama and I.Oppenheim,AIP New York,1999,p148. [3]T.Takeda,Y.Kawabata,H.Seto,S.Komura,S.K.Ghosh and M.Nagao,D.Okuhara: J.Phys.Chem.Solids(1999) in press. [4]A.G.Zilman and R.Granek:Phys.Rev.Letters77,4788-4791(1996).	178
1-4-10	[1]O.Yamamuro et al.,J.Chem.Phys.,105,732(1996). [2]O.Yamamuro et al.,J.Phys.Chem.,106,2997(1997). [3]K.Takeda et al.,J.Chem.Phys.,103,3457(1996). [4]O.Yamamuro et al.,ISSP Activity Report,5,117(1998).	180
1-4-11	[1]For example;U.Buchenau,in Dynamics of Disordered Materials,edited by D.Richter,A.J.Dianoux,W.Petry,J.Teixeira(Springer,Berlin,1989). [2]O.Yamamuro,K.Harabe,K.Takeda,I.Tsukushi,T.Kanaya and T.Matsuo,ISSP Activity Report,5,117 (1998). [3]O.Yamamuro,Proceedings of International Workshop on JHF Science(JHF98) (KEK Proceedings 98-5),Vol.III,160(1998). [4]O.Yamamuro,K.Harabe,K.Takeda,I.Tsukushi,T.Kanaya and T.Matsuo,J. Chem.Phys.,Submitted. [5]T.Kajitani,K.Shibata,S.Ikeda,M.Kohgi,H.Yoshizawa,K.Nemoto,K.Suzuki, Physica B 213&214,872(1995). [6]T.Nakayama and N.Seto,J.Phys.:Cond.Matter 10,L41(1998).	182

1-4-12	[1]G.M.Schneider,Ber.Bunsenges.Physk.Chem.76,325(1972). [2]J.Teixeira,M.C.Bellissent-Funel,S.H.Chen and A.J.Dianoux,Phys.Rev.A31, 1913(1985).	184
1-4-13	[1]Jobic H,J.Chem.Phys.76,2693(1982). [2]Kobayashi M.,Kaneko F.,Sato K. and Suzuki M.,J.Phys.Chem.90,6371(1986). [3]Kajitani T.,Shibata K.,Ikeda S.,Kohgi M.,Yoshizawa H.,Nemoto K. and Suzuki K.,Physica B213&214 872(1995). [4]Schaufele R.F. and Shimanouchi T., J.Chem.Phys.47,3605(1967).	185
1-4-14	[1]Pohl and Zeller,Phys.Rev.B5(1971)2029. [2]Y.Inamura et al.,Physica B 241-243(1998)903. [3]Hiramatsu et al.,Physica B 219-220(1996)287. [4]M.A.Romos et al.,Phys.Stat.Sol.135(1993)477. [5]S.Sugai and A.Onodera,Phys.Rev.Lett.,77(1996)4210. [6]A.P.Sokolov et al.,Phys.Rev.Lett.,69(1992)1540. [7]S.R.Elliott,Phys.Rev.Lett.,67(1991)711. [8]T.Nakayama,Phys.Rev.Lett.80(1998)1244. [9]U.Buchenau, et al.,Phys.Rev.B43(1991)5939. [10]P.W.Anderson et al.,Phil.Mag.25(1972)1,W.A.Philips,J.Low Temp.Phys.7 (1972)351. [11]A.P.Sokolov et al.,Phys.Rev.Lett.78(1997)2405. [12]T.Nakayama,J.Phys. :Condens.Matter 10(1998)L41-L47. [13]W.A.Philips,J.Low Temp.Phys.7(1972)351.	187
1-5-1	[1]M.Yashima,S.Sasaki,M.Kakihara,Y.Yamaguchi,H.Arashi and M.Yoshimura, Acta Crystallogy.B50,663-672(1994). [2]M.Yashima,S.Sasaki,Y.Yamaguchi,M.Kakihara,M.Yoshimura and T.Mori, Applied Physics Letters,72,182-184(1998). [3]P.Aldebert and J.P.Traverse,J.Am.Ceram.Soc.,68,34-40(1985). [4]O.Yokota,Ph D.Thesis,Tokyo Institute of Technology,(1998). [5]M.Yashima,K.Ohtake,M.Kakihara and M.Yoshimura,J.Am.Ceram.Soc.,77, 2773-2766(1994);O.Yokota, M.Yashima,M.Kakihara,A.Shimofuku and M.Yoshimura,J.Am.Ceram.Soc.82 in press(1999).	191
1-5-4	[1]T.Vogt and W.W.Schmahl,Europhys.Lett.24,281-285(1993).	196
1-5-6	[1]S.Miyajima and T.Hosokawa,Phys.Rev.B,52,4060(1995).	198
1-6-1	[1]Y.Izumi,K.Soma,K.Aizawa,S.Koizumi, and H.Tomimitsu,JAERI-Rev.99-003, p.27(1999). [2]K.Aizawa&H.Tomimitsu,Physica B213&214(1995)884-886.	201
1-6-2	[1]Y.Takahashi,T.Sato,H.Tadokoro,and Y.Tanaka,J.Polym.Sci.Polym.Phys. Ed.11,233(1973). [2]Y.Takahashi,Rep.Progr.Polym.Phys.Jpn.,41,363(1998). [3]A.V.Fratini,P.G.Lenherth,T.J.Resch,and W.W.Adams,Mat.Res.Soc.Symp.Proc. 134,431(1989).	202
1-6-3	[1]M.Teraguchi and T.Masuda,J.Polym.Sci.,A Polym.Chem.,36,2721(1998) and references herein.	203

1-6-5	[1]Takahashi Y.,Kitade S.,Noda M.,Ochiai N.,Noda I.,Imai M., and Matsushita Y.,Polym.J.30,388(1998).	206
1-6-6	[1]T.Hashimoto et al.,Macromolecules,30,6819(1997).	207
1-6-7	[1]M.Shibayama and H.Hirose,Macromolecules,31,5336(1998).	208
1-6-11	[1]H.Takeno et al.,Polymer J.,29,931(1997).	213
1-6-12	[1]Nakano, M;Deguchi,M.;Matsumoto,K.;Matsuoka,H;Yamaoka,H. Macromolecules,submitted. [2]Nakano, M;Matsuoka,H;Yamaoka,H.;Poppe,A.;Richter,D.Physica B 1998, 241-243,1038.	214
1-6-14	[1]M.Sugiyama,K.Hara,N.Hiramatsu and H.Iijima:Jpn.J.Appl.Phys.37(1998) L404. [2]E.Kamata:New Food Industry,36(1994)59(in Japanese). [3]Y.Izumi,A.Uchida,H.Nogami,K.Kajiwara,H.Urakawa,Y.Yuguchi, M.Hashimoto and T.Takahashi:Activity Rep.Neutron Scattering Res.,4(1997) 205.	216
1-6-15	[1]Y.Matsushita et al.,Macromolecules 21(1998)1802-1806.	217
1-6-17	[1]T.Kanaya,M.Ohkura,K.Kaji,M.Furusaka,M.Misawa,Macromolecules,1994,24, 5609. [2]P.G. de Gennes,Physics,3,37(1967). [3]R.Oeser,B.Ewen,D.Richter and B.Farago,Phys.Rev.Lett.,60,1041(1988).	219
1-6-18	[1]T.Kanaya et. al. J.Chem.Phys.104(1996)3841.	221
1-6-20	[1]H.Takeno et al.Macromolecules,29,2440(1996).	223
1-6-21	[1]K.Tashiro et al.,Macromolecules 25,1801(1992);25,1809(1992);27,1221 (1994);27,1228(1994);27,1234 (1994);27,1240(1994);28,8477(1995);28,8484 (1995). [2]K.Tashiro,Acta Polymerica,46,100(1995). [3]S.Sasaki et al.,Polym.J., in press.	224
1-7-1	[1]Y.Ohgo and S.Takeuchi,J.Chem.Soc.,Chem.Commun.21(1985). [2]T.Yoshimiya,Master Thesis,Tokyo Institute of Technology,1996.	229
1-7-2	[1]S.Fujiwara et al.,JAERI Review 99-003(1999)13. [2]Z.Otwinowski and W.Minor:Methods Enzym.276(1997)307-326.	230
1-7-7	[1]M.Hirai et al.,Biophys.J.70,1761(1996);J.Phys.Chem.100,11675(1996); Themochim.Acta 308,93(1998);J.Chem.Soc.Faraday Trans.92,4533(1996); Biophys.J.74,3010(1998);J.Phys.Chem.B102,3062(1998).	235
1-8-1	[1]L.Koester,H.Rauch and E.Seymann:Atomic Data and Nuclear Data Tables 49 (1991)65. [2]H.Tomimitsu,Y.Hasegawa,K.Aizawa and S.Kikuta:Nucl.Instr. and Meth. in Phys.Res.A420(1999)453.	239

1-8-2	<p>[1]Achiwa N.,Hino M.,Tasaki S.,Ebisawa T.,Akiyoshi T. and Kawai T.,J.Phys. Soc.Jpn.65,Suppl.A 183(1996).</p> <p>[2]Achiwa N.,Hino M.,Tasaki S.,Ebisawa T.,Akiyoshi T. and Kawai T.,Physica B 241-243,1068(1998).</p> <p>[3]Hino M.,Achiwa N.,Tasaki S.,Ebisawa T.,Akiyoshi T. and Kawai T.,Physica B 241-243,1083(1998).</p> <p>[4]Achiwa N.,Hino M.,Kakurai K. and Kawano S.,Physica B 241-243,1204 (1998).</p> <p>[5]Guigay J.P. and Schlenker M.,J.Mag.Mag.Mat.14 340(1979).</p>	241
1-8-3	[1]M.Hashimoto,T.Takahashi,ISSP7'98.	243
1-8-4	<p>[1]H.Funahashi,T.Ebisawa,T.Haseyama,M.Hino,M.A.Masaike,Y.Otake,T.Tabaru, S.Tasaki,Phys.Rev.A54,649(1996).</p> <p>[2]T.Ebisawa,S.Tasaki,T.Kawai,M.Hino,N.Achiwa,Y.Otake,H.Funahashi, D.Yamazaki, and T.Akiyoshi,Phys.Rev.A57,4720(1998).</p>	244
1-8-5	<p>[1]A.Steyerl,T.Ebisawa,K.A.Steinhauser and M.Utsuro,Z.Phys.B.41(1981)283.</p> <p>[2]M.Maaza,B.Pardo,J.P.Chauvineau,A.Raynal,A.Menelle,F.Bridou,Phys.Lett. A223(1996)145.</p> <p>[3]M.Hino,N.Achiwa,S.Tasaki,T.Ebisawa,T.Kawai and T.Akiyoshi,Physica B241-243(1998)1083.</p> <p>[4]M.Hino,N.Achiwa,S.Tasaki,T.Ebisawa,T.Kawai and T.Akiyoshi,Phys.Rev. A59(1999)2261.</p> <p>[5]T.Ebisawa,H.Funahashi,S.Tasaki,Y.Otake,T.Kawai,M.Hino,N.Achiwa and T.Akiyoshi,J.Neutron Research vol 4,157(1996).</p>	245
1-8-6	<p>[1]M.Hino,N.Achiwa,S.Tasaki,T.Ebisawa,T.Kawai and D.Yamazaki,Phys.Rev. A59 2261(1999).</p> <p>[2]S.Yamada,T.Ebisawa,N.Achiwa,T.Akiyoshi and S.Okamoto,Annu.Rep.Res. Reactor Inst.Kyoto Univ.,11,8(1978).</p> <p>[3]T.Ebisawa,T.Akiyoshi,N.Achiwa,S.Yamada and S.Okamoto,Annu.Rep.Res. Reactor Inst.Kyoto Univ.,14,10(1981).</p>	246
1-8-7	<p>[1]D.Yamazaki,T.Ebisawa,T.Kawai,S.Tasaki,M.Hino,T.Akiyoshi,N.Achiwa, Physica B 241-243(1998)186-188.</p> <p>[2]W.Besenböck,P.Hank,M.Köppe,R.Gähler,T.Keller,R.Golub,J.Phys.Soc.Jpn.65 Suppl.A(1996)215.</p> <p>[3]T.Ebisawa,S.Tasaki,M.Hino,T.Kawai,Y.Iwata,D.Yamazaki,N.Achiwa, Y.Otake,T.Kanaya,K.Soyama,Journal of Physics and Chemistry of Solids (1999)in press.</p> <p>[4]D.Yamazaki., et al.. to be published.</p>	247
1-9-1	<p>[1]I.Tanaka,K.Kurihara,Y.Haga,Y.Minezaki,S.Fujiwara,S.Kumazawa,and N.Niimura,J.Phys.&Chem.Solids(1999),in press.</p> <p>[2]Niimura N.,Karasawa Y.,Tanaka I.,Miyahara J.,Takeshi K.,Saito H., Koizumi S., and Hidaka M., Nucl. Instr.Meth.A349,(1994)521.</p> <p>[3]I.Tanaka,N.Niimura&P.Mikula,J.Appl.Cryst.,32(1999),525.</p> <p>[4]Haga Y.,Kumazawa S., and Niimura N.,J.Appl.Cryst.,(1999), in press.</p> <p>[5]Tanaka I.,Minezaki Y.,Harada K., and Niimura N., Physica B 241-243(1998) 227.</p>	251

1-9-3	<p>[1] S.Kawano et al. Physica B 241-243(1998)145-147.</p> <p>[2] H.Fujii, T.Shigeoka, J.Magn.Magn.Mat.90&91(1990)115-120.</p> <p>[3] S.Kawano et al. Physica B 241-243(1998)657-659.</p> <p>[4] J.A.Blanco et al.J.Magn.Magn.Mat.97(1997)4-1.</p>	254
1-9-4	<p>[1] T.Takeda, S.Komura, S.Seto, M.Nagai, H.Kobayashi, E.Yokoi, C.M.E Zeyen, T.Ebisawa, S.Tasaki, Y.Ito, S.Takahashi and H.Yoshizawa: Nucl.Instr. and Methods in Phys.Research, A346(1995)186.</p> <p>[2] T.Takeda, H.Seto, S.Komura, S.K.Ghosh, M.Nagao, J.Matsuba, H.Kobayashi, T.Ebisawa, S.Tasaki, C.M.E Zeyen, Y.Ito, S.Takahashi, H.Yoshizawa; J.Phys.Soc. Jpn.65 Suppl.A(1996)189.</p> <p>[3] T.Takeda, H.Seto, Y.Kawabata, D.Okuhara, T.Krist, C.M.E Zeyen, I.S.Anderson, P.Hghfj, M.Nagao, H.Yoshizawa, S.Komura, T.Ebisawa, S.Tasaki and M.Monkenbusch: J.Phys.Chem.Solids(1999) in press.</p>	255
1-9-5	[1] Y.Kawabata et al., Nucl.Instru. and Meth.in Phys.Res.A420(1999)213-217.	256
1-9-6	<p>[1] T.Kawai, T.Ebisawa, S.Tasaki, M.Hino, D.Yamazaki, H.Tahata, T.Akiyosi, Y.Matsumoto, N.Achiwa and Y.Otake, Physica B, 241-243(1998)133.</p> <p>[2] M.Hino, T.Kawai, T.Ebisawa, S.Tasaki, N.Achiwa, Physica B(1999), in press.</p>	257
1-9-7	<p>[1] K.Soyama et al.: ICANS-XIV, ANL-98/33 Vol.I(1998)132.</p> <p>[2] K.Soyama et al.: J. of Phys. and Chem. of Solid in press.</p>	258
1-9-8	[1] S.Tasaki, T.Ebisawa, T.Akiyosi, T.Kawai, and S.Okamoto, Nucl.Inst.Meth. Phys.Res., A355(1995)501.	259
1-10-1	[1] S.Okido, M.Hayashi, K.Tanaka, Y.Akino, N.Minagawa, and Y.Morii, Proc.7th Iner.Conf.Nuclear Engng, ICONE, Tokyo, 1999.	263
1-10-2	<p>[1] K.Tanaka, M.Matsui, R.Shikata and T.Nishikawa, J.Soc.Mat.Sci.Japan, Vol.41, No.464(1992), 593.</p> <p>[2] J.Otsuka, S.Iio, Y.Tajima, M.Watanabe, K.Tanaka, J.Ceramic Soc.Japan, Vol.102, No.1(1994), 29.</p>	264
1-10-3	[1] K.INOUE et al., Jpn.J.Appl.Phys.37(1998)5680.	265
1-10-4	<p>[1] T.Sasaki and Y.Hirose, J.Soc.Mat.Sci., Japan, vol.44, No.504(1995)1138-1143.</p> <p>[2] T.Sasaki and Y.Hirose, Trans.Japan Soc.Mech.Eng., vol.61, No.590, A, (1995) 2288-2295.</p> <p>[3] T.Sasaki, Y.Hirose and S.Yasukawa, Trans.Japan Soc. Mech.Eng., vol.63, No.607, A, (1997)533-541.</p>	266
2-1	<p>[1] 呉田昌俊他 2 名, 「中性子ラジオグラフィによるサブクール沸騰流中のボイド率分布計測技術の開発」, JAERI-Research 99-023, 1999.</p> <p>[2] 呉田昌俊他 3 名, Void Fraction Measurement of Subcooled Boiling of Water by Using the High-Frame-Rate Neutron Radiography, proc.The Sixth World Conference on Neutron Radiography, AP-144, May 17-21, 1999.</p> <p>[3] 呉田昌俊他 3 名, Visualization and Void Fraction Measurement Subcooled Boiling of Water Flow in a Narrow Rectangular Channel Using High-Frame-Rate Neutron Radiography, proc.Two-Phase Flow Modeling and Experimentation 1999, p.1509-1514, May 23-26, 1999.</p>	271

2-2	<p>[1]柴本泰照他 6 名,「溶融金属中に落下する水ジェット挙動の可視化」日本原子力学会99春の年会(111),(1999).</p> <p>[2]柴本泰照他 6 名,Visualization of Plunging Jet Behavior in Molten Alloy, Proc.of ICONE-7254(1999).</p> <p>[3]Coolant Jet Behaviors during its Penetration into Melt,Proc.of NURETH-9 (on submitting,1999).</p>	272
2-3	<p>[1]松林政仁他 2 名,「中性子ラジオグラフィ用蛍光コンバータの発光スペクトル測定」,中性子ラジオグラフィ技術の応用と実用化専門研究会報告(KURRI-KR-27),9-15.</p> <p>[2]松林政仁,Preparation of a beam quality indicator for effective energy diterminations of continuum beams-Establishment of traceability,Nuclear Instruments & Methods in Physics Research section A424,165-171(1999).</p> <p>[3]松林政仁,Advancement of Neutron Radiography Technique in JRR-3M, Symposium on Research Reactor,March29-31(1999).</p> <p>[4]松林政仁他 5 名,Application of Neutron Radiography Systems in JRR-3M to Nuclear Engineering,Proceedings of the 7th international Conference on Nuclear Engineering,FP7143(1999).</p> <p>[5]松林政仁他 2 名,Development of a High-frame-rate Neutron Radiography System,The Sixth World Conference on Neutron Radiography,May14-21 (1999).</p>	273
2-4	<p>[1]Tamaki,M.,Oda,M.,Takahahi,K.,Tanimoto,W. and Funahashi,T., "Study on neutron imaging techniques and processings for developing quantitative neutron radiography" Nucl.Instr.Meth.,A377, pp.102-106(1996).</p> <p>[2]Oda,M.,Tamaki,M.,Takahashi,K. and Tasaka,K., "Removal of scattered neutrons in thermal neutron radiography using a multichannel collimator" Nucl.Instr.Meth.,A379,pp.323-329(1996).</p> <p>[3]Oda,M.,Tamaki,M.,Tsuruno,A.,Yoneda,K. and Kobayashi,H., "Transmittance measurements of cold neutrons for some materials by means of neutron radiography" Nucl.Instr.Meth.,A377, pp.72-75(1996).</p> <p>[4]小田将広、玉置昌義、松林政仁、森線千鶴夫” 冷中性子計算機断層撮影の定量性におけるビームスペクトルの影響”、日本原子力学会誌、39、pp.647-656(1997).</p> <p>[5]Oda,M.,Tamaki,M.,Matsubayashi,M. and Kobayashi,H., "Dependence of Attenuation Coefficient on Penetrating Path Length in Cold Neutron Radiography",Proc.5th World Conference on Neutron Radiography,ed. C.O.Fischer(DGZfP,Berlin,1997)199-205.</p> <p>[6]小田将広(学位論文)” 冷中性子ラジオグラフィ技術の定量解析性向上に関する基礎研究”、課程博士論文(1997.11,名古屋大学)。</p> <p>[7]Tamaki,M.,Oda,M. and Tsuruno,A., "Film Imaging and Processing Techniques for Quantitative Neutron Radiography", Proc.5th World Conference on Neutron Radiography,ed. C.O.Fischer(DGZfP,Berlin,1997) 391-398.</p> <p>[8]M.Tamaki(Invited Talk) "Imagoing plates,Converters and Neutron energies for developing quantitative neutron radiography," Presented at 6th World Conference on Neutron Radiography,(Osaka,1999.5.17-21).</p> <p>[9]Y.Masunaga,M.Tamaki,O.Nishiguchi,K.Yoneda,Y.Kukita, "Characterization of imaging plates for quantitative neutron radiography, "Presented at 6th World Conference on Neutron Radiography,(Osaka,1999.5.17-21).</p>	275

	<p>[10] O.Nishiguchi,M.Tamaki,M.Oda,M.Matsubayashi,Y.Kukita, "Application of imaging plates for quantitative thermal and cold neutron radiography," Presented at 6th World Conference on Neutron Radiography, (Osaka,1999.5.17-21).</p> <p>[11] M.Tamaki,Y.Masunaga,K.Tsuchida,S.Taguchi,K.Yoshi,S.Fujine, H.Kobayashi, "Application of imaging plates for fast and epi-thermal neutron radiography," Presented at 6th World Conference on Neutron Radiography,(Osaka,1999.5.17-21).</p> <p>[12] M.Tamaki,O.Nishiguchi,Y.Masunaga,S.Tazaki,S.Iwai,Y.Kukita, "Diminishing procedure of gamma-ray fogging using new type imaging plates for advanced quantitative neutron radiography," Presented at 6th World Conference on Neutron Radiography,(Osaka,1999.5.17-21).</p> <p>[13]西口 蔵、玉置昌義、小田将広、久木田豊、松林政仁、"イメージングプレートを用いた高感度間接法中性子ラジオグラフィ(2)"、日本原子力学会、1997年秋の大会(沖縄)、A64.</p> <p>[14]玉置昌義、西口 蔵、舟橋隆之、田崎誠二、江藤雅弘、"γ線不感処理イメージングプレート中性子ラジオグラフィ法"、日本原子力学会、1997年秋の大会(沖縄)、A65.</p> <p>[15]玉置昌義、岩井定彦、鍊石恵子、田崎誠二、"中性子画像変換方法" 特願平9-190530.</p> <p>[16]Santoso,B.,Tamaki,M.,Oda,M.,Honda,M. and Ikeda,Y., "Neutron Radiography with a one-dimensional image sensor having a high linearity range" Nucl.Meth.,A377,pp.133-136(1996).</p> <p>[17]Tamaki,M.,Hara,Sh.,Kondoh,I.,Yoneda,K.,Tsuruno,A. and Kobayashi,H., "Visualization and Analysis of forced diffusion of hydrogen in palladium by electrotransport", Nucl.Meth.,A377,pp.166-169(1996).</p> <p>[18]Y.Tsuji,S.Matsueda,M.Oda,M.Matsuda,T.Yagi,M.Tamaki,M.Matsubayashi and S.Fujine, "Visualization and correlation analysis of counter-current two-phase flow in a thermosyphon by neutron radiography", Nucl.Meth.,A377, pp.148-1152(1996).</p> <p>[19]T.Funahashi,M.Tamaki,M.Oda,S.Somyoy,M.Matsubayashi, "Application of neutron computed tomography for liquid film measurement in simulated liquid-bonded sphere-packed nuclear fuel element", Presented at 6th World Conference on Neutron Radiography,(Osaka,1999.5.17-21).</p>	
2-5	<p>[1]K.Mishima,T.Hibiki,Y.Saito,H.Nakamura,Y.Kukita, "Visualization study of molten metal-water interaction by using neutron radiography," Proc. Workshop on Severe Accident Research in Japan,SARJ-96,Oct.28-30,1996, Tokyo,Japan.</p> <p>[2]K.Mishima and T.Hibiki, "Development of high-frame rate neutron radiography and quantitative measurement method for multiphase flow research, "Proc.OECD/CSNI Specialist Meeting on Advanced Instrumentation and Measurement Techniques,March 17-20,1997,Santa Barbara,USA.</p> <p>[3]K.Mishima,T.Hibiki,Y.Saito,A.Yamamoto,K.Moriyama,J.Sugimoto, "Visualization study of molten metal-water interaction by using neutron radiography," Proc.International Seminar on Vapor Explosion and Explosive Eruptions,May 22-24,1997,Sendai,Japan,101-109.</p>	279

	<p>[4] K.Mishima, T.Hibiki, Y.Saito, K.Moriyama and J.Sugimoto, "Visualization study on hot particle-water interaction by using neutron radiography," Proc. Workshop on Severe Accident Research in Japan, SARJ-98, Nov.4-6, 1998, Tokyo, Japan.</p> <p>[5] Y.Saito, K.Mishima, T.Hibiki, A. Yamamoto, J.Sugimoto and K.Moriyama "Application of high-frame-rate neutron radiography to steam explosion research," Nucl.Instru.Meth.Phys.Res.A424(1999)142-147.</p> <p>[6] Y.Saito, T.Hibiki, K.Mishima, K.Moriyama and J.Sugimoto, "Visualization study on hot particle-water interaction by using neutron radiography," Proc. Two-Phase Flow Modelling and Experimentation, May 23-25, 1999, Pisa, Italy.</p> <p>[7] K.Mishima, T.Hibiki, Y.Saito, J.Sugimoto and K.Moriyama, "Visualization study of molten metal-water interaction by using neutron radiography," Nucl.Eng.Design 189(1999)391-403.</p>	
2-7	<p>[1] K.Saito, T.M.Nakanishi, M.Matsubayashi and G.Meshitsuka: Development of New Lignin Derivatives as Soil Conditioning Agents by Radical Sulfonation and Alkaline-Oxygen Treatment. Mokuzai Gakkaishi 43(8), 669-677 1997.</p> <p>[2] T.M.Nakanishi, A.Tsuruno and M.Matsubayashi: Water Movement in Plant. Proc. of Fifth World Conference on Neutron Radiography, C.O.Fischer, J.Stade and W.Bock (Eds.) DGZfp (Deutsche Gesellschaft für Zertörungsfreie Prüfung E.V.) Publisher 716-719 1997.</p> <p>[3] T.M.Nakanishi and M.Matsubayashi: Water Imaging of Seeds by Neutron Beam. Biomages 5(2), 45-48 1997.</p> <p>[4] T.M.Nakanishi and M.Matsubayashi: Nondestructive Water Imaging Neutron Beam Analysis in Living Plants. J.Plant Phys. 151, 442-445 1997.</p> <p>[5] T.M.Nakanishi, K.Okano, I.Karakama, T.Ishihara and M.Matsubayashi: Three Dimensional Imaging of Moisture in Wood Disk by Neutron Beam During Drying Process. Holzforschung, 52, 673-676 1998.</p> <p>[6] T.M.Nakanishi, J.Furukawa and M.Matsubayashi: A Preliminary Study of CT Imaging of Water in Carnation Flower. Nucl.Instr.Meth.Phys.Res.A424, 136-141 1999.</p> <p>[7] J.Furukawa, T.M.Nakanishi and M.Matsubayashi: Neutron Radiography of the Root Growing in Soil with Vanadium. Nucl.Instr.Meth.Phys.Res.A424, 116-121 1999.</p> <p>[8] T.M.Nakanishi, I.Karakama, T.Sakura and M.Matsubayashi: Moisture Imaging of a Camphor Tree by Neutron Beam. Radioisotopes, 47, 387-391 1999.</p> <p>[9] T.M.Nakanishi, J.Furukawa and M.Matsubayashi: CT Imaging of Water in Root-Soil System by Neutron Beam. Soil Phys. Conditions and Plant Growth, Japan, in Press.</p>	294
3-1	<p>[1] 第34回理工学における同位元素発表会 講演要旨集、(1997)PP.92</p> <p>[2] 第35回理工学における同位元素発表会 講演要旨集、(1998)PP.168</p> <p>[3] 平成9年度国立機関原子力試験研究成果報告書、第38集、(1999)84-1~4, 85-1~4.</p>	299

3-2	<p>[1]C.Yonezawa,H.Matsue,T.Adachi,M.Hoshi,E.Tachikawa,P.P.Povinec,S.W.Fowler,M.S.Baxter,"Neutron-induced prompt γ-ray analysis of Gulf marine environmental samples",Extended Synopses of International Symposium on Marine Pollution,IAEA,p.296(1998).</p> <p>[2]松江秀明、米沢伸四郎：「中性子即発γ線分析法におけるk_0法の適用」、第42回放射化学討論会予稿集、p.37(1998).</p> <p>[3]C.Yonezawa,"Prompt γ-ray analysis using cold and thermal guided neutron beam at JAERI",Proceedings of International Conference on Nuclear Analytical Material in the Life Sciences,in press,Humana,(1999).</p> <p>[4]C.Yonezawa,H.Matsue,"Usefulness of prompt gamma-ray analysis with guided neutron beams comparing to neutron activation analysis",J.Radioanal.,Nucl.Chem.,in press(1999).</p> <p>[5]H.Matsue,C.Yonezawa,"k_0 Standardization approach in neutron-induced prompt gamma-ray analysis at JAERI",J.Radioanal.Nucl.Chem.,in press (1999).</p> <p>[6]C.Yonezawa,P.P.Ruska,H.Matsue,M.Magara,T.Adachi"Determination of boron in Japanese geochemical reference samples by neutron-induced prompt γ-ray analysis",J.Radioanal.Nucl.Chem.,239,571(1999).</p>	301
3-3	<p>[1]T.Kishikawa,K.Nishimura,S.Noguchi,Nucl.Instrum.Meth.A353(1994)285.</p> <p>[2]A.Ore,J.L.Powell,Phys.Rev.,75(1949)1696.</p> <p>[3]T.Kishikawa,S.Noguchi,C.Yonezawa,H.Matsue,A.Nakamura,H.Sawahata "Photopeak profile of full energy and escape peaks in neutron capture prompt gamma ray spectra ",J.Radioanal.Nucl.Chemistry.215(1997)211-217.</p>	303
4-2	[1]日本土壤肥料学会（北海道大会）で発表予定、1999.7.30 .	312
4-6	<p>[1]N.Imai, et al.,Geochemical Journal 29,91(1995).</p> <p>[2]K.Furuno, et al.,Nucl.Instr. and Meth.A 421 211(1999).</p>	317
4-7	<p>[1]T.M.Nakanishi,J.Takahashi and H.Yagi:Partition of Transition Elements between Soil and Caatinger Wood Grown in North -East Brazil Determined by Neutron Activation Analysis.J..Radioanal.Nucl.Chem.,Letters 214(6), 517-527 1996.</p> <p>[2]T.M.Nakanishi,J.Takahashi and H.Yagi:Rate Earth Element,Al, and Sc Partition between Soil and Caatinger Wood Grown in North -East Brazil by Instru Neutron Activation Analysis.Biological Trace Element Research 60 ,163174 1997.</p> <p>[3]T.Kataoka,M.Mori,T.M.Nakanishi,S.Matsumoto and A.Uchiumu:Highly Sensitive Analysis Method for Aluminum Movement in Soybean Root through Lumogallion Staining.J.Plant Res.110,305-309(1997)</p> <p>[4]T.Kataoka,H.Iikura and T.M.Nakanishi:Aluminum Distribution and Viability of Plant Root and Cultured Cells.Plant nutrition-for sustainable food production and environment.427-431 1997.</p> <p>[5]T.M.Nakanishi and M.Tamada:Kinetics of Element Profile Pattern during Life Cycle Stage of Morning-Glory.J.Radioanal.Nucl.Chem.,239(3),489-494 1999.</p> <p>[6]T.M.Nakanishi and M.Tamada:Kinetics of Transition Element Profile during the Life Cycle of Morning-Glory.Proc.of Tenth International Conference on Modern Trends in Activation Analysis.Bethesda,USA 1999</p> <p>[7]J.Furukawa and T.M.Nakanishi:A Study of Nutrient Recycling System in Plant-Soil System using Neutron Activation Analysis.ibid,1999</p>	319

	<p>[8] T.M.Nakanishi, S.Ueoka and J.Furukawa: A Simulation of an Environmental Effect to a Soybean Plant Derived from the Kinetics of Ca and Mg throughout the Generation. Proc. of the 45th Conference on Bioassay, Analytical & Environmental Radiochemistry, Washington DC 1999.</p> <p>[9] S.Ueoka, J.Furukawa and T.M.Nakanishi: An Effect of Al and V on an Element Uptake Manner in a Soybean Plant. <i>ibid</i> 1999.</p>	
4-8	<p>[1] 黒沢悦郎, 鈴木稔(1983). "紅藻ソゾ(Laurencia)の代謝産物", 化学と生物, 21, 23-32.</p> <p>[2] K.L.Erickson(1983). "Constituents of Laurencia" in "Marine Natural Products; Chemical and Biological Perspectives", P.J.Scheuer ed., Vol.5, pp 131-257, Academic Press, New York.</p> <p>[3] 鈴木稔, 野矢洋一, 大西俊之(1997). "放射化による含臭素化合物の海産生物内の代謝研究", 原研施設利用共同研究成果報告書(平成8年度), pp63-65.</p> <p>[4] M.Suzuki, Y.Takahashi, S.Nakano, Y.Noda and T.Ohnishi, in preparation.</p> <p>[5] T.Abe, M.Masuda, T.Suzuki and M.Suzuki(1999). "Chemical races in the red alga Laurencia nipponica(Rhodomelaceae, Ceramiales)", <i>Phycol.Research</i>, 47, 87-95.</p> <p>[6] T.Irie, M.Izawa and E.Kurosawa(1970). "Laureatin and isolaureatin, constituents of Laurencia nipponica Yamada", <i>Tetrahedron</i>, 26, 851-870.</p> <p>[7] T.Irie, M.Suzuki and T.Masamune(1968). "Laurencin, a constituent of Laurencia glandulifera Kützinger", <i>Tetrahedron</i>, 24, 4193-4205.</p> <p>[8] B.M.Howard and W.Fenical(1975). "Structures and chemistry of two new halogen-containing chamigrene derivatives from Laurencia", <i>Tetrahedron, Lett.</i>, 1687-1690.</p> <p>[9] M.Suzuki, A.Furusaki and E.Kurosawa(1979). "The absolute configurations of halogenated Chamigrene derivatives from the marine alga, Laurencia glandulifera Kützinger", <i>Tetrahedron</i>, 35, 823-831.</p> <p>[10] Y.Takahashi, M.Suzuki, T.Abe and M.Masuda(1999). "Japonenynes, halogenated C₁₅ acetogenins from "Laurencia japonensis", <i>Phytochemistry</i>, 50, 799-803.</p> <p>[11] D.J.Kennedy, I.A.Selby, H.J.Cowe, P.J.Cox and R.H.Thomson(1984). "Bromoallenes from the alga Laurencia microcladia", <i>J.Chem.Soc.Chem. Commun.</i>, 153-155.</p> <p>[12] M.Suzuki, S.Nakano, Y.Takahashi, Y.Noya, T.Ohnishi, T.Abe and M.Masuda, in preparation.</p> <p>[13] 鈴木稔, 中野智, 高橋義宣, 阿部剛史, 増田道夫, 野矢洋一, 大西俊之(1998). 「海藻由来のハロゲン化合物の生合成研究」日本化学会北海道支部 1998年夏季研究発表会(7月26日, 釧路)</p> <p>[14] 中野智(1999). 「海藻由来のハロゲン化合物の生合成研究」北海道大学大学院地球環境科学研究科修士論文(3月).</p>	323
4-9	<p>[1] L.M.MOSULISHVILI, M.A.KOLOMITSEV, V.YU.DUNDUA, N.I.SHOMIA, O.A.DANILOVA, <i>J.Radioanal.Chem.</i>, 26(1975)175.</p> <p>[2] D.I.LEYPUNSKYSYS, V.I.DRYNKIN, B.V.BELENKY, M.A.KOLOMITSEV, V.YU.DUNDUA, N.V.PACHULIA, <i>J.Radioanal.Chem.</i>, 26(1975)293.</p> <p>[3] D.H.ANDERSON, J.J.MURPHY, W.W.WHITE, <i>Anal.Chem.</i>, 44(1972)2099.</p> <p>[4] D.H.ANDERSON, J.J.MURPHY, W.W.WHITE, <i>Anal.Chem.</i>, 48(1976)116.</p> <p>[5] J.W.MICHELL, L.D.BLITZER, T.Y.KOMETAIN, T.GILIS, L.CLARK Jr., <i>J.Radioanal.Chem.</i>, 39(1977)335.</p> <p>[6] A.R.DATE, <i>Analyst</i>, 103(1978)84.</p>	328

	<p>[7]K.MATSUMOTO,N.SUZUKI,Radiochem.Radioanal.Lett.,42(1980)99.</p> <p>[8]N.SUZUKI,Y.IWATA,H.IMURA,Anal.Sci.2(1986)335.</p> <p>[9]K.KUDO,N.SUZUKI,J.Radioanal Nucl Chem.,88(1985)75.</p> <p>[10]N.SUZUKI,Y.IWATA,Appl.Organomet.Chem.,4(1990)287.</p> <p>[11]Y.IWATA,H.NAITOH,N.SUZUKI,J.Radioanal Nucl Chem.,159(1992)121.</p> <p>[12]N.SUZUKI,Y.IWATA,H.IMURA,Intern.J.Environ.Anal.Chem.,30(1987)289.</p> <p>[13]Y.IWATA,N.SUZUKI,Anal.Chem.Acta,259(1992)159.</p> <p>[14]Y.MURAMATSU,R.M.PARR,Survey of Currently Available Reference Materials for Use in Connection with the Determination of Trace Elements in Biological and Environmental materials,IAEA/RL/128,IAEA,Vienna, 1985.</p> <p>[15]NIST Standard Reference Materials Catalog 1995-6,NIST Special Publication 260, National Institute of Standards and Technology, Gaithersburg,MD,1995.</p> <p>[16]NIES Certified Reference Materials No.9 "Sargasso", National Institute for Environmental Studies,Ibaraki,JAPAN 1988.</p> <p>[17]Y.IWATA,H.IMURA,N.SUZUKI,J.Radioanal Nucl. Chem.,172(1993)305.</p> <p>[18]Advantage of Synthetic Multi-Element Reference Material with Pseudo-Biological Matrix in Activation Analysis,Y.Iwata and N.Suzuki,J.Radioanal Nucl Chem.,233(1998)49.</p>	
4-10	<p>[1]M.Ebihara(1996) Solar and solar system abundances of the elements.J.Royal Soc.West.Australia 79,51-57.</p> <p>[2]M.Ebihara and T.Mimura(1996)Chemical characteristics of Cretaceous, Tertiary and their boundary layers at Gubbio,Italy.Geochim.Cosmochim.Acta 60,5133-5144.</p> <p>[3]M.Ebihara,P.Kong and K.Shinotsuka(1997)Chemical composition of Y-793605, a Martian lherzolite.Antarct.Meteorite Res.10,83-94.</p>	334
5-1	<p>[1]小林勝利他 1 名,ガドリニウム造影剤の体内残留を高感度で検出,Isotope News,12-14(1998).</p> <p>[2]羽鳥晶子他 6 名,A Novel autoradiography technique:Neutron activation whole body autoradiography,The Society for wholebody autoradiography, Ann Arbor,Michigan(1997).</p>	345
5-2	<p>[1]大石哲也他 1 名,放射性ガスのパルス注入によるガスモニタの校正法,RADIOISOTOPES,23-31 (1999).</p> <p>[2]大石哲也他 1 名,放射性ガスモニタのパルス注入校正と閉ループ校正との比較,第37回日本原子力学会要旨集,第 I 分冊,104(1999).</p>	346
6-1	<p>[1]八巻大樹他 2 名,Helium release from neutron-irradiated Li₂O single crystals, J.Nucl Mater 258-263(1998)349-354.</p>	349
7-1	<p>[1]須貝宏行他 2 名,Release of tritium,protium,and helium from neutron-irradiated Li-Al alloy II,Journal of Nuclear Materials,Vol.151,p254-258 (1998).</p>	353

7-2	<p>[1]Bellemans,F. et al.(1995):Radiat.Meas.,24,153-160.</p> <p>[2]De Corte,F. et al.(1981):Jour.Radioanal.Chem.,62,209-255.</p> <p>[3]Hurford,A.J.(1990):Chem.Geol.,80,171-178.</p> <p>[4]Hurford,A.J. and Green,P.F.(1983):Isot.Geosci.,1,285-317.</p> <p>[5]鈴木達郎(1992):放射線,18,16-24.</p> <p>[6]鈴木達郎(1998):国内研究用原子炉の照射場の特性からみたフィッシュョン・トラック年代測定と放射化分析. 日本地質学会西日本支部会報. No.112,p.3-4.</p>	354
7-3	<p>[1]N.Fukada,Nihon Kagaku Zasshi,Vol.75,378 and 1141(1953).</p> <p>[2]O.Kujirai,N.Ikeda,Radiochem.Radional.Letters,Vol.15,67(1973).</p> <p>[3]H.Shoji,"Some Specific Features of the Recoil Behaviour of Central Metal Atoms in the Solid System of Water-Soluble Matalloporphyrin Ion Associates,"Res.Report of Lab.of Nucl.Sci.,Tohoku Univ.Vol.29,57(1996).</p> <p>[4]H.Shoji,"Correlation of Some Recoil Features in the Water-Soluble Matalloporphyrin Ion Associate Solid System with Structural Factors," J.Radional.Nucl.Chem.,Vol.239,191(1999).</p>	358
7-4	<p>[1]Ikeya,M.(1993)New Applications of Electron Spin Resonance,Dating, Dosimetry and Microscopy,World Scientific,Singapore.</p> <p>[2]Odom,A.L. and Rink,W.J.(1989)Natural accumulation of Shottky-Frenkel defects:Implications for a quartz geochronometer,Geology,17,55-58.</p> <p>[3]Rink,W.J. and Odom,A.L.(1991)Natural alpha recoil particle radiation and ionizing radiation sentivities in quartz detected with EPR:implications for geochronometry,Nucl.Tracks Radiat.Meas.,18,163-173.</p> <p>[4]Toyoda,S. and Ikeya,M.(1991)Thermal stabilities of paramagnetic defect and impurity centers in quartz:Basis for ESR dating of thermal history,Geochem. J.25,437-445.</p> <p>[5]Toyoda,S. and Ikeya,M.,Morikawa,J., and Nagamoto,T.(1992)Enchancement of oxygen vacancies in quartz by natural external β and γ ray dose:a possible ESR Geochronometer of Ma-Ga range,Geochem. J.26,111-115.</p> <p>[6]Toyoda,S. and Ikeya,M.(1994)Formation of oxygen vacancies in quartz and its application to dating,Quatern.Geochnol.13,607-609.</p> <p>[7]Toyoda,S.,Rink,W.J.,Schwarcz,H.P., and Ikeya,M.(1996)Formation of E_i precursors in quartz:application to dating and dosimetry,Appl.Radiat.Isot.,47, 1393-1398.</p> <p>[8]Ziegler,J.F.(1989)Software-TRIM version 5.0 IBM Research(unpublished).</p> <p>[9]Toyoda,S. and Hattori,W.(submitted)Formation and decay of the E_i center and of its precursor,Appl.Radiat.Isot.</p> <p>[10]豊田新・池谷元伺 γ線による石英の酸素空格子の生成 研究会・放射線検出器とその応用1998年1月21-23日 高エネルギー加速器研究機構</p> <p>[11]Toyoda,S. and Hattori,W. and Ikeya,M.,Formation and decay of the E_i center and of its precursor.International Conference on Biodosimetry and 5th International Symposium on ESR Dosimetry and Applications,June, 22-26,1998,Medical Radiological Research Center of Russian Academy of Medical Sciences,Obninsk,Russia.</p> <p>[12]豊田新 石英中のE_i中心の生成過程と年代測定への応用 第14回ESR応用計測研究発表会 1998年11月21日 大阪大学 豊中</p>	362

付 録 (2)

Appendix (2)

This is a blank page.

付 録(2)

事情により、研究炉利用の成果・連絡票のみの提出となった利用者について、その内容をここに示す。

研 究 テ ー マ 「表 題」	所 属 担 当 者	利用原子炉 及び装置名	報 告 書 等	利用分野
陸上系環境放射能 安全性実証試験	(財)環境科学技 術研究所 塚田 祥文	JRR-4 PN	本研究テーマでは土壌、農作物 等の環境試料中元素濃度を放射 化分析により測定しています。 なお本研究は、科学技術庁から の依託により行われており、平 成10年度の成果については報告 できません。	放射化分 析
元素定量のための 放射化分析法の応 用	(財)放射線利用 振興協会 吾勝 常勲	JRR-3M IIR-1,2 PN-1,2,3 JRR-4 T,S,D- pipe PN	放射線利用振興協会では、諸機 関から依頼された試料の放射化 分析を行っています。結果につ いては機密保持が契約条件であ るため、成果報告の提出ができ ません。	放射化分 析
中性子照射による シリコン半導体の 製造	(財)放射線利用 振興協会 坪 長	JRR-3M SI-1	シリコンインゴットに中性子を 照射してシリコン半導体を定常 的な業務として製造している。	その他

This is a blank page.

付 録 (3)

Appendix (3)

This is a blank page.

付 録(3)

原研研究炉の利用設備一覧

1. JRR-3M

1) 実験設備

実 験 孔	実 験 装 置
1 G	高分解能粉末中性子回折装置 (HRPD)
1 G-A	生体高分子結晶構造解析用中性子回折計 (BIX-I)
2 G	三軸型中性子分光器 (偏極機能付、TAS-1)
3 G	中性子トポグラフィ及び精密光学実験装置 (PNO)
4 G	汎用三軸型中性子分光器 (GPTAS)
5 G	偏極中性子散乱装置 (PONTA)
6 G	東北大学中性子散乱分光器 (TOPAN)
7 R	中性子ラジオグラフィ装置 (TNRF)
T1-1	中性子偏極回折装置 (HQR)
T1-2	単結晶中性子回折装置 (KSD)
T1-3	粉末中性子回折装置 (HERMES) (KPD)
T1-4-1	即発ガンマ線分析装置 (PGA)
T1-4-3	TOF型中性子反射率計 (TOF)
T2-1	残留応力測定用中性子回折装置 (RESA)
T2-2	中性子単結晶4軸回折装置: 未設置
T2-3	中性子イメージングプレート付生体物質中性子回折計 (BIX-II)
T2-4	高分解能三軸型中性子分光器 (TAS-2)
C1-1	高エネルギー分解能三軸型中性子分光器 (HER)
C1-2	二次元位置測定小角散乱装置 (SANS-U)
C1-3	超高分解能後方散乱装置 (ULS)
C2-1	冷中性子散乱実験デバイス開発装置 (LTAS)
C2-2	中性子スペクトル変調・時間分析装置 (NSM) 中性子スピネコー分光器 (NSE)
C2-3-1	冷中性子ラジオグラフィ装置 (CNRF)
C2-3-2	即発ガンマ線分析装置 (PGA)
C2-3-4	TOF型中性子反射率計 (TOF)
C3-1-1	高分解能パルス冷中性子分光器 (AGNES)
C3-1-2	多層膜中性子干渉計 (MINE)
C3-2	中性子小角散乱装置 (SANS-J)

2) 照射設備

水 力 照 射 設 備	H R - 1, 2
気 送 照 射 設 備	P N - 1, 2
放射化分析用照射設備	P N - 3
均 一 照 射 設 備	S I - 1
回 転 照 射 設 備	D R - 1
垂 直 照 射 設 備	V T - 1, R G - 1 ~ 4 B R - 1 ~ 4, S H - 1

2. J R R - 4

1) 実験設備

ブ ー ル
中性子ビーム設備
散 乱 実 験 設 備
冷却水循環ループ
医療照射設備 (B N C T)
即発ガンマ線分析装置

2) 照射設備

簡 易 照 射 筒	T パイプ (水力)
	S パイプ
	D パイプ
	N パイプ
気送管照射設備	P N

Appendix(3)

Utilization Facilities of Research Reactor

1.JRR-3M

1) Experimental Equipments

Beam Port	Experimental equipments
1G	High Resolution Powder Diffractometer (HRPD)
1G-A	Diffractometer for Biological Crystallography- I (BIX- I)
2G	Triple-Axis Spectrometer-1(TAS-1)
3G	Apparatus for Precise Neutron Optics and Neutron Diffraction Topography (PNO)
4G	Triple-Axis Spectrometer (GPTAS)
5G	Polarized Neutron Triple-Axis Spectrometer (PONTA)
6G	Tohoku-University Polarization Analysis Neutron Spectrometer (TOPAN)
7R	Thermal Neutron Radiography (TNRF)
T1-1	High Q-Resolution Triple-Axis Spectrometer (HQR)
T1-2	KINKEN Single-Crystal Diffractometer (KSD)
T1-3	KINKEN Powder Diffractometer (HERMES) (KPD)
T1-4-1	Prompt Gamma-Ray Analysis (PGA)
T1-4-3	TOF Neutron Reflectometer (TOF)
T2-1	Diffractometer for Residual Stress Analysis (RESA)
T2-2	Four-Circle Diffractometer:Under Construction
T2-3	Diffractometer for Biological Crystallography- II (BIX- II)
T2-4	Triple-Axis Spectrometer-2(TAS-2)
C1-1	High E-Resolution Triple-Axis Spectrometer (HER)
C1-2	Small Angle Neutron Scattering Instrument University of Tokyo (SANS-U)
C1-3	Ultra Small Angle Neutron Scattering Instrument (ULS)
C2-1	Low Energy Triple-Axis Spectrometer (LTAS)
C2-2	Neutron Spectral Modulation Spectrometer (NSM) Neutron Spin Echo Spectrometer (NSE)
C2-3-1	Cold Neutron Radiography (CNRF)
C2-3-2	Prompt Gamma-Ray Analysis (PGA)
C2-3-4	TOF Neutron Reflectometer (TOF)
C3-1-1	Angle Focusing Cold Neutron Spectrometer (AGNES)
C3-1-2	Multilayer Interferometer for Neutrons (MINE)
C3-2	Small Angle Neutron Scattering Instrument (SANS-J)

2) Irradiation Facilities

Hydraulic Rabbit Irradiation Facility	HR-1,2
Pneumatic Rabbit Irradiation Facility	PN-1,2
Activation analysis Irradiation Facility	PN-3
Uniform Irradiation Facility	SI-1
Rotating Irradiation Facility	DR-1
Capsule Irradiation Facility	VT-1, RG-1~4 BR-1~4, SH-1

2.JRR-4

1) Experimental Equipments

Pool
Scattering Experimental Facility
Neutron Beam Facility
Coolingwater Circulation Loop
Medical Neutron Irradiation (BNCT)
Prompt Gamma-Ray Analysis

2) Irradiation Facilities

Irradiation Tubes	T-Pipe
	S-Pipe
	D-Pipe
	N-Pipe
Pneumatic Rabbit Irradiation Facility	PN

国際単位系 (SI) と換算表

表1 SI基本単位および補助単位

量	名称	記号
長さ	メートル	m
質量	キログラム	kg
時間	秒	s
電流	アンペア	A
熱力学温度	ケルビン	K
物質の量	モル	mol
光の度	カンデラ	cd
平面角	ラジアン	rad
立体角	ステラジアン	sr

表3 固有の名称をもつSI組立単位

量	名称	記号	他のSI単位 による表現
周波数	ヘルツ	Hz	s^{-1}
力	ニュートン	N	$m \cdot kg / s^2$
圧力、応力	パスカル	Pa	N / m^2
エネルギー、仕事、熱量	ジュール	J	$N \cdot m$
工率、放射束	ワット	W	J / s
電気量、電荷	クーロン	C	$A \cdot s$
電位、電圧、起電力	ボルト	V	W / A
静電容量	ファラド	F	C / V
電気抵抗	オーム	Ω	V / A
コンダクタンス	ジーメン	S	A / V
磁束	ウェーバ	Wb	$V \cdot s$
磁束密度	テスラ	T	Wb / m^2
インダクタンス	ヘンリー	H	Wb / A
セルシウス温度	セルシウス度	$^{\circ}C$	
光の束度	ルーメン	lm	$cd \cdot sr$
照射度	ルクス	lx	lm / m^2
放射能	ベクレル	Bq	s^{-1}
吸収線量	グレイ	Gy	J / kg
線量当量	シーベルト	Sv	J / kg

表2 SIと併用される単位

名称	記号
分、時、日	min, h, d
度、分、秒	$^{\circ}, ', ''$
リットル	l, L
トン	t
電子ボルト	eV
原子質量単位	u

$$1 \text{ eV} = 1.60218 \times 10^{-19} \text{ J}$$

$$1 \text{ u} = 1.66054 \times 10^{-27} \text{ kg}$$

表4 SIと共に暫定的に維持される単位

名称	記号
オングストローム	\AA
バ	b
バ	bar
ガ	Gal
キュリー	Ci
レントゲン	R
ラ	rad
レ	rem

$$1 \text{ \AA} = 0.1 \text{ nm} = 10^{-10} \text{ m}$$

$$1 \text{ b} = 100 \text{ fm}^2 = 10^{-28} \text{ m}^2$$

$$1 \text{ bar} = 0.1 \text{ MPa} = 10^5 \text{ Pa}$$

$$1 \text{ Gal} = 1 \text{ cm/s}^2 = 10^{-2} \text{ m/s}^2$$

$$1 \text{ Ci} = 3.7 \times 10^{10} \text{ Bq}$$

$$1 \text{ R} = 2.58 \times 10^{-4} \text{ C/kg}$$

$$1 \text{ rad} = 1 \text{ cGy} = 10^{-2} \text{ Gy}$$

$$1 \text{ rem} = 1 \text{ cSv} = 10^{-2} \text{ Sv}$$

表5 SI接頭語

倍数	接頭語	記号
10^{18}	エクサ	E
10^{15}	ペタ	P
10^{12}	テラ	T
10^9	ギガ	G
10^6	メガ	M
10^3	キロ	k
10^2	ヘクト	h
10^1	デカ	da
10^{-1}	デシ	d
10^{-2}	センチ	c
10^{-3}	ミリ	m
10^{-6}	マイクロ	μ
10^{-9}	ナノ	n
10^{-12}	ピコ	p
10^{-15}	フェムト	f
10^{-18}	アト	a

(注)

- 表1～5は「国際単位系」第5版、国際度量衡局 1985年刊行による。ただし、1 eV および 1 uの値はCODATAの1986年推奨値によった。
- 表4には海里、ノット、アール、ヘクタールも含まれているが日常の単位なのでここでは省略した。
- barは、JISでは流体の圧力を表わす場合に限り表2のカテゴリーに分類されている。
- EC閣僚理事会指令ではbar、barnおよび「血圧の単位」mmHgを表2のカテゴリーに入れている。

換算表

力	$N (=10^5 \text{ dyn})$	kgf	lbf
	1	0.101972	0.224809
	9.80665	1	2.20462
	4.44822	0.453592	1

$$\text{粘度 } 1 \text{ Pa} \cdot \text{s} (= \text{N} \cdot \text{s} / \text{m}^2) = 10 \text{ P (ポアズ)} (\text{g} / (\text{cm} \cdot \text{s}))$$

$$\text{動粘度 } 1 \text{ m}^2 / \text{s} = 10^4 \text{ St (ストークス)} (\text{cm}^2 / \text{s})$$

圧	MPa (=10 bar)	kgf/cm ²	atm	mmHg (Torr)	lbf/in ² (psi)
	1	10.1972	9.86923	7.50062×10^3	145.038
力	0.0980665	1	0.967841	735.559	14.2233
	0.101325	1.03323	1	760	14.6959
	1.33322×10^{-4}	1.35951×10^{-3}	1.31579×10^{-3}	1	1.93368×10^{-2}
	6.89476×10^{-3}	7.03070×10^{-2}	6.80460×10^{-2}	51.7149	1

エネルギー・仕事・熱量	$J (=10^7 \text{ erg})$	kgf·m	kW·h	cal (計量法)	Btu	ft·lbf	eV
	1	0.101972	2.77778×10^{-7}	0.238889	9.47813×10^{-4}	0.737562	6.24150×10^{18}
	9.80665	1	2.72407×10^{-6}	2.34270	9.29487×10^{-3}	7.23301	6.12082×10^{19}
	3.6×10^6	3.67098×10^5	1	8.59999×10^5	3412.13	2.65522×10^6	2.24694×10^{25}
	4.18605	0.426858	1.16279×10^{-6}	1	3.96759×10^{-3}	3.08747	2.61272×10^{19}
	1055.06	107.586	2.93072×10^{-4}	252.042	1	778.172	6.58515×10^{21}
	1.35582	0.138255	3.76616×10^{-7}	0.323890	1.28506×10^{-3}	1	8.46233×10^{18}
	1.60218×10^{-19}	1.63377×10^{-20}	4.45050×10^{-26}	3.82743×10^{-20}	1.51857×10^{-22}	1.18171×10^{-19}	1

$$1 \text{ cal} = 4.18605 \text{ J (計量法)}$$

$$= 4.184 \text{ J (熱化学)}$$

$$= 4.1855 \text{ J (15 } ^{\circ}C)$$

$$= 4.1868 \text{ J (国際蒸気表)}$$

$$\text{仕事率 } 1 \text{ PS (馬力)}$$

$$= 75 \text{ kgf} \cdot \text{m/s}$$

$$= 735.499 \text{ W}$$

放射能	Bq	Ci
	1	2.70270×10^{-11}
	3.7×10^{10}	1

吸収線量	Gy	rad
	1	100
	0.01	1

照射線量	C/kg	R
	1	3876
	2.58×10^{-4}	1

線量当量	Sv	rem
	1	100
	0.01	1

(86年12月26日現在)

